

Transactions

of the

ASME

Recent Experience in Examination of High-Temperature Catalytic-Cracking Pressure Equipment	<i>D. B. Rossheim, J. J. Murphy, R. H. Coughrey, and W. B. Hoyt</i>	1099
Frequency-Response Analysis for Industrial Automatic-Control Systems	<i>D. W. St. Clair, W. F. Coombs, Jr., and W. D. Owens</i>	1133
The Effect of High-Frequency Sound Waves on an Air-Propane Flame	<i>C. J. Kippenhan and H. O. Croft</i>	1151
Photographic Analysis of Sprays	<i>J. L. York and H. E. Stubbs</i>	1157
Design and Performance of an Extended-Surface Regenerator for a Gas-Turbine Plant	<i>Sven Holm and R. L. Lyerly</i>	1163
Heat-Transfer and Flow-Friction Characteristics of Some Compact Heat-Exchanger Surfaces—Part 3	<i>A. L. London, W. M. Kays, and D. W. Johnson</i>	1167
Convective Heat-Transfer and Flow-Friction Behavior of Small Cylindrical Tubes—Circular and Rectangular Cross Sections	<i>W. M. Kays and A. L. London</i>	1179
Variation in Heat Absorption in a Natural-Gas-Fired, Water-Cooled Steam-Boiler Furnace	<i>A. R. Mumford and R. C. Cory</i>	1191
The New-Type Code Chart for the Design of Vessels Under External Pressure	<i>E. O. Bergman</i>	1217
A Procedure for Determining the Allowable Out-of-Roundness for Vessels Under External Pressure	<i>Marshall Holt</i>	1225
On the Accuracy of Extrapolated Creep-Test Relations for Plexiglas Subjected to Various Stresses	<i>Joseph Marin and Yeh-Han Pao</i>	1231
Heat Transfer From Spheres to a Rarefied Gas in Supersonic Flow	<i>R. M. Drake, Jr., and G. H. Bacher</i>	1241
An Experimental Investigation of Convective Heat Transfer to Air From a Flat Plate With a Stepwise Discontinuous Surface Temperature	<i>Steve Scusa and F. M. Sauer</i>	1251
Dynamic Buckling of Thin Elastic Plates	<i>G. A. Zizicas</i>	1257
Friction Surfaces for Spin-Up Simulation in Landing-Gear Drop Tests	<i>D. W. Drake</i>	1269
The Mean Flow in Kaplan Turbines	<i>R. E. Meyer</i>	1283

OCTOBER, 1952

VOL. 74, NO. 7

Transactions

of The American Society of Mechanical Engineers

Published on the tenth of every month, except March, June, September, and December

OFFICERS OF THE SOCIETY:

R. J. S. PROOFT, *President*

JEROME L. KEMP, *Treasurer*

EDGAR J. KATH, *Asst. Treasurer*

C. E. DAVIES, *Secretary*

COMMITTEE ON PUBLICATIONS:

C. B. CAMPBELL, *Chairman*

GEORGE R. RECH

PAUL T. NORTON, JR.

MORRIS GERR

JOSEPH SCHMIDLER, *Junior Advisory Member*

GEORGE A. SYMON, *Editor*

OTTO DE LORENZO

COLIN CARMICHAEL

K. W. CAMBERMUND, *Managing Editor*

REGIONAL ADVISORY BOARD OF THE PUBLICATIONS COMMITTEE:

KERR ATKINSON—I
J. DE S. COOTNER—II
W. E. BRANN—III
F. C. SMITH—IV

HENRY BLACKBURN—V
CHESTER R. EARLE—VI
R. G. ROBINSON—VII
M. A. DURLAND—VIII

Published monthly by The American Society of Mechanical Engineers. Publication office at 20th and Northampton Streets, Easton, Pa. The editorial department is located at the headquarters of the Society, 29 West Thirty-Ninth Street, New York 18, N. Y. Cable address, "Dynamic," New York. Price \$1.50 a copy, \$12.00 a year for Transactions and the Journal of Applied Mechanics to members and subscribers, \$1.00 a copy, \$5.00 a year. Changes of address must be received at Society headquarters four weeks before they are to be effective on the mailing list. Please send old as well as new address. . . . By-Law: The Society shall not be responsible for statements or opinions advanced in papers or . . . printed in its publications (B13, Sec. 4). . . . Entered as second-class matter March 2, 1928, at the Post Office at Easton, Pa., under the Act of August 24, 1912. . . . Copyrighted, 1952, by The American Society of Mechanical Engineers. Reprints from this publication may be made on condition that full credit be given the Transactions of the ASME and the author, and that date of publication be stated.

Recent Experience in Examination of High-Temperature Catalytic-Cracking Pressure Equipment

By D. B. ROSSHEIM,¹ J. J. MURPHY,² R. H. CAUGHEY,³ AND W. B. HOYT,⁴ NEW YORK, N. Y.

The welded seams of three integral-clad catalytic-cracking unit reactors have been found to contain cracks after about 7 years of service. Examination has detected graphite in the carbon-steel base metal and heat-affected zones. This paper reports the findings of investigations made on these three and other reactors, both clad, lined and unlined, in similar service. The results of mechanical tests and microscopic examinations made on specimens removed from reactors and other high-temperature equipment in the same service are presented. Possible causes of the cracks are discussed with particular emphasis on the role of thermal stresses in bimetallic construction and the effect of graphite on mechanical properties. Recommendations are included relative to existing equipment and new construction for service at elevated temperatures.

INTRODUCTION

THE purpose of this paper is to present the results of some examinations made since the beginning of 1951 on pressure equipment operating at high temperatures in fluid catalytic-cracking units, to discuss the possible causes of cracking discovered in three integral-clad reactors, to describe the extent of graphitization found in this equipment, and to offer suggestions concerning existing high-temperature equipment and projected new construction.

On February 8, 1951, a leak developed in the reactor of a fluid catalytic-cracking unit constructed of Type 347 integral-clad carbon steel after 53,000 hr of operation at 900 to 975 F (designated unit A herein). Examination disclosed a crack adjacent to and paralleling a longitudinal weld, and further examination disclosed numerous cracks of a similar type in the carbon steel at welds throughout the vessel, as well as cracks in the inside alloy weld deposits. Examination of samples cut from the vessel revealed the carbon-steel base metal to be graphitized. The graphite was nodular and, in general, uniformly distributed. A tendency toward local concentrations was evident, at heat-affected zones, but only one sample showed graphite approaching a chain type; no "eyebrow" type formations were observed.

There are seven other clad reactors of essentially identical construction with similar service and operating time. Two of these (units B and C) have been found subsequently to contain numerous cracks similar to those in the first reactor. Specimens

from unit B had only relatively small amounts of graphite while those obtained from unit C contained substantially no graphite. Two others, units D and E, have been reported free from cracks, although samples of base metal from unit D contain heavy nodular graphite. The other three units have not been examined fully; however, one, unit F, visually examined while in operation, has been reported to have one 9-in.-long crack adjacent to the weld joining the top cone to the overhead line.

To date, the sampling and examination has been extended to include other carbon-steel reactors in similar service, some without alloy linings and some with 18 per cent Cr-8 per cent Ni or 11-13 per cent Cr alloy-steel spot-welded liners. Pipe operating above 900 F also has been sampled. No cracks have been found; although some samples contain nodular graphite in varying degree of concentration, most are not graphitized.

The discovery of graphite in conjunction with cracks in pressure equipment in petroleum refineries was a new experience and was disturbing because of the history of failures in steam piping in power plants caused by severely graphitized welded joints. Consequently, primary emphasis has been placed on the detection of graphite in operating pressure equipment and on the evaluation of its possible contribution to the failures in these reactors. Consideration also has been given to other factors which may have contributed to formation of cracks in these reactors; in particular, the influence of differential expansion strains inherent in bimetallic clad steel has been extensively studied.

The experience of the petroleum industry with graphitization dates from the early days of thermal cracking when carbon-steel still tubes were found to be graphitized as a result of prolonged exposure to elevated temperatures. Examination of a failed carbon-steel tube and identification of graphite was reported by A. B. Kinzel and R. W. Moore⁵ in 1935.

Prior to the failure in 1943 of a welded joint in a carbon-moly-steel steam line of the West Penn Power Company at Springdale, Pa., no particular attempt was made to detect graphite in the steel of high-temperature equipment. If it was found it was usually accidentally during the examination of a furnace tube which had ruptured, usually as the result of overheating, and the presence of graphite was considered of academic interest only. Since the detection of graphite by microscopic examination requires highly experienced polishing and etching techniques to retain the exposed graphite particles, it is possible that some cases of graphitization may have gone undetected in the examination of material from failed equipment.

From the time of the Springdale failure until early in 1951, the petroleum industry had carried out a limited examination of operating equipment for graphite. Most of these examinations yielded negative results, although in a few instances some graphite has been found. The graphite found was of a scattered nodular character not associated with serious impairment of the metallic structure or its load-carrying capacity.

With the failure of a welded joint at Springdale, graphite was

¹ Staff Engineer, The M. W. Kellogg Company. Mem. ASME.
² Mechanical Development Engineer, The M. W. Kellogg Company. Mem. ASME.

³ Assistant Chief Metallurgist, The M. W. Kellogg Company.

⁴ Materials Engineer, The M. W. Kellogg Company.

Contributed by the Petroleum Division and Effect of Temperature on Metals Research Committee and presented at the Annual Meeting, Atlantic City, N. J., November 25-30, 1951, of THE AMERICAN SOCIETY OF MECHANICAL ENGINEERS.

NOTE: Statements and opinions advanced in papers are to be understood as individual expressions of their authors and not those of the Society. Manuscript received at ASME Headquarters, November 14, 1951. Paper No. 51-A-26.

⁵ "Graphite in Low Carbon Steel," by A. B. Kinzel and R. W. Moore. Trans. AIME, vol. 116, 1935, pp. 318-329.

found for the first time to be concentrated in chain or "eyebrow" type formation at the outer edge of the heat-affected zone in the parent metal, and serious deterioration of physical properties could be attributed to it. Subsequent examination of other steam-power equipment resulted in the detection of graphite in carbon-moly and carbon-steel piping. In most cases the graphite was of the scattered nodular type primarily occurring in the heat-affected zones of welded joints. In a few cases the graphite occurred in chain-type formations which caused planes of weakness adjacent to the welds, and in one or two instances concentrations of graphite were located in strain lines in the base metal away from welded joints.

As a result of these findings the power industry is selecting materials with emphasis on long-time resistance to graphitization. Practically all of the individual and co-operative research efforts on this problem have been directed toward an understanding of the factors contributing to and the mechanism of graphitization in carbon and low-alloy steels, with emphasis placed on the development and selection of graphitization-resistant steels. Difficulty has been experienced in laboratory tests in reproducing heavy chain-type graphite formations adjacent to welds. Additional knowledge is required on the influence of nodular graphite on room- and high-temperature tensile properties, shock resistance, and fatigue properties for better evaluation of the serviceability of equipment.

Until early in 1951 no chain graphite was found in the limited number of samples obtained from petroleum-refinery equipment. With a successful background of experience and absence of definite evidence that graphitization will result in failures, the use of carbon steel has been continued, principally because of its economic advantage and ease of field fabrication, alterations, and repairs. The power industry's unsatisfactory experience with carbon-molybdenum steel has had some influence in that this analysis has been increasingly avoided in new refinery installations in favor of low-chrome-molybdenum steels which have the added advantage of increased high-temperature strength.

FAILED REACTORS

Of the catalytic-cracking units which have been designed and built by the company with which the authors are associated,

eight have reactors which are constructed of integral-clad steel plate composed of ASTM Specification A201, Gr. A, carbon-steel backing with Type 347 alloy-steel cladding. The vessel shell size of 23 ft diam \times 47 ft shell length, with 90-deg-included-angle top and bottom cones, necessitated field erection, and stress-relieving at 950 to 1000 F was employed due to the shell and cone thickness of $1\frac{1}{2}$ in. and $1\frac{29}{32}$ in., respectively. Fig. 1 shows an outline sketch of a typical reactor, clad plate being used except for the top and bottom torus sections which were made of ASTM

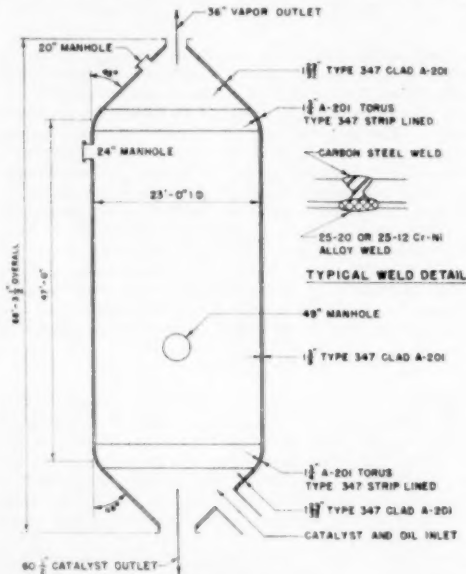


FIG. 1 TYPICAL CLAD REACTOR

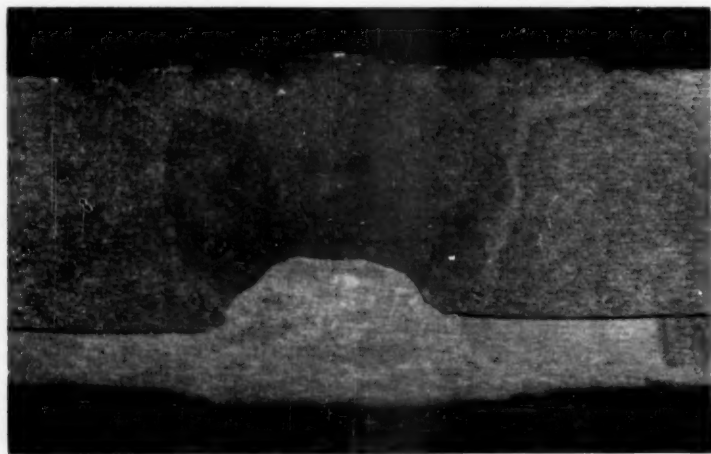


FIG. 2 REFINERY A—TYPICAL COMPOSITE BUTT WELD

A-201 Gr. A plate and strip-lined with Type 347 alloy sheet. The vessels were designed and constructed in accordance with the 1936 API-ASME Unfired Pressure Vessel Code, and the ASME interpretations. The cladding thickness is nominally 20 per cent but varied considerably as supplied, usually on the heavy side. The butt welds are also composite as shown in Fig. 2, the base-metal portion being welded with carbon-steel rod and the alloy portion welded with 25-20 and 25-12 Cr-Ni electrodes.

All of these units began operation between November, 1943, and August, 1944. The operating conditions of these reactors are quite steady. They contain hydrocarbon gases and powdered catalyst under pressure of from about 15 to 25 lb, and operating temperatures have been between 900 and 1000 F. Their exteriors are heavily insulated so that the shell metal temperature is reasonably uniform and close to the internal gas temperature, although arrangement of internals and coke deposits lower the metal temperature in some areas. Continuous operating runs of a year or more are not unusual. Fig. 3 shows a typical layout of the arrangement of the reactor, regenerator, and interconnecting piping in a fluid catalytic-cracking unit. Of these eight integral-

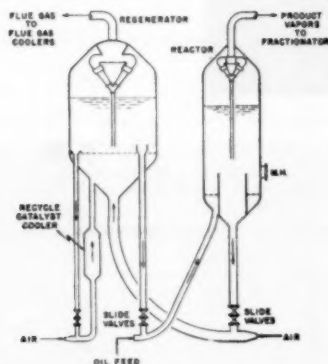


FIG. 3 SIMPLIFIED FLOW DIAGRAM OF FLUID CATALYTIC-CRACKING UNIT

clad reactors, three have been found to contain extensive cracking. Three more have been examined partially and the only crack found was a 9-in.-long crack in the top head-nozzle neck at the fillet weld to one of the vessels. The remaining two reactors have been in continuous operation with no opportunity for inspection since the first reported discovery of cracking.

As mentioned in the Introduction, unit A developed a leak in service after 53,000 hr of operation at 900 to 975 F. Following shutdown, visual examination disclosed a crack which was 8 ft long on the outside and about 4 ft long on the inside. After preparation of the exterior weld surfaces by sandblasting and grinding, visual inspection supplemented by Magnaflex examination disclosed numerous other cracks of variable lengths and depth at the edge of both longitudinal and girth welds. Some cracks also were found at the edge of fillet welds attaching nozzle necks or manhole reinforcing pads to the shell. The total length of cracks at the main seams was approximately 75 ft in a total weld footage of about 1500 ft. The upper portion of the shell showed the greatest percentage of cracks, and cracks adjacent to girth welds were at least as extensive as at longitudinal welds.

Following preparation of the interior alloy weld surfaces by grinding, visual inspection supplemented by Zygo examination

revealed profuse cracks in the alloy weld metal throughout the entire vessel. These cracks were of two types. One was the crazed random-directional type characteristic of the micro-cracking common in austenitic weld deposits; the other was a transverse-type crack which stopped at the junction of the alloy weld and cladding. These latter cracks occurred in some locations as frequently as 1 or 2 in. apart, and examinations of trepanned plugs and cutouts showed that they generally penetrated no farther than the junction of the alloy weld with the carbon steel, although a few penetrated into the carbon-steel weld metal. The cracks in the alloy welds are disturbing and deserve study; however, they appear to be a separate problem from that of graphitization and of the cracks in the carbon-steel portion of the clad plate, and consequently will be considered in this paper only in so far as they may have influenced the development of cracks in the base metal.

The cracks in the carbon steel appeared to have originated on the outside carbon-steel surface at or near the edge of the heat-affected zone. Macro and microscopic examination of trepanned plugs and cutouts showed the path of the cracks tended to parallel the contour of the welds at the far edge of the heat-affected zone and to propagate into the base metal perpendicular to the surface. All the cracks were of the branching, intergranular type characteristic of those found in the laboratory at the fractured surface of long-time stress-rupture specimens. There was no indication that the cracks originated at the junction of the carbon-steel and alloy weld deposits. Fig. 4 shows the orientation of a typical crack.

The results of examination and tests of samples and cutouts are given in Tables 1 to 5 inclusive, for this unit as well as for other units subsequently examined. The tabulations include the results of examinations and tests performed by others which have been made available to the authors. The following comments apply to unit A.

The examinations of the cracks in the carbon-steel base metal revealed the presence of graphite in all of the samples examined. No graphite was found in weld metal. In general, the base metal consisted of free ferrite, spheroidized carbides, mostly at ferrite grain boundaries, and nodules of graphite as large as 0.0015 in. diam. These nodules were scattered throughout the base metal, with heavier concentrations in the heat-affected areas. In the areas containing a system of intergranular cracks, nodules of graphite were observed to be located in the cracks, as shown in Fig. 4, indicating that the graphite particles constitute a preferred path of propagation, if they did not actually enhance the cracking.

In one sample the structure of the metal at the base of a crack system appeared to contain graphite in a continuous platelike form outlining grain boundaries in an orientation parallel to the direction of the cracks. This is shown in Fig. 5. Accurate identification of this structure is difficult and questionable and there is some belief that this constituent may consist of oxides rather than of graphite.

Mechanical tests were made on plate material and welded joints cut from the vessel to determine the degree to which the carbon steel had deteriorated. The results of these tests are to be found in Tables 1 to 5. Room-temperature tensile tests on base metal showed average yield-strength values of 25,000 psi and tensile strength of about 45,000 to 46,000 psi, which is about what might be expected of extremely low-carbon steel. Ductility as shown by tensile and bend tests was of the order of 50 to 60 per cent. Similar properties were found in specimens including welded seams with one notable exception. At one location, two free-bend test specimens broke at the edge of the heat-affected zone with substantially no elongation, and examination showed the fractured surfaces to be peppered with tiny black particles.

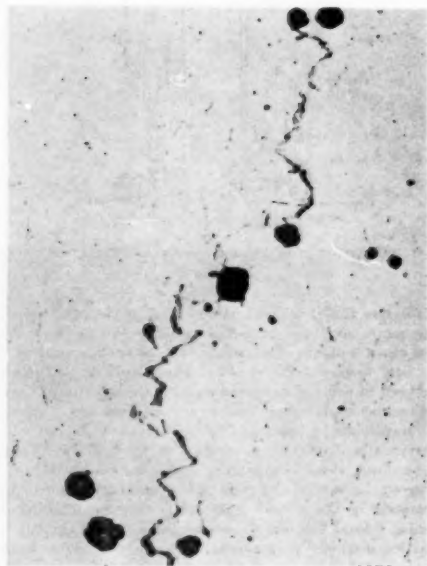


FIG. 4 REFINERY A—TYPICAL CRACK AT EDGE OF WELD JOINT HEAT-AFFECTED ZONE
(Top, Crack system at $\times 4$. Lower left, Crack system at $\times 100$. Lower right, Graphite nodules in crack system at $\times 100$.)

TABLE 1 TYPES OF EQUIPMENT TESTED

Unit designation	Equipment	Sample	Material	Approximate service conditions		
				Temp, deg F	Time, hr	Cycles
A	Reactor shell	Type 347 clad A201, Gr. A	FBQ	920	53000	28
B	Reactor shell	Type 347 clad A201, Gr. A	FBQ	900-950	37-50000	11
C	Reactor shell	Type 347 clad A201, Gr. A	FBQ	900-950	35-60000	
D	Reactor shell	Type 347 clad A201, Gr. A	FBQ	1000	58000	20
E	Regenerator internal	Carbon steel		1100		
F	Reactor internal	Type 347 clad A201, Gr. A	FBQ	960	55-60000	12
G	Recycle cat. standpipe	A201, Gr. B	FBQ	1060		
H	Reactor			920	55-60000	
I	Reactor shell	A201, Gr. A	FBQ	920	35-50000	
J	Reactor shell	A201, Gr. A	FBQ	920	19000	3
K	Regen. cat. standpipe	A201, Gr. B	FBQ	1060		
L	Reactor shell	A201, Gr. A, FBQ lined Type 347		900	55-60000	
M	Reactor shell	A201, Gr. A, FBQ lined Type 405		910	48000	
N	Cat. standpipes	A106, seamless C. S.		1060		
O	Reactor shell	A201, Gr. A, FBQ lined Type 405		875	40-45000	

TABLE 2 CHEMICAL COMPOSITION

REFINERY	IDENTIFICATION SPECIMEN	MATERIAL	SERVICE HRS. $\times 10^3$	F	ELEMENT %						
					C	MN	P	S	SI	AL	AL ₂ O ₃
A	REACTOR	ASTM A201 GR. A	53	920	.04	.36	.010	.022	.23	.006	.007
					.08	.43	.010	.026	.23	.006	.006
					.10	.34	.011	.026	.25	.004	.002
					.06	.44	.010	.019	.25	.005	.003
					.06	.39	.012	.027	.23	.006	.002
B	REACTOR	ASTM A201 GR. A	57-60	900-950	.07	.40	.005	.026	.23	.007	.004
					.02	.29	.010	.023	.24		
					.04	.46	.012	.026	.23	.006	.011
E	REACTOR O ² LINE CAT. STANDPIPE	ASTM A201 GR. A	55-60	980	.10	.42	.011	.029	.27	.004	.003
					.06	.40	.012	.026	.28	.002	.010
					.20	.52	.006	.062	.20	.030	.004
G	REACTOR	ASTM A201 GR. A	55-60	920	.20	.46	.033	.025	.16	.005	.003
					.20	.46	.027	.025	.15		
J	REACTOR	ASTM A201	55-60	900	.23	.42	.006	.035	.21	.003	NIL
K	CAT. STANDPIPE	ASTM A 106	40-45	1060	.30	.36	.006	.025	.19	.019	.002
					.27	.37	.006	.031	.18	.024	.008
					.23	.37	.006	.027	.22	.026	.003
L	REACTOR	ASTM A201 GR. A	40-45	875	.18	.45	.030	.032	.22		
					.18	.46	.030	.034	.22	.004	.010
H	REACTOR	ASTM A201 GR. A	19	920	.13	.54	.018	.045	.18	.002	.010
					.14	.40	.015	.030	.13		

It is apparent that in at least this one location sufficient concentration of nodular graphite may have existed to produce a serious plane of weakness.

Before concluding this summary it is of interest to note that a sample taken from the top torus ring, which was not integral-clad plate, showed only slight spheroidizing of the carbide phase but no graphite. The carbon content of the torus plate was 0.21 per cent compared with 0.08 to 0.11 per cent in the base metal of the clad plate.

The second clad reactor to fail was that of unit B. The seams of this vessel were being stripped of insulation for inspection when a leaking crack, approximately 30 in. long, was discovered adjacent to a circumferential weld joint in the shell. After the unit was shut down and the welds prepared for examination by sandblasting, cracks in the base metal and alloy welds were found which were of the same type and to approximately the same extent as in the reactor of unit A. Although the total linear extent of the cracks in the carbon steel was about the same, the cracks

in unit B were not as severe in depth or individual length as those in unit A. There was one new type of crack as described in the following paragraph which is of interest, but which appears unrelated to graphitization or cracks in the heat-affected zones.

During the fabrication of the vessel, some defects were found in the carbon-steel weld metal which were chipped out and the cavities rewelded. When these defects were so deep that the repair weld might fuse into the alloy-steel cladding or weld metal, the repair weld was made with austenitic stainless-steel electrodes. At the location of these full-penetration alloy welds, a crack frequently was found at the junction between the alloy weld metal and the carbon-steel base metal. Microscopic examination of a section including such a crack showed heavy concentrations of carbides in the alloy weld metal which have migrated from the carbon steel. The crack appears to be located in the band of pure ferrite in the carbon steel immediately adjacent to this carburized band.

It is worth noting that this type of crack is not uncommon in

TABLE 3 SHORT-TIME TENSION TESTS

REFINERY	IDENTIFICATION		SERVICE HRS. X10 ³	F	TENSION TESTS				
	SPECIMEN	MATERIAL			TEST TEMP.	0.2% YIELD PSI	ULT. STR. PSI	% ELONG. IN 2 IN.	R.A. %
A	REACTOR	ASTM A 201 GR. A	53	920	ROOM	25,800 25,300	50,000 49,500	41.0 43.0	74.2 75.2
					950F		28,000 27,300	49.0 44.5	62.0 61.7
A	REACTOR	ASTM A201 GR. A	53	920	ROOM	23,100 23,000	45,500 47,200	43.0 40.5	74.4 79.5
					950F		30,400 28,100	40.0 51.5	70.6 77.1
A	REACTOR	ASTM A 201 GR. A	53	920	ROOM	29,400	48,600	32.5	57.5
					950F		25,300	51.5	61.0
B	REACTOR	ASTM A201 GR. A	57- 80	900- 950	ROOM	25,800	49,400	41.5	74.6
					950F		28,000	22.0	28.5
C	REACTOR	ASTM A201 GR. A	55- 60	920	ROOM	28,500 28,000	54,600 54,600	37.0 38.0	62.3 59.1
					950F		29,600 29,600	54.0 53.5	61.6 61.0

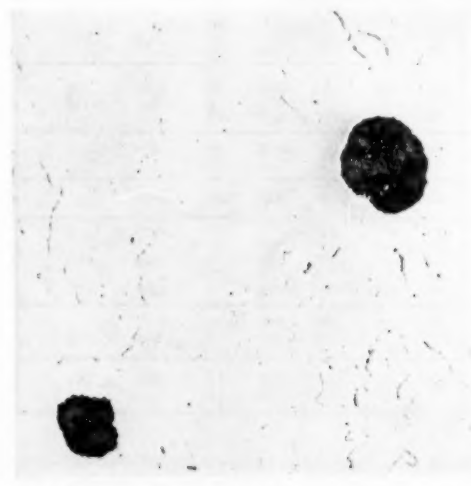


FIG. 5 REFINERY A—TERMINATION OF CRACK SYSTEM; GRAPHITE NODULES
(Heat-affected zone, Fig. 4, Pical etch; X100.)

welded joints between austenitic and ferritic steels operating at elevated temperatures. This type of construction needs study to determine the conditions under which it will perform satisfactorily or cause trouble in service.

Microexamination of samples removed from the reactor of unit B revealed some scattered graphite particles located principally in the heat-affected areas of the carbon-steel base metal. The amount of graphite was considerably less than that found in the unit A reactor, and there was no evidence of heavy concentrations which might cause planes of weakness. Mechanical tests showed excellent ductility across welded joints. The cracks in the carbon steel of this reactor have since been repaired and the

unit is back on stream. Until such time as a new reactor can be made available, the repaired reactor is operating with an internal insulating liner to decrease the metal temperature to a point where further deterioration is unlikely.

The third clad reactor found to be badly cracked is designated as unit C herein. This unit was shut down for inspection in May, 1951, and after preparing the outside surfaces of the welds by sandblasting and some local grinding, Magnaflex inspection revealed cracks in the carbon steel adjacent to the welds to approximately the same lineal extent as found on units A and B.

The majority of these cracks were shallow although one crack about 3 ft long in a shell girth seam extended practically through the entire plate thickness. The cracks were of the same type as found in unit B, that is, in the heat-affected base metal adjacent to carbon-steel welds and along the junction between carbon-steel base metal and alloy-steel repair welds.

Approximately 90 per cent of the alloy welds on the inside of the vessel were sandblasted and examined by the Zygo method. Except for one section about 12 ft long which contained some transverse cracks, the alloy welds were sound and free of cracks.

A limited number of weld probe specimens obtained from the vessel shell and cone seams contained traces of graphitization away from the welds with no concentrations of graphite in the base-metal heat-affected zones.

This reactor has since been repaired, and the unit is back on stream with an internal insulating liner installed to minimize the possibility of further deterioration.

EXPLORATION OF CAUSES OF CRACKING

General. The occurrence of cracks along the edge of welds in high-temperature pressure vessels is a more general problem than indicated by the specific cases reported herein. When such cracks have occurred in the past, the problem of why the affected area should be inherently weak usually has received only the limited attention necessitated by the repair or replacement of the vessel affected. Vessels in cyclic service, such as hydro-former reactors or coke drums, which are subject to repeated changes of temperature, have been found to be susceptible to cracking at weld edges.

The following factors have been considered as to their possible

TABLE 4. COMPARISON, MICROSTRUCTURE AND BEND TESTS

IDENTIFICATION			SERVICE		MICROSTRUCTURE GRAPHITE	MCQUAID ENH		COMPOSITION		REMARKS SIDE BEND TEST
REFINERY	SPECIMEN	MATERIAL	HRS X10 ³	F		GRAIN SIZE	ABNORM- ALITY	%AL	%AL ₂ O ₃	
A	REACTOR	ASTM A201 GR. A	53	920	SCATTERED NODULAR HAZ AND BASE METAL LOCALIZED AREAS IN HAZ	4	3	.006	.007	FAILED HAZ
						3	3	.006	.006	FAILED HAZ
						3	3	.004	.002	PASSED
						3	3	.006	.003	FAILED HAZ
						3	2	.006	.002	FAILED HAZ
B	REACTOR	ASTM A 201 GR. A	57- 60	900/ 950	SCATTERED NODULAR HAZ AND BASE METAL	2(1-3)	3	.007	.004	PASSED
						3	1	.009	.011	PASSED
E	REACTOR O-B LINE	ASTM A201	55- 60	980 1060	NONE SCATTERED NODULAR HAZ AND BASE METAL	3-2	1	.004	.003	PASSED
						3-2	1	.002	.010	PASSED
G	REACTOR	ASTM A201 GR. A	55- 60	920	NONE NONE	3	2	.005	.003	PASSED
						3	1			PASSED
J	REACTOR	ASTM A201	55- 60	900	SCATTERED NODULAR	2-1	2	.003	NIL	PASSED
K	CAT. STANDPIPE RE-REGEN.	ASTM A 106 ASTM A201	45- 50	1060 910	HEAVILY GRAPHITIZED HAZ AND BASE METAL	6	3	.019	.002	FAILED HAZ
						6	3			FAILED HAZ
						6	3			FAILED HAZ
L	REACTOR	ASTM A201 GR. A	40- 45	875	NONE NONE	6	1	.025	.003	FAILED HAZ
						6	1			FAILED HAZ
H	REACTOR	ASTM A201 GR. A	59	920	NONE NONE	4	1	.002	.010	PASSED
						4	2			PASSED
K	REACTOR	ASTM A201 GR. A	40- 45	910	NONE NONE SCATTERED NODULAR SCATTERED NODULAR SCATTERED NODULAR SCATTERED NODULAR NONE NONE	3-2	1			PASSED
						3-2	1			PASSED
						3-2	1			PASSED
						3-2	1			PASSED
						3-2	1			PASSED
						3-2	1			PASSED
J	REACTOR	ASTM A201	55- 60	900	NONE	3-2	1			PASSED
G	REACTOR	ASTM A 201 GR. A	55- 60	920	NONE NONE NONE	3	2			PASSED
						3	2			PASSED
						3	2			PASSED
H	REACTOR	ASTM A201 GR. A	19	880	NONE NONE NONE NONE NONE NONE NONE NONE	3	1			PASSED
						3	1			PASSED
						3	1			PASSED
						3	1			PASSED
						3-4	2			PASSED
						3-4	1			PASSED
						3-4	2			PASSED
						4	1			PASSED
D	REACTOR	ASTM A201	58	1000	LARGE NODULAR	4-3	1			PASSED
						4	1			PASSED
E	REACTOR O-B LINE	ASTM A201			NONE					
J	REACTOR	ASTM A201	55- 60	900	SCATTERED NODULAR					

TABLE 5 ROOM-TEMPERATURE MECHANICAL TESTS

IDENTIFICATION			SERVICE		ROOM TEMPERATURE TENSION TESTS			
REFINERY	SPECIMEN	MATERIAL	HRS.	F	TYPE SPECIMEN	YIELD STR. PSI	ULT. STR. PSI	% ELONG. IN 2 IN. FRACTURE
A	REACTOR	ASTM A201 GR. A	53	920	WELD	26,300	44,040	52.5
						25,600	44,600	42.5
						24,300	47,000	55.0
						25,000	46,600	50.0
					PLATE	26,300	49,100	60.0
						25,800	47,500	62.0
B	REACTOR	ASTM A201 GR. A	57-60	900-950	WELD	30,000	59,800	13.0
					PLATE	35,000	50,000	38.0
A	REACTOR	ASTM A201 GR. A	53	920	FREE BEND TESTS ON WELD SPECIMENS			
					ANGLE OF BEND	REMARKS		
					5	FRACTURED AT FUSION LINE OF WELD		
					180	SATISFACTORY		
					0	FRACTURED ON LOADING		
					180	SATISFACTORY		
A	REACTOR	ASTM A201 GR. A	53	920	FREE BEND TESTS ON PLATE SPECIMENS			
					ANGLE OF BEND	REMARKS		
					180	SATISFACTORY		
					180	SATISFACTORY		
					180	SATISFACTORY		
					180	SATISFACTORY		
A	REACTOR	ASTM A201 GR. A	53	920	SIDE BEND TESTS ON WELD SPECIMENS			
					ANGLE OF BEND	REMARKS		
					180	SATISFACTORY		
					180	SATISFACTORY		
					180	SATISFACTORY		
					180	SATISFACTORY		
A	REACTOR	ASTM A201 GR. A	53	920	SIDE BEND TESTS ON PLATE SPECIMENS			
					ANGLE OF BEND	REMARKS		
					180	SATISFACTORY		
					180	SATISFACTORY		
					180	SATISFACTORY		
					180	SATISFACTORY		
B	REACTOR	ASTM A201 GR. A	57-60	900-950	180	SATISFACTORY		
					180	SATISFACTORY		

influences on the initiation or propagation of the cracks at the edge of welds in the three integral-clad reactors:

1 Underhead cracks.

Although these might be a factor in the case of high-carbon or low-alloy steels, such cracks were not encountered during the fabrication of these vessels, which are mild steel, and no evidence was found to indicate that they developed during service.

2 Stress concentration due to undercutting at the edge of welds or heavy weld reinforcement.

A limited amount of undercutting and heavy reinforcement was present on the main seam welds on each of the three reactors; however, no correlation with cracks was observed. Some of the cracks occurred at the edge of such welds requiring grinding to enable correct interpretation of Magnaflex indications.

3 Hydrogen embrittlement due to the use of electrodes not of the "low-hydrogen" variety.

The use of low-hydrogen-type electrodes has been of benefit in eliminating cracking in heavy welds and welds under a high degree of restraint. Although these vessels were welded before the low-hydrogen-type rods were extensively used, no unusual trouble was encountered during fabrication with cracks in the carbon-steel weld metal and no cracks occurred in the base metal. The only seams which involved considerable cracking difficulties were at the intersections of the cones to shell where intersection effects enhanced the shrinkage stresses. Since hydrogen embrittlement due to welding would be at its maximum during fabrication and would subsequently diminish as the hydrogen diffused out of the steel, it does not appear that such embrittlement would be responsible for the development of the reported cracks.

4 Fatigue in cyclic service.

The conditions under which these vessels operate are not

cyclic in the usual sense, the total number of operating cycles ranging from 11 to 26. Apparently a limited number of cycles is of importance in evaluating the effect of thermal stresses inherent in a bimetallic structure, as will be discussed later.

5 Impact and vibration effects.

The inertia effect of the fluid-catalyst bed and incoming catalyst stream does result in low-frequency vibration of low amplitude which increases during start-up and shutdown operations. The magnitude of the vibration amplitudes in the vessel are minor as compared with that in the connecting catalyst pipe lines and are considered relatively unimportant.

6 Effects of graphitization on mechanical properties.

There is no positive connection between the graphitization and the development of the cracks. In the reactor in unit A which showed appreciable nodular graphite, the cracks primarily followed the heat-affected zone where there was a tendency for graphite concentrations. The segregated graphite observed in heat-affected zones, however, was not of the eyebrow type found on the Springdale failure, but was nodular and might be more descriptively termed "bead" type, Fig. 6. Bend tests have shown that moderate amounts of bead-type graphite do not adversely affect ductility, although a few tests of welded joints with particularly heavy concentrations have shown reduced ductility in a degree proportionate to the quantity of graphite present. Little is known about the possible effect of such segregation on the long-time high-temperature strength and ductility or the fatigue or shock resistance of welded joints. While segregated graphite appears to have been an influence in the development of cracks in the case of unit A, this is not supported by the findings on units B and C, unit B having little graphite and unit C being practically free of graphite. The degree of spheroidization also varied. The steel for all three vessels was supplied from the same source at the same time; in fact,

some heats are represented by plates in more than one vessel. The difference in degree of deterioration is not readily explained but the difference is sufficiently marked that graphite cannot be ascribed as a primary influence in causing the cracking.

7 Notch effect at edge of alloy weld deposit due to its greater depth than the alloy cladding thickness.

In no case were cracks found which originated at this location.

8 Propagation of initial fabrication cracks in alloy or carbon-steel welds, such as micro-cracks or cracks at the junction between the carbon and alloy steel.

It is known that some difficulty with micro-cracking of alloy weld deposits was experienced during fabrication and it is probable that some such cracking existed at the start of service. These cracks undoubtedly propagated within the alloy weld deposit although the depth of these multidirectional cracks was quite shallow; in most cases they could be eliminated by surface-grinding. Transverse cracks also developed; however, the origin of these is not clear since this type of crack was not observed during the fabrication and original inspection of these vessels. Even though these cracks did not propagate into the carbon steel to any extent they could have had an important influence on the development of cracks in the base metal since the internal force system due to thermal and other effects would be disturbed locally. This could introduce appreciable additional local stress concentration on the base metal at this point. It should be noted, however, that the alloy welds in the reactor of unit C were reported to be sound except for one 12-ft length so that in that instance at least, alloy-weld-metal cracks could not contribute to the carbon-steel cracking that occurred.

As pointed out in (3), there was negligible trouble with cracks in carbon-steel welds during fabrication. With the inspection means employed it is unlikely that cracks of significant dimensions would have been present at the time the reactors began serv-

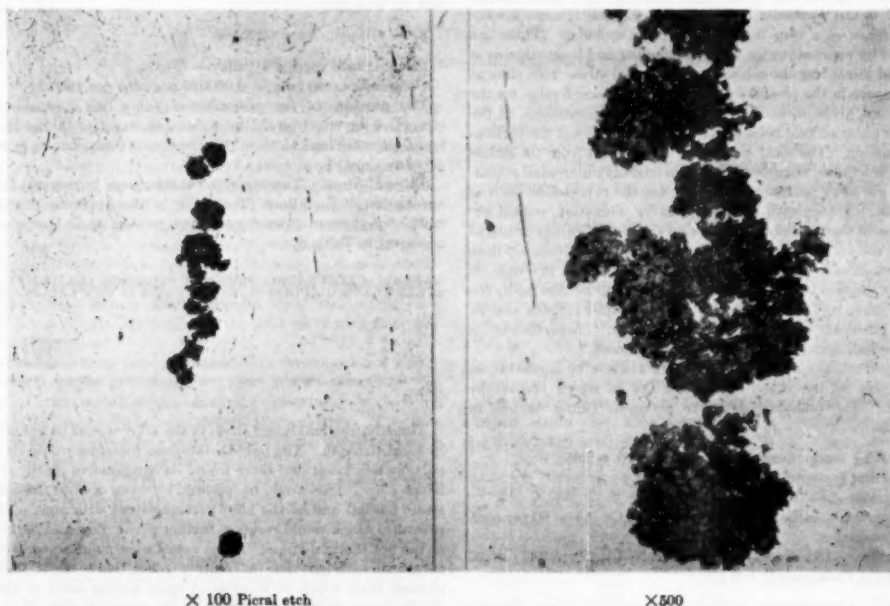


FIG. 6 REFINERY K—WELD JOINT HEAT-AFFECTED ZONE; CONCENTRATION OF GRAPHITE NODULES

ice; also it would be expected that large cracks would have propagated and become evident in a much shorter time period.

9 Thermal stress resulting from difference in expansion of alloy and carbon steel in integral-clad plate or composite welds.

10 Fatigue attendant to thermal cycling in integral-clad plate construction.

11 Stress-rupture failure due to combined operating stresses.

These last three factors require more detailed consideration and are discussed in the following section.

THEORETICAL STUDY OF STRESSES AND PLASTIC STRAINS IN INTEGRAL-CLAD PRESSURE VESSELS

Since the integral-clad plates of the reactors discussed in units A, B, and C involve cladding and base metals of different thermal-expansion characteristics, the contribution of thermal stresses to the interaction and/or propagation of flaws should be assessed. It is the purpose of this section to examine the stress cycle and attendant deformation for such vessels.

The API-ASME Code to which these reactors were built accepts part or all of the alloy thickness of integral-clad plate as part of the required thickness, provided the allowable stress for the base material is used for the entire thickness. This practice stems from reasoning that in high-temperature service, thermal stress as a form of internal loading would rapidly be lowered by creep or relaxation, similar to that in boiler or furnace tubes, so that essentially only pressure stress would exist under service conditions.

For vertical refinery vessels of the type being discussed, other influences such as dead load, piping reactions, wind load, and so on, are insignificant at the shell areas where the cracks occurred. Attention therefore can be confined to thermal expansion and pressure effects.

In an effort to gain a better understanding of actual behavior of a clad vessel in high-temperature service, expressions are developed in the Appendix for the elastic thermal stresses for the general case of a thin integral-clad plate cylinder. These are followed by expressions for the local bending and hoop stresses at a welded joint; for the relaxation of thermal stress with time at temperature in the presence of pressure stress; and finally, for the subsequent division, under steady-state creep conditions, of the internal pressure load between the alloy cladding and the carbon-steel backing. The local stresses at welds result from the difference in thickness, composition, and attendant differential expansion of the alloy portion of the weld, and the expressions derived for them, together with the equations for relaxation, permit exploration of their possible influence on the cracks. Only principal stresses are calculated and, for convenience, available creep data under uniaxial tension is assumed to apply. The precision of strain evaluation and load-carrying capacity will be affected by the meager creep and other high-temperature data available and by certain necessary simplifying assumptions; nevertheless, a valuable indication of general trends is achieved.

The general formulas of the Appendix will now be applied to an exploration of the integral-clad reactors in which cracks developed. The following data are pertinent (units defined in Appendix):

- Operating temperature... $(T = 975 - 70 = 905)$
- Operating pressure... $P = 16$ to 25 psi
- Composite shell thickness... $t = 1\frac{1}{2}$ in.
- Base metal... carbon steel (ASTM A201 Gr. A) = 80 per cent of t nominal
- Cladding... 18 per cent Cr-8 per cent Ni-Cb (Type 347) = 20 per cent of t nominal ($B = 0.2$)

(Note: Alloy-cladding thickness exceeded the nominal thickness in areas.)

Thermal expansion coefficient

Carbon steel... $\alpha_s = 7.95 \times 10^{-6}$

Type 347 steel... $\alpha_c = 10.15 \times 10^{-6}$

Modulus of elasticity

Carbon steel... $E_s = 29 \times 10^6$ at 70 F

$= 19.3 \times 10^6$ at 975 F

Type 347 steel... $E_c = 29 \times 10^6$ at 70 F

$= 19.3 \times 10^6$ at 975 F

(Note that E_c is taken equal to E_s for convenience since little error is introduced)

Poisson's ratio $\nu = 0.3$ (assumed constant for all temperatures)

Pressure Stress: Considering internal pressure stress alone, if thermal stresses were to relax completely with time at temperature and the vessel is maintained at the operating temperature, the alloy cladding and base metal would divide the pressure load so that each creeps at the same rate. The expressions relating creep, stress, and time at the operating temperature of 975 F are taken as follows:

For carbon steel

$$\epsilon_c = \frac{(S_c)^{3.51}}{6.46 \times 10^{17}} \text{ in. per in. per hr}$$

For Type 347 steel

$$\epsilon_c = \frac{(S_c)^{3.51}}{1.26 \times 10^{18}} \text{ in. per in. per hr}$$

Application of Equations [14] and [15] in the Appendix for the maximum operating pressure of 25 psi gives for $B = 0.2$

$S_s = 1364$ psi; $S_c = 7250$ psi

Per cent load carried by alloy = 57

Composite creep rate = 0.000052 per cent per 1000 hr and for $B = 0.3$

$S_s = 970$ psi; $S_c = 6200$ psi

Per cent load carried by alloy = 73

Composite creep rate = 0.000019 per cent per 1000 hr

The presence of the austenitic cladding has a considerable strengthening effect on the base metal in so far as taking the internal pressure load alone is concerned, and creep due to internal pressure would be at a very low rate.

Thermal Stress. Turning to a consideration of thermal stress, application of Equations [2] and [3] in the Appendix results in calculated thermal stresses upon first coming up to temperature as shown in Table 6.

TABLE 6 CALCULATED THERMAL STRESS IN 18-8 CR-NI CLAD STEEL PLATE ON FIRST HEATING FROM 70 TO 975 F ASSUMING NO YIELDING

B	S_s	S_c
0.2	+11000	-44000
0.3	+16500	-38500
0.4	+22000	-33000

NOTE: Plus sign indicates tensile stress; minus sign indicates compression stress.

Actually, the maximum stress in the alloy would be limited by its yield strength. The base-metal stress therefore would be proportionately lower and there would be compressive plastic strain in the alloy. This would be followed by creep of both the carbon steel (tensile) and of the alloy (compressive) with time at temperature, which would result in further plastic flow and reduction of the hot thermal stress. If the vessel were maintained at temperature a sufficient time for complete relaxation to occur, thermal stresses again would be introduced upon cooling down to atmospheric temperature and would be of reversed sign from the original stresses when hot. In the cold condition the calculated

TABLE 7 STRAINS IN 20 PER CENT INTEGRAL-CLAD (TYPE 347) STEEL REACTOR ($P = 25$ PSI)

Cycle	Total operating time, hr	Temp, deg F	Thermal stress, psi		Elastic strain, in./in.		Added plastic strain, in./in.		Net plastic strain per cycle, in./in.	
			S_a	S_b	Cladding	Base metal	Cladding	Base metal	Cladding	Base metal
1	0	975	-20000	+5000	-0.000725	+0.000181	-0.001084	0		
	5000	975	0	0	0	0	-0.000129	+0.000777		
	5000	70	+30000	-7500	+0.000724	-0.000181	+0.001085	0	-0.000128	+0.000777
2	5000	975	-20000	+5000	-0.000725	+0.000181	-0.000179	0		
	10000	975	0	0	0	0	-0.000129	+0.000777		
	10000	70	+30000	-7500	+0.000724	-0.000181	+0.001085	0	+0.000777	+0.000777

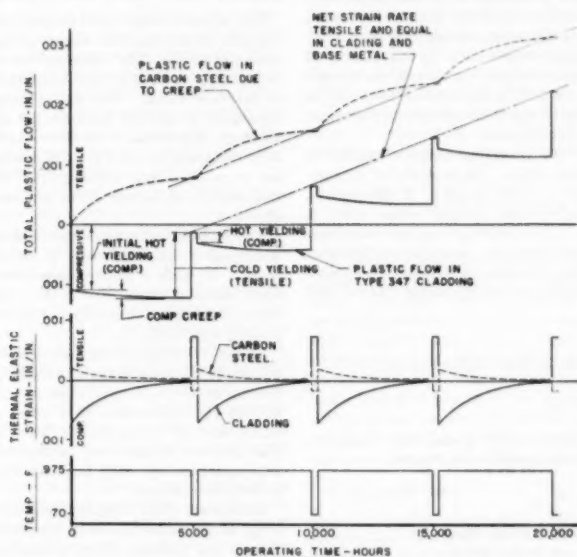


FIG. 7 THERMAL STRAINS IN TYPE 347 CLAD-STEEL REACTOR WITH OPERATING CYCLES

values would be equal to the values given in Table 6, increased by the ratio of the cold to the hot modulus of elasticity. The stress in the cladding would exceed the cold yield strength of the alloy which again would limit the actual stress level, and there would be tensile plastic flow in the alloy. The establishment of a residual stress system of reversed sign in the cold condition is favorable since it reduces the hot thermal strain in all succeeding cycles. Depending on the percentage cladding thickness, little or no further hot plastic flow would occur in the alloy because of exceeding the hot yield strength. Relaxation due to creep, however, would continue during each cycle and there also would be a repetition of tensile plastic flow in the alloy on cooling to atmospheric temperature.

Table 7 has been prepared to indicate the amount of plastic flow which might be expected to occur in the carbon-steel and alloy cladding on successive operating cycles, each cycle being sufficiently long to permit relaxation of thermal stress. The plate is assumed to be stress-free to start with and the time indicated is that estimated for complete relaxation by application of Equation [12] of the Appendix in the presence of an internal pressure stress of 2540 psi corresponding to the maximum operating pressure of 25 psi. Relaxation was assumed to take place in the carbon steel and alloy in the ratio of 6:1. This ratio, while not exact, seems reasonable from the creep properties of the two materials at 975 F. The yield strength of the alloy was assumed as 30,000 psi at 70 F and 20,000 psi at 975 F. Two cycles are tabulated, but any subsequent cycles of similar duration would repeat the second cycle.

It is noted that on each cycle there is tensile plastic strain of the base metal which occurs owing to creep in the hot condition and a net tensile strain of equal amount in the alloy. The net tensile alloy strain is the result of tensile yielding upon cooling to room temperature, which is only partially offset by compressive yielding and creep in the hot condition. The plastic and elastic strains are more effectively shown in curve form in Fig. 7. These curves bring out the greater amount of working of the alloy even though the net tensile growth per cycle is the same for both materials.

If the time of a cycle were to be increased beyond that which causes complete relaxation, the rate of creep during the additional time would be dictated by pressure stress alone and the net rate of creep per cycle would decrease. If the time were to be shortened, the net rate of creep would increase. The effect of the number and duration of the temperature cycles is therefore of interest.

Table 8 has been prepared to indicate the effect of cycling on the total strain which might be expected for the same total operating time, taken as 50,000 hr.

TABLE 8 EFFECT OF OPERATING CYCLES ON NET RATE OF CREEP: TYPE 347 INTEGRAL-CLAD STEEL REACTOR; TOTAL OPERATING TIME CONSTANT AT 50,000 HR

Number of cycles	Duration of each cycle, hr	Total elongation, in. per in.		
		$P = 25$ psi $B = 0.3$	$P = 16$ psi $B = 0.3$	$P = 25$ psi $B = 0.3$
2	2500	0.00176	0.00188	0.000818
5	10000	0.00402	0.00402	0.00412
10	5000	0.00777	0.00845	0.00821
15	3333	0.01090	0.01090	0.01225
20	2500	0.01316	0.01638	0.01654
30	1667	0.01680	0.01329	0.02145

In preparing Table 8, a favorable residual-stress system of reversed sign was considered to have been established prior to the first cycle, as would be accomplished by the thermal stress relief which these reactors received. The influence of the number of cycles is quite marked. Since the results are affected by the cladding thickness and the pressure stress, three elongation columns are included to show the effect of changes in these variables. The first column is based on a pressure of 25 psi and 20 per cent cladding thickness; in the second column the pressure is reduced to 16 psi; in the third column the pressure is again 25 psi but the cladding thickness is increased to 30 per cent. In the range of 10 to 30 cycles, lowering the pressure 36 per cent lowered the elongation approximately 20 per cent, while an increase from 20 to 30 per cent in cladding thickness raised the elongation 6 per cent for 10 cycles and 27 per cent for 30 cycles.

Local Effects at Welds. The preceding analysis applies to integral-clad plates away from welds. An analysis for approximating the stress conditions at welds is given in the section, Local Temperature Stress in Welded Circumferential Joint in Clad Plate, of the Appendix. The resulting equations have been applied to the vessels under consideration, assuming the following weld proportions and cladding thickness as typical of the actual construction; weld metal was 25 per cent chromium—12 per cent nickel-alloy steel:

$$B_1 = 0.3; B_2 = 0.5$$

$$t_2 = 1\frac{1}{2} \text{ in. (allows for } \frac{1}{4} \text{ in. weld reinforcement)}$$

$$w = 1 \text{ in.}$$

$$\alpha_w = 9.72 \times 10^{-6}; E_w = E_s$$

Other data are as given in the preceding analyses. Equations [6] to [9] of the Appendix yield the following results:

$$S_{L1} = \pm 342 \text{ psi}$$

$$S_{L2} = \pm 287 \text{ psi}$$

$$S_{M1} = + 85 \text{ psi (outside fiber)}$$

$$+ 291 \text{ psi (inside fiber)}$$

$$S_{M2} = -3816 \text{ psi (outside fiber)}$$

$$-3644 \text{ psi (inside fiber)}$$

These stresses must be superimposed on the thermal stresses calculated separately for the clad plate and the composite weld by Equations [2] and [3]. These thermal stresses are given in Table 6 for the clad plate. For the weld metal the values are

$$S_M = +22,050 \text{ psi}$$

$$S_w = -22,050 \text{ psi}$$

The net stresses are therefore as follows:

At outside fiber of carbon-steel base material, part (1)

$$+16,842 \text{ psi longitudinal}$$

$$+16,585 \text{ psi circumferential}$$

At outside fiber of carbon-steel weld metal, part (2)

$$+22,337 \text{ psi longitudinal}$$

$$+18,234 \text{ psi circumferential}$$

At inside fiber of alloy cladding, part (1)

$$-38,842 \text{ psi longitudinal}$$

$$-38,209 \text{ psi circumferential}$$

At inside fiber of 25-12 alloy weld metal, part (2)

$$-22,337 \text{ psi longitudinal}$$

$$-25,694 \text{ psi circumferential}$$

The actual stresses would be lower as dictated by the hot yield strength of the material which has not been considered in the foregoing figures. The values indicate that less plastic flow would occur in the 25-12 alloy weld metal than in the Type 347 cladding of the base metal. The discontinuity stresses obtained from Equations [6] to [9] of the Appendix are surprisingly small. It is apparent that owing to the lower coefficient of expansion of the weld compared to the Type 347 cladding of the base metal, the use of an alloy weld depth greater than the adjacent cladding thickness is advantageous in lowering the local discontinuity effects.

The stress in the carbon-steel weld metal is shown to be somewhat higher than the stress in the adjacent carbon-steel base metal. To gain a better appreciation of what influence this might have on plastic flow in the weld metal with temperature cycles, Table 9 has been prepared for the composite weld for comparison with Table 7.

The yield strength of the weld metal was assumed as 35,000 psi at atmospheric temperature and 25,000 psi at 975 F. It is apparent that on the second and all subsequent cycles the net plastic flow in both the carbon-steel weld metal and the 25-12 weld metal would tend to be appreciably lower than in the adjacent clad plate because of the lower coefficient of expansion of the alloy weld metal and the more favorable residual stress system set up in the cold condition.

Discussion. The foregoing analyses are useful in judging the trend of the many variables involved and the relative role of thermal and pressure effects in causing plastic flow. The plastic flow indicated cannot be taken as an accurate estimate as it can be altered by variations in the assumptions made in the approach and for the physical properties of the materials used. Variation of the actual metal temperature from the assumed 975 F would have a very marked effect. Raising the cold yield strength as a result of straining also would operate to reduce the plastic deformation per cycle.

Pressure stress has been shown to have a negligible influence on total creep as compared to thermal cycling. The number of temperature cycles in a given total operating period is indicated to have a direct influence on total creep. The unit A reactor is reported to have had 53,000 hr of total operating time and to have had 26 cycles with temperature ranging from 900 to 975 F and pressure from 16 to 25 psi. The unit B reactor had approximately the same total time and temperature but only 11 cycles with pressure at 16 psi. Table 8 would indicate a total creep of approximately 1.4 per cent for unit A reactor and 0.7 per cent for unit B reactor, assuming 975 F metal temperature and 20 per cent cladding thickness. Heavier cladding thickness would increase this, but lower metal temperature would reduce it con-

TABLE 9 LONGITUDINAL STRAINS IN COMPOSITE GIRTH WELD IN 18-8 CR-NI-CLAD STEEL REACTOR

(Cladding thickness taken as 30 per cent, alloy weld depth 50 per cent, alloy weld metal 25 per cent Cr-12 per cent Ni alloy. Pressure = 25 psi)

Cycle no.	Total operating time, hr	Temp, deg F	Thermal stress, psi		Elastic strain, in/in		Added plastic strain, in/in	
			Alloy weld	CS weld	Alloy weld	CS weld	Alloy weld	CS weld
1	0	975	-22337	+22337	0.00081	0.00081	0	0
	9100	975	0	0	0	0	-0.00021	+0.00139
	9100	70	+33500	-33500	0.00081	0.00081	0	0
2	9100	975	0	0	0	0	0	0

siderably. While no original strapping dimensions are available, circumferential strappings at various levels on the shell after failure showed several readings at or close to the theoretical circumference when new and a maximum difference between minimum and maximum readings of $2\frac{1}{4}$ in. for the unit A reactor and $3\frac{1}{4}$ in. for the unit B reactor. These correspond to elongations of only 0.3 and 0.4 per cent, respectively.

The cracks under consideration herein were located at welds. Neither the base metal nor cladding showed ill effects away from welds. The approximate analyses described herein indicate that stress conditions in the composite welds are such that both carbon- and alloy-steel weld metal would be expected to have less total plastic flow than the adjacent carbon-steel base metal and alloy cladding. However, differential strains would be encountered at the edge of welds owing to different stress conditions and variations in the yield and creep properties of weld and base materials, the effects of which cannot be assessed accurately.

Stress-rupture test data are not applicable in evaluating thermal effects, as we are dealing with internal stresses which are the result of strains rather than forces and which vary with time. On each temperature cycle there is a locked-up thermal strain of limited magnitude. The relief of this strain is dependent on the ductility of the material rather than its load-carrying ability. The approximate analysis herein presented indicates that the total elongation would be 1.4 per cent or less, and vessel measurements indicate actual elongations were considerably lower. The materials used in these vessels normally would be expected to yield such amounts without distress as is evidenced by the absence of any cracks away from welds. Analysis indicates less strain at welds than away from welds and hence offers no explanation for the cracking at welds or for the peculiar regular pattern of transverse cracks in the alloy weld metal.

It is the opinion of the authors that thermal strains and strain gradients at welds were not sufficiently severe to initiate cracks in sound material of the expected physical properties. However, cyclic thermal strains could initiate cracks in zones of low ductility or fatigue resistance or propagate existing flaws or cracks. The prevalence of cracks adjacent to welds points to some weakness which is inherent or which developed in the structure of this zone. The extent of cracking at girth welds, which was at least as extensive as at longitudinal welds, would appear to be an indication that thermal rather than pressure effects were responsible for disclosing weak zones. It is known that some difficulty was encountered with micro-cracking of the alloy weld deposits during the vessel fabrication and that the original welds contained some such defects. These may have contributed to stress concentrations at the weld areas. Another factor which would add to the local stress effects at welds is the variation in the cladding thickness encountered on these plates, which varied up to 40 per cent of the total thickness and might be different on either side of the weld. The unit B reactor was cracked practically as badly as the unit A reactor even though it had only 11 cycles as compared to 26 for the latter vessel, while the unit D reactor of the same design and operating time is still intact after having gone through 20 cycles; other units are not in difficulty as far as is known. Experience, therefore, does not permit any firm conclusions to be drawn.

Comparison With 11-13 Per Cent Chromium-Clad Steel. While dis-

cussing the thermal effects in integral-clad plates it may be of interest to include a comparison of the expected performance of 11-13 per cent chromium integral-clad steel on the same basis, since there are vessels of this type operating in similar service. Assuming the same vessel dimensions and operating conditions as used previously, but changing the cladding material to 11-13 per cent Cr steel, gives the following results:

Against pressure loading alone the alloy cladding again would have a strengthening effect because of its greater creep strength. For 25 psi operating pressure and 20 per cent cladding thickness, it is estimated that after relaxation of thermal stress the carbon-steel stress would be 1940 psi and the alloy stress 4950 psi, the alloy carrying 39 per cent of the total pressure load.

In so far as thermal strains are concerned, Tables 10 and 11 are given for comparison with Tables 6 and 7. In calculating the values shown in these tables the following data were used:

$$\alpha_{cl} = 6.47 \times 10^{-6}, E = 19.3 \times 10^6 \text{ at } 975 \text{ F}$$

$$\text{Alloy yield strength} = 35,000 \text{ psi at } 70 \text{ F}$$

$$25,000 \text{ psi at } 975 \text{ F}$$

The initial calculated stresses are lower than those for Type 347 integral-clad steel since the differential strain is reduced one third. The plastic flow per cycle on each cycle after the first is indicated as very low and as compressive rather than tensile. This brief comparison indicates that 11-13 Cr clad plate is more favorably disposed to absorb thermal strains without difficulty. However, conditions at composite welds where the alloy weld layer is made with 25-12 or 25-20 Cr-Ni electrodes involve local discontinuity effects as great or greater than with Type 347 cladding. Application of Equations [2] to [9] of the Appendix for $B_1 = 0.2$ and $B_2 = 0.4$ give the following results:

Longitudinal stress	
Outside fiber C.S. base plate.....	-5870 psi
Outside fiber C.S. weld.....	+26700
Inside fiber alloy cladding.....	+27900
Inside fiber 25-12 weld.....	-18870
Circumferential stress	
Outside fiber C.S. base plate.....	+590
Outside fiber C.S. weld.....	+8920
Inside fiber alloy cladding.....	+37370
Inside fiber 25-12 weld.....	-33740

It is noted that at the edge of the weld the stresses in the adjacent parts are of opposite sign; therefore differential straining in this area can be expected which would accentuate any local weakness, should such exist, as in the case of 18-8 Cr-Ni cladding. No difficulty has been reported thus far, and experience must remain the proof of whether such effects are of practical significance or not. It would be well to follow the service performance of such composite welds, and, for that matter, the performance of all

TABLE 10. CALCULATED THERMAL STRESSES IN 11-13 PER CENT CR INTEGRAL-CLAD STEEL PLATES

B	S_b	S_c
0.1	-3690	+33200
0.2	-7380	+29500
0.3	-11070	+25800
0.4	-14760	+22130

TABLE 11. EFFECT OF OPERATING CYCLES: 11-13 PER CENT CR INTEGRAL-CLAD REACTOR (25 PSI, $B = 0.3$)

Cycle	Total operating time, hr	Temp, deg F	Thermal stress, psi		Elastic strain, in./in.		Added plastic strain, in./in.		Net plastic strain per cycle, in./in.	
			Cladding	Base metal	Cladding	Base metal	Cladding	Base metal	Cladding	Base metal
1	0	975	+25000	-8250	+0.000905	-0.000226	+0.00021	0	+0.00049	-0.00057
	8700	975	0	0	0	0	+0.00057	0	0	0
	8700	70	-35000	+8750	-0.000843	+0.000210	-0.00029	0	0	0
2	8700	975	+7990	-1590	+0.000231	-0.000058	0	0	0	0
	17900	975	0	0	0	0	+0.000145	-0.000145	-0.000145	-0.0001
	17900	70	-35000	+8750	-0.000843	+0.000210	-0.00029	0	0	0

welds involving materials having dissimilar coefficients of expansion and operating at high temperature.

INSPECTION OF OTHER REACTORS

The API Subgroup on Graphitization is currently circularizing the petroleum industry with the aim of initiating a program of sampling and examining high-temperature equipment of all kinds in an effort to accumulate experience on the tendency of carbon- and low-alloy steels to develop graphite, particularly of the segregated variety. Because of the particular interest focusing on catalytic-cracking units as a result of the reported deterioration found in three reactors, some inspections already have been made in these units and the more pertinent findings will be described herewith.

Tables 1 to 5 list the reactors which have been inspected, their description and history, and the results of tests and the examination of samples. A summary of this information is as follows:

Of the three other Type 347 integral-clad reactors which have been inspected, the first is designated unit D herein. During a regular shutdown in March, 1951, two series of vertical seams were uncovered and Magnafluxed and one series of vertical seams on the alloy side were examined by "Dyecheck." No cracks were found. Two plugs were removed from a shell plate away from the welded seams and were found to contain heavy nodules of graphite, with almost complete spheroidization of the carbide phase. No specimens were obtained from welded seams.

The next integral-clad reactor, unit E, also was inspected in March, 1951, by Magnafluxing the outside surface and Zyglolting the inside alloy surface of about one-half of the vessel seams. No cracks were found. No samples were cut from the vessel although a specimen was obtained from an extension into the top of the reactor of the overhead vapor line, which also is of Type 347 integral-clad plate. This was found to contain a small amount of carbide spheroidization but no graphite.

The integral-clad reactor, unit F, at the time of preparing this paper, had not been shut down for inspection although about 20 per cent of the vessel seams had been uncovered and visually examined. No cracks were detected; however, a 9-in-long crack was observed in the overhead vapor line, which also is of Type 347 integral-clad steel, immediately adjacent to the butt weld joining this line to the reactor-top cone.

In addition to the six integral-clad reactors which have been discussed, five other reactors of ASTM Specification A201, Gr. A carbon steel also have been inspected or sampled; two are unlined, two have resistance spot-welded linings of Type 405 stainless steel, and one has a resistance spot-welded lining of Type 347 stainless steel.

The two carbon-steel reactors are designated as units G and H. Unit G began service in 1944, and unit H in April, 1949. Weld-probe specimens were taken from both vessels and although the metal from the older vessel shows the carbides to be about 50 per cent spheroidized, neither one contains any graphite. No cracks have been observed.

The reactor of unit J has a resistance spot-welded liner of Type 347 and began operation early in 1944. Plugs cut from a welded seam and base plate in the top cone showed scattered nodular graphite with heavier concentrations in the base metal heat-affected zones. Despite these concentrations of graphite, miniature bend specimens had good ductility in base metal and across welded joints.

The reactors of units K and L are both lined with resistance spot-welded liners of Type 405 and both went into service in 1946. Examination of a sample removed from the unit L reactor in February, 1951, reveals about 50 per cent spheroidization but no signs of any graphite. Weld-probe specimens obtained in April from the unit K reactor show the steel in the top and bottom cones

to be substantially unchanged by service, while material from the shell shows some spheroidization and traces of graphite in the base material and in the heat-affected zone. Magnaflux examination of a series of vertical seams and adjacent portions of girth seams in the unit K reactor revealed no cracking.

INSPECTION OF OTHER EQUIPMENT

In addition to the inspection and sampling of reactors, some samples have been taken from carbon-steel and Type 347 integral-clad carbon-steel pipe lines and vessel internals which are operating at high temperatures in these catalytic-cracking units. Results are included in Tables 1 to 5. There are two cases which have been examined in the laboratory of the authors' company which are of some interest.

A plug was cut from a carbon-steel internal in the regenerator of unit D. This material had been exposed to temperatures of approximately 1050 F for about 58,000 hr. Visual observation of the saw-cut surface of the plug revealed smeared black specks which microscopic examination showed to be massive nodules of graphite with diameters as large as 0.020 in. These nodules have a definite structure and probably consist of mixtures of pure graphite and one or more other constituents whose identity is not yet determined. Fig. 8 is a photomicrograph of one of these massive nodules.

The other case concerns the regenerated catalyst standpipes joining the regenerator to the reactor inlet lines of unit K. These lines are made of ASTM Specification A-106 seamless carbon-steel pipe and have been exposed to flue gas and powdered catalyst at approximately 1050 F for a period of about 48,000 hr. During the April, 1951, shutdown these lines were cut in sections and removed from the structure to permit the installation of internal insulating linings which would permit operation at higher temperatures than those for which the lines were designed. After the insulation was installed they were rewelded in place and continued in service. Samples cut from the original welded joints in these lines were examined and found to contain large graphite nodules which were scattered throughout the base metal with heavy concentrations in the heat-affected areas. In some areas these concentrations were sufficient to cause planes of weakness which resulted in definite impairment of ductility in miniature side bends tested with the heat-affected zones at the point of maximum bending. Instead of being able to obtain full 180-deg bends as was the case when testing the graphitized base metal away from welds, it was possible to bend two specimens only about 90 deg with 6 per cent and 12 per cent elongation, respectively, before rupture occurred at the edge of the heat-affected zone. It is interesting to note that despite the severity of the graphitization which has occurred in this pipe, the mechanical properties are such that further satisfactory life is anticipated.

WELDING ON GRAPHITIZED STEEL

The discovery that graphite in the plate materials was associated with the cracks in the unit A reactor posed the problem as to whether or not suitable and serviceable weld repairs could be made. Favorable precedent established in the power industry notwithstanding, noticeable differences in the form and distribution of the graphite observed in refinery-equipment materials suggested that preliminary weldability tests probably were warranted. In samples removed from the unit A reactor graphite was found concentrated in the heat-affected zone of weld joints, which was not unlike the power piping experience. However, it was observed that graphite was also present in the unaffected base metal, in certain cases in copious quantities; this condition, in the experience of the authors with power-piping equipment, has been the exception rather than the rule. Repair of graphitized weld joints in steam piping usually has involved the complete removal

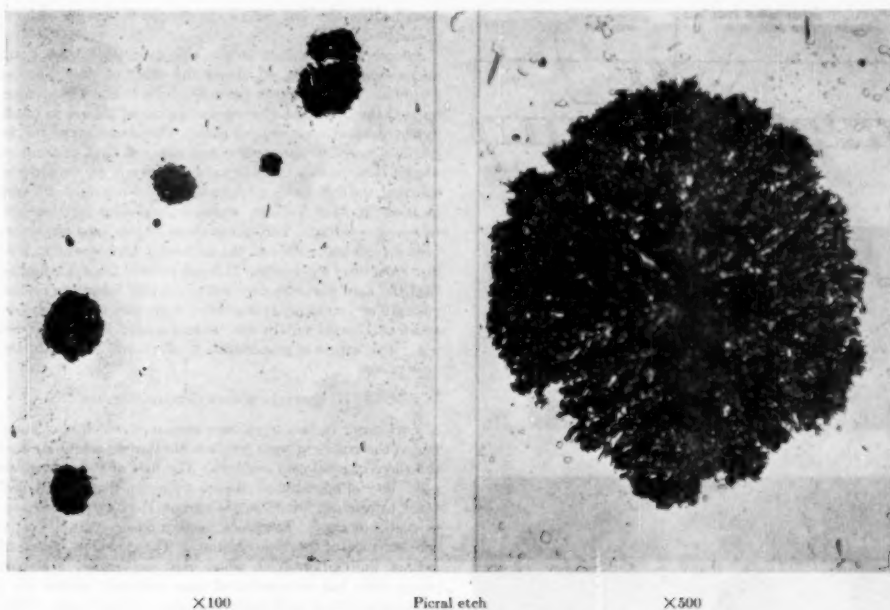


FIG. 8 REFINERY D—BASE METAL: MASSIVE GRAPHITE NODULES

of a weld joint including the graphitized heat-affected zones. The new welds were then made on material substantially free from graphite and it has been found that this procedure has insured the elimination of graphite effects for limited service at least. Since comparable procedures were not practicable in the repair of a reactor shell, the question was raised as to what effect welding would have on graphite particles in the initially unaffected base metal, and the associated effects on the mechanical behavior of a repair weld joint. This problem is now under consideration by a subgroup of the ASME-ASTM Joint Research Committee. Pending the completion of these studies it may be of interest to report the results of some limited test welds made in heavily graphitized carbon steel.

Two test repair welds were made in the shell plates of the integral-clad reactor of unit A. The first was made on a vertical seam in the vessel and followed a procedure which was being considered as a possible method of repairing the cracked vessel seams.

A crack adjacent to the carbon-steel weld was ground out to a depth of approximately $\frac{1}{4}$ in.; total shell plate thickness was $1\frac{1}{4}$ in. The resultant groove was then repaired by the deposition of three beads of weld metal, each bead being inspected by Magnaflux. The alloy weld on the inside of the shell contained transverse cracks and this was then gouged out by metal-arc melting. In removing the alloy weld metal, the groove was flared out to a width of approximately 8 in. with a depth of about $\frac{1}{2}$ in. at the center.

The reason for this method of removing the alloy was a tentative suggestion that the vessel might be temporarily salvaged by repairing the cracks in the carbon steel and cutting out the cracked alloy welds without replacing them. The thickness of the backing material without the cladding was adequate for the operating conditions of pressure with metal temperatures reduced

by the addition of an internal insulating liner, and corrosion had not been found to be a factor.

It was observed that the carbon-steel welding on the outside caused the joint to move inward, radially, approximately $\frac{1}{8}$ in. in the 18-in. length of the repair weld. The melting of the alloy from the inside caused an additional $\frac{1}{8}$ in. of distortion. The bending appeared to take place within 12 in. of the joint and was presumed to be caused by residual stresses in the integral-clad shell.

A 12-in. \times 12-in. plate containing this repair weld was cut from the shell and sectioned for mechanical testing. Fig. 9 is a sketch of a cross section showing the relation of the repair weld to the original weld and also indicating the locations where cracks occurred during the bend tests. It may be noted that one crack system which was located underneath the repair weld coincides with the location of the far edge of the heat-affected zone of the original weld. The other crack system originated at the toe of the repair weld on the side removed from the original weld and extended to a depth of about $\frac{1}{4}$ in. in a direction perpendicular to the plate surface. The results of this preliminary test cast grave doubts on the possibility of repairing satisfactorily the cracks in graphitized plate.

Another test weld was made in plate cut from the reactor from which the alloy had been machined. No original weld metal was involved in this test plate. Mechanical tests cut from this second test weld were satisfactory, with reduced-section tensile bars showing strengths of about 47,500 psi and ductilities of about 43 per cent, with fractures in the base metal.

As mentioned previously, the amount of graphite found in the reactor of unit B was much less than that in the reactor of unit A. No difficulty was experienced in making test welds and in repairing the cracks in the carbon-steel base metal of this reactor. The reactor of unit C contained even less graphite, and here also there was no difficulty in making repair welds.

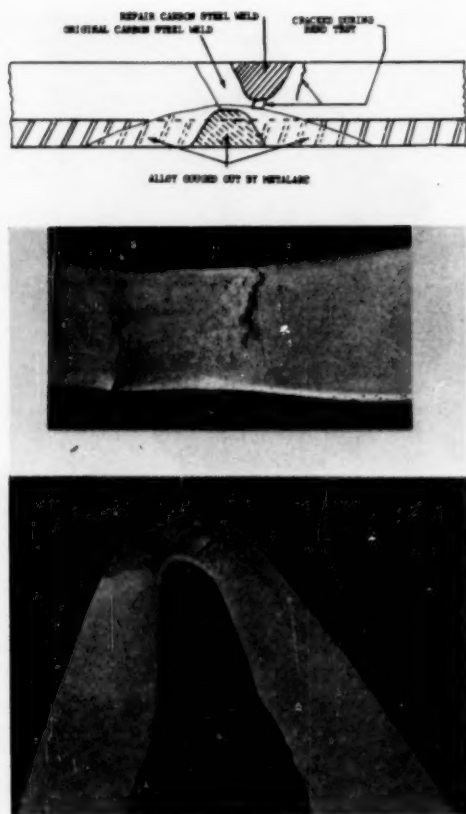


FIG. 9 REFINERY A—SKETCH AND PHOTOGRAPHS OF A TEST REPAIR WELD

The only other example of welding on a heavily graphitized carbon steel, related to the recent refinery-equipment investigations of which the authors are aware, was in the case of the recycle catalyst standpipes in unit K which were ASTM A106 seamless pipe. Large nodules of graphite, Fig. 10, were observed to be concentrated in the heat-affected zones and randomly dispersed throughout the base metal. A test weld joint was made on a sample section of the graphitized pipe, using a preheat temperature of 500 F and holding the preheat temperature as a postheat for 30 min after welding. The preheat and postheat conditions were chosen with the realization that the graphite nodules are potential carburizers, and when rapidly cooled from temperatures above about 1350 F can produce localized hard spots which also might initiate cracks. No difficulty was reported in making the test weld and visual inspection did not disclose cracks. Subsequently, 180-deg-bend tests, including both root and face bends, were made satisfactorily without evidence of crack failure. However, the outside surface of the bend at the maximum radius did show a myriad of superficial surface fissures which could not be accounted for on subsequent microscopic examination.

These standpipes have been rewelded by the same procedure

described for the test weld and replaced in service without any apparent difficulty.

Sample cross sections of the test weld joint were examined microscopically. Fig. 11 shows the effect of weld heat on the graphite. Each graphite particle in the heat-affected zone carburized the immediately surrounding metal matrix to produce a hypereutectoid zone around each. The structure of the former graphite nodules apparently has changed and micro-hardness examination reveals them to have a hardness on the order of 450 Vickers; the surrounding hypereutectoid zones showed a hardness of about 200-220 Vickers, which is consistent for the slow-cool following welding. The composition of the hard phase has not been established, although the microstructure resembles the cast-iron eutectic of ledeburite. It is not assured from this limited test that the hard particles may not effectively lower the mechanical strength of a weld joint; however, it appears to be probable that satisfactory weld repairs can be made, hard spots notwithstanding. This aspect of graphitization effects will receive further investigation.

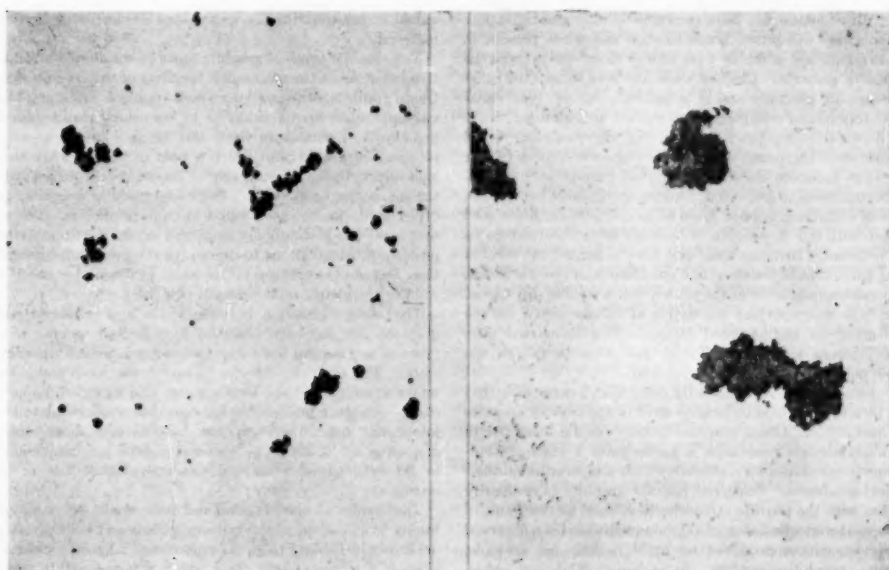
METALLURGICAL CONSIDERATIONS

Two major factors have been examined which may have promoted the cracks at weld joints in the carbon-steel base metal of the three integral-clad reactors. The first of these considers the possibility of operational stresses acting on the integral-clad material to produce failure in the carbon steel by the creep-to-rupture phenomenon. The crack pattern observed in almost every case is typical of this type of failure. The second is the graphitization of the carbon steel, which past experience in the power-piping field has demonstrated may seriously impair the load-carrying ability of weld joints and cause sudden failure. Although graphite does not appear to be a primary cause for the cracks in the three integral-clad reactors, the presence of concentrations of graphite in the areas of cracks in the unit A reactor and the impaired ductility shown in bend tests of welded joints containing concentrations of graphite suggest that graphitization may have contributed to failure to an indeterminate degree. For this reason, and with the view toward future selection of materials to resist graphitization it is pertinent to review the outstanding metallurgical considerations which have been developed by laboratory research and service experience on carbon and carbon-molybdenum steels.

Graphite may be expected to develop in carbon or carbon-molybdenum steels with long-time exposure at temperature ranging from about 850 to 1200 F. It is the result of decomposition of iron carbide (cementite) and is considered a nucleation and growth phenomenon. Its form is usually nodular and it occurs scattered in the matrix. However, in some operating equipment the graphite has been aligned or concentrated as "chains" which formed planes of weakness and in a few cases resulted in failures. It should be emphasized that the chain formations were localized in weld joint heat-affected zones only and were peculiar to operating equipment; attempts to duplicate these formations in the laboratory have been unsuccessful. Laboratory experimentation has succeeded in producing concentrations of nodular graphite but not the chain or eyebrow formations which were the cause of failure in steam piping.

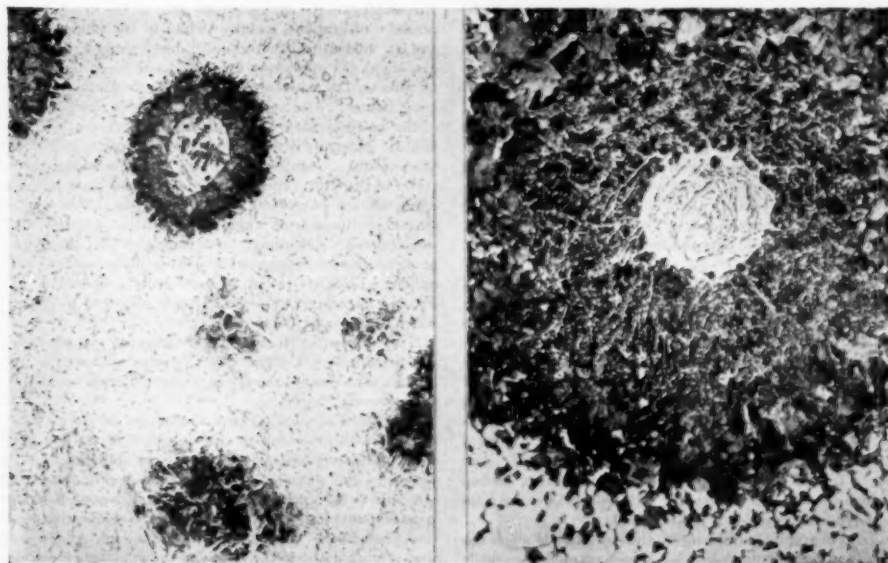
The potentiality of a steel, carbon or carbon-molybdenum, to graphitize at elevated temperature is dependent on such factors as composition, deoxidation practice, heat-treatment, and the effects of welding and working processes.

With respect to the effects of composition, carbon content influences both the amount of graphite and its rate of formation; thus the higher the carbon the greater is the amount of graphite. Manganese, phosphorus, sulphur, and silicon are not considered to have an influence in the normal amounts in which they occur in



X100 Picral etch X500

FIG. 10 REFINERY K-BASE METAL: SCATTERED NODULAR GRAPHITE



X100 Picral etch X500

FIG. 11 REFINERY K—AFFECTED GRAPHITE NODULES AS RESULT OF HEAT FROM REWELD, HEAT-AFFECTED ZONE

steels. Molybdenum has been shown to inhibit graphitization. Chromium also will retard graphitization and when present in sufficient quantities, probably 1 per cent or more, will prevent the formation of graphite. Limited work has been done with other carbide-forming elements and it is generally agreed that vanadium, titanium, and columbium also will act as inhibitors.

The deoxidation practice in steel melting, with particular regard for quantities of aluminum added, was recognized early as having the greatest influence on the potential of carbon and carbon-molybdenum steels to graphitize. Additions of about 1 lb per ton or more of aluminum tend to promote graphitization, while steel produced with 0.5 lb per ton or less has been observed to be highly resistant. Investigations also have indicated the level of residual aluminum in the steel, but not alumina, to be a reasonably dependable indication of the tendency of a steel to graphitize. Later it was observed that the degree of "abnormality" in the microstructure of the accepted McQuaid-Ehn carburized tests for the inherent grain size of steel also would establish the probable potential of a steel to graphitize.

The microstructure developed by prior heat-treatment of the steel is believed by some to be indicative of the type of graphite which may occur. Chain graphite usually can be identified in carbon-molybdenum steels with a coarse-grain Widmanstätten-like structure produced by a relatively high-temperature normalizing heat-treatment. Scattered nodular graphite is ordinarily associated with the pearlite structures developed as the result of low-temperature normalizing. In carbon steel it has been observed that microstructures produced by rapid cooling, for example, martensite, graphitize readily; in carbon-molybdenum steels, however, this structure is highly resistant.

Laboratory tests have not yielded clear results concerning the effects of welding on graphite formations. On the other hand, literally hundreds of service examinations which have been made by the power industry almost always have shown graphite to be located in the weld-heat-affected zone. The reason for the latter is not well understood. It is generally agreed, however, that the temperature gradient established during welding is probably a contributing factor, steep gradients causing more localized graphitization. The use of high preheat temperatures to avoid localized graphite has been suggested. It is of interest to note that graphite, except for one unexplained case, never has been found in weld metal. The relatively low carbon content of weld deposits is probably a reasonable explanation.

The influence of certain other fabrication procedures on graphitization is not entirely clear. The effects of hot-working, cold-working, and postweld heat-treatments have all been subject to limited investigation.

Hot-working as such does not appear to be a factor. Cold-working, on the other hand, is definitely suspected of promoting graphitization; important examples have shown graphite to be localized in "Lüders lines" in the macrostructure of steel which could be traced to fabrication strain. Accordingly, residual strain or stress also probably accelerates graphitization. Relatively high-temperature post-heat-treatments (1300 to 1400 F) for periods as long as 4 hr have been found in the case of carbon-molybdenum steels to inhibit graphitization; it is understood that the effect is to produce a more stable iron-molybdenum carbide. This practice has not, to the authors' knowledge, been employed for carbon steels, which would not be expected to be benefited since the form of iron-molybdenum carbide is not involved.

The effects of graphite on the mechanical behavior of steels has received attention in thousands of laboratory examinations made on weld-joint probe specimens. These examinations have consisted primarily of room-temperature miniature bend tests supplemented by microscopic examinations. Unfortunately, there is a dearth of data on elevated-temperature tests which would be

valuable in estimating the anticipated service life of graphitized material.

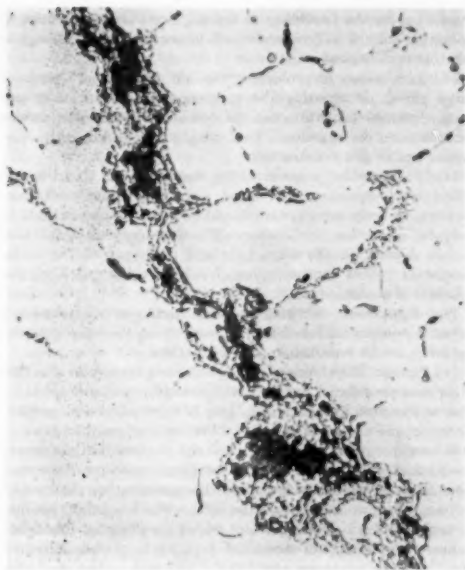
Two distinct types of graphite must be considered in their relative influence on the mechanical behavior of the graphitized steel. Chain graphite, or formations which approach chain graphite, invariably cause brittle behavior in room-temperature miniature bend tests—a miniature bend test being a thin cross-sectional specimen of a weld joint which is bent in two places so that the heat-affected zone on each side of the weld deposit is located at the maximum bend radius. Scattered nodular graphite, on the other hand, has not been found to impair ductility. The miniature bend test is commonly employed in periodic examinations of power pipe installations to determine the progress of graphitization, and serves as a basis for decisions as to whether or not to re-weld or completely replace steam-pipe lines.

The same distinction between chain and scattered nodular graphite also has been observed in a limited number of other types of mechanical tests which have been made on graphitized steels. For example, Charpy impact tests, room and elevated-temperature short-time tensile tests, and elevated-temperature stress-to-rupture tests all have shown that chain graphite at weld joints may impair seriously the ductility and shock resistance of a material; the effect of scattered nodular graphite seems only to be reflected in a lowered but insignificant loss in tensile strength.

The results of observations and tests made on samples obtained from certain of the refinery vessels and component parts are shown in Tables 1 to 5. The macro and microscopic characteristics of a representative crack which occurred within the heat-affected zone of a weld seam in the carbon-steel base material of the reactor at unit A is shown in Fig. 4. This crack propagated through about one third of the vessel wall and probably only in this respect is it different from the crack which caused the leak. Noteworthy is the intergranular path of the crack system, the presence of graphite nodules (white in the photomicrograph), and an unidentified intergranular black particle phase. Fig. 5 also shows the presence of the latter-mentioned phase located in an area on the same specimen apparently away from the open crack failure. Also notable is the somewhat marked orientation of the intergranular constituent relative to the path of the crack failure. Attempts to resolve this phase microscopically have been unsuccessful. Cognizant, however, of the potential carburizing power of graphite, a specimen containing this black intergranular phase was heated at 1550 F for 15 min. Fig. 12 shows this heat-treated specimen, from which it appears that a carburizing effect was attained. Accordingly, it is suggested that the black intergranular phase represents a high-carbon phase which behaves not unlike graphite in this test. Whatever its composition, the intergranular phase probably incorporated planes of weakness along which cracks could have propagated.

It is noteworthy that a similar structure was observed associated with a crack in the unit C reactor, although no graphite nodules were observed in the heat-affected zones (see Fig. 13 and compare with Fig. 5).

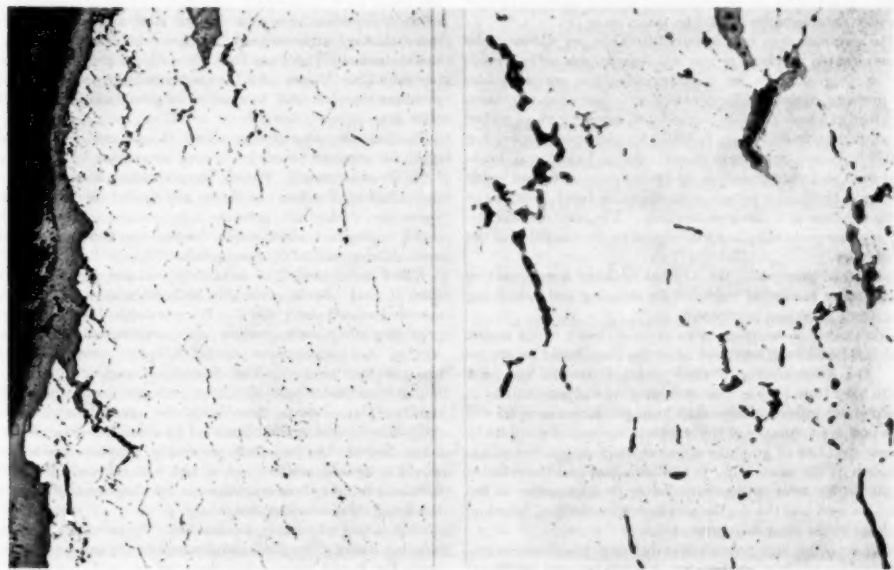
The results of routine chemical analyses are shown in Table 2, together with the results of analyses made for Al and Al_2O_3 contents. The compositions, exclusive of the aluminum data, do not vary from the normal expected for each steel analyzed. On the other hand, the aluminum content in certain cases indicates that large amounts may have been used in the steel-melting deoxidation procedures. In Table 4 the aluminum contents are repeated and related to the results of the miniature bend tests and microstructure observations. Noteworthy are the test results on samples from ASTM Specification A106 seamless pipe. Correlation between high aluminum content (0.020-0.025 per cent), the quantity of graphite observed, and the high degree of abnormality



X500 Picral etch

FIG. 12 REFINERY A—INTERGRANULAR PHASE; EFFECT OF 1550 F—15-MIN EXPOSURE (Reference Fig 4.)

Main crack



X100

Picral etch

X500

FIG. 13 REFINERY C—CRACK PATTERN OF HEAT-AFFECTED ZONE

in the McQuaid-Ehn test seems to be established. Relative to the level of aluminum contents which may promote graphitization, although a clear-cut maximum has not been established, it has been claimed that graphitization steels contain aluminum in amounts greater than 0.003 per cent. On this basis it appears that most of the steels examined are susceptible to graphitization.

The results of mechanical tests which were made to investigate the probable service behavior of equipment in which graphitization was evident and sample materials could be provided are shown in Tables 3 and 5. The average tensile strength of 28,000 psi at 950 F and the high-ductility results are in line with observations made concerning the probable effects of scattered nodular graphite on the mechanical properties. Also, the comparable room-temperature tests for this same material are consistent with the reported effect of scattered nodular graphite.

Shown in Table 5 are the results of mechanical tests which were made at unit A on reactor-plate sections including weld joints. Graphite was present in all the samples tested. The reported ultimate strengths and ductility are considered normal for low-carbon steel. The free-bend specimens made on welded joints show definitely that planes of weakness within the heat-affected zones were present in this vessel, even if only in localized areas.

Certain conclusions appear warranted, based on the foregoing history of graphitization as related to the experience of the power industry and the evidence presented in this paper for graphite occurrence in refinery equipment.

1 The damaging effects of graphite in refinery equipment to the degree experienced by the power industries is not obvious at this time.

2 Graphitization does not appear to be solely responsible for the cracks in three integral-clad reactors.

3 Added limitations on the use of carbon steels in refinery equipment appear unwarranted in view of the limited hazard of graphitization so far established.

4 As with any form of material instability, continued use of susceptible materials should be accompanied by service examinations to develop its progress and serve as a basis for rehabilitation considerations.

5 One fundamental gleaned from research on graphitization to date probably should be incorporated in future materials specifications with the view toward increased resistance to graphitization; that is, restrictions on the quantities of aluminum permitted for deoxidation purposes in steel melting would be justified.

6 It seems likely that the economics of large initial investments and early obsolescence relative to refinery equipment compared with the power industry would dictate that certain amounts of graphite can be tolerated. In this light, continued research should assess the effects of both "chain" and scattered nodular graphite on the load-carrying ability of carbon steel at elevated temperatures.

CONSIDERATIONS PERTAINING TO EXISTING AND PROJECTED PRESSURE EQUIPMENT

Existing Equipment. For carbon or carbon-moly steel in service above 850 and 900 F, respectively, the following precautions should be considered:

(a) All equipment operating at temperatures where there is continuous plastic flow with time should be inspected periodically for the possibility of cracking at welded seams and locations of stress concentration. The frequency and extent of inspection should be based on the severity of the operating conditions—temperature, pressure, thermal or mechanical shock, fatigue effects, and so on. Visual inspection should be supplemented by magnetic-particle examination in so far as practical, and any doubtful area should be ground to facilitate examination. Such inspection practice can be expected to give reasonable warning of any unsafe condition, whether due to graphite or other cause. If any cracking should be discovered, the examination should be extended and intensified, grinding where necessary and using magnetic-particle examination, and samples should be taken as in (b).

(b) For equipment in service over 30,000 hr, or where cracks have been located by visual or magnetic-powder inspection, weld-prober or plug samples for micro-examination are desirable. Where pressure equipment is operating well above the minimum temperature at which graphite might form, sampling at an earlier period would be advisable, say, 10,000 hr for carbon steel operating at 1000 F or more. Specimens should contain base metal, heat-affected zone and weld metal; weld-prober samples across welds are preferred since they permit miniature side-bend tests of the heat-affected zone as a check on ductility. The need for and frequency of subsequent sampling will depend on the condition of the initial samples.

As mentioned previously, the API has initiated a co-operative program among interested refineries for securing and examining samples from operating equipment.

The limitations of sampling as an accurate index of the status of graphitization in a given piece of equipment should be appreciated. The susceptibility of steel to graphitization has been known to vary from heat to heat and even over adjacent areas of a single plate or pipe so that freedom from graphite in samples will not give positive assurance of the complete absence of graphite or that concentrations of graphite may not be present. Sampling, nevertheless, is the most valuable available tool and the reliance to be placed on information obtained is proportionate to the variables present and the degree to which the selection, location, and number of the samples represent them.

(c) Where cracks, significant loss in ductility, heavy concentrations of nodular graphite, or chain graphite are present, additional specimens are desirable to assess their extent. Decision must be

reached as to the feasibility of repairs, and safety in continued operation subject to frequent check inspection and sampling, or whether replacement is desirable.

(d) As a means of prolonging the life of impaired vessels or large piping or arresting the progress of graphitization at any stage, internal insulation can be considered where the service permits such construction. Insulating concrete linings are discussed under new construction.

(e) Where welded joints involving materials with dissimilar coefficients of expansion operate at elevated temperatures, particularly in cyclic service, care should be taken to subject them to periodic inspection for cracks. The frequency of inspection should depend on the magnitude and frequency of the cyclic service as well as on the degree of difference between their coefficients of expansion.

New Equipment. For projected construction or replacement of pressure equipment the following suggestions are offered in the light of present knowledge of graphitization:

(a) *Piping:* The choice of piping materials for service over 850 F involves considerations of material strength, resistance to oxidation and corrosion, availability, ease of fabrication and possible alterations or repair, as well as stability against graphitization.

Where operating pressures are low and the possibility of severe mechanical shock or vibration effects are remote, carbon steel would seem to be justifiable choice. The use of carbon steel would be particularly appropriate for use in lines which normally operate at temperatures below 850 F but which are designed for higher temperatures because of occasional operation for periods of limited duration at temperatures over 850 F. Although carbon steel with unspecified deoxidation practice may be used, it would be desirable to obtain, where possible, steel which is melted with controlled deoxidation practice as indicated in (c).

For service considered to be more critical as a result of high pressures, shock or fatigue effects, possible overloads, inaccessibility, and so on, the use of an alloy steel is justified. Except for improved high-temperature strength, carbon-molybdenum steel offers little advantage over carbon steel and, in view of the unsatisfactory experience in the power industry, its use is not recommended. The 1 per cent Cr - $\frac{1}{2}$ per cent Mo or the $1\frac{1}{2}$ per cent Cr - $\frac{1}{2}$ per cent Mo steel provides good elevated-temperature strength and immunity to graphitization to at least 1050 F.

For large-diameter piping, above 30 in. diam., the suggestions given for pressure vessels in (b) may be applied.

(b) *Pressure vessels:* Three alternatives may be examined. For individual applications the choice will depend on the influence of vessel size, desired life, pressure, temperature, degree of cyclic or shock loading, service, necessity for field erection and alterations, maintenance, and relative economics.

Killed carbon steel: For metal temperatures over 850 F carbon steel, if used, should preferably be low-aluminum-deoxidized as specified subsequently in (d). Its use should be on the basis of providing adequate inspection and metallurgical examination in service. For temperatures over 900 F, design provisions should be incorporated in the inside dimensions, supporting steel and foundations for a possible future internal insulation. Should significant graphite be discovered, the internal lining could be economically and readily installed to arrest its progress at any stage desired. As indicated previously, graphite in base metal would be of little concern but on any indication of a tendency to form and build up concentrations in the weld-heat-affected zones the lining should be installed.

Carbon steel with internal insulation: By providing internal insulation initially the shell-metal temperature can be maintained below 800 F with internal flow temperatures well above this. The type of steel used and the deoxidation practice is not important

from considerations of graphitization unless overheating occurs due to loss or ineffectiveness of insulation. This should be guarded against by special attention to insulation choice and details and by providing a reasonable margin between expected metal temperature and actual design metal temperature. With design metal temperature of 650 F, which permits full use of the material strength, the metal weight saving will often offset the cost of the liner, and for higher flow temperatures (over 900 F) and larger-size vessels, the relative cost is in favor of internally insulated construction.

Graphitization-resistant steel: It is indicated that $1/2$ per cent Cr - $1/2$ per cent Mo, and 1 per cent Cr - $1/2$ per cent Mo steels are resistant to graphitization up to 950 F and 1050 F, respectively, and are presently the most economic choice of resistant materials. Both are slightly air-hardening, the former comparable to carbon-moly steel, and are commonly considered to require preheat to 400 F and thermal stress relief. Tests and fabrication experience in the Jersey City plant of the authors' company indicate that underbead cracking is effectively eliminated by the use of low-hydrogen electrodes so that welds in low-carbon (about 0.08 per cent C) 1 per cent Cr - $1/2$ per cent Mo steel can be made safely with preheat reduced to 200 F, with no postheat necessary to reduce hardness or obtain desirable ductility. These elements are not very significant on shop-constructed pressure vessels where the higher preheat and stress relief can be provided without great difficulty, and are still advised; however, for field fabrication involving position welding and limited experience of local welders with low-hydrogen electrodes, a simple procedure which is not too sensitive to variations in preheat and postheat is practically essential. Even so, unsuspected difficulties and excessive repairs might be encountered on initial field installations which might compromise fabrication economics and safe construction. An example is the unexpected root cracking cited by A. H. Goodger⁴ in trying to use low hydrogen electrodes in welding 1 per cent Cr - $1/2$ per cent Mo pipe.

As yet, no known installations of 1 per cent Cr - $1/2$ per cent Mo steel pressure vessels have been field-fabricated; however, it is understood that one vessel is scheduled for construction with carbon content probably around 0.12 per cent. It remains to determine whether this carbon content will be found practical under field conditions. With either shop or field fabrication, radiographic examination would be considered essential and stress relief desirable even though limited to 900 F. A serious drawback under present conditions is the procurement problem, since ingots are not available and amounts less than full heats are subject to parallel orders for scheduling, which can cause serious delay and expense.

(c) Specification requirements: For high-temperature service (over 850 F) all carbon-steel material (plate, forgings, castings, tubing, pipe, shapes, and so on) should be produced from steel melted in accordance with a deoxidation practice restricted to the use of $1/2$ lb of aluminum per ton maximum. Further, the material should have a coarse grain size and be free of abnormality on McQuaid-Ehn carburization test.

(d) Insulation liners: Internal insulation has been employed extensively over many years in high-temperature equipment. With adequate design, materials, fabrication, and inspection, linings have been satisfactory. Large-diameter fluid-catalyst regenerators lined with panels of gunite-applied insulating concrete with a surface of refractory concrete reinforced with steel grating and supported at frequent intervals to the vessel shell by welding studs have given maintenance-free service for over 5 years. Similar linings have been used and are being specified for reactors in fluid-catalyst cracking units. Insulating concrete

linings with aggregate selected for structural strength and without surface reinforcement have been used in regenerators; they involve lower first cost, but are more likely to involve extensive maintenance. In reactor service the insulation will be infiltrated by coke which will raise its thermal conductivity, requiring proper allowance in design; this may cause cracking or spalling unless the surface is suitably retained. It is highly desirable to omit external insulation, thus exposing the exterior to observation for evidence of overheating or deterioration. Vessels having both inside and outside insulation are much more sensitive to overheating owing to deterioration or ineffectiveness of the internal insulation.

Internal insulation may lower the inside steel shell temperature below the dew point of the flowing medium; also condensate may be retained during shutdowns unless lengthy drying out with non-condensable vapor is exercised. While ganister concrete linings have been reasonably effective against corrosion in thermal cracking, such installations were provided with external insulation and the dense concrete, aided by coke, probably sealed off the shell surface. It is possible that cement wash from the insulating concrete will serve as reasonable protection; on the other hand, porous aggregate may penetrate to the metal, providing paths for liquid flow. It may be advisable to protect the metal shell against condensation by a thin first coat of dense concrete, a cement wash, two coats of acid-resistant high-temperature paint, or a silicate-of-soda wash, or similar treatment.

(e) Dissimilar metal weldments: For elevated-temperature cyclic service it is advisable to avoid wherever possible the use of welded joints involving austenitic and ferritic steels. This is not always possible since many times carbon-steel vessels must be provided with stainless liners for corrosion resistance. Where lined vessels with composite welds operate in cyclic service, provision should be made for periodic inspection of all main seams.

ACKNOWLEDGMENTS

Grateful acknowledgment is made to those companies who have made available the samples and data on which this paper is based; also to the Timken Roller Bearing Company and General Electric Company, who helped by making the aluminum and alumina determinations.

Particular credit is given to Mr. Howard Richards of the Metallurgical Laboratory of the M. W. Kellogg Company, who prepared the photomicrographs and performed most of the mechanical tests reported herein. Credit is also given to Mr. H. S. Blumberg, Chief Metallurgist of the M. W. Kellogg Company, whose advice and helpful criticism have been appreciated.

Appendix

NOMENCLATURE

The following nomenclature is used in the Appendix:

- α = mean coefficient of thermal expansion from 70 F to operating temperature (in./in./deg F)
- A = constant in creep equation
- B = per cent cladding thickness (expressed as decimal)
- Δ = radial displacement, in.
- e = unit elongation, in./in.
- E = modulus of elasticity, psi
- M = internal longitudinal bending moment (in.-lb per in. circumference) at weld
- n, m = exponents in creep equation
- ν = Poisson's ratio
- P = internal pressure, psi
- R = mean radius, in.

⁴ "Heat Treatment Welds in Pipelines," by A. H. Goodger, *Engineering*, vol. 172, July 27, 1951, pp. 125-127.

S = stress psi
 t = thickness (in.); t_r — relaxation time (hr)
 T = temperature rise, deg F
 V = radial shear (lb per in. circumference) at weld
 w = width of weld, in.

Subscripts:

b = base metal
 c = cladding
 h = hoop (circumferential) stress
 L = longitudinal stress
 w = weld metal

TEMPERATURE STRESSES—CLAD PLATE—THIN CYLINDER

The unit thermal expansion, if unrestrained, is

$$\alpha_b T \text{ for base metal} \\ \alpha_c T \text{ for cladding}$$

When a clad plate is in cylindrical form there is biaxial restraint to free expansion. Temperature stresses will be equal in the longitudinal and circumferential directions. Let ϵ_b and ϵ_c be the elastic unit strain caused by stress. Then for equality of strains between the base metal and cladding (radial stress assumed negligible, which is true for a thin cylinder)

$$\alpha_b T + \epsilon_b = \alpha_c T + \epsilon_c$$

Now

$$\epsilon_b = \frac{S_b(1-\nu)}{E_b}, \quad \epsilon_c = \frac{S_c(1-\nu)}{E_c}$$

Hence

$$\alpha_b T + \frac{S_b(1-\nu)}{E_b} = \alpha_c T + \frac{S_c(1-\nu)}{E_c} \quad [1]$$

Since there must be equilibrium of internal forces, the forces in base metal and cladding for unit width must balance, Fig. 14.

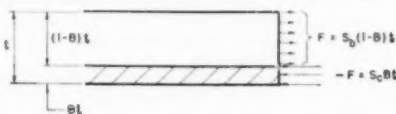


FIG. 14

Hence

$$-S_c B t = S_b(1-B)t; \quad S_c = -\left[\frac{(1-B)}{B}\right] S_b$$

Substitution in Equation [1] gives

$$\alpha_b T + \frac{(1-\nu)S_b}{E_b} = \alpha_c T + (1-\nu)\left[\frac{B-1}{B}\right] \frac{S_b}{E_c}$$

from which

$$S_b = \frac{(\alpha_c - \alpha_b)TE_b}{1-\nu} \left[\frac{B}{B + \frac{E_b}{E_c}(1-B)} \right] \quad [2]$$

and

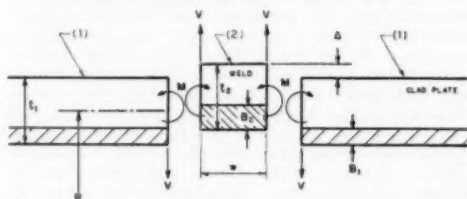
$$S_c = -\frac{(\alpha_c - \alpha_b)TE_b}{1-\nu} \left[\frac{1-B}{B + \frac{E_b}{E_c}(1-B)} \right] \quad [3]$$

where positive sign indicates tensile stress.

LOCAL TEMPERATURE STRESS AT WELDED CIRCUMFERENTIAL JOINT IN CLAD PLATE DUE TO ALLOY WELD DEPTH BEING GREATER THAN THE CLADDING AND ALSO BEING OF DIFFERENT ANALYSIS

This local effect can only be approximated. The following approximation can be made for a girth weld in a cylinder. It would be expected that local effects at a longitudinal weld would be about the same:

In Fig. 15, part (1) represents the clad plate and part (2) represents the weld. The internal thermal stresses in parts (1) and (2), exclusive of local effects, can be obtained by applying Equations [2] and [3]. The local discontinuity stresses can be determined by evaluating the shear and moment induced at the junction by the differential radial deflection Δ between the two parts.



NOTES: Shear and moment assumed positive when in direction shown.

w is assumed sufficiently small that shear V and moment M may be assumed constant over the weld width.

FIG. 15 LOCAL TEMPERATURE STRESS AT WELDED CIRCUMFERENTIAL JOINT IN INTEGRAL-CLAD PLATE

Radial extension due to temperature and stress of part (1) (away from weld) is given by

$$\Delta_1 = \alpha_b RT + (1-\nu) \frac{S_b R}{E_b} \\ = \alpha_b RT + (\alpha_c - \alpha_b) RT \left[\frac{B_1}{B_1 + \frac{E_b}{E_c}(1-B_1)} \right]$$

and similarly for part (2), if free, the radial extension would be

$$\Delta_2 = \alpha_c RT + (\alpha_w - \alpha_b) RT \left[\frac{B_2}{B_2 + \frac{E_b}{E_w}(1-B_2)} \right]$$

The differential radial displacement is

$$\Delta = \Delta_2 - \Delta_1 \quad [4]$$

Let Δ_3 = deflection of part (1) due to the induced shear V and moment M at the junction⁷

$$\Delta_3 = \frac{-VR^2\lambda}{E_b t_1}$$

where

$$\lambda = \frac{1.285}{\sqrt{Rt_1}}$$

Note that modulus of elasticity of base metal and cladding are assumed equal.

⁷ "Formulas of Stress and Strain," by R. J. Roark, McGraw-Hill Book Company, Inc., New York, N. Y., 1943, case 8, table 13.

Let Δ_2 = deflection of part (2)

$$\Delta_2 = \frac{2VR^2}{E_2 l_2 w}$$

For equal net deflection at the junction

$$\Delta_1 + \Delta_2 = \Delta_2 + \Delta_1 \text{ or } \Delta_2 - \Delta_1 = \Delta_2 - \Delta_1 = \Delta$$

$$-\frac{VR^2}{E_1 l_1} - \frac{2VR^2}{E_2 l_2 w} = \Delta$$

from which

$$V = \frac{-E_2 \Delta}{R^2} \left(\frac{l_1 l_2 w}{2l_1 + l_2 w} \right) \quad [5]$$

From Roark's formulas²

$$M = \frac{V}{2\lambda}$$

and stresses due to discontinuity effects at the junction become (upper sign applies to outer fiber; + denotes tension)

Longitudinal bending stress in part (1)

$$S_{L1} = \mp \frac{6M}{l_1^3} = \mp \frac{3V}{\lambda l_1^3} \quad [6]$$

Longitudinal bending stress in part (2)

$$S_{L2} = \mp \frac{6M}{l_2^3} = \mp \frac{3V}{\lambda l_2^3} \quad [7]$$

Hoop stress in part (1)

$$S_{M1} = -\frac{VR\lambda}{l_1} - \nu S_{L1} \quad [8]$$

Hoop stress in part (2)

$$S_{M2} = \frac{2VR}{l_2 w} - \nu S_{L2} \quad [9]$$

These stresses may be superimposed on those calculated from Equations [2] and [3] to obtain the total stress.

RELAXATION OF THERMAL STRESS DUE TO CREEP WITH TIME AT TEMPERATURE IN PRESENCE OF PRESSURE STRESS

Relaxation of thermal stress will occur due to creep in both the base metal and the alloy cladding, one being tensile and the other compressive creep. An evaluation of the simultaneous creep of the two materials proved too complex. Therefore in the following development the relaxation is assumed to occur entirely in the base metal and the pressure and thermal stresses are assumed to be of the same sign; ϵ'_0 and ϵ' are taken as the sum of thermal elastic strains in both the base metal and alloy. The relaxation time indicated is therefore too long. If the relation between the amount of creep which occurs in the alloy and base metal can be approximated, a closer approximation can be made by reducing ϵ'_0 accordingly. Let

ϵ'_0 = initial locked-up elastic strain at time $t = 0$

ϵ' = residual locked-up elastic strain at any time t

S_0 = initial thermal stress in the base metal at time $t = 0$ (bi-axial)

S_p = pressure stress (based on assumed uniformity over cross section)

S = total stress at any time t , in base metal

$$\epsilon'_0 = (S_0 + S_p + S_0 - S_p) \frac{(1-\nu)}{E} = (S_0 + S_p) \frac{(1-\nu)}{E}$$

and since $S_p = S_0(1-B)/B$ (absolute value)

$$\epsilon'_0 = \frac{S_0(1-\nu)}{BE} \quad [10]$$

$$\epsilon' = \left(S + (S - S_p) \frac{(1-B)}{B} - S_p \right) \frac{(1-\nu)}{E} = \frac{(S - S_p)(1-\nu)}{BE} \quad [11]$$

From Equations [10] and [11]

$$\epsilon' = \frac{S - S_p}{S_0} \epsilon'_0$$

The amount of plastic relaxation is given by

$$\epsilon = \epsilon'_0 - \epsilon'$$

Hence

$$\epsilon + \epsilon'_0 \left(\frac{S - S_p}{S_0} - 1 \right) = 0$$

Differentiating gives

$$\frac{d\epsilon}{dt} + \left(\frac{\epsilon'_0}{S_0} \right) \frac{dS}{dt} = 0$$

and if $(d\epsilon)/(dt) = AS^n$ in accordance with the usual assumed empirical creep relation

$$AS^n + \left(\frac{\epsilon'_0}{S_0} \right) \frac{dS}{dt} = 0$$

Substitution for ϵ'_0 from Equation [10] and rearranging gives

$$\frac{dt}{t} = -\frac{(1-\nu)}{BEA} \frac{dS}{S^n}$$

$$t_r = \int_0^{t_r} \frac{dt}{t} = -\frac{(1-\nu)}{BEA} \int_{S_0+S_p}^S \frac{dS}{S^n}$$

from which

$$t_r = \frac{(1-\nu)}{(n-1)BEAS^{n-1}} \left[1 - \left(\frac{S}{S_0+S_p} \right)^{n-1} \right] \quad [12]$$

DIVISION OF INTERNAL PRESSURE LOAD BETWEEN CLADDING AND BASE METAL UNDER STEADY-STATE CREEP CONDITIONS AFTER THERMAL STRESSES HAVE RELAXED TO ZERO

The pressure stress in the cladding and base metal must produce equal rates of creep in each. If $A_b(S_b)^n$ and $A_s(S_s)^n$ express the creep rates in base metal and cladding, respectively, then

$$A_b(S_b)^n = A_s(S_s)^n; S_b = \left(\frac{A_s}{A_b} \right)^{1/n} S_s^{n/n} \quad [13]$$

Now for a cylinder under internal pressure and stress in the circumferential direction

$$S_b(1-B) + S_s B = \frac{PR}{t}$$

$$S_b = \frac{\frac{PR}{t} - S_s B}{1-B} \quad [14]$$

Equations [13] and [14] give

$$\frac{PR}{t} - S_b B = (1 - B) \left(\frac{A_2}{A_1} \right)^{1/n} S_a^{m/n} \quad [15]$$

from which S_a can be determined by trial.

The percentage of the total load carried by the base metal is given by

$$100 S_b (1 - B) \left(\frac{t}{PR} \right) \quad [16]$$

and the percentage carried by the cladding is

$$100 S_b B \frac{t}{PR} \quad [17]$$

Discussion

H. F. BROWN, J. S. CLARKE, F. J. FEELY, JR., R. H. MAASS, AND M. S. NORTHUP.⁸ The background of failures in bimetallic reactors and a discussion of the possible causes have been presented by representatives of the M. W. Kellogg Company. This discussion summarizes the views of the Standard Oil Development Company as to the most likely various possible causes.

In the investigation of these failures, the authors' company and that of the writers have independently explored all of the conceivable causes of failure. It is felt that certain ones can be reasonably eliminated. For instance, none of the many weld sections from these reactors had weld defects of a nature contributing to the observed failures. We agree with the paper on the type of structural changes which occurred, namely, spheroidization and nodular graphitization of the carbon steel. Particularly, we agree with the statement, "graphitization does not appear to be solely responsible for the cracks." In fact, cracks occurred in the carbon steel of one of the three reactors where graphitization was not found.

All investigators are agreed that the cracking of the carbon steel is typical of stress rupture, i.e., intergranular cracking re-

sulting from stress at elevated temperature. Since stress rupture occurred, any plausible analysis must provide for the possibility of failure in the time these vessels were in service.

Certain facts of the reactor failures point to the conclusion that rather large stresses were present. Primarily, the nature of the failure has been identified as typical of rupture due to stress operating at elevated temperature. Next, the failures occurred in both the circumferential and longitudinal seams, a circumstance that indicates stresses from some source other than internal pressure. Finally, the observed ruptures do not appear to be associated with piping or supports and cannot be explained by assuming such effects.

Both the Kellogg and S. O. D. parallel calculations show the probability of tensile stresses in the carbon steel of from 6000 to 20,000 psi resulting from the differential expansion of the bimetallic plate on initial heating. This variation is over the range of 10 to 50 per cent cladding thickness as actually observed. Calculation of the relaxation of these stresses indicates that thermal effects are the most logical source of stresses leading to the observed failures.

For one explanation leading to results not at variance with the observed failures, we refer to Fig. 16 of this discussion. In this figure the following information is given:

1 The range of stress to produce elevated-temperature stress rupture in low-carbon steel at 920 F, based on information given in the Miller-Heger report on "The Strength of Wrought Steels at Elevated Temperatures."

2 Stress-rupture data for killed carbon steel at 920 F, extrapolated from information contained in the Timken "Digest of Steels for High Temperature Service." This steel is believed to compare with that used in the reactors.

3 The limits of stress relaxation from an initial stress of 20,000 psi at 920 F, as calculated from creep-rate data given in the Miller-Heger report.

4 Stress relaxation from an initial stress of 20,000 psi at 920 F, based on creep data from the Timken Digest.

The temperature of 920 F was selected as a basis for stress calculations as it appears to be representative of the average metal

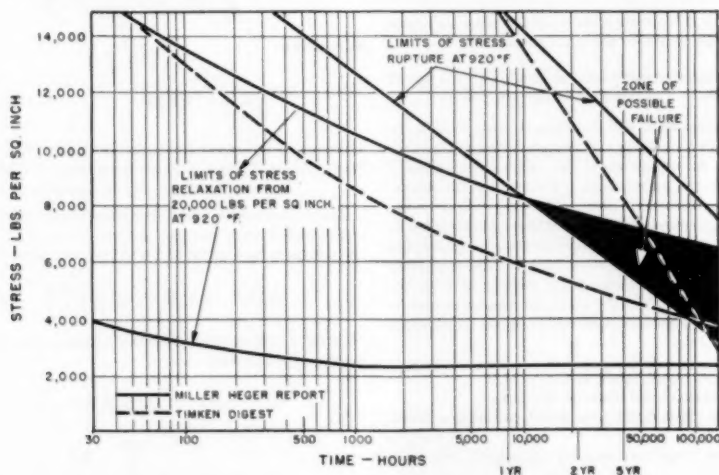


FIG. 16 STRESS-RELAXATION AND STRESS-RUPTURE CURVES LOW-CARBON STEEL

⁸ Standard Oil Development Co., Linden, N. J.

temperature of the reactors at units A, B, and C, where failures of the vessels occurred.

The stress-relaxation curves were calculated from the initial thermal stress caused by the differential thermal expansion of a bimetallic plate with 50 per cent cladding thickness, but neglecting the effect of the alloy cladding on stress relaxation. From this plot it is seen that the zone of possible failure begins at about 10,000 hr, with the time of most probable failure at approximately 100,000 hr. While this is a rough check on the observed failures, which occurred after about 60,000 hr, if the effect of the alloy cladding on relaxation is considered, the residual stress at any given time is somewhat higher.

Referring to Fig. 17 of this discussion, there is plotted the following:

1 Stress rupture of killed carbon steel at 920 F, based on Timken data.

2 A family of curves showing relaxation of the initial stress in the carbon-steel base metal with thickness of cladding varying from 10 to 50 per cent. These relaxation stresses are based on Timken creep data interpolated for 920 F. The 10 per cent curve is dotted because actually the alloy cladding will be plastically deformed and the stress in the carbon steel will be reduced accordingly.

The stress-relaxation curves were calculated from the equation shown. In deriving this equation, it was realized that the elongation of the base metal must equal the elongation of the cladding. The deformation of the base metal is the sum of the thermal expansion, the elastic tensile deflection, and the tensile creep. The total deformation of the cladding is its thermal expansion minus the elastic compressive deflection and minus the compressive creep.

These terms may be expressed as follows: Deformation of base metal is

$$\alpha_1 \Delta T + \frac{\sigma_1 l}{E_1} + \Sigma a_1 \Delta t \times 10^{-6} \quad [18]$$

Deformation of cladding is

$$\alpha_2 \Delta T - \frac{\sigma_2 l}{E_2} - \Sigma a_2 \Delta t \times 10^{-6} \quad [19]$$

where

α_1 = coefficient of thermal expansion of base metal, in/in/deg F

α_2 = coefficient of thermal expansion of cladding, in/in/deg F

l = unit length, in.

ΔT = temperature of bimetallic plate minus atmospheric temperature, deg F

σ_1 = instantaneous thermal stress in base metal, psi

σ_2 = instantaneous thermal stress in cladding, psi

E_1 = Young's modulus of base metal at temperature T , psi

E_2 = Young's modulus of cladding at temperature T , psi

a_1 = creep rate of base metal, per cent per 1000 hr at temperature T , in./in./hr

a_2 = creep rate of cladding in per cent per 1000 hr at temperature T , in./in./hr

Δt = incremental time, hr

Since the deformations are equal, then

$$\alpha_1 \Delta T + \frac{\sigma_1 l}{E_1} + \Sigma a_1 \Delta t \times 10^{-6} = \alpha_2 \Delta T - \frac{\sigma_2 l}{E_2} - \Sigma a_2 \Delta t \times 10^{-6} \quad [20]$$

For the particular case in question where the cladding represents an appreciable portion of total thickness, the term $\Sigma a_2 \Delta t \times 10^{-6}$ has been neglected since the creep rate in the cladding at 920 F is negligible compared to that of the carbon steel.

Now, since the force in the base metal must equal the force in the cladding to satisfy equilibrium, then

$$F_1 = F_2 = \sigma_1 A_1 h = \sigma_2 A_2 h \quad [21]$$

and

$$\sigma_2 = \sigma_1 \frac{A_1}{A_2} \quad [22]$$

where

A_1 = per cent thickness of base metal

A_2 = per cent thickness of cladding

h = thickness of bimetallic plate

Then, substituting for σ_2 , dividing by l , and rearranging, we have

$$\sigma_1 = \frac{(\alpha_2 - \alpha_1) \Delta T - \Sigma a_1 \Delta t \times 10^{-6}}{\left[\frac{1}{E_1} + \frac{A_1}{A_2 E_2} \right]} \quad [23]$$

The circumferential pressure stress can be expressed as

$$\sigma_p = \frac{PD}{2h} \quad [24]$$

where

P = internal pressure, psi

D = mean diameter, in.

For the bimetallic reactors of units A, B, and C, the instantaneous stress in the carbon-steel base metal σ_b , and in the 18 per cent Cr-8 per cent Ni cladding σ_c , can be calculated from the following equations

$$\sigma_b = \frac{[167.5 - \Sigma a_1 \Delta t] 100}{[0.495 + 0.427 A_1/A_2]} + 2200 \quad [25]$$

$$\sigma_c = \frac{[167.5 - \Sigma a_1 \Delta t] 100}{[0.427 + 0.495 A_2/A_1]} - 2200 \quad [26]$$

when

$T = 850$ F

$\alpha_1 = 7.96 \times 10^{-6}$ in/in/deg F

$\alpha_2 = 9.93 \times 10^{-6}$ in/in/deg F

$E_1 = 20.2 \times 10^6$ psi

$E_2 = 23.4 \times 10^6$ psi

$P = 22$ psi

$D = 23$ ft

$h = 1.375$ in.

The initial instantaneous stress in the carbon steel and alloy at various cladding thicknesses upon heating to 920 F are listed as follows:

Per cent cladding	Stress, psi	
	CS	Alloy
50	20400	16000
40	17000	20000
30	13400	24000
20	9800	28200
10	6100	32500

The variable term in Equation [23] of this discussion is the summation of creep in carbon steel over short increments of time

with relaxation stresses being calculated by mechanical integration. For example, with 50 per cent cladding and an initial total stress of 20,400 psi, the creep rate is 1.5×10^{-6} in. per in. In 10 hr the elongation at this rate is 1.5×10^{-5} in. per in., indicating relaxation of the stress to 18,000 psi. The creep rate at this stress is 0.9 per cent per 1000 hr. The stress relaxation for subsequent intervals may be calculated similarly.

The calculated stress-relaxation curves for 30 and 50 per cent cladding intersects the Timken stress-rupture curve for killed carbon steel at 80,000 and 90,000 hr, respectively, Fig. 17. Actual failures occurred at approximately 60,000 hr. The shorter time is directionally correct because of other factors which tend to increase these stresses. Also, it is within the range of expected accuracy for the calculation basis employed. In our calculations we made certain simplifying assumptions such as neglecting the effect of operating temperature fluctuation, periodic return to atmospheric temperature, and stress concentrations. It was assumed also that creep in the thicker alloy cladding (30 to 50 per cent) was negligible. Some of these factors may have increased and others reduced the stresses. For instance, the effect of the periodic return of the vessels to atmospheric temperature is not clear inasmuch as the extent of cracking on unit A, which experienced 26 plant shutdowns, was approximately the same as that of units B and C, which were subjected to only 11 shutdowns. In our opinion, the simplifications we have made do not alter the fact that the stresses in these vessels were above tolerable limits. Also, the stress-rupture curve is based on application of a constant stress. In the case of the relaxation curves, the stresses have been at higher levels and failure should occur somewhat prior to the times indicated.

While these calculations have been based on plain bimetallic material, there are several factors that cause stress concentration near the welds. The effects of these stress raisers are indeterminable but explain why failure may be expected at the welds. Some of these factors are as follows:

- 1 Local flattening of the plates at the welds resulting from forming and welding shrinkage.
- 2 The effects of a reinforcing bead such as remained on the reactor of unit A and/or undercutting.

3 The effect of an abrupt change in alloy depth where plates of different cladding thickness adjoin with the resultant wedge action of the alloy weld as shown in Fig. 18 which shows a section through a trepanned plug from unit A.

The effect of such concentrations of stress would either maintain the stress at higher levels or use up the total elongation before failure at the localized regions of the welds. It may be concluded, therefore, that the region of the welds provided the most probable location of failure due to stress application.

It is our opinion that these reactors failed primarily because of continuing stresses of unforeseen magnitude resulting from the thermal expansion difference of the thickly clad bimetallic plate of carbon and austenitic steels.

From the metallurgical standpoint, we are not overly con-



FIG. 18 SECTION SHOWING DEPTH OF ALLOY WELD

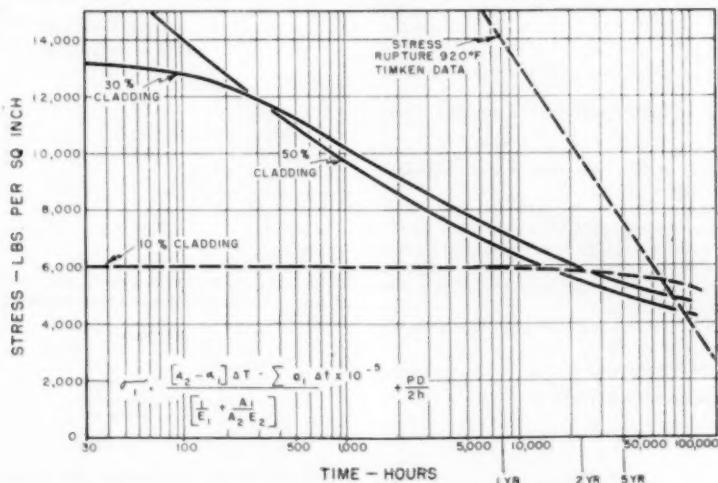


FIG. 17 STRESS-RELAXATION OF CARBON-STEEL BASE METAL IN BIMETALLIC PLATE

cerned by the effects of spheroidization and nodular graphitization of the carbon steel such as used in these reactors at these temperatures. We do plan, however, to follow the effect of temperature on the structure of carbon-steel vessels now in service.

The writers wish to make the following acknowledgments: To the M. W. Kellogg Company for assistance in evaluating the failures of the bimetallic reactors and on determining the disposition of these vessels. To Prof. J. P. den Hartog of the Massachusetts Institute of Technology, for his review of the stress analysis and for his helpful suggestions in preparing this discussion.

M. A. SCHEIL² AND R. A. HUSEBY.³ The examinations and conclusions reported by the authors in this paper are of great interest to us since the writers' company fabricates reactors with applied linings. The performance of mild-steel and stainless-lined equipment in cyclic thermal service has been followed by our staff since the first welded equipment was furnished to the industry.

At this time we would like to contribute some data on welds which have a bearing on cyclic thermal service. Physical properties of welded joints are commonly available; however, it is not generally appreciated that a wide range in yield strength can be set up between weld and plate under certain conditions, even though welding is done with comparable electrodes. In Table 12 of this discussion, data on the properties of stress-relieved all-weld standard 0.505-in. round tensile specimens tested at room temperature and 900 F are given with average properties of mild steel and Type 347 plate added for comparison. Specimens were taken from two full penetration welded joints made in 1 1/2-in.-thick ASTM A-201 Grade A stock which were welded from one side with mild-steel electrodes, then turned over, root pass chipped out, and completed with stainless electrodes.

Dilution of the stainless-steel deposit was held to a minimum by butting the scarfed edge of the stainless-steel portion of the weld with the same stainless electrode. The welded plates were furnace-stress-relieved at 1000 F for 2 hr and furnace-cooled at 150 F maximum per hr. Standard 0.505 in. all-weld tensiles were prepared from each deposit and tested at room temperature and at 900 F. All tests were made using a Peters' high-temperature extensometer and Southwark-Templin automatic strain-recording equipment. The class E-6030 electrode used represents a good shop electrode for positioned welding of heavy plate while the E-6013 is a universal a-c-d c-all-position electrode very popular for field work.

The significant point in Table 12 is the yield-strength value of the weld as compared to the yield strength of the base plate. The average value of 42,000-psi yield strength at room temperature and 20,000-psi yield strength at 900 F, given by ASTM for the ASTM A201 steel, represents the average in a range of 0.08 to 0.30 per cent carbon. The minimum yield strengths of 34,000

psi at room temperature and 16,500 psi at 900 F, taken from the same ASTM source, are probably more applicable to the yield strength of the backing material from the clad plates. In fact, the authors, in Table 7, report 46,000 to 48,000-psi ultimate strength and 25,000 to 26,000-psi yield strength at room temperature for the backing material of reactor A with a carbon content ranging from 0.04 per cent to 0.10 per cent. In the same table data for the welds are given but from the remark that fracture took place in the base metal we judge these to be joint specimens.

If in operation thermal stresses of yield-point magnitude are set up due to uneven heating or due to dissimilar coefficients of expansion a fairly sharp stress gradient may exist between weld and adjacent plate. This condition as regards dissimilar coefficient of expansion will be aggravated as the depth of alloy weld deposit is increased. Plastic strain of the base material would also tend to concentrate near the weld junction. We feel that the fissuring and possibly the graphite concentration, shown by the authors in their Fig. 4, may be a result of these dissimilar yield strengths. While we have no data to support the statement it seems likely that creep rates follow the same general pattern which would mean that somewhat the same conditions would apply during steady-state operation.

The authors have made a very detailed study of the problem but the difference in yield-strength properties may not be fully appreciated and we have submitted these data for their consideration.

V. A. STANTON, JR.¹⁰ The conclusion that graphitization does not appear to be solely responsible for the failure of three reactors is well substantiated.

We have had an opportunity to examine sections of the shell, conical head, and torus ring of one of the cracked vessels from the standpoint of susceptibility of the steels to graphitization. These three steels were found to have all the characteristics of a straight silicon-killed, coarse-grained steel which is known to possess an appreciable resistance to graphitization. We found only a very few isolated graphite nodules in the weld-heat-affected zone of the shell plate, and none in the cone and torus ring. The fact that this type of steel did graphitize, though only to a limited extent, points to unusual stress conditions. In so far as carbon steel goes, this silicon-killed coarse-grained type of material is the best steel available and one which is generally not prone to form dangerous chain graphite. This type of steel can be identified by very low residual metallic aluminum, by its grain-coarsening characteristics, and by coarse grain size and normal carbide structure in the McQuaid-Ehn test. The chemical, microstructural, and mechanical properties of the three steels examined by us are given in Tables 13 and 14, and Figs. 19 to 22 of this discussion.

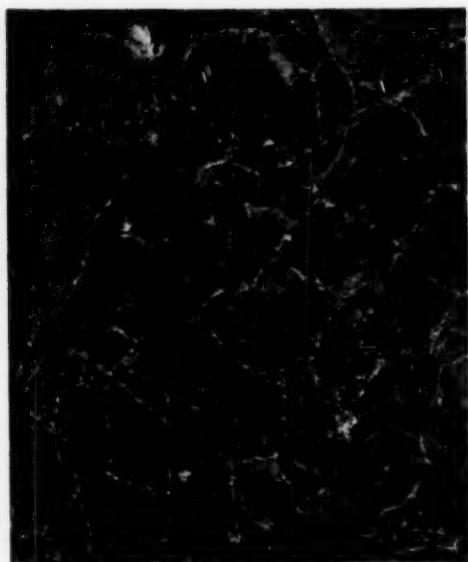
¹⁰ Associate Research Metallurgist, Research and Development Department, The Babcock & Wilcox Company, Alliance, Ohio.

² A. O. Smith Corporation, Milwaukee, Wis.

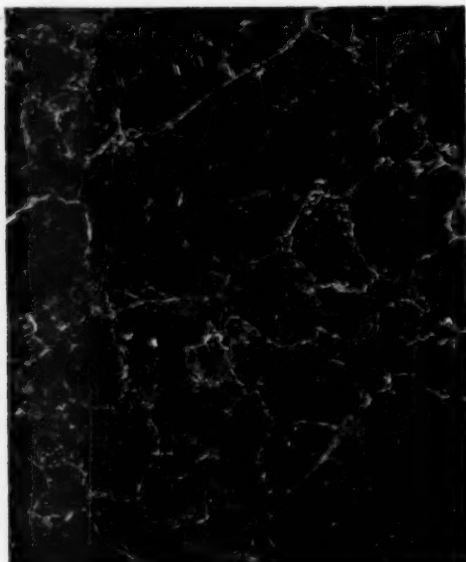
TABLE 12 TENSILE PROPERTIES OF WELDS AFTER STRESS-RELIEVING AT 1000 F

Type	Class	Test temperature	Ultimate strength, psi	Yield strength, 0.2 per cent, psi	Elongation in 2 in., per cent	Reduction in area, per cent	E, 28.5×10^6 psi
Mild steel	E 6013	Room temperature	73500	60000	23.5	57	28.5
Mild steel	E 6030	Room temperature	71000	56500	23	60.5	20.0
Stainless	25-20	Room temperature	84700	59000	26.5	29	21.8
Stainless	25-12	Room temperature	85000	56500	37	42.5	21.25
Mild steel	E-6013	900 F	47000	39500	17	81.5	20.2
Mild steel	E-6030	900 F	49000	38000	23.5	68.5	18.2
Stainless	25-20	900 F	60000	39000	28.5	38	16.9
Stainless	25-12	900 F	64500	37000	32	37.5	18.25
A-201 plate*	Roller	Room temperature	62000	42000	36	62	...
A-201 plate*	Roller	900 F	35000	20000	42	78	...
Type 347*	Roller	Room temperature	92000	42000	50	70	...
Type 347*	Roller	900 F	64000	32000	35	68	...

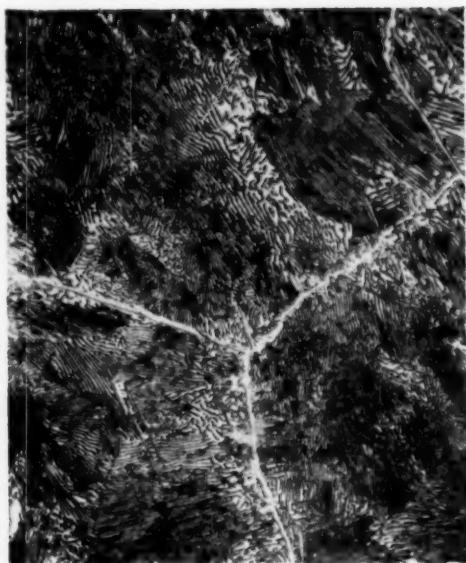
* From ASTM Special Technical Publication No. 100 "Strength of Wrought Steels at Elevated Temperatures." Figures given are average values representing a range of compositions.



X100

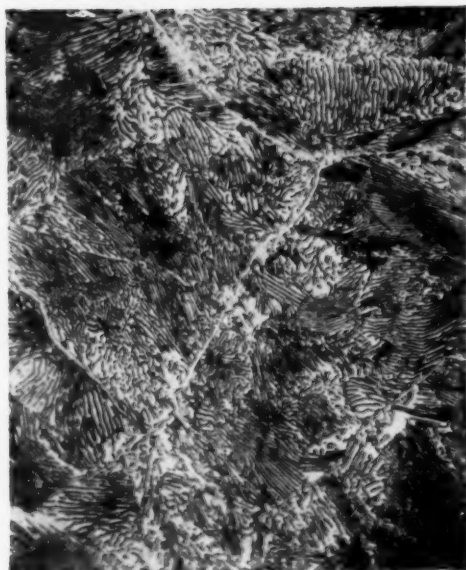


X100



X500

FIG. 19 SHELL—McQUAID-EHN GRAIN SIZE ASTM No. 3; NORMALITY 1

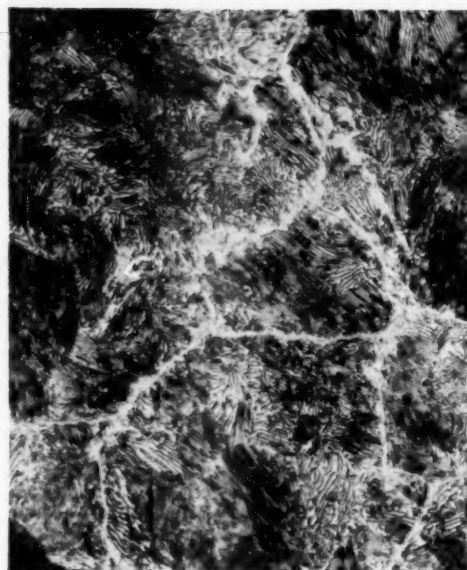


X500

FIG. 20 CONICAL HEAD—McQUAID-EHN GRAIN SIZE ASTM No. 0-3; NORMALITY 1



X100



X500

FIG. 21 TORUS RING—McQUAID-EHN GRAIN SIZE ASTM No. 1-3(4); NORMALITY 1

TABLE 13 CHEMICAL PROPERTIES OF STEELS EXAMINED

	C	Mn	Si	S	P	Total N	Total Al	Acid soluble Al
Shell	.07	.30	.25	.025	.011	.02	.003	.001
Conical head	.07	.32	.24	.024	.012	.02	.003	.001
Torus ring	.22	.44	.060	.015	.03	.006	.001	.001

TABLE 14 PHYSICAL PROPERTIES OF STEEL EXAMINED

	Yield strength, psi	Tensile strength, psi	Elongation in 2 in., per cent	Reduction in area, per cent	Type of fracture
ASTM A-201	minimum	55000	minimum		
Grade A	27000	62000	22		
Shell	23500	48250	45.5	71.6	1/2 cup
	23250	48350	45.5	72.9	1/2 cup
Conical head	27250	48000	45.5	70.1	1/2 cup
	28000	49000	43.0	71.8	1/2 cup
Torus ring	40120	99950	34.0	59.4	1/2 cup
	49000	66830	35.0	58.8	1/2 cup

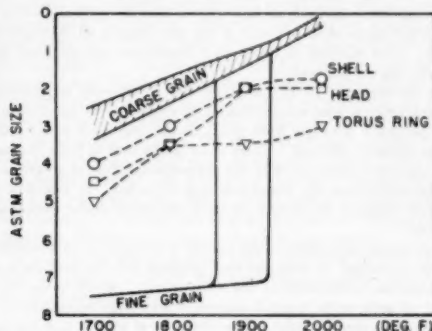


FIG. 22 LIMITS OF COARSE-GRAIN AND FINE-GRAIN TYPES OF STEEL (Taken from "Metals Handbook," 1948, page 341.)

A. B. WILDER.¹¹ The program being conducted by API on examining materials in various types of high-temperature oil-refinery equipment will establish valuable information concerning metal behavior. Graphitization is primarily a function of chemical composition, metal structure, exposure time, and temperature. Secondary factors such as those discussed by the authors are encountered in the operation of oil-refinery equipment and have considerable influence on the behavior of materials. Chain graphite, for example, is seldom observed in laboratory weld tests after exposure at elevated temperatures. However, chain graphite is considered much more objectionable in operating units than nodular graphite.

The authors propose that carbon-steel pipe and tubing for temperatures above 850 F be made in accordance with a deoxidation practice restricted to the maximum use of 0.5 lb per ton of aluminum. Further, the material should have a coarse grain size and be free of abnormality in the McQuaid-Ehn carburizing test. The producers of this material would have considerable difficulty in meeting these requirements. Usually carbon-steel seamless pipe and tubing are made with greater quantities of aluminum and very little experience is available concerning the normality of this type of steel.

It is important to have a properly killed steel for the manufacture of carbon-steel seamless products by the Mannesmann process and if graphitization is a problem, chromium in conjunction with molybdenum should be employed. The use of molybdenum not only increases the creep strength but also reduces the tendency

¹¹ Chief Metallurgist, National Tube Division, U. S. Steel Co., Pittsburgh, Pa.

for embrittlement at elevated temperatures. Chromium will inhibit the formation of graphite.

J. G. WILSON.¹³ The authors have presented a fine report with reference to the studies they have made on the causes of failure of three catalytic-cracking-plant reactors, 23 ft ID \times 68 ft straight side. These are cylindrical vessels with cone heads and are made of carbon steel clad with ± 25 per cent of type 347 stainless steel. The inside welds are 25–20 stainless and are ± 50 per cent of the total weld thickness. Of the three vessels which have failed, two show signs of some graphitization and one does not, which goes a long way to prove that graphitization is not the principal cause of failure. The extensive cracking encountered in the carbon steel at or near the weld is of a brittle nature with little evidence of plastic flow. It would seem that further explanation is necessary to pin down the cause of such failures.

In our stress analysis we have shown that the critical section is the weld where ± 50 per cent of the thickness is 25–20 stainless steel. This analysis is based on a bimetallic cylinder and the results are as follows:

In the region of 75 F, for every 100 F, increase or decrease in temperature from a condition of no stress due to temperature, the resultant stress is 5100 psi. In the region of 975 F, the stress value is 3400 psi. There is no doubt that in both the carbon steel and stainless steel the proportional limit is greatly exceeded every time the vessel is heated or cooled. It would be of interest to know the fatigue limits of the steels under these conditions.

Another consideration is the nature of the stresses at a location where a "wedge" of stainless steel projects into the carbon steel (a condition which exists at the weld areas). At the inner "corners" of such welds, triaxial stresses of very large magnitude and of the same sign do exist. The concepts of plastic flow cannot prevail under this condition and the steel will act in a brittle manner. Steel subject to such operating conditions could easily fail in a brittle manner. The vessels have failed in such a manner in or near the carbon-steel welds.

With reference to the use of graphitization-resistant alloy steel for use in vessel fabrication, we quite agree that greater difficulty is to be expected in welding this steel than would be expected in welding low-carbon or low-carbon-molybdenum steels. However, two such reactor vessels made of $1/2$ chrome $1/2$ molybdenum steel already have been built and are in operation. It would appear that the authors have overemphasized the difficulties to be expected in the use of such materials for construction. However, we are in agreement that a graphitization-proof carbon steel for high-temperature service is greatly needed and should be developed.

Since the time when this paper was presented, the one chrome half-moly vessel 24 ft. in diameter referred to the paper, has been built and placed in operation. The vessel was welded with one chrome half-moly rod of the low-hydrogen type. The carbon content of the steel plate varied between 0.13 per cent and 0.17 per cent carbon. No unusual difficulties were encountered in the fabrication of this vessel.

A. W. ZEUTHEN.¹² Relative to the exploration of causes of cracking, thermal stresses resulting from differences in expansion of alloy and carbon steel appear to be largely responsible for the intergranular cracking which was observed. Graphitization apparently played a minor role since the cracking was reported as nearly the same irrespective of the extent of graphitization. A factor which may have had an influence on cracking and which unfortunately has not been evaluated is grain size. Immediately

adjacent to every weld is found an area of coarse grain structure where the base metal has attained a high temperature (above 1800 F). This is bounded by a fine-grained zone where grain refinement has occurred to the extent that the grain size is considerably smaller than that of the unaffected base metal. Further, since it is known that fine-grained materials have considerably poorer creep and stress-rupture properties, and since the cracks were typically high-temperature intergranular fractures and were located in this area, it appears that grain refinement may have influenced the failures.

Metallurgical examination of a repair weld made during the fabrication of the vessel with austenitic stainless-steel electrodes, disclosed a crack in the carbon-steel base metal in an area from which carbon diffused to the stainless-steel weld metal. Since it was stated that this type of crack is not uncommon in joints between austenitic and ferritic steels operating at elevated temperatures, it would be of interest to know where similar cracks have been found, at what temperatures has the diffusion been observed to initiate and proceed to a serious extent, and has the diffusion appeared to be as rapid for all alloy weld metals or is it perhaps most severe for the austenitic materials?

J. G. ALTHOUSE¹⁴ and L. W. WILLIAMS.¹⁵ The authors are to be congratulated on their collection of data on catalytic reactors and their excellent mathematical analysis of the problem. However, while the authors have been most thorough in examining all phases of the problem, they fail to make clear that the clad material they refer to as integral-clad was made by the now obsolete Pluramelt process, and not by the sandwich method. This distinction has an important bearing on the problem of graphitization, because those factors contributing most to the promotion of graphitic formation and stress concentration, i.e., overdeoxidation of the backing steel with three or four pounds of aluminum per ton and large variations in the thickness of the clad material (20 to 40 per cent), are inherent in the Pluramelt process but, for all practical purposes, do not exist in clad material manufactured by the sandwich method.

The production of the Pluramelt-type clad plate required base-metal steel very low in carbon to prevent pickup of carbon in the stainless cladding (in order to maintain the maximum corrosion resistance of the stainless) during manufacture of the slabs. To produce this type of base steel, excessive amounts of aluminum were added to the metal during deoxidation in the open hearth. Because of this particular practice, the base metal was made susceptible to the formation of graphite when subjected to long-time exposure at high temperature and stress. Excessive stress was present in the plates themselves during the operation of the vessel due to the nonuniformity of the austenitic stainless cladding. This nonuniformity of cladding thickness was further exaggerated by stainless welds deposited at the seams. These deposits, for the most part, were quite heavy and produced a concentration of stress in these areas.

Stainless-clad plates now being manufactured by the sandwich method do not have these excessive cladding-thickness irregularities. Consequently, the magnitude of stress left in the plate is not as great. In addition, the backing steel on clad plates now being produced is of a normal coarse-grain type which is less susceptible to graphitization than the Pluramelt type. It is of interest to note that in reactor A, no graphite was found in the torus section which was 0.21 per cent carbon, while the low-carbon, overdeoxidized backing steel of the Pluramelt clad material was heavily graphitized. The uniform cladding thickness of the currently

¹³ Shell Oil Company, New York, N. Y.

¹² Consulting Engineer, Port Washington, N. Y.

¹⁴ Metallurgical Engineer, Lukens Steel Company, Coatesville, Pa.

¹⁵ Manager, Technical Service, Lukens Steel Company, Coatesville, Pa.

produced clad-steel plates reduces the local stresses created around welded joints.

To date there has been no evidence of detrimental graphitization in installations of stainless-clad steels operating under high temperatures and pressures where the base metal has been coarse-grained and not excessively aluminum-deoxidized.

As mentioned by the authors, until 1951 the main concern for graphitization was in power-plant equipment. Since that time the same detrimental graphite was found in some austenitic stainless-clad vessels. This equipment was examined, as well as considerable other equipment made from clad-steel or lined-steel plates, each with austenitic stainless or straight-chromium steel, also unlined or nonclad steels. The only material which had detrimental graphite present had the same condition present in the steel and had been subjected to the same general operating conditions.

The only product in which detrimental graphitization in service had occurred had been in those steels which in their manufacture were deoxidized with aluminum to a degree where the inherent grain size had been affected for the chemical composition involved. The function of the aluminum addition to steel in steelmaking is to remove as much iron oxide from the molten metal as possible in order to prevent reaction of this iron oxide with the carbon in the steel, which results in the formation of gas holes in ingots during solidification. When aluminum is added over the particular amount needed for this purpose, its next action is to reduce the inherent grain size of the metal. However, in order to accompany this function, some of the aluminum added must be in solid solution with the steel and occur in the steel as aluminum, and not as an oxide of aluminum.

In all the steels which contained detrimental graphite, aluminum had been added in excess of the amount necessary to achieve its prime function, and all had been given sufficient aluminum to affect the inherent grain size of the steel.

It is to be noted from this paper, and other experience, that graphitization has not been found to occur in boiler-steel plates of straight carbon, carbon-molybdenum, or clad steels when the steel has received a normal deoxidation practice during its manufacture. The majority of steel plates made for boiler or high-temperature services are of so-called coarse-grain nature. Consequently, it is our definite opinion, and proved by available facts, that from a steelmaking standpoint, a material having little, if any, tendency for the formation of detrimental graphite can be produced by adding a few simple requirements to existing specifications for steel which is intended for use at high temperature and where high stresses may be present. These simple requirements would be that not more than $\frac{3}{4}$ lb of aluminum per net ton of steel be added during deoxidation and that the McQuaid-Ehn grain size be between 1 and 4.

This requirement for high-temperature service mentioned previously would apply only when operating temperatures exceeded 900 F. Graphitization in plate products has not been found at temperatures below this figure.

We agree with the authors' conclusions regarding the addition of alloying elements to steels to inhibit the formation of graphite. Theoretically, and actually, the addition of both molybdenum and chromium to high-temperature steels improves their high-temperature properties. Both of these elements are carbide-forming, and the carbide forms are more resistant to change at high temperature than those that would occur in straight carbon steels. However, graphitization of these will also occur during service if deoxidation of the metal by aluminum is of such a degree as to affect the grain size.

The advantage these alloying elements give to steels for high-temperature service, in addition to forming carbides, is the formation of solid solutions in the ferrite constituent. Ferrite

with molybdenum and/or chromium in solution is stronger at high temperatures than just normal ferrite. Consequently, they can withstand stresses more readily without too much movement of the metal during operation. Advantage can be taken of these superior high-temperature features in service above 900 F, whether it be solid homogeneous plate or the use of clad plate in the base steel.

It is agreed that the chromium-molybdenum steels are slightly air-hardening. However, it is believed that the authors are perhaps overconcerned with the difficulties anticipated in welding these steels in the field, especially since the authors have demonstrated, both in test and in fabrication experience, that preheat can be lowered to 200 F and postheat is not necessary.

All of the Pluramelt reactors were clad with type 347 stainless, which the authors agree is not as suitable, relative to thermal stresses, as the straight-chrome type. However, the authors state that the discontinuity stresses at the weld are as great, or greater, than in a type 347 material; but since the magnitude of these stresses is of a low order, it remains to experience to prove their significance. In the past five or six years, clad steels with types 410 and 405 cladding made by the sandwich method have been used in petroleum applications with no difficulties to prove there are any serious discontinuity stresses at the weld.

It is surprising that in the recommendations made by the authors, mention was not made of clad steels made by the sandwich method which can produce a product incorporating the corrosion resistance of stainless steels and the graphitization-resistant backing steels, the two salient features demanded by conditions existing in various petroleum applications.

In conclusion, the authors are again to be congratulated on the thorough manner in which they have collected their data and on their fine presentation.

AUTHORS' CLOSURE

The authors wish to express their appreciation for the interest displayed by the discussers in this subject and for their comments and supplementary information. Many of the points raised are valuable, and will undoubtedly contribute to a better understanding of the causes for the cracking of integral-clad pressure equipment operating at high temperatures.

Regarding the statements and hypotheses advanced by Messrs. Brown, Clarke, Feely, Maass, and Northup, the authors wish to make the following points:

The concept of predicting failure by a comparison of the stress-relaxation and stress-rupture curves, Fig. 16, is certainly novel and merits attention. The basic concept of this approach is, however, questionable, inasmuch as it involves a comparison of stresses which result from dissimilar considerations and are accompanied by different modes of straining of the material. In the stress-rupture test the stress results from a constant load; plastic strain continues until the limiting strain for the material is reached. With stress relaxation the maximum strain (elastic) is fixed to start with and stress reflects only a change from elastic to plastic strain, without change in the total strain.

The total strain due to differential thermal expansion initially locked up between the base metal and alloy cladding in the reactors in question is only 0.0017 in. per in. Ignoring creep due to pressure stresses, the plastic flow due to the relaxation of thermal stresses cannot exceed this value over any single thermal cycle. The authors believe that failure is not likely to occur in a stress-relaxation test, provided the magnitude of the initial strains does not closely approach the limiting strain the material can sustain. If this were not the case, one would be compelled to drastically reconsider the concepts relating to localized stress concentrations inherent in the design of high-temperature equipment, omis-

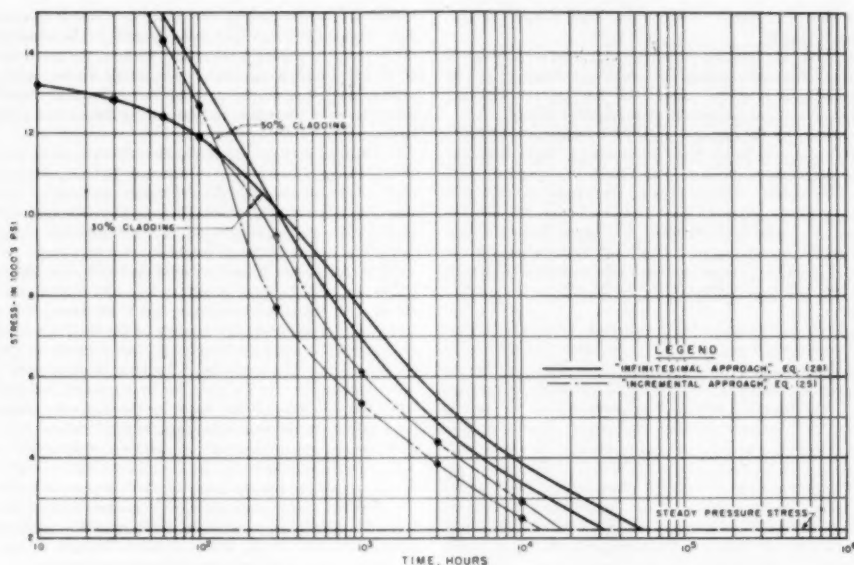


FIG. 23 STRESS-RELAXATION CURVES FOR BIMETALLIC REACTORS AT 920 F

sion of or thoroughness of stress-relieving processes, and the self-springing tendency of piping systems.

A more satisfactory examination would result if the plastic flow developing over a given period of time were compared with the values of ductility developed in the stress-rupture test. Unfortunately, data on the long-time ductility of materials are seldom encountered in the literature, and extrapolation from short-time stress-rupture ductility values is of uncertain accuracy.

The formulas developed by Messrs. Brown, Clarke, Feely, Maass, and Northrup are fundamentally sound. Except for the fact that an incremental approach has been substituted for the integration involved in Equation [12], their derivation is basically equivalent to the expressions developed in the first and third sections of the Appendix, noting that different moduli of elasticity for base material and cladding have been used and biaxial effects are omitted. Equation [12] can be modified to take care of different moduli of elasticity and unidirectional relaxation and becomes

$$t_r = \frac{B + (1-B) \frac{E_b}{E_s}}{(n-1)AE_bBS^{n-1}} \left[1 - \left(\frac{S}{S_b + S_p} \right)^{n-1} \right] \quad [28]$$

As the equivalence of these approaches is not self-evident, stress relaxation curves for 30 and 50 percent cladding were calculated using Equation [28] and also using Equation [25] of the discussion based on the numerical values and physical constants following Equation [25] and the following expression for creep rate at 920 F which was considered representative of interpolated creep data

$$\text{Creep rate (in/in/hr)} = \frac{S^4}{1.153 \times 10^{21}} \quad [27]$$

where S is the stress promoting creep.

These curves are shown in Fig. 23. The curves for the incre-

mental approach lie to the left of the Equation [28] curves predicting shorter relaxation time for a given stress. Had more and shorter time intervals been chosen for use with Equation [25] the error involved would be considerably reduced. Fig. 23 is directly comparable to Fig. 17 of the discussion; that it indicates shorter relaxation times for a given stress is undoubtedly due to the use of different creep data by the discussers than indicated by Equation [27].

The authors also believe that if the effect of creep in the alloy cladding were considered, lower residual stress at any time would result.

With reference to the test data presented by Messrs. Scheil and Huseby, the generally increased mechanical strength, especially the yield strength, of weld metal compared to wrought base metal of similar composition is well known and has been recognized by the authors in considering this problem. However, so long as the yield strength of the weld metal is as high as assumed in the paper, the analytical results would not be affected. It was realized and pointed out in the paper that these differences in the strength of weld and base metal can produce localized stress concentrations at the weld junction. Notwithstanding the variance in load-carrying ability, it is suggested that the relief of locked-up thermal strain is dependent on the ductility of the material. Relative to the cracks, the accompanying elongation was observed to be markedly low and well under the normal expected range, which suggests that zones of inherently low ductility or fatigue resistance may have existed at the weld joints.

The results reported by Mr. Stanton are interesting and somewhat surprising. That the carbon-steel portion of a clad steel from one of the cracked vessels has the characteristics of a straight silicon-killed coarse-grained steel is contrary to the statement by Messrs. Althouse and Williams concerning the steelmaking practice employed which indicates that substantial amounts of aluminum were customarily added to the metal for deoxidation.

Analysis of specimens covered by this report appear to be half-way between these extremes.

Mr. Stanton's statement to the effect that the finding of graphite in such a steel indicates unusually high stress conditions is not supported by the available literature or the findings of this report. Although research into the phenomenon of graphitization has indicated the probable accelerating effect of stress, the preponderance of data points to time-temperature relationship as the important governing factor. Many examples have been reported where moderate to severe graphitization has been encountered in carbon steels even though the residual aluminum was low and the steel otherwise apparently normal in all respects. It is generally accepted belief that any carbon steel, regardless of melting practice, will graphitize in time if the conditions of temperature and possibly stress are critical.

Mr. Wilder states that producers of seamless carbon-steel pipe would have difficulty in meeting restrictions on the use of aluminum in deoxidation practice on this product at this time. Basing their decision on this viewpoint, a subgroup of ASTM Subcommittee XXII, Section on Pipe, have recommended against any restrictions on deoxidation of steel for seamless pipe. However, it is believed by the authors that restrictions on aluminum are not out of the question. For example, in the case of carbon-moly steel, as early as 1938 a coarse inherent grain was found to promote increased high-temperature strength. About 1939 the carbon-moly pipe Specification ASTM A-206 was revised to provide such steel and consequently carbon-moly pipe produced since that time has been made of steel melted with aluminum of about 0.5 lb per ton. It is also known that during World War II the use of aluminum for deoxidation was restricted by government order and allocated on the basis of 0.6 lb per ton. Accordingly, although occasional heats may have required a greater quantity, the majority of heats were probably deoxidized with 0.6 lb per ton or less. Since it is well recognized that steels deoxidized with large quantities of aluminum are susceptible to the formation of graphite, it is believed that a greater effort should be made to produce a more resistant-type carbon steel. The authors particularly deplore the growing tendency to recommend against the use of all-carbon steel for service at elevated temperatures where experience has shown lengthy and successful operation.

Mr. Wilson has offered the theory that the cracks may result from large triaxial stresses of like sign which exist at the inner corners of the alloy weld "wedge" with plastic flow restrained. The authors doubt the existence of high tensile triaxiality at this location and have pointed out that no cracks were found to initiate at the junction of the alloy weld and base metal.

It is welcome news that a one per cent chromium one-half

per cent molybdenum steel vessel has been successfully field-fabricated without difficulty, and the authors are pleased to learn of this successful experience. It should be noted that ASTM Specification A-301 Grade B permits carbon contents of 0.21 per cent maximum, while the highest carbon content Mr. Wilson reported was 0.17 per cent. It is hoped that plates with the higher carbon contents can be fabricated as readily.

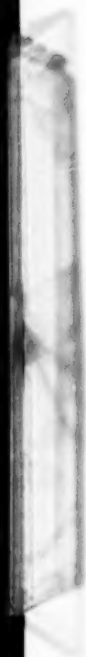
The authors agree with Mr. Zeuthen that the high-temperature strength of the heat-affected zones of welded joints is subject to question. Data available on this subject are scarce and as a result the Petroleum and Chemical Panel of the Joint ASTM-ASME Committee on the Effect of Temperature on the Properties of Metals has initiated a project to investigate the high-temperature strength characteristics of welded joints.

Cracks at the junction of austenitic welds and carbon-steel base metal have not been extensively discussed, being a problem separate from the type of deterioration with which this paper is concerned and on which a number of published papers dealing with weldments of dissimilar materials are available.

At the time this paper was presented the authors were of the opinion expressed by Messrs. Althouse and Williams that coarse-grained, silicon-killed steels were not as susceptible to graphitization as the heavily aluminum-killed steels. However, recent preliminary reports by Battelle upon examination of samples submitted by petroleum refiners in connection with the API program indicate that in material from one refiner silicon-killed steels have heavily graphitized while aluminum-killed steels have not.

Apparently Messrs. Williams and Althouse have misinterpreted the authors' statements to the effect that the magnitude of local discontinuity stresses at a composite weld in ferritic chromium clad steel are of a low order when the welds are austenitic steel. The authors have pointed out that differential straining at the edge of the welds can be expected; however, whether or not this is significant remains for experience to prove.

In closing, the following additional inspection results are given. The integral-clad reactor of Unit F was shut down for inspection in November, 1951. Magnaflux examination of the carbon-steel side of the welded seams revealed cracks of the same type observed on the reactors from Units A, B, and C. These cracks were repair-welded and the vessel was returned to service with an internal insulation lining. The integral-clad reactor of Unit D was removed from service in June, 1952, and replaced by a new reactor of 1 per cent chromium— $\frac{1}{2}$ per cent molybdenum steel. Examination of the scrapped reactor revealed some cracks in the carbon steel adjacent to the welded joints of large pipe connections in the bottom cone and of the large manway in the shell section.



Frequency-Response Analysis for Industrial Automatic-Control Systems

By D. W. ST. CLAIR,¹ W. F. COOMBS, JR.,² AND W. D. OWENS,² ROCHESTER, N. Y.

The authors outline the fundamental principles of frequency-response analysis in terms familiar to the industrial automatic-control engineer, as well as present data obtained by frequency-response methods descriptive of the effect of typical variables on the behavior of the control system. These variables are gain, derivative time, reset rate, transportation lag, and capacity lag, with period of oscillation and stability as dependent variables. They have been combined to form three basic controllers and four basic processes, the data being presented for the various combinations of controller and process. The method of calculation and a specific example are given in the Appendix.

INTRODUCTION

THERE is, without question, a need in the industrial automatic-control field for a more exact method of control analysis than the currently used empirical and rule-of-thumb methods, and which at the same time can be understood by more than a few. Such a method is available and is called frequency-response analysis. This versatile and powerful method of study was originally and thoroughly developed for use in feedback amplifier design and subsequently has been widely applied in the servomechanism field. It is now generally realized that servomechanisms and industrial automatic-control systems are basically the same and, therefore, the methods of study used in one field can be applied directly to the other merely by a change in terminology and point of view or emphasis.

The frequency-response method of analysis is based on sound mathematical principles, yet it is uniquely different from other mathematical approaches to control analysis in that it can be used with almost no reference to the mathematics. It is equally suited for either qualitative or quantitative studies, and the accuracy of the results obtained is in keeping with the accuracy of the information furnished. Considering the complex nature of control systems it is a method easily learned and easily applied since the experience gained from studying only a few examples provides avenues of reasoning afforded by no other method. The purpose of this paper is twofold—to explain in terms familiar to the industrial automatic-control engineer some of the salient features of frequency-response analysis and to present data on the effects of typical control-system variables as obtained by frequency-response methods.

As a beginning, what is meant by frequency response? It is

¹ Mechanical Engineer, Instruments and Control Group, Engineering Division, Kodak Park, Eastman Kodak Company.

² Formerly, Eastman Kodak Company; at present, Physics Department, University of Rochester, Rochester, N. Y.

³ Formerly, Eastman Kodak Company; at present, Research Engineer, Aero Division, Minneapolis-Honeywell Regulator Company, Minneapolis, Minn.

Contributed by the Industrial Instruments and Regulators Division and presented at the Annual Meeting, Atlantic City, N. J., November 25-30, 1951, of THE AMERICAN SOCIETY OF MECHANICAL ENGINEERS.

NOTE: Statements and opinions advanced in papers are to be understood as individual expressions of their authors and not those of the Society. Manuscript received at ASME Headquarters, October 9, 1951. Paper No. 51-A-127.

well known that the response of a thermometer to a step change in temperature is called the step response of the thermometer. Similarly then, the response of the thermometer to a cycling or sinusoidal change in temperature over a range of frequencies is called the frequency response of the thermometer. In control analysis these terms are not confined to describing thermometers; they may refer to any part or combination of parts in the control loop. For each step response there is only one corresponding frequency response and vice versa. Frequency-response information is like a common denominator in dealing with fractions, for information can be directly added to or subtracted from the whole. The importance of this lies in the fact that if the frequency response of the entire system is known, then the behavior of the system when in control is also known, with an accuracy generally sufficient for studying industrial systems. Thus by studying the effect of each variable on the frequency response of the entire system, its effect on control will also be known.

A study of a control system by frequency-response methods is divided broadly into three parts: (a) Transforming all information about the system into frequency-response information; (b) combining this information and studying the effect of each variable on the entire system in terms of frequency response; and (c) interpreting these results to predict the behavior of the system when in control. Admittedly, performing these steps for the first time on an actual control problem is long and difficult; however, as familiarity with the procedure grows much of the effort is reduced. Experience with the system is much like filling in the blanks of a multiplication table, for once they have been filled in the work need not be repeated.

To aid in establishing this foundational knowledge, the authors have chosen four basic types of processes and have shown the effects of typical variables on the control system. Specifically the variables studied are gain, derivative time, reset rate, transportation lag, and capacity lag, with stability and period of oscillation as dependent variables. (These terms are defined under "Terminology.") The results obtained can be used and understood without understanding the frequency-response method used to obtain them, but in keeping with the dual purpose of this paper, some understanding of the basic principles involved is desirable for it enables one to use the data more flexibly or investigate variables other than those specifically studied here.

The frequency-response method of analysis as described here is strictly applicable only to those systems commonly referred to as linear. While this term is based on the type of differential equation representing the system, it means only that effect is always in direct proportion to cause. In this sense all physical systems are nonlinear to some extent but, generally speaking, those industrial systems which are continuous are linear enough over a small range to be analyzed by the method described here. However, it may be necessary to analyze a single system under different operating conditions in order to complete the study of the system.

EXAMPLE OF BASIC PRINCIPLES

To illustrate the steps involved in obtaining control information by frequency-response methods, first picture a control system as a loop as shown in Fig. 1. For present purposes the part of the loop from the controller output around to the recording pen will

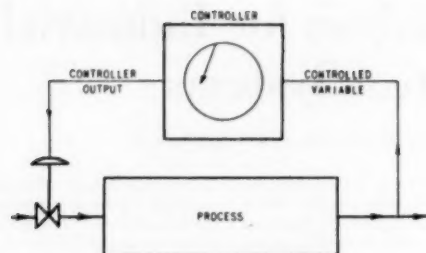


FIG. 1 SCHEMATIC DIAGRAM OF A CONTROL SYSTEM TO SHOW EXISTENCE OF A LOOP

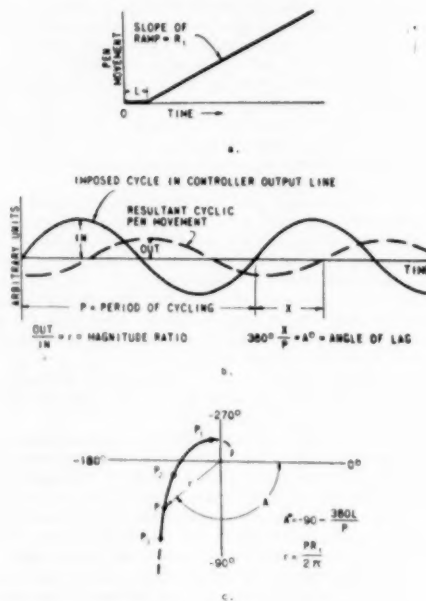


FIG. 2

- (a) STEP RESPONSE OF A NON-SELF-REGULATING PROCESS HAVING TRANSPORTATION LAG
 (b) DIAGRAM ILLUSTRATING IMPORTANT VARIABLES OF FREQUENCY RESPONSE, PERIOD, ANGLE, AND MAGNITUDE RATIO
 (c) FREQUENCY RESPONSE OF THE PROCESS WHOSE STEP RESPONSE IS SHOWN IN FIG. 2(a)

be called the process and the remainder called the controller. If the controller is disconnected and a step change is applied in the controller output line, the pen will draw the step response of the process. Assume this response curve to be non-self-regulating with a transportation lag as shown in Fig. 2(a) and assume the controller to have only proportional action. All physical systems will exhibit some hesitation before the rising part of the curve even though it may be extremely small.

First, it is necessary to determine the frequency response of the process. Frequency-response data include three variables: the period of cycling, the ratio of the magnitudes of the resultant and imposed cycles, and the phase angle between the imposed and re-

sultant cycle. To illustrate these on the foregoing process suppose that instead of the step change, a sinusoidal change had been applied in the controller output line. Then the cycle would have passed through the process and resulted in a cyclic pen movement as shown in Fig. 2(b). The three variables of interest—period, magnitude ratio, and phase angle—are shown in this figure. Note that this is an imposed cycle while the loop is open and should not be confused with the closed-loop cycle of an unstable controlled system. Values of r and A will vary as the period of cycling varies and while these variables usually can be determined by test as outlined, they very often can be calculated easily. As explained in the Appendix, this is the case for the process described and for all of the other variables considered in this paper.

These three variables of frequency, magnitude ratio, and phase angle can be collected into one plot to form a single curve as shown in Fig. 2(c). Each point on the curve represents a definite period of cycling and is plotted at a distance from the origin equal to r and at an angle equal to A , the nomenclature being the same for Fig. 2(c) as for Fig. 2(b). This curve is the frequency-response curve of the process and is a picture of the process characteristics in the same sense that Fig. 2(a) is the step-response curve and is a picture of the process characteristics. While complete frequency-response data would include all periods of cycling from zero to infinity, generally only those periods necessary to form as much of the curve as shown in solid are of interest. For the process chosen, the curve terminates in the origin for periods approaching zero and goes to infinity at a -90 deg angle for periods approaching infinity.

Since a frequency-response curve must represent the entire loop before it can be evaluated in terms of system behavior when in control, the frequency response of the controller must be obtained and combined with that already obtained for the process. The rule for combining frequency-response data is to multiply the radii (magnitude ratio) and add the angles for corresponding periods of cycling. An ideal controller with only proportional action has a phase shift of -180 deg and a magnitude ratio which is fixed for each controller setting. The -180 -deg shift is inherent in a controller which is to produce corrective action because the controller output must be in opposition to the error signal; it is the result of a mathematical minus sign which the controller puts into the loop rather than the result of lags in the controller. Since it is a factor common to all systems, convention is to disregard it in the combining step and base all reasoning on 180 deg less phase shift than is actually occurring in the loop. Thus the effect of adding the controller frequency response to the process frequency response is to proportion the radii in accordance with the controller setting as shown in Fig. 3(a). An increase in controller gain (decrease in throttling range) increases each radius in that proportion and may be thought of as changing the scale of the plot without changing the shape.

The combined curve could be obtained by test by breaking the controller output line and imposing a sinusoidal air pressure to the valve as before. The relationship between this pressure and the controller output pressure would then be the frequency response of the complete system. Actually, it is immaterial where the loop is broken but the location suggested is probably as easily visualized as any. Not enough stress has been put on the fact that the frequency response is the common denominator for combining all information. It can be either calculated or obtained by test and it can be readily added to or subtracted from other data by the rule described. Thus control loops may be built up as desired by assembling the frequency-response data of the individual components in the loop. In fact, the frequency response of the process in this example as shown in Fig. 2(c) is a combination of that for a transportation lag (for which $A = -360L/P$

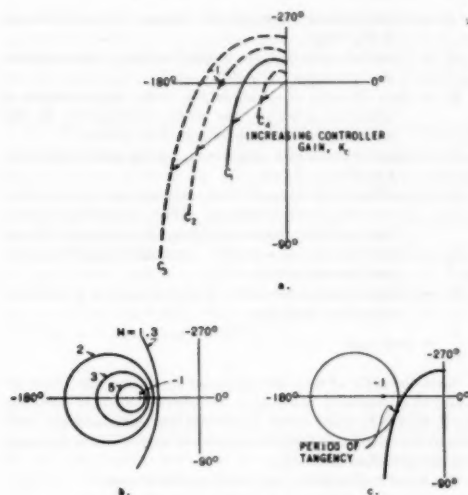


FIG. 3

- (a) EFFECT OF CONTROLLER GAIN ON FREQUENCY-RESPONSE CURVE
 (b) DIAGRAM SHOWING PATTERN OF M -CIRCLES
 (c) COMBINATION OF FIGS. 3(a) AND 3(b) TO SHOW HOW GAIN CAN BE VARIED TO CAUSE M -CIRCLE TANGENCY

deg and $r = 1$) and that for a ramp (for which $A = -90$ deg and $r = PR_1/2\pi$).

Since the curves in Fig. 3(a) represent the frequency response of the entire loop (each curve being for a particular controller gain) they can be analyzed in terms of system behavior when in control. The criteria for this evaluation are as follows: If the curve passes to the right of the -1 point (the point on the -180 -deg line at a distance 1 from the origin) as curve C_1 , the system is stable if it passes through the -1 point as curve C_2 the system is unstable with a constant amplitude of cycling and has a period of oscillation represented by that point on the curve. If it passes to the left as curve C_3 the system is unstable with increasing amplitudes of cycling. Thus the -1 point quickly establishes stability or instability. If the curve is peculiarly shaped near the -1 point more complete rules must be applied (1, 2, 3).⁴

Generally speaking, the further a stable curve misses the -1 point the more stable the system is; that is, curve C_1 is more stable than C_2 . The transition from the complete loop frequency response to the transient response to be expected after set point changes or load changes in the controlled closed loop is not, in a mathematical sense, exact. For each frequency response there will be a definite transient response but all of the methods for making this transition analytically are, to the authors' knowledge, only approximate. While work has and is being done in this field (3, 4) to make the transition more exact there exists a criterion which is sufficiently accurate for use in the industrial automatic-control field. This criterion is based on a closed-loop magnitude ratio and will be discussed more fully in the Appendix along with the -1 point criterion. For present purposes the criterion may be thought of as being based on what are called M -circles. These are circles of radius $M/(M^2 - 1)$ with their centers on the -180 -deg line and at a distance $M^2/(M^2 - 1)$ from the origin.

⁴ Numbers in parentheses refer to the Bibliography at the end of the paper.

A family of M -circles is shown in Fig. 3(b). By changing the scale of the plot as shown in Fig. 3(a), the curve can be made tangent to a selected M -circle in the manner shown in Fig. 3(c).

Stability increases as the value of M decreases. For instance, the transient response of the system to a small change in set point when the curve is tangent to an $M = 2$ circle will have approximately the stability shown in Fig. 4(a), while Fig. 4(b) shows the stability to be expected from tangency to an $M = 1.3$ circle. For values of M around 1.3 the ratio of the peak on the first overshoot to the change in set point is very nearly M , while for higher values of M this ratio is less than M . The period at the point of tangency between the curve and the M -circle approximates the period of the damped oscillation, this approximation being very good for an M of 2 or more and reasonably close for an M of 1.3. Since load changes generally do not occur as abruptly as the step change in set point the load-change stability will be better than shown in Fig. 4 (5). The value of 1.3 for M has been chosen be-

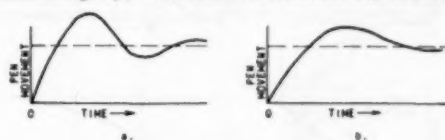


FIG. 4

- (a) TYPE OF CONTROLLED RESPONSE TO A STEP CHANGE IN SET POINT TO BE EXPECTED FROM TANGENCY TO AN $M = 2$ CIRCLE
 (b) TYPE OF CONTROLLED RESPONSE TO A STEP CHANGE IN SET POINT TO BE EXPECTED FROM TANGENCY TO AN $M = 1.3$ CIRCLE

cause it is popular in servomechanism studies and the other value 2, has been chosen because it is an integer and represents a degree of stability often sought in industrial control systems.

The steps involved in a frequency-response analysis of a control system have been outlined and at best are somewhat lengthy when compared to empirical and rule-of-thumb methods. However, as pointed out, once a few examples of basic systems are worked out the results are useful not only for the particular systems studied but form a basis of reasoning for studying all systems. Also, as familiarity with the system grows it will become evident that there are many short cuts and simplifications which can be applied to the methods used to obtain the results. It is not the purpose of this paper to develop or advocate the method of approach and analysis for there are numerous ways of treating the data which are described in servomechanism books (2, 3). Much can be said in favor of plotting the frequency-response data on rectangular co-ordinates rather than circular co-ordinates but since it is perhaps easier to learn the circular method first (even though it is more difficult to use) that is the method described. It is quite conceivable that a technique of analysis and synthesis might be developed which is more suitable for use on industrial systems than on servomechanisms.

While controller settings can be determined by frequency-response methods the primary value of the system does not lie here but in its ability to show the effect each variable has on the whole. It is a means of studying why a system behaves in a certain manner, or in a more positive and aggressive sense, what can be done to improve the behavior to meet certain requirements. The authors are not advocating frequency-response analysis as a cure-all or even as a substitute for empirical methods, for empirical methods will always play a major part in industrial-control analysis. Rather it is a tool which can be used where empirical methods are not satisfactory and where the expected results justify the additional effort. Before the method can be applied with facility, however, files or libraries of actual test data must be established.

TERMINOLOGY

Somewhat thorough descriptions of the symbols and terms used are in order before presenting the data. Letters have been assigned to each of the specific processes studied to avoid a complete description with each reference.

Type A refers to a process consisting of a transportation lag and a ramp or non-self-regulating response and has a step response as shown in Fig. 5(a).

Type B refers to a process consisting of a transportation lag and a single capacity and has a step response as shown in Fig. 5(b).

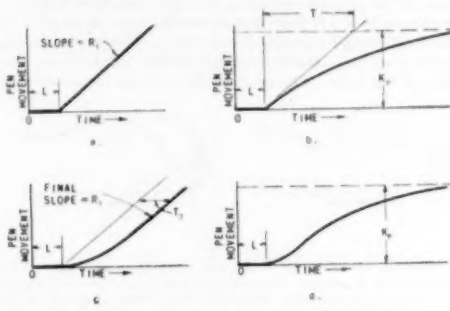


FIG. 5

- (a) STEP RESPONSE OF A TYPE A PROCESS
(b) STEP RESPONSE OF A TYPE B PROCESS
(c) STEP RESPONSE OF A TYPE C PROCESS
(d) STEP RESPONSE OF A TYPE D PROCESS

Type C refers to a process consisting of a transportation lag, a single capacity, and a ramp, and has a step response as shown in Fig. 5(c). It is a type A process with an added capacity.

Type D refers to a process consisting of a transportation lag and two capacities and has a step response as shown in Fig. 5(d). It is a type B process with an added capacity. Ramp refers to the non-self-regulating step response shown in Fig. 5(a).

Capacity refers to the classical capacity whose step response is the exponential shown in Fig. 5(b).

Degrees of stability are noted in the following manner:

Ultimate refers to conditions existing when the frequency-response curve passes through the -1 point.

$M=2$ refers to conditions existing when the frequency-response curve is tangent to the $M=2$ circle.

$M=1.3$ refers to conditions existing when the frequency-response curve is tangent to the $M=1.3$ circle.

M is a closed-loop magnitude ratio and will be defined further in the Appendix.

For sake of brevity, letters have been assigned to the co-ordinates on the polar plot but have not been used directly as variables under discussion. The co-ordinates are as follows:

A = phase angle, deg. Lag angles are minus, lead angles are plus

r = radius vector or magnitude ratio, arbitrary units

The variables fall into two classes, those which are in terms of time and those which are not. The following variables are functions of time:

L = transportation lag or velocity-distance lag and is shown in Fig. 5(a)

P = period of oscillation, the oscillation being either continuous or damped

R_1 = slope of ramp as shown in Fig. 5(a). Its dimension is somewhat arbitrary but when multiplied by K_p the product must have the dimension of $1/\text{time}$

T = time constant of a single-capacity lag and is shown in Fig. 5(b)

T_1 = another single-capacity time constant used in conjunction with type D process (The symbol T_1 has not been used in order to avoid possible confusion with T_d)

T_d = derivative time of controller: sometimes called rate, hyper, or preact action

T_i = integral time or reset time of the controller: is the reciprocal of reset rate

$\frac{1}{T_i}$ = reset rate

Since the units of time are only relative, all the results are reduced to a time scale based on L by referring the time variables R_1, T, T_1, T_d, T_i , and P to L . This technique eliminates one variable in the calculation and presentation of results and is necessary in a dimensionless approach.

The following variables are not a function of time:

K_c = controller gain, sometimes referred to as controller sensitivity; it is the reciprocal of throttling range or proportional band of controller

K_p = process gain and is shown in Fig. 5(b); its units are arbitrary as are those of K_c , but they must be the reciprocal of the units of K_c . For instance, if K_c is in psi/in. then K_p will be in in./psi so that the product $K_c K_p$ is dimensionless

$K = K_c K_p$ = loop gain in process types B and D

$K_p L R_1$ = loop gain in process types A and C

loop gain = product of all individual gains in loop

It is realized that many of these definitions could be expressed mathematically but the authors believe the foregoing to be less confusing and sufficiently defining.

PRESENTATION OF DATA

The following sections are classified according to the type of process A, B, C, or D, and in each section the use of controllers having proportional only, proportional-plus-derivative, and proportional-plus-reset actions are discussed. The general pattern in which the data are presented is to show the loop gain and period of oscillation along the vertical axis of the graphs and one of the independent variables along the horizontal axis. Logarithmic co-ordinates have been used throughout in order to present an undistorted picture but one disadvantage is that a zero cannot be shown. In order to overcome this disadvantage, the authors have introduced a vertical line on the left side of each graph which represents zero for the independent variable. Thus, if the derivative action in a proportional-plus-derivative controller is plotted along the horizontal axis and it is desirable to know the data for proportional control only, one need only refer to the data for zero derivative action which is shown on the additional vertical line mentioned. All data for ultimate conditions were obtained directly by slide-rule calculation while data for $M=2$ and $M=1.3$ conditions were obtained graphically.

Because process requirements are quite variable and indeed sometimes opposite, the authors purposely have avoided any statement of optimum conditions and have concentrated on showing the effects of common variables over a wide range. It is believed this type of information is particularly valuable for the

process industries because industrial systems are notably prone to changes in process parameters (lags, gain, and so on) with changes in operating conditions (load, through-put, and so on). In general, the optimum conditions defined by others (6, 7, 8, 9) fall near the $M=2$ conditions.

A NON-SELF-REGULATING PROCESS WITH TRANSPORTATION LAG

For a process whose step response consists of a transportation lag and ramp as shown in Fig. 5(a), the effects of using controllers having proportional only, proportional-plus-derivative, and proportional-plus-reset actions are shown in Fig. 6 and the corresponding frequency-response information is shown in Fig. 7.

Proportional Action Only. The control system with only proportional control action is represented in Fig. 6(a) when T_d is 0, or in Fig. 6(b) when $1/T_i$ is 0. These curves show that the ultimate period will be 4 times the lag ($P/L = 4$) and that the controller gain, K_c , at ultimate stability is

$$\frac{\pi}{2LR_1}$$

The fact that $K_c LR_1$ can be treated as a single variable can have several interpretations but they are all basically the same. Probably the most popular interpretation is that with all other variables held constant, controller gain is inversely proportional to lag and to the slope of the ramp which is consistent with the empirical-control theory. Thus, while the data are plotted in terms of

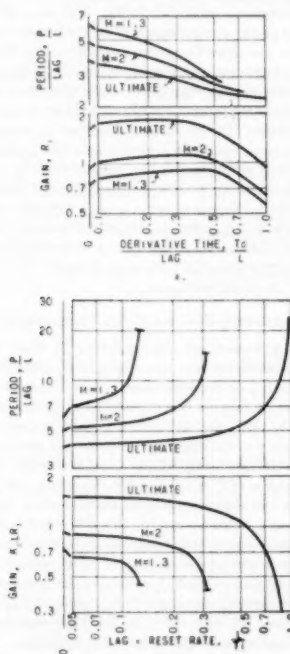


FIG. 6

- (a) USE OF A PROPORTIONAL-PLUS-DERIVATIVE CONTROL ON TYPE A PROCESS
(b) USE OF PROPORTIONAL-PLUS-RESET CONTROL ON A TYPE A PROCESS

$K_c LR_1$, they can be converted quickly to any of the variables K_c , L , or R_1 . Actually, it is believed the results are as useful in the relative sense as in the absolute sense, in which case the variables need not be separated.

For $M=2$ and $M=1.3$ stability the period increases to $5L$ and $6.3L$ or 25 and 57 per cent above the period for ultimate stability. The loop gain has to be reduced to 0.92 and 0.73 which, for a fixed process, means a reduction in controller gain to 59 and 46 per cent of the controller gain for ultimate stability.

The frequency-response curves for this process and a proportional controller have been discussed already.

Proportional-Plus-Derivative Action. Data on the system when using a proportional-plus-derivative controller are given in Fig. 6(a). For any degree of stability, it is seen that an increase in derivative action always decreases the period but that the allowable loop gain first increases and then decreases. The curves show that derivative times in the order of 0.5 to $0.6L$ will allow the same controller gain as with no derivative action but, will re-

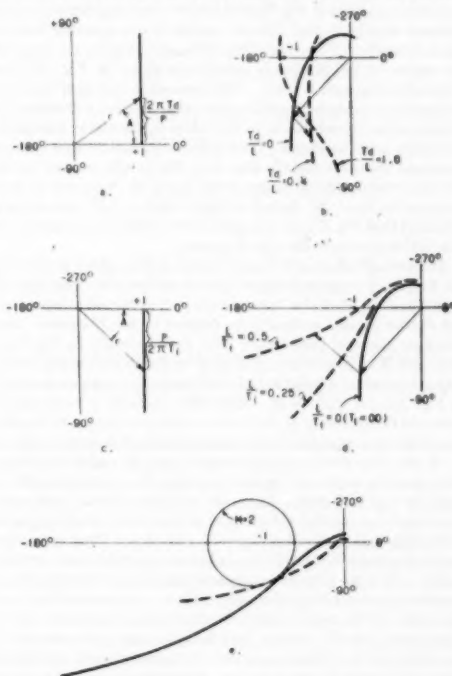


FIG. 7

- (a) FREQUENCY RESPONSE OF AN IDEAL PROPORTIONAL-PLUS-DERIVATIVE CONTROLLER, CONTROLLER GAIN UNITY
(b) SHAPING EFFECT FROM ADDITION OF DERIVATIVE ACTION TO A TYPE A PROCESS
(This is a combination of Figs. 2(a) and 7(a).)
(c) FREQUENCY RESPONSE OF AN IDEAL PROPORTIONAL-PLUS-RESET CONTROLLER, CONTROLLER GAIN UNITY
(d) SHAPING EFFECT FROM ADDITION OF RESET ACTION TO A TYPE A PROCESS
(This is a combination of Figs. 2(c) and 7(c).)
(e) FREQUENCY-RESPONSE DIAGRAM TO SHOW HOW GAIN REDUCTION CAN CAUSE M -TANGENCY IF RESET ACTION IS USED ON TYPE A PROCESS

duce the period to about $2.6L$ almost regardless of the degree of stability desired. The gain for $M=2$ to $M=1.3$ stability is about one half that for ultimate stability when derivative action is in use. For these and all gain curves shown in this paper the region above the ultimate gain curve represents unstable conditions and the region below it, stable conditions.

Derivative times greater than 0.5 to $0.6L$ do not reduce the period materially and require a considerable reduction in gain, it being almost inversely proportional to T_d/L for values of T_d/L above 1 , and the minimum period which can be approached is $2L$. Since this system does not have reset action, a decrease in gain increases the offset due to a load change.

A technique commonly used in combining frequency-response curves is first to separate those variables which affect only the scale of the plot from those variables which affect the shape. Then, after the shape is determined using a loop gain of unity, the loop gain is varied to establish the desired scale of the curve. The frequency response of an ideal proportional-plus-derivative controller is shown in Fig. 7(a), the word ideal meaning one which adheres exactly to the defining equation, not meaning best or most desirable. The effect derivative action has on the shape of the curve for the process in question is shown in Fig. 7(b) for which the loop gain is unity. The new curve is shaped from the original by moving each point on the original curve a distance T_d/L along a line perpendicular to the radius vector and in a counterclockwise sense as shown. The points obtained in this manner represent the same periods that they did on the original curve. Having established the shape of the curve, the loop gain is then adjusted to meet the desired stability criteria. It must be emphasized that Fig. 7(a) is a general curve while its application in Fig. 7(b) is specific to the type A process.

The over-all effect as derivative action is first added is to swing the frequency-response curve counterclockwise away from the -1 points and the M -circles, bringing the part of the curve representing shorter periods around to be tangent to the M -circles. The effect on gain and period have been shown already in Fig. 6(a). However, if large amounts of derivative action are added, the effect is to produce a bulge in the curve near the -1 point as shown in Fig. 7(b) for $T_d/L = 1$. This effect requires a reduction in gain and the geometry of the curve is such as to permit little additional decrease in period for the large amounts of derivative action.

On the polar plot, it is customary to refer to angles in a clockwise sense as angles of lag and to angles in a counterclockwise sense as angles of lead. From the stability criteria, it is easily visualized that increasing lag angles tend toward instability while increasing lead angles tend toward stability. Thus derivative action in general is a stabilizing influence because it provides lead angles. However, the phase angle is not the only variable to be considered when adding derivative action. As seen in Fig. 7(a), the length of the radius vector also increases as derivative action is increased, slowly at first, and then at large angles almost in proportion to it. At the same time, the proportionate increase in lead angle becomes less and less. Realizing the way the radius vector and angle vary with each other makes just another way of visualizing the results already shown in Fig. 6(a).

Proportional-Plus-Reset Action. Fig. 6(b) shows the effect of reset action on the variables period and gain for various degrees of stability. An increase in reset rate always increases the period and decreases the allowable gain for all degrees of stability. Data can be collected from these curves to indicate that provided gain, $K_c L R_i$, is held constant, the period of oscillation is not greatly affected by varying reset rates, only the degree of stability is affected. These curves also show that in certain ranges if reset rate is held constant and gain varied, the period of oscillation can change appreciably without comparable changes in the degree of stability.

As the product of reset rate times the lag approaches 1 , the allowable gain goes to zero and the period to infinity for this particular process and the process cannot be stabilized for values of L/T_i greater than 1 by changing the proportional action. The terminations of the $M=2$ and $M=1.3$ curves signify that there is a limit to the amount of reset action which can be used and still meet the M -circle criterion. These curves are the only ones presented in this paper which have such a termination. The reason for the termination will be more evident after viewing the frequency-response curve. Fig. 7(c) shows the frequency response of an ideal proportional-plus-reset controller and is a general curve corresponding to Fig. 7(a). The way proportional-plus-reset action shapes the curve for the particular process in question is shown in Fig. 7(d). With the gain factor unity, points representing the same period are moved a distance

$$r \left(\frac{P}{2\pi T_i} \right)$$

along a line perpendicular to the radius in a clockwise sense.

Again the loop gain was chosen as unity for plotting purposes. Note that in a sense reset action is opposite to derivative action but that the perpendicular distance plotted increases as the radius increases, having its greatest moving effect on the long periods while derivative action has its greatest effect on short periods.

After reset is added to the process in question, the tail of the curve, instead of approaching -90 deg, approaches -180 deg as the period increases. As shown in Fig. 7(e), this effect could be interpreted as partly encircling an M -circle because sufficient reduction in gain can draw the curve away from the M -circle on its right side, but cause tangency on its left side. This point of tangency represents a longer period of oscillation than did the previous point of tangency and further reductions in gain only tend toward instability. In this relationship lies the reason there is a limit to the amount of reset action which can be used and still meet an M -circle criterion, for the curve can remain so close to the -180 -deg line that it always passes through the desired M -circle rather than becomes tangent to it. Actually the curves for M stability of Fig. 6(b) reverse themselves to allow two values of gain and period for one reset rate but the other gain is so low and the period so long that the curves have been terminated rather than reversed, to avoid confusion.

SELF-REGULATING PROCESS WITH TRANSPORTATION LAG

Since most processes are self-regulating to some extent, it is necessary to determine how their behavior might differ from a non-self-regulating or ramp process. As a first approximation of the self-regulating process it is considered to have a step response as shown in Fig. 5(b), and is called a type B process for convenience. The study of this process involves one more independent variable than did the study of the type A process, this variable being T or the ratio of T to L . The components in the loop gain for the B process are slightly different from those in the loop gain for the A process. The reason for this difference stems from the fact that in the A process the slope can be treated as a gain but in the B process it cannot be so treated with universal accuracy. The data are shown in Figs. 8, 9, and 10 in the manner previously used, it being necessary to choose finite values of T/L to show the information since for each curve in the A process there is now a family of curves because of the additional variable.

Proportional Action Only. The type B process differs noticeably from a type A process at low values of T/L and imperceptibly at high values of T/L . Fig. 8 provides a picture of this difference from which it is seen that the allowable loop gain is always higher in the type B process and never less than 1 , while the period is always less in the type B but never being less than $2L$.

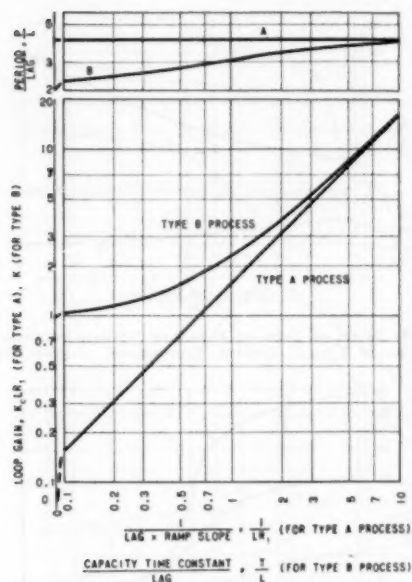


FIG. 8 COMPARISON OF PERIOD AND GAIN AT ULTIMATE STABILITY FOR TYPES A AND B PROCESSES, PROPORTIONAL CONTROL ONLY

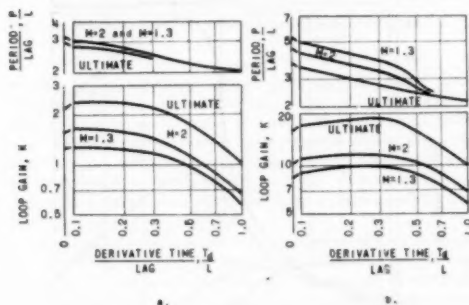


FIG. 9

- (a) USE OF PROPORTIONAL-PLUS-DERIVATIVE CONTROL ON TYPE B PROCESS, $T/L = 1$
 (b) USE OF PROPORTIONAL-PLUS-DERIVATIVE CONTROL ON TYPE B PROCESS, $T/L = 10$

For all practical purposes, the two types of processes are the same for values of T/L of 10 and above. Exactly what the lowest values of T/L are that is of practical importance is not known though it is possibly around 1. Lower values of T/L are of academic if not of practical interest.

If a load change is imposed on a type B process controlled with proportional action only it is well known that there will be a resulting offset of pen and pointer. If the controller is not acting, i.e., the valve is held fixed, and the same load change is applied, there will be a larger steady-state offset. The ratio of the uncontrolled to controlled offset is $1 + K$ on any self-regulating system, a relationship which forms a quick basis for estimating the K

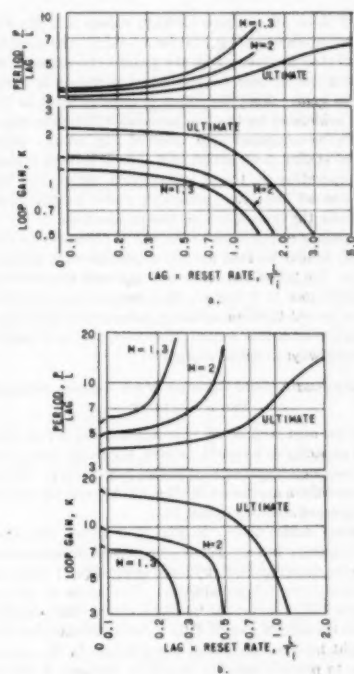


FIG. 10

- (a) USE OF PROPORTIONAL-PLUS-RESET CONTROL ON TYPE B PROCESS, $T/L = 1$
 (b) USE OF PROPORTIONAL-PLUS-RESET CONTROL ON TYPE B PROCESS, $T/L = 10$

of an existing system or for choosing a desirable K . This relationship does not exist on a type A process.

Proportional-Plus-Derivative Action. The curves for proportional-plus-derivative action on the type B process are shown in Fig. 9(a) for $T/L = 1$ and in Fig. 9(b) for $T/L = 10$. For high values of T/L , Fig. 6(a) may be used by substituting T/L for $1/(R/L)$. As for the type A process, the general effect as derivative action is added is to reduce the period toward some limit (which can be less than $2L$ for a type B process) and allow some increase in gain at first but then require a reduction in gain. These effects of decreased period and increased gain become less as the value of T/L decreases until at $T/L = 0$ (not shown) there is no gain peak and only slight period reduction. Notice that the loop gain for $M = 2$ and $M = 1.3$ stability bears about the same relationship to ultimate gain as it did for the type A process but that the period of oscillation for these degrees of stability approaches the period at ultimate stability as the ratio of T/L decreases. Thus it is seen that as the value of T/L decreases, derivative action becomes less effective as a period reducer and stabilizer.

The frequency-response curve of a type B process differs from that of a type A process in that its tail swings around counter-clockwise in a sort of semicircle and terminates on the 0-deg line at a point equal to K . In the extreme when $T/L = 0$ and $K = 1$, the curve is a circle of radius 1 with its center at the origin.

Proportional-Plus-Reset Action. The effect of reset rate on period and gain is shown in Fig. 10(a) for $T/L = 1$ and in Fig.

10(b) for $T/L = 10$. Again, for high values of T/L , Fig. 6(b) may be used by substituting T/L for $1/(R/L)$. The most noticeable effect is that the lower T/L the greater the amount of reset action which can be used for equivalent increases in period and decreases in gain. Also, the effect is more gradual as T/L decreases as evidenced by the less pronounced knee in the curves of Fig. 10(a) as compared with those of Fig. 10(b). Otherwise, the effect of adding reset action to a type B process is similar to the same operation on the A process and within the limits of practical interest the first paragraph under proportional-plus-reset action for the type A process also applies here.

The frequency-response curve for the B process with reset action will be similar to that for the A process with proportional action only; the tail of the curve will approach the -90-deg line as the period goes to infinity. As a consequence the M -circle criteria can be met through sufficient reduction in gain regardless of how much reset action is used; however, the sacrifice for large reset rates is always in period and gain.

A NON-SELF-REGULATING PROCESS WITH TRANSPORTATION LAG AND A CAPACITY

Perhaps the next step in the approximation of actual processes is to add a capacity to a type A process, the result being a type C process whose step response is as shown in Fig. 5(c). Curves for ultimate conditions are shown in Figs. 11, 12, and 14, and for the various degrees of stability in Fig. 13.

Proportional Action Only. In Fig. 11 is shown the effect the additional capacity has on period and gain at ultimate stability. The loop gain decreases from $\pi/2$ and approaches 1 while the period increases from $4L$ indefinitely. The slope of the period curve after a T/L of about 2 is $1/2$, which means that period is proportional to the square root of T/L . One interpretation of these curves might be that the use of a restriction in the controller-output line to provide stability is a futile attempt if the process is originally a type A process controlled with proportional action only for it serves only to decrease allowable gain rather than increase it, and in addition, the period is greatly lengthened (the restriction and the capacity of the valve top offer a capacity lag, an increase in restriction being an increase in T/L in Fig. 11). Another factor which aggravates this situation still further but which is not shown in Fig. 11, is that as T/L increases there is a greater spread both in period and gain between ultimate conditions and $M=2$ or $M=1.3$ conditions. Thus, if the loop gain of a type C process having a T/L of 10 changes, say, due to valve characteristics, then stability does not vary greatly, only the period varies. This same effect was noted for proportional-plus-reset action on the type A process and stems from the same reasoning on the frequency-response curve.

Proportional-Plus-Derivative Action. There are two major differences between the type A and the type C processes when derivative action is used. One is that much greater benefits can be derived in the way of decreased period and increased gain, and the other is a lack of uniform correspondence between ultimate, $M=2$, and $M=1.3$ stability. By the latter is meant the lack of parallelism or near parallelism between the ultimate, $M=2$, and $M=1.3$ curves which was so evident in the type A process, Fig. 6(a).

Fig. 12 shows the data for ultimate conditions from which it is seen that the processes having the higher T/L are the ones most benefited by derivative action. However, too many conclusions must not be drawn from these curves alone because the conditions for $M=2$ and $M=1.3$ stability are not shown. For these conditions on a type C process with $T/L=10$ refer to Fig. 13. Note that for no derivative action the gains for $M=2$ and $M=1.3$ stability are considerably less than one-half ultimate; in fact, for $M=1.3$ the gain is about 0.1 ultimate. There is also a larger

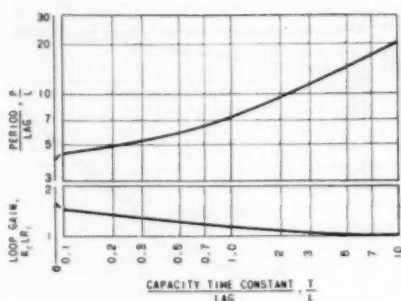


FIG. 11 EFFECT ON GAIN AND PERIOD AT ULTIMATE STABILITY OF CAPACITY IN TYPE C PROCESS, PROPORTIONAL CONTROL ONLY

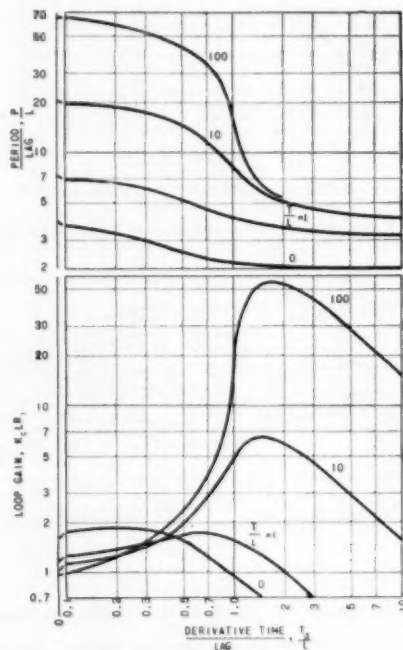


FIG. 12 USE OF PROPORTIONAL-PLUS-DERIVATIVE CONTROL ON TYPE C PROCESS, ULTIMATE STABILITY

sacrifice in period for M -stability as compared with the type A process. These features were mentioned in connection with proportional action only. On processes such as this it would be difficult to determine ultimate loop gain exactly by test because a wide range of gains would produce slowly damped cycling which might be judged just short of the continued cycling of ultimate stability.

There is little effect on either gain or period as derivative action is first added but then a region is reached in which there is great effect on both as shown; in fact, the effects are more prominent on the M -curves than on the ultimate curves. These effects also

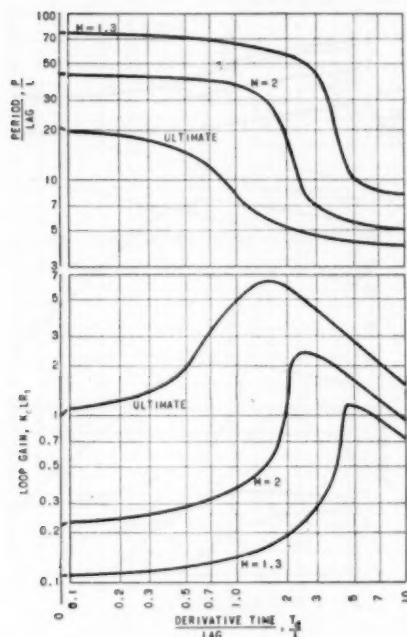


FIG. 13 Use of Proportional-Plus-Derivative Control on Type C Process, $T/L = 10$

increase as T/L increases. Shortly after the gain peak is passed the periods are near their minimum and at a T_d/L of 10 the system is the same as a type A process, with proportional action only. This is true because if in a proportional-plus-derivative controller the derivative time equals the time constant of a capacity the effect of the capacity is canceled. Note that it is not desirable to have a derivative time large enough to cancel completely the effect of the capacity.

The frequency-response curve for the foregoing process crosses the -180 -deg line at a shallower angle than that for the type A process. Thus to obtain tangency with a given M -circle the gain must be reduced from ultimate much more than previously. But it is on just such curves that derivative action is most effective as a stabilizing tool because of the general counterclockwise rotation it imparts to the curve. There is, however, a practical limit to the attainment of the high gain peaks and that is the difference between actual and ideal derivative functions. An ideal derivative function can produce a phase advance approaching 90 deg while actual derivative functions must fall short of this, the amount depending on the design. It is for such applications that double derivative or two derivatives in series are valuable but it is not within the scope of this paper to discuss this function. Probably other practical limitations on the attainment of the high gain peak and great period reduction are friction, dead spot, and noise.

Proportional-Plus-Reset Action. Reset action is generally less exciting than derivative action and in most cases is only a necessary evil to obtain zero error. Fig. 14 shows the application of the proportional-plus-reset controller to the type C process for ultimate stability from which it can be seen that all curves are

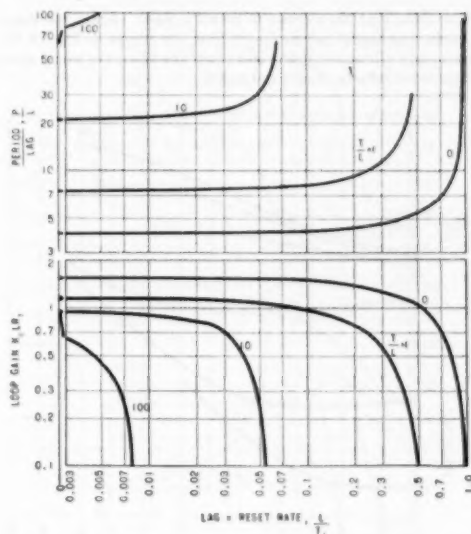


FIG. 14 Use of Proportional-Plus-Reset Control on Type C Process, Ultimate Stability

basically the same except for the location of the knee in the curve. The vertical distribution of the curves corresponds to Fig. 11.

A Two-Capacity Process With Transportation Lag

A two-capacity process with transportation lag or type D process is a type B process with one more capacity. The added capacity has the effect on the step response of making it S-shaped or "toed in" as shown in Fig. 5(d). While the time constants of the two capacities T and T_1 can be determined from the step-response curve it is not as direct a procedure as it was for the type B or C process.

For each curve used in describing the type B process there is now necessarily a family of curves because of the additional variable. The curves pertaining to the type D process are shown in Figs. 15 through 22, all of them being for ultimate conditions only, except for Fig. 19 which shows M -stability also. It is immaterial which capacity is considered T and which T_1 , so there is some duplication in the presentation of the curves as necessary to provide a complete picture. For instance, curves for $T/L = 1$ and $T_1/L = 10$ are identical to those for $T/L = 10$ and $T_1/L = 1$.

Proportional Action Only. Fig. 15 provides an over-all picture in terms of loop gain and period of the effect of adding the second capacity to a process already characterized by T/L of 1, 10, and 100. The effect on the allowable loop gain as the new capacity is added is first to decrease it and then finally to increase it. It is interesting to note that the ultimate loop gain is very nearly its original value when the time constant of the additional capacity is one half the time constant of the original capacity ($T_1/T = 1/2$). The period, however, is not subject to this reversal and continues to increase as the new capacity is added, approaching some limit and essentially reaching it by the time T_1/T is 10. Thus, while an added capacity could not be used to stabilize a type A process, it can be used to stabilize a type B process, and the sacrifice in period is dependent on the original value of T/L . Generally those processes having a low T/L are the ones difficult to stabilize within the limits of the controller gain and it

is on those that the sacrifice in period is least. Again, too many conclusions should not be drawn from the curves in Fig. 15 because only ultimate stability is shown; the M -curves would show more severe effects on gain and period.

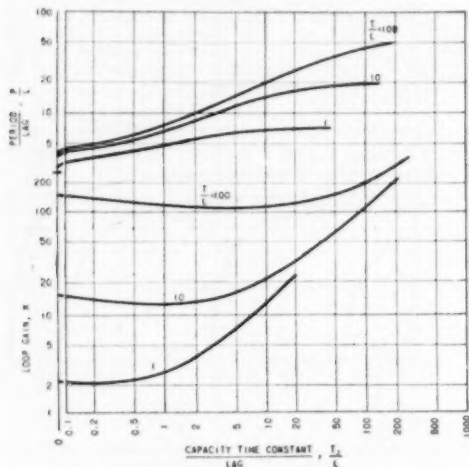


FIG. 15 EFFECT ON GAIN AND PERIOD AT ULTIMATE STABILITY OF SECOND CAPACITY IN A TYPE D PROCESS, PROPORTIONAL CONTROL ONLY

Proportional-Plus-Derivative Action. Data for ultimate stability using proportional-plus-derivative action for the type D process are shown in Figs. 16, 17, and 18. For each figure one of the capacities is held constant and the other is varied to form a family of curves. The same general effects of derivative action are again noted and the vertical distribution of the curves corresponds to Fig. 15. The period is uniquely tied to the gain and a derivative time setting slightly longer than that for the peak gain provides most of the reduction in period which can be achieved with the derivative function. Again, however, too much stress cannot be put on curves for ultimate stability because $M = 2$ and $M = 1.3$ stability might be vastly different.

As an extreme case, the $M = 2$ and $M = 1.3$ stability curves have been worked out for $T/L = T_2/L = 100$ and are shown in Fig. 10. The effects are the same as those in Fig. 13 but more extreme both in the separation of the curves at T_d/L near zero and in the improvement effected by the use of derivative action. The peculiar reversal of the curves indicates more vividly than previously that gain can be varied over a very wide range without influencing stability to any extent, the period being the factor affected. The possible limitations on the attainment of such benefits on a physical system have been mentioned already in connection with Fig. 13, but at least it is enjoyable to speculate that period might be reduced 30-fold and gain increased 100-fold through the use of derivative action. Another point of interesting consideration is that of purposely changing a process approaching the type B into one decidedly a type D through use of a restriction and capacity and then, through use of derivative action, obtain high gain. This seems contrary to common sense and there will be a sacrifice in period, but the thought is interesting in any event.

Proportional-Plus-Reset Action. Figs. 20, 21, and 22 are offered as a guide for visualizing the effect of reset action on a type D

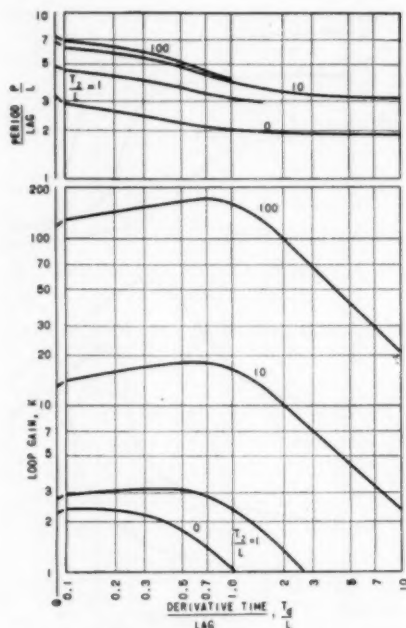


FIG. 16 USE OF PROPORTIONAL-PLUS-DERIVATIVE CONTROL ON TYPE D PROCESS, $T/L = 1$, VARIABLE T_2/L , ULTIMATE STABILITY

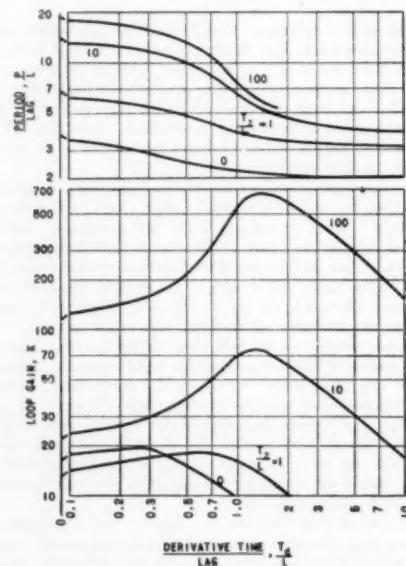


FIG. 17 USE OF PROPORTIONAL-PLUS-DERIVATIVE CONTROL ON TYPE D PROCESS, $T/L = 10$, VARIABLE T_2/L , ULTIMATE STABILITY

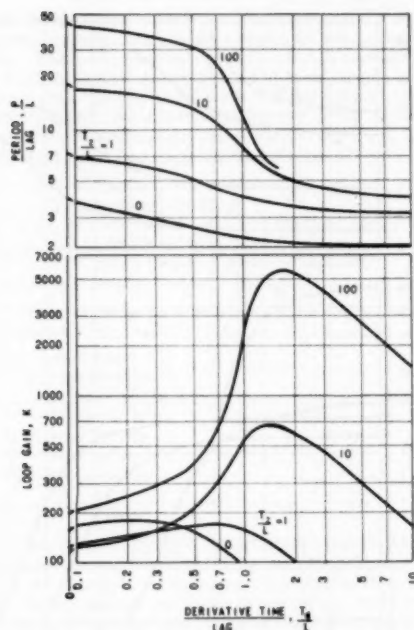


FIG. 18 USE OF PROPORTIONAL-PLUS-DERIVATIVE CONTROL ON TYPE D PROCESS, $T/L = 100$, VARIABLE T_d/L , ULTIMATE STABILITY

process, but since they represent only ultimate conditions no comment will be made.

CONCLUSION

The foregoing treatment of the method and data illustrates that frequency-response analysis can be largely free from the complicated mathematics usually associated with control theory. The practical interpretations which may be applied to the data presented are abundant but only a few have been mentioned for it is not within the scope of this paper to discuss the numerous physical factors which contribute toward transportation lags, capacity lags, ramps, or the gain, derivative, and reset effects which may manifest themselves in the process as well as in the controller. Rather, the authors have concentrated on presenting the information in a perfectly general form for simple processes, which data can form stepping stones toward the interpretation of specific process problems.

In view of the fact that frequency response is such a versatile basis on which to assemble knowledge, it would seem advisable for the process and instrument industries to accumulate and tabulate such information about the component parts of the control loop and about the closed loop. This information can be from actual frequency-response tests, from accurately converted step-response tests, or from applicable theoretical considerations. While concepts derived from studying the few systems presented do form a concrete basis of reasoning in the design or revision of processes or in the explanation of existing phenomena, a collection of quantitative data as suggested would be invaluable in the design or selection of equipment. In this connection, frequency-response data provide a consistent basis on which to compare

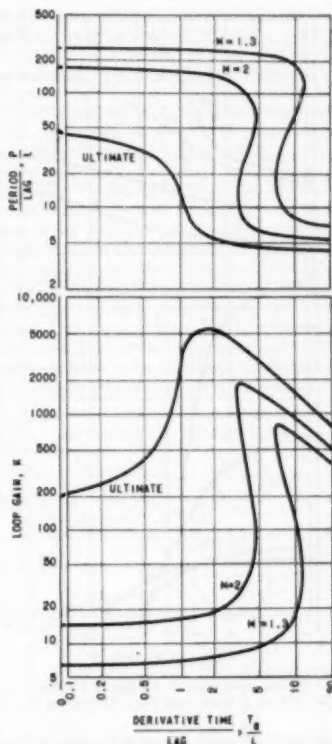


FIG. 19 USE OF PROPORTIONAL-PLUS-DERIVATIVE CONTROL ON SPECIFIC TYPE D PROCESS, $T/L = T_d/L = 100$

competitive or alternate pieces of equipment or evaluate new equipment.

In a sense the types A, B, and C processes are all special cases of the type D process, but rather than treat them as such the authors have chosen to discuss them separately for purposes of simplicity. However, the types C and D or even only D approximate real processes more closely than do types A and B and therefore deserve a fuller treatment than has been given in this paper. Also, the use of a three-term controller (proportional-plus-derivative-plus-reset) is of widespread interest but the problem of presenting the data for such a controller on a type D process in an easily interpretable manner is not a small one. The fuller coverage of the types-C and D process as well as the introduction of a three-term controller are left for a possible later paper.

BIBLIOGRAPHY

- 1 "The Analysis and Synthesis of Linear Servomechanisms," by A. C. Hall, The Technology Press, Massachusetts Institute of Technology, 1943.
- 2 "Principles of Servomechanisms," by G. S. Brown and D. P. Campbell, John Wiley & Sons, Inc., New York, N. Y., 1948.
- 3 "Servomechanisms and Regulating System Design," by H. Chestnut and R. W. Mayer, John Wiley & Sons, Inc., New York, N. Y., vol. 1, 1951.
- 4 "Servomechanism Transient Performance From Decibel Log Frequency Plots," by H. Harris, Jr., M. J. Kirby, and E. F. von Arn.

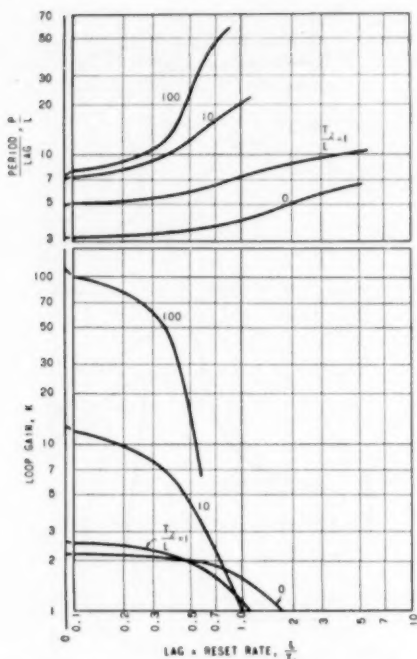


FIG. 20 USE OF PROPORTIONAL-PLUS-RESET CONTROL ON TYPE D PROCESS, $T/L = 1$, VARIABLE T_1/L , ULTIMATE STABILITY

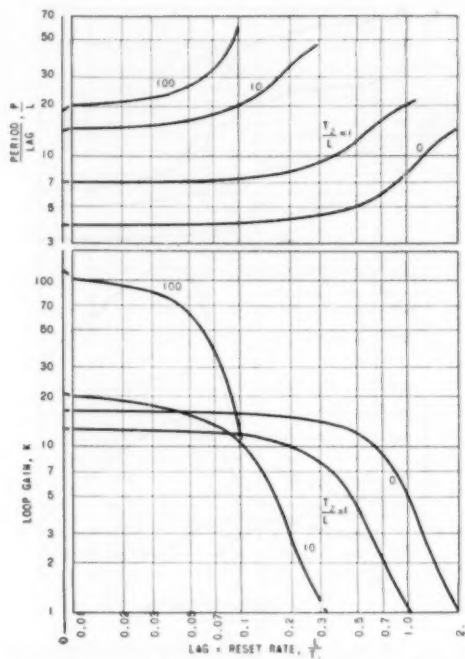


FIG. 21 USE OF PROPORTIONAL-PLUS-RESET CONTROL ON TYPE D PROCESS, $T/L = 10$, VARIABLE T_1/L , ULTIMATE STABILITY

advance copy, technical paper, American Institute of Electrical Engineers, printed May 24, 1951.

5 "On the Automatic Control of Generalized Passive Systems," by K. L. Chien, J. A. Hrones, and J. B. Roswick, *Trans. ASME*, vol. 74, 1952, pp. 175-185.

6 "Optimum Settings for Automatic Controllers," by J. G. Ziegler and N. B. Nichols, *Trans. ASME*, vol. 64, 1942, pp. 759-765.

7 "The Optimum Adjustment of Regulators," by P. Hasebroek and B. L. van der Waerden, *Trans. ASME*, vol. 72, 1950, pp. 317-322.

8 "Theoretical Considerations on the Optimum Adjustment of Regulators," by P. Hasebroek and B. L. van der Waerden, *Trans. ASME*, vol. 72, 1950, pp. 309-315.

9 "Controller Settings for Optimum Control," by W. A. Wolfe, *Trans. ASME*, vol. 73, 1951, pp. 413-418.

10 "The Dynamics of Automatic Controls," by R. C. Oldenbourg, and H. Sartorius, translated and edited by H. L. Mason, published by ASME, 1948.

11 "The Practical Application of Frequency Response Analysis to Automatic Process Control," by C. I. Rutherford, *Proceedings of The Institution of Mechanical Engineers*, vol. 162, 1950, pp. 334-354.

Appendix

The Appendix is intended to show how the data presented in the body of this paper were calculated and at the same time show how similar data not presented in the paper can be obtained. In connection with the method, a typical example is set up and discussed. A little more information is given about the -1 point and M -circle criteria and a method of obtaining time constants from a two-capacity step response is also discussed. No proof of any of the algebra or trigonometry is given for it can be obtained elsewhere.

Method. One of the important concepts in the field of control

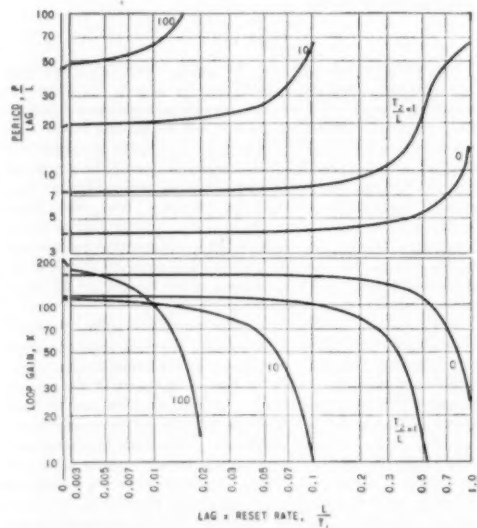


FIG. 22 USE OF PROPORTIONAL-PLUS-RESET CONTROL ON TYPE D PROCESS, $T/L = 100$, VARIABLE T_1/L , ULTIMATE STABILITY

theory is the relationship between what comes out of a piece of equipment to what goes in, or more briefly, the ratio of output to input. This ratio, called the transfer function, is normally written in algebraic form and is the basis of calculating frequency-response data. In Fig. 23 are shown the step response, the frequency response, and the transfer function for all of the independent variables studied in the body of this paper.

The symbols not used previously are defined as follows:

- e = Napierian base = 2.718
 j = imaginary symbol, $j^2 = -1$
 K_1, K_2 , etc. = individual gains of each function; their product for the complete loop is K
 s = complex variable = real + j imaginary
 ω = angular frequency = $2\pi/P$

A brief review of the symbols previously used which also occur in the table are listed below:

- A = phase angle
 L = transportation lag
 P = period of oscillation
 r = magnitude ratio
 R_1 = slope of ramp
 T = capacity lag
 T_d = derivative time
 $1/T_i$ = reset rate

To obtain frequency-response data from the transfer function, substitute j for s and separate the real from the imaginary part. Then plot these data, for variable ω , on rectangular co-ordinates with the real axis horizontal and the imaginary axis vertical. The result will be exactly the same as shown in the frequency-response column of Fig. 23 whose co-ordinates are polar rather than rectangular.

The unitized frequency-response curves and the transfer functions shown in Fig. 23 are building blocks for assembling a complete loop. If the components they represent are in series or cascade, as they are in all the systems treated in the body of the paper, the frequency response of the complete loop can be obtained by the addition of angles and the multiplication of radii, as mentioned previously, or the transfer function of the complete loop may be obtained by multiplication. For instance, if the process in question is a type D process and it is to be controlled by proportional-plus-derivative action the transfer function is

$$\frac{K_1 e^{-Ls} K_{2a} K_{2b} K_3 (1 + T_d s)}{(Ts + 1)(T_s + 1)} \quad [1]$$

or

$$\frac{K(e^{-Ls})(1 + T_d s)}{(Ts + 1)(T_s + 1)} \quad [2]$$

The subscripts a and b are used to differentiate the two capacity-lag gains. As used in the body of the paper (K_1) (K_{2a}) (K_{2b}) = K_p and $K_3 = K_v$. The frequency-response co-ordinates for the foregoing process and controller would be

$$r = \frac{K_1 K_{2a} K_{2b} K_3 \sqrt{1 + (T_d \omega)^2}}{\sqrt{1 + (T \omega)^2} \sqrt{1 + (T_s \omega)^2}} \quad [3]$$

and

$$A = \frac{-180L\omega}{\pi} - \tan^{-1}T\omega - \tan^{-1}T_s\omega + \tan^{-1}T_d\omega \dots [4]$$

To obtain ultimate conditions merely equate r to 1 at $A = -180$ deg. To obtain $M = 2$ and $M = 1.3$ conditions the fre-

quency-response curve must be calculated and plotted in the region of the M -circles and a tangency produced. There are graphical techniques which can be used to determine the K necessary to produce tangency to a given M -circle but these will not be discussed here.

This in brief is how the data which have been shown in the body of this report were obtained. As mentioned earlier, the open-loop frequency-response plots on circular co-ordinates are possibly easier to understand on first encounter than other methods of presentation but such plots do not lend themselves to synthesis as well as other methods of plotting do. It is definitely not the purpose nor within the scope of this paper to describe a method of synthesis but a few words are not out of order. Widely accepted and used in the servomechanism field are rectangular plots of phase and log magnitude versus log frequency. These are convenient for analyzing, combining, and filing test and calculated data. They also lend themselves to graphical approximations of the frequency-response information and thereby by-pass most of the calculating labor. Plots of the frequency-response curve on rectangular co-ordinates using log magnitude ratio ver-

FUNCTION OR COMPONENT	STEP RESPONSE	FREQUENCY RESPONSE	TRANSFER FUNCTION
TRANSPORTATION LAG			$K_1 e^{-Ls}$
CAPACITY LAG			$\frac{K_2}{Ts + 1}$
RAMP			$\frac{K_3 R_1}{s}$
PROPORTIONAL ONLY CONTROLLER			K_4
PROPORTIONAL PLUS DERIVATIVE CONTROLLER			$K_5 (1 + T_d s)$
PROPORTIONAL PLUS RESET CONTROLLER			$K_6 \left(1 + \frac{1}{T_i s}\right)$

FIG. 23 FREQUENCY-RESPONSE BUILDING BLOCKS

quency-response curve also have advantages over the circular co-ordinate plots, after a reasonable acquaintance with frequency response is established.

Example. As an example, consider an air-heating system whose loop is assembled in the following manner: The controller output operates a 3-way valve which mixes hot and cold water and supplies it to a finned-tube heater. Air passes over the heater and

the temperature is sensed by a mechanical tube system. The tube system operates a pen in a proportional-only pneumatic controller.

Taking a trip around the loop the lags and gains might be analyzed in the following manner: The resistance in the controller output tubing and the capacity in the valve top offer a capacity lag which is small in this case, by observation having a time constant less than $1/3$ sec. The gain is 10 per cent of valve travel per psi. Next there is a negligible lag in achieving a new water temperature once the valve has been moved but there is a gain of 100 F for 100 per cent valve travel. Then there is a transportation lag of 2 sec to get the mixed water to the heater and the gain is 1 F/F, assuming the pipe effects little cooling. Once inside the heater the distribution to the heating surfaces is somewhat complicated and the lags do not fit well into any of the simple types discussed but it is known from design data that the gain of the heater is 0.6 F change in air temperature per 1 F change in water temperature entering the heater. Continuing around the loop there is next a transportation lag in the air from heater to bulb which from the velocity-distance considerations is calculated to be $1/4$ sec, and the gain is again 1 as it was for the other transportation lag. From previous test data it is known that the bulb represents a double capacity lag having time constants of $1/3$ and 40 sec in air for the velocity at hand and the gain, almost by definition, is unity. In view of the other lags in the system the controller lag is negligible.

A review of the loop shows it to have two transportation lags which total $3/4$ sec, capacity lags whose time constants are 40, $1/3$, and less than $1/4$ sec, and a complicated heater lag.

For simplification the small capacity lags may be added to the transportation lag to give a total of 4 sec. Thus the frequency response of every component in the loop may be calculated except for that of the heater.

The process gain is

$$\left(\frac{10 \text{ per cent}}{\text{psi}}\right) \left(\frac{100 \text{ F}}{100 \text{ per cent}}\right) \left(\frac{1 \text{ F}}{\text{deg F}}\right) \left(\frac{0.6 \text{ F}}{\text{deg F}}\right) \left(\frac{1 \text{ F}}{\text{deg F}}\right) \left(\frac{1 \text{ F}}{\text{deg F}}\right) = \frac{6 \text{ F}}{\text{psi}} \quad [5]$$

A step-response curve of the process would suggest that the heater acts like a single capacity having a long time constant but since it is one of the important lags in the system some frequency-response test data could very well be called for. Since there is no convenient way to separate it as a unit from the rest of the system its frequency response must be found indirectly. This can be done by first determining the frequency response of the process by test and then removing the effects of the known lags and gains by calculation, the remainder being the frequency response of the heater alone. For purposes of completing this example assume the heater was found to behave as a single capacity having a time constant of 200 sec.

Now having complete frequency-response information it is possible to investigate cause and effect in whatever direction is desirable. Because a frequency-response test on the process has been made, the calculated gain and period at ultimate conditions will agree with actual gain and period, but if all data were calculated then it would be desirable to check these conditions by test if possible and then if necessary revise some of the lag and gain approximations in order to bring the calculated and actual into agreement.

While the actual system is made up of a number of lags, it has been reduced to a loop approximated by a transportation lag of 4 sec and two capacity lags of 40 and 200 sec, respectively. Thus

$$\begin{aligned} L &= 4 \text{ sec} \\ T &= 40 \text{ sec} \\ T_2 &= 200 \text{ sec} \end{aligned}$$

or

$$\frac{T}{L} = 10 \quad [6]$$

$$\frac{T_2}{L} = 50$$

and

$$K_p = \frac{6 \text{ deg F}}{\text{psi}}$$

From Fig. 15 it is seen that the ultimate loop gain is 60; therefore the ultimate controller gain is $60/6 = 10 \text{ psi/deg F}$. From this figure it is also seen that $P/L = 18$ or $P = 18 \times 4 = 72 \text{ sec}$. While no data have been presented which show the $M = 2$ and $M = 1.3$ stability for this particular process, Fig. 13 can be used as a first approximation by substituting T_2/L for $1/(LR_1)$. If this is done the ultimate loop gain K is 50 which is reasonably close to the 60 obtained from Fig. 15, and $P/L = 20$ which is in good agreement with the value of 18 previously determined. The values of gain and period for proportional only or proportional-plus-derivative control can be determined from this figure with reasonable accuracy.

If the time constant of the sensing element could be cut from 40 sec to 4 sec ($T/L = 1$) then Fig. 15 shows that loop gain at ultimate stability will be somewhat less than previously but not appreciably, while the period will be reduced to $7L$ or 28 sec. However, there will not be the spread between ultimate gain and period and $M = 2$ or $M = 1.3$ gain and period that there was when the process approximated Fig. 13; the spread will be more like that shown in Fig. 6(a). This will result in the controller gain at $M = 1.3$ stability being higher than it was for the slower temperature-sensing bulb, even though the ultimate gains are essentially the same, and the improvement in period will be even more pronounced than the 72 to 28-sec ratio indicated.

Returning to the original system but evaluating a different variable, Fig. 15 shows that further increases in the time constant of the heater T_2 will increase the ultimate controller gain almost in proportion without affecting the period of oscillation to any extent. This is also borne out by the fact that Fig. 13 is a close approximation of the system as it exists and becomes closer as T_2/L becomes larger, of course substituting T_2/L for $1/(LR_1)$.

The same type of reasoning just described can be used to evaluate the effect of transportation lag or the small capacity lags included in transportation lag, but enough curves have not been provided for a quick or limitless evaluation of all variables. It was not within the purpose or scope of this paper to provide the great variety of curves which would be necessary to study a process fully by the procedure outlined here.

In this study the frequency response of a particular heater used in a particular way was determined. For purposes of simplifying the example it was assumed to be a single capacity lag but in any instance, whether it is simple or complicated, that information has been determined and may be used if the heater is applied elsewhere in a similar manner or may be used as a basis of comparing the performance of this heater with another.

The -1 Point and M-Circles. As explained before, the frequency response of the complete loop can be established experimentally by breaking the loop anywhere, conveniently in the controller-output line, and imposing a cycle, the relationship between the imposed and resultant cycle being the complete frequency response. If the frequency and loop gain are such that the resultant magnitude is identical to the imposed magnitude and lags it by a full cycle or 360 deg, then it is obvious the loop

could be closed and the cycle would sustain itself, ultimate stability existing. In terms of frequency response this means the magnitude ratio is 1 and the phase lag is 180 deg since the other 180-deg phase lag of the controller has been allowed for in plotting the frequency-response curve. Thus the connection of the —1 point with the ultimate stability becomes obvious.

Until now all frequency-response information pertained to open loops or individual pieces of equipment from which there was no feedback. If the loop is closed and the set point is varied sinusoidally there will be a resultant sinusoidal variation shown by the pen. The ratio of the resultant magnitude to the imposed magnitude is the closed-loop magnitude ratio M . M -circles are the loci of points representing the same magnitude ratio in the closed loop when the open-loop frequency-response data are plotted in the manner described. The closed-loop magnitude ratio and phase angle are uniquely related to the open-loop magnitude ratio and phase angle, for the closed-loop magnitude ratio is the ratio of the length of the radius vector to the length of the vector drawn from the —1 point and the phase angle is the angle between these two vectors. (Graphs are available for making the conversion from open to closed loop or vice-versa.)

Discussion

E. G. HOLMANN.⁵ In any classification of systems and presentation of data, some degree of selective sampling is inevitable, and the choice will depend largely on the relative importance placed upon the various performance aspects. The choice of M -circle stability as a performance criterion has gained almost universal acceptance in the servomechanisms control field in the last decade. This criterion has proved to be of immense value in the design of the simpler type of systems.

Even so, it may not be out of place to utter a word of warning for the benefit of the industrial-control engineer who is not too familiar with the mathematics underlying the frequency and transient-response concepts. In making the transition from frequency response to transient response, band width plays a part that is about as important as the amount of maximum response ratio. In using the M -circle criterion, band width is ignored—a procedure that is justifiable only because in the majority of problems we are dealing with systems that are effectively low-pass filters, and because the frequency at M -stability is usually indicative also of the order of magnitude of the cutoff frequency.

While it is true that graphical or numerical methods for making the transition from frequency response to transient response are approximate, the authors' statement that they are not aware of any exact analytical methods is somewhat surprising. The inverse Laplace or Fourier transformation is a tool designed to do just that. For example, the transient response, to a unit impulse, of a system characterized by the complex frequency response $H(j\omega)$ is uniquely given by

$$h(t) = \frac{2}{\pi} \int_0^{\infty} \operatorname{Re} H(j\omega) \cos \omega t d\omega$$

RUFUS OLDENBURGER.⁶ This paper emphasizes the great importance of the frequency-response approach to control problems. Advantages of this powerful approach are well known. To be up to date a designer of automatic controls must have a knowledge of frequency-response techniques.

Important though it may be, the frequency-response approach is but one of many tools available to the control engineer. It has

limitations which should be borne in mind; in fact, frequency-response methods should be used only where indicated. That will depend on the nature of the problem. The frequency-response approach has the advantage that it can be taught to technicians unacquainted with the mathematical theory underlying this approach but has the obvious disadvantage that it may be employed by incompetent personnel in situations or in a manner not justified by the theory.

The frequency-response approach as we understand it arose in the telephone field, where a primary concern is how a system responds to periodic inputs. Thus it is desired to transmit the human voice without distortion from one place to another, in which case the signal at the receiving end is to be in a sense identical with the input. The telephone designer must concentrate to a considerable extent on the transmission of sinusoids involving the steady-state solution of the differential equations, and he often does not care about the exact nature of the transients as long as they die out rapidly enough so that they can be neglected. On the other hand, in the control of a physical variable, such as temperature, transients play an important and often dominant role. Suppose that the temperature of a system is to be kept constant. If there is an undesirable disturbance L , the temperature is not to respond to L but is to remain constant, in so far as possible. If we think of L as information, it is information we wish to suppress. It is when the temperature setting is changed that we wish the temperature to change also. Changes in temperature setting as a function of time may be thought of as input information and the actual variation of temperature as the output. Here we have a case of transmission of information. Not only is the setting change often nonperiodic, but in a wide variety of applications the setting is kept fixed most of the time. While it is fixed, one is concerned only with the suppression of responses to undesired disturbances.

Since there is so much emphasis on transients in the design of automatic controls, it appears that it is desirable to study the transients as directly and accurately as possible. For rough design purposes only, certain readily obtained properties of the transients, rather than the transients themselves, are needed. Some of these follow immediately from frequency-response information.

In the communication field it is customary to design for certain gain and phase margins, which are a measure of stability. The "servo" people do a similar thing when they design on the basis of M -curves. This is in a sense equivalent to using the Routh stability inequalities and making the convention that if $a > b$ is any one of the inequalities to be satisfied, we design our system for $a > 2b$ to be on the safe side. The Routh stability criterion applies to algebraic equations and therefore does not hold for systems with transportation or dead time and cannot be applied unless the equation of the system is available. The Nyquist stability method does not suffer these disadvantages. Application of the Routh criterion to an algebraic equation is a very simple computation and can be done much faster than the plotting of curves on the Nyquist plane, so that in this sense the Routh method is to be preferred when it can be used.

Although under rather general mathematical assumptions the transient solutions can be obtained from the frequency-response curves, the actual computation of these curves is a serious matter. Various authors have concerned themselves with methods for rapidly obtaining important properties of transients from frequency response curves.^{7,8,9} The writer refers to maximum

⁵ Electrical Engineering Department, Shell Development Company, Emeryville, Calif.

⁶ Mathematician, Woodward Governor Company, Rockford, Ill. Mem. ASME.

⁷ "Servomechanism Transient Performance From Decibel-Log Frequency Plots," by H. Harris, Jr., M. J. Kirby, and E. F. von Arx, Trans. AIEE, vol. 70, part 2, 1951, pp. 1452-1459.

⁸ "Comparison of Steady-State and Transient Performance of Servomechanisms," by Harold Chestnut and R. W. Mayer, Trans. AIEE, vol. 68, 1949, pp. 765-777.

overswing, the duration of the transient, and similar factors. Curves have been prepared so that the analyst need but refer to them to obtain these properties. Unfortunately, all of the rapid techniques for obtaining properties of transients from open-loop frequency-response curves or transfer functions are based on the assumption that the system is second order, or that there are no complex characteristic roots, or that other restrictions of a similar nature hold. When the necessary assumptions are satisfied, these techniques are valuable and are not to be minimized. However, in the governor and allied fields, where the writer's control experience lies, the systems are almost always fundamentally of the third order or more, even when all possible numerically large characteristic roots are discarded, and economic considerations make it often necessary to be satisfied with roots that are definitely oscillatory.

The frequency-response approach thus lends itself to qualitative studies of system transients, but it is by no means equally suited to quantitative analyses of the transients.

In an old highly developed field, such as the governing of prime movers, qualitative information about transients is not generally sufficient. Direct study of the transients is indicated, at least to the point of obtaining characteristic roots. By proper techniques the solution for the roots is not difficult.¹¹ Each problem has its own peculiarities. If use is made of these, the solution for roots will be very rapid; but unfortunately there is little published material on this subject of help to the control engineer. Analog computers are especially useful for obtaining the actual transient curves, the plotting of which is a laborious procedure.

Frequency-response runs on system components have been most useful to the writer's company for checking transfer functions. It is our experience that it is desirable to derive these functions from basic mathematical laws and check the derivations with the frequency-response runs. The process of obtaining transfer functions by matching transfer functions to experimental data is laborious and inaccurate as compared to the derivation of transfer functions from basic laws. However, experimental frequency responses will show up neglected factors, unsuspected nonlinearities, and other equally pertinent information. Thus by frequency-response runs we have found a dead time on the order of $1/16$ sec between the fuel flow at the fuel valve and the speed of a gas turbine, a dead time not yet explained by theory. This dead time accounted for serious design troubles. The company has a mobile truck equipped with a mechanical oscillator, oscillographs, and other devices for making frequency-response runs in the field.

There are situations where limitations of time, or other factors, make it necessary to obtain the transfer function experimentally. This may involve merely working with the frequency-response curves and not actually matching a formula to these curves. The transfer function so obtained has some disadvantages: (a) Common factors in numerator and denominator will not show up in frequency-response runs. As an example, consider the transfer function $f(s)$ given by

$$f(s) = \frac{s+1}{s+1}$$

relating the variables y and x in the equation

$$y' + y = x' + x$$

where the primes denote differentiation with respect to time t , x is the input, and y the output of a physical component. The frequency-response runs will give the transfer function $g(s)$, where $g(s) = 1$. If we have a transient where y is initially different from x , due, for example, to a load disturbance on the system, the transient is not $y = x$, as is to be inferred from $g(s)$, but rather

$$y = x + Ce^{-t}$$

for a constant of integration $C \neq 0$.

(b) Another disadvantage of an experimentally determined transfer function, and thus a differential equation for a physical component, is that it does not show how this differential equation is physically derived from others. This may affect the initial conditions for the transients, and hence the transients, as we shall illustrate. Consider the equation

$$y'' + \frac{3}{2}y' + y = x' + x$$

with the transfer function $f(s)$, where

$$f(s) = \frac{s+1}{s^2 + \frac{3}{2}s + 1}$$

This equation will represent, for example, the physical configuration composed of a weight A with co-ordinate y free to move in the vertical y -direction only, attached to a vertical dashpot B , whose other end is fixed, and attached to a spring C , and dashpot D whose other ends are rigidly connected at a point E above A with co-ordinate x , free to move in the vertical direction. Consider a unit step change in x defined by the relations

$$\begin{array}{ll} x = 1 & t \geq 0 \\ x = 0 & t < 0 \\ x' = 0 & t \neq 0 \\ x' \text{ undefined} & t = 0 \end{array}$$

Since x' is undefined at $t = 0$, the differential equation in y and x is undefined at this instant. We assume that the system is at rest for $t < 0$. We can then obtain a solution for y in the usual manner¹² with the initial conditions

$$y = y' = 0, \quad t = 0^+$$

The same second-order differential equation in x and y can be obtained by combining the equations

$$y' + \frac{y}{2} = x + z$$

$$z' + z = -\frac{y}{2}$$

The first equation may be taken to represent an engine where y is the speed of the engine, x the load, and z the throttle position, provided proper units are employed. The second equation can then be interpreted to be a droop-governor equation. If now we make the step change in x employed in the foregoing, we have the initial conditions

$$y = 0, y' = 1, t = 0^+$$

based on the assumption that $y = z = 0$ at $t = 0$.

The same initial conditions for y and y' are obtained in either case by replacing the unit step function for x by an approximating curve with no discontinuities in x and x' , and taking the limit of

¹¹ "The Analysis and Optimum Synthesis of Linear Servomechanisms," by Donald Herr and Irving Gerst, Trans. AIEE, vol. 66, 1947, pp. 959-970.

¹² "Principles of Servomechanisms," by G. S. Brown and D. P. Campbell, John Wiley & Sons, Inc., New York, N. Y., 1948.

¹³ "Practical Computational Methods in the Solution of Equations," by Rufus Oldenburger, American Mathematical Monthly, vol. 55, June-July, 1948, pp. 335-342.

¹² "Introduction to Applied Mathematics," by F. D. Murnaghan, John Wiley & Sons, Inc., New York, N. Y., 1948.

the solution $y = y(t)$ as the approximating curve approaches the unit step function. However, there may be cases where different initial conditions are to be used for the different physical situations. The assumptions $y = z = 0$, $x = 1$ at $t = 0^+$ and the two first-order equations determine y' at $t = 0^+$, whereas the combined second-order equation with $y = x' = 0$, $x = 1$ at $t = 0^+$ does not determine y' , but only the value 1 of the combination $y'' + \frac{3}{2}y'$. If we choose $y' = 0$, we have $y'' = 1$ so that the step change in x affects y'' but not y and y' .

The authors are to be congratulated on their excellent exposition of certain aspects of the frequency-response approach.

W. E. VANNAH.¹³ Perhaps the greatest task we have at present in the application of the frequency-response technique is that of education. The authors of this paper have made a significant contribution to the required education by a clear presentation of the fundamentals with a minimum of mathematics. Figs. 1, 2, 3, and 4 of the paper and the corresponding text are excellent basic reference material for the engineer who wishes to understand. They constitute a translation of previously published material which has examined thoroughly the theoretical background. Previous authors on the subject have found it necessary to explain the fundamentals of the technique before presenting application. With the fundamentals now well covered, we look forward to papers reporting on applications. As a step in this direc-

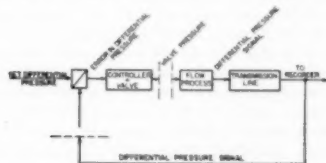


FIG. 24 BLOCK DIAGRAM OF FLOW-CONTROL SYSTEM

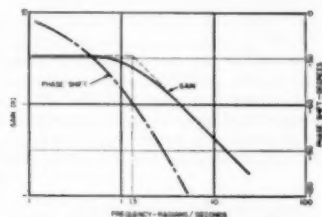


FIG. 25 GAIN-PHASE PLOT OF FLOW PROCESS

tion and as an illumination of the present paper, we offer a simple example of application.

Fig. 24 of this discussion is a block diagram of a flow-control system. The broken lines show the points at which sinusoidal disturbances may be applied and measured.

Fig. 25 is the frequency response of a flow process with gain (output magnitude)/(input magnitude) and frequency of applied sinusoidal disturbances plotted on logarithmic scales, and with phase shift between output and input plotted on a linear scale superimposed along the right of the graph. Plotting of the frequency response on these co-ordinates produces curve shapes which reveal significant characteristics. For instance, the observed slope of one-half gain per frequency double indicates the

process is a single-capacity one. The intersection between zero slope and the slope of one-half gain per frequency double determines the time constant.

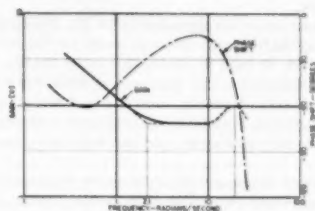


FIG. 26 GAIN-PHASE PLOT OF A CONTROLLER AND VALVE MOTOR

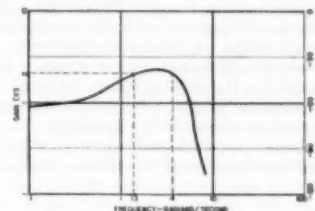


FIG. 27 GAIN PLOT OF CLOSED LOOP

In Fig. 26 the frequency response of a controller is plotted on the same co-ordinates as those of Fig. 25. Reset action is evidenced by the portion of the curve coming in at a slope of one-half gain per frequency double to intersect the proportional gain of the controller at a frequency which is a measure of the reset time constant.

The process is known to have a transportation lag L , of 0.1 sec. Time constants are taken from Figs. 25 and 26. Hence

$$\begin{aligned} \frac{L}{T_1} &= 0.17 & T &= 0.77 \text{ sec (Fig. 25)} \\ \frac{T}{L} &= 7.7 & T_2 &= 0.05 \text{ sec (Fig. 26)} \\ \frac{T_2}{L} &= 0.5 & T_1 &= 0.6 \text{ sec (Fig. 26)} \end{aligned}$$

Application of these values to the curves given in the paper indicates that the period will be 0.6 sec at $M = 2$, and that the controller gain must be doubled to go from $M = 2$ to ultimate stability. Both of these indications agree with our observations within 85 per cent, although the absolute values of indicated controller gain do not check closely. The frequency (gain only) response of the closed loop is shown in Fig. 27.

AUTHORS' CLOSURE

The authors wish to thank each of the discussers for his interest in the paper. Several points have been raised which will be discussed as follows:

The authors are grateful to Mr. Holzmann for emphasizing an unintended interpretation which might be applied to the statement in the paper regarding exact transient solutions. The interpretation intended was that there is no way of obtaining the exact transient response from frequency-response data in tabular or graphical form. Unless $H(j\omega)$ is known analytically the inverse Fourier transform must be approximated by numerical methods and hence is not exact.

¹³ Research and Development, The Foxboro Company, Foxboro, Mass.

It is not clear to the authors how Mr. Holmann has connected band width to stability; perhaps he has reference to the effect the shape of the curve near M -circle tangency has on the character of the transient.

The authors are in full agreement with Mr. Oldenburger when he states that the frequency-response method is but one of several tools which can be used in automatic-control studies, that each tool has its limitations, and that each problem has its one best method of attack. However, only one tool meets the requirements of simplicity, versatility, and sufficient accuracy essential for wide-scale industrial usage, and that is the frequency-response tool.

The transient response is the information of interest to the industrial-control engineer. The authors find that in every case treated in the paper for which exact transient data are available, the agreement between transients predicted from M -circles and the exact transient solution is good. Thus the use of M -circles as a rapid conversion technique is not limited to second-order systems or to systems with complex characteristic roots. The only restriction that the authors are aware of is that, if the curve is peculiarly shaped in the stability region, the rapid conversion techniques become less reliable. As yet the authors have not encountered a physical system with this peculiarity.

Mr. Oldenburger's approach to an industrial-control problem is somewhat different from that of the authors. Rather than writ-

ing theoretical equations and then complementing them with test data, the authors find it easier to obtain test data and then complement them with theory. Perhaps the basic difference is in the type of system studied. This different approach places emphasis on different phases. If the data are obtained first then they can be handled by well-known and rapid techniques without curve-fitting to determine the transfer function. Thus the opportunity of using the Routh stability criteria empirically would never exist. The only occasion for writing the transfer function would be to place it in a computer to determine a more accurate transient than that available from M or gain and phase-margin criteria.

The authors have not as yet experienced the disadvantage of experimentally determined transfer functions that Mr. Oldenburger mentions. If the input-output transfer function is incomplete because of the possibility of intermediate load disturbances, then the load-output transfer function can be determined experimentally and incorporated in the study.

Mr. Vannah's comments in support of the simplicity of presentation is encouraging; his example of application is a valuable addition to the paper.

Frequency-response techniques will by no means answer all questions which arise in connection with the dynamics of industrial automatic-control systems, but they represent a sizable step in that direction. With this everyone seems to be in agreement. The problem currently is one of accumulating usable data.

The Effect of High-Frequency Sound Waves on an Air-Propane Flame

By C. J. KIPPENHAN¹ AND H. O. CROFT²

This paper describes measurements of normal flame velocity of propane-air mixtures by the "burner method." The experimental burner was so arranged that high-frequency sound could be introduced into the burner and allowed to travel through the gas-mixture column and combustion zone. Experimental measurements indicate that high-frequency sound does not change the magnitude of the normal flame velocity. Visual observations disclose a change of combustion-zone configuration of sound-influenced flames from the usual "cone" to a flattened bowl shape for laminar flames, and to a suspended violently agitated zone in the case of turbulent flames, both possessing remarkable stability.

INTRODUCTION

THERE is considerable literature on the theory of flame propagation in the case of so-called "stationary" flames burning on the rim of a tubular burner. This material is well presented by Lewis and von Elbe (1), Jost-Croft (2), and others. These authors also discuss the burner method of normal flame-velocity determination. A considerable amount of work has been performed on studies of the effect of electric fields of both constant and alternating voltages applied both longitudinally and transversely on combustion zones. Work of this character is reported by Malinowski and co-workers (3), Haber (4), and others. Experimental work is reported by Hannemann and Ehret (5), on the effect of low-frequency, high-intensity sound on the combustion process. The effect of sound on flame stability is reported by Markenstein (6), and by Loschek, Fein, and Olsen (7). The last authors also report effect on normal flame velocity.

The term "normal flame velocity" as used here alludes to the velocity at which a stable flame front advances normally to itself relative to the unburned mixture flowing from a burner tube. The work herein reported was an attempt to assess the influence of high-frequency sound waves of considerable intensity on the combustion process and, in particular, the effect on normal flame velocity.

EXPERIMENTAL ARRANGEMENTS

The first requisite for this study was the production of rather large intensity-high frequency sound waves and a method of applying or coupling these disturbances to the combustion system.

The production of waves at the frequencies desired [in the

ultrasonic range roughly from 20 kilocycles (kc) per sec up] can be achieved by a variety of arrangements.

The prime difficulty the experimenter meets, however, is the effective coupling of the vibrating source to the system. The effectiveness of coupling varies in direct proportion to the acoustical resistance of the medium (ρc = product of medium density and velocity of sound) (for solids $\rho c \approx 1.5 \times 10^4$, liquids $\rho c \approx 1.5 \times 10^3$, gases $\rho c \approx 40$). Effective coupling of the piezo and magnetostriction apparatuses at the intensities and frequencies required for this study is virtually impossible. The final choice of the sound generator was thus limited to one producing the waves directly in a gaseous medium. The only unit capable of meeting the requirements set out at the time of this investigation, was a Hartmann-type gas-current generator. This choice was of necessity a compromise, the main items sacrificed being frequency regulation and wave form of the produced sound.

The principle of the Hartmann generator is not generally well known, so a brief résumé seems justified. The reader is referred to Hartmann's (8) original paper for more complete detail. The operation of this generator depends upon the inherent instability of a jet of gas discharging from a straight-sided or convergent nozzle into a region of subcritical pressure to form the disturbance waves. The curve of impact-pressure variation with distance from the nozzle assumes a dampened sinusoidal shape. Thus a cavity or resonator body, axially aligned with the jet axis, and introduced at one of the pressure peaks, alternately fills and empties with a definite period, depending primarily on the volume of the cavity. This alternate filling and emptying of the cavity sets up a sound wave which is propagated through the gaseous medium.

A generator of the Hartmann type was designed to produce sound at frequencies of approximately 20, 40, and 100 kc. Tests of the jet nozzles and resonators constructed revealed the actual frequencies produced to be approximately 26.4, 44.8, and 57.5 kc.

In the first part of this investigation the propane-air mixture was allowed to expand through the sound-generator nozzle, the entire system being confined within an enclosure to collect the spent gas and to conduct it through the burner tube to the combustion zone. This experimental arrangement is shown in Fig. 1. Maximum sound intensity could be applied to the combustion zone in this manner. This direct application required a compromise since the flow rate of propane-air mixture was fixed quite definitely both in maximum and minimum by the pressure and rate flow requirements of the sound producing jet. The quantities of mixture burned were thus dependent upon the experimental frequency.

It is apparent that for any particular mixture composition, the supply velocity for stable flames lies in a very narrow range. Thus with the fixed flow rate dictated by the requirements of the sound generator, the diameter of the burner had to be adjusted to yield suitable supply velocities. This resulted not only in a rather cumbersome experimental arrangement, but also limited this phase of the investigation to turbulent-mixture flow.

Some considerable difficulty was experienced owing to flame fluctuations induced by this turbulence. These flames were photographed by means of ordinary speed motion-picture photography. Mean combustion-surface areas were evaluated from a

¹ Associate Professor of Mechanical Engineering, Washington University, St. Louis, Mo. Jun. ASME.

² Dean, College of Engineering, University of Missouri, Columbia, Mo. Mem. ASME.

³ Numbers in parentheses refer to the Bibliography at the end of the paper.

Contributed by the Gas Turbine Power, Fuels, and Applied Mechanics Divisions and presented at the Annual Meeting, Atlantic City, N. J., November 25-30, 1951, of THE AMERICAN SOCIETY OF MECHANICAL ENGINEERS.

NOTE: Statements and opinions advanced in papers are to be understood as individual expressions of their authors and not those of the Society. Manuscript received at ASME Headquarters, August 4, 1949. Paper No. 51-A-112.

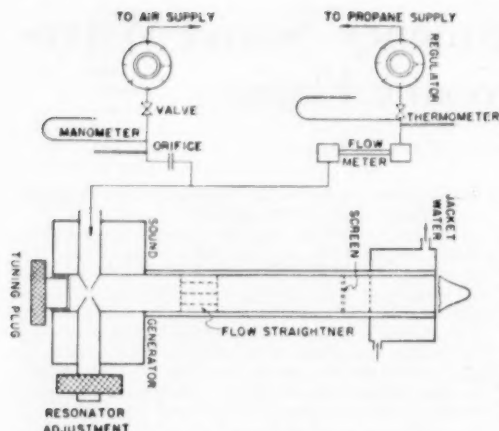


FIG. 1 SCHEMATIC DIAGRAM SHOWING EXPERIMENTAL EQUIPMENT ARRANGEMENT FOR TESTS CONDUCTED ON TURBULENT FLAMES

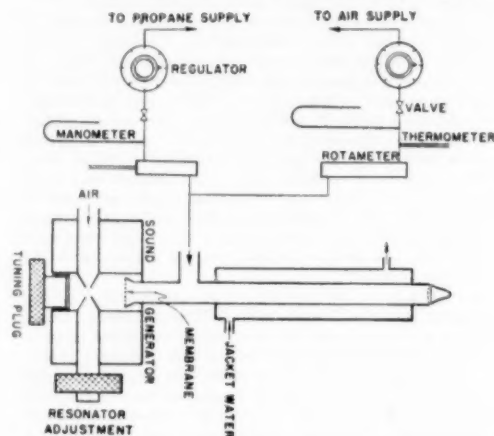


FIG. 2 SCHEMATIC DIAGRAM SHOWING EXPERIMENTAL EQUIPMENT ARRANGEMENT FOR TESTS CONDUCTED ON LAMINAR FLAMES

sample of 10 frames chosen at random from a population of 300 to 400 frames and analyzed to determine the areas of each flame. The mean area was chosen as the numerical average of the ten samples. A check of sample size of 20 and 30 frames from the same population showed a maximum change in the mean of 7 per cent. The maximum deviation from the mean of any individual sample was 14 per cent. From areas so determined and the propane and air flow rates, the normal flame velocity and mixture composition could be determined.

Laminar flames were investigated by separating the air-driven sound source from the burner-mixture supply by means of a thin membrane. Experimental measurements showed transmission of sound waves of considerably smaller amplitude to burner mouth. Fig. 2 shows this experimental arrangement.

Since the mixture flow rates were quite small and little fluctuation of the flames was noted, single still photographs for combus-

tion-zone-area determination were taken once steady-state conditions had been achieved, and normal flame velocities were calculated in the usual manner.

The introduction of flexible membranes between the sound source and the burner tube did without question distort the wave forms to an undetermined degree, as well as considerably diminish the sound intensity.

EXPERIMENTAL MEASUREMENTS

The calculation of normal flame velocities can proceed when the quantities of gas-air mixture flows per unit of time and the area of the combustion zone are established. The flow rates of air and propane were measured by means of calibrated flowmeters, at measured pressure and temperature conditions. Thus both volumetric and weight flow rates could be calculated.

Determination of combustion-zone area was accomplished from measurements of enlarged photographs. Unbounded flame areas, closely approximating cones, can be computed easily from photographs showing flame cross section. In the case of bounded flames it was necessary to apply a graphical construction on the basic photograph before planimetry because of rounding of flame shape.

The average normal flame velocity over the entire combustion zone can then be calculated by application of the continuity principle

$$W_m = (W_a + W_p) = v_m \gamma_m = \text{const} \\ = (v_a \gamma_a + v_p \gamma_p) = V_n S \gamma_m$$

Thus

$$V_n = \frac{V_a \gamma_a + v_p \gamma_p}{S \gamma_m} = \frac{v_a + v_p}{S}$$

where

- W = weight rate of flow, lb per sec
- v = volume rate of flow, cfs
- γ = specific weight of gas, cu ft per lb
- V_n = average normal flame velocity, fps
- S = surface area of combustion zone, sq ft

Subscripts:

- a = air at inlet condition
- p = propane inlet condition
- m = mixture at inlet conditions

The normal flame velocities reported in this paper are corrected to standard inlet conditions, 29.92 in. Hg pressure and 70 F.

These flame velocities are plotted against per cent theoretical air.

The determination of the sound-characterizing quantities, frequency and intensity, concluded the experimental quantities requiring measurement. Considerable search revealed no ready solution to the sound-intensity measurement—in fact, only a very rough estimate of sound intensity above a vibrating membrane was attempted using a hot-wire anemometer. This indicated an order of magnitude of about 1 milliwatt per sq cm. Sound-frequency determinations were made using the standing-wave method in a horizontal tuned tube, with a liquid layer as an indicating agent. Half-wave lengths thus measured combined with velocity of sound yielded estimates of sound frequencies.

VISUAL OBSERVATIONS

Several interesting phenomena were noted while experimenting with sound-affected flames:

- 1 In most cases turbulent flames subjected to high-frequency

direct sound radiation tended to lift from the burner rim and to burn with considerable agitation, but remarkable stability, in a suspended position approximately 1 diam above the burner rim. Special flow-straightening and stilling devices had to be introduced to seat the flames. A quantitative estimate of sound intensity made by visual observation of the tuned-frequency-determination tube gave a positive indication of sound waves, but of diminished magnitude due to blocking by these flow-straightening devices.

2 In the case of laminar flames influenced by sound waves the combustion zone was changed from a quite sensitive cone shape to an inherently stable flattened-bowl shape, Fig. 3. This directly extends the work of Hannemann (5) to these considerably higher frequencies.

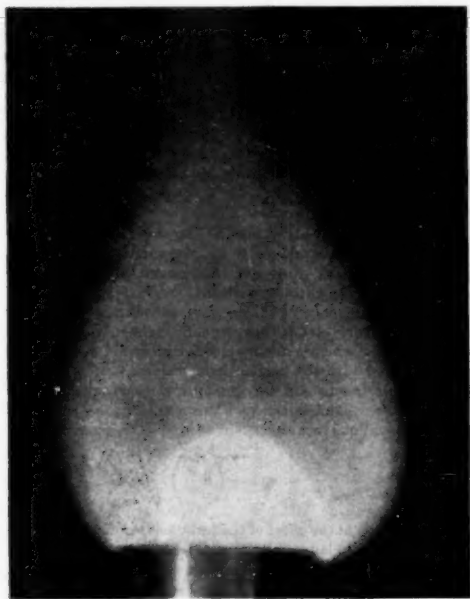


FIG. 3 FLATTENED-BOWL SHAPE OF COMBUSTION ZONE IN CASE OF LAMINAR FLAMES INFLUENCED BY SOUND WAVES

EXPERIMENTAL RESULTS

The normal flame velocities calculated from the experimental data are shown in Fig. 4. Both the turbulent- and the laminar-flame velocities are shown in this illustration as functions of per cent theoretical air.

The solid curve drawn through the mean of the laminar-flame data exhibits the characteristic peak or maximum flame velocity near the stoichiometric-mixture composition. The values obtained check quite well with the work of other experimenters. It should be noted that the points representing the flames influenced by 44.8-ke-per-sec sound lie within the normal scatter of points from the mean. Therefore it must be concluded that the normal flame velocity of sounded laminar flames was not changed in this particular study. This fact stands despite the shape change of the combustion zone previously described.

The dashed curve in Fig. 4 is drawn through the mean of the data taken from turbulent flames. This mean curve again ex-

hibits the peaked shape at very slightly fuel-rich mixture. The value of the maximum velocity is somewhat greater than the laminar maximum. Application of the criteria for estimating turbulent-flame maximum normal velocities (9) yields theoretical results 15 per cent greater than those found experimentally in this study. The tendency of the maximum point shift toward richer mixtures for turbulent flames is reasonable and may be explained as due to enhanced mixing with surrounding air. The experimental points representing sound-influenced turbulent flames lie within normal scatter limits and do not depart systematically from the nonsounded data. This leads to the conclusion that sound within the range of frequencies and intensities used in this study does not change the normal flame velocity of simple laminar- and turbulent-burner flames.

SUMMARY

1 Experimental measurements of normal flame velocity made by the burner method indicate that high-frequency sound waves within the range used have little or no effect on this important parameter. This was verified for flames formed on a burner tube in which the flow Reynolds number was above and below the lower critical limits (turbulent and laminar flames).

2 Visual observations indicate that while resultant flames are of a dissimilar nature as regards shape and configuration of the combustion zone, high-frequency sound tends to stabilize the flames against blowoff or flashback due to small external or internal perturbations.

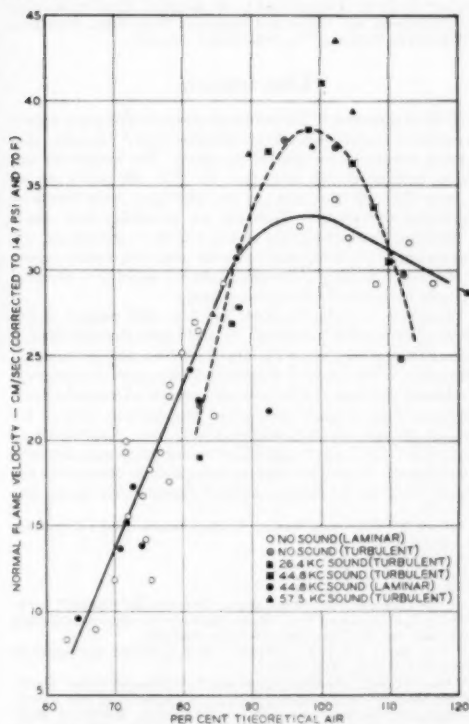


FIG. 4 NORMAL FLAME VELOCITY AS A FUNCTION OF PER CENT THEORETICAL AIR

BIBLIOGRAPHY

- 1 "Combustion, Flames and Explosions of Gases," by B. Lewis and G. von Elbe, Cambridge University Press, London, England, 1958.
- 2 "Explosion and Combustion Processes in Gases," by W. Jost, translated by H. O. Croft, McGraw-Hill Book Company, Inc., New York, N. Y., 1946.
- 3 "Influence of Electric Longitudinal Fields on the Combustion of Acetylene," by A. E. Malinovski and F. A. Lavrov, *Physik, Sowjetunion*, vol. 2, 1932, pp. 52-58.
- 4 "Effect of Frequency of an Electric Field on the Velocity of Combustion of Gases," by A. E. Malinovski, V. S. Russuklin, and V. P. Timkovskii, *Physik Z. Sowjetunion*, vol. 5, 1934, pp. 902-905 (see also pp. 212-220).
- 5 "Über die Rolle der Elektrizitätsträger bei der Explosion Brennbaren Gase in Gemisch mit Luft" ("On the Role of Electricity Carriers in the Explosion of Combustible Gases Mixed With Air"), by F. Haber, *Sitzungsberichte der Akad. Wissenschaften*, Berlin (Preuss.), *Phys.-Math.*, vol. 2, 1929, pp. 162-170.
- 6 "Einfluss Starker Schallwellen auf eine Stationäre Gas-Flamme," ("Effect of Strong Sound Waves on a Stationary Gas Flame"), by H. Hannemann and L. Ehret, *Zeitschrift für Technische Physik*, vol. 24, 1943, pp. 228-242.
- 7 "Interaction of Flame Propagation and Flow Disturbances," by G. H. Markstein, Third Symposium on Combustion and Flame and Explosion Phenomena, University of Wisconsin, Madison, Wis., September 7-11, 1948.
- 8 "The Effect of Sound on the Normal Velocity and Stability Limits of Laminar Propane-Air Flames," by S. Loshaek, R. S. Fein, and H. L. Olsen, University of Wisconsin, NOrd, Report 9938 CN 553, July, 1949.
- 9 "New Method for the Generation of Sound Waves," by J. Hartmann, *Physical Review*, vol. 22, 1922, pp. 719-727.
- 10 "The Effect of Turbulence on Flame Speeds of Burner Type Flame," by D. T. Williams and L. M. Bollinger, Third Symposium on Combustion and Flame and Explosion Phenomena, University of Wisconsin, Madison, Wis., September 7-11, 1948.

Discussion

G. H. MARKSTEIN.⁴ The results presented in this paper appear to confirm a conclusion reached in previous work,⁵⁻⁹ namely, that burning velocity is not affected by sound. The frequencies employed in these studies range from less than 100 cycles per sec to more than 50 kilocycles per sec, but leave wide bands of frequencies unexplored. Therefore the possibility that effects of sound on chemical kinetics and/or transport phenomena and thus on burning velocity may occur for other frequencies cannot be excluded; coupling phenomena between sound and chemical reactions have indeed been contemplated.¹⁰

No agreement seems to exist, however, with respect to the effects of sound on flame shape. It would seem desirable that in future studies of this nature visual and conventional photographic observation of the flame be supplemented by spark shadowgraph or schlieren photography, in order to ascertain whether the flame surface actually remains smooth and stationary in spite of the presence of high-frequency sound disturbances. Exploration of the flow field by means of particle or smoke traces may also help to understand the peculiar changes of flame shape observed in the present study and by Hannemann and Ehret,⁴ as well as the lift-

ing that occurred in the present work only for turbulent flames but which was observed by Loshaek^{7,8,9} with laminar flames.

The conclusion reached by the present authors regarding the effect of sound on blowoff and flashback stability is at variance with the results of Loshaek, et al.,^{7,8,9} that were obtained in very careful and quantitative work; moreover, it does not seem to be substantiated by their own experimental results.

It may be worth while to mention that although the effects of sound waves on burner flames appear to be of minor significance, flames burning in tubes were found to be affected by sound to a much larger extent, regardless of whether the sound was applied artificially¹¹ or whether it was generated spontaneously by the flame.^{12,13} The essentially negative results of the work on burner flames would seem to confirm the writer's opinion¹⁴ that the phenomena which occur in tubes should be ascribed primarily to variations of flame-surface area rather than of burning velocity.

A. A. PUTNAM.¹⁵ An interesting question regarding these tests is brought up by the similarity between the shape of an acoustically disturbed flame front, as shown by Markstein's¹⁴ photographs, and the shape of the turbulent flame front, as shown by Karlovitz, et al.,¹⁷ the distortions of the fronts given by both workers are of approximately the same size. Since Markstein used frequencies below 1000 cycles, we may ask what distortion in flame front should be expected when an ultrasonic frequency is used.

If a value of jet velocity of about 4 fps, and a sound frequency of 50 kc are assumed, sound pulses will pass through the flame at a spacing of about $1/4$ in. However, these pulses will not affect the flame directly. The effect will occur through the production of vortices, at the boundary of the stream, as shown by Markstein. The spacing of vortices and their size will be not $1/4$ in., but about 0.001 in. Thus, whereas low frequencies produced disturbances large compared with the laminar-flame thickness of about 0.01 in., ultrasonic frequencies may produce vortices much smaller than the laminar-flame thickness. This means that we should no longer use equations such as Shelkin's¹⁸ large-scale equation

$$\frac{F_t}{F} = \sqrt{1 + \left(\beta \frac{u'}{F}\right)^2} \quad [1]$$

for the prediction of the effect of the turbulent velocity, u' , on the ratio of turbulent to laminar-flame speed, because this equation is based on the concept of a distorted flame front. We should use a relation such as that given by Shelkin for small-scale turbulence

¹¹ "Über den Einfluss starker Schallwellen auf fortschreitende Gasflammen in Röhren," by L. Ehret, V. Neubert, and H. Hannemann, MÖS (A) Volkenrode, Reports and Translations No. 650, ATI No. 9452, February, 1947.

¹² "Flame Propagation, Particularly With Reference to Vibratory and True Detonation Flames," by R. P. Frazer, "The Science of Petroleum," Oxford University Press, vol. 4, 1938, p. 2983.

¹³ "Einfluss der Eigenschwingungen brennender Gasgemische auf ihre Brenngeschwindigkeit," by H. Nielsen, *Forschung auf dem Gebiete des Ingenieurwesens*, vol. 4, 1933, p. 300.

¹⁴ "Interaction of Flow Pulsations and Flame Propagation," by G. H. Markstein, *Journal of the Aeronautical Sciences*, vol. 18, 1951, p. 428.

¹⁵ Fuels Research Division, Battelle Memorial Institute, Columbus, Ohio, Jun. ASME.

¹⁶ "Interaction of Flame Propagation and Flow Disturbance," by G. H. Markstein, Third Symposium on Combustion, Flame, and Explosion Phenomena, Williams and Wilkins, Baltimore, Md., 1949, p. 162.

¹⁷ "Investigation of Turbulent Flames," by Bela Karlovitz, D. W. Denniston, Jr., and F. E. Wells, *Journal of Chemical Physics*, vol. 19, May, 1951, p. 541.

¹⁸ "On Combustion in a Turbulent Flow," by K. I. Shelkin, NACA Technical Memorandum No. 1110, February, 1947.

⁴ Head of Combustion Section, Cornell Aeronautical Laboratory, Inc., Buffalo, N. Y.

⁵ Reference (5) of paper.

⁶ Reference (6) of paper.

⁷ Reference (7) of paper.

⁸ "The Effect of Sound on Laminar Propane-Air Flames," by S. Loshaek, R. S. Fein, and H. L. Olsen, *Journal of the Acoustical Society of America*, vol. 21, November, 1949, pp. 605-612.

⁹ "The Effect of Sound on Flames," by S. Loshaek, University of Wisconsin-CM-612, May, 1950.

¹⁰ "Leontropische Zustandsänderungen in dissoziierenden Gasen und die Methode der Schalldispersion zur Untersuchung sehr schneller homogener Gasreaktionen," by G. Damköhler, *Zeitschrift für Elektrochemie*, vol. 48, 1942, pp. 62 and 116; cf. NACA TM 1268 and TM 1269, 1950.

$$\frac{F_1}{F} = \sqrt{1 + \frac{\alpha u' l C_p \rho}{k}} \quad [2]$$

which, it may be seen, includes a scale term l .

In tests at Battelle on an apparatus similar to that used by Kippenhan and Croft, but with the combustible mixture driven by the bottom plate of the resonator cavity, an intensity of 5 watts per sq cm was attained at 20 kc. Using the root-mean-square velocity corresponding to this intensity as the measure of turbulent intensity, and the scale previously estimated, Equation [2] becomes

$$\frac{F_1}{F} = \sqrt{1 + \sim 10} \cong 3.3 \dots \dots \dots [3]$$

Although this indicates a large effect of the sound, not only is the estimate too large because of the assumption that all of the intensity appears in vortex generation and that there is no dissipation, but the effect is confined to a region of the flame of about the size of the vortex. Therefore the effect on average flame speed would be imperceptible.

Ultrasonics do have an effect on flow pattern, however, as many investigators have shown. This phase of the problem appears worthy of further investigation.

AUTHORS' CLOSURE

We wish to thank the discussers for their thoughtful and stimulating discussions. The authors agree with Dr. Markstein that more elaborate techniques for observing the flame fronts such as schlieren or shadowgraph are much needed in order to interpret the exact nature of the flame front under the influence of high-frequency disturbances.

An attempt was made to study quantitatively the stability limits. However, the experimental apparatus was not well suited for such a study; hence it was decided to place the main emphasis on normal flame velocity. The term stability is perhaps unopportunately chosen when suspended flames, lifted from the burner mouth, are discussed. Such suspended flames fall in the region between flashback and blowoff limits, but were not useful for study of normal burning velocity.

The phenomena qualitatively observed in combustion chambers, where high gas velocities require use of flame-holding devices, seem to indicate a much larger and more complex interaction between sound waves and the combustion front. The effects observed on burner flames fail to provide an answer to this most critical problem.



Photographic Analysis of Sprays

By J. L. YORK¹ AND H. E. STUBBS,² ANN ARBOR, MICH.

This paper describes an experimental method for determining the size distribution and velocities of drops in a spray. Photographs are taken of a small known volume of the spray, and the images of the drops are counted and measured to give the size distribution. Velocities are determined by taking two exposures on the same film and measuring the displacement of the drops in the interval between exposures. Since a photographic method does not require any objects in the spray, the results are free of bias from disturbances of the flow pattern. The technique is applicable to sprays in which the diameters of drops range from 15 to 500 microns and gives results which differ by less than 20 per cent from the metered values of total flow rate.

INTRODUCTION

THE study of sprays and their properties has been hampered by difficulty in obtaining trustworthy measurements of the number, sizes, and velocities of drops at various locations within a spray. Many attempts to evaluate the character of a spray have been concerned only with the distribution of the flow and give no information about the drops. An example is the patternator, which operates with cups placed at various locations in the spray. After the spray fills the cups for some period of time, the contents of each cup can be measured to evaluate the flow rate at that location. Other methods of analysis attempt to measure the number and size of the drops of a spray. Most of these depend on physical sampling of the spray or on the scattering of light by the spray. Physical sampling is usually accomplished by having drops impinge on cups or microscope slides in the spray or by sucking them out of the spray through a tube. The captured sample can then be analyzed leisurely for number and size of drops. These procedures are untrustworthy because it is questionable if the sample analyzed is representative of the original spray.

The work of Langmuir and Blodgett,³ Sell,⁴ and others,^{5,6,7} indicates that any impingement process discriminates against

capturing small drops. Analyses based on light scattering are free of the bias arising from impingement, but the interpretation of light-scattering data is extremely difficult when the drops of the spray are not in a very narrow range of sizes. Furthermore, any interpretation depends on a long chain of theory containing questionable assumptions. None of these methods gives any information about drop velocities.

The photographic method of spray analysis here described was developed to give spray measurements which are not biased by physical sampling and which are susceptible to direct interpretation in terms of number, sizes, and velocities of the drops.

DETAILS OF METHOD

Principle. In the photographic technique of spray analysis, pictures are taken of a small volume in the spray without disturbing the flow pattern with any objects. The drop images on the film are measured and counted, giving the size distribution of drops in the small volume of the spray (the spatial distribution). For most applications, however, the information desired is the size distribution of drops passing a cross-sectional area in a unit time (the temporal distribution). Since the temporal distribution is the product of the spatial distribution and the average velocity of drops of each size, it is necessary to measure drop velocities to obtain the temporal distribution. Therefore we take double exposures of regions in the spray with a small known interval between exposures. The resulting photographs show a pair of images for each drop, one image made at each exposure. The velocity of each drop can be calculated from the distance between images and the interval between exposures.

Camera. The camera is a light-tight wooden box with a receptacle for film holders and a viewing screen on the back and a threaded fitting for a lens in front. The lens is an Argus Coated Cintar with a 50-mm focal length and $f/3.5$ aperture. Although the lens and front part of the camera are wet by the periphery of a wide-angle spray, no special precautions have proved necessary to prevent the entry of water. The lens fittings are normally lubricated with a heavy grease, and this evidently has been a sufficient barrier to the water. The optical properties of the lens are not distorted seriously by the water on the front surface.

The distance from the lens to the film is such that there is a magnification of 10 (about 20 in.). This magnification produces images of a convenient size and also gives virtually the best resolution obtainable with a given lens.

Film. We have used Kodak Contrast Process Ortho film because it has high contrast and high resolution. The high contrast makes close control of the illumination necessary.

Illumination. The open-shutter method is used in all photographs. The camera shutter remains open, and the length of exposure is determined by the duration of the illumination. For the light source we have used a "Photolight,"⁸ which produces light by the discharge of a capacitor through an arc, the duration of useful illumination being about 1 microsecond. In the early stages of the development of this technique we placed the photolight so that the light reflected from the drops into the camera. The photographs taken with this arrangement showed images which were reflections of the light source in the surface of the drops. The size of the image was not easily related to the size of the drop and we abandoned this arrangement in favor of one

¹ Associate Professor of Chemical and Metallurgical Engineering, University of Michigan. Mem. ASME.

² Research Associate, Engineering Research Institute, University of Michigan.

³ "A Mathematical Investigation of Water Droplet Trajectories," by I. Langmuir and K. B. Blodgett, AAF Technical Report 5418, Army Air Forces, Air Materiel Command, Dayton, Ohio, 1946.

⁴ "The Precipitation of Dust on Simple Bodies and in Air Filters," by W. Sell, *Forschungsheft* No. 347, Ausgabe B, vol. 2, 1931.

⁵ "Theoretical Investigation Concerning the Deposition of Dust From Air Flow," by F. Albrecht, *Physikalische Zeitschrift*, vol. 32, 1931, p. 48.

⁶ "Electronic Spray Analyzer for Electrically Conducting Particles," by J. M. Geist, J. L. York, and G. G. Brown, *Industrial and Engineering Chemistry*, vol. 43, 1951, pp. 1371-1373.

⁷ "Sampling of Liquid Aerosols by Wires, Cylinders, and Slides and the Efficiency of Impaction of Droplets," by H. O. Landahl and R. G. Hermann, *Journal of Colloid Science*, vol. 4, 1949, p. 103.

⁸ Contributed by the Gas Turbine Power, Fuels, and Applied Mechanics Divisions and presented at the Annual Meeting, Atlantic City, N. J., November 25-30, 1951, of THE AMERICAN SOCIETY OF MECHANICAL ENGINEERS.

NOTE: Statements and opinions advanced in papers are to be understood as individual expressions of their authors and not those of the Society. Manuscript received at ASME Headquarters, September 9, 1951. Paper No. 51-A-48.

⁸ General Electrical Photolight, Catalog 9364688G1.

in which the light shines directly into the camera giving a silhouette picture with the background illuminated and the drops appearing as shadow. In the arrangement we now use, the light from the photolight passes through a water cell out to a ground-glass diffusing screen, then through the spray and into the camera as shown in Fig. 1. Fig. 4 shows the resulting photograph. The water cell is a lucite vessel with flat sides containing a solution of nigrosin to control the intensity of illumination.

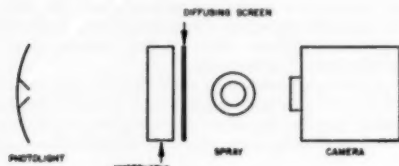


FIG. 1 ARRANGEMENT OF ELEMENTS

The concentration of nigrosin required for correct exposure varies as different parts of a spray are photographed. The concentration can be adjusted by trial exposures, but this procedure is inconvenient since the result of each adjustment is not known until after the film is processed. A photoelectric cell cannot be used directly for immediate measurements of the intensity of the illumination because it will not respond to the high intensity and short duration of the light from a photolight. We have therefore used the following method to permit immediate measurements with a photoelectric cell to adjust the nigrosin concentration:

By a series of trial exposures we established the correct nigrosin concentration for one point of a spray. Leaving the spray and nigrosin unchanged we placed a photoelectric cell at the plane of the film and an incandescent light so that it would shine through the water cell, spray, and into the camera. The reading of the photoelectric cell was taken as a measure of correct exposure conditions, and for any other photographs the nigrosin concentration is adjusted to give the same reading. The diffusing screen makes the illumination of the spray more uniform.

METHOD OF COUNTING DROPS

After the films are processed the negatives are placed in a Jones and Lamson bench comparator and projected onto a ground-glass screen. The projection produces a magnification of 10; hence the image on the screen is 100 times the size of the drop. An operator then classifies the drops by sizes and counts the drops of each size. This gives the spatial distribution.

The volume of the spray which is photographed with one exposure is bounded in two dimensions by the view of the camera and in the third dimension by the depth of field of the optical system as shown in Fig. 2. The extent of depth of field is not as sharply defined as is the extent of field of view. The images of drops that are successively further from the object plane are more and more blurred. The operator who sizes and counts the images must judge from the amount of blur whether a drop is within the arbitrary limits of the depth of field. In the early stages of the development of this technique, judgments of various operators did not agree, and the judgment of a single operator changed over a period of time. To co-ordinate the judgments of various operators over a period of time, we made "standard images." These are images of various sizes of drops known to be at the limit of field depth. They are projected on the screen along with images of the drops to be sized and counted. Thus an operator needs to judge only whether a given image is more or less blurred than a standard image of the same size.

The standard images were selected by comparison with a series of photographs of glass fibers having diameters in the same range as the diameters of the drops of the spray. Between photographs, the lens of the camera was advanced on a screw toward the fibers. The photographs thus showed the fibers at successive locations in the field of the camera. Since the movement of the lens was known, the photographs indicated the degree of blur corresponding to a certain distance from the object plane. A convenient limit of field was chosen and the corresponding images of fibers provided a measure of permissible blur for each diameter. Drop images with the same amount of blur were then chosen as standard images for each size.

The depth of field for any fixed blur depends on the lens aperture. If the depth of field is to be maintained constant for a series of photographs, the aperture must remain unchanged and

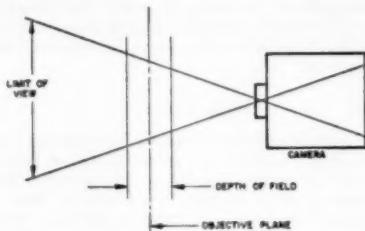


FIG. 2 LIMITS OF KNOWN VOLUME PHOTOGRAPHED

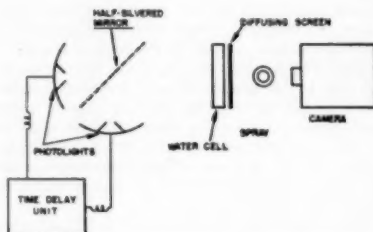


FIG. 3 ARRANGEMENT FOR DOUBLE EXPOSURE

the illumination must be controlled some other way. This is why a water cell is used rather than a variable aperture.

MEASUREMENT OF VELOCITIES

Drop velocities are measured by means of double exposures necessitating two flashes of light. Since the interval between flashes must be less than the recovery time of a photolight, two are necessary, one firing after the other. The light beams are brought into the spray from the same direction by using a half-silvered mirror as a beam splitter. Otherwise, the optical arrangements are the same as when single exposures are made. Fig. 3 shows the arrangement and Fig. 5 a typical photograph. The interval between flashing of the first photolight and the second is controlled by an electronic delay unit. The circuit diagram for this is given in Fig. 6. The exact length of the interval is not critical, but it must be reproducible. If the delay is very long it becomes difficult to associate the two images of a single drop. If the delay is very short the movement of the drops is difficult to measure, and small uncontrollable delays inherent in the flash units themselves become significant. A delay of



FIG. 4 TYPICAL SILHOUETTE PHOTOGRAPH



FIG. 5 DOUBLE EXPOSURE FOR VELOCITY MEASUREMENT

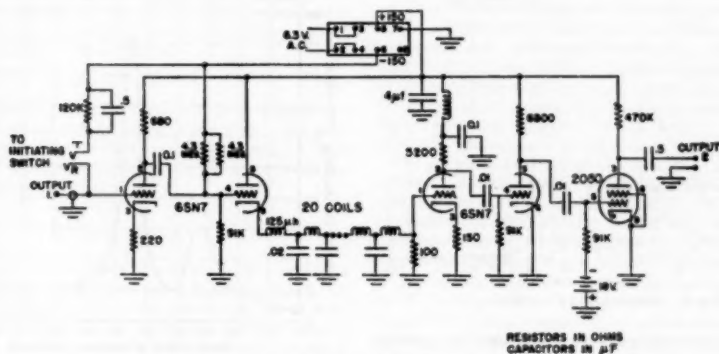


FIG. 6 TIME-DELAY CIRCUIT

25 microseconds proved reasonable for the optical arrangement described here and drops moving about 20 fps.

After making several unsuccessful attempts to calibrate the delay unit using electronic timing equipment, we turned to a mechanical calibration which has been quite successful. In this method a double-exposure photograph is taken of a rotating saw blade. The arrangement is exactly the same as shown in Fig. 3 except that the rotating saw blade replaces the spray. By measuring the angular velocity of the saw and the distance a tooth moves between exposures, the interval between flashes can be calculated.

The negatives with the double exposures of drops are placed in the comparator and the displacement of pairs of images is recorded as a function of drop diameter. From this information the average velocity in each size range is obtained and then this is used to calculate the temporal drop-size distribution.

By repeating the whole procedure described in the foregoing at successive locations in the spray, the character of the whole spray can be determined.

RESULTS OF ANALYSIS OF A SPRAY

The results of this analytical method as applied to a Monarch

simplex nozzle spraying water at the rate of 200 lb per hr are shown graphically in Figs. 7, 8, 9, and 10. This nozzle has a hollow-cone spray that is symmetrical about an axis. The character of the spray 6 in. from the nozzle tip and at different angles from the axis is shown.

Fig. 7 shows the average drop-velocity pattern. At a distance of 6 in. from the nozzle tip the velocity is far from uniform. This indicates that the drops are moving at velocities considerably different from that of the surrounding air. Fig. 8 shows the temporal drop-size distribution. In this figure the number of drops per centimeter, per steradian, per cubic centimeter of flow is plotted against size of drop for various locations in the spray. Such a plot is not of immediate use in spray applications but it is of interest in making complete comparisons between nozzles and in design of nozzles. The ordinate f in this plot at diameter x and angle α is

$$f = \frac{1}{q} \lim_{\Delta x \rightarrow 0} \frac{1}{(\Delta x)(\omega)}$$

as Δx and ω approach zero; n is number of drops with diameter between x and $x + \Delta x$ passing across a surface having solid

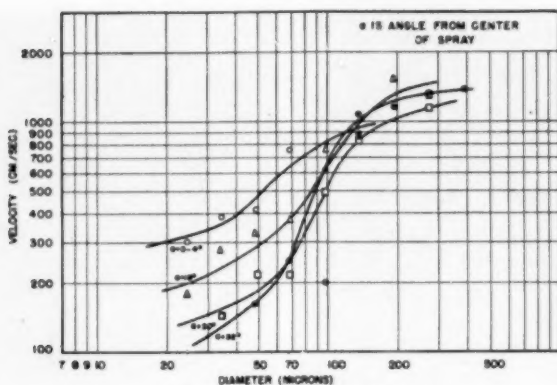


FIG. 7 AVERAGE DROP VELOCITY

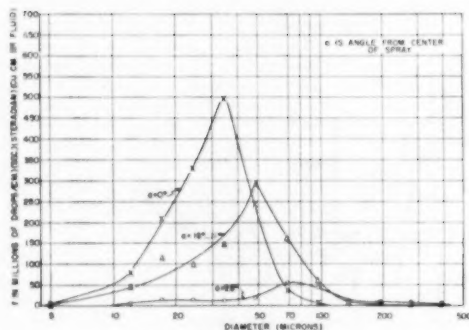


FIG. 8 DISTRIBUTION FUNCTION

angle ω with respect to the tip of the nozzle while the quantity of fluid q is sprayed through the nozzle. If the function f is integrated over all drop sizes and all solid angles, the result will be the total number of drops produced in the spray for each cubic centimeter of fluid sprayed.

We have chosen to present this plot and the succeeding ones in terms of unit solid angles rather than in terms of unit cross-sectional area. If the functions plotted were in terms of cross-sectional area, they would change radically as the distance from the nozzle changes, reflecting the divergence of the spray instead of any fundamental change in the character of the spray. When the functions are expressed in terms of solid angle it is possible to compare directly data taken at different distances from the orifices of nozzles.

Fig. 8 contains all the distribution information about the spray. From it can be derived the mass or surface distribution throughout the spray, the specific surface, the total surface, or any other distribution information desired. Some of the information derivable from the distribution curves is given in Figs. 9 and 10.

By integrating the surface and volume distributions over the whole spray, values can be obtained for the total surface and volume produced in the spray in a unit of time. Since the volume per unit time entering the nozzle can be obtained independently by metering the flow, it is possible to check the over-all accuracy of the analysis by comparing the two values. For this analysis the discrepancy was less than 20 per cent.

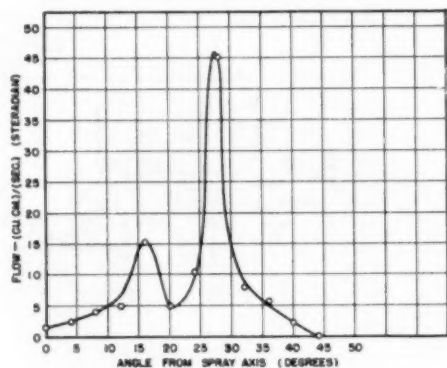


FIG. 9 FLOW DISTRIBUTION

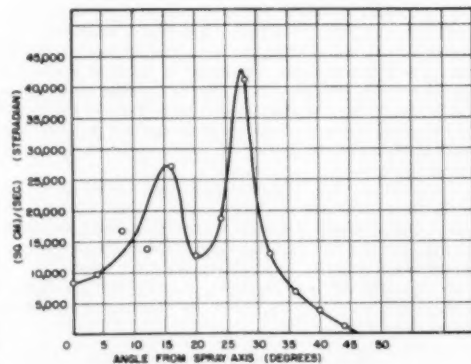


FIG. 10 SURFACE DISTRIBUTION

DISCUSSION

We have determined drop velocities and the spatial size distribution from different series of photographs because the double exposure necessary for velocity measurement tends to obscure the smaller drops. This effect is less objectionable in velocity measurements, since a fraction of the small drops will suffice to determine the average velocity of such drops. For a spray which diffuses little light and consequently gives very sharp drop shadows, or if only larger drops (over 50 microns) are of interest, it might be feasible to use double exposures for both distribution and velocity measurements.

The number of photographs which must be taken and drops which must be counted rise sharply as the desired accuracy increases. The problem is a statistical one.

Even though a large part of the work of an analysis can be made routine, and does not require highly trained personnel, it is still quite laborious to apply the technique described in this paper to a large number of points throughout a spray. In many applications it may not be worth while to obtain the detailed quantitative analysis of which the method is capable. Often the effort can be better spent getting semiquantitative information at a few points of a spray which would be sufficient to indicate the trends and general nature of the spray. Adaptations of this method also might be used to examine the mechanism of formation of a spray or its behavior as it impinged on an object or at some other point of special interest.

ACKNOWLEDGMENT

We wish to acknowledge with thanks the help of many colleagues and assistants at various stages of this work. We especially acknowledge the financial assistance and encouragement of the Air Materiel Command, United States Air Force, who have released this paper for publication.

Discussion

J. P. LONGWELL.⁹ When one wishes to study the evaporation or combustion of a cloud of liquid drops, it is immediately apparent that lack of information on the size distribution of drops and their relative velocity to the air stream prevents detailed consideration of these processes. This is generally recognized and this lack of information does not result from lack of interest in the subject but is due to lack of suitable experimental technique for making the necessary measurements. It is, therefore, of interest to hear of the development of another technique for making such measurements.

This new technique must compete with other available methods such as those which collect drops on a slide for later counting and measuring. As pointed out by the authors, there is a tendency to collect a larger proportion of big drops rather than of small drops on an obstacle placed in an air stream. By use of reference (3) of this paper, it is possible to calculate the magnitude of such errors.

Table 1 of this discussion gives the error in size distribution due to this selective sampling for the case of a spray from an air-atomizing nozzle giving a mass median drop diameter of 20 microns. The air velocity was 70 fps and the collecting plate width was 0.3 in.

It is seen that the mass median partial diameter would be about 10 per cent too large and the error for smaller drops would be somewhat greater. More accurate results would be obtained for the coarser sprays generally encountered and, by knowing collection efficiencies, it is possible to correct these results and

⁹ Esso Laboratories, Standard Oil Development Company, Linden, N. J.

TABLE 1 EFFECT OF SAMPLING ERROR ON SIZE DISTRIBUTION

Fraction of total mass above a given diameter	Diameter for original spray, microns	Diameter for sample, microns	Error per cent
0.9	11.5	13.1	14
0.75	15.3	17.3	13
0.5	20	22.1	10
0.25	28.7	28.5	7
0.1	32.0	32.7	2

therefore improve the accuracy. It is felt that this accuracy is adequate for many purposes; so comparison of this technique with the photographic technique would be on the basis of the time consumed in procuring data. In measuring a sample on a slide, one would generally photograph it for future counting. In this case the photographic technique is not critical, since all drops can be in the focal plane. Measuring the drops on the negative is also easier, since it is not necessary to use judgment as to when a spot is in or out of focus and machines have been developed to count and measure drops on such a negative.

The photographic technique described in this paper can give information on drop velocity which the other techniques do not give; however, it is not certain that this technique is necessarily more accurate or less time-consuming than other available techniques.

J. M. PILCHER.¹⁰ The authors have made a valuable and noteworthy contribution to the complex problem of characterizing a spray in terms of drop-size distribution. The greatest difficulty involved in this problem is accurate sampling of the spray to eliminate discrimination against either the larger or smaller drops; and, in this regard, they have made a wise choice in selecting the photographic method which obviates the placement of collecting objects such as slides in the spray.

The principal shortcoming of this method appears to be the complex counting operations and the measure of drop sizes which require much time and tedious effort. This objection might be overcome, however, by the use of a semiautomatic device for counting and sizing the drops such as the "differentiating droplet counter" developed at Douglas Aircraft Company by J. H. Rupe, or the scanning device developed at the University of Wisconsin by W. R. Marshall and his associates. These instruments are capable of scanning at rates of about a thousand drops per minute, and the human element is eliminated from the counting process; however, a sharp negative with high contrast between drops and background is required.

It appears that the method described in the paper may be most suitable as a primary means of calibrating some less tedious and time-consuming indirect method. Such a method might be based upon the absorption or diffraction of light, or upon the electrical charges carried by the droplets.

AUTHORS' CLOSURE

As both Mr. Longwell and Mr. Pilcher point out, the method described in this paper is laborious and time consuming. We agree that for many problems of spray analysis, faster methods are more suitable.

We have considered the use of mechanical counting devices like those mentioned by Mr. Pilcher, but we have not been able to work out a satisfactory way to use any of them on our negatives.

Mr. Longwell suggests the use of Langmuir and Blodgett's work (footnote 3) to compute correction factors to compensate for discrimination against small drops in samples collected on slides. Under some circumstances this may be feasible, but this procedure must be used with great caution. For their calculations, Langmuir and Blodgett assume that the air mass is free of turbulence

¹⁰ Battelle Memorial Institute, Columbus, Ohio. Mem. ASME.

and that at a distance from the obstacle the air is moving at uniform velocity and the drops are at rest with respect to the air. These conditions are not even remotely approached in many sprays. Fig. 7 shows that for the spray described there the average velocities of drops varied through a tenfold range. The

velocities of individual drops had an even wider variation. Under such conditions, calculations from footnote 3 might indicate where discrimination begins to be an important factor in collection on slides, but it cannot be relied on for numerical corrections.

Design and Performance of an Extended-Surface Regenerator for a Gas-Turbine Plant

BY SVEN HOLM¹ AND R. L. LYERLY,² WELLSVILLE, N. Y.

This paper describes a new type of extended-surface heat exchanger developed for application to a gas-turbine plant for a natural-gas pipe-line pumping station. This regenerator features compactness and low weight, although the particular unit described is not as compact and light as could be made since primary consideration was given to material strength and service life, thus involving the use of relatively heavy sections for both primary and extended surfaces. Smaller-scale component parts would give higher heat-transfer coefficients and increase heating surface per unit volume by as much as 3 to 1.

INTRODUCTION

THE basic requirements for a regenerator in this gas-turbine plant were an air-side temperature effectiveness of 75 per cent, relatively low pressure drops, and a long service life with natural gas as the fuel in the cycle.

The general arrangement of the plant is shown in Fig. 1 with the air and gas flow directions indicated. The air from the com-

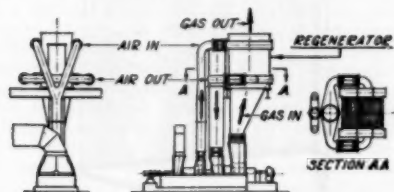


FIG. 1 GENERAL PLANT ARRANGEMENT
(Courtesy of Clark Brothers Company, Olean, N. Y.)

pressor enters the regenerator on both sides at the top and leaves the regenerator from both sides at the bottom. The expanded gases from the turbine pass upward through the heater in true counterflow relationship to the air and exhaust through the stack and weather hood, which are not shown in Fig. 1. All ductwork is equipped with expansion joints of the universal type and self-restrained hinge type to relieve the regenerator and other machinery of loads imposed by thermal expansion.

The regenerator performance is given in Table 1. These are calculated values for full-load flow. Physical data for the unit are given in Table 2.

MECHANICAL DESIGN

All parts of the regenerator were made from open-hearth steel,

¹ Research Engineer, Air Preheater Corporation. Mem. ASME.

² Research Engineer, Air Preheater Corporation. Jun. ASME.

Contributed by the Gas Turbine Power and Heat Transfer Divisions and presented at the Annual Meeting, Atlantic City, N. J., November 25-30, 1951, of THE AMERICAN SOCIETY OF MECHANICAL ENGINEERS.

NOTE: Statements and opinions advanced in papers are to be understood as individual expressions of their authors and not those of the Society. Manuscript received at ASME Headquarters, September 18, 1951. Paper No. 51-A-106.

TABLE 1 REGENERATOR PERFORMANCE

Cycle conditions:	Full-load design
Flow rate, air, lb per hr.	242,380
Flow rate, gas, lb per hr.	250,524
Inlet pressure, air, psia.	74
Inlet pressure, gas, psia.	15
Inlet temperature, air, deg F.	417
Inlet temperature, gas, deg F.	839
Design factors:	
Flow velocity, air, fpm.	18.6
Flow velocity, gas, fpm.	92.1
Mass velocity, air, lb/sq ft-hr.	12,940
Mass velocity, gas, lb/sq ft-hr.	11,440
Reynolds numbers, air.	6,520
Reynolds numbers, gas.	4,780
Film coefficient, air, Btu/sq ft-deg F-hr.	48.1
Film coefficient, gas, Btu/sq ft-deg F-hr.	15.2
Temp effectiveness of surface, air, per cent.	80.5
Temp effectiveness of surface, gas, per cent.	96.7
Overall heat-transfer coefficient based on air side, including safety factor (U), Btu/sq ft-deg F-hr.	11.3
$NTU = \frac{\text{Air-side heating surface} \times U}{\text{Air flow} \times C_p \text{ air}}$	2.80
Performance:	
Pressure drop, $\Delta P/P$, air, per cent.	0.88
Pressure drop, $\Delta P/P$, gas, per cent.	2.00
Pressure drop, $\Delta P/P$ total, per cent.	2.88
Exit temperature, air, deg F.	724
Exit temperature, gas, deg F.	944
Heat transferred, Btu per hr.	19,100,000
Air-side temperature effectiveness, per cent.	75
Maximum operating gas temperature, deg F.	900

NOTE: $\Delta P/P$ = pressure drop/absolute static pressure.

TABLE 2 PHYSICAL DATA

Volume of core, cu ft.	480
Weight of core, lb.	68,500
Total weight (Fig. 5), lb.	85,500
Plate wall thickness, in.	0.0625
Air side:	
Total heating surface, sq ft.	15,900
Direct, per cent.	43
Extended, per cent.	57
Pin diameter, in.	0.120
Hydraulic diameter, ft.	0.0361
Heating surface/cu ft of core, sq ft.	31.8
Gas side:	
Total heating surface, sq ft.	18,700
Direct, per cent.	31
Extended, per cent.	69
Pin thickness, in.	0.0625
Hydraulic diameter, ft.	0.03175
Heating surface/cu ft of core, sq ft.	39.5

NOTE: The manifold surface was not considered in the heat-transfer calculations.

$$\text{Hydraulic diameter} = \frac{4 \times \text{free area} \times \text{flow length}}{\text{Heating surface}}$$

joined by copper brazing and arc welding. A single element of the heat-transfer core is substantially a flat tube or envelope with extended surface in the form of pin fins on the inside and strip fins on the outside, Fig. 2. The pin-fin surface is made by bending wire into a sinusoidal shape, clipping it between two small channels, and then placing it between the two plates which form the envelope. The strip-fin surface is formed by attaching channel-shaped sections to the outer sides of the plates. These parts are then brazed together to form the heating-surface envelope. An envelope complete with manifold sections is shown in Fig. 3.

Fig. 4 illustrates a number of envelopes assembled into a bundle of weight and size suitable for convenient handling. The envelopes are placed side by side, almost touching each other, and are welded to the section of air header at each end. Six bundles

with gas inlet and outlet connections complete the unit as shown in Fig. 5.

LABORATORY TEST

For calculating the performance of the regenerator, laboratory test results were used to determine the heat-transfer and pressure drops. Laboratory test pieces are shown in Fig. 6. Safety factors were added to allow for fouling, imperfect flow distribution, and possible discrepancies.

The investigation for heat-transfer and pressure-drop data began with small test pieces of several different pin arrangements. The tests were conducted in a 4-in. \times 4-in. wind tunnel, using saturated steam in a crossflow relationship as a heat source. Then manufactured envelopes were made into final test pieces about

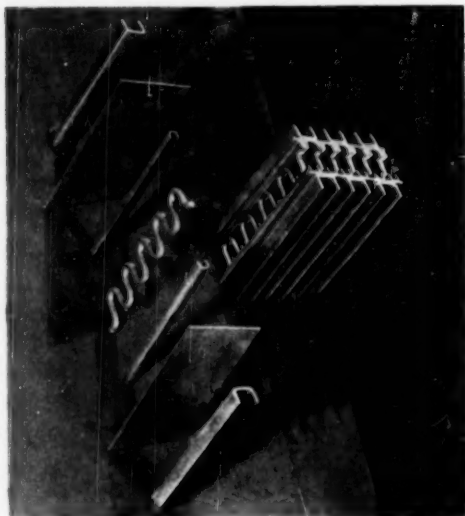


FIG. 2 ENVELOPE CONSTRUCTION DETAIL

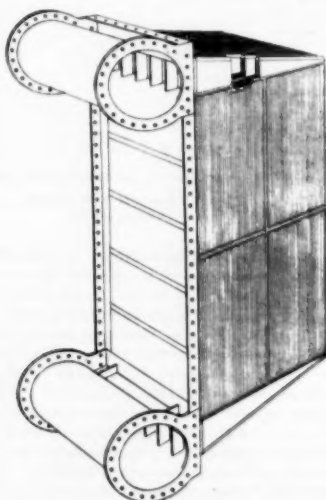


FIG. 4 ENVELOPE BUNDLE

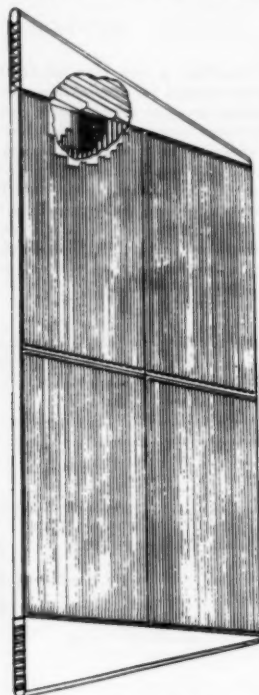


FIG. 3 HEATING-SURFACE ENVELOPE

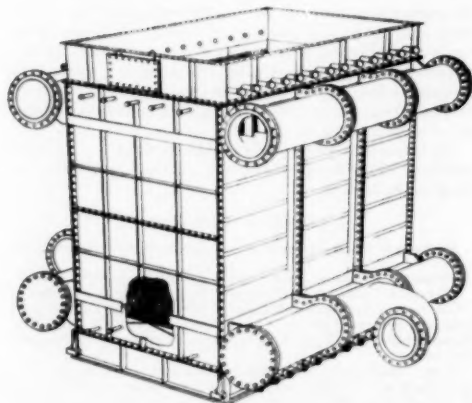


FIG. 5 REGENERATOR ASSEMBLY

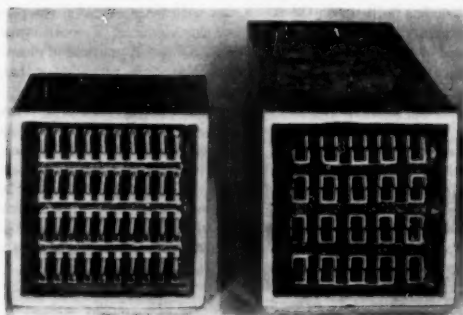


FIG. 6 LABORATORY TEST PIECES

4 times the size of the original ones; the steam passages contained no extended surface and had about one fourth the free area of the air passages. The tests on channel surfaces showed characteristics in close agreement with flow inside round pipe.

HEAT-TRANSFER DESIGN

The first approach to a design for this regenerator was a two-pass cross-counterflow unit with the gas on the inside of the envelope and the air on the outside. A major difficulty was encountered in attempting to design a lightweight rectangular shell to carry the air pressure of 60 psig. The core was satisfactory but the large flat sides required an excessive amount of reinforcing. To eliminate this difficulty, the high-pressure air was switched to the inside of the envelope, since wires brazed between two plates form an extremely rigid pressure vessel. Sample envelopes tested hydrostatically at room temperature held firm at pressures above 1500 psi; the strength will drop off to about one half at operating temperatures, assuming the joints to be no stronger than the brazing material. Therefore this structure adapts itself to the high-pressure air without the use of any external members to carry the load.

Arranging for air flow on the inside of the envelope fortunately made possible a counterflow unit. With the free areas about the same, the mass velocities were almost the same on the air side and the gas side. The heat-transfer coefficients were much higher on the air side than on the gas side. Since both sides had about the same amount of surface, the heat-transfer balance was less desirable than that obtained in the initial design.

The reduction in required NTU from two-pass crossflow to counterflow was greater than the reduction in the over-all heat-transfer coefficient caused by the unbalance so that a size reduction was achieved by using counterflow.

BRAZING EXTENDED SURFACE

Brazing in a controlled-atmosphere furnace with copper as the brazing material was the basic manufacturing method for joining the extended surface to the plates, forming an envelope. Copper was chosen in preference to three other brazing materials as a result of an investigation of the tensile and metallurgical properties of brazed samples which had been heated in air at 750 to 900 F for varying lengths of time. The average test values did not reveal any change in tensile strength with length of exposure in this temperature range. The metallurgical examinations revealed exceptionally good wetting and bonding of the copper to the steel base metal. The joints were sound and without evidence of internal oxidation or porosity due to shrinkage. Etching revealed a fine dendritic cast structure.

The small channels into which the formed wires were inserted performed a very important function in obtaining positive and uniform metal-to-metal contact between the wire and the plates. Without these channels, any irregularity in the wire loops or a small warpage of the plate would result in points of poor or no contact. The channels compensated for any lack of uniformity by providing side contact with the wire loops.

AIR-FLOW DISTRIBUTION

A test was performed on a full-sized envelope to determine how well the tapered manifolds distributed the air across the envelope. The test envelope was cut in the middle and a special section was welded in for inserting Pitots across the width of the envelope.

As expected, the velocity profile showed the highest velocity in the shortest air-flow path while the longest air path was about average. The velocity profile is shown in Fig. 7 for the design-load Reynolds number.

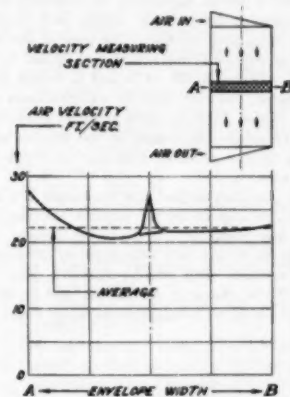


FIG. 7 AIR-FLOW DISTRIBUTION INSIDE ENVELOPE AT DESIGN-LOAD REYNOLDS NUMBER

The peak in the profile at the center of the envelope was caused by a nonuniform structure of extended surface due to manufacturing methods. Each envelope was made from four rectangular brazed pieces, welded together in the middle in both directions. This procedure resulted in a larger gap between the center row of pins than between the rest. An improvement in manufacturing will eliminate this deviation in future units.

Neglecting the center peak condition, a smooth velocity pattern exists. To lower the velocity in the shortest path in an effort to flatten the velocity curve, more resistance could be added in that particular section of the envelope. Larger ports would lower the velocity at entrance and exit with less flow friction in manifolds and would result in improved flow distribution.

FIELD TEST

The gas-turbine plant was erected at the factory to examine thoroughly the operating characteristics of each component part as well as to test the entire plant. In addition to the elaborate instrumentation of the complete plant, the authors' company installed an independent thermocouple system for measuring the air and gas temperatures in and out of the regenerator. Fifteen thermocouples were placed in the hot-gas stream immediately below the core, and fifteen more were placed just above the core for the cooled gas. Two thermocouples were placed to measure the air in and two for the hot air out.

The regenerator performed satisfactorily over a large range of loads, with an air-temperature effectiveness slightly higher than the calculated value for any particular load. The air-side pressure drops were somewhat higher than anticipated but the gas-side pressure drops were considerably lower, resulting in a lower sum of $\Delta P/P$ for air and $\Delta P/P$ for gas than predicted.

An inspection of the surfaces after the tests were completed revealed the surfaces completely clean and free from any deposits.

CONCLUSION

This regenerator possesses many advantages above a conventional tubular heater, principally a substantial saving in volume and weight requirements, made possible by a counterflow design and a higher over-all heat-transfer coefficient. The rectangular shape fits very well into the general plant arrangement.

A regenerator using 1-in.-OD tubes as heating surface has been described by George R. Fusner.¹ A comparison between this regenerator and a pin-fin regenerator as described in this paper shows a considerable difference in volume and weight required to obtain the same performance. The core of the tubular unit has a volume of 1050 cu ft and a weight of 92,000 lb. The pin-fin core has a volume of 400 cu ft and a weight of 57,000 lb. It should be noted, however, that the wall thickness of the tubes was 0.095-in., which might be more than required for corrosion resistance. Therefore the weight of the tubular unit may be reduced using thinner material, reducing the weight advantage of the pin-fin core.

The pin-fin extended-surface heat exchanger is a result of an extensive research program by the authors' company in the field of gas-to-gas heat exchange. Many other designs were tested and found superior to this heat exchanger for other applications. Two pin-fin surfaces with smaller-diameter pins have been described by W. M. Kays, A. L. London, and D. W. Johnson.² These surfaces are useful in applications where space is at a premium.

Discussion

G. R. FUSNER.³ A "pin-fin" extended-surface heat exchanger, as described in the paper, has many attractive features. For gas-turbine applications where space is limited, such as in locomotive cabs, mobile railway cars and ships, the shape and low weight of such a regenerator make it very attractive. This design also lends itself well to applications where a relatively short life requirement demands a low weight. The relatively low weight mentioned in the paper can be reduced still further for these applications by simply making the plates and channel extended surface of thinner material.

The relatively short gas-path length of the pin-fin design should make it very easy to clean with soot blowers when the unit is in operation. Experience with the Oklahoma Gas and Electric Company gas turbine and recuperator operating with natural-gas fuel shows that after several months' operation a thin layer of carbon varying in thickness builds up on the tubes. During a 730-hr period this deposit built up to a maximum of 0.010 in. This deposit can be removed with a soot blower.

To date it has not been necessary to clean the regenerators on oil-burning units manufactured by the writer's company, but the number of operating hours is relatively small. A slight ash de-

posit has built up on the tubes, but with little effect on the performance. When the time comes for cleaning, if soot-blower type of equipment turns out to be a satisfactory method of cleaning, it will be an easier job with the plate-type regenerator than with the shell-and-tube equipment.

At the moment the cost of the plate-type regenerator appears higher than the shell-and-tube design when using the existing manufacturing techniques. Therefore, on stationary applications where space and weight are not important factors and where capital investment must be kept down, it is hard to justify the use of the pin-fin surface. However, on mobile applications where weight and space-saving features have a high value, the pin-fin regenerator is very attractive. If manufacturing costs can be reduced, it will have an important effect on the situation.

P. R. TRUMPLER.⁴ The possible use of extended surface for the difficult gas-to-gas heat-transfer problem of the gas-turbine regenerator has interested a number of heat-exchanger designers. The type of analysis involving heat-transfer rates, surface per unit volume, and power loss made by A. L. London, W. M. Kays, and co-workers of Stanford University, is only a first step. The practical realization of the advantages of extended surfaces depends on a satisfactory mechanical design. To the writer's knowledge, this paper presents the first successful design of a full-scale commercial extended-surface regenerator.

At this time it is too early to say whether or not corrosion or fouling problems will be encountered during the exchanger operating life. The first few hundred hours of experimental operation, under conditions probably much more severe with respect to certain operating variables than will be encountered in practice, were satisfactory in every respect. There is no reason to expect difficulties in the future.

The writer personally feels that this heater design marks an important forward step in gas-turbine technology and that this form of regenerator will prove economically attractive for a large number of gas-turbine installations.

It should be emphasized that the exchanger to which the authors refer operates with a gas-fired combustor. This minimizes the fouling problem. Perhaps the authors could express their opinions concerning fouling problems which might be encountered with oil- or pulverized-coal firing.

AUTHORS' CLOSURE

Referring to the question of possible fouling of the gas-side surface by deposits, it is our opinion that this will not be a severe problem in gas-turbine practice due to high cold-end metal temperatures, high gas velocities, and high degree of dilution of products of combustion.

One procedure used to study the fouling and cleaning characteristics of the pin-fin surface was as follows:

Envelope samples about 6 × 6 in. were installed in the cold end of a Ljungstrom type of air preheater used with a stoker-fired boiler-burning midwestern high sulfur bituminous coal. The surface was blown with steam once a day. After about four months of continuous operation, the samples were removed and inspected. The examination proved that build-up of deposits of the pin-fin type of surface could be controlled by soot blowing, even under very adverse conditions such as encountered in this particular application.

The authors are grateful for the constructive comments of the discussers.

¹ "Heat-Exchange Equipment for a 5000-Kw Gas-Turbine Generator," by G. R. Fusner, *Mechanical Engineering*, vol. 72, 1950, p. 316.

² "Gas-Turbine Plant Heat Exchangers," by W. M. Kays, A. L. London, and D. W. Johnson, *THE AMERICAN SOCIETY OF MECHANICAL ENGINEERS*, New York, N. Y., 1951.

³ Gas Turbine Engineering Division, General Electric Company, Schenectady, N. Y. *Jun. ASME*.

⁴ Professor, Mechanical Engineering, Illinois Institute of Technology, Chicago, Ill. Consultant, Clark Brothers Company, Inc., Olean, N. Y. *Mem. ASME*.

Heat-Transfer and Flow-Friction Characteristics of Some Compact Heat-Exchanger Surfaces

Part 3—Design Data for Five Surfaces

By A. L. LONDON,¹ W. M. KAYS,² AND D. W. JOHNSON,³ STANFORD, CALIF.

New developments in prime-mover and process equipment have created a more urgent need for compact heat-transfer surfaces. This paper presents basic heat-transfer and flow-friction design data for five such surfaces. Three of these are variations of the finned-circular-tube type. The other two are flow inside small rectangular (6:1 aspect ratio) and circular tubes. In addition to the use of conventional nondimensional heat-transfer and flow-friction correlations, the various surfaces are compared on a heat-transfer coefficient versus flow-friction-horsepower basis. The results represent a continuation of a program started in 1945 and bring to a total of 39 the number of compact surfaces for which design data have been reported.

NOMENCLATURE

The following nomenclature is used in the paper:

- A = transfer area, sq ft
- A_s = minimum free-flow area, sq ft
- A_{fs} = frontal area, sq ft
- c_p = specific heat at constant pressure, Btu/(lb deg F)
- D = circular tube inside diameter, in., ft
- D_o = over-all outside diameter of fins, in.
- D_t = outside diameter of tube alone, in.
- E_{std} = friction power evaluated at specified standard gas properties (see caption of Fig. 10), hp/(sq ft of A)
- f = friction factor defined by Equation [2], dimensionless
- G = mass velocity based on A_s , lb/(hr sq ft of A_s)
- g = proportionality factor in Newton's second law, 32.2 (lb/g) (ft/sec²)
- h = unit conductance for thermal convection, Btu/(hr sq ft deg F)
- h_{std} = unit conductance evaluated at specified standard gas properties (see caption of Fig. 10), (Btu/(hr sq ft deg F))
- k = unit thermal conductivity, Btu/(hr sq ft deg F/ft)
- L = flow length, ft, in.

- n = number of fins per inch of tube length, in.⁻¹
- P = flow-stream pressure, ΔP is pressure drop, inches of water, lb/sq ft
- r_h = flow-passage hydraulic radius, ft ($r_h/L = A_c/A$)
- V = flow velocity, ft per sec
- α = ratio of total transfer area on one side of exchanger to total volume of exchanger, sq ft/cu ft
- α^* = aspect ratio of a rectangular cross section, long to short side, dimensionless
- β = ratio of total transfer area on one side of a plate-fin heat exchanger to volume between plates of that side, sq ft/cu ft
- δ = fin thickness, in.
- ρ = gas density, lb/cu ft
- σ = ratio of free-flow area to frontal area, A_c/A_n , dimensionless
- τ = surface flow-friction force per unit area, lb/sq ft
- μ = gas viscosity, evaluated at bulk average temperature, lb/(hr ft)
- μ_f = gas viscosity, evaluated at film average temperature, lb/(hr ft)
- N_{St} = Stanton number, (h/Gc_p) , a heat-transfer modulus
- N_{Pr} = Prandtl number, $(\mu c_p/k)$, a fluid-properties modulus evaluated at film average properties
- $N_{St} N_{Pr}^{1/3}$ = generalized heat-transfer parameter. This factor versus N_{Re_f} defines heat-transfer characteristics of surface
- N_{Re} = Reynolds number, $(4r_h G/\mu)$, modulus characterizing type of flow
- N_{Re_f} = $(4r_h G/\mu_f)$
- f = friction factor; $f = N_{Re_f}$ relation defines friction characteristics of surface

INTRODUCTION

Recognizing the need for ascertaining and making generally available basic heat-transfer and flow-friction design data for compact heat-transfer surfaces, the USN Bureau of Ships initiated in 1945 a test program at the USN Engineering Experiment Station, Annapolis, Md. This program was supplemented in 1947, when the Office of Naval Research, in co-operation with the Bureaus of Ships and Aeronautics, established a similar project at Stanford University. A number of co-operating manufacturers fabricated test cores for these investigations.

The test results from these programs have been published in two ASME papers (1, 2)⁴ and in several USN EES reports (3). Up to May, 1950, a total of 34 surfaces had been tested on the two programs. These data were collected and recalculated where necessary so that a common treatment of the basic test data was employed throughout, and were published under one cover (4). Diagrams of the various surfaces reported in this reference are shown in Fig. 1.

⁴ Numbers in parentheses refer to the Bibliography at the end of the paper.

¹ Professor of Mechanical Engineering, Stanford University. Mem. ASME.

² Assistant Professor of Mechanical Engineering, Stanford University. Jun. ASME.

³ Instructor, Mechanical Engineering, Stanford University. Jun. ASME.

Contributed by the Gas Turbine Power and Heat Transfer Divisions and presented at the Annual Meeting, Atlantic City, N. J., November 25-30, 1951, of THE AMERICAN SOCIETY OF MECHANICAL ENGINEERS.

NOTE: Statements and opinions advanced in papers are to be understood as individual expressions of their authors and not those of the Society. Manuscript received at ASME Headquarters, October 9, 1951. Paper No. 51-A-129.

Between May, 1950, and May, 1951, five more test cores were studied—three of the finned-circular-tube type, one of the rectangular-cylindrical-tube type, and one of the common circular-cylindrical-tube type. These surfaces are described schematically in Fig. 2. It is the object of this paper to present this later design information, bringing to a total of 39 the number of test cores investigated and reported.

EXPERIMENTAL METHOD AND TEST CORES

The arrangement of the test equipment and method of analyzing the direct test results are covered in considerable detail in (5). Consequently, only a brief summary will be presented here.

The test system provided for condensing-steam-to-air heat transfer with air flow on the surface of interest. The direct test data allowed determination of the over-all steam-to-air heat-transfer coefficient and the air-side core pressure drop. Allowance for the ineffectiveness of the extended surface and the steam-side condensate film resistance permitted the evaluation of the average unit conductance for thermal convection on the air side. The friction factor was extracted from the core pressure-drop data by allowing for entrance and exit flow stream mechanical energy losses (6), and for flow acceleration accompanying density changes due to both pressure and temperature variations along the flow length. Friction factors were established from isothermal flow tests as well as from runs with core heating.

The test cores were all of $8\frac{3}{4} \times 9\frac{3}{4}$ in. air-flow frontal area, with air-flow lengths ranging from 4 in. for the three finned-circular-tube cores to 18.3 in. for the direct-surface circular-tube core, ST-1. The steam-flow length in all cases was 8.4 in. These cores are shown in Fig. 2. Detailed core geometry used in reducing the direct test results are given in Table 1. Note that all the cores, except the circular-tube core ST-1, are of the extended-surface type.

For the finned-circular-tube cores, four semicircular cylindrical baffles were installed vertically on each of the two side panels of the core test assembly. This insured the same maximum mass velocity through each row by providing a total of ten tubes for each row transverse to the flow. However, in the five-row-deep core, rows 2 and 4 had only 9 effective tubes for heat transfer giving a total number of 48 active heat-transfer tubes. As a point of criticism, this procedure, while it satisfied the mass-flow requirement for each row, failed to duplicate completely the influence of fins on the flow turbulence for the tubes adjacent to the side panels. As a recommendation for future work, a better procedure would be to use longitudinally cut finned tubes for the wall baffles.

In contradistinction to the test-core factors given in Table 1, Table 2 summarizes the geometry of the air-side surface alone, as would obtain exactly in a core of infinite extent. The relatively minor differences for the finned-circular-tube surface, between these dimensions and the corresponding items in Table 1, arise from the influence of tube-sheet transfer area and the fact that an integer number of active heat-transfer tubes must be employed in each row.

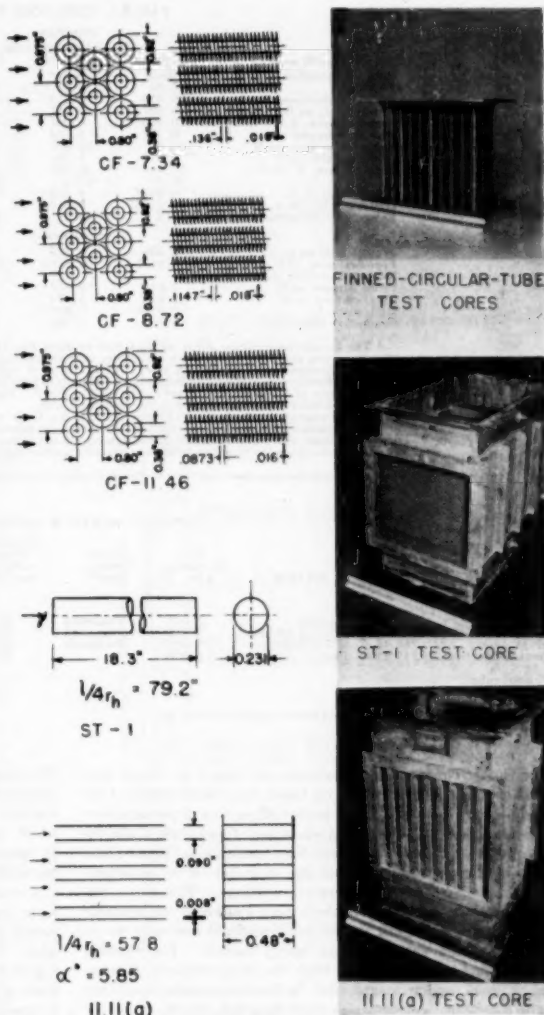


FIG. 2 GEOMETRY OF FIVE COMPACT SURFACES REPORTED IN PAPER (See Table 2 for additional information on the surfaces and Table 1 for details of test cores.)

HEAT-TRANSFER AND FLOW-FRICTION DESIGN DATA

Table 3 summarizes the reduced test data and the results of calculations for the basic heat-transfer and flow-friction design data for a typical core, CF-8.72. Included along with the heat-transfer information are both the isothermal-core friction and the hot-core friction behavior. The general excellence of the energy balances attests to the accuracy of the air-flow rate and temperature measurements. Energy balances for the other cores show average deviations of the order of 2.5 per cent, with the exception of the latter half of the runs for the rectangular-

TABLE 1 TEST-CORE DATA

Air side	Air Side			Rectangular tubes 11.11(a)	Circular tubes ST-1
	CF-7.34	CF-8.72	CF-11.46		
Core construction	Notes ^a	Notes ^a	Notes ^a	Notes ^b	Notes ^c
Fins/inch	7.34	8.72	11.46	11.11	...
Fins mean thickness, in.	0.018	0.018	0.016	0.008	...
Frontal area, sq ft	0.567	0.567	0.567	0.567	0.567
Free-flow area, A_c , sq ft	0.304	0.297	0.289	0.2245	0.3004
Free flow/total area, ϕ	0.536	0.524	0.510	0.396	0.530
Extended surface, sq ft	22.0 ^a	26.82 ^a	35.29 ^a	43.1 ^b	...
Prime surface, sq ft	3.34 ^a	3.24 ^a	3.17 ^a	8.9	95.175
Total surface, A , sq ft	25.94 ^a	30.06 ^a	38.46 ^a	52.0	95.175
A/A_c	85.3	101.2	133.1	232	317
Flow length, L , ft	0.333 ^a	0.333 ^a	0.333 ^a	0.667	1.325
Hyd. dia., $4r_H$, ft = $4L/(A/A_c)$	0.0156 ^d	0.0132 ^d	0.0100 ^d	0.0115	0.0193
Extended/total surface, per cent	87.2	89.3	91.8	82.9	0

STEAM SIDE

Frontal area, sq ft	0.338	0.338	0.338	0.542	1.21
Free-flow area, sq ft	0.0177	0.0177	0.0177	0.245	0.1907
Extended surface, sq ft	47.6	...
Prime surface, sq ft	2.97 ^a	2.97 ^a	2.97 ^a	7.8	99.6
Total surface, sq ft	2.97 ^a	2.97 ^a	2.97 ^a	55.2	99.6
Hyd. diam., ft	0.017 ^e	0.017 ^e	0.017 ^e	0.0125	0.00536
Steam-flow length, ft	0.700	0.700	0.700	0.700	0.700

^a The finned-circular-tube cores all had 0.92-in.-diam fins on 0.380-in.-OD, 0.260-in.-ID tubes. The aluminum fins are extruded from an aluminum over copper liner. Tube-wall thicknesses are 0.03 in. for both the aluminum and copper. $A_c = 110$ Btu/(hr sq ft deg F/ft) was used for evaluating the temperature effectiveness of the extended surface. Details of tube layout can be seen in Fig. 2.

^b Geometry of this plate-fin surface can be seen in Fig. 2. Plate material 0.03-in.-thick brass, fin material 0.008-in.-thick copper ($k = 218$ Btu/(hr sq ft deg F/ft)).

^c Tube material aluminum, $k = 110$ Btu/(hr sq ft deg F/ft), wall thickness 0.006 in.

^d Prime surface includes 0.60 sq ft for tube-sheet heat-transfer surface.

^e Flow length taken as tube center-line distance for 5-rows-deep core.

^f Hydraulic diameter based on total heat-transfer surface including 0.6 sq ft of tube-sheet effective surface.

^g Hydraulic diameter based on total surface excluding tube-sheet transfer area.

TABLE 2 SURFACE GEOMETRY

Surface	Fins/inch	Fin type	Fins thickness, in.	Tube arrangement ^b	Extended/total surface, per cent	Hyd. radius r_H , ft	α sq ft/cu ft	β sq ft/cu ft	ϕ	$L/4r_H$
Finned-circular-tube type:										
CF-7.34	7.34	Circular	0.018	Staggered	89.2	0.00385	139.8	...	0.338	...
CF-8.72	8.72	ID = 0.38 in.	0.018	Staggered	91.0	0.00322	162.8	...	0.524	...
CF-11.46	11.46	OD = 0.92 in.	0.016	Staggered	93.1	0.00244	209.0	...	0.810	...
Rectangular tube ^a	11.11	Plane	0.008	...	82.9	0.00288	...	312	...	57.8
Circular tube:										
ST-1	0.00482	79.2

^a The rectangular flow cross section has an aspect ratio of 3.85.

^b See Fig. 2.

tube core. These energy unbalances are from 7 to 18 per cent on the wrong side of expectations based on a consideration of the steam-metering system (5). The first 50 per cent of the runs were generally good. This difficulty was traced to a failure of the desuperheater on the inlet steam line, resulting in liquid-phase carry-over into the steam side of the core in spite of indicated gas-phase superheat from temperature readings. This error was corrected subsequently. As check runs confirmed the previous Stanton-number results, it was not considered necessary to re-run all the tests showing a poor energy balance. This decision was fortified by the fact that while the energy-balance discrepancies are of random magnitudes, the Stanton-number results are quite consistent, as is apparent from the graph, Fig. 6.

Table 4 summarizes the recommended design data as extracted from smoothed curves based on the test results shown in Figs. 3 through 7. The recommended f versus Na_f tabulations are based on the isothermal friction runs. The recommended Na_f $Ne^{1/2}$ versus Na_f correlation includes an allowance for steam-side resistance, the magnitude of which can be visualized from the ordinate difference between the plotted data points and the recommended curve shown in Figs. 3 to 7 inclusive. In effect, the plotted points do not represent an air-side Stanton number, but rather an "over-all coefficient Stanton number" corrected only for the temperature ineffectiveness of the extended surfaces.

The steam-side-resistance correction, for the case of steam flow through the inside of the vertical tubes of the finned-circular-tube cores, was based on the analysis of Nusselt given in reference (7).

The h_{steam} used ranged from 2500 to 5000 depending on the magnitude of the condensate rate. The blow steam rate was kept constant at about 270 lb per hr compared to the condensate rate which varied from 25 to 150 lb per hr. This blow steam, used to minimize the steam-side resistance, was separated from the condensate and metered as described in reference (5).

A similar procedure was used for the steam-side resistance estimate for the ST-1 core. Here again film condensation was assumed and the empirical results given by McAdams (7) were used. The h_{steam} so estimated ranged from 900 to 2500 depending on the condensate rate, with no allowance being made for the effect of the blow steam scouring off the condensate layer. It is believed that the resulting correction is conservative, but since the relative magnitude is small, less than 5 per cent from Fig. 7, this conservatism is of minor consequence.

For the rectangular-tube core 11.11(a), the finned steam-side surface was not of a simple configuration and no basic information was available for a firm estimate of the steam-side conductance. Consequently, in lieu of better information, an $h_{\text{steam}} = 2000$ was used, and the temperature ineffectiveness of the extended surface on the steam side was allowed for. Note from Fig. 6 that the corrections to Stanton number are less than 5 per cent, so that if the estimated conductance is of the right order of magnitude, only a small uncertainty is introduced into the recommended formulation.

Throughout this paper and the previous papers of this series (1, 2, 4), the length dimension employed in the Reynolds num-

TABLE 4 SUMMARY OF BASIC HEAT-TRANSFER AND FRICTION DATA

$(h/Gc_p)N_{Pr}^{1/4}$, f versus N_{Re} from smoothed curves					
N_{Re}	$(h/Gc_p)N_{Pr}^{1/4}$	f	h_{old}	f_{old}	
Core CF-7.34					
10000	0.00234	0.0314	33.4	0.953	
8000	0.00267	0.0339	30.4	0.527	
6000	0.00316	0.0341	27.0	0.235	
5000	0.00350	0.0345	24.9	0.131	
4000	0.00399	0.0351	22.8	0.0881	
3000	0.00469	0.0375	20.1	0.0307	
2500	0.00521	0.0390	18.6	0.0185	
2000	0.00592	0.0404	16.9	0.00980	
1500	0.00700	0.0428	15.0	0.00438	
1200	0.00799	0.0450	13.7	0.00236	
1000	0.00885	0.0470	12.6	0.00143	
800	0.01018	0.0499	11.2	0.000775	
600	0.0119	0.0541	10.2	0.000355	
500	0.0133	0.0570	9.41	0.000216	
Core CF-8.72					
6000	0.00368	0.0338	37.6	0.379	
5000	0.00395	0.0346	33.7	0.224	
4000	0.00433	0.0345	29.5	0.115	
3000	0.00492	0.0354	25.2	0.0486	
2500	0.00530	0.0368	22.0	0.0298	
2000	0.00602	0.0387	20.5	0.0161	
1500	0.00699	0.0420	17.9	0.00735	
1200	0.00788	0.0430	16.1	0.00406	
1000	0.00870	0.0449	14.8	0.00233	
800	0.00989	0.0478	13.5	0.00127	
600	0.0117	0.0525	12.0	0.000588	
500	0.0130	0.0560	11.1	0.000303	
400	0.0148	0.0612	10.1	0.000203	
Core CF-11.46					
8000	0.00356	0.0261	64.1	1.503	
6000	0.00390	0.0269	52.6	0.693	
5000	0.00415	0.0275	46.7	0.410	
4000	0.00450	0.0284	40.5	0.217	
3000	0.00504	0.0296	34.0	0.0953	
2500	0.00547	0.0307	30.8	0.0572	
2000	0.00605	0.0321	27.2	0.0306	
1500	0.00699	0.0341	23.6	0.0137	
1200	0.00790	0.0361	21.1	0.00749	
1000	0.00885	0.0379	19.2	0.00432	
800	0.00965	0.0405	17.4	0.00247	
600	0.0113	0.0449	15.2	0.00116	
500	0.0125	0.0482	14.1	0.000718	
400	0.0142	0.0538	12.8	0.000410	
Core 11.11(a)					
10000	0.00288	0.00768	54.88	0.5566	
8000	0.00303	0.00807	46.19	0.2965	
6000	0.00324	0.00862	37.04	0.1362	
5000	0.00338	0.00900	32.20	0.08153	
4000	0.00353	0.00958	26.90	0.0444	
3000	0.00368	0.01050	21.34	0.02055	
2500	0.00373	0.0112	17.77	0.01268	
2000	0.00375	0.0119	14.29	0.006900	
1700	0.00386	0.0127	12.47	0.004522	
1500	0.00420	0.0137	12.00	0.003351	
1200	0.00505	0.0166	11.55	0.002079	
1000	0.00586	0.0198	11.17	0.001435	
800	0.00704	0.0243	10.73	0.0009017	
600	0.00860	0.0319	10.17	0.0005040	
500	0.0103	0.0380	9.813	0.0003443	
Core ST-1					
15000	0.00288	0.00668	49.26	0.3502	
12000	0.00300	0.00667	41.05	0.1871	
10000	0.00310	0.00725	35.35	0.1126	
8000	0.00314	0.00760	28.64	0.06044	
6000	0.00294	0.00770	20.11	0.02583	
5000	0.00254	0.00725	14.48	0.01408	
4000	0.00193	0.00635	8.803	0.006313	
3000	0.00202	0.00672	6.910	0.002818	
2500	0.00229	0.00750	6.528	0.001820	
2000	0.00269	0.00902	6.135	0.001121	
1500	0.00334	0.01170	5.713	0.0006134	
1200	0.00399	0.01425	5.460	0.0004825	
1000	0.00463	0.1680	5.279	0.0003621	
800	0.00558	0.0206	5.090	0.0001638	
600	0.00707	0.0266	4.837	0.00008025	

ber is 4 times the hydraulic radius, defined in the following manner

$$4r_H = \frac{4L A_s}{A} = \frac{4\sigma}{\alpha} \quad [1]$$

where σ is the free-flow area to frontal area ratio and α expresses the area compactness of the surface geometry under consideration. This dimension is identical to the hydraulic diameter for cylindrical tube surfaces.

The friction factor, in conformity with the previous procedure,

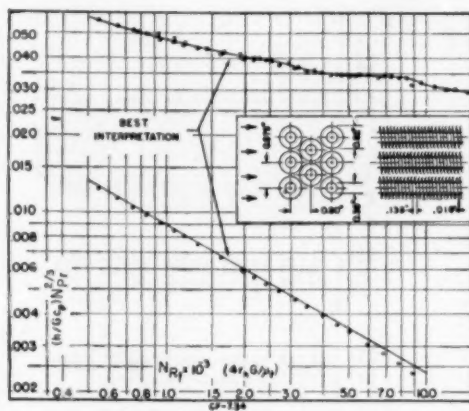


FIG. 3 HEAT-TRANSFER AND FLOW-FRICTION DESIGN DATA FOR SURFACE CF-7.34

(o denotes hot-core data; x denotes isothermal flow-friction data.)

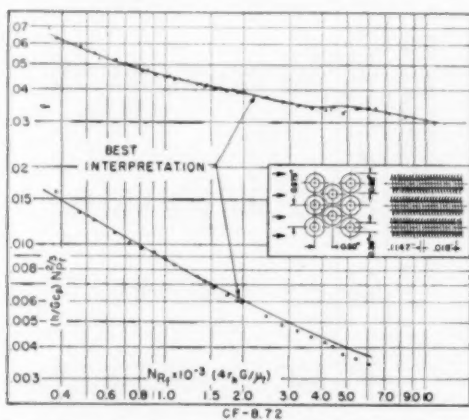


FIG. 4 HEAT-TRANSFER AND FLOW-FRICTION DESIGN DATA FOR SURFACE CF-8.72

(o denotes hot-core data; x denotes isothermal flow-friction data.)

has the following alternative and equivalent definitions

$$\frac{\Delta P}{\rho} = f \frac{L}{r_H} \frac{V^3}{2g} = f \frac{A}{A_s} \frac{V^3}{2g} = f \frac{L}{(\sigma/\alpha)} \frac{V^3}{2g} \quad [2]$$

$$f = \frac{\tau}{\rho \frac{V^2}{2g}}$$

Here $\Delta P/\rho$ is the "friction pressure drop" that would obtain for incompressible flow; τ is the friction force per square foot of surface area, including form drag as well as skin-friction effects.

Properties of air, as for the previous reports of this series, were taken from reference (8). More recent data (9) confirm that used, for the temperature range covered in the test work, and suggest that the uncertainty in N_{Pr} is of the order of 2 per cent rather than the previously used 5 per cent, reference (5).

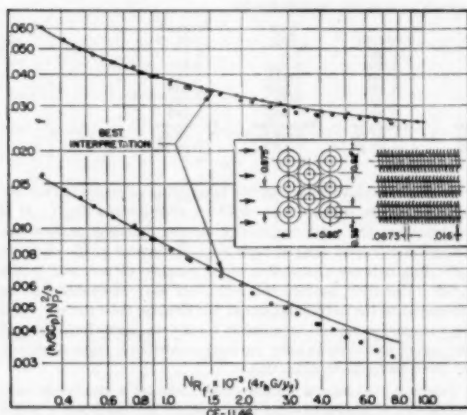


FIG. 5 HEAT-TRANSFER AND FLOW-FRICTION DESIGN DATA FOR SURFACE CF-11.46
(o denotes hot-core data; x denotes isothermal flow-friction data.)

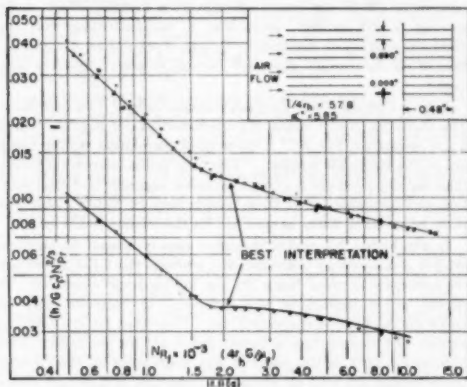


FIG. 6 HEAT-TRANSFER AND FLOW-FRICTION DESIGN DATA FOR SURFACE ST-1
(o denotes hot-core data; x denotes isothermal flow-friction data.)

The procedure for the evaluation of experimental accuracy was considered in some detail in reference (5). For the surfaces reported here, this procedure yielded the following estimates:

Estimated uncertainty in				
Surface	Nu_f	Nu_c	Nu_f	f
CF-7.43	± 2	± 4	± 2	± 3.5
CF-8.72	± 2	± 4	± 2	± 3.5
CF-11.46	± 2	± 4 at $Nu_f = 1000$ ± 6 at $Nu_f = 8000$	± 2	± 3.5
ST-1	± 1.6	± 3	± 2	± 3.5 at $Nu_f = 1000$ ± 7.5 at $Nu_f = 15,000$
11.11 (a)	± 1.6	± 3	± 2	± 5.5 at $Nu_f = 1000$ ± 8 at $Nu_f = 13,000$

The greater uncertainty in the friction factors for the cylindrical tube surfaces arises from the relatively large contribution of entrance- and exit-flow losses to the over-all pressure drop and the uncertainty of the coefficients applying to these losses (6).

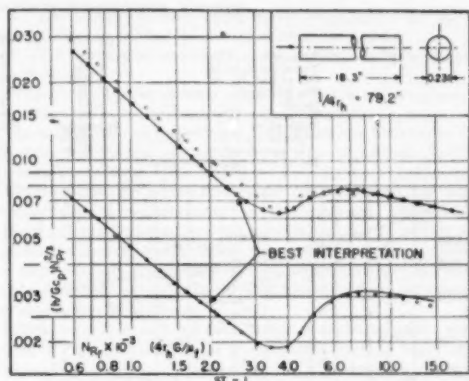


FIG. 7 HEAT-TRANSFER AND FLOW-FRICTION DESIGN DATA FOR SURFACE ST-1
(o denotes hot-core data; x denotes isothermal flow-friction data.)

For the finned-circular-tube surfaces, on the other hand, no such corrections need to be made, as such losses are chargeable directly to these surfaces, in the same manner as for flow normal to tube banks.

Some possible uncertainty might be introduced in the heat-transfer characteristics of the circular-finned-tube surfaces as a result of the very large ratio of air-side to steam-side area. This ratio is as high as 13:1 for surface CF-11.46. Any unaccounted-for scale resistance due to fouling on the steam side, or contact resistance between the copper liner and the finned aluminum tube, would result in calculated magnitudes of $Nu_c N_{f,0.5}$ for the air side which are lower than actuality. A resistance due to these factors of $1/100$ (hr sq ft deg F)/Btu, based on inside tube area, could account for an error of as much as 45 per cent at the highest Reynolds-number test point for the CF-11.46 core. At the other extreme, the lowest Reynolds-number test point for CF-7.34, the possible error is 7 per cent. However, an examination of the steam-side surfaces after completion of the tests showed no evidence of scale deposits, nor were any expected because of the relatively high "blow" steam velocity (approximately 100 fps), and the fact that the test cores were in service for only a few hours. Moreover, a sectioned sample tube taken from the test core showed excellent bonding. It also should be noted that the steam-side resistance was estimated employing the analysis of Nusselt which assumes a laminar condensate layer. This analysis is believed to be very conservative and should, if anything, introduce an error in the other direction.

DISCUSSION

The surface characteristics, as reported in Figs. 3 to 7, inclusive, will be considered in this discussion under two classifications, namely, the finned-circular-tube surfaces and the cylindrical-tube surfaces.

Finned-Circular-Tube Surfaces—Friction Characteristics. As is apparent from the data points shown in Figs. 3, 4, and 5, there is excellent agreement between the isothermal and hot-core friction factors over the complete Reynolds-number test range. For the hot-core runs, the viscosity in the Reynolds number is taken at a mean film temperature, defined as the arithmetic average of tube wall and bulk average flow temperature. The bulk average flow temperature is taken as the arithmetic average of core inlet and exit air temperatures. This agreement of isothermal and hot-core friction factors evidences the well-mixed

TABLE 5 COMPARISON OF FINNED-CIRCULAR-TUBE GEOMETRIES

	CF-7.34	CF-8.72	CF-11.46	Kata (11)	Jameson (10)
Fins/inch	7.34	8.72	11.46	7.8	8.7
Tube diam. D_t , in.	0.380	0.380	0.380	0.625	0.621
OD of fin, D_o , in.	0.920	0.920	0.920	1.315	1.12
Fin height, in.	0.270	0.270	0.270	0.347	0.248
D_o/D_t	2.42	2.42	2.42	2.12	1.29
Fin spacing/tube diam.	0.36	0.30	0.23	0.205	0.185
Tube pitch	Triangular	Triangular	Triangular	Triangular	Triangular
Transverse, p_t	1.06 D_t	1.07 D_t	1.07 D_t	1.07 D_t	1.10 D_t
Longitudinal, p_l	0.87 D_t	0.87 D_t	0.87 D_t	1.14 D_t	1.20 D_t
No. of rows deep in test core	5	5	5	2	8

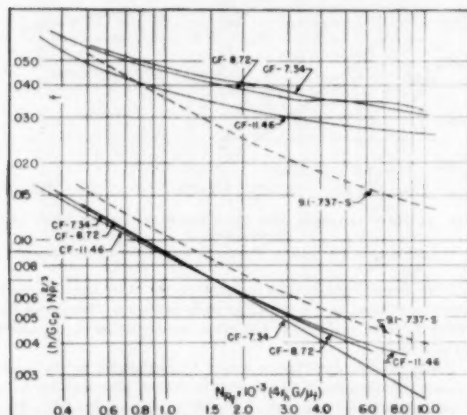


FIG. 8 COMPARISON OF FRICTION AND HEAT-TRANSFER CHARACTERISTICS OF FINNED-CIRCULAR-TUBE SURFACES (Dotted lines are characteristics of finned-flat-tube surface 9.1-737-S described in Fig. 1.)

flow arising from the high turbulence introduced by the flow geometry. In contrast, for the cylindrical-tube surfaces to be considered later, in the low-Reynolds-number regions there is a substantial difference between the isothermal and hot-core friction factors owing to the laminar-type flow.

The friction-factor characteristics for the three finned-circular-tube surfaces are compared, Fig. 8. The "bumps" in the characteristics for the CF-8.72 and CF-7.34 surfaces are interpreted as due to shifts in the point of separation for the flow around the circular tubes. No such effects are in evidence for the more closely spaced fin surface CF-11.46, and this fact supports the conclusion that the closer fin spacing stabilizes the flow to the extent that the point of separation in the tubes remains fixed, at least for the Reynolds-number range of the tests.

The fact that the friction factors for the three surfaces do not agree more closely (± 15 per cent deviation from the average) is evidence that the dimension selected for the Reynolds-number characterization ($4r_H = 4\sigma/\alpha$) is not sufficient, and that additional moduli involving ratios of dimensions are required. As the surfaces reported here did not include marked variations of geometry (see Tables 2 and 5) no generalized correlation is recommended. The results reported for f in Figs. 3, 4, and 5, are applicable only to cases where strict geometrical similarity is maintained. Interpolation and a limited extrapolation of these data may be valid within the following limits:

Fin spacing to tube diameter ratio: 0.2 to 0.4

Fin to tube diameter ratio, D_o/D_t : 2 to 3

Longitudinal pitch, p_l : 0.85 D_t to 0.90 D_t

Transverse pitch, p_t : 1.0 D_t to 1.1 D_t

Two comparisons with previously reported friction characteristics of somewhat similar surfaces are considered.

In Fig. 8 is plotted f versus N_D taken from reference (2) for the finned-flat-tube surface, 9.1-737-S, described in Fig. 1. It is evident that the aerodynamically cleaner flat-tube surface has a much lower form drag at high N_D . Estimates of the circular-tube drag indicate a contribution of roughly 45 per cent to the total. Moreover, surface 9.1-737-S has continuous fins as compared to the individual fins of the circular-tube surface; and here is another reason for a lower form drag, since form drag of the fins of the circular-tube surfaces contributes approximately 20 per cent to the total friction.

Jameson (10) reports friction-factor data for a number of configurations of finned-circular-tube surfaces and proposes a single f versus N_D correlation based on a complex equivalent diameter for the N_D length dimension. Converting the f versus N_D data reported here to Jameson's definitions results in quite excellent agreement (± 10 per cent). However, a definite effect of fin spacing is still evident, as in Fig. 8, demonstrating that the Jameson equivalent dimension, though representing a combination of all the surface geometry factors, is not completely adequate.

Finned-Circular-Tube Surfaces—Heat-Transfer Characteristics. The three $N_{St} N_D^{1/3}$ versus N_D characteristics of Figs. 3, 4, and 5 are compared, Fig. 8. A quite good correlation results using $4r_H$ in the Reynolds number. This correlation, somewhat better than for the f versus N_D characteristics, suggests that interpolation and extrapolation of these results may be valid within the same geometrical limits as specified for the friction behavior.

In the higher N_D region the more closely spaced fin surfaces exhibit a concave-up characteristic, whereas the CF-7.34 surface characteristic is quite linear on the log-log scale employed. A partial rationalization of this difference in behavior may be based on the friction characteristics. Note that for the CF-7.34 surface the f -curve has a bump down at $N_D \sim 3000$. This indicates a shift in the point of flow separation on the circular tubes further aft with an attendant reduction of flow turbulence and a decrease in N_{St} . In contrast, at an $N_D \sim 4000$ the f for CF-8.72 has a bump up suggesting a shift of the separation point forward with more form drag, resulting in additional turbulence tending to increase N_{St} . The behavior of the CF-11.46 surface neither supports nor denies these contentions.

Three comparisons with previously reported heat-transfer characteristics are considered.

In Fig. 8 the behavior of the finned-flat-tube surface, 9.1-737-S, described in Fig. 1, is superimposed. Quite similar curve shapes obtain for both this and the CF-11.46 and CF-8.72 surfaces. However, the flat-tube surface has roughly a 15 per cent higher N_{St} over the test range. Comparison of the geometries, Figs. 1 and 2, reveals that the average flow mass velocity, for a given G_{max} used in N_{St} , is higher for the flat-tube surface. This may account for the greater N_{St} in spite of a smaller amount of flow energy going into turbulence, as evidenced by the lower form drag relative to the circular-tube surfaces.

In Fig. 9 the heat-transfer data reported by Kata, et al. (11) and Jameson (10), are compared with the results reported here. The relative geometries of the surfaces considered are summarized in Table 5.

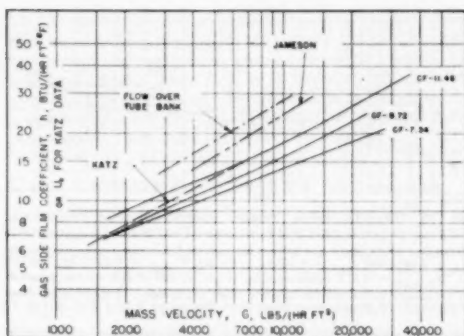


FIG. 9 FINNED-CIRCULAR-TUBE HEAT TRANSFER—COMPARISON WITH RESULTS OF OTHER EXPERIMENTERS
(Solid lines denote present data. Dashed lines denote data of Katz, et al., reference (11). Jameson reference (10), and flow over unfinned-tube banks, reference (7). See Table 5 for comparison of geometries.)

The Katz and Jameson surfaces were selected so as to most closely conform to the tube layout and fin-pitch geometries of the finned-circular-tube surfaces of this paper. In a nondimensional sense the most notable differences in geometry are with respect to the longitudinal spacing of the tubes and the fin spacing to tube diameter ratio.

Any attempt to make a comparison of heat-transfer behavior on a nondimensional basis is open to serious question as to the proper length dimension to use in Reynolds number. To avoid this difficulty, the convection coefficient h is plotted versus the mass velocity G_{max} . As Katz only reports an over-all coefficient U , from condensing steam to air, this is used in place of h and may be expected to be of the order of 5 to 10 per cent low as a consequence.

The most notable feature of this comparison is the substantial difference in h at the same G for comparable fin pitches, the data of Jameson running high by 30 to 50 per cent and that of Katz by 5 to 20 per cent. Considering the fact that Katz's data are only for a two-row-deep core one would expect even a larger discrepancy for a five-row core. Moreover, the slopes of the characteristics are quite different. These contradictions, which are significant from a design point of view, cannot be accounted for plausibly in terms of the different surface geometries, as shown, Table 5.

Several serious objections exist with respect to the test methods employed to obtain the older data. Katz and his co-workers did not meter the air flow directly, but rather calculated it from the experimental steam-condensate rate and inlet- and outlet-air temperatures measured at only a single point in the air-stream cross section. Jameson employed hot-air to cold-water heat transfer and estimated air-side conductances from a Wilson plot intercept using, in general, only two magnitudes of water velocity. The magnitudes of the water-side coefficients, which could have been deduced from this method, are not reported.

An obvious conclusion from these considerations is that additional careful experimental work has to be done on the finned-circular-tube surface, and until consistent data are obtained by different experimenters, designs using these quite common surfaces will be somewhat speculative.

Cylindrical-Tube Surfaces—Friction Behavior. The main objective in investigating these two cylindrical-tube surfaces was to obtain supplementary information for previously reported work (2) with a view to studying the following:

- 1 The influence of cross section on the heat-transfer and friction behavior in the transition Reynolds-number regime.
- 2 The influence of tube length, $L/4r_h$, particularly in the laminar-flow regime.

This is a subject for another paper (12), and as a consequence the discussion presented here will be quite limited.

As evident from an inspection of Figs. 6 and 7 for both the rectangular and circular tubes, the friction-factor behavior with Reynolds number is quite similar to the $N_{Re} N_{Pr}^{1/4}$ behavior. Flow-transition Reynolds numbers are duplicated and, for the circular tubes, the transition-dip region is reproduced. Note that fully developed turbulent flow is not evident until $N_{Re} \sim 7000$ is established, and, moreover, laminar flow persists up to $N_{Re} \sim 3000$ to 4000. From a design point of view, this departure from the quite commonly accepted $N_{Re} = 2300$ transition from turbulent to laminar flow is significant.

Both isothermal and hot-core friction-factor data points are given in Figs. 6 and 7 and the recommended curve is based on the isothermal runs. Note that in the turbulent-flow regime very good agreement obtains between these two sets of data where, for the hot-core runs, a viscosity based on the arithmetic-average film temperature is employed in the N_{Re} evaluation. This is in agreement with the behavior of the finned-circular-tube surfaces. However, for the laminar-flow regime a 5 to 10 per cent difference exists, with the hot-core points showing the highest f . This phenomenon is of course associated with the increase of gas viscosity and decrease of density with temperature and the preservation of the hot fluid layer adjacent to the wall by the smooth flow characteristics of the surface.

For a liquid, on the other hand, as viscosity decreases with temperature increase, the reverse would be true and the hot-core f -data would fall below the isothermal. Apparently there is sufficient distortion of the velocity profile as a result of viscosity and density variations so that even using a viscosity evaluated at wall temperature in N_{Re} will not correlate the hot-core runs with the isothermal characteristic. Introducing a viscosity ratio, bulk-fluid-to-wall correction factor to the f -ordinate scale has been proposed (7), and this can certainly be done in the present case. However, the difference in fluid viscosities evaluated at wall and bulk-fluid temperature, amounted to less than 20 per cent and remained fairly constant for the tests reported here. Consequently, no recommendations in this respect can be made.

The rectangular-tube-surface friction factors agree closely with the previously reported (2) behavior of the plate-fin surface, 19.86, described in Fig. 1. For the circular tube, the turbulent flow f agrees closely with previously accepted data. In the laminar region it approaches the $16/N_{Re}$ magnitude for long tubes. Further consideration of the friction behavior in cylindrical tubes is contained in reference (12) where a detailed study of the influence of $L/4r_h$ effects is presented.

Cylindrical-Tube Surfaces—Heat-Transfer Behavior. As the heat-transfer behavior of these cylindrical tube surfaces is discussed in some detail in reference (12), only a few of the most striking features will be examined here.

The most marked difference between the characteristics of the rectangular-tube and the circular-tube surfaces is the pronounced dip region for the latter extending from N_{Re} of 3000 to 7000.

Another departure from what has been somewhat common practice, is the fact that turbulent flow is not fully established until N_{Re} is greater than 8000, as compared to the traditional 2300.

In the laminar zone, much higher coefficients obtain for the rectangular as compared to the circular tube. This is in conformity with theoretical considerations as outlined in reference (12) where the importance of the aspect ratio of the rectangular tube is considered.

Possibly the most important single point arising from the foregoing comparison is that a dip region is an area of design uncertainty, and the factors such as approach flow turbulence, details of the flow contraction at inlet to the tubes, and roughness of the surfaces may influence the character of the dip. In contrast, for rectangular tubes of large aspect ratio, such as 11.11(a), no dip exists and, as a consequence, designs in this region are established on a firmer basis.

The performance of the 11.11(a) surface, with 11.11 fins per inch, is closely approximated by that of the plate-fin surface with 19.86 fins per inch, described in Fig. 1, and previously reported (2). In this reference the influence of tube length, $L/4r_H$, was emphasized and this point is examined in some detail in reference (12).

Heat Transfer—Friction Power Characteristics. In the previous discussions, friction and heat-transfer characteristics were considered separately. In many design applications, however, such as the gas-turbine regenerator, the relation of heat-transfer rates and flow-friction power requirement is of paramount interest. To provide this comparison Figs. 10, 11, 12 are presented. Here, as in reference (2), the heat-transfer conductance for standard, or reference, gas properties is evaluated as a function of Reynolds number, Table 4. Also, the friction power requirement per square foot of transfer area is similarly established. Figs. 10 and 11 are plots of the resulting h_{std} versus E_{std} for the five surfaces tested. The caption of Fig. 10 specifies the reference gas properties. Fig. 11 is a similar type of plot but here the compactness of the surface α is included, and the conductance per unit of core volume (αh_{std}) in Btu/(hr deg F cu ft) is graphed versus the friction-power requirement (αh_{std}) fhp/cu ft. Note that as much as a 6 to 1 disparity exists in friction power at an $h_{std} = 20$ between the CF-11.46 and the CF-7.34 surfaces. On a unit volume basis the disparity is increased to 40:1. Because of the flatness of the curves, the difference between h_{std} for the various surfaces at a given friction power is less marked, but, nevertheless, quite significant.

Fig. 12 strikingly illustrates the heat-transfer versus friction-power advantage of the flat-rectangular-tube versus circular-tube surface for operation in the laminar- and transition-flow regions, and the disappearance of this advantage in the turbulent-flow regime.

To extrapolate from the $h_{std} - E_{std}$ conditions given in Table 4 and Figs. 10, 11, and 12, to fluid properties different from the reference properties, the following relations may be employed

$$h = h_{std} \left[\frac{c_p}{c_{p, std}} \right] \left[\frac{\mu}{\mu_{std}} \right] \left[\frac{N_{Pr(Std)}}{N_{Pr}} \right]^{1/3} \quad (3)$$

$$E = E_{std} \left[\frac{\rho_{std}}{\rho} \right]^2 \left[\frac{\mu}{\mu_{std}} \right]^2$$

This extrapolation is founded on keeping Reynolds number and flow geometry constant. The derivation of these equations is available in reference (1).

CONCLUSIONS

As a summary of the foregoing discussion, the following conclusions are offered:

1 Design data for gas flow are presented for five additional configurations of compact surfaces to supplement the information contained in reference (4), bringing to a total of 39 the number of surfaces tested and reported.

2 The finned-circular-tube data, while in good agreement with respect to friction as compared to the results of Jameson (10), differ significantly with the previously available heat-transfer data given in references (10) and (11).

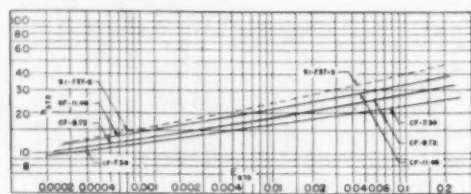


FIG. 10 HEAT-TRANSFER VERSUS FRICTION-POWER COMPARISON FOR FINNED-CIRCULAR-TUBE SURFACES—UNIT SURFACE AREA BASIS (Reference or standard gas properties selected for this representation are $\rho_{std} = 0.0413$ pcf, $\mu_{std} = 0.0678$ lb/(hr ft), $c_{p(Std)} = 0.2477$ Btu/(lb deg F), $N_{Pr(Std)} = 0.671$ corresponding to air at 500 F and 1 atm pressure. See Equations (3) for extrapolation to other conditions. Dotted line is characteristic of the finned-flat-tube surface designated 9.1-0.737-8 in Fig. 1.)

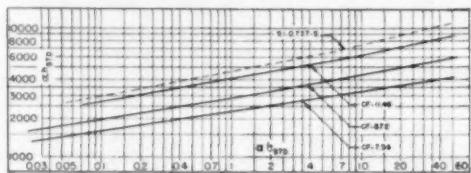


FIG. 11 HEAT-TRANSFER VERSUS FRICTION-POWER COMPARISON FOR FINNED-CIRCULAR-TUBE SURFACES—UNIT CORE VOLUME BASIS (See caption of Fig. 10 for standard gas properties and Equations (3) for extrapolation to other conditions. Dotted line is characteristic of finned-flat-tube surface designated 9.1-0.737-8 in Fig. 1.)

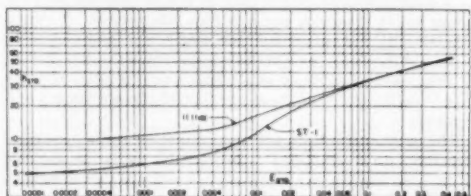


FIG. 12 HEAT-TRANSFER VERSUS FRICTION-POWER COMPARISON FOR RECTANGULAR AND CIRCULAR-CYLINDRICAL-TUBE SURFACES—UNIT SURFACE AREA BASIS (See caption of Fig. 10 for standard gas properties and Equations (3) for extrapolation to other conditions.)

3 These discrepancies suggest the urgent need for additional careful test work to obtain adequate design data for this very common type of surface. Until different experimenters can obtain reasonable agreement on basic data, design applications will remain uncertain.

4 A re-examination of the accepted heat-transfer correlation for flow in circular tubes is indicated, with special emphasis on the transition-flow region, which is a design region of interest for air flow in small tubes of the order of 0.25 in. diam. This is accomplished in reference (12).

5 The elimination of a "dip" region by the use of rectangular tubes of large aspect ratio, is attractive from the point of view of minimizing design uncertainties. Moreover, such tubes possess substantial heat transfer-friction power advantages in the laminar-flow region relative to circular-section tubes.

6 Some uncertainty exists for the problem of estimating friction factors for laminar-type flow with heat transfer from isothermal-friction data, as in cylindrical-tube flow. However, where the flow is well mixed, as for the finned circular-tube surfaces, no such question exists.

7 A number of configurations of interesting surfaces remain to be tested and reported before the designer will have the basic heat-transfer and flow-friction information needed to make optimum applications. These data, to be useful, must be obtained using adequate methods and instrumentation such as described in detail in reference (5). Standardization of such test procedures is believed to be highly desirable.

ACKNOWLEDGMENTS

The USN Office of Naval Research, the Bureau of Ships, and the Bureau of Aeronautics are currently sponsoring the research program on compact heat-transfer surfaces at Stanford University. The authors prepared this paper as a part of this program and express their appreciation to the sponsoring organizations.

The test cores were obtained from the Wolverine Tube Division of the Calumet and Hecla Consolidated Copper Company, the Modine Manufacturing Company, and the AiResearch Manufacturing Company. Mr. J. S. Rodgers and Mr. J. S. Marshall of Wolverine, Mr. Clyde Simpelaar of Modine, and Mr. S. K. Andersen of AiResearch were most co-operative. Without the assistance of the heat-exchanger industry this program would not have been feasible.

A number of Stanford University engineering students assisted in the testing and the performance of necessary computations and drafting. Chief among these were Messrs. Robert K. Lo, M. Talsania, and M. Potter. Their careful and painstaking work contributed to the validity of the reported results.

BIBLIOGRAPHY

- 1 "Test Results of High-Performance Heat-Exchanger Surfaces Used in Aircraft Intercoolers and Their Significance for Gas-Turbine Regenerator Design," by A. L. London and C. K. Ferguson, Trans. ASME, vol. 71, 1949, pp. 17-26.
- 2 "Heat-Transfer and Flow-Friction Characteristics of Some Compact Heat-Exchanger Surfaces—Part 2. Design Data for Thirteen Surfaces," by W. M. Kays and A. L. London, Trans. ASME, vol. 72, 1950, pp. 1087-1097.
- 3 "USN Engineering Experiment Station Reports C-2171-D, C-2171-E, C-2171-F, C-2171-G," by J. J. Dinan, August, 1947, to June, 1949.
- 4 "Gas-Turbine Plant Heat Exchangers—Basic Heat Transfer and Flow Friction Design Data," by W. M. Kays, A. L. London, and D. W. Johnson, ASME Research Report published in 1951.
- 5 "Heat-Transfer and Flow-Friction Characteristics of Some Compact Heat-Exchanger Surfaces, Part 1, Test System and Procedure," by W. M. Kays and A. L. London, Trans. ASME, vol. 72, 1950, pp. 1075-1085.
- 6 "Loss Coefficients for Abrupt Changes in Flow Cross Section With Low Reynolds Number Flow in Single and Multiple Tube Systems," by W. M. Kays, Trans. ASME, vol. 72, 1950, pp. 1067-1074.
- 7 "Heat Transmission," by W. H. McAdams, McGraw-Hill Book Company, Inc., New York, N. Y., 1942.
- 8 "An Investigation of Aircraft Heaters—Part II, Properties of Gases," by M. Tribus and L. M. K. Boelter, NACA Wartime Report W-9, 1942.
- 9 "A Summary of Viscosity and Heat-Conduction Data for He, A, H₂, O₂, N₂, CO, CO₂, H₂O, and Air," by F. G. Keyes, Trans. ASME, vol. 73, 1951, pp. 589-596.
- 10 "Tube Spacing in Finned-Tube Banks," by S. L. Jameson, Trans. ASME, vol. 67, 1945, pp. 633-642.
- 11 "Heat Transfer Through Tubes With Integral Spiral Fins," by D. L. Katz, K. D. Beatty, and A. S. Foust, Trans. ASME, vol. 67, 1945, pp. 665-674.
- 12 "Convective Heat Transfer and Flow-Friction Behavior in Small Cylindrical Tubes—Circular and Rectangular Cross Sections," by W. M. Kays and A. L. London, published in this issue, pages 1179-1189.
- 13 "Heat Transfer Coefficients for Air Flowing in Round Tubes in Rectangular Ducts, and Around Finned Cylinders," by R. E. Drexel and W. H. McAdams, NACA Wartime Report W-108, 1945.
- 14 "The Performance of Finned-Circular-Tube Heat Exchanger Surfaces," by D. W. Johnson, Technical Report No. 12, Navy Contract N6-onr-251, Task Order 6 (NR-035-104), January 1, 1951.

- 15 "Basic Heat Transfer and Flow Friction Design Data for Gas Flow in Circular and Rectangular Cylindrical Tube Heat Exchangers," by W. M. Kays, Technical Report No. 13, Navy Contract N6-onr-251, Task Order 6 (NR-035-104), June 15, 1951.

Discussion

R. H. NORRIS.⁵ What evidence can be presented by the authors on the magnitude of the thermal resistance of the bond between the helical fins and the tube, and what is the effect of this resistance on the magnitude and significance of the test results on the air-side heat transfer for the helically finned tube?

AUTHORS' CLOSURE

The point raised by Mr. Norris, as well as by some of the other discussions at the oral presentation, resolve to the following two questions relating specifically to the bi-metal construction of the finned-circular-tube surfaces: (1) What is the magnitude of the fouling resistance of the steam side? (2) What is the magnitude of contact resistance between the copper liner and the outer aluminum-extruded fin-tube combination? To answer these questions additional tests were performed since the original preparation of this paper, and it is the purpose of this closure to present the results and conclusions of this later work.

Fouling Resistance. The original CF-8.72 core, see Fig. 2, was retested at several points over the Reynolds number range after chemical and mechanical cleaning of the steam side of the tubes. No detectable difference was apparent in the heat-transfer characteristics as reported in Fig. 4. Visual inspection before cleaning indicated only a very light copper-oxide coating on the steam side. It is concluded as a consequence that the fouling resistance for the original tests was entirely negligible.

Contact Resistance. To resolve this question a new core, designated as CF-8.72(c) was tested. This consisted of finned circular tubes, formed out of solid copper stock, instead of the bimetal construction of the original tubes. Duplication of the geometry of the original CF-8.72 surface was only approximated as indicated in Table 5(a).

TABLE 5(a) ADDITIONAL COMPARISON OF FINNED-CIRCULAR-TUBE GEOMETRIES

	CF-8.72	Jameson (10)	CF-8.72(c)
Fins/in.	8.72	8.7	8.72
Tube diam., D_t , in.	0.380	0.621	0.42
OD of fins, D_o , in.	0.920	1.12	0.86
Fin height, in.	0.270	0.248	0.22
D_o/D_t	2.42	1.79	2.05
Fin spacing/tube diam.	0.30	0.185	0.273
Tube pitch	triangular	triangular	triangular
Transverse, x , in.	1.06 D_o	1.19 D_o	1.13 D_o
Longitudinal, z , in.	0.87 D_o	1.20 D_o	0.93 D_o
No. of rows deep in test core	5	8	5
Extended/total surface area	0.910	0.875	0.877

The results of these tests are summarized in Fig. 4(a) in a form directly comparable to the previous results shown in Fig. 4.

With respect to flow friction the new tests reveal a higher f factor by 8 to 12 per cent and this small difference may well be accounted for in terms of the increased tube diameter and smaller fin length as revealed by Table 5(a). An approximate breakdown of the friction factor into the components—skin friction of the fins, form-drag of the fins, and skin friction plus form-drag of the tubes, indicates that this last component amounts to about 50 per cent of the total. Consequently the 30 per cent greater fraction of tube area relative to fin area could account for the observed increase of the over-all friction as contained in the f factor.

In contrast to the small and easily explained discrepancy in

⁵ Engineer, General Electric Company. Mem. ASME.

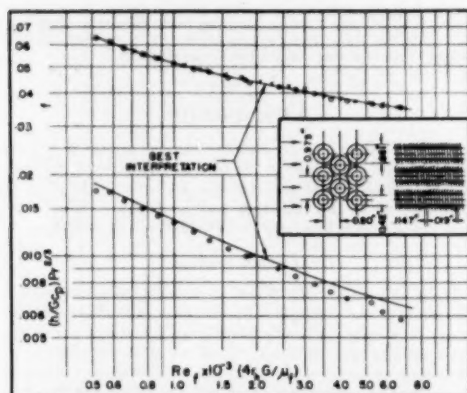


FIG. 4(a) HEAT-TRANSFER AND FLOW-FRICTION DESIGN DATA FOR SURFACE CF-8.72(c)

Surface Geometry. Fins/in., 8.72; fin ID, 0.42 in.; OD, 0.86 in.; fin thickness, 0.010 in.; tube arrangement, staggered; extended/total surface, 87.6 per cent; hydraulic radius, r_h , 0.00363 ft; μ , 136 ft²/ft²; ϵ , 0.494. See Table 2 for comparison with other surface geometries.

friction behavior, the heat-transfer results for the new core are strikingly different, ranging from 40 per cent higher at $Re = 600$ to 80 per cent higher at $Re = 6000$. This difference cannot be completely accounted for in terms of a "contact resistance" associated with the bimetal construction of the previous core. For reasons that will be considered later a thermal contact resistance of the order of $1/1000$ (hr deg F ft² of contact surface)/Btu appears to be a reasonable expectation, but this still leaves a discrepancy of 25 to 30 per cent. This cannot be accounted for in terms of the slight differences in air-side geometry between the CF-8.72 and CF-8.72(c) surfaces as shown in Table 5(a).

The later heat-transfer results agree very well with those of Jameson (10), either on the nondimensional basis of Fig. 4(a), or the dimensional basis of Fig. 9. A consideration of the comparison of the nondimensional geometrical factors shown in Table 5(a) points out both strong similarities and differences in air-side geometry of the two surfaces. Consequently this good agreement in heat-transfer behavior may be viewed as at least partially fortuitous.

For the bimetallic tube construction of the CF-8.72 surface the copper liner has the smaller coefficient of thermal expansion by about 3.8×10^{-6} in/(in deg F). As a result, if no prestress condition exists at room temperature, the aluminum outer cylinder with the integral fins will expand away from the copper liner for the test conditions, as the tube wall is then about 140 F above room temperature. The air gap thus formed will be of the order of 0.7×10^{-3} ft and, as a consequence, will provide a contact resistance. Additionally, the extrusion process used in forming the aluminum fins over the copper liner employs a grease lubricant. Visual inspection suggests that this grease layer may be of the order of 10^{-3} ft and the effect will make a further small contribution to the contact resistance. On the basis of the foregoing estimates a contact resistance of $1/1000$ (hr deg F ft² of contact surface)/Btu is estimated. Another method of estimating the contact resistance is to discover the resistance magnitude required to bring the heat-transfer characteristic of the previous CF-8.72 surface, Fig. 4, into parallelism with the CF-8.72(c) surface, Fig. 4(a). This procedure results in a magnitude of $1/1000$. But even this large resistance still leaves a discrepancy of 25 to 30 per cent between the "corrected" behavior of the CF-8.72 surface and the new results.

The following conclusions are offered as the main observations to be made from the foregoing considerations:

(1) The results reported in Figs. 3, 4, and 5 are not adequate for design purposes because the bi-metal tube construction introduces a contact thermal resistance not characteristic of the fin-side surface geometry and flow conditions. This contact resistance may be expected to vary substantially in magnitude depending on service conditions.

(2) The magnitude of this contact resistance for the particular set of bi-metal tube tests is believed to be of the order of $1/1000$ to $1/1000$ (hr deg F ft² of contact surface)/Btu. This still leaves about one half of the difference in heat-transfer behavior—monometal versus bimetal construction—as unaccounted for.

(3) The results reported in Fig. 4(a) of this closure are believed adequate for design providing geometrical similarity is maintained as indicated in the CF-8.72(c) quote of Table 5(a).

(4) These new results agree quite well with the previously reported data of Jameson (10).

(5) It is important to reiterate the conclusion stated in the main body of this paper—that additional carefully obtained design data are needed for the finned circular-tube surface before this very common configuration may be employed with confidence in heat-exchanger designs.

Convective Heat-Transfer and Flow-Friction Behavior of Small Cylindrical Tubes—Circular and Rectangular Cross Sections

By W. M. KAYS¹ AND A. L. LONDON,² STANFORD, CALIF.

Recent heat-transfer and flow-friction test data (1)³ for gas flow in small circular and rectangular cylindrical tubes, in the laminar, transition, and low-Reynolds-number turbulent-flow regimes, are examined and compared with earlier results. For circular tubes in laminar flow, the heat-transfer results substantiate very well analytical predictions as summarized by Norris and Streid (2). In turbulent flow, circular-tube heat transfer is correlated by an empirical nondimensional equation of the same form, but with a somewhat lower coefficient than has been commonly employed in the past. The difference is attributable in part to the use of more recent data on air properties in the reduction of test results to a nondimensional form. The transition region for circular tubes is found to extend from about $N_{Re} \sim 2000$ to $N_{Re} \sim 10,000$, and heat-exchanger design in this "dip" region is discussed. Laminar-flow circular-tube friction factors show an entrance length effect, similar to that found for heat transfer, and it is demonstrated that the analysis of Langhaar (3) for flow in a single tube can be employed to predict friction factors with acceptable accuracy for flow through a tube bundle even with the sudden change of flow area at the contracted tube-entrance section. For small circular tubes, as a result of this analysis, recommended design correlations in graphical form are given for the N_{Re} range 500 to 50,000.

The turbulent-flow heat-transfer and friction performance of rectangular tubes is in close agreement with the characteristics for circular tubes. However, there is a marked difference in the laminar and transition behavior, where the aspect ratio of the rectangular cross-section is demonstrated to have an important influence. It is concluded that considerable additional work, both analytical and experimental, is needed to ascertain laminar and transition flow-friction and heat-transfer characteristics in rectangular tubes.

NOMENCLATURE

The following nomenclature is used in the paper:

- A = heat transfer area, sq ft
- A_c = free-flow area, sq ft
- c_p = specific heat at constant pressure, Btu/(lb deg F)
- D = $4r_h$ inside diameter of circular tube, or hydraulic diameter of rectangular section tube, ft

¹ Assistant Professor, Mechanical Engineering, Stanford University, Jan. ASME.

² Professor, Mechanical Engineering, Stanford University. Mem. ASME.

³ Numbers in parentheses refer to Bibliography at end of paper. Contributed by the Gas Turbine Power and Heat Transfer Divisions and presented at the Annual Meeting, Atlantic City, N. J., November 25-30, 1951, of THE AMERICAN SOCIETY OF MECHANICAL ENGINEERS.

NOTE: Statements and opinions advanced in papers are to be understood as individual expressions of their authors and not those of the Society. Manuscript received at ASME Headquarters, October 9, 1951. Paper No. 51-A-130.

- f = Fanning friction factor, dimensionless
- G = mass velocity, lb/(hr sq ft)
- g = proportionality factor in Newton's second law, $g = 32.2$ (lb/ft)(ft/sec²)
- h = unit conductance for convective heat transfer, Btu/(hr sq ft deg F)
- K_c = contraction loss coefficient for pressure loss at heat-exchanger entrance, dimensionless
- K_d = momentum-velocity distribution correction factor, dimensionless
- K_e = expansion-loss coefficient for pressure loss at heat-exchanger exit, dimensionless
- k = unit thermal conductivity, Btu/(hr sq ft deg F/ft)
- L = flow length, ft
- r_h = hydraulic radius, $A_c L/A$ = flow cross section/wetted perimeter for cylindrical tubes, ft
- V = velocity, fps
- α^* = aspect ratio of rectangular section, long side over short side, dimensionless
- ρ = density, lb/ft³
- σ = ratio of free flow to frontal area, dimensionless
- τ_0 = wall shear stress, lb/ft²
- μ = viscosity, lb/(hr ft)
- Na = Stanton number, h/Gc_p
- N_{Pr} = Prandtl number, $\mu c_p/k$
- N_{Re} = Reynolds number, $4r_h G/\mu$, or DG/μ

NOTE: In all of the correlations proposed in this paper the fluid properties are evaluated at "film average" temperature, defined as the arithmetic average of the wall temperature and the bulk-average fluid temperature.

INTRODUCTION

The heat-transfer and flow-friction characteristics for gas flow in small circular tubes have been the subject of a great deal of experimentation, but there are surprisingly few reliable data upon which to base heat-exchanger design, unless an uncertainty of ± 15 to 20 per cent can be tolerated. This is especially true for Reynolds numbers in and near the transition region, and it is just this Reynolds-number range that becomes of importance when employing tubes with hydraulic diameters of the order of $1/4$ in. or less with low-density gases. There are considerably less experimental data available for rectangular tubes. The characteristics of rectangular tubes at low Reynolds numbers are becoming increasingly important because this is the flow-passage geometry for very compact plate-plain-fin-type heat-exchanger surfaces (4).

For heat transfer in the turbulent-flow region, Drexel and McAdams (5) correlated the previously available experimental data by the equation

$$N_{Re} N_{Pr}^{1/4} = 0.021 N_{Re}^{-0.3} \dots \dots \dots [1]$$

This equation averaged a fairly wide scatter of test points obtained by different experimenters employing different test techniques. It was recommended for both circular and rectangular

tubes, employing a hydraulic diameter, $4r_h$, as the N_R length dimension in both cases. Many heat-exchanger designers employ the Colburn equation, which is similar to Equation [1], but with the coefficient changed from 0.021 to 0.023.

In the laminar region for gas flow there have never been sufficient reliable test data to form any empirical generalizations, and in laminar flow the problem is further complicated by the fact that the heat-transfer performance becomes a strong function of the length-to-hydraulic-diameter ratio of the flow tubes, $L/4r_h$; and in the case of rectangular tubes, of the aspect ratio of the rectangular section. Natural convection also may affect test results at very low velocities. Fortunately, laminar-flow heat transfer can be analyzed theoretically. Norris and Streid present an extension of the work of Graetz and Leveque for flow through circular tubes with constant wall temperature, and flow between parallel planes with constant wall temperature (2). Adequate experimental confirmation, however, is lacking. Analyses also are available for some cases for laminar flow with constant heat input per unit of length, again without experimental confirmation.

There are extensive data available for the friction-factor behavior for circular tubes in turbulent flow. Heat-exchanger designers often employ the simple equation given by McAdams (6) for smooth tubes

$$f = 0.046 N_R^{-0.2} \quad [2]$$

For Reynolds numbers greater than 30,000 this equation corresponds closely to most of the more complex correlations, but at lower Reynolds numbers it yields a somewhat lower friction factor than the generally accepted best correlations, i.e., Blasius, Kármán-Nikuradse, etc. (7). For rectangular tubes the same equation is generally employed.

For laminar flow, the friction factor is readily derived analytically for fully established parabolic velocity distribution for both circular and rectangular cross sections (6) but there are no analytical results to demonstrate the influence of entrance length, except for the recent work on a circular tube with bellmouth entrance system by Langhaar (3).

There are insufficient heat-transfer and friction design data for gas flow in the transition region between fully established laminar and turbulent flow for both circular and rectangular tubes. What few data there are, however, indicate that the common procedure of extrapolating turbulent-flow correlations down to $N_R = 2300$ is not valid. Previous work on the Office of Naval Research Stanford University program reported in (4) was for air flow in cylindrical tubes of approximately rectangular section. However, owing to manufacturing limitations, these cores had a relatively short uninterrupted flow length, $L/4r_h$ 10 to 35. Moreover, the aspect ratio of the flow cross section, α^* , varied from 2.5 to 5. As a consequence, the separate effects of $L/4r_h$ and α^* could not be established quantitatively from these tests.

In view of the uncertainties in the design characteristics of these geometrically simple and quite commonly used heat-exchanger surfaces, the Navy-Stanford program included tests of a long circular-tube core and a long rectangular-tube core. The surface geometry of these cores is briefly described as follows:

Circular-Tube Surface—Designation ST-1

Tube ID = $4r_h = 0.231$ in.

Flow length, $L = 18.3$ in.

$L/4r_h = 79.2$

Free flow to frontal area ratio, $\sigma = 0.530$

1033 drawn aluminum tubes rolled into tube sheets providing an air-flow frontal area of 0.567 sq ft

Rectangular Tube Surface—Designation 11.11(a)

Tube inside dimensions, 0.48×0.082 in.

Aspect ratio, $\alpha^* = 5.85$

Hydraulic diameter, $4r_h = 0.1382$ in.

Flow length, $L = 8$ in.

$L/4r_h = 57.8$

Free flow to frontal area ratio $\sigma = 0.396$

Plate-fin type of core formed from 0.008-in. continuous copper fins (11.11 fins/in.) and brass plates, to provide an air-flow frontal area of 0.567 sq ft; Dip solder construction.

These cores are described in more detail in reference (1). The method of test, involving condensing steam-to-air heat transfer, and the method of reduction of test data, are given in reference (8).

Smoothed curves, representing the heat-transfer and flow-friction characteristics of these surfaces (1) are reproduced in Fig. 1 for the circular tubes (ST-1), and in Fig. 2 for the rectangular tubes (11.11a). The Reynolds-number test range extended from well into the laminar-flow regime, through transition flow, into the fully developed turbulent range, from N_R of 600 to 15,000 for (ST-1) and 400–12,000 for (11.11a). Only isothermal friction-factor results are reported here. However, reference (1) also reports the friction behavior associated with the hot-core runs.

The major objective of this paper is to critically compare the results of these tests with the analytical and experimental information contained in the literature. By this means, at least tentative recommendations for correlations to use for heat-exchanger design purposes are formulated. Particular consideration is given to the laminar and transition-flow regions, the influence of tube length $L/4r_h$ for circular tubes, and the effect of aspect ratio for rectangular tubes. Additionally, the work that remains to be accomplished for rectangular tubes is emphasized.

CIRCULAR-TUBE HEAT-TRANSFER PERFORMANCE

Comparison With the Conventional Correlations. In Fig. 1 the heat-transfer and flow-friction test results for the circular tube surface, ST-1, are plotted as $N_{St}N_{Pr}^{1/3}$ and f versus N_R . These particular parameters were chosen in order to show the similarity between the heat-transfer and friction performance, and to emphasize the flow-transition-region behavior. Superimposed are some of the commonly employed correlations for laminar- and turbulent-flow conditions.

The laminar-flow heat-transfer curves were evaluated from Norris and Streid's analytical results (2). These curves had to be calculated for the particular Prandtl number of the tests since $N_{St}N_{Pr}^{1/3}$ versus N_R is not an adequate set of parameters for laminar flow. The two turbulent-flow heat-transfer correlations are the ones recommended by Drexel and McAdams (5) (Equation [1]), and the older Colburn equation which has a coefficient of 0.023 instead of 0.021.

An examination of the test curve indicates laminar flow below $N_R = 3000$, a gradual transition from laminar to turbulent flow from $N_R = 3000$ to $N_R = 10,000$, and apparently fully established turbulent flow for $N_R > 10,000$, although the heat-transfer test range extended only to $N_R = 16,000$.

In the laminar-flow region, the test data agree closely with the Norris and Streid analytical curves for the particular L/D of the test core. The analytical curves are based on the idealization of fully established parabolic velocity distribution throughout the tube length, whereas in the tests the tubes start with an abrupt contraction followed by a re-expansion and then the build-up of the laminar-flow velocity distribution. From this point of view the test results support Norris' contention that for $L/D > 5$ the initial velocity distribution is of secondary importance. It also is worth noting that for laminar flow, $L/D = 80$ is still by no means a "long" tube, since both the test results and the analysis show a very marked entrance length effect.

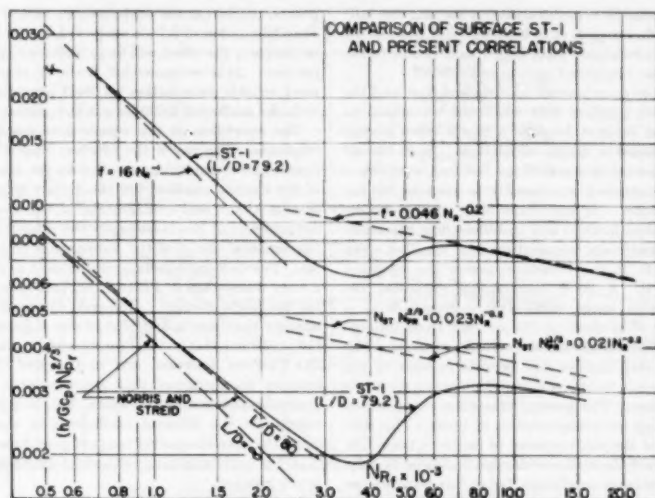


FIG. 1 CIRCULAR-TUBE HEAT-TRANSFER AND FLOW-FRICTION CHARACTERISTICS
(Comparison of surface ST-1, $L/D = 79.2$, with commonly used correlations.)

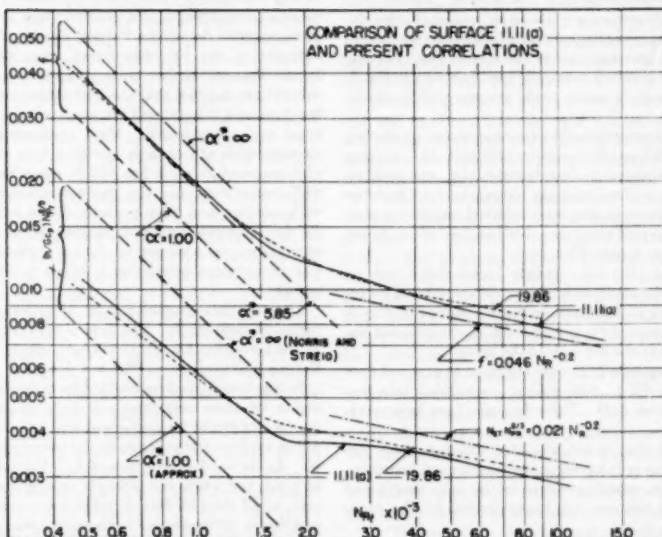


FIG. 2 RECTANGULAR-TUBE HEAT-TRANSFER AND FLOW-FRICTION CHARACTERISTICS
(Comparison of the surface 11.11 a, $L/4a = 57.8$, with previous results and recommendations, including predictions from laminar-flow theory.)

Although the test range does not extend very far into the fully established turbulent-flow region, it is apparent that both of the commonly employed correlations yield higher unit conductance. This discrepancy will be considered later in more detail.

The gradual transition from laminar to turbulent flow, and the wide range of Reynolds numbers over which the transition extends, is of particular interest because a much more abrupt transition is often assumed in design calculations. Since the air temperatures on the downstream side of the test core were determined by a 27-point traverse it was possible to examine the behavior of individual tubes. It was found that whereas in the region of fully established laminar and turbulent flow the maximum variation of downstream temperature over the flow cross section was about 2 F, in the transition region the variation was as great as 20 F. A 20 F temperature variation, occurring in the Reynolds range, 5000-6000, corresponds to a variation of $Nu_N Pr^{1/4}$ of as much as 50 per cent from tube to tube. Furthermore, this variation was perfectly random. The conclusion is evident that laminar flow persists in some of the tubes to $Nu > 8000$, while in others a transition occurs at much lower Reynolds numbers. The gradual transition curve shows only the integrated effect for a large number of tubes. This substantial variation in the Reynolds number of incipient transition would be expected where there is considerable variation in tube dimensions and tube-entrance conditions, but in this test core the drawn aluminum tubes were sized accurately. Also, the core has an abrupt flow-area contraction at the tube entrances ($\sigma = \text{free flow}/\text{frontal area} = 0.530$) which would be expected to produce an early and a consistent transition rather than the actual variable transition which in some tubes is as late as $Nu \sim 8000$.

Comparison With Other Small-Tube Test Results. Rather than attempt to draw definite recommendations for heat-exchanger design from the foregoing comparisons alone, the actual test data of a number of previous investigations of gas flow in small circular tubes at low Reynolds numbers were compared as shown in Fig. 3. These were all obtained in steam-to-air systems with multiple-tube test cores.

The London and Brewster data (9) were recalculated employing more recent information on air properties (10) and (11); making a correction for an estimated steam-side resistance; and evaluating fluid properties at a "film" average temperature. The tubes of this test core had hex ends that were soldered together so that a rather smooth convergent entrance existed instead of an abrupt contraction entrance as for the ST-1 core.

The Harrison data (12) were likewise recalculated but no correction was made for steam-side resistance, there being no information upon which to base any estimate. However, this is approximately compensated by the omission of a correction for the heat-transfer area in the hex ends of the tubes.

The Green and King data (13) were obtained from a test core very similar to core ST-1, with abrupt contraction tube entrances, but with shorter L/D . These data also have been recalculated.

An examination of Fig. 3 indicates that although there are considerable differences in behavior in the laminar and transition regions, all of the test results converge in the fully established turbulent-flow region and are well approximated by the equation

$$Nu_N Pr^{1/4} = 0.020 N_{Re}^{-0.7} \quad [3]$$

This equation is 5 per cent below the correlation recommended by Drexel and McAdams and 15 per cent below the Colburn equation.

An important point to note is that the Prandtl number employed in the reduction of the test data was evaluated at a film-average temperature and was about 0.69 for most of the test

points, employing the air-properties data of (10) and (11). If a Prandtl number of 0.74 is employed, as has been frequently done in the past, the effect will be to increase $Nu_N Pr^{1/4}$ by just about 5 per cent. It is recommended, however, that the most recent and most reliable information on fluid properties be used together with the coefficient 0.020 for gas flow, rather than 0.021.

The restriction of this equation to gas flow is worth special emphasis. The use of the j -factor, $Nu_N Pr^{1/4}$, specifies that the heat-transfer conductance varies as the minus-two-thirds power of the Prandtl number, but this is only an empirical approximation of the actual contribution of the Prandtl number. The actual effect of Pr is currently the subject of a great amount of fundamental study of the mechanisms of turbulent heat transfer. The Colburn equation can be used as an approximation for a very wide range of Prandtl numbers (except for $Pr < 1$ as for the liquid metals). However, comparison with some of the analogy analyses such as that of von Kármán (14), or Martinelli (15) indicates that in the Prandtl-number range of gases, 0.6-0.8, the Colburn equation, due to the $Pr^{1/4}$ factor, yields heat-transfer conductances that are somewhat high, while in the Prandtl-number range of water, 2-6, it is low. This, then, accounts for the different coefficients in the j -factor equations. Since the Prandtl-number range of gases is rather small, the use of $Pr^{1/4}$ is quite adequate, but extrapolation outside the gas range is not justified.

It also should be noted that all of the data considered were obtained with essentially constant wall temperature. In laminar flow there is about a 20 per cent difference between the unit conductances for constant wall-temperature conditions, and for what might be considered the other extreme, constant heat input per unit of tube length. Seban and Shimazaki (16) have shown that there is also a difference for turbulent flow and that this difference increases with decreasing Prandtl number, having an important influence in the Prandtl-number range of the liquid metals. In the Prandtl-number range of gases considered here, Seban's calculations indicate that the unit conductance for constant heat input per unit of length will run 4 to 5 per cent above that for a constant wall temperature. Most applications with gas flow in circular tubes will occur in crossflow heat exchangers where the wall-temperature variation will be somewhere between constant wall temperature and the wall-temperature variation obtained with constant heat input per unit of tube length. The correction for nonisothermal wall conditions would then be within the range of experimental accuracy of the data upon which the constant wall-temperature correlation is based in the turbulent flow Nu regime.

The test data examined show no apparent L/D effect in the turbulent-flow region. The data of (17) indicate that for $L/D > 25$ the correction for entrance-length effects is probably less than the experimental error of the test data.

In Fig. 3 analytical curves have been drawn in the laminar-flow region for three magnitudes of L/D , employing the results of Norris and Streid for isothermal wall conditions. The comparison of analysis and experiment has already been made for $L/D = 80$. At the lower magnitudes of L/D the comparison is not quite as good, but when the probable experimental accuracy, ± 5 per cent, of all the test data, is taken into consideration, the Norris and Streid curves appear to be a quite reasonable approximation of laminar-flow heat-transfer characteristics in a circular tube with constant wall temperature. Norris originally presented his results as a tabulation of Nusselt number versus $Nu_N Pr/(L/D)$, and then presented as an approximation to the tabulation two asymptotic equations. As an improvement over these approximations, the following very simple equation is presented, which for $Nu < 2000$ and $L/D > 25$ has a maximum deviation of 2 per cent from the original analytical results

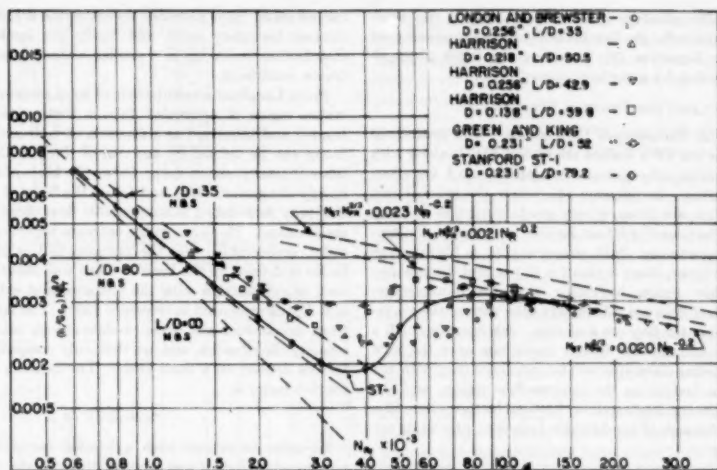


FIG. 3 CIRCULAR-TUBE HEAT-TRANSFER CHARACTERISTICS
 (Influence of L/D and entrance flow conditions. Comparison with results of other experiments and with laminar-flow theory.)

$$N_{St} N_{Pr} = 3.66/N_{Re} + 0.05 N_{Pr}/(L/D) \dots [4]$$

For large magnitudes of L/D , or for very low Reynolds numbers this equation approaches the theoretical limiting Nusselt number of 3.66 ($N_{St} = N_{Pr}/N_{Re}$). The unit conductance considered here is based on the logarithmic mean temperature difference so that the limiting magnitude is also the limiting local conductance. Another virtue of this empirical equation is its symmetry with Equation (7) which is proposed for f as a function of N_{Re} .

It should be emphasized that the laminar-flow data discussed are strictly applicable only for constant wall-temperature conditions. For constant heat input per unit of length the limiting Nusselt number (18) is 4.36. This gives a unit conductance 19 per cent above the constant wall-temperature case. No analysis is currently available for other than the limiting Nusselt number.

Another aspect for laminar-flow convection which should be considered is the effect of natural convection. It will be noted that no account is taken of the influence of natural convection in the comparison of analysis and experiment. For low-velocity laminar flow in large tubes, there is no question that there will be considerable natural-convection effects. However, the equations which have been proposed would involve a correction which for these tests appears entirely out of line. It is believed that for tubes of less than $1/4$ in. diam and for Reynolds numbers greater than 500 the natural convection influence is negligible.

Since all of the test data examined were obtained with air under similar heating conditions, it is not possible to determine the effect of temperature-dependent fluid properties, i.e., variation of fluid properties over the flow cross section. For gases this is not as serious a problem as for liquids, since the μ , k , N_{Pr} properties do not change as strongly with temperature. The use of a film-average temperature at which to evaluate fluid properties is a simple expedient which appears to be quite adequate for turbulent flow of gases, but whether this is adequate for laminar flow is open to question. An examination of the comparison of isothermal friction factors, and friction factors obtained with air heating in reference (1) indicates that a better method is needed for handling the influence of variable properties for at least the friction factors in laminar flow.

All of the data plotted on Fig. 3 show the gradual transition from laminar to turbulent flow as for the ST-1 surface. However, there is a definite difference in the transition range. It is especially notable that the London and Brewster data show a transition range at quite high Reynolds numbers, whereas the Green and King data show a transition range at Reynolds numbers approximately 50 per cent lower. The Green and King data are based on somewhat greater L/D , 52 as compared to 35, but the principal difference lies in the fact that the Green and King core had an abrupt contraction at the entrance whereas the London and Brewster core had a fairly smoothly convergent entrance owing to the manner of header construction. All three of the Harrison test cores had smoothly convergent entrances, while the ST-1 core had an abrupt contraction. If the cores with different entrance conditions are compared separately, consistent behavior is noted. A smoothly convergent entrance tends to preserve laminar flow to higher Reynolds numbers than an entrance with an abrupt contraction, and with the smooth entrance the transition range extends to higher Reynolds numbers for short tubes than for long tubes. For the two cores with abrupt contraction entrances, the transition appears to take place in about the same Reynolds-number range.

The foregoing considerations, both experimental and analytical, of the heat-transfer performance for small circular tubes, yields the following conclusions:

(a) The Norris and Streid calculations for laminar flow are very well substantiated and are closely approximated for $N_{Re} < 2000$ and $L/D > 25$ by Equation (4). A correction for natural convection effects for tubes of $1/4$ inch diameter or less, and for Reynolds numbers greater than 500, does not appear to be warranted.

(b) The transition from laminar to turbulent flow will extend from $N_{Re} \sim 2000$ to $N_{Re} \sim 10,000$, or even greater. For multiple-tube systems the transition will be gradual, but the position of the transition curve will depend upon the length-to-diameter ratio, L/D , and the entrance conditions. In general, with an abrupt contraction at the entrance, transition will start, and will be complete, at a lower N_{Re} than if the entrance is smoothly convergent. For these reasons heat-exchanger design with circular tubes in this range is quite uncertain.

(c) For Reynolds numbers greater than 10,000, the heat-transfer characteristics for gas flow in small circular tubes are best approximated by Equation [3], providing the latest physical-properties information for gases is employed (11).

CIRCULAR-TUBE FRICTION PERFORMANCE

Comparison With Conventional Correlations. The isothermal friction factors for the ST-1 surface are shown, Fig. 1, along with two commonly employed equations for laminar and turbulent flow in circular tubes. In reference (1), where the original test data for this surface are given, a very good correlation between isothermal and "hot-core" friction factors is obtained for turbulent flow, by evaluating fluid properties at a film-average temperature. However, there is about a 10 per cent discrepancy in the laminar-flow region indicating that the film-average-temperature method does not adequately take care of the variation of viscosity over the flow cross section. Additionally, such a procedure cannot account for density variations over the flow section. The following discussion will be concerned only with the isothermal friction factors, in the laminar-flow region, and the question of correlating laminar-flow friction factors where film properties vary, although of considerable technical interest, is not considered further.

In the laminar-flow region the test friction factors show a definite L/D effect similar to that found for the heat-transfer results. The transition from laminar to turbulent flow is similar to that for the heat-transfer results, the only difference being that the dip is less pronounced.

In the turbulent-flow region the test friction factors agree very well with Equation [2], which is somewhat surprising when it is considered that this equation, while agreeing with the Kármán-Nikuradse equation for $N_R > 30,000$, yields friction factors that are about 8 per cent low at $N_R = 10,000$. Since the heat-transfer results indicate that fully established turbulent flow is not attained until Reynolds numbers greater than 10,000, it may be that the correlation with the $f = 0.046 N_R^{-0.2}$ curve at low Reynolds numbers is fortuitous and due to the part laminar, part turbulent characteristic of the transition range. Shapiro and Smith (19) note this entrance effect in experiments on tubes with bellmouth entrances, and find that for Reynolds numbers less than 100,000 the apparent friction factor is generally lower than the friction factor given by the Kármán-Nikuradse equation for fully established turbulent flow.

There is another reason why the friction factors may be somewhat lower than anticipated. As employed here, f is defined on the basis of the mean wall shear stress, $\tau_0 = \rho V^2/2g$, rather than the pressure drop. The change in pressure due to changes in velocity distribution is taken care of by the entrance abrupt-contraction coefficient K_e of reference (20). The abrupt contraction at the entrance to the flow tubes is followed by a vena contracta of the flow stream a few diameters downstream, and then a re-expansion. In the region of the vena contracta there is actually a flow reversal at the wall and thus reversed shear. The result is that the integrated shear along the entire tube may be less than the local shear at points downstream where there is fully established turbulent flow.

Effect of L/D on Laminar-Flow Friction Factors. It was mentioned previously that in the laminar-flow region the friction factors for surface ST-1 show a similar L/D effect as do the heat-transfer results. What appears to be the best analytical study of the entrance region of a tube in laminar flow is that of Langhaar (3). This analysis includes the idealization of a uniform velocity distribution at the entrance, a condition hardly satisfied by the abrupt contraction entrance for the ST-1 core, or by the entrance conditions in most heat-exchanger applications. However, the effect of the abrupt contraction is noticed for only a few diameters

downstream. It is plausible that after the first few diameters the laminar boundary layer, and finally the laminar-flow velocity distribution builds up in a similar manner regardless of the entrance conditions.

From Langhaar's calculations of total pressure drop in the entrance region of a circular tube a friction factor can be extracted and tabulated as a function of L/D and N_R . A friction factor can be defined by any one of three methods: (a) On the basis of total pressure drop; (b) on the basis of mean mechanical energy-dissipation rate; and (c) on the basis of mean wall shear. For fully established incompressible flow these three definitions are identical. However, in the entrance region of a tube they will differ considerably. For the purposes of this paper the friction factor is defined on the basis of mean wall shear so that it can be used in conjunction with the entrance and exit coefficients, K_e and K_x , as presented in reference (20). The latter were derived from momentum and force considerations, taking into account velocity distribution, and are thus only compatible with friction factors defined on a force basis. The defining equation for the friction factor is

$$\tau_0 = \rho V^2/2g \quad [5]$$

In order to extract such a friction factor from Langhaar's pressure-drop data it was necessary to evaluate, from his velocity-distribution data, a momentum-velocity distribution correction factor K_d , as a function of the parameter, $4(L/D)/N_R$. The momentum correction factor is defined (20) as

$$K_d = \frac{1}{A_s V^2 \tau_0} \int_0^{A_s} V^3 dA_s \quad [6]$$

These results are presented in Table 1. It will be noted that as L/D is increased, or N_R decreased, K_d approaches the familiar magnitude of 1.333 for parabolic velocity distribution.

TABLE 1 MOMENTUM-VELOCITY DISTRIBUTION CORRECTION FACTORS FOR LAMINAR FLOW IN SHORT CIRCULAR TUBES

$4(L/D)/N_R$	K_d^a
0.006	1.110
0.008	1.124
0.010	1.138
0.015	1.158
0.020	1.174
0.025	1.187
0.030	1.199
0.050	1.221
0.050	1.238
0.060	1.255
0.080	1.282
0.100	1.300
0.150	1.318
0.200	1.326
0.250	1.330
0.300	1.332
.....	1.333

^a K_d is defined by Equation [6].

The friction factors are then presented in Table 2 in the form $4f(L/D)$ versus $4(L/D)/N_R$. It will be noted that for $4(L/D)/N_R > 0.25$ the complex functional relation is closely approximated by the simple equation

$$f = 16/N_R + 0.152/(L/D) \quad [7]$$

The mean friction factor thus approaches the well-known relation, $f = 16/N_R$, for fully established laminar-flow velocity distribution, as (L/D) is increased, and also as N_R is decreased. This equation has the same form as Equation [4] for heat transfer in laminar flow.

Comparison With Other Small-Tube Test Data. In order to check the applicability of friction factors from Langhaar's analysis to systems with an abrupt contraction entrance, four sets of test results were examined, for laminar flow with differing L/D .

TABLE 2 LAMINAR-FLOW FRICTION FACTORS FOR SHORT CIRCULAR TUBES*

$4(L/D)/N_{Re}$	$4f(L/D)$
0.00722	0.333
0.0143	0.324
0.0214	0.690
0.0335	0.949
0.0549	1.353
0.0715	1.646
0.0947	2.043
0.1365	2.554
0.1795	3.467
0.2479	4.575
0.3040	5.475

For $4(L/D)/N_{Re} > 0.25$
 $f = 16/N_{Re} + 0.153/(L/D)$

* Based on uniform velocity distribution at tube-inlet section.

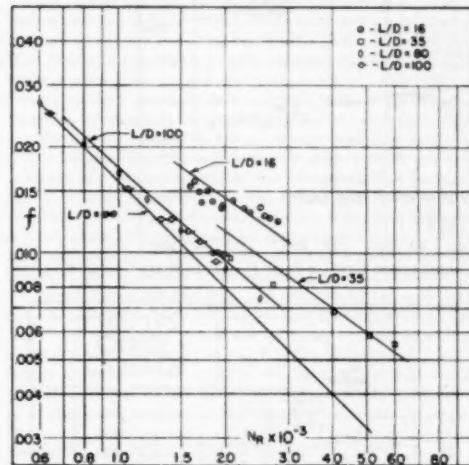


FIG. 4 CIRCULAR-TUBE LAMINAR-FLOW FRICTION FACTORS (Influence of L/D . Comparison with results of other experimenters and with laminar-flow theory.)

To extract the friction factor from over-all core pressure-drop data, entrance and exit loss coefficients, K_e and K_x , were evaluated by the methods of reference (20) employing the momentum-velocity distribution correction factor K_d , described previously. These test data along with friction factors from Table 2, are shown in Fig. 4.

The test data for $L/D = 80$ are from surface ST-1. For $L/D = 35$ the London and Brewster data reference (9) were employed. The heat-transfer test results had indicated in this case that laminar flow persisted to $N_{Re} = 5000$. The $L/D = 100$ data were obtained from reference (21). The $L/D = 16$ test points are unpublished data (22).

The $L/D = 80$ test points lie somewhat low and practically coincide with the data for $L/D = 100$. The latter, however, correlate fairly well with the analysis. For $L/D = 35$ the two lowest N_{Re} test points appear to be low, but the other three correlate fairly well with the analysis. The correlation between the analysis and the test points for $L/D = 16$ is excellent considering the experimental difficulties of measuring accurately the small pressure drops encountered in these tests, especially at low N_{Re} .

In general, the test points tend to lie slightly below the curves from Langhaar's analysis. This is to be expected since the friction factors are defined on the basis of mean wall shear, and the reversed shear in the vicinity of the vena contracta at the entrance would tend to reduce the apparent friction factors in the manner shown.

As a general conclusion to this discussion, there is no question that a very definite L/D influence on the laminar-flow friction factors exists, and the friction factors predicted from Langhaar's analysis are in substantial quantitative agreement with the experimental results.

RECOMMENDED HEAT-TRANSFER AND FLOW-FRICTION CORRELATIONS FOR FLOW INSIDE CIRCULAR TUBES

In the foregoing sections the flow of a gas inside small smooth circular tubes in the laminar, transition, and low N_{Re} turbulent regimes has been investigated, and the results of a number of different experimenters have been examined and correlated. The conclusions from this investigation are presented graphically in the form of recommended design curves, Fig. 5, and represent a summary of the current best interpretation of the available test data for gas flow inside small circular tubes.

The laminar-flow heat-transfer curves are based on analysis, as presented by Norris and Streid (2), which has been shown to be supported by experiment. These curves are evaluated for a Prandtl number of 0.672, corresponding to air at 500 F. Very little error is introduced by this specification for the Prandtl-number range of gases, and it has the virtue of allowing both laminar and turbulent-flow correlations to be shown on the same plot.

The dashed line in the laminar-flow heat-transfer region is for constant heat input per unit of length, and $L/D = \infty$, instead of constant wall temperature which is the basis of the Norris and Streid analysis. This is the situation which would be encountered in a counterflow heat exchanger with equal capacity rates for each fluid, as, for example, a gas-turbine regenerator. The laminar-flow characteristic for the counterflow arrangement with capacity-rate ratios other than unity, and for crossflow arrangements, probably will lie between these curves. For short tubes with constant heat input per unit of length, it is recommended in lieu of other data that either the constant wall-temperature data or the long-tube constant heat-input data be used, whichever yields the higher $N_{Re} N_{Pr}^{1/4}$ magnitude.

The laminar-flow friction-factor curves are based on the analysis of Langhaar (3), and these $f - N_{Re}$ characteristics have been shown to be supported by experiment. It should be noted that these curves are for isothermal conditions. For heating gases the friction factor may be from 5 to 15 per cent higher, and for cooling gases the friction factor may be lower to the same extent.

The transition behavior for both heat transfer and friction is based on the observed behavior of a number of multiple-tube systems. Design in this region is quite uncertain and the estimated error of ± 15 per cent indicated in Fig. 5 may be optimistic.

The turbulent-flow heat-transfer curve is based on the very good correlation obtained for a number of test cores with varying L/D . Although there is undoubtedly a small L/D effect in turbulent flow, the correction for $L/D > 25$ is less than the probable experimental discrepancy upon which the given curve is based.

The turbulent-flow friction curve is admittedly the least substantiated recommendation in Fig. 5. It is based primarily on the behavior of surface ST-1. At Reynolds numbers greater than 30,000 the curve checks very well with most accepted data for very smooth tubes, but between 10,000 and 30,000 the curve lies somewhat below the most generally accepted data. It should also be noted that the turbulent-flow friction factors for rough tubes will be higher, but for small-tube heat exchangers constructed of drawn tubes, the smooth-tube curve should apply.

The friction factors as given here are defined on the basis of mean wall shear. The entrance and exit effects, due to the contraction and free expansions associated with abrupt area changes at core entrance and exit, and the pressure changes associated with changes in velocity distribution, must be taken into consideration

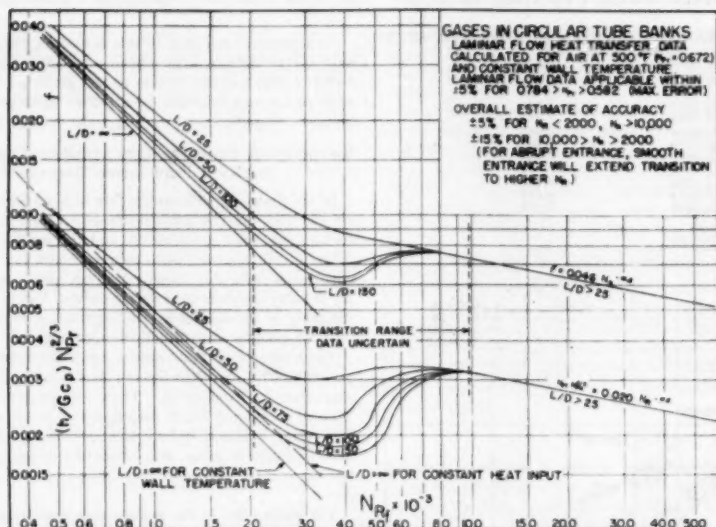


FIG. 5 RECOMMENDED HEAT-TRANSFER AND FLOW-FRICTION DESIGN CORRELATIONS FOR GAS FLOW INSIDE OF SMALL CIRCULAR TUBES

by separate entrance and exit coefficients, K_e and K_x . The entrance and exit coefficients for a multiple circular-tube system with essentially uniform velocity distribution upstream and downstream of the core are given in Fig. 6. This illustration, taken from reference (20), has been supplemented with additional curves calculated for short tubes in laminar flow, employing the K_d velocity-distribution correction factors of Table 1.

RECTANGULAR TUBE HEAT-TRANSFER AND FRICTION PERFORMANCE

The heat-transfer and flow-friction characteristics for the rectangular tube surface, 11.11(a), are shown, Fig. 2. Represented, too, are the test data for surface 19.86, a plain-plate-fin configuration, with approximately rectangular tubes, $\alpha^* = 5.5$, and $L/4r_h = 35$, reported in reference (4). Equations [1] and [2] for turbulent flow in circular cylinders also have been recommended for rectangular tubes and, consequently, these relations are given graphically for purposes of comparison. In the laminar-flow region the dashed lines for $\alpha^* = 1, 5.85$, and ∞ represent analytical predictions for long tubes. The analytically established laminar-flow friction factors were taken from reference (6) where the complete variation with aspect ratio α^* is given. The laminar-flow heat-transfer curves were taken from Norris and Streid (2) for flow between parallel planes, $\alpha^* = \infty$, and from Glaser (18) for flow through a square tube, $\alpha^* = 1.00$, both for isothermal tube-wall conditions. No analytical results are yet available for other aspect ratios. Moreover, analyses are lacking for the effect of $L/4r_h$ on the laminar-flow friction factors and heat-transfer conductances, except for flow between parallel planes, $\alpha^* = \infty$.

Surface 11.11(a) was tested primarily to determine the characteristics of a typical plain-plate-fin surface with large $L/4r_h$. The plain-plate-fin surfaces that had been tested previously and reported in reference (4) actually had interrupted fins, and the greatest ratio of uninterrupted fin length to hydraulic diameter, $L/4r_h$, was 35 for surface 19.86, as compared to 57.8 for surface 11.11(a).

Turbulent-Flow Characteristics. When the estimated experimental accuracy is taken into consideration, the agreement is

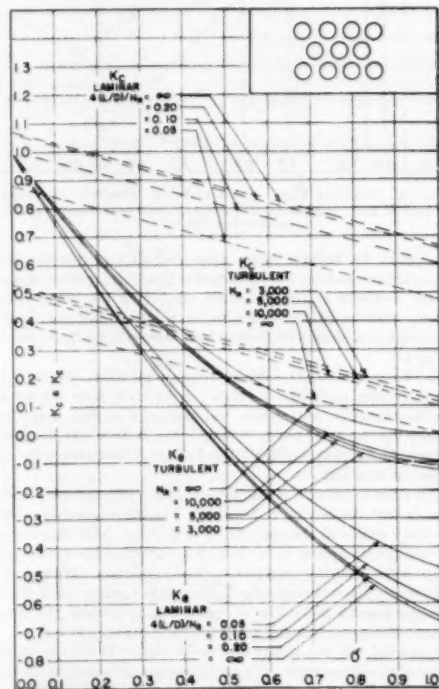


FIG. 6 FLOW CONTRACTION AND EXPANSION-LOSS COEFFICIENTS, K_e AND K_x , IN MULTIPLE CIRCULAR-TUBE SYSTEMS (Calculations from analysis of reference 20, based on idealization of uniform velocity distribution in upstream and downstream ducts. For laminar flow, calculations are based on K_d of Table 1.)

excellent between the characteristics of the 19.86 and 11.11(a) surfaces, for both heat transfer and friction, over entire Reynolds-number test range. For turbulent flow there is apparently little tube-length influence for $L/4r_s \geq 35$. A re-examination of the data in reference (4) indicates that for turbulent flow both the heat-transfer and friction characteristics for plain-plate-fin surfaces for $L/4r_s > 25$ be approximated by the following equations

$$Nu_s Nu_{Pr}^{1/4} = 0.019 Nu_s^{-0.3} \quad [8]$$

$$f = 0.050 Nu_s^{-0.3} \quad [9]$$

regardless of the magnitude of the aspect ratio. Somewhat higher friction factors may be encountered in practice since plate-fin surfaces are generally of brazed construction and excess brazing material on the fins and prime surface can produce a rough wall. However, it is important to note that the 11.11(a) and 19.86 surfaces were built by different manufacturers using different brazing methods and materials (copper and brass dip solder as compared to aluminum furnace brazing) and yet their basic heat-transfer and flow-friction characteristics are essentially similar.

It is believed that the turbulent-flow characteristics are little influenced by the aspect ratio of the rectangular flow passages, and it is also expected that the characteristics of roughly triangular and square flow passages that are sometimes employed in plain-plate-fin systems can be approximated closely by the foregoing equations. The close agreement of Equation [8] with Equation [3] for circular tubes supports these last contentions.

Laminar-Flow Characteristics. In contrast to the turbulent-flow characteristics, both the laminar-flow heat-transfer and friction characteristics for rectangular tubes are strongly dependent on aspect ratio, as shown in Fig. 2. The laminar-flow friction factors of surface 11.11(a) agree closely with the analytically evaluated friction factors for $\alpha^* = 5.85$ for a fully established laminar velocity distribution (6). The friction factors for surface 19.86 also coincide closely; which is to be expected since the aspect ratio is only slightly lower, $\alpha^* = 5.5$.

The laminar-flow heat-transfer curves for both of the test surfaces under consideration are in substantial agreement and lie between the extremes predicted analytically for $\alpha^* = \infty$ and $\alpha^* = 1.00$ for constant wall temperature. However, there is no analysis

yet available against which to compare test data between these extremes.

The slopes of both the experimental heat-transfer and friction curves, compared to the analytical curves (based on $L/4r_s = \infty$), show an $L/4r_s$ effect which is more pronounced for heat transfer than for friction. The tube-length influence is more accentuated for surface 19.86 with $L/4r_s = 35$ than for surface 11.11(a) with $L/4r_s = 58$, as expected from previous experience with circular tubes.

Transition-Flow Behavior. The most notable aspect of the transition behavior of the rectangular tube surfaces under consideration is the lack of a pronounced "dip" region as exists for circular tubes. To emphasize this contrast, in Fig. 7 the heat-transfer behavior of surfaces ST-1 and 11.11(a) are compared. There are two reasons apparent for the lack of a dip for the rectangular tube surfaces. The transition for both surfaces 11.11(a) and 19.86 tends to take place at a considerably lower Reynolds number, 1500-2000, as compared to $Nu_s > 3000$ for the circular tube surface. For rectangular passages of large aspect ratio both the friction factors and the heat-transfer unit conductances for laminar flow are much higher than for circular tubes, while the turbulent-flow characteristics are quite similar. There is thus no opportunity for a dip unless laminar flow could be made to persist to a very high Reynolds number. This argument, together with the analytical data available for laminar flow in square passages ($\alpha^* = 1$), leads to the conclusion that there should be a considerable dip for square passages, except for the case of a very early transition, $Nu_s < 800$, which is improbably low. However, there are as yet insufficient experimental data to determine how the transition point will vary with aspect ratio. The early transition for surfaces 11.11(a) and 19.86 may be due to the relatively rough walls as compared to the circular tube systems considered which had drawn tubes.

The lack of a pronounced transition dip for rectangular passages with large aspect ratio is an important consideration in heat-exchanger design. Even if the Reynolds number of transition cannot be determined, little design uncertainty is introduced because in the transition range the laminar and turbulent-flow characteristics do not differ markedly. This is in marked contrast to circular tubes where there is a large degree of uncertainty, and

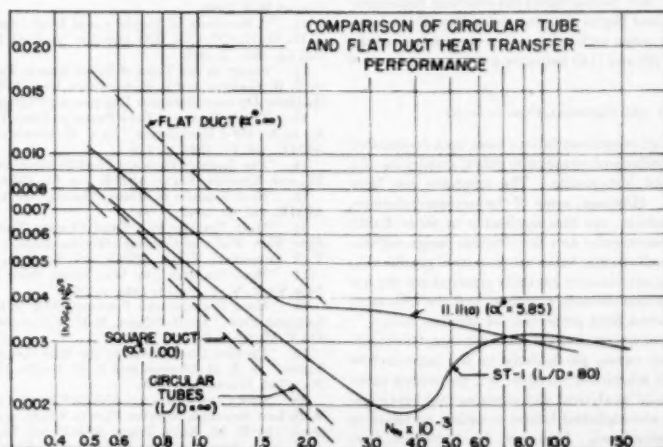


FIG. 7 TRANSITION-FLOW HEAT-TRANSFER BEHAVIOR, COMPARISON OF RECTANGULAR AND CIRCULAR TUBES

the assumption of turbulent flow at, for example, $N_R = 5000$, can introduce a design error of from 30 to 50 per cent in the heat-transfer performance of an exchanger.

CONCLUSIONS FOR RECTANGULAR TUBES

The addition of another variable, the aspect ratio, which strongly affects both the heat-transfer and friction performance in the laminar-flow region makes it impossible at this time to provide complete design recommendations for the use of rectangular tubes such as was done in Fig. 5 for circular tubes. For turbulent flow it is believed that Equations [8] and [9] are adequate within ± 5 per cent, regardless of aspect ratio, but it should be noted that these equations are based on tests at Reynolds numbers less than 12,000, so that extrapolation beyond 12,000 may be speculative.

Before adequate design recommendations for the laminar-flow region can be formulated, both analytical and experimental work must be done on the following open questions:

- (a) The variation of the heat-transfer unit conductance for large $L/4r_h$ for both constant wall temperature and constant heat input per unit of length, for all aspect ratios.
- (b) The influence of $L/4r_h$ on heat transfer for all aspect ratios, and for both constant wall temperature and constant heat input per unit of length.
- (c) The influence of $L/4r_h$ on friction factor for all aspect ratios. Tentatively, however, it is recommended that for $L/4r_h > 35$ the long-tube analytical formulations for f given by McAdams (6) may be used.
- (d) The effect of aspect ratio, if any, on the Reynolds number of transition.

In addition there are the same problems of temperature-dependent fluid properties as for circular tubes.

Until such analyses are completed, the laminar-flow characteristics of rectangular tubes for other than the approximate geometry of surfaces 11.11(a) and 19.86 can be estimated only from a rough interpolation of the results shown, Fig. 2. In this regard it should be noted that the difference between the heat-transfer conductance for constant wall temperature and constant heat input per unit of length is apparently not the same for rectangular as for circular tubes. For circular tubes the constant heat-input conductance is 19 per cent higher than for constant wall temperature. For rectangular tubes with $\alpha^* = \infty$, a comparison of the analyses of references (2) and (18) indicates a difference of only 8 per cent.

SUMMARY AND GENERAL CONCLUSIONS

Heat-exchanger design recommendations have been formulated for the use of small circular and rectangular tubes, employing as a basis recently obtained test results. The emphasis has been primarily on gas flow. However, some of the recommendations, with suitable modifications, are also applicable to other fluids. The recommended heat-transfer and flow-friction design correlations for gas flow in small circular tubes are presented graphically, Fig. 5. Questions that remain only partially resolved are the uncertain behavior in the transition-flow regime, and the treatment of temperature-dependent fluid properties for laminar flow.

There are more serious uncertainties in the heat-transfer characteristics of rectangular tubes, particularly in the laminar-flow regime, because of the additional variable, α^* , the aspect ratio. Consequently, additional analytical and experimental investigations will have to be accomplished before complete correlations for design can be formulated. However, for turbulent flow, Equations [8] and [9] may be used for $L/4r_h > 25$ irrespective of α^* ; and the formulations for the laminar flow f -characteristics,

a function of N_R and α^* , given in reference (6), also appear to be adequate providing $L/4r_h > 35$.

ACKNOWLEDGMENTS

The USN Office of Naval Research, the Bureau of Ships, and the Bureau of Aeronautics are currently sponsoring the research program on compact heat-transfer surfaces at Stanford University. The authors prepared this paper as part of this program and express their appreciation to the sponsoring organizations.

The test cores used as a basis for this work were obtained from the AiResearch Manufacturing Company, the Modine Manufacturing Company, and the Harrison Radiator Division of the General Motors Corporation. The co-operation of Mr. S. K. Andersen of AiResearch, Mr. Clyde Simpelaar of Modine, and Messrs. L. P. Saunders and J. W. Godfrey of Harrison is gratefully acknowledged.

BIBLIOGRAPHY

- 1 "Heat Transfer and Flow Friction Characteristics of Some Compact Heat-Exchanger Surfaces, Part 3—Design Data for Five Surfaces," by A. L. London, W. M. Kays, and D. W. Johnson, published in this issue of the Transactions, pp. 1167-1178.
- 2 "Laminar-Flow Heat-Transfer Coefficients for Ducts," by R. H. Norris and D. D. Streid, Trans. ASME, vol. 62, 1940, p. 525.
- 3 "Steady Flow in the Transition Length of a Straight Tube," by H. L. Langhaar, *Journal of Applied Mechanics*, Trans. ASME, vol. 64, 1942, p. A-55.
- 4 "Heat-Transfer and Flow-Friction Characteristics of Some Compact Heat-Exchanger Surfaces, Part 2—Design Data for Thirteen Surfaces," by W. M. Kays and A. L. London, Trans. ASME, vol. 72, 1950, p. 1087.
- 5 "Heat Transfer Coefficients for Air Flowing in Round Tubes, in Rectangular Ducts and Around Finned Cylinders," by R. E. Drexel and W. H. McAdams, NACA Wartime Report W-108, 1945.
- 6 "Heat Transmission," by W. H. McAdams, McGraw-Hill Book Company, Inc., New York, N. Y., 1942.
- 7 "Elementary Mechanics of Fluids," by Hunter Rouse, John Wiley & Sons, Inc., New York, N. Y., 1946.
- 8 "Heat-Transfer and Flow-Friction Characteristics of Some Compact Heat-Exchanger Surfaces, Part 1—Test System and Procedure," by W. M. Kays and A. L. London, Trans. ASME, vol. 72, 1950, p. 1075.
- 9 "Test and Predicted Oil-Cooler Performance," by A. L. London and J. I. Brewster, Trans. ASME, vol. 66, 1944, p. 73.
- 10 "An Investigation of Aircraft Heaters—Part II. Properties of Gases," by Myron Tribus and L. M. K. Boelter, NACA Wartime Report W-9, 1942.
- 11 "A Summary of Viscosity and Heat Conduction Data for He, A, H, O, N, CO, CO₂, H₂O, and Air," by F. G. Keyes, Trans. ASME, vol. 73, 1951, p. 589.
- 12 "Steam to Air Tests of Small Round Tubes With Flex Ends," by J. W. Godfrey and L. P. Saunders, Report No. RER-58, Harrison Radiator Division Research Engineering Department, April 11, 1943.
- 13 "The Influence of Tube Shape on Heat-Transfer Coefficients in Air to Air Heat Exchangers," by F. H. Green and L. S. King, Trans. ASME, vol. 68, 1946, p. 115.
- 14 "The Analogy Between Fluid Friction and Heat Transfer," by Th. von Kármán, Trans. ASME, vol. 61, 1939, p. 705.
- 15 "Heat Transfer to Molten Metals," by R. C. Martinelli, Trans. ASME, vol. 69, 1947, p. 947.
- 16 "Heat Transfer to a Fluid Flowing Turbulently in a Smooth Pipe With Walls at Constant Temperature," by R. A. Seban and T. T. Shimasaki, Trans. ASME, vol. 73, 1951, p. 803-809.
- 17 "Heat Transfer," by Max Jacob, John Wiley and Sons, Inc., New York, N. Y., vol. 1, 1949, p. 548.
- 18 "Heat Transfer and Pressure Drop in Heat Exchanges With Laminar Flow," by H. Glaser, MAP Volkenrod Ref.: MAP-VG 96-818 T, March 1, 1947.
- 19 "Friction Coefficients in the Inlet Length of Smooth Round Tubes," by A. H. Shapiro and R. D. Smith, NACA Technical Note No. 1785, November, 1948.
- 20 "Loss Coefficients for Abrupt Changes in Flow Cross Section With Low Reynolds Number Flow in Single and Multiple-Tube Systems," by W. M. Kays, Trans. ASME, vol. 72, 1950, p. 1067.
- 21 "An Investigation of Losses of Flow Stream Mechanical Energy at Abrupt Changes in Flow Cross Section in Single Tube Systems," by P. G. Bissiri, thesis for the Degree of Engineer, Depart-

ment of Mechanical Engineering, Stanford University, Stanford, Calif., September, 1949.

22 "An Investigation of Losses of Flow Stream Mechanical Energy at Abrupt Changes in Flow Cross Section," by W. M. Kays, Technical Report No. 1, Navy Contract N6-onr-251 T.O. 6, Stanford University, Stanford, Calif., September 15, 1948.

23 "Basic Heat Transfer and Flow Friction Design Data for Gas Flow in Circular and Rectangular Cylindrical Tube Heat Exchangers," by W. M. Kays, Technical Report No. 14, Navy Contract N6-onr-251 T.O. 6, Stanford University, Stanford, Calif., June, 1951.

Discussion

C. F. KAYAN.⁴ This and its companion paper (1) present results which appear to rely for homogeneity in the laminar and turbulent regions on an assumption of a characteristic dimension for the computation of the Reynolds number. This characteristic length is $4r_h$, where r_h is the hydraulic radius, as defined by the authors. Whereas they recognize lack of agreement of the heat-transfer data, primarily, for the narrow rectangular flow passages as compared with circular flow passages for which the laminar-turbulent pattern is more or less accepted, their attention is invited to the nonhomogeneity of the heat-transfer mechanism for the two types of flow, i.e., laminar versus turbulent.

With heat transfer in laminar fluid flow more directly associ-

⁴Department of Mechanical Engineering, Columbia University, New York, N. Y. Mem. ASME.

ated with conduction, it is suggested that the smallest dimension of the flow stream might be more apt to control, rather than the "hydraulic" dimension used.

The authors venture that the aspect ratio of the rectangular channels might have some effect on the Reynolds number of transition. The suggestion is made, herewith, that perhaps some other characteristic dimension than the hydraulic one used in the Reynolds number would facilitate the general correlation of the excellent data, both thermal and friction, produced in the authors' programs.

AUTHORS' CLOSURE

In reply to Professor Kayan's remarks concerning the use of a hydraulic diameter $4r_h$ it is possible that a single more suitable length dimension might be chosen to correlate laminar-flow data. The hydraulic diameter was selected in this paper for design convenience, so as to have a single type of presentation for both turbulent and laminar flow, and for the purpose of maintaining a consistent presentation of all of the design data obtained on this research project. At the present time additional work, both analytical and experimental, is being done on laminar flow in rectangular tubes, and when this is completed the possibility of a single generalized treatment of rectangular tubes will be greatly enhanced.

[Illegible text block]

[Illegible text block]

[Illegible text block]

[Illegible text block]

[Illegible text block]

[Illegible text block]

[Illegible text block]

[Illegible text block]

[Illegible text block]

[Illegible text block]

[Illegible text block]

[Illegible text block]

Variation in Heat Absorption in a Natural-Gas-Fired, Water-Cooled Steam-Boiler Furnace

By A. R. MUMFORD¹ AND R. C. COREY²

This paper covers the first comprehensive study of the distribution of heat absorption in a natural-gas-fired, water-cooled, steam-boiler furnace. The use of a fuel free of incombustible residue revealed factors in furnace performance because ash was not present to mask the influence of such factors. The tube-surface temperatures on the furnace walls were essentially constant at any given rating and excess air, and were completely reproducible. After a lapse of more than a week a check test was made, and it was found that the indicated tube-surface temperatures were within a degree or two of their previous values. The obvious conclusion is that the shape of the "flame" envelope (invisible with natural gas) was independent of load, at least with fixed burner position and at fixed mixing-vane angles. There is no reason to suppose that the flame envelope and gas path in a furnace fired with pulverized coal would not also be the same at the same rating and excess air and with fixed positions of burners and mixing devices. This factor has not been apparent on previous tests because of the masking effect of variable ash deposits on the furnace tube surfaces. The test boiler, in normal service, was used at high load factor and high capacity. The mixing vanes and flows in the burners had been adjusted properly for this load condition after extended experience. Readjustment for each test load would have been time-consuming so vane adjustment was not attempted. When isotherms were drawn on plots of the furnace walls it was strikingly apparent that the pattern was similar at all loads with eight burners and with four burners. The gradient, or space between isotherms, varied with rating but the pattern was constant. This constancy of pattern indicated that as long as burners and mixing devices were not readjusted, the hot gases would impinge on the walls at the same spots at all ratings and, therefore, that the path of gases through a furnace is determined by the burner position and the geometry of the furnace and not significantly by rating or excess air. This factor was not apparent from the results of the previous pulverized-coal-fired tests because of the masking action of ash deposits on the surface of the furnace tubes. The usual flame, as observed in coal and oil-fired furnaces, was completely invisible in this natural-gas-fired furnace. Computations of radiant transfer indicate that

about 80 per cent of the heat absorbed by the furnace was transferred by radiation. Estimates for luminous flames indicated that from 95 to 100 per cent of the heat absorbed in the furnace is transferred by radiation. In the first attempts to measure the furnace gas temperature at the burner level several impressive occurrences indicated that we were dealing with much higher temperatures than were expected. The porcelain shields, used to reduce radiation loss, shattered upon reaching the hot gases. The platinum and even the platinum-rhodium wires of the thermocouple melted. The analysis of the data indicated, by extrapolation, that temperatures of 3400 F were common within 10 ft of the burner. Such temperatures indicated effective mixing of fuel and air and very rapid combustion. Conservative estimates of heat release indicated values of 160,000 Btu per cu ft of space utilized for the completion of combustion. When the velocities of gas and air were lowered, for testing at lower loads, temperature measurements indicated that the mixing action was not as effective because the burner vanes were not readjusted to compensate for the reduced velocities. At partial loads studies of the gas temperature indicated that the impingement of the hot gases on the rear or target wall produced sufficient mixing to complete combustion at the burner level. No unburned products were found in the gas samples taken above the burner level at any load. It can be concluded, therefore, that with sufficient hot-air pressure and with a well-designed mixing burner, natural gas can be burned rapidly and completely at high heat-release rates. The temperatures of the gases leaving the furnace at constant steam load decreased with increase in excess air but the heat content of the mixture increased. The patterns of the isotherms of gas temperature at the furnace outlet vary markedly with the load. The addition of a widely spaced screen of tubes in front of the rear wall reduced the gas temperatures leaving the furnace from 50 to 100 F but also changed the pattern of isotherms so that the pattern was essentially the same at all loads. Probably the furnace-wall screen not only absorbed additional heat but also aided in the mixing action of the gases impinging on the wall and thus made the isotherms more uniform.

INTRODUCTION

THIS report covers the co-operative investigation conducted by the Louisiana Power & Light Co., the Research Department of the Combustion Engineering-Superheater, Incorporated, and the Combustion Research Section of the Bureau of Mines, U. S. Department of the Interior. The purpose of the investigation was to learn more about combustion of natural gas in boiler furnaces in view of the rapid expansion of the use of natural gas for steam generation.

The investigation was carried out on boiler 9 at the Sterlington Steam Electric Station of the Louisiana Power & Light Co. at

¹ Research Department, Combustion Engineering-Superheater, Inc., New York, N. Y. Fellow ASME.

² Supervising Engineer, Combustion Research Section, Bureau of Mines, U. S. Department of the Interior, Pittsburgh, Pa. Mem. ASME.

Contributed by the Furnace Performance Factors Research Committee and the Power, Fuels, and Heat Transfer Divisions and presented at the Annual Meeting, Atlantic City, N. J., November 25-30, 1951, of THE AMERICAN SOCIETY OF MECHANICAL ENGINEERS.

NOTE: Statements and opinions advanced in papers are to be understood as individual expressions of their authors and not those of the Society. Manuscript received at ASME Headquarters, January 3, 1952. Paper No. 51-A-147.

Sterlington, La. The methods established by the Special Research Committee on Furnace Performance Factors of the ASME were followed during this project.

Just as it was necessary to break down the over-all performance of a steam-generating unit into its components to improve the early design and economic efficiency of such units, it is necessary to break down the over-all performance of a furnace in order that any uneconomic or inefficient parts may be improved. This is the broad object of such an investigation as is described in this paper.

Accordingly, tests were made to determine the variation and distribution of heat absorption on the furnace walls and the progress of combustion in the furnace cavity at several values of load and excess air.

In addition to making available the test boiler and acting as cosponsor of the program, the Louisiana Power & Light Co. offered the mechanical-engineering students at Tulane University and at Louisiana Polytechnic Institute the rare opportunity to work on the tests as technicians and thus gain valuable experience in practical application of their engineering training. About 30 or 40 students from each institution were made available in rotation under the direction of faculty members B. T. Bogard, H. B. Richardson, and J. J. Thigpen of Louisiana Polytechnic Institute.

GENERAL

This paper covers the results of four series of tests, comprising 14 complete runs, on a natural-gas-fired boiler furnace. These tests, made at $1/4$, $1/2$, $3/4$, and full load and at low, medium, and high excess-air values, were designed to determine the relative heat absorption by the four walls and the progress of combustion, as affected by load, excess air, and burners in service.

In previous work by the Furnace Performance Factors Committee, where furnace-wall heat-absorption rates were determined from tube-surface temperature measurements, ash deposits on the wall tubes complicated the correlation of the measured tube temperatures with the over-all furnace heat absorption. The investigation of heat absorption in a gas-fired furnace eliminated ash as a variable, and the only factors influencing the heat absorption at any point in the furnace were the radiant and convective heat-transfer components of the flame body and the radiant transfer from the incandescent brickwork.

Although no flame body was directly visible, owing to the non-luminous character of the natural-gas flame, its extent could be inferred from color differences of the exposed incandescent brickwork and the variation in the tube-surface temperatures of the walls.

In measuring the surface temperature of a tube at its exposed crown, it was not the impression that the amount this temperature exceeded the saturation temperature of the cooling fluid was the temperature drop through the tube wall at all points on its exposed semicircumference. If this were the condition, then the product of the temperature drop through the wall and the conductivity of the metal and inner film would give the heat absorption per unit area, or for the entire furnace if a proper weighted average of the individual delta t were computed. However, it is well known that the distribution of heat absorption around the exposed semicircumference is affected by radiation and convection from different directions, and the measurement of the temperature at the exposed crown of the tube only will not suffice for all portions of the semicircumference of the tube. However, an "apparent" average conductivity of the metal and film can be obtained when the total heat absorption is determined from the difference between the heat input and heat leaving the furnace in the products of combustion. This apparent average conductivity or heat transferred per degree delta t will include

such factors of circumferential distribution and exposure as normally would be applied if the distribution were known. It is almost certain that the circumferential distribution will change with rating, flame body, and flame path, so the apparent conductivity of the metal and film or the heat transferred per degree delta t will not remain constant for all conditions of operation. Nevertheless, the apparent average conductivity offered a satisfactory index of local rates of heat absorption on the walls.

EQUIPMENT

The steam-generating unit investigated is an outdoor natural-gas-fired unit with a water-cooled furnace, superheater, economizer, and air heater. The unit was supplied by Combustion Engineering Co., now Combustion Engineering-Superheater, Inc. The air heater was supplied by the Air Preheater Corp. The two side walls, upper front wall, and roof have some exposed refractory tile between tubes. The lower front wall has tubes arranged in front of a heavy refractory wall in which the burners are located. These lower front tubes are bent around the burners to permit free passage of the combustion gases. The only convection evaporative surface in the unit is the screen formed from the rear-wall tubes and located in front of the superheater. The rear wall is composed of 3-in. tubes on $3\frac{1}{2}$ -in. centers with metallic sealing strips between tubes and with tile backing over the entire wall below the superheater screen.

A sectional side elevation of the unit is shown in Fig. 1. In Fig. 2 is shown the sections of the four variations in wall construction. These four types of wall construction introduced four undetermined factors to modify the observed crown temperature in determining the heat absorbed per degree delta t . The average delta t for the entire furnace is based on averages for each wall, weighted by the corresponding projected exposed areas and, therefore, the application of the average heat transferred per degree delta t to an individual wall will be in error by the difference in the undetermined individual factors and the average factor for the entire furnace. The burner is a ring burner, with air entering the furnace both outside and inside of the ring of gas jets. The inside vanes are adjustable, and the outside vanes are fixed. In all cases the inner and outer vanes on the same burner are set to cause rotation in opposite directions. The complete transparency of the flame indicates that the mixing action of the burners was rapid when operated at normal velocities or above.

The unit is designed for 975 psig, and operating conditions are 900 psig and 915 F at the superheater outlet. The unit normally operates continuously at about 380,000 lb of steam per hr, but on occasion carries loads of 410,000 to 425,000 lb of steam per hr. The eight gas burners are installed in the lower front wall in two rows of four burners each. All eight burners were utilized for runs at full and $3/4$ loads, while only the bottom row of four burners was used for the $1/2$ and $1/4$ -load runs. Because the unit is normally operated at full load and at about 100 per cent load factor, the air-directing vanes were not readjusted for best mixing action at $3/4$ and $1/4$ loads. At $1/2$ load, the same velocities existed as existed at full load, because only four instead of eight burners were used. As will be shown in the analyses later, the lower velocities existing at $3/4$ and $1/4$ loads, uncompensated for by vane adjustments, introduced evidences of less complete mixing of fuel and air at the burners, but this was corrected by the mixing action owing to impingement on the rear wall.

Seventy-one tube-surface thermocouples were installed, 20 on the front wall and roof, 18 on each side wall, and 15 on the rear wall. The thermocouples on all walls were of the welded guarding type as described by Humphreys.¹ The location and

¹ "Thermocouples for Furnace-Tube Surface Temperature Measurements," by C. G. R. Humphreys, *Combustion*, December, 1944, p. 53.

designation of thermocouples is shown in Fig. 3, which is an "unfolded" view of the furnace walls and roof. For the rear wall of the furnace, which was backed by tile to form one of the walls of the superheater chamber, it was necessary to run the thermocouple wires through the sealing strips to the back of the tubes. Stainless-steel tubing, of small diameter, was spot-welded to the back of the wall tube at intervals to constitute a conduit to carry thermocouple wires through the bottom of the superheater chamber to the outside. The backing tiles were replaced after the conduit was installed and the circuit checked. The lower front wall, with its screening tubes standing away from the refractory surface, was handled by inserting a stainless-steel tube through the refractory into the air duct supplying the burners. The thermocouple wires were passed through this

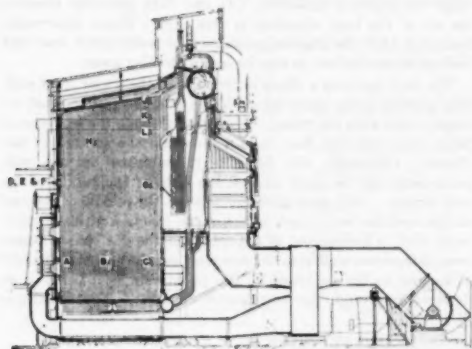


FIG. 1 SECTIONAL SIDE ELEVATION OF UNIT

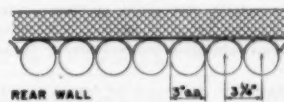
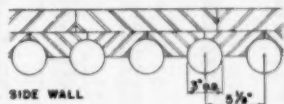
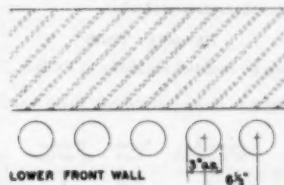
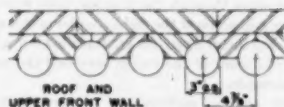


FIG. 2 TYPES OF WALL CONSTRUCTION

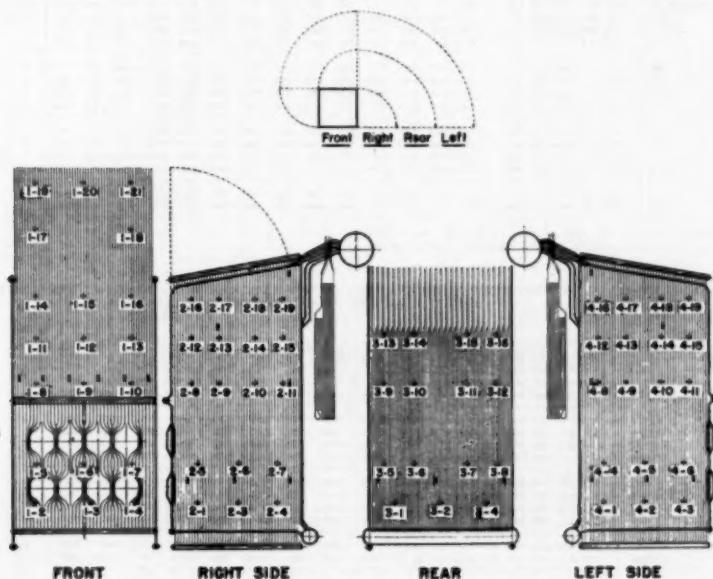


FIG. 3 LOCATION AND DESIGNATION OF WALL COUPLES

TABLE 4 AVERAGE OF OBSERVED TUBE-SURFACE TEMPERATURES BOILER, NO. 9, STERLINGTON STEAM ELECTRIC STATION, 1949

Rear Wall Position	3-1	3-2	3-3	3-4	3-5	3-6	3-7	3-8	3-9	3-10	3-11	3-12	3-13	3-14	3-15	3-16	Approx. Load
Run No. 1	596 616	-	604 630	637 650	624 597	618 610	669 597	599 595	592								Full
2	597 608	-	596 625	653 625	619 594	613 601	664 595	597 588	587								"
3	602 615	-	599 652	641 626	622 596	618 604	676 594	599 592	591								"
4	580 597	-	597 610	626 616	617 590	612 595	651 589	597 585	582								"
8	585 597	-	582 611	619 605	600 585	594 593	647 584	582 582	579								↓
9	582 596	-	582 612	618 605	600 583	583 589	651 582	581 581	579								"
10	579 590	-	577 604	611 599	595 581	589 586	639 580	580 576	575								"
14	582 594	-	579 606	612 600	595 580	587 587	639 579	576 576	572								"
5	582 595	-	599 600	615 600	600 566	561 570	608 565	549 560	559								↓
6	585 576	-	591 605	616 599	598 568	559 571	610 567	548 561	560								"
7	585 600	-	599 600	612 604	601 587	580 572	605 564	550 561	559								"
13	585 599	-	592 608	598 602	599 571	560 573	610 569	547 565	560								"
11	546 545	-	551 559	566 562	567 549	548 552	574 546	545 548	546								↓
12	546 552	-	554 560	559 567	565 552	552 557	572 550	546 552	547								"

Note: Position 3-3 used as wall identification on recorder.

TABLE 5 AVERAGE OF OBSERVED TUBE-SURFACE TEMPERATURES BOILER, NO. 9, STERLINGTON STEAM ELECTRIC STATION, 1949

Left Wall Position	4-1	4-2	4-3	4-4	4-5	4-6	4-7	4-8	4-9	4-10	4-11	4-12	4-13	4-14	4-15	4-16	4-17	4-18	4-19	Approx. Load
Run No. 1	613 590 587	-	606 599 617	594 601	586 579	581 586	580 565	573 575	561 557											Full
2	607 583 576	-	599 595 623	589 593	581 573	577 579	573 560	570 569	559 555											"
3	610 588 581	-	601 596 618	592 599	585 577	580 583	577 562	571 572	560 596											"
4	607 579 572	-	598 604 621	582 585	576 563	572 575	567 554	567 568	560 556											"
8	589 574 569	-	584 581 600	581 579	575 569	571 572	586 554	554 563	556 553											↓
9	591 573 567	-	584 580 604	580 579	573 567	570 571	565 552	562 561	554 550											"
10	584 569 565	-	580 576 591	575 573	570 563	566 566	560 550	559 558	550 547											"
14	589 570 565	-	580 578 593	574 572	567 561	564 565	560 549	559 558	550 548											"
5	595 573 568	-	585 580 584	564 559	552 545	554 553	548 542	540 548	543 541											↓
6	592 571 566	-	580 589 583	564 558	551 544	555 553	547 541	550 549	545 542											"
7	598 576 570	-	586 591 590	565 561	555 548	555 555	551 544	551 549	546 544											"
13	591 572 566	-	581 591 583	563 556	550 544	555 550	547 541	564 549	543 542											"
11	559 555 549	-	559 559 548	546 540	539 536	541 539	556 555	559 559	553 557											↓
12	560 559 555	-	557 557 551	548 543	541 539	543 540	540 538	542 542	541 539											"

Note: Position 4-4 used as wall identification on recorder.

TABLE 6 AVERAGE DIFFERENCE BETWEEN TUBE-SURFACE AND SATURATION TEMPERATURES (Δt), BOILER NO. 9, STERLINGTON STEAM ELECTRIC STATION, 1949

Front Wall and Roof Position	1-1	1-2	1-3	1-4	1-5	1-6	1-7	1-8	1-9	1-10	1-11	1-12	1-13	1-14	1-15	1-16	1-17	1-18	1-19	1-20	Approx. Load
Run No. 1	34	54	45	73	95	-	50	56	27	50	46	29	24	35	17	99	137	40	33	20	Full
2	96	50	40	63	90	-	44	39	29	29	56	27	22	33	17	92	141	38	30	67	"
3	98	53	45	67	93	-	48	35	27	35	42	27	24	35	16	97	148	40	39	67	"
4	78	46	39	57	89	-	27	26	35	23	34	25	23	34	16	89	136	35	29	61	"
8	76	42	35	60	84	-	37	26	20	25	30	22	21	28	17	74	159	35	27	54	↓
9	77	43	35	57	84	-	38	25	19	25	31	21	20	27	14	74	144	32	27	51	"
10	71	38	31	57	80	-	43	20	21	22	26	18	16	21	11	66	151	28	24	49	"
14	71	39	32	55	81	-	34	21	16	21	28	18	15	23	10	67	129	28	25	47	"
5	69	40	39	44	38	-	15	16	14	13	20	15	12	17	10	45	115	19	20	29	↓
6	72	40	37	42	36	-	13	15	12	15	20	15	11	17	10	46	105	19	22	29	"
7	71	41	40	45	39	-	17	16	15	15	19	16	13	17	11	44	99	20	21	30	"
13	74	40	36	37	38	-	15	17	15	15	22	18	11	18	12	45	107	20	26	34	"
11	55	21	14	15	20	-	6	6	4	6	8	5	5	6	3	25	61	10	12	15	↓
12	57	24	17	17	25	-	9	9	8	10	12	9	8	9	8	50	70	15	16	19	"

Note: Position 1-1 used as wall identification on recorder.
1-7 failed shortly after tests started.

TABLE 7 AVERAGE DIFFERENCE BETWEEN TUBE-SURFACE AND SATURATION TEMPERATURES (Δt), BOILER NO. 9, STERLINGTON STEAM ELECTRIC STATION, 1949

Right Wall Position	2-1	2-2	2-3	2-4	2-5	2-6	2-7	2-8	2-9	2-10	2-11	2-12	2-13	2-14	2-15	2-16	2-17	2-18	2-19	Approx. Load
Run No. 1	56	-	51	55	66	69	63	52	49	45	58	28	32	43	45	24	24	33	39	Full
2	49	-	45	60	80	64	62	29	50	40	56	27	30	40	43	24	24	30	37	"
3	58	-	50	57	70	68	63	30	45	43	56	30	29	42	45	23	24	32	37	"
4	57	-	36	46	84	47	55	30	64	37	53	23	32	38	40	21	21	29	35	"
8	41	-	39	42	58	58	50	24	38	37	48	21	27	36	38	21	21	28	33	↓
9	42	-	38	40	65	58	48	23	37	36	47	21	26	34	37	18	19	27	32	"
10	38	-	37	40	56	52	45	19	35	32	43	19	25	30	33	18	18	25	29	"
14	32	-	37	40	63	57	45	18	28	32	43	18	23	30	33	18	17	24	28	"
5	38	-	42	45	44	50	44	14	25	23	31	14	18	20	23	14	15	18	20	↓
6	41	-	41	46	50	51	44	13	24	21	34	13	18	21	25	14	15	19	21	"
7	42	-	41	47	47	49	44	16	28	24	33	14	19	22	24	14	14	19	21	"
13	44	-	43	49	55	56	50	15	23	27	38	15	20	27	29	17	17	21	25	"
11	15	-	14	11	13	22	18	4	8	8	16	4	8	9	11	7	7	9	11	↓
12	18	-	18	14	16	26	20	7	10	12	19	9	10	13	17	10	10	13	14	"

Note: Position 2-2 used as wall identification on recorder.

TABLE 8 AVERAGE DIFFERENCE BETWEEN TUBE-SURFACE AND SATURATION TEMPERATURES (40), BOILER NO. 9, STERLINGTON STEAM ELECTRIC STATION, 1949

Rear wall		Position																Approx.
Run No. 1		5-1	5-2	5-3	5-4	5-5	5-6	5-7	5-8	5-9	5-10	5-11	5-12	5-13	5-14	5-15	5-16	Load
	0	65	81	-	69	95	102	95	89	62	85	75	134	62	64	58	57	Full
	2	62	73	-	61	90	98	88	84	59	78	68	129	58	62	55	52	"
	3	67	80	-	64	97	106	91	87	61	83	69	141	59	64	57	56	"
	4	45	62	-	62	78	91	81	82	55	77	60	116	54	62	48	47	"
	5	50	64	-	49	78	86	72	67	52	61	60	114	51	49	49	46	"
	6	49	65	-	49	79	85	72	67	50	60	62	118	49	48	48	46	"
	10	46	57	-	44	71	78	66	60	49	56	55	106	47	47	43	40	"
	14	49	61	-	46	73	79	67	60	47	54	54	106	46	43	43	39	"
	5	51	62	-	68	69	84	69	69	35	50	59	77	52	18	29	28	"
	6	52	65	-	60	74	85	68	67	37	28	40	79	36	17	30	29	"
	7	51	66	-	67	68	80	72	69	35	28	40	73	32	18	29	27	"
	15	54	68	-	61	77	67	71	68	40	29	42	79	36	16	52	29	"
	11	15	12	-	20	26	55	31	36	18	17	21	45	17	12	17	15	"
	12	15	21	-	23	29	28	36	34	21	21	26	41	19	15	21	16	"

Note: Position 5-3 used as wall identification on recorder.

TABLE 9 AVERAGE DIFFERENCE BETWEEN TUBE-SURFACE AND SATURATION TEMPERATURES (50), BOILER NO. 9, STERLINGTON STEAM ELECTRIC STATION, 1949

Left Wall	Position	6-1	6-2	6-3	6-4	6-5	6-6	6-7	6-8	6-9	6-10	6-11	6-12	6-13	6-14	6-15	6-16	6-17	6-18	6-19	Approx. Load
Run No.		7	55	42	-	71	64	82	59	66	51	44	46	51	45	38	40	38	40	38	Full
2	72	48	41	-	64	60	88	54	58	46	58	42	44	58	25	35	34	24	20	"	"
3	75	53	46	-	66	61	83	57	64	48	42	45	48	42	27	36	37	25	21	"	"
4	72	44	37	-	61	69	86	47	50	41	28	37	40	52	19	32	31	25	21	"	"
5	56	41	36	-	51	46	67	48	46	42	36	58	39	33	21	31	30	23	20	"	"
6	58	40	34	-	51	47	71	47	46	40	34	57	38	32	19	29	28	21	17	"	"
10	51	36	32	-	47	45	58	42	40	37	30	33	33	27	17	26	25	17	14	"	"
14	56	37	32	-	47	45	60	41	39	34	28	51	32	27	16	26	25	17	15	"	"
5	64	42	37	-	54	59	53	33	28	21	14	23	22	17	11	18	17	12	10	"	"
6	61	40	36	-	49	58	52	33	27	20	13	24	22	16	10	19	18	11	11	"	"
7	66	44	38	-	54	59	58	33	29	23	16	23	23	19	12	19	17	14	12	"	"
13	60	41	35	-	50	60	52	32	25	19	13	24	19	18	10	19	18	14	11	"	"
11	28	24	18	-	28	28	17	15	9	8	5	10	8	5	4	8	8	6	6	"	"
12	29	28	24	-	26	26	20	17	12	10	8	12	9	9	7	11	11	10	8	"	"

Note: Position 6-4 used as wall identification on recorder.

between left and right in the figure may be caused by differences in burner flows and adjustment. Some evidence will be shown later that it also may be partly due to nonuniform cooling by heat absorption on the rear wall.

The right wall shows a pattern of isotherms, indicating that the delta t decreases toward the junction of the upper front wall and roof. There is evidence that with increase in excess air the tendency to impinge on the side wall at the burner level and near the burners increases. This tendency is evidenced at all loads. There is some tendency, at the low loads, for the isotherms to bend back toward the front wall at the top of the side walls. There is, however, no indication of impingement at the upper levels of the side walls even though the roof impingement is great near this wall, and we conclude that the hot gases are not directed to the hot spot on the roof by the right side wall.

The rear wall is the target wall, and its pattern of isotherms indicates two areas of impingement. The one between the burner levels is normally the less pronounced, but on runs 5 and 6, during which only the lower row of burners was in operation, it is the more pronounced. The second area is above the burner level at the right of the rear wall in the figure. The evidence of heavy impingement is quite clear and may, because of the cooling action, cause the unbalance from left to right shown on the roof section. This suggests that the principal cause of unbalance lay in the uneven distribution at the burners. At the top of each plot of isotherms is shown the unfolding diagram and a glance at this shows that this second area is in the right position to influence the cooling of the gases and cause the unbalance at the area of impingement on the roof. The obvious explanation for the impingement areas on the rear wall is in the amount of flow and direction of firing of some of the burners. Excess air has the same general effect as with the other walls. The top of the rear wall is the area showing the lowest delta t on the wall. It is

quite evident, therefore, that the gas stream has receded from the rear wall and moved toward the front of the furnace in order to make the turn into the superheater chamber in an arc with the longest possible radius.

The left side wall shows an isotherm pattern very similar to that of the right wall, but there is evidence of considerably more impingement on the left wall. In only one case (run 13) did the average delta t for the right wall exceed that for the left.

The uniformity of the pattern of the isotherms is rather conclusive evidence that the gas stream flowing through this furnace follows the same path at all ratings and at all excess-air values. Differences in gas volume (rating) do not appear to change the path but only the gradient or intensity of the wall temperatures at points of contact. It is evident that with this method of firing the entire furnace is not filled with the main body of swiftly moving hot gases. The uniformity of pattern also is conclusive evidence that any lack of uniformity of flow and adjustment in the individual burners produces differences which persist at all ratings in this method of firing which does not involve direct impingement of one flame upon another. It is practically impossible to carry such investigations as these to a point of incontrovertible proof, so it is common practice to formulate conclusions based on such evidence as develops. Such a conclusion is that the geometry of each furnace, including the location of the fuel-feeding devices and the post-furnace path available, sets the shape and path of the gas stream within the furnace at all normal ratings. The evidence herewith is fairly conclusive, but in furnaces utilizing fuels which produce deposits on walls, the evidence is not so clear. Deposits change the isotherm gradients and thus conceal the evidence, but this in itself is not evidence that the flame shape and path have changed in such a furnace.

Average of Indicated Delta t . The average delta t for any wall or the whole furnace may be obtained by arithmetic averages of

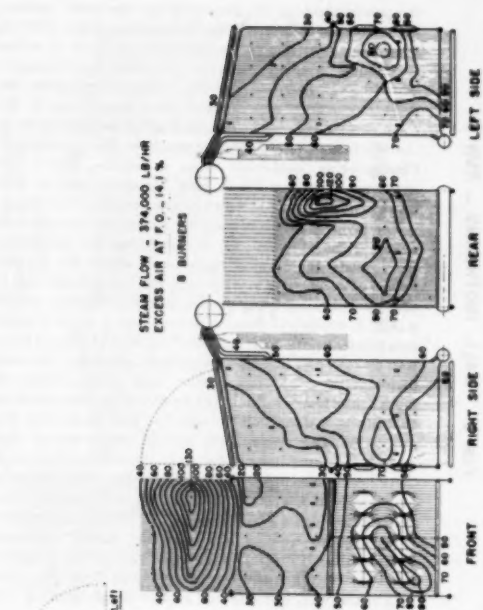


FIG. 4 WALL ISOTHERMS - RUN 1

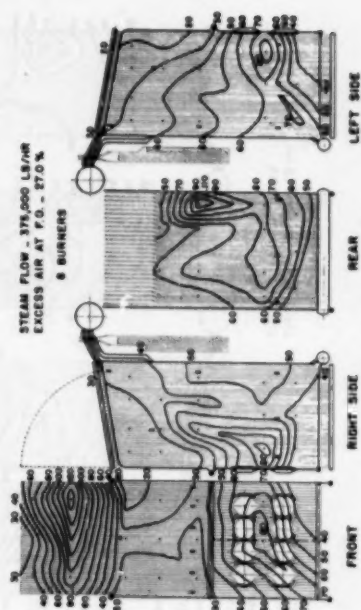


FIG. 5 WALL ISOTHERMS - RUN 2

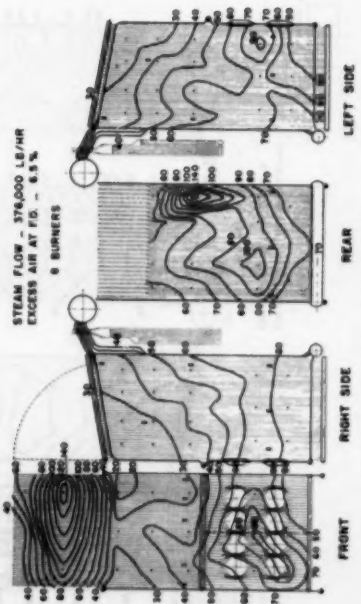


FIG. 6 WALL ISOTHERMS - RUN 3

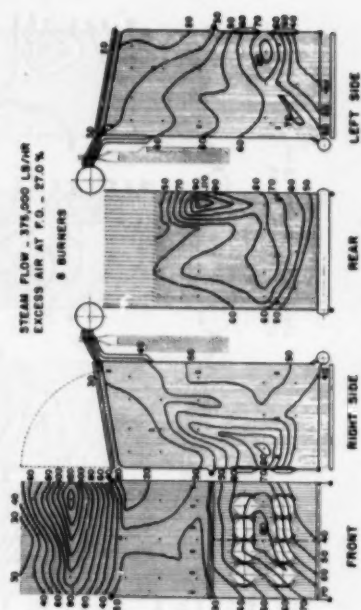
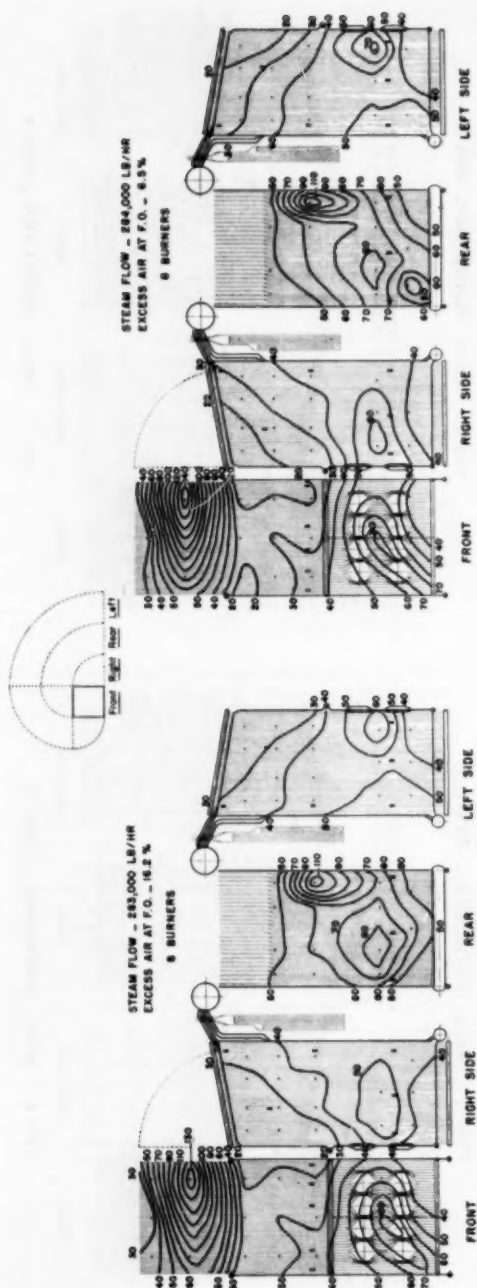


FIG. 7 WALL ISOTHERMS - RUN 4





the point values, or by planimetry the areas between the isotherms, thus weighting the average values with an area factor. Arithmetic averaging is easy but it makes no attempt to compensate for differences in areas represented by the points. For the tests at Sterlington, the measuring points were located after observation of the color of exposed brickwork and after consideration of the erection of scaffolding necessary for the installation. Planimetry of isothermic areas is tedious, but if the isotherms have been drawn with reasonable care, it does introduce an area factor which results in weighted averages.

The average values of Δt for each wall are given in Table 10 as obtained by planimetry of the isotherms. In all cases the rear or target wall shows the highest values of Δt . As tabulated, the lower front wall is next, probably reflecting the construction which, as shown in Fig. 2, consists of furnace tubes about 3 in. in front of incandescent refractory. If the data from the upper front wall and the roof had been considered separately, the roof undoubtedly would have shown high average values of Δt , but because the upper front wall is constructed so that its tubes continue to form the roof tubes, this was not done. The upper front wall is comparatively cool and by including it with the roof, the average values of Δt rank third in order among the walls. The side walls average about the same with the left wall running a degree or two higher except on test 13. Burner adjustment is believed to have caused somewhat greater impingement on the left wall. The last column shows the weighted averages for the entire furnace obtained from the products of the wall averages and factors proportional to the water-cooled area of each wall.

Table 11 compares averages obtained arithmetically and by planimetry. The differences are not consistent as to magnitude nor direction. The areas included between isotherms, of constant interval distance, vary with the difference in temperature between adjacent points and with the judgment of the draftsman.

Our conclusion is that planimetry is warranted when the distribution of measuring points is not uniform and when large differences in temperature exist between adjacent points.

Analysis and Interpretation of Wall-Temperature Data. The absence of solid particles of ash or slow-burning heavy hydrocarbons makes a natural-gas-fired furnace free from effects which, with other fuels, mask the influence of the flame path and relative area of the flame envelope. Increase in excess air lowers the theoretical flame temperature but increases the convective transfer by increasing velocities. The indications are, however, that the increase in convective transfer does not compensate for the lowered radiation transfer as is shown in Fig. 18. In Fig. 18 the furnace average Δt is plotted against rating for three groups of excess air. Although the correlation is not as good as desired, the relative positions on the curves encourage the conclusion that the lowering of the combustion temperature through raising the excess air effects a net reduction of average heat absorption in the furnace.

In Fig. 19 is plotted the furnace average Δt at four loads against the excess air in the gases leaving the furnace. The furnace average Δt decreases with increasing excess air at both full and $3/4$ loads and at approximately the same rate. However, the $1/2$ -load runs (with only the bottom row of four burners in use) show a rising tendency of furnace average Δt with increased excess

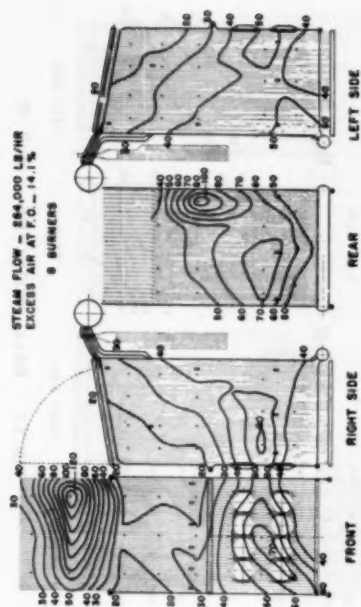


FIG. 11 WALL ISOTHERMS - RUN 14

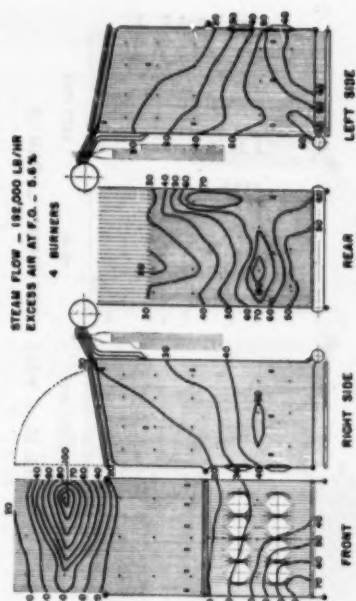


FIG. 13 WALL ISOTHERMS - RUN 6

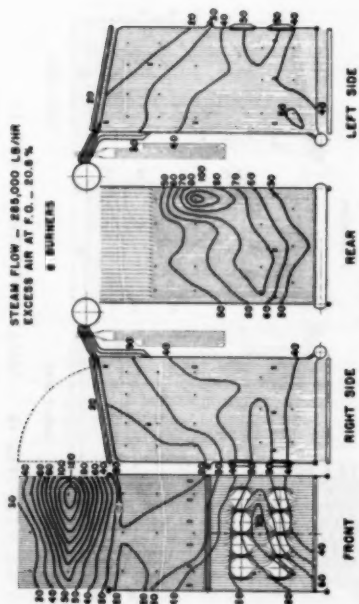


FIG. 10 WALL ISOTHERMS - RUN 10

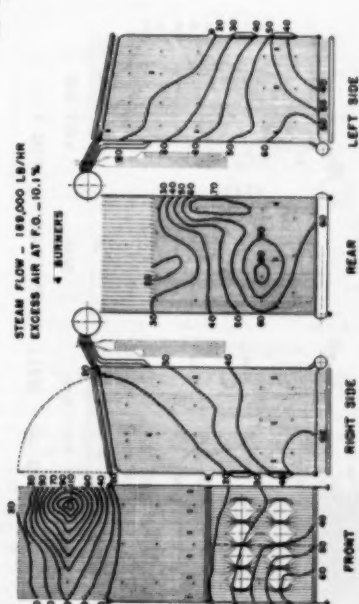


FIG. 12 WALL ISOTHERMS - RUN 5



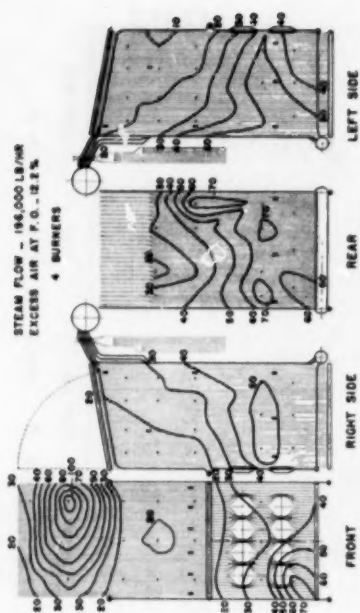


FIG. 15 WALL ISOTHERMS - RUN 13

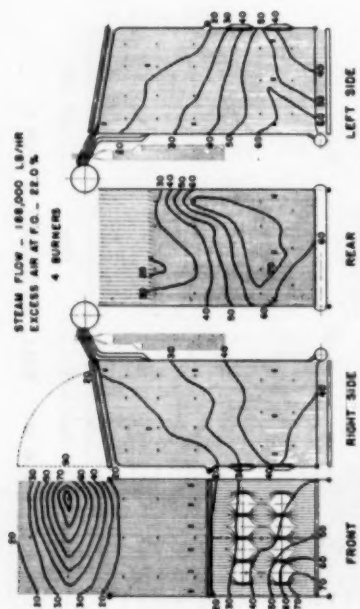


FIG. 14 WALL ISOTHERMS - RUN 7

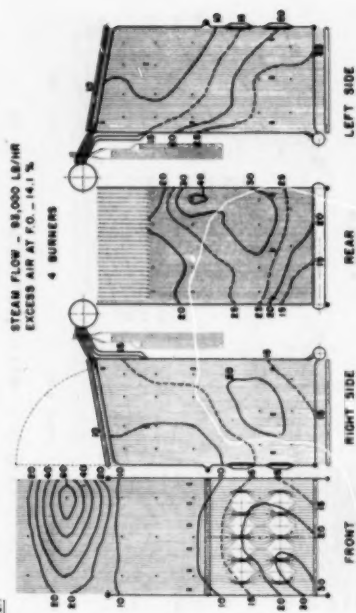


FIG. 17 WALL ISOTHERMS - RUN 12

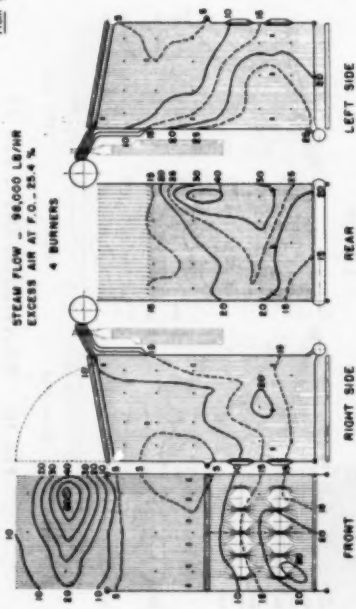


FIG. 16 WALL ISOTHERMS - RUN 11

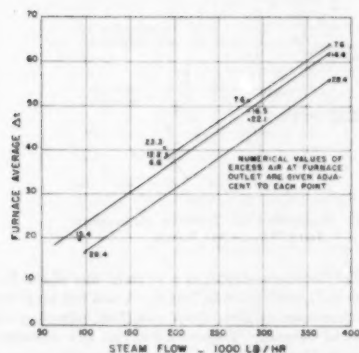


TABLE 10 AVERAGE BY WALLS OF DIFFERENCE BETWEEN TUBE-SURFACE AND SATURATION TEMPERATURES (Δt), AVERAGES DETERMINED BY PLANIMETERING ISOTHERMAL AREAS, BOILER NO. 9, STERLINGTON STEAM ELECTRIC STATION, 1949

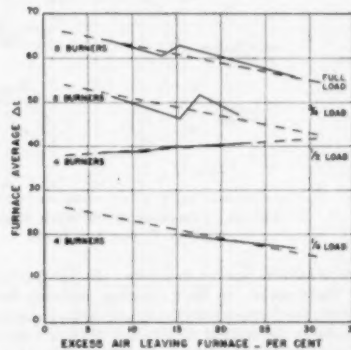
Run No.	Approx. Load	Lower Front	Upper Front And Roof	Right	Rear	Left	Furnace Ave. (Weighted by Exposed Areas)
1	Full	60.3	53.7	46.7	76.2	49.7	60.5
2	"	58.0	57.1	47.9	80.1	54.0	62.8
3	"	64.0	56.6	47.8	80.9	52.3	63.8
4	"	58.8	49.9	43.2	68.0	45.4	55.7
8	$\frac{1}{2}$	52.2	46.8	38.3	65.5	41.9	51.7
9	"	53.8	46.2	37.5	64.5	40.0	51.2
10	"	50.0	41.9	34.1	60.0	35.6	47.1
14	"	48.3	40.3	34.7	58.6	36.3	46.3
5	$\frac{1}{4}$	37.9	30.8	25.5	53.0	33.6	39.9
6	"	35.6	29.8	31.3	51.8	32.5	38.6
7	"	39.5	31.1	30.5	54.8	34.6	40.7
13	"	34.2	33.9	33.7	52.0	32.6	39.5
11	$\frac{1}{4}$	16.5	14.8	11.1	22.2	15.5	16.7
12	"	19.7	18.4	14.5	24.9	16.1	19.6

TABLE 11 COMPARISON OF ARITHMETIC AND PLANIMETER AVERAGES BY WALLS OF DIFFERENCE BETWEEN TUBE-SURFACE AND SATURATION TEMPERATURES (Δt), BOILER NO. 9, STERLINGTON STEAM ELECTRIC STATION, 1949

Run No.	Ave.	1	2	3	4	8	9	10	14	5	6	7	13	11	12
Ler. Fr.	Plan	60.3	58.0	64.0	58.8	92.2	53.8	50.0	48.3	37.9	35.6	39.5	34.2	16.5	19.7
	Arith.	72.2	67.8	71.2	61.8	90.4	59.2	55.4	55.6	46.0	45.4	47.2	45.0	20.2	24.0
Uppr. Fr.	Plan	53.7	57.1	56.6	49.9	46.8	46.2	41.9	40.3	30.8	29.8	31.1	33.9	14.8	18.4
	Arith.	48.9	45.0	48.6	42.2	39.8	39.0	35.4	34.5	25.5	24.8	25.2	26.8	12.3	16.7
Right	Plan	46.7	47.9	47.8	43.2	38.3	37.5	34.1	34.7	25.5	31.3	30.5	33.7	11.1	14.5
	Arith.	45.1	45.9	44.6	40.4	36.7	36.0	32.9	32.4	27.6	28.4	28.6	21.7	10.7	14.2
Rear	Plan	76.2	80.1	80.9	68.0	65.5	64.5	60.0	58.6	53.0	51.8	54.8	52.0	22.2	24.9
	Arith.	79.3	74.2	78.8	67.8	65.2	65.0	57.8	57.8	50.7	49.6	50.5	51.4	22.8	24.4
Left	Plan	49.7	54.0	52.3	45.4	41.9	40.0	35.6	36.3	33.6	32.5	34.6	32.6	15.5	16.1
	Arith.	50.8	46.2	48.7	42.9	39.2	38.3	33.8	33.7	29.7	29.0	31.1	28.8	13.2	15.4
Approx. Furn. Ave.	Full Load	60.5	62.8	63.8	55.7	51.7	51.2	47.1	46.3	38.9	38.6	40.7	39.5	16.7	19.6
	Arith.	62.6	58.6	61.8	53.8	50.5	49.8	45.6	45.4	38.3	37.8	38.7	39.1	16.0	19.9

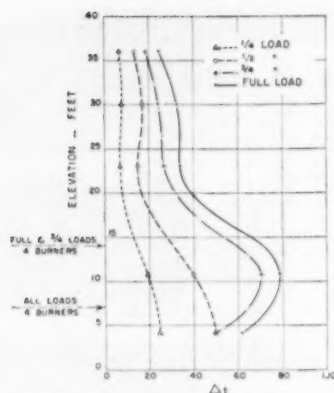
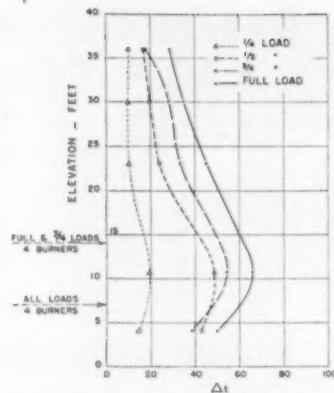
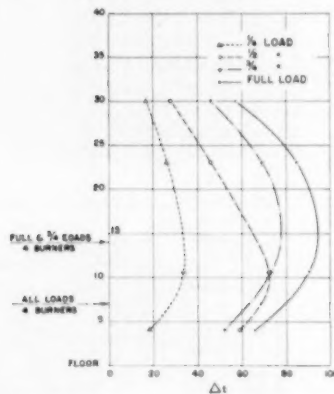
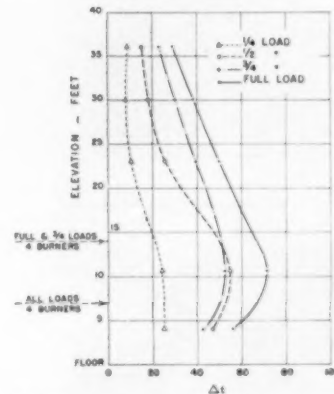
FIG. 18 VARIATION OF FURNACE AVERAGE Δt WITH RATING

air. These $\frac{1}{8}$ -load runs show a better correlation than the other series, so the evidence must be accepted. The explanation is probably that the increase in convective transfer, due to the longer path of gases when using four burners, exceeds the decrease of radiant transfer. Although a line parallel to the full and $\frac{1}{2}$ -load lines has been drawn through the two $\frac{1}{4}$ -load points, it is uncertain that this is correct because only two points were determined. No very low excess air were possible at this rating because the forced-draft-fan dampers, already closed at 15 per cent excess air, could not be made tight enough to control a lower air supply. However, a difference exists between four and eight-burner operation, probably explained by the difference in length of flame path. On the preceding chart, Fig. 18, the points for $\frac{1}{2}$ load are all above the lines drawn.

FIG. 19 VARIATION OF FURNACE AVERAGE Δt WITH EXCESS AIR LEAVING FURNACE

Lines of two slopes could have been drawn indicating a steeper slope for four-burner operation than for eight-burner operation, and this might be more logical. The lack of a full range of excess-air values at the $\frac{1}{4}$ -load series still leaves an uncertainty. However, there is good evidence that the increase in rating increases the convective component of the heat transfer and it is possible that with four-burner operation it will increase faster than with eight-burner operation because of the longer flame path.

Fig. 20 shows the vertical distribution of Δt on the front wall for each of the four loads. The parallelism of the full and $\frac{1}{2}$ -load curves shows that about the same drop in Δt existed at all elevations above the furnace floor with this change in load. These two curves also bulge to the right between burner-row elevations. For the $\frac{1}{4}$ and $\frac{1}{8}$ loads, no bulge exists because the

FIG. 20 VARIATION OF Δt WITH ELEVATION FRONT WALL—ALL LOADSFIG. 21 VARIATION OF Δt WITH ELEVATION RIGHT WALL—ALL LOADSFIG. 22 VARIATION OF Δt WITH ELEVATION REAR WALL—ALL LOADSFIG. 23 VARIATION OF Δt WITH ELEVATION LEFT WALL—ALL LOADS

upper row of burners was not in service. Except for the indication of a slight rise at the 30-ft elevation, probably due to gas impingement, the decrease from the 4-ft elevation is continuous.

Fig. 21 shows the vertical distribution of delta t on the right side wall for each of the four loads. At full load, above the bulge between burner elevations, the decrease in delta t with increase in elevation is almost a straight line. At $1/4$ -load, there was practically no change in delta t from the 23-ft elevation up. In no case is a rise in delta t indicated at the top elevation near the junction with the furnace roof. At $1/4$ load, the delta t at the 4-ft elevation is lower than that at the $1/2$ -load point, probably because the burner velocities were higher at $1/4$ load through the lower row of four burners than at $1/2$ load. Apparently the impingement at $1/4$ load was somewhat greater at the 10.5-ft elevation than at $1/2$ load, as indicated by the higher delta t . Except for the falling off of the $1/2$ -load delta t at the 36-ft elevation, the variation of delta t with load is as expected.

Fig. 22 shows the vertical distribution of delta t on the rear wall for each of the four loads. The shape of the curves reflects the differences caused by rating, by operation of one or two rows of burners, and by velocities through the burners. In general,

the delta t decreases almost as a straight line above the 10.5-ft elevation at $1/4$ and $1/2$ loads, but at $3/4$ and full loads the curves reach a maximum at about 15-ft elevation, reflecting the use of two rows of burners. The delta t at the 4-ft elevation for $1/2$ load exceeds that for $3/4$ load, reflecting the more intense mixing action of the velocities through the burners. Apparently, since the velocities through the bottom row of burners were the same at $1/4$ and at full loads, the small difference in delta t reflects the slower upward turning (or longer turning radius) of the gas stream from eight burners as compared with four. The peaks reached at elevation 15 ft at $3/4$ and full loads reflect the target character of the rear wall and the wiping action of convective transfer caused by the changing direction of the main gas stream.

Fig. 23 shows the vertical distribution of delta t on the left wall for each of the four loads. Apparently burner adjustment was such that there was greater impingement on this wall than on the right wall at the burner levels. The more complete mixing of fuel and air at the burners is evidenced by the higher delta t at $1/2$ load than at $3/4$ at both the 4-ft elevation and the 10.5-ft. The delta t at $1/4$ and full loads decreases in a straight line with

increase in elevation above the 10.5-ft point, even though burners were in service at the 4-ft elevation. It must be assumed, therefore, that the convective transfer due to impingement was greater for the bottom row than for the top row or that measurement at an elevation of 15 ft would have shown a peak. At the 23-ft elevation and above, the Δt are in the relation to be expected at the respective rating.

The four preceding charts, Figs. 20 to 23, inclusive, show that the heat transfer at any rating decreases more or less uniformly with distance above the burners. In addition, the convective component increases the heat transfer where impingement is to be expected. This latter factor is most pronounced, of course, on the rear wall.

Fig. 24 shows the vertical distribution of Δt at full load for each of the four walls. The rear wall, with the greatest impact of gas, has the highest indicated heat-transfer rate at all elevations.

The lower front wall is next in magnitude of Δt , but the upper front wall is the lowest of the four. It is apparent that the gas radiation from the very high-temperature flame near the lower front wall is not as great as the sum of the gas radiation and con-

vective heat transfer to the rear wall from the lower temperature gases reaching it.

The two side walls show the same variation with elevation but the left has higher Δt at all elevations, probably indicating greater impingement. All three walls are close at the 36-ft elevation and an extrapolation of the rear-wall curve would bring it into the same group.

Fig. 25 shows the vertical distribution of Δt at $3/4$ load for each of the four walls. The rear and lower front walls are very closely the same at the 4-ft and 10.5-ft elevations. As at full load the upper front wall shows the lowest Δt of the four walls. Again the left wall shows a generally higher Δt than the right except at the 10.5-ft elevation where the difference is small, and at the top where no difference is indicated.

Fig. 26 shows the vertical distribution of Δt at $1/2$ load for each of the four walls. At this load the effect of using only the bottom row of burners is evident. The rear wall still shows the highest Δt at all elevations, but the absence of the top row of burners explains the more rapid fall-off between 10.5-ft and 23-ft elevations. The side-wall curves show that the left wall falls below the right at the upper two elevations perhaps because the

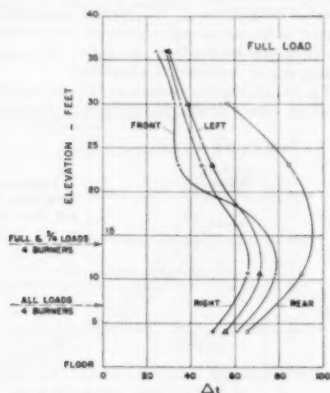


FIG. 24 VARIATION OF Δt WITH ELEVATION ALL WALLS—FULL LOAD

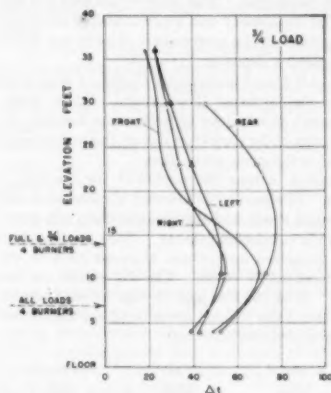


FIG. 25 VARIATION OF Δt WITH ELEVATION ALL WALLS— $3/4$ LOAD

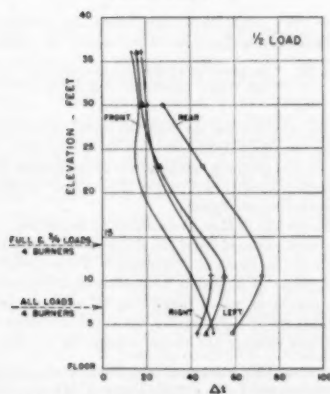


FIG. 26 VARIATION OF Δt WITH ELEVATION ALL WALLS— $1/2$ LOAD

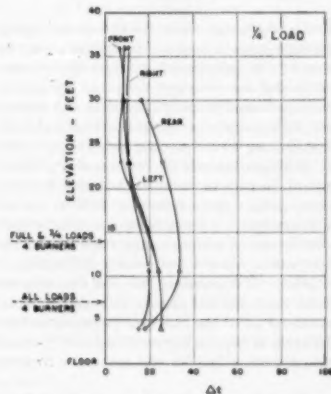


FIG. 27 VARIATION OF Δt WITH ELEVATION ALL WALLS— $1/4$ LOAD

gases were cooled more by convection on the left wall at the lower levels. Front-wall delta t is above side-wall delta t only at the lowest elevation.

Fig. 27 shows the vertical distribution of delta t at $1/4$ load for each of the four walls. The two side walls and the front wall are close together at all elevations. The rear wall again shows the highest delta t of the four walls but the minimum variation. Since furnace-gas velocities are lower at this rating, impingement on the lower rear wall is less, and gas radiation, accounting for the greater fraction of total heat transfer, produces more uniform delta t .

Figs. 24 to 27, inclusive, show consistently that the distribution of delta t varies among the walls rather widely. Convective transfer resulting from flame impingement is the probable cause of this variation. Obviously, more effective utilization of the convective component would increase the total heat absorption, and this can be achieved by appropriate design.

Application of the surface-temperature method of determining the distribution of heat absorption to a natural gas-fired furnace has demonstrated a consistency in pattern and distribution and a reproducibility that could not be determined when coal ash was present to mask the indications. The authors feel that the evidence of fundamental consistency and reproducibility presented will be of aid in the study of the performance of solid and liquid fuels that produce masking deposits.

Variation of Over-All Heat-Transmission Coefficient With Wall Thickness and Film Conductance. The amount of heat transmitted through the wall of a furnace or boiler tube depends not only on the conductivity of the metal but also on the transmission coefficient of the film on the inside of the tube.

The usual assumption is that the coefficient for the film is reasonably constant. Obviously, the velocity of circulation will vary with the output of steam and the film thickness will be affected somewhat by the circulation velocity. The rate of rupture of the film by the formation and release of steam bubbles will also vary with the output of steam. The differences are not marked in this unit. Both the film and the over-all conductance are fairly constant above the $1/4$ -load series based on the net absorption in the furnace, as in the following:

Load	U metal	U film	U over-all
Full	1560	3309	1057
$3/4$	1560	3544	1075
$1/2$	1560	3029	1026
$1/4$	1560	5665	1176

Assuming that the film conductance does not change materially at constant load, the differences in over-all conductance may be attributed to differences in the relationship between the average delta t around the tube and the measured delta t at the crown. The differences in excess air would produce differences in temperature and consequently, differences in radiant transfer; and the different volume of gases flowing would produce a difference in the convective transfer. For these reasons the relation of the delta t measured at the crown of the tube to the average around the tube at the same elevation can be expected to vary with excess air when the boiler load is constant. Although the film conductance also will vary with distribution of surface temperature around the tube, the difference is probably slight because the differences in distribution are not great. If we assume that the film conductance at constant boiler load does not change with change in excess air and if we attribute all of the observed variation in heat transmission to differences in the circumferential distribution of heat, we can compute a delta t that we can assume to be more representative.

Such computations have been made and the results indicate that an increase in excess air does increase the average delta t

relative to the crown delta t almost uniformly at full load but to a decreasing extent as the load is decreased. Obviously, the flame volume decreased with load, and we would expect a decreasing effect of excess air on surface-temperature distribution at such lower loads. Some measurements of the temperature distribution around the exposed semicircumference of wall tubes in a coal-fired furnace have been reported by Mumford and Powell.⁴ These measurements show the effect of flame direction as well as the influence of the coal ash.

The following conclusions regarding the over-all conductance through the tube are offered for consideration:

- 1 That changes in over-all conductance with change in boiler load are due to changes in the conductance of the internal film.
- 2 That changes in over-all conductance with change in excess air at constant boiler load are due to changes in the distribution of temperature around the surface of the tube which changes the relation of the measured crown temperature to the average.

These conclusions are offered as an explanation of observed variations of the over-all U and are not intended as a criticism of the method used by the Research Committee on Furnace Performance Factors. Obviously, the assumption that the circumferential distribution of tube-surface temperature is constant is implied in the use of only the crown temperature. Fortunately, the variations are not large, so that at this stage of the work the assumption of constancy is acceptable.

Fig. 28 indicates the variation of U_0 with wall thickness at three constant values of film conductance. The relative importance

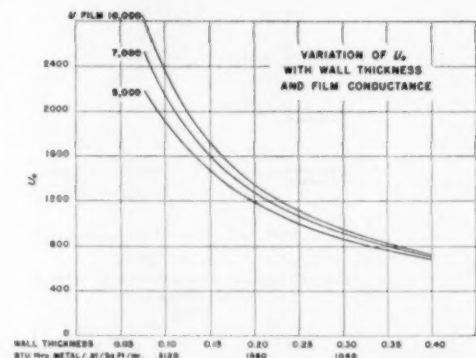


FIG. 28 VARIATION OF OVER-ALL COEFFICIENT OF HEAT TRANSFER WITH WALL THICKNESS AND FILM CONDUCTANCE

of the conductance through the metal obviously is much greater than the conductance through the inside film. With thick-wall tubes, the resulting temperature drop through the inside film is a relatively insignificant part of the over-all temperature drop under evaporating conditions.

Proportion of Heat Transmitted by Radiation. Computations of the heat radiated from the flame have been made in accordance with the methods of McAdams.⁵ From sketches of flame path and shape as indicated by furnace-wall temperatures and flame temperatures, mean beam lengths were computed for the two conditions of eight-burner operation and four-burner operation without refining the flame volume for $3/4$ and $1/4$ loads. The

⁴ "Heat-Flux Pattern in Fin Tubes Under Radiation," by A. R. Mumford and E. M. Powell, Trans. ASME, vol. 67, 1945, p. 693.

⁵ "Heat Transmission," by W. H. McAdams, second edition, McGraw-Hill Book Company, Inc., New York, N. Y., 1942.

values obtained were 18.9 ft for eight-burner operation and 13.8 ft for four-burner operation. Partial pressures of water vapor and carbon dioxide were computed from the fuel analysis and from the analyses of gas leaving the furnace. Averages of gas temperatures measured along the gas path were assumed to be the averages for the furnace. Wall temperatures were computed from the measured tube-surface temperatures and estimated refractory temperatures.

Fig. 29 shows the relation between average net heat absorption in the furnace and average transmitted by radiation, as computed for each of the four load points. The proportion of the heat absorbed transmitted by radiation is essentially constant at a value of 80 per cent of the total. With luminous flames, such as pulverized-coal flames, the amount transmitted by radiation has been estimated as 95 per cent of the total furnace absorption. Apparently the presence of radiating solids in pulverized-coal flames increases the radiant transmission over that of transparent natural-gas flames.

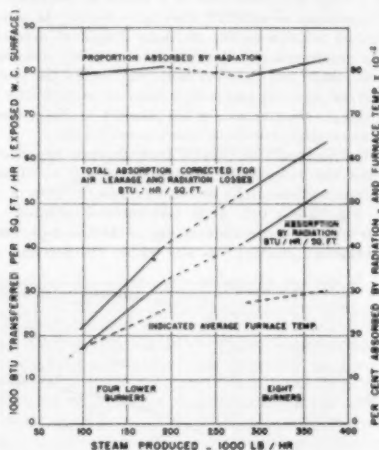


Fig. 29 PROPORTION OF HEAT ABSORBED BY RADIATION

Summary of Analysis of Wall-Temperature Data. The uniformity of the pattern of the isotherms on the wall diagrams is rather conclusive evidence that the gas stream flowing through the Sterlington furnace follows the same path at all ratings and at all excess-air values. Differences in rating do not appear to change the gas path but only the gradient or intensity of the wall temperatures at points of contact owing to mass-velocity changes. It is evident that with this method of firing the entire furnace is not filled with the main body of swiftly moving hot gases. It is further evident, therefore, that the shape of the gas stream is controlled by distribution at the inlet (burners) and by the available area and path even beyond the outlet, at least in the gas-volume range covered by these investigations. The uniformity of pattern also is conclusive evidence that any lack of uniformity of flow and adjustment in the individual burners produces differences that persist at all ratings in this method of firing, which does not involve the direct impingement of one flame upon another. A possible conclusion is that the geometry of each furnace, including the location of the fuel-feeding devices and the post-furnace gas passages, sets the path of the gas stream within the furnace at all normal ratings. The indications are that a difference exists between four and eight-burner

operation, probably explained by the difference in length of flame path. The wall-temperature peaks reached at elevation 15 ft at $2/3$ and full loads reflect the target character of the rear wall, and the wiping action caused by the change in direction of the main gas stream increasing the convective heat transfer at this elevation.

Charts of vertical distribution of wall temperatures show, in general, that the heat transfer at any rating decreases more or less uniformly with distance above the burners. In addition, the convective component increases the heat transfer where impingement is to be expected. This latter factor is most pronounced, of course, on the rear wall.

Charts show the relative effectiveness of each of the walls when fired with natural gas mixed with air to produce a non-luminous flame. The rear wall, with the greatest impact of gas, has the highest indicated heat-transfer rate at all elevations. The lower front wall is next, but the upper front wall is the lowest of the four. The two side walls show the same variation with elevation, but the left has higher Δt at all elevations, indicating greater impingement. The Δt for the side walls and the front wall are nearly the same at the 36-ft elevation and extrapolation of the rear-wall curve would bring it into the same group.

Application of the surface-temperature method of determining the distribution of heat absorption to a natural-gas-fired furnace has demonstrated a consistency in pattern and distribution and a reproducibility that could not be determined had coal ash been present to mask the indications. The evidence presented of fundamental consistency and reproducibility will aid study of the performance of solid and liquid fuels that produce masking deposits.

PROGRESS OF COMBUSTION AND OVER-ALL FURNACE HEAT ABSORPTION

The over-all furnace heat absorption is determined from measurements of gas temperature and composition at the furnace outlet and a knowledge of the heat input. Such measurements require special equipment and technique and, in this case, additional sampling points were utilized to obtain information as to the progress of combustion along the path of the flame between the furnace inlet and outlet.

Equipment. Henry Kreisinger and J. F. Barkley⁴ reported that measurements of gas temperature in a tube bank of a water-tube boiler were increasingly lower as the diameter of the thermocouple wire increased. The errors introduced by the size of the wire were attributed to loss of heat by radiation from the thermocouple weld to the surrounding cooler surfaces. Several investigators have taken part in the development of means of reducing the radiation loss. Surrounding the couple with a refractory shield reduced the radiation from the couple because of the interposition of a surface at an intermediate temperature. Drawing hot gas between the couple and shield raised and maintained the shield temperature at a higher point by convective transfer and thus further reduced the radiation loss from the couple. Some temperature difference between the gas and the couple must exist but this has been reduced by increasing the mass flow of gases between the couple and the shield. If the hot gases contain ash particles, deposits form on the couple and in the passages, increasing the resistance beyond the capacity of the suction equipment and impeding the mass flow of gases over the couple. In the case of a natural-gas-fired furnace, however, no dust is present and the optimum mass flow of gases can be maintained.

⁴ "Measuring the Temperature of Gases in Boiler Settings," Bulletin 145, U. S. Bureau of Mines, 1918.

Instead of a simple hollow cylinder of porcelain, or such a cylinder partly filled with pieces of porcelain tubing, the shields used on these tests were extruded shapes equivalent to a double cylindrical shield.

Fig. 30 shows sections of the several shields used and the relation of the shield, thermocouple, and water-cooled probe. Type

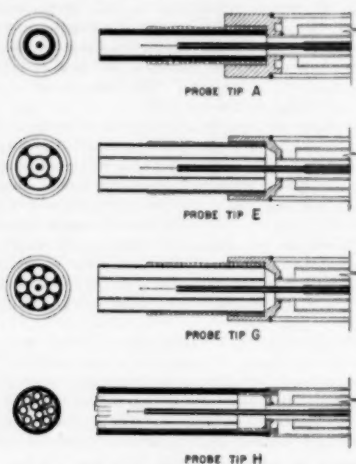


FIG. 30 TYPES OF PORCELAIN SHIELDS USED WITH WATER-COOLED PROBE

A is the simple cylindrical shield or single shield and type H is a high-velocity multiple shield. The passages in the latter shield clog rapidly in gases containing dust, and allowable exposures under such conditions are not long enough to be certain of results. Type E shield is of relatively large gas area and is structurally strong enough to permit use, even with dust-laden gases, for several observations. Type G shield is similar to type E but with round instead of kidney-shaped holes. The free areas available for gas flow, the resistance to flow, and the ease of manufacture differ in the types tested. Owing to the simple construction and the ease of handling the types E and G were used for all gas-temperature measurements.

A full description of the probes and the aspirating apparatus is given in a paper by Cohen, Corey, and Myers.⁷

Temperature Measurements. Fig. 31 shows the observed temperature plotted against the approximate mass flow of gases through the instrument at point *J(r)*. In this location the shielded couple is approximately 2 ft in front of the screen of evaporative tubes in front of the superheater. At this point the gas temperatures are approximately 1800 F above the tube-surface temperature, and radiation losses from the shield can be expected to be high. All shields, except type A, show a rising-temperature indication between low and high mass flows of gases through the instrument. Shields A and G show a sharp rise in temperature indication between no flow and low mass flow. Shield G indicated a temperature 190 F higher at low flow than at no flow, and 100 F higher at high flow than at low flow. It is evident, therefore, that substantial radiation losses existed which were corrected by drawing gas through the shields.

⁷ "Methods and Instrumentation for Furnace Heat-Absorption Studies: Temperature and Composition of Gases at Furnace Outlet," by Paul Cohen, R. C. Corey, and J. W. Myers, *Trans. ASME*, vol. 71, 1949 pp. 965-978.

The indicated temperatures differed by about 50 F at approximately 15,000 lb of gas per sq ft of free area, except for type A, which was about 180 F low.

Comparisons were made between the various thermocouples at a location in the furnace (door H) where the gas temperature was normally lower than that at the furnace outlet (door *J(r)*). The couples were inserted 6 ft from the side wall, and the temperatures were measured with mass velocities from zero to about 16,000 lb per hr per sq ft. The results are shown in Fig. 32 and it is seen that above a mass velocity of 5000 lb per hr per sq ft the change in indicated temperature with mass velocity is relatively small, and the differences between the type H and other types of shields are considerably less than when compared at door *J(r)*. These observations illustrate the effect of the temperature of the surroundings, relative to the true gas temperature, on the errors in the observed temperatures for a given type of radiation shield.

The platinum-platinum 10 per cent rhodium thermocouple was 5 ft long and connected to a Leeds & Northrup single-point Speedomax recorder by alloy leads having the same emf-temperature relation as the platinum couple at normal cold-junction temperatures. However, the junction between the platinum couple and the alloy leads was within the probe 5 ft from the hot junction, and tests were made to determine the effect of the gas temperature on the junction at this point, when the gas was aspirated at the optimum mass velocity.

The thermocouple was drawn back through the shield and probe and the temperature measured every 2 in. Gas flows were maintained essentially constant as were the flows of cooling water. Fig. 33 is a plot of the temperatures recorded. There was only a slight temperature change in the first 2 in., probably because the hot junction was still within the porcelain shield.

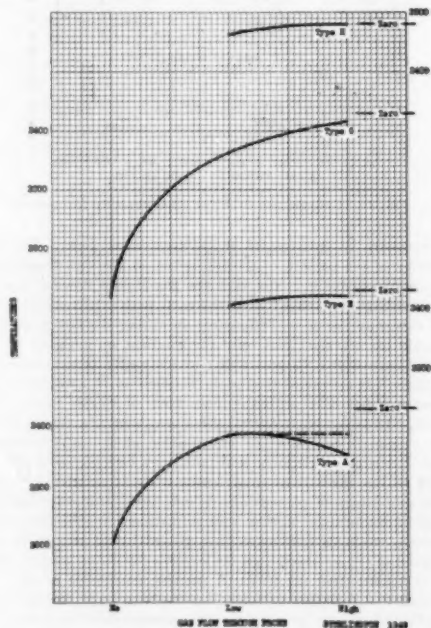


FIG. 31 COMPARISON OF SHIELDS AT POINT *J(r)*

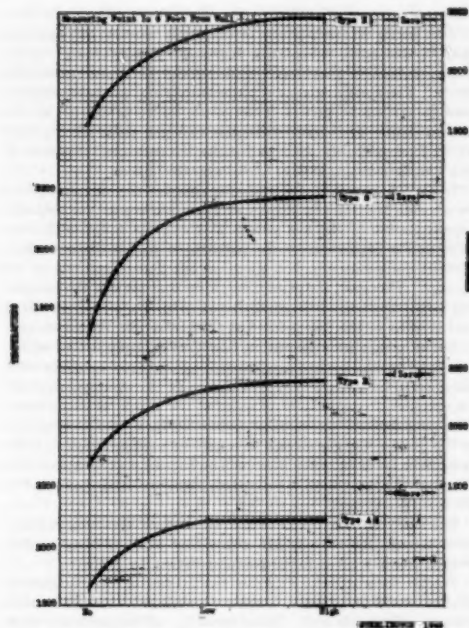


FIG. 32 COMPARISON OF SHIELDS AT POINT H

The reversal indicated on the chart is unexplained and is assumed to represent an inaccuracy in the measurement. Thereafter there was a rapid temperature drop as the gases were giving up heat to the water-cooled probe. At distances from the normal position of the hot junction, from 10 to 100 in., the temperature falls on a curve of the normal characteristics for convective cooling. At 60 in. from the normal position of the hot junction, the position of the junction with the alloy leads, the recorded temperature was 565 F. At such a temperature a "cold" junction correction is necessary and was applied for the temperatures used in the following study of the progress of combustion.

PROCEDURE AND RESULTS

With the unit operating under steady conditions, the probe was inserted successively in holes A, B, C, G, J, K, and L shown in Fig. 1 approximately distances of 3, 6, and 9 ft into the furnace from the right side wall. Points A, B, and C are in a horizontal line just above the center line of the bottom row of burners. Point G is about 17 ft above point C, and points J, K, and L are at the entrance to the screen in front of the superheater. By sketching the probable path of the gases through the furnace, as indicated by gas and wall temperatures, it was possible to estimate the distance along the flame path of each measuring position from the burner. These distances are the abscissas in each of the following figures, while temperature is the ordinate. The maximum reading of the Speedomax recorder was 3000 F, and the melting point of platinum is 3224 F, while the melting point of platinum-rhodium alloy is higher. On some charts, temperatures at points A, B, and C are incomplete because they were above the range of the recorder or because the platinum, the platinum-rhodium, or both melted. Such high tempera-

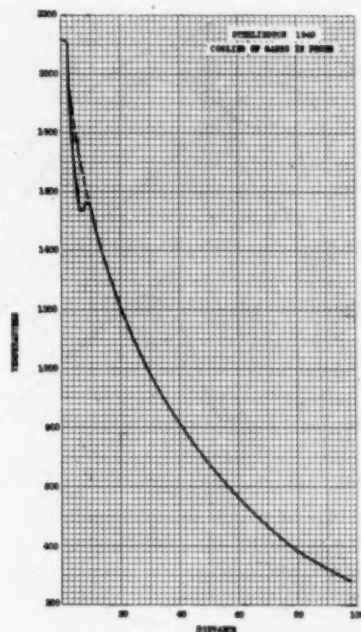


FIG. 33 COOLING OF GASES IN PROBE

tures were observed at full load and at part loads in the hotter zones of the flame.

Temperature About 3 Ft From Wall. In Fig. 34 are plotted the average temperatures of all tests at each load at position 3, that is, approximately 3 ft from the side wall at points A, B, C, G and J, K, and L. The points, in each case, are connected by continuous curves, but it must be kept in mind that the changes in temperature may be more abrupt than indicated. For the $1/4$ -load condition, we find a comparatively low temperature about 2 ft from the burner rising rapidly to a maximum about 9 ft from the burner. The temperature drops almost as rapidly up to a distance of about 18 ft from the burner when a rise to a secondary peak takes place. Thereafter the temperature drops to the furnace outlet. A similar dip, or reversal, occurs on the curve of temperatures for the $3/4$ load. On this curve, the secondary peak is higher than the peak 9 ft from the burner. No dip or reversal is indicated for the curve of $1/2$ -load temperatures. The peak at 9 ft from the burner is indicated as the maximum temperature, and the fall of temperature thereafter is indicated as being directly proportional to the flame travel. It is also to be noted that the temperatures measured up to 19 ft from the burner are higher at $1/2$ than at $3/4$ load. Only two points were recorded for the full-load condition because the temperatures at the burner level were all above the range of the recorder and couple.

To operate the unit at $1/4$ and $1/2$ loads, the four burners in the bottom row were used. For $3/4$ and full loads, the upper row of four burners was put in service in addition. Thus the individual burners were operated at the same gas and air velocities at full and $1/2$ loads, but the velocities were $1/2$ as much at $1/4$ loads as at $3/4$ load and $3/4$ as much at $1/2$ load as at full load. No adjustments were made in the directing vanes for the air between loads

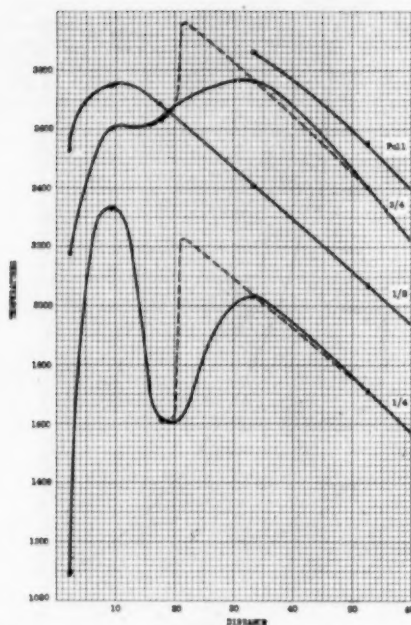


FIG. 34 GAS TEMPERATURE ALONG FLAME-PATH VARIATION WITH RATING—POSITION 3

to compensate for the decreased air and gas velocities. We can conclude, therefore, that the mixing action induced by the burner mechanism was the same at full and $1/4$ loads, was $3/4$ as great at $3/4$ load as at full load, and was only $1/2$ as great at $1/4$ load as at full load.

The characteristic curve for this furnace is indicated, we believe, by the complete $1/4$ -load curve. Very intense combustion starts at the burner and is completed 9 to 11 feet from the burner. We believe this is so, and roughly this indicated a completed heat-release rate of approximately 160,000 Btu per cu ft. The parallelism of the part of the full-load temperature curve shown encourages extrapolation leading to an indicated temperature of about 3200 F 10 feet from the burner. The direct proportionality of cooling and distance after complete temperature development may be the result of a fortunate choice of the sketched-in flame path from which the distances were measured. Again, the parallelism of all four curves from 33 to 53 ft from the burner indicates the same direct proportionality of cooling to distance although the temperatures differ by approximately 900 F between full and $1/4$ loads.

Bearing in mind that individual burner velocities are three quarters as much at $1/4$ load as at full load and one half as much at $1/2$ load as at full load, it is evident that mixing is less intense near the burners at the lower velocities. Thus the complete development of temperature does not occur at $1/4$ load until the flame has been deflected by splashing against the rear furnace wall approximately 20 ft from the burner. If the incomplete combustion is rapidly completed by this mixing, the temperature curve might be as indicated by the broken line.

Similarly, at the lowest burner velocities met with at $1/4$ load, the development of temperature is less rapid near the burner

but rises more rapidly than at the other loads. The rapid drop is due partly to cooling the incompletely burned mixture and may be due partly to a lesser degree of "mushrooming" of the flame so that it may have turned away from the measuring point. The splashing against the rear wall may produce complete enough mixing to give a temperature curve indicated by the broken line. The lower velocities (67 per cent) at $1/4$ than at $3/4$ load probably account for the temperature indication of less complete mixing at the $1/4$ load near the burner.

In the foregoing and the following analyses the assumption has been made that all of the temperatures are correct and equally representative of the gas stream at the given point. This assumption is supported by the patterns of wall isotherms which showed comparatively hot spots at the same locations at all ratings. However, the possibility exists that some of the measuring points are more representative at some loads than at others and if some of the low points (at the bottom of dips) were neglected as being unrepresentative, the effect of impingement on the rear wall would be less pronounced. If the gas analyses were assumed to be correct, they would support the assumption of the unrepresentative character of some of the points at some loads. The temperatures measured at points D, E, F, and H were not in the path of the gas stream as originally sketched and, in addition, were lower by some hundreds of degrees than temperatures at about the same level, which were, therefore, indicated to be in the main gas stream.

The analyses have been made on the basis of the temperatures, even though the authors are aware that some, perhaps equal, weight, could be given to the gas composition.

Temperatures About 6 Ft From Wall. In Fig. 35 are plotted similar curves for position 6, approximately 6 ft into the furnace from the right side wall. Unfortunately, all temperatures close to the burner were beyond the range of the instruments available.

Extrapolation at full load indicates the existence of temperatures as high as 3400 F 10 ft from the burner. The cooling rate is not markedly different at position 6 than at position 3 after temperature development has ceased.

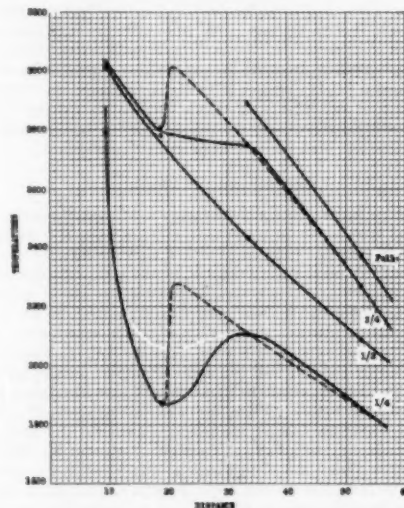


FIG. 35 GAS TEMPERATURE ALONG FLAME-PATH VARIATION WITH RATING—POSITION 6

At $1/2$ load, proportionality of cooling to distance from the burner is indicated as being almost direct for all measured points.

At $3/4$ and $1/4$ loads, we note again the indication that final mixing of combustible and air may be taking place at the rear wall.

Temperatures About 9 Ft From Wall. In Fig. 36 are plotted curves for position 9, approximately 9 ft into the furnace from the right side wall. The general characteristics of the curves are the same as those drawn for position 6, but the direct proportionality of cooling to distance is not as evident. At position 9 the measuring point is quite evidently in the main body of the flame and this may account for the slight downward convexity in the cooling region.

As for position 6, all temperatures close to the burner at position 9 were above the range of the instruments as were all measuring points at the burner level at full load.

Extrapolation of the full-load curve again indicates temperatures of about 3400 F 10 feet from the burner.

The lack of complete mixing is again indicated at the lower burner velocities existing at $3/4$ and $1/4$ loads. The effect of the mixing caused by the rear wall is probably as indicated by the broken curves.

In general, there are some variations in the slope and in the convexity of the cooling sections of these temperature curves. Some of these variations may be due to draftsmanship in drawing a continuous smooth curve through the measured temperature points and in part, also, to differences in accuracy at different distances from cold walls. In addition, development of temperature or release of heat may be proceeding even though the curves do not indicate major developments at the full-velocity conditions of $1/2$ load. A minor continuation of heat release would, of course, alter the slope or convexity of the cooling sections of the curves, but insufficient data were taken to estimate such a condition; in any case, such detailed work would be difficult to justify economically.

Effect of Distance From Wall at Constant Load. To indicate the variation of temperature with distance from the right side wall, three tests at $1/4$ load each with a different excess air have been chosen. Because the amount of excess air changes the velocity through the burner and, therefore, the mixing action of fuel gas and air, separate figures are presented for each value of excess air. Obviously, there should be somewhat better or quicker mixing action at the higher excess air because of higher velocities.

At 6.5 Per Cent Excess Air at Furnace Outlet. In Fig. 37 the temperatures measured are plotted for positions 3, 6, and 9, at $1/4$ load with only 6.5 per cent excess air as indicated by gas analyses at the furnace outlet. One measurement at position 6 and two at position 9 were above the range of the recorder and probably above that of the thermocouple. All positions show a rise in temperature between 17 and 33 ft from the burner. With good mixing, temperatures higher than normal should develop with such a low excess air, but velocities through the burners are somewhat low because of the load compared to full-load velocities and the mixing action was probably less. Position 3, closest to the right side wall, shows the lowest temperatures except at the furnace outlet where this position shows the highest temperatures. This reversal of recorded temperatures is shown for all excess air at this load and was found to be characteristic of the furnace at all loads. Temperatures increased toward the center of the furnace at the burner level, became almost uniform about 33 ft from the burner, after the turn at the rear wall, and decreased toward the center of the furnace at the furnace outlet.

At 16.2 Per Cent Excess Air at Furnace Outlet. In Fig. 38 the recorded temperatures for positions 3, 6, and 9 are shown for run 8 at $1/4$ load and 16.2 per cent excess air. The effect of the increase in excess air over the 6.5 per cent of Fig. 37 is not pronounced but all temperatures about 18 ft from the burner are

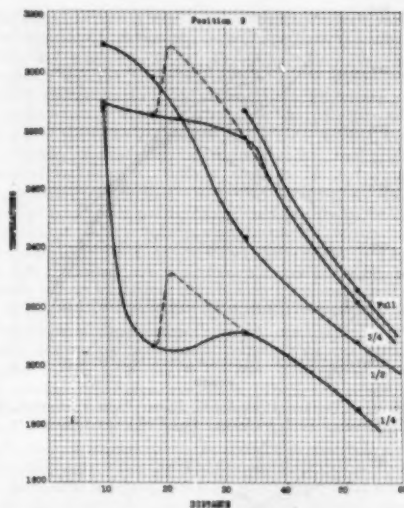


FIG. 36 GAS TEMPERATURE ALONG FLAME-PATH VARIATION WITH RATING—POSITION 9

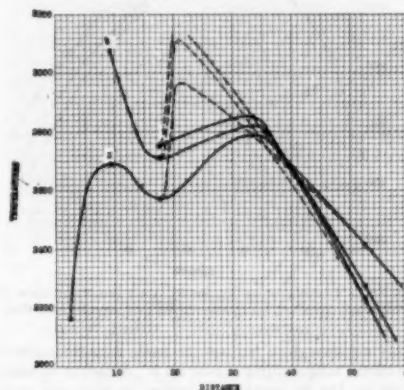


FIG. 37 GAS TEMPERATURE ALONG FLAME-PATH VARIATION WITH POSITION—RUN 9, $1/4$ LOAD—6.5 PER CENT EXCESS AIR

higher with the higher excess air, indicating more of the available heat had been released at the burner level. The rough indication (broken curves) of the mixing action of impingement on the rear wall at low excess air (6.5 per cent) was from 300 F to 400 F rise in gas temperature, whereas at 16.2 per cent excess the indicated temperature rise was from 100 to 150 F. Again, the temperature at the furnace outlet, 52.6 ft, falls as the distance from the side wall increases, a reversal of the conditions existing at the burner level.

At 20.8 Per Cent Excess Air at Furnace Outlet. In Fig. 39 the recorded temperatures at positions 3, 6, and 9 from the right side wall are plotted for run 10 at $1/4$ load and 20.8 per cent excess air. The increased excess air has increased the burner velocities to such an extent that mixing is almost complete near the burner but

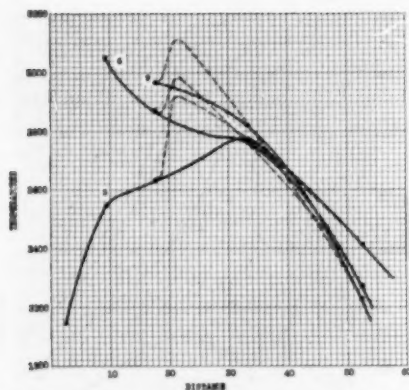


FIG. 38 GAS TEMPERATURE ALONG FLAME-PATH VARIATION WITH POSITION—RUN 8, $3/4$ LOAD—16.2 PER CENT EXCESS AIR

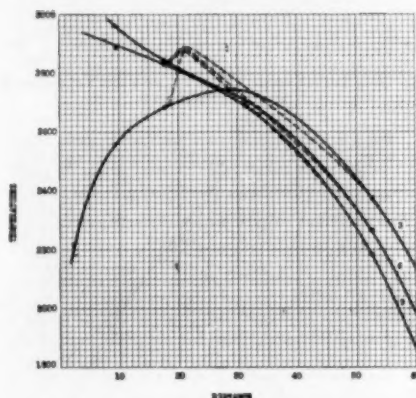


FIG. 39 GAS TEMPERATURE ALONG FLAME-PATH VARIATION WITH POSITION—RUN 10, $3/4$ LOAD—20.8 PER CENT EXCESS AIR

probably not enough to fan out the flame near the burners, as shown by the temperatures at position 3. Some rise in temperature, 50 to 150 F, probably occurred at the rear wall as indicated by the broken curves. Such a rise would alter the upward convexity shown by the full continuous curves. The same reversal of temperature gradient is shown at the furnace outlet as compared to the burner level temperatures.

This study of the progress of combustion along the flame path as indicated by temperature measurements indicates that air and gas velocities of the proper magnitude through the burner will produce rapid mixing with complete combustion occurring during a short flame travel. Where burner adjustments cannot readily be made to produce the desirable velocities at different loads, impingement with a change in the direction of flow is desirable and will produce the required additional mixing. It is reasonable to assume that with a burner capable of producing intense mixing at all rates, by mechanical adjustment, the required volume for complete combustion will be comparatively small. Such a small furnace would necessitate replacement of the radiant cooling surface normally installed by more effective convective steam-

generating surface. The high temperatures actually measured, those that melted the platinum couple and those that would have melted the couple if we had persisted in attempting to measure such temperature, all confirm the existence of rapid mixing and intense combustion with natural-gas fuel.

Distribution of Temperature at Furnace Outlet. Gas temperatures were measured at 18 points at the furnace outlet, using the same equipment described previously for determining gas temperatures in the furnace.

Isotherms and point readings have been placed on a rectangular plot for each test to show the interesting pattern of isotherms, the variation of the pattern with load and excess air, and the effect on the pattern of a change in rear-wall construction.

Fig. 40 shows the isotherm patterns and point values of the temperature at the furnace outlet for the full-load tests and at various excess-air values. The arithmetic and planimetric averages of the temperatures are given on each chart. The general pattern of isotherms is essentially the same for all the full-load tests, being asymmetrical about a vertical center line with the temperatures increasing as the sides are approached. The temperature on the right side is slightly higher than on the left, which is probably due to greater flame impingement on the left wall. The upper part of the outlet is cooler than the lower part owing to the flow of gases along the roof tubes. The wall and roof delta t confirm this conclusion. The excess air appears to have a significant effect on the gas temperature at the furnace outlet. The temperatures are highest for the lowest excess air (run 3, 6.5 per

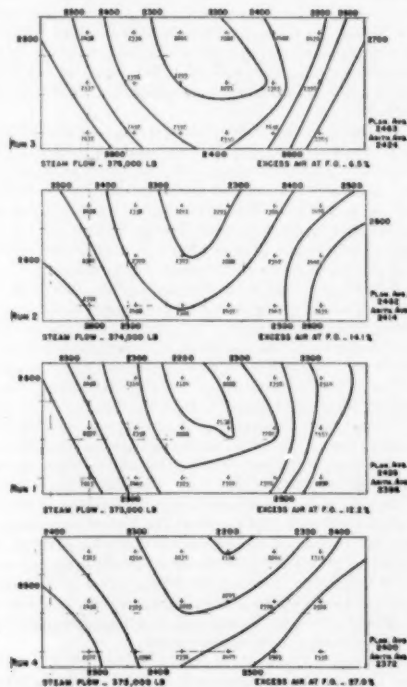


FIG. 40 ISOOTHERMS AND POINT VALUES OF TEMPERATURE AT FURNACE OUTLET FULL LOAD RUNS

cent excess air) and lowest for the highest excess air (run 4, 27.0 per cent). The isotherms seem to be more nearly vertical at low excess air and flatter at high excess air. This may have some relationship to the cross-sectional shape of the flame and to the heat transfer to the walls.

The four charts for the $1/2$ -load condition (runs 5, 6, 7, and 13, Fig. 41), show the same relationship of average temperature to excess air that was shown by the full-load isotherm diagrams. The highest average temperature was obtained during the lowest excess-air run and vice versa. It is interesting to note that the planimeter and arithmetic averages correspond very closely for the $1/2$ -load runs, whereas for the full-load tests, the planimeter averages were appreciably higher than the arithmetic averages. The isotherms for the $1/2$ -load tests are essentially horizontal, although wavy. This pronounced change in the nature or shape of the isotherms is probably due to the fact that only the bottom row of four burners was in use at $1/2$ load, whereas both upper and lower rows of four burners each were used for the full load.

The four charts of isotherms at the furnace outlet at $1/2$ load for runs 8, 9, 10, and 14, Fig. 42, show an isotherm pattern much the same as the full-load pattern but tending slightly toward the $1/2$ -load pattern. The planimeter averages are higher than the arithmetic averages for these $1/2$ -load tests as they were for the full-load tests, but the differences are not as pronounced. Although eight burners were in use at $1/2$ load, as at full load, the velocities were lower.

The two charts for $1/2$ -load runs 11 and 12, Fig. 43, are different. For run 11, the pattern is similar to the $1/2$ -load pattern,

but for run 12, it is an inversion of the full-load pattern, with the higher temperatures toward the center rather than the sides.

This study of the isotherms at the furnace outlet indicates that the pattern changes rather markedly with rating but not as markedly with excess air. The change in pattern occurring with only an increase in velocity is a widening of the space between isotherms as is shown by comparison of full and $1/2$ loads, both of which utilized two rows of four burners each. This might be called a normal change. However, when the number of burners changes from eight to four, the pattern of isotherms changes markedly from nearly vertical lines to nearly horizontal lines. The explanation offered for this change is that the vertical width of the flame, near the burners, is halved when the top row is shut down and less change in flow pattern or turbulence is required to reach the velocity and cross section fixed by the vertical dimension of the furnace outlet and the horizontal dimension of the path through the superheater.

Table 12 gives the three average values of the temperature of the gases leaving the furnace. The first column gives the arithmetic averages of the observed values. The second column gives the arithmetic averages of the observed values corrected for the special cold junction within the probe. The third column gives the planimetric averages of the corrected observed values. The larger differences between the arithmetic and planimetric averages occur on those isothermic charts having the steeper gradient. In the case of the $1/2$ -load runs, planimetry produced an average less than the arithmetic average.

Effect of Change in Rear-Wall Construction on Temperature

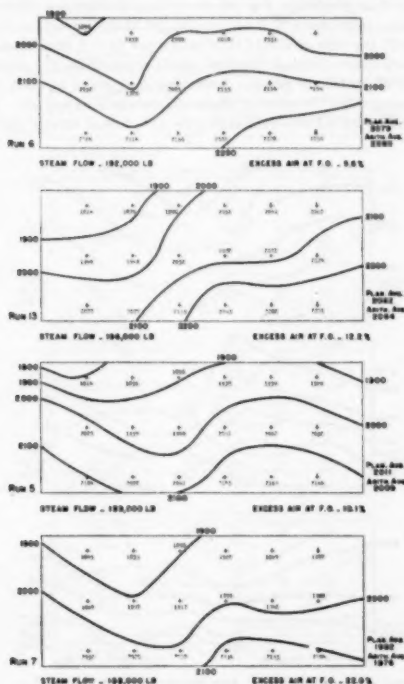


FIG. 41 ISOTHERMS AND POINT VALUES OF TEMPERATURE AT FURNACE OUTLET $1/2$ LOAD RUNS

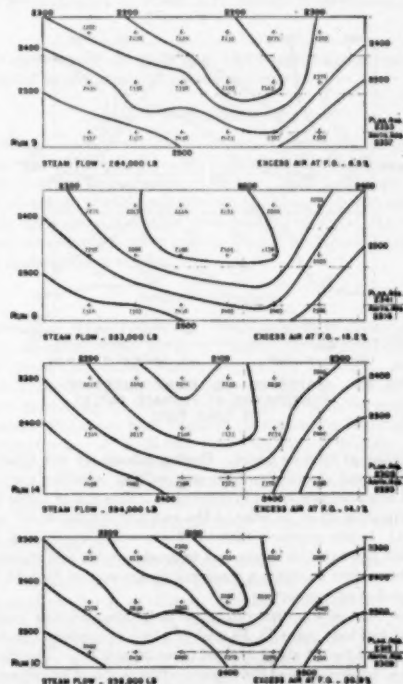
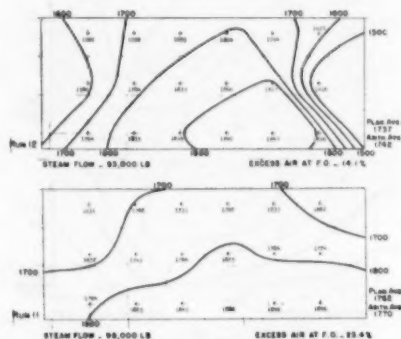


FIG. 42 ISOTHERMS AND POINT VALUES OF TEMPERATURE AT FURNACE OUTLET $1/2$ LOAD RUNS

TABLE 12 TEMPERATURE OF GASES LEAVING FURNACE, BOILER NO. 9, STERLINGTON STEAM ELECTRIC STATION, 1949

RUN	Arithmetic	Arithmetic	Planimeter
	Averages Of	Averages Of	Averages Of
	Observed	Observed	Observed
	Temperatures	Temperatures	Temperatures
		Corrected	Corrected
		For Special	For Special
		Cold Junction	Cold Junction
1	2545	2586	2426
2	2510	2414	2402
3	2579	2424	2465
4	2551	2572	2400
5	1908	2009	2011
6	2057	2080	2079
7	1957	1976	1982
8	2279	2516	2541
9	2299	2557	2555
10	2258	2509	2512
11	1796	1770	1762
12	1768	1762	1757
13	2056	2084	2082
14	2249	2285	2505

FIG. 43 ISOTHERMS AND POINT VALUES OF TEMPERATURE AT FURNACE OUTLET $1/4$ LOAD RUNS

Distribution at Furnace Outlet. Further advantage was taken of the active heat absorption of the rear wall by installing a widely spaced row of screen tubes in front of it. This row of tubes was approximately 12 in. in front of the wall and spaced on 19 1/2-in. centers. It was expected that the flame would impinge on the rear wall through this screen and in mushrooming and changing direction would transmit a considerable amount of heat to the screen tubes by convection.

Three load series were run after installation of this screen, three at full load (runs 15, 16, and 17), two at overload (runs 18 and 19), and two at about $1/4$ load (runs 20 and 21). The distribution of temperature at the furnace outlet is shown on rectangular diagrams, Figs. 44 and 45, of the furnace outlet as before by point measurements and isotherms.

Although the average temperatures are lower at the same rating

than without the screen tubes, as would be expected, a rather great change in the pattern of isotherms is evident. The isotherms, after the installation of the new screen, are essentially horizontal at full load, whereas they were formerly essentially vertical. Even at overload the isotherms remain essentially horizontal.

The three full-load patterns are shown in Fig. 44. The two overload patterns and the two $1/4$ -load patterns are shown in Fig. 45. Comparison of patterns before and after the screen installation have a generally similar top to bottom distribution; namely, the higher temperatures are at the bottom. If the gas stream had "hugged" the rear wall throughout its height, lower instead of higher temperatures should have been found at the bottom. However, the original assumption, that the gas stream utilized the longest possible radius in making the turn out of the furnace and therefore scrubbed the roof, explains the lower temperatures at the top and the screen tubes did not change this condition. The side temperatures at the higher loads represented by these figures are no longer substantially higher than the middle temperatures as indicated by the horizontal character of the isotherms. This greater uniformity of temperature distribution across the furnace outlet is probably the result of increased mixing action produced by the screen.

Variation of Furnace Efficiency With Load. Furnace efficiency, computed as the difference between heat entering and heat leaving, corrected for air leakage and radiation, and divided by heat entering, measures the portion of the heat input absorbed in the furnace.

The data plotted in Fig. 46 show that the furnace efficiency decreases from about 47.5 per cent at 100 M lb of steam per hr to about 33 per cent at 375 M lb of steam per hr. A smooth curve has been drawn through the four points representing the average results at each load point. Averaging the results at each load point suppresses the effect of slight differences in excess air. The points also have been connected with two dotted curves, one for

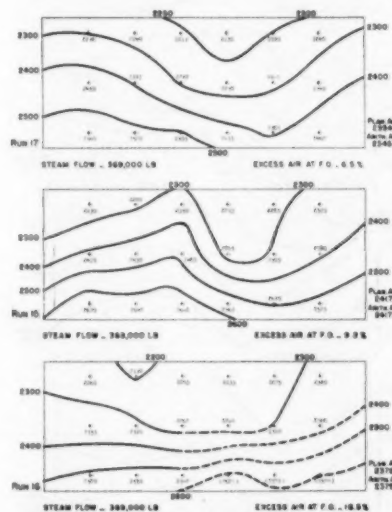


FIG. 44 ISOTHERMS AND POINT VALUES OF TEMPERATURE AT FURNACE OUTLET WITH ADDITIONAL FURNACE COOLING FULL LOAD RUNS

the low loads for which only the bottom row of burners was used and one for the high loads for which both rows of burners were used. The two dotted curves are approximately parallel and indicate a drop in furnace efficiency when the upper row of burners is added to the lower row. This drop may be due to a shortening of the mean flame path. The two dotted curves probably approximate actual conditions more closely than the single curve. An intermediate rating at about 240 M lb of steam per hr, produced with one and with two rows of burners, would have established this effect, but would have necessitated compensating adjustments of burner vanes to compare properly the high burner velocities of four-burner operation with the low burner velocities of eight-burner operation at this load. Such adjustments were not undertaken because normal operation was at 375 M lb of steam per hr or higher.

Variation of Furnace Efficiency With Excess Air at the Furnace Outlet. At $1/2$, $3/4$, and full loads, four tests were made, each with a different excess air. In each case, two of the four tests were made at about 10 to 15 per cent excess air at the furnace outlet. Limits of damper control and fan speed made it impossible to operate at low excess air at $1/4$ load, so only two test points are available for this load.

Fig. 47 shows that the furnace efficiency decreases with increasing excess air at all loads. Here again, a difference between four and eight-burner operation is indicated by the difference in slope between the two low-load curves and the two high-load curves. Apparently, the effect of increasing excess air is slightly greater

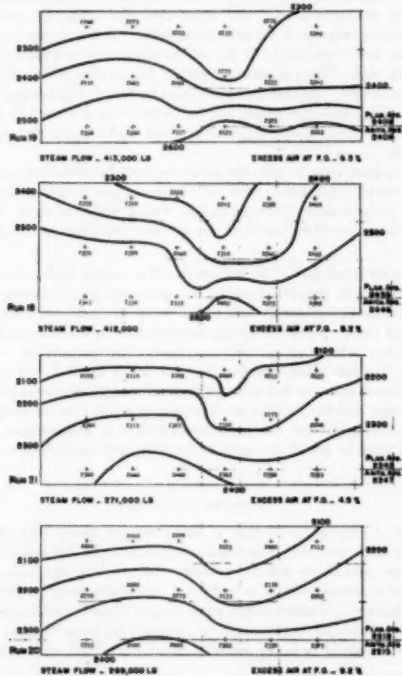


FIG. 45 ISOTHERMS AND POINT VALUES OF TEMPERATURE AT FURNACE OUTLET WITH ADDITIONAL FURNACE COOLING OVERLOAD AND $1/4$ LOAD RUNS

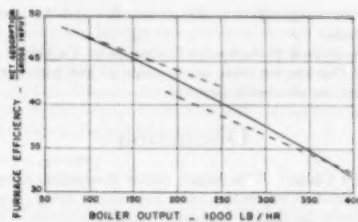


FIG. 46 VARIATION OF FURNACE EFFICIENCY WITH LOAD

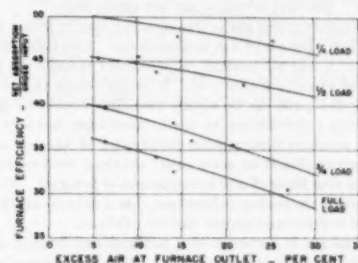


FIG. 47 VARIATION OF FURNACE EFFICIENCY WITH EXCESS AIR AT FURNACE OUTLET

with eight-burner operation than with four-burner operation, as indicated by the general slope of the curves.

CONCLUSION

We may conclude that the arrangement permitting the longest flame travel is the best from the standpoint of minimizing the effect of excess air on furnace efficiency. With natural-gas fuel, full advantage of this condition can be taken, but with solid or liquid fuels associated with incombustible material, the flame length and burner location may be limited by deposit formation and slagging characteristics.

ACKNOWLEDGMENTS

Bureau of Mines Personnel. For permission to participate in the co-operative work: Dr. A. C. Fieldner, Chief Fuels Technologist, Bureau of Mines, Washington, D. C.; Dr. R. L. Brown, Fuels Technology Co-ordinator, Bureau of Mines.

For conducting the work on furnace gas temperature and composition: P. Cohen, Fuel Engineer (now with the Westinghouse Electric Corp.); J. W. Myers, Fuel Engineer; J. Jonakin, Fuels Chemist; C. H. Schwartz, Fuel Engineer; J. J. Pfeiffer, Fuel Engineer; G. R. Kollar, Engineering Aide. All of the Combustion Research Section, Bureau of Mines, Pittsburgh, Pa.

To J. W. Myers for careful review of the manuscript and many valuable suggestions.

Combustion Engineering-Superheater, Inc., New York; C. G. R. Humphreys, Research Department.

Louisiana Power & Light Company, Sterlington; C. E. Dickey, C. D. Brooks, J. R. Horton, R. L. Phillips, W. T. Hess.

Particular thanks are due to J. R. Horton for his untiring interest, for his efforts to secure the desired loads and to supervise the adjustments of the unit, and for his freely given valuable advice. To R. L. Phillips is due special appreciation for his interest and for the kind of co-operation which makes such a project a pleasure. To W. T. Hess, our gratitude for his making

possible the co-operation of the universities and the services of the students.

Electric Bond & Share Service Corporation: To Arthur Krause and Paul Gordon, for their co-operation in the initial stages of the project, we are deeply grateful.

Discussion

OLLISON CRAIG.⁵ This paper, which constitutes a report of data obtained in connection with natural-gas firing in a boiler furnace, gives the data of heat-absorption distribution in the furnace envelope, in a manner similar to that which has been done previously in reports of similar tests on boilers fired with pulverized coal. The data of course are self-explanatory.

The firing of natural gas in this case was done in such a manner that the flame produced was nonluminous. This being the case, it apparently was not possible to determine visually the path of the flow of gases in the furnace. It is interesting to note, however, that this path can be readily visualized merely by the pattern of delta t distribution on the furnace walls and roof. It is generally assumed that uniform distribution of gas flow across a furnace outlet should be more easily obtained with natural-gas firing than with firing of coal in suspension or firing oil. There has been reason in the past to believe that this is not true and the data contained in this paper supply further evidence.

If natural gas is burned with a nonluminous flame it is a fair assumption that this is because of the intimate mixture of gas and air to such an extent that combustion is not retarded. To the contrary, if a luminous gas flame is desired, it is obtained by delaying gas and air mixture. However, the data in the paper indicate that even though the mixture is sufficiently intimate as to produce a nonluminous flame, it still is not complete by the time the gases pass from the front to the rear of the furnace, as evidenced by the rise in gas temperature after further mixing has taken place at the rear wall because of the turbulence produced by wall impingement. Presumably combustion could be completed in the shortest distance from the burners if the gas and air were thoroughly premixed before passing from the burners. This of course is done in some types of industrial processes.

The paper points out the lesser percentage of heat absorption in the furnace walls by radiation, and a greater percentage of absorption by convection, as compared to pulverized-coal or oil-firing. It also points out the additional mixing that occurred and additional convection heat absorption by the tube screen that was placed in front of the rear wall. This might lead to the idea that still further tubes could be placed in the furnace space to produce additional mixing and to absorb more heat by convection. This of course would be possible with gas firing while it would not be practical with pulverized-coal or oil-firing.

It would be useful if a comparison were made of the data reported in this paper with data reported on previous tests with pulverized-coal-firing. For example, with a given rate of heat release per square foot of tube surface exposed in the furnace, what is the relative rate of heat absorption, or what are the differences in delta t , what differences are there in the temperature of gases leaving the furnace, and reasons for these differences?

It can be assumed that the difference in heat-radiating ability of a nonluminous gas flame as compared to a luminous pulverized-coal or oil flame accounts for the difference in proportion of heat absorbed in the furnace envelope as radiated heat. It also can be assumed that if the natural-gas flame was luminous instead of nonluminous it would have a greater radiating capacity. As a matter of fact, tests at Battelle have indicated that luminous

gas flame will radiate more heat than will nonluminous gas flame. It would be of interest if comparative tests could be made in the same furnace and under the same conditions but varying only the difference in the luminosity of the gas flame, determining the comparative heat absorption in the furnace walls, and comparing the average temperature of gases leaving the furnace. Some such method could reduce the difference in superheated-steam temperature in multiple fuel-fired furnaces as between pulverized coal, oil, and natural gas, fired in the same furnace.

F. G. ELY.⁶ As the authors point out, this report on the performance of a natural-gas-fired furnace, which is free from ash deposits on the heat-absorbing surfaces, should provide a valuable reference for comparison with coal-fired furnaces in which ash is a prominent factor.

From Fig. 46 of the paper it is noted that in spite of the clean surface, the values of furnace-absorption efficiency are appreciably lower than those of coal-fired furnaces reported in previous committee tests. This may be due in part to the difference in flame luminosity, to the influence of gas-flow patterns, and to the specific arrangement of tubes and refractory in the furnace-wall construction.

It would be of interest to include further information on the construction of the water-cooled floor area, the over-all dimensions of the furnace shown in Fig. 1 of the paper, and a sketch showing the arrangement of rear-wall screen tubes installed prior to test No. 15.

As regards the gas-flow pattern, the authors' interpretation, based on furnace-wall isotherms and the observed color of refractory, appears to be quite reasonable. It is unfortunate that means were not available for introducing some additive which would make the gas stream visible for confirmation of these observations. Further interest would be afforded by comparative tests using only the upper row of burners, to disclose the effect on Δt profiles, gas-flow patterns, and furnace-absorption efficiency.

It is gratifying to note the progress made in calibration checks on testing equipment, such as thermocouple radiation shields, and furnace-tube thermocouples, under circumstances where advantage could be taken of the ash-free condition of the gas.

RALPH SCORAH.¹⁰ The authors in collaboration with the owners of this steam generator are to be congratulated on having presented an exceptionally fine paper based on very carefully conducted tests. We note that gas temperatures above about 3000 F were not attempted in order to preserve the instrument. However, the gas temperatures observed below 3000 F can be extrapolated so as to indicate the probable maximum furnace temperature, and this extrapolated temperature can then be compared with the calculated adiabatic temperature of combustion. We would like to ask if the authors could include such data in their closure.

AUTHORS' CLOSURE

Mr. Craig suggests that a luminous gas flame will radiate more heat than will a nonluminous flame. In the same flame volume and shape this is probably true, but for the same heat input, luminosity could be achieved practically only by delaying combustion. Consequently, even though the effective emissivity of the luminous flame would be greater, the mean radiant temperature would be lower and it is conceivable that no net change

⁵ Vice-President, Riley Stoker Corporation, Worcester, Mass. Fellow ASME.

⁶ Consultant, The Babcock & Wilcox Company, Research & Development Department, Alliance, Ohio. Mem. ASME.

¹⁰ Professor of Mechanical Engineering, University of Missouri, Columbia, Mo.

in total radiation would occur. This is a recurring question, particularly in open-hearth and glass-tank firing, but in these cases a long flame is preferred because of more uniform distribution of heat; the fact that it is luminous is the result of delayed combustion.

Mr. Craig suggests that the results of these tests be compared with those obtained from tests made of pulverized-coal-fired furnaces. The Furnace Performance Factors Committee plans at a later date to make a comprehensive correlation of its work with the objective of finding such general relationships as may exist.

Mr. Ely's comments regarding furnace heat-absorption efficiency are probably correct, and it is interesting to note in this connection that the heat absorption rates up to about 60,000 Btu per hr ft² were attained at Sterlington, whereas it was about 40,000 in two pulverized-coal-fired furnaces studied previously.

In answer to Mr. Scolah's discussion, the adiabatic flame temperature was calculated for three different values of excess air, namely, 0, 14, and 27 per cent. The last value is the highest

excess air for any of the tests, as measured at the furnace outlet. Owing to furnace leakage the excess air in the vicinity of the burners will be somewhat less than that at the furnace outlet. The corresponding adiabatic flame temperature will, therefore, lie between the temperature of a stoichiometric mixture and the temperature for the gas composition at the furnace outlet.

Following are the values calculated:

Excess air, per cent.	0	14	27
Flame temperature, F.	3765	3600	3410

In making these calculations the average values of the preheat temperature, and of the atmospheric humidity for all the full-load tests were assumed. The heating value of the gas was taken as the average of determinations on several samples obtained during the test series. Allowance was made for the dissociation of CO₂ to CO and O₂ and for the dissociation of H₂O to H₂, O₂, and OH. However, at the temperatures prevailing it was not considered necessary to allow for dissociation of H₂, O₂, and N₂ into their corresponding atoms.

The New-Type Code Chart for the Design of Vessels Under External Pressure

By E. O. BERGMAN,¹ ALHAMBRA, CALIF.

This paper presents a new Code chart for shells and heads of pressure vessels under external pressure. The chart is especially adaptable to materials like nonferrous metals that have a nonlinear stress-strain curve. The curves for shells consist of two families with a common abscissa scale and different ordinate scales. One family represents the dimensional variables and is the same for all materials. The other family represents the mechanical property variables of a given material at different temperatures. Each curve is constructed from a stress-strain diagram of the material at the temperature it represents. A "head-line" curve provides for the design of hemispherical heads.

NOMENCLATURE

The following nomenclature is used in the paper:

- D = outside diameter of shell, in.
- D' = inside skirt diameter of ellipsoidal head, in.
- E = tangent modulus of elasticity for a material with a nonlinear stress-strain curve, psi
- E_0 = constant modulus of elasticity for a material having a linear stress-strain curve, psi
- L = length of unsupported shell between heads or between circumferential stiffener rings, in.
- L' = inside crown radius of torispherical heads, in.
- L_h = effective radius of formed heads, in.;
= inside radius of spherical heads, in.
- n = number of lobes in a complete circumferential belt at time of collapse
- p = collapsing pressure, psi
- P = allowable working pressure, psi
- S = average compressive stress at collapsing pressure, psi
- S_y = yield strength of material that has a definite yield point, psi
- t = thickness of shell, in.
- t_h = thickness of head, in.

INTRODUCTION

Circular cylindrical shells under external pressure may fail either by yielding or by buckling. Vessels with relatively thick walls fail by plastic deformation under load. Relatively thin-walled vessels fail by instability or buckling under stresses that on an average are below the yield strength of the material. The buckling may be entirely elastic or it may be accompanied by more or less plastic deformation.

The collapsing strength of vessels under external pressure may be increased by means of circumferential rings attached to the inside or outside of the vessel at intervals to stiffen it. The shell

length, for purpose of analysis, becomes the length between centers of stiffeners. For closely spaced stiffeners, the average stress to produce buckling is greater than the yield stress and failure is by plastic deformation.

As the stiffener spacing is increased, the stress required to produce buckling decreases and eventually becomes less than the yield stress. The circumference of the shell then buckles in a series of lobes whose number decreases as the stiffener spacing is increased. A spacing is finally reached where the stiffeners have no effect on the resistance to buckling of the portion of the shell midway between stiffeners. Beyond this "critical length" or spacing of stiffeners, the collapsing pressure is independent of the length.

INSTABILITY FORMULAS

The region of instability has been the subject of numerous analytical studies. The principal instability formulas developed prior to 1934 are given by Windenburg and Trilling (1),² together with an evaluation of the formulas and a bibliography. Sturm (2) has presented a more recent analysis, also accompanied by an extensive bibliography.

The instability formulas give the ratio of the collapsing pressure to the modulus of elasticity of the material in terms of four dimensionless variables. One of these, Poisson's ratio, may be considered constant for design purposes. The geometry of the shell appears in two dimensionless ratios, the thickness-to-diameter ratio t/D , and the length-to-diameter ratio L/D . These ratios appear in the charts now given in the Code (3). The fourth dimensionless quantity n , in the instability formulas, is the number of lobes into which the shell buckles. The effect of n is shown by the nodes that appear in the curves for t/D when they are plotted against L/D and a function of the collapsing pressure as variables (2), (4).

For design purposes it is desirable to eliminate n from the instability formulas. Two methods for doing this have been proposed. One is a graphical method by Sturm and O'Brien, illustrated in Fig. 9 of reference (5). The other method is that of Windenburg and Trilling (1). They obtain an approximate formula, independent of n , that has an average deviation of about 1 per cent from the exact formula of von Mises (1). For Poisson's ratio equal to 0.30, the formula is

$$p = \frac{2.60 E (t/D)^{3.5}}{L/D - 0.45(t/D)^{2.5}} \quad [1]$$

When the modulus of elasticity E has a constant value, this equation plots as straight lines on log-log paper, except for very small values of L/D for which the second term in the denominator is not negligible.

Above the critical length, the collapsing pressure is given by the Bresse-Bryan formula (1) for tubes of infinite length. For Poisson's ratio equal to 0.30, this equation is

$$p = 2.2 E (t/D)^3 \quad [2]$$

² Numbers in parentheses refer to the Bibliography at the end of the paper.

¹ Consulting Engineer, C. F. Braun & Company. Mem. ASME. Contributed by the Committee on Strength of Vessels Under External Pressure and presented at the Annual Meeting, Atlantic City, N. J., November 25-30, 1951, of THE AMERICAN SOCIETY OF MECHANICAL ENGINEERS.

NOTE: Statements and opinions advanced in papers are to be understood as individual expressions of their authors and not those of the Society. Manuscript received at ASME Headquarters, September 18, 1951. Paper No. 51-A-137.

CONSTRUCTION OF PRESENT CODE CHARTS

The charts in the ASME and the API-ASME Codes for Unfired Pressure Vessels were developed for a group of carbon and low-alloy steels at room temperature. The construction of these charts is explained in references (6, 7, 8). Only a brief summary will be given here.

These charts are drawn for a material that has a definite yield point. The modulus of elasticity is taken as constant up to the yield point. The stress-strain diagram is assumed to consist of two straight lines, a line through the origin having a slope equal to the modulus of elasticity, and a horizontal line with an ordinate equal to the yield-point stress.

A series of curves representing constant values of t/D are plotted on log-log paper against values of P as ordinates and L/D as abscissas, as shown in Fig. 1. The t/D -curves consist of three straight-line segments, each of which is determined by a different formula. The straight-line segments are connected by short arbitrarily drawn transition curves.

The horizontal segments at the left represent the region of plastic flow. The collapsing pressure is figured by a modified hoop-stress formula (6) as follows

$$p = 2S_y(t/D)/1.05 \quad [3]$$

Failure in carbon steel is assumed to take place when the mate-

rial reaches the yield-point stress S_y , which is taken as 27,500 psi in Fig. 1. Theoretical considerations and experience are given as the basis for the reduction factor of 1.05 in the denominator.

The inclined segments of the t/D -curves in the middle of the chart represent the region of buckling in which the stiffening rings are more or less effective. The collapsing pressure in this region is figured by Equation [1] using a value of E_0 equal to 29,000,000 psi.

The horizontal segments at the right of the chart represent the region of buckling where the stiffeners are spaced too far apart to have any effect on the collapsing pressure. For t/D -values below 0.023, the curves are based on Equation [2] divided by 1.27, that is, on

$$p = 50,200,000 (t/D)^3 \quad [4]$$

For t/D -values above 0.023, the collapsing pressure is figured from the equation

$$p = 86,670 t/D - 1386 \quad [5]$$

The formulas for the t/D -curves in this region are empirical equations based on tests made by Stewart (9) in 1906, on lap-welded steel tubes having a yield point of 37,000 psi. Jasper and Sullivan (10) indicate that the average variation between the minimum and the average thickness of Stewart's tubes was 12 per cent and the average out-of-roundness was 1.4 per cent.

Theoretically, this material should buckle according to Equation [2] up to a t/D -value of about 0.035. For t/D greater than 0.035, the material should deform plastically when the hoop stress reaches the yield point. Stewart's Fig. 47 indicates that Equation [4] fits the plotted test results for t/D -values up to about 0.032. Thus the chart would have been satisfactory if it had been based on Equation [4] only.

MATERIALS WITH NONLINEAR STRESS-STRAIN CURVES

We have seen that the stress-strain diagram for many carbon steels can be approximated by two straight lines. The inclined line has a constant slope equal to the modulus of elasticity E_0 . The horizontal line has an ordinate S_y , and zero slope. Such an idealized stress-strain diagram permits the collapsing pressure to be read directly from the type of chart shown in Fig. 1.

Unfortunately, this type of stress-strain diagram is the exception rather than the rule, being limited practically to carbon and low-alloy steels at temperatures not over 500 F. Other materials, such as high-alloy steels, nonferrous metals, and carbon steel above 500 F, have a nonlinear stress-strain curve with a variable modulus of elasticity and no definite yield point. Charts of the type of Fig. 1 cannot be used directly for such materials.

Three methods of dealing with materials not covered by Fig. 1 were presented at the Annual Meeting of the ASME in 1946. The first method (7, 8) involves a change in the abscissa and ordinate scales so as to make the chart applicable to materials having a yield point other than $S_y = 27,500$ psi and a modulus of elasticity other than $E_0 = 29,000,000$ psi. A second chart is needed to take care of vessels whose length exceeds the critical length.

Charts based on this method are included in Appendix II of the ASME Code for Unfired Pressure Vessels, Section VIII, 1950 edition. These charts are to be used for steel at elevated temperatures. Since no change has been made in the shape of the stress-strain diagram, these charts give results that decrease in accuracy as the knee in the stress-strain curve become less prominent with increasing temperature.

Windenburg (8) has outlined a method for avoiding the error caused by using a chart based on a constant modulus of elasticity for a material that has a nonlinear stress-strain curve. The method is one of trial and error. It requires a stress-strain dia-

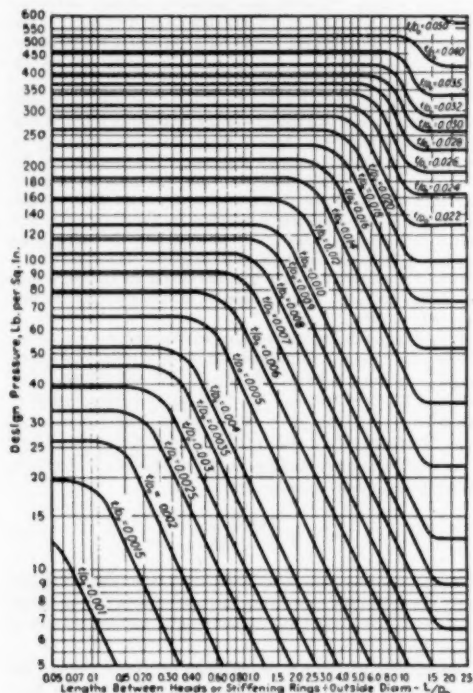


FIG. 1 CHART FOR DETERMINING SHELL THICKNESS OF CYLINDRICAL SHELL VESSELS UNDER EXTERNAL PRESSURE— $E_0 = 29,000,000$ Psi, $S_y = 27,500$ Psi

(This chart is Fig. UG-28.2 of the ASME Code for Unfired Pressure Vessels, reference 3. It is based on a factor of safety of 4; that is, the design pressure is one fourth of the collapsing pressure.)

gram of the material from which a diagram of the reduced modulus or the tangent modulus of elasticity is plotted against stress. Windenburg's paper (8) should be consulted for a discussion of these moduli.

Another method is discussed by Sturm and O'Brien (5). They present a type of chart based on a variable modulus of elasticity. The mechanical property terms that appear in the equations for collapsing pressure are considered as two additional variables. They are the tangent modulus of elasticity E , of the material and the corresponding value of compressive stress S . The pattern of the t/D -curves depends on the mechanical property variables so that a different chart is required for each material and each temperature range of the material. Sturm and O'Brien show in detail the work required to prepare the chart for A-nickel at room temperature. They also develop a chart for 17-7 chromium-nickel stainless steel. Hartman (11) gives two charts of the same type for pure aluminum and aluminum-manganese alloy.

Hartman also has three charts for nickel alloy, later adopted in ASME Code Case 1074, that have the general shape of the chart for carbon steel in Fig. 1. A comparison with Sturm and O'Brien's chart for A-nickel indicates that the t/D -curves obtained by Sturm and O'Brien's method have been warped into the more familiar shape of the curves in Fig. 1. This may indicate a feeling that the t/D -curves, representing a geometrical relationship, should maintain their pattern regardless of the material.

SEPARATION OF MECHANICAL PROPERTY VARIABLES FROM DIMENSIONAL VARIABLES

Sturm and O'Brien (5) point out that the instability equations can be written so that the mechanical property variables are on one side of the equation and the dimensional variables are on the other. This separation of the geometrical and mechanical variables is the basis on which the new-type Code chart is constructed.

Instability formulas with the dimensional variables on one side of the equation may be derived readily from Equations [1] and [2] with the help of the hoop-stress formula for the average compressive stress in the shell. This equation can be written in the form

$$p = 2S(t/D) \quad [6]$$

Equating the values of p given by Equations [1] and [6] and dividing by E gives

$$\frac{S}{E} = \frac{1.30(t/D)^{1.5}}{L/D - 0.45(t/D)^{0.5}} \quad [7]$$

The second term in the denominator has no discernible effect on the curves within the range of the chart and can be neglected. This gives

$$\frac{S}{E} = \frac{1.30(t/D)^{1.5}}{L/D} \quad [8]$$

In like manner, Equation [2] reduces to

$$S/E = 1.1(t/D)^2 \quad [9]$$

In constructing the present Code chart shown in Fig. 1, this equation was multiplied by Stewart's out-of-roundness factor of $1/1.27$ giving the formula

$$S/E = 0.87(t/D)^2 \quad [10]$$

Thus the present chart introduces an out-of-roundness factor in the portion of the chart where Equation [10] applies, while omitting it in the rest of the chart. In this paper, Fig. 2 is based on Equation [10] to permit direct comparison with the present

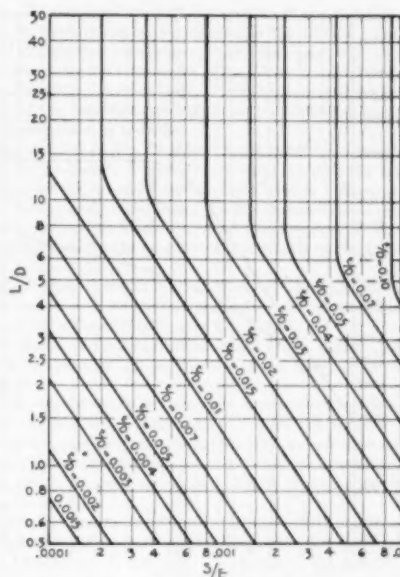


Fig. 2 CHART SHOWING RELATION BETWEEN DIMENSIONAL RATIOS t/D AND L/D AND THE MECHANICAL PROPERTY RATIO S/E
(This chart is the same for all materials.)

chart. New-type charts for adoption as part of the Code should, however, be based on Equation [9], thus, in effect, doing away with Stewart's factor for out-of-roundness.

Fig. 2 is a graph of Equations [8] and [10] in which a family of t/D -curves is plotted with values of S/E as abscissas and L/D as ordinates. Since S and E are simply simultaneous values of the stress and modulus of elasticity considered as variables, the curves in Fig. 2 give general relations that are applicable to all materials.

The advantage that the chart in Fig. 2 possesses of applying to all materials, carries with it the disadvantage of not applying specifically to any particular material. Fig. 2 gives the incidence of failure, not in terms of collapsing pressure p as in the present charts, but in terms of S/E . To obtain the collapsing pressure, charts are needed showing the relation between p and S/E for particular materials.

Such charts can be constructed readily with the help of a stress-strain diagram of the material together with the hoop-stress formula. Using a factor of safety of 4, so that $p = 4P$, Equation [6] for hoop stress can be written as

$$P D/t = S/2 \quad [11]$$

Materials curves based on this equation give results in terms of allowable working pressure.

A graphical method of obtaining simultaneous values of S and E is explained in detail by Sturm and O'Brien (5). Values of S/E and $P D/t = S/2$ are computed from such data, and a curve is drawn having S/E as abscissa and $P D/t = S/2$ as ordinate. Two such curves are shown in Fig. 3, one for a steel at room temperature where the modulus of elasticity is constant, and one for a steel at 650 F where the modulus of elasticity is a variable.

The two families of curves are shown on separate charts to explain their construction. In practice it is better to have them

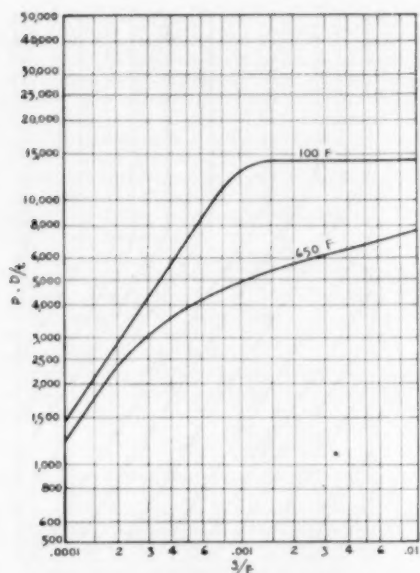


FIG. 3 CHART SHOWING RELATION BETWEEN MECHANICAL PROPERTY RATIO S/E AND $P D/t = S/2$ FOR A PARTICULAR STEEL AT 100 F AND 650 F

superposed on a single chart with the common abscissa S/E , as shown in Fig. 4. The ordinate scale for values of L/D is at the left and that for $P D/t$ is at the right. The variable S/E is ordinarily not needed in using the charts. It may be considered as a parameter that serves to tie the two sets of curves together.

The horizontal lines at the right in Fig. 1 are represented by the vertical lines in Figs. 1 and 4. These line segments apply to shells that exceed the critical length. The horizontal lines at the left in Fig. 1 apply to shells that fail by yielding. For any given value of t/D , the collapsing pressure is constant over a range of L/D -values. The pressure is constant only because failure takes place at the yield stress, which is assumed to be constant. The same constant collapsing pressure over a range of L/D -values is obtained in Fig. 4 for a given t/D -value when the material curve has a horizontal segment such as that of the curve for 100 F.

USE OF NEW CODE CHART

Pressure-vessel problems, like many other engineering problems, are of two kinds, investigation and design. In problems of investigation, the pertinent dimensions of the vessel are known, the diameter, the length between stiffeners, and the shell thickness. The loading condition, which in this case is the allowable external pressure, is to be determined.

This is the form in which the problem ordinarily presents itself to the inspector. He computes the values of L/D and t/D , the same as for the present charts. He then enters the chart at the computed L/D -value on the left-hand scale, follows the L/D -ordinate to its intersection with the computed t/D -curve, then follows vertically along the S/E -line through the intersection to where it cuts the material curve for the operating temperature. He then follows the horizontal line through this intersection to the scale on the right where he reads the value of $P D/t$. Multi-

plying this value by the computed value of t/D gives the allowable external pressure for the vessel.

In problems of design, the operating pressure and temperature are given and, in most cases, the diameter of the vessel. Usually both the shell thickness and the stiffener spacing are to be determined. The problem of the designer is to determine corresponding values of thickness and spacing that meet Code rules, satisfy service requirements, and make the combined cost of shell and stiffeners as low as possible.

Since t is a factor both in t/D and $P D/t$, the designer should begin by assuming a value of t , in a commercial plate thickness, for use in figuring t/D and $P D/t$. The traverse of the chart in a design problem is made in the opposite direction to that followed in an investigation problem.

The designer enters the chart at the computed $P D/t$ value on the right-hand scale, follows the $P D/t$ -ordinate to its intersection with the material curve for the operating temperature, then follows vertically along the S/E -line through the intersection to where it cuts the computed t/D -curve. He then follows the horizontal line through this intersection to the scale on the left where he reads the value of L/D . Multiplying this value by D gives the stiffener spacing corresponding to the value assumed for t .

A second and often a third value of t must be tried to obtain the most economical combination of shell thickness and stiffener spacing. More than one trial may be needed also when a specified stiffener spacing must be met.

FORMED HEADS UNDER EXTERNAL PRESSURE

Rules for formed heads under external pressure are given in Par UG-33 and Par UA-5 of the ASME Code for Unfired Pressure Vessels. The Code gives two formulas. One applies to relatively thin heads in which failure originates from instability; the

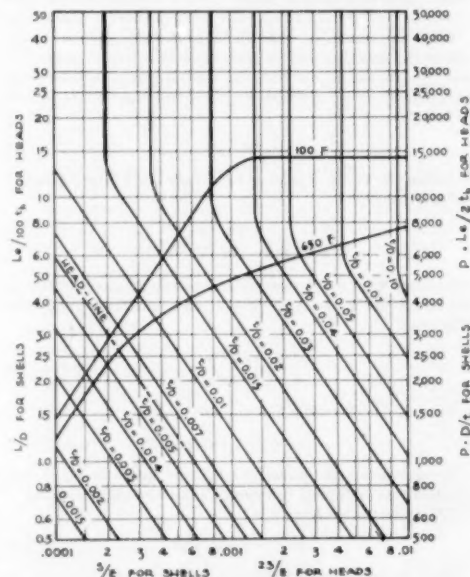


FIG. 4 NEW-TYPE CODE CHART FORMED BY SUPERPOSITION OF FIGS. 2 AND 3

(Head line permits the chart to be used for hemispherical heads.)

other applies to relatively thicker heads where failure starts with plastic deformation.

Like the chart in Fig. 1 for shells, these formulas for heads are directly applicable only to materials that have a constant modulus of elasticity. For materials with a nonlinear stress-strain curve, cut-and-try methods are necessary in order to arrive at a solution that is based on simultaneous values of S and E . A chart embodying the materials curves shown in Fig. 3 will simplify the design of heads made from such materials.

The equations for formed heads may be shown graphically on the same chart as that used for shells. The geometrical relations can be shown by a single curve instead of a family of curves, since the head can be specified with one less dimension than is needed for shells.

The instability formula for heads, as given in Par UA-5, is based on the von Kármán-Tsien equation for spheres (12), with reductions for out-of-roundness and factor of safety. It is

$$P = E/16 (t_h/L_h)^3 \dots \dots \dots [12]$$

where L_h , the spherical radius of the head, is substituted for the symbol L of the formula to avoid confusing it with the symbol for stiffener spacing used in this paper.

The dimensional variables may be separated from the mechanical property variables by combining Equation [12] with the equation for average compressive stress in a hemispherical head

$$S = PL_h/2t_h \dots \dots \dots [13]$$

Eliminating P and rearranging

$$2S/E = 1/16 (t_h/L_h) \dots \dots \dots [14]$$

This equation plots as an inclined straight line on the log-log chart. An abscissa value of $2S/E$ is used in order that the "head line" will satisfy the requirements in the region of plastic deformation. The ordinates are plotted as $L_h/100t_h$ in order to fit the scale used to plot L/D -values for shells.

In the region where plastic deformation occurs, the Code sets the allowable external working pressure as 60 per cent of the allowable internal working pressure. The 60 per cent reduction factor was set up in the Code at the same time that provision was made for formed heads under external pressure. The primary value of a factor such as this would seem to lie in the increased resistance against failure in the range of thickness-to-diameter ratios where buckling occurs.

Since the allowable pressure varies with the square of t_h/L_h in the region of instability, the correction factor to be applied to a pressure based on the first power of t_h/L_h should itself be a function of t_h/L_h . The constant factor of 0.60 was found to be too low for small values of t_h/L_h and as a result, Equation [12] was adopted. Equation [12] applies to all thickness-to-diameter ratios at which failure is due to elastic instability.

The use of the 0.60 per cent factor in the design of heads in the thickness range where failure is by plastic deformation is open to question, particularly since no such factor is applied to shells that are in the same thickness range. If the 60 per cent factor is not applied, the equation for stress in a hemispherical head in the plastic range is given by Equation [13].

The material curves on the chart were constructed with $S/2$ as ordinate and S/E as abscissa. Values of $PL_h/2t_h = S$ may be read from these curves provided both ordinate and abscissa scales are doubled. It will be remembered that the head line was drawn to a scale of $2S/E$ so as to permit this change in scales.

The head line shown in Fig. 4 is a graphical representation of Equations [13] and [14] for hemispherical heads. The design pressures obtained from Fig. 4 for steel at 100 F compare as follows with those obtained from the rules of Par UG-33 of the

Code. The inclined straight-line portion of the material curve gives the same values as the equation in Par UG-33. The horizontal straight-line portion gives values that agree with the Code rules except for the elimination of the 60 per cent reduction factor. The curved section used to join the two straight-line segments of the materials curve gives values somewhat lower than the values figured by the rules.

The head line in Fig. 4 has been constructed for hemispherical heads on the basis of Equations [13] and [14], with the quantity L_h equal to the spherical radius of the head in both equations. Fig. 4 can be used for the design of other shapes of heads provided the effective radius in the formulas corresponding to Equation [13] is the same as the effective radius defined in Par UG-33 for use in Equation [14].

The effective radius in Par UG-33 of the Code is $K_1 D'$ for ellipsoidal heads, and L' for torispherical heads. From Equations [1] and [3] in Par UA-4, the effective radius is KD' for ellipsoidal heads and L/M for torispherical heads. The values of K_1 , K , and M are given in Tables UG-37, UA-4.1, and UA-4.2, respectively.

With this difference in definition, a separate head line is required for each shape ratio of each of these two types of heads. A separate chart for heads would be needed to show such a family of head lines. Even two more head lines for 2-to-1 ellipsoidal heads and 6 per cent torispherical heads might clutter up the chart too much.

The use of the one head line for all three shapes requires that the definitions of L_h be changed so as to have the same value for both Equations [13] and [14]. A change in the definitions for Equation [14] would result in a thicker head in the region of elastic instability and would provide greater security against collapse due to out-of-roundness. Since the Code does not set limits for out-of-roundness for heads, such added security would appear desirable.

NEED FOR FURTHER CONSIDERATION

The Subcommittee on Strength of Vessels Under External Pressure has approved the new-type chart for use in the ASME Code for Unfired Pressure Vessels. This paper has brought up the following points on which decisions are needed before construction of charts of the new type begins:

- 1 The elimination of the 1.05 factor in Equation [3] for vessels that fail by plastic deformation. This may be looked upon as a minor change in the factor of safety. In considering the need for this factor, it should be remembered that for vessels under external pressure the factor of safety in the region of yielding is based on yield strength, while for vessels under internal pressure, the factor of safety is based on the tensile strength which is much higher.

- 2 The inapplicability of Equation [5] to pressure vessels. This equation applies primarily to the range where failure is by plastic deformation. This range is adequately covered when provision is made against failure by plastic deformation.

- 3 The elimination of Stewart's reduction factor which is now applied to Equation [2] for shells that exceed the critical length.

- 4 The elimination of the 60 per cent factor for formed heads when they are figured by the rules for heads under internal pressure. This factor should have been eliminated when the von Kármán-Tsien type of formula was adopted.

- 5 Consideration of the rules for ellipsoidal and torispherical heads to determine whether the effective radius in the region of elastic instability should be the same as that in the region of plastic deformation.

SUMMARY

- 1 The present Code charts are designed for use with mate-

rials that have a constant modulus of elasticity up to the yield point.

2 The new-type Code charts can be used with materials that have either a constant or a variable modulus of elasticity.

3 The family of curves that depends on the dimensional variables of the vessel is the same for all materials. The family of curves that depends on the physical properties of a particular material is readily constructed from stress-strain curves of the material at a number of different temperatures.

4 An additional line of the chart allows it to be used in the design of hemispherical heads. Ellipsoidal and torispherical heads designed by this method have greater resistance to out-of-roundness in the region of elastic instability than when designed under the Code rules.

ACKNOWLEDGMENTS

The author wishes to express his appreciation to Messrs. G. B. Farkas, M. Holt, and P. J. Smith of the Subgroup on Vessels Under External Pressure of the Subcommittee on Nonferrous Materials, and to J. E. Soehrens of C. F. Braun & Company for their contribution to the development of the new type of chart.

BIBLIOGRAPHY

- 1 "Collapse by Instability of Thin Cylindrical Shells Under External Pressure," by D. F. Windenburg and C. Trilling, Trans. ASME, vol. 56, 1934, p. 819.
- 2 "A Study of the Collapsing Pressure of Thin-Walled Cylinders," by R. G. Sturm, University of Illinois, Engineering Experimental Station, Bulletin No. 329, 1941.
- 3 "Rules for Construction of Unfired Pressure Vessels," Section VIII, ASME Boiler Construction Code, 1950 edition.
- 4 "Theory of Elastic Stability," by S. Timoshenko, McGraw-Hill Book Company, Inc., New York, N. Y., 1936.
- 5 "Computing Strength of Vessels Subjected to External Pressure," by R. G. Sturm and H. L. O'Brien, Trans. ASME, vol. 69, 1947, pp. 353-358.
- 6 "Theoretical and Empirical Equations Represented in Rules for the Construction of Unfired Pressure Vessels Subjected to External Pressure," by D. F. Windenburg, *Mechanical Engineering*, vol. 59, 1937, pp. 601-608.
- 7 "API-ASME Code for the Design, Construction, Inspection, and Repair of Unfired Pressure Vessels for Petroleum Liquids and Gases," fourth edition, 1943.
- 8 "Master Charts for the Design of Vessels Under External Pressure," by D. F. Windenburg, Trans. ASME, vol. 69, 1947, pp. 345-351.
- 9 "Collapsing Pressure of Bessemer Steel Lap-Welded Tubes, Three to Ten Inches in Diameter," by R. T. Stewart, Trans. ASME, vol. 27, 1906, pp. 789-822.
- 10 "The Collapsing Strength of Steel Tubes," by T. M. Jasper and J. W. W. Sullivan, Trans. ASME, vol. 53, 1931, pp. 219-245.
- 11 "Unfired Cylindrical Vessels Subjected to External Pressure," by F. V. Hartman, Trans. ASME, vol. 69, 1947, pp. 337-344.
- 12 "Buckling of Spherical Shells by External Pressure," by T. von Kármán and H. Tsien, *Journal of the Aeronautical Sciences*, vol. 7, 1939, pp. 43-50.

Discussion

F. V. HARTMAN.² This paper will serve a useful purpose in outlining the thought behind the charts that are being included in the 1952 edition of Section VIII of the Code. There are certain discrepancies between the method of drawing such charts as presented by the author and that used in preparing the charts submitted to the Boiler Code Committee.

The charts submitted to the Boiler Code Committee are composite charts of the general type described but the geometry lines which are considered applicable to vessels of all materials are based on the theory developed by Dr. R. G. Sturm (author's reference 2) rather than on the earlier work of Dr. Windenburg

and Mr. Trilling. This choice was based on the thought that Dr. Sturm's work is more complete and is independent of empirical equations such as Equation [5].

Reference 2 shows the development of an equation for the collapsing pressure of circular cylindrical vessels which is of the form

$$p = KE_1 \left(\frac{t}{D} \right)^3 \quad [15]$$

where

K = coefficient dependent on proportions of vessel, that is, ratio of diameter to thickness and length to diameter
 E_1 = initial slope of stress-strain curve, that is, Young's modulus

and the other terms are as defined in the nomenclature. Charts showing the variation of K with the proportions of the vessel are given in references (2) and (5). For long, thin-walled tubes, Equation [15] of this discussion reduces to Equation [2] of the paper. Although reference (2) gives values of K for only six values of the ratio of diameter to thickness there are many ways in which interpolation can be made for other values of the ratio in order to avoid lengthy calculations.

The development of Equation [10] of the paper contains the factor 1.27 which is an empirical constant required to give good agreement between Equation [2] and the average experimental results obtained by Prof. R. T. Stewart from tests on long lap-welded steel tubes (author's reference 9). Saunders and Windenburg¹ emphasize that Professor Stewart's tests were made on commercial tubing yet some of the test results are in agreement with Equation [2]. Also Jasper and Sullivan, in reference (10) advocate the use of Sturm's analysis in the field of elastic buckling. The charts submitted to the Boiler Code Committee do not include this factor of 1.27. The author concurs with this step.

Fig. 5, herewith, shows a comparison of some of the lines from

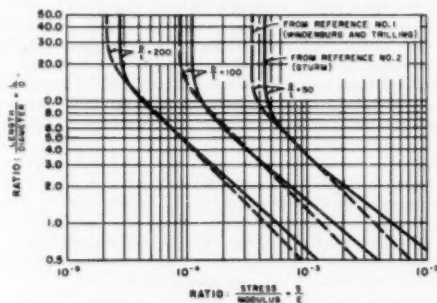


Fig. 5 COMPARISON OF GEOMETRY LINES FROM AUTHOR'S REFERENCES (1) AND (2)

Fig. 2 of the paper, and the corresponding lines from the charts submitted to the Boiler Code Committee for inclusion in the 1952 edition of Section VIII. The divergence in the vertical portions of the curves lies in Mr. Stewart's empirical factor 1.27. The divergence in the lower part of the sloping portions lies in the difference in the theories for short shells as developed by Sturm, and by Windenburg and Trilling. For length-diameter ratios commonly used, for example, L/D between 2.5 and 11, and for D/t

² Mechanical Engineer, Technical Division, Aluminum Ore Company, East St. Louis, Ill. Memo. ASME.

¹ "Strength of Thin Cylindrical Shells Under External Pressure," by H. E. Saunders and D. F. Windenburg, Trans. ASME, vol. 53, 1931, pp. 207-218.

equal to 100, the two sets of lines yield ratios of stress to modulus which agree within about 5 per cent.

The use of the tangent modulus as the effective modulus deserves additional comment. It should be recognized that Equations [1], [2], [4] of the paper and Equation [15] of this discussion were developed on the assumption of elastic action of the material and hence do not apply rigidly in the region of plastic action. In other buckling problems such as columns and stiffened flat sheet it has become common practice to redefine modulus of elasticity for the range of plastic action as the "effective" modulus of elasticity. In column problems it is customary to use the tangent modulus as the effective modulus (author's reference 5). The material lines in both the author's chart and in those submitted to the Boiler Code Committee are developed on this basis and are therefore in agreement.

The sphere line on the chart submitted to the Boiler Code Committee represents the equation of von Kármán and Tsien which is

$$p = 0.183 E_1 \left(\frac{t_0}{L_0} \right)^3 \dots \dots \dots [16]$$

The factor of safety of 4 is introduced in the material lines of the chart. The use of Equation [12] leads to a factor of safety of about 12 for a perfectly formed spherical shell.

It is believed that Equation [16] is valid for spherical segments large enough to develop the natural buckle pattern of a sphere of the same proportions. It also would seem reasonable for use with formed heads of ellipsoidal or other shape provided the effective radius of curvature can be determined. The factors in Table UG-37 [author's reference (3)] lead to the maximum radius of curvature of a four-centered ellipse having the axis ratios indicated. The Subcommittee on Vessels Under External Pressure recently voted to accept the sphere line and the factors in Table UG-37 for ellipsoidal heads of nonferrous materials. A similar proposal for heads of the ferrous materials is before the Subcommittee.

M. B. HIGGINS.⁶ It is the writer's feeling that the new-type chart is more desirable, and, no doubt, more correct for use at elevated temperatures than the Windenburg charts now in the Code. However, the new charts should be constructed using the two correction factors introduced by Dr. Windenburg and which have been in the Code Rules for vessels subject to external pressure, since their inception. These factors were based both on theoretical consideration and experience, and to bring the Bresse-Bryan theoretical formula in agreement with the Stewart formula which was developed from experimental research.

In regard to the construction of the Code chart, the author states that a constant modulus of elasticity was used up to the yield point and that the straight-line segments were connected by short arbitrarily drawn transition curves. This is not quite correct as Dr. Windenburg did consider the stress-strain curve for steel at room temperature, and the transition curves are supposedly tangent to the sloping lines at points where the stress equals the proportional limit.

Equation [5] of the paper is Stewart's empirical equation for cylindrical vessels having a t/D -ratio above 0.023, and made of steel having a yield strength of 37,000 psi. Dr. Windenburg, in reference (8), gives an equation [4c], by which the strength of a vessel with known mechanical properties can be determined. By this formula, the Stewart formula for a steel with a 27,500-psi yield strength becomes

$$p = 64,460 (t/D) - 901$$

⁶ Supervising Engineer, The Texas Company, New York, N. Y. Mem. ASME.

Referring to the upper limit of the Bresse-Bryan Formula [2] or the Stewart Formula [4], in 1946 Dr. Dana Young developed the following formula to determine this upper limit

$$t/D = 0.682 (S_y/E)^{1/2}$$

According to this formula, the upper limit buckling for a 27,500-psi yield-strength steel vessel would be $t/D = 0.021$ instead of 0.035 as given in the paper.

The method outlined for the design of heads should prove quite satisfactory.

It is the writer's feeling that in the construction of the new chart all of the present code precepts, notations, and range of the chart should be retained.

A word about the material lines for carbon steel to be put on the new chart. This is not an easy task, as the stress-strain curves available are on material that is much stronger than specified, and, therefore, must be reduced. Also, since the proportional limit and yield strength start to reduce at temperatures above 100 F, it means that material curves must be developed for frequent temperature intervals.

MARSHALL HOLT.⁷ The interpretation and revision of the Boiler Code in the years to come will be facilitated because of the recording of the development of this new type of chart. There are some points, however, that need further clarification.

The author has made a poor choice of words in differentiating between the stress-strain curve of mild steel as being linear and those of the other materials of construction as being "nonlinear." Fig. 6 of this discussion shows parts of stress-strain curves for a number of materials.⁷ It will be seen that each of them has a linear portion for small stresses while the departures from the

⁶ Assistant Chief, Engineering Design Division, Aluminum Research Laboratories, New Kensington, Pa. Mem. ASME.

⁷ Fig. 2 of "Some Stress-Strain Studies of Metals," by R. L. Templin and R. G. Sturm, *Journal of the Aeronautical Sciences*, vol. 7, 1940, pp. 189-198.

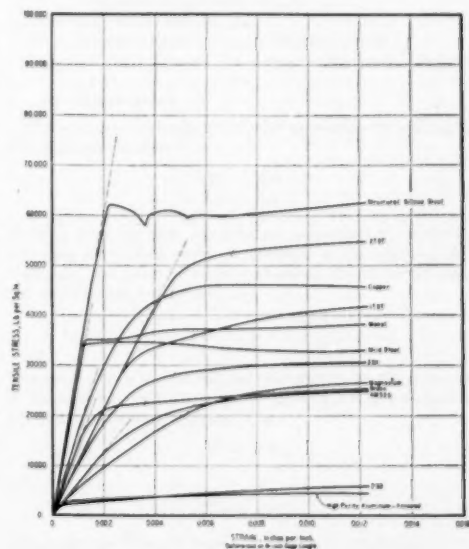


FIG. 6 PART OF STRESS-STRAIN CURVES FOR SEVERAL MATERIALS

initial slopes are more or less rapid. In the case of mild steel and Monel, the departures are quite rapid while, for the other materials, the departure is more or less gradual. Judging from these curves, one cannot differentiate any as being linear and others as being nonlinear.

The author is incorrect in stating that charts of the type of Fig. 1 cannot be used with materials having stress-strain curves that depart gradually from the initial slope. Such curves are given in the author's references (5) and (11). The new type of chart lacks the one desirable feature contained in charts of the type of Fig. 1, that is, it is not direct reading. The necessity for the new type of chart arose from the fact that the type of chart in Fig. 1 is valid for only one material and for only one temperature range; consequently each material and each temperature to be considered in Section VIII would require a separate chart. Obviously, with the expansion of the Code to cover additional materials, the number of charts required to cover adequately these materials and the temperature ranges would be excessive. The new type of chart, while not direct-reading, covers the whole temperature range for one or more tempers of a given material.

The author points out that the direct-reading chart of Sturm and O'Brien for A-nickel at room temperature appears to be "warped into the more familiar shape of the curves in Fig. 1" for mild steel. In view of the variety of stress-strain curves shown in Fig. 6 of this discussion it should not be surprising that some charts are very much alike and others quite different.

AUTHOR'S CLOSURE

The author wishes to thank the discussers for their contribution to a better understanding of the new-type code chart. It is grati-

fying that the objections are on the manner of presentation and not on the method of developing the chart.

Mr. Hartman points out that the geometry lines may be based either on the work by Windenburg and Trilling or that by Sturm. The author used Sturm's work in his original development of the chart. The equation of Windenburg and Trilling was used in the paper because it simplified the explanation of the method of developing the chart.

Since the paper was presented, the Subcommittee on Vessels Under External Pressure has considered the points listed in the section preceding the summary to the paper. Mr. Hartman states the action taken by the Subcommittee.

Mr. Higgins discusses the basis for the Windenburg-type charts now in the Code. He points out quite correctly that the author's use of the term, arbitrarily drawn transition curves, does not correctly describe the method of constructing the transition portion of the curves. He gives two formulas from reference (9) to indicate that the upper limit of buckling occurs at a t/D -value of 0.021. These equations are developed mathematically from an empirical equation proposed by Stewart (9). Since the test points on which Stewart's expression was based were for the most part in the region of plastic flow, the validity of these derived equations is open to question.

While the term, nonlinear, as applied to stress-strain diagrams, was borrowed from one of the reference papers, the author can find no fault with Dr. Holt's objection that it is a poor choice of words. In connection with the discussion of Fig. 1, the statement was made that the chart cannot be used directly with materials having stress-strain curves that depart gradually from the initial slope. Reference was made to two methods which make indirect use of the charts.

A Procedure for Determining the Allowable Out-of-Roundness for Vessels Under External Pressure

By MARSHALL HOLT,¹ NEW KENSINGTON, PA.

The procedure developed in the paper is based on the theory of thin shells developed by Dr. R. G. Sturm.² The formula for determining the allowable out-of-roundness contains two factors, one based on the proportions of the shell and the other based on the properties of the material as measured by the allowable design stress. The procedure is applicable to elevated as well as to room temperatures.

INTRODUCTION

ALTHOUGH the allowable working pressures for vessels under external pressure are usually computed by means of a theory that assumes mathematical perfection of form, it is practically impossible to fabricate such perfect vessels. Therefore it is expedient that a certain degree of imperfection be tolerated in the construction of commercial pressure vessels. This situation is recognized by the ASME Boiler Construction Code in that rules are given for determining the allowable out-of-roundness.

The present rules and chart in the Boiler Construction Code were developed by The Special Research Committee on the Strength of Vessels Under External Pressure, largely through the efforts of Dr. D. F. Windenburg and under the chairmanship of Mr. W. D. Halsey.³ They were intended for use with carbon and low-alloy steels. The problem of allowable out-of-roundness is revived by the extension of the Code to include nonferrous materials and high-alloy steels. In developing new charts for the new materials it would seem desirable to follow a procedure that is applicable to all materials and needs only a single factor which is developed from the mechanical properties of the particular material under consideration.

It is the purpose of this paper to develop a procedure for computing the allowable out-of-roundness of a cylindrical vessel subjected to external pressure and to illustrate the application.

OUTLINE OF PROCEDURE

The fundamental theory to be used in this study was developed by Dr. R. G. Sturm.² In addition to formulas and coefficients for the collapse of perfect cylinders, an equation is given for computing the ultimate pressure for a vessel having an initial

out-of-roundness of the same shape as the buckle pattern of a perfect shell. In the case under consideration, as the pressure increases, the out-of-roundness merely increases in magnitude until the stresses reach a value analogous to modulus of failure, at which time the external pressure reaches a maximum value. This behavior is similar to that of an eccentrically loaded or crooked column.

The equation for computing the strength of a shell with the prescribed out-of-roundness is

$$\bar{W} = \frac{2S \frac{t}{D}}{1 + \frac{4A_e}{t} \frac{E \left(N^2 - 1 + \mu \frac{\pi^2 D^2}{4L^2} \right) \frac{t^3}{D^3}}{(1 - \mu^2)(W_c - \bar{W})}} \quad [1]$$

in which

- \bar{W} = maximum pressure for out-of-round cylinder, psi
- S = maximum stress that can be developed in the shell wall, corresponds to the modulus of failure, psi
- t = wall thickness, in.
- D = outside diameter, in.
- A_e = out-of-roundness or maximum deviation from radius of corresponding perfect shell, in.
- E = modulus of elasticity, psi
- N = number of lobes in out-of-roundness pattern
- W_c = collapsing pressure for corresponding perfect cylinder, psi
- μ = Poisson's ratio

This equation can be given a simpler appearance by making the following substitutions

$$(a) \quad \frac{W_c}{K} = \frac{Et^3}{D^3} \quad [2]$$

which is from the basic equation for computing the collapsing pressures for perfect circular cylindrical shells, where K is a coefficient, the value of which depends on the proportions and not on the material of the shell

$$(b) \quad M = N^2 - 1 + \mu \frac{\pi^2 D^2}{4L^2} \quad [3]$$

The value of this term is affected only slightly by the properties of the material; since the range of values of μ is rather small for the common materials of construction.

$$(c) \quad \bar{W} = \alpha W_c \quad [4]$$

and

$$(d) \quad \mu = 1/\lambda \quad [5]$$

This value for Poisson's ratio is a reasonable approximation for the range of values for the materials under consideration.

Now Equation [1] can be rewritten as

¹ Assistant Chief, Engineering Design Division, Aluminum Research Laboratories. Mem. ASME.

² "A Study of the Collapsing Pressure of Thin-Walled Cylinders," by R. G. Sturm, University of Illinois Engineering Experiment Station Bulletin No. 329.

³ "Vessels Under External Pressure," by D. F. Windenburg, *Mechanical Engineering*, vol. 59, 1937, pp. 601-608.

Contributed by the Committee on Strength of Vessels Under External Pressure and presented at the Annual Meeting, Atlantic City, N. J., November 25-30, 1951, of THE AMERICAN SOCIETY OF MECHANICAL ENGINEERS.

NOTE: Statements and opinions advanced in papers are to be understood as individual expressions of their authors and not those of the Society. Manuscript received at ASME Headquarters, Sept. 18, 1951. Paper No. 51-A-136.

$$\alpha W_e = \frac{2S}{1 + \frac{4A_e}{t} \frac{9M}{8K(1-\alpha)}} \quad [6]$$

Whence

$$\frac{A_e}{t} = \left(\frac{2S}{\alpha W_e} - 1 \right) \frac{2K(1-\alpha)}{9M} \quad [7]$$

and

$$A_e = tQ \left(\frac{2S}{\alpha W_e} - 1 \right) \quad [8]$$

in which

$$Q = \frac{2K(1-\alpha)}{9M} \quad [9]$$

It should be noted that the value of Q depends on the proportions of the shell and the reduction in strength produced by the out-of-roundness and is only slightly affected by the material from which the vessel is made.

It has been the policy of the Boiler Code Committee to allow an out-of-roundness that reduces the ultimate pressure to 80 per cent of that of the corresponding perfect shell. Thus, taking α equal to 0.8 and values of K and N from Sturm,³ the variation of Q with the proportions of the vessel can be shown. This is done in Fig. 1 where it can be seen that the value of Q can be represented for practical purposes by a single curve. It should be borne in mind that the plotted points are computed values and not test results. For further use in this paper the curve mentioned is shown in Fig. 2.

The term within the parentheses of Equation [8] involves the material, since the value of S is probably closely related to the tensile strength of the material and the value of W_e depends on the effective modulus of the material.

Tests on beams of wide rectangular cross section indicate that the modulus of failure is greater than the tensile strength of the material; hence Sturm³ suggests that S be taken as 15 per cent greater than the tensile strength. In view of the fact that the tensile strength varies with the temperature and is different for each of the materials under consideration, it would appear necessary to have a curve for each material giving the tensile strengths at various temperatures. Since most of the allowable design stresses in the Code are controlled by the tensile strength, it seems reasonable to use the ratio of the design stress to the design pressure rather than the ratio of the modulus of failure to the collapsing pressure. Any irregularities brought about by the design stress being controlled by the yield strength of the material rather than the tensile strength will be on the conservative side.

Equation [8] is thus reduced to

$$A_e = tQ \left(\frac{3S}{P} - 1 \right) \quad [10]$$

in which S = design stress at the operating temperature, psi, P = design pressure, psi, and the other terms as defined previously. The factor 3 arises from taking the modulus of failure as 20 per cent greater than the tensile strength. If the 15 per cent increase suggested by Sturm³ had been used, this factor would have been 2.88. The implied accuracy of this value is not warranted.

It should be pointed out that A_e is the maximum radial deviation from a perfect circle when measured over an arc length corresponding to one-half lobe length of the out-of-roundness

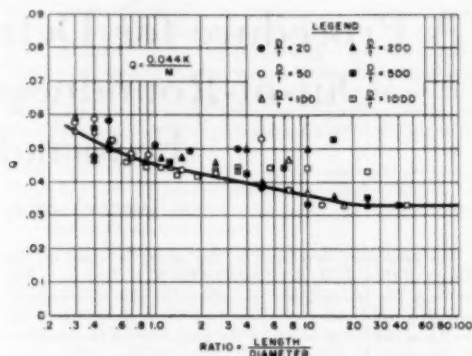


FIG. 1 VARIATION OF Q WITH PROPORTIONS OF SHELL

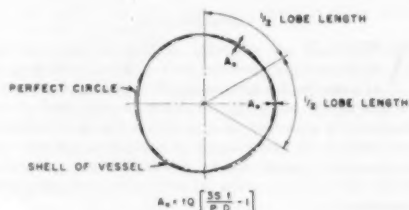


FIG. 2 VALUES OF Q FOR DETERMINING ALLOWABLE OUT-OF-ROUNDNESS

pattern. In the case of an even number of lobes this is also one fourth of the difference between the maximum and minimum diameters. For odd numbers of lobes this relation does not hold.

The number of lobes into which a circular cylinder will buckle is a function of the proportions of the shell and not of the material of which it is made. The arc length of a complete lobe can be deduced from the number of lobes as follows

$$\text{arc length} = \theta R = \frac{2\pi R}{N} = \frac{\pi D}{N} \quad [11]$$

The arc length and chord length corresponding to one-half lobe can be determined by the following equations

$$A = \text{arc length of one-half lobe} = \frac{\pi D}{2N} \quad [12]$$

$$C = \text{chord length of one-half lobe} = D \sin \frac{\pi}{2N} \quad [13]$$

The values of N given by Sturm³ lead to the chart shown in Fig. 3 where the various fields represent a given number of lobes,

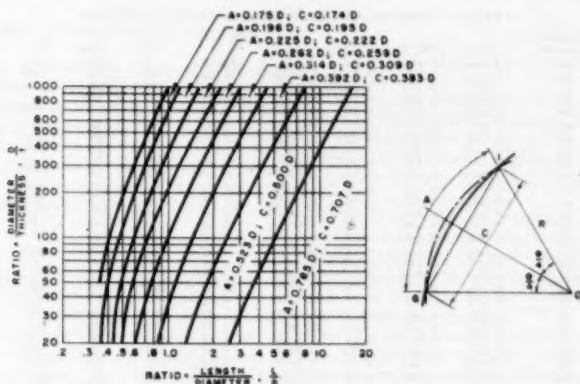


FIG. 3 CHART FOR DETERMINING ARC LENGTH OR CHORD LENGTH OVER WHICH OUT-OF-ROUNDNESS IS TO BE MEASURED

and the indicated values of arc length and chord length correspond to all the ratios of length to diameter and diameter to thickness defined by points within the field.

PROPOSED PARAGRAPH FOR CODE USE

The paragraph to be used in the new Code might be as follows:

Par. UG-80(b) For vessels operating under external pressure, the shell shall be so constructed that the out-of-roundness does not exceed the value computed by the formula

$$A_o = tQ \left(\frac{3S}{P D} - 1 \right)$$

in which

A_o = maximum plus or minus deviation from the true circular form measured on outside or inside of vessel, using an arc or chord length defined by Fig. 3

t = thickness of shell course under consideration (exclusive of corrosion allowance), in.

Q = factor defined by Fig. 2

S = maximum allowable design stress for material and temperature under consideration, psi

P = external design pressure, psi

D = outside diameter of shell course under consideration, in.

ILLUSTRATION

To illustrate the use of this proposed rule, consider the example worked out in Par. UA-271 of the 1950 edition of Section VIII. The data given are

$$\frac{L}{D} = 1.5$$

$$t = 0.41 \text{ in.}$$

$$D = 96 \text{ in.}$$

$$\frac{t}{D} = 0.00425$$

$$P = 15 \text{ psi}$$

From Table UG-23, the value of S will be taken as 13,750 psi. In Fig. 2 the value of Q is found to be 0.044. Equation [10] now yields

$$A_o = 0.41(0.044) \left[\frac{3(13,750)(0.00425)}{15} - 1 \right] = 0.192 \text{ in.}$$

The arc length over which the out-of-roundness is to be measured is found from Fig. 3 to be 0.314 D or 30.1 in., while the chord length is 0.309 D or 29.7 in. The corresponding values in Par. UA-271 are as follows:

Allowable out-of-roundness = 0.369 in.

Reference chord length = 25.92 in.

By comparison, the proposed procedure allows approximately 50 per cent as much out-of-roundness as the 1950 edition of Section VIII. It should be pointed out, however, that the 1950 edition liberalized the requirements for out-of-roundness as compared to the 1949 edition. For vessels that collapse into an even number of lobes, the liberalization amounted to a fourfold increase in allowable out-of-roundness. Since the vessel in this example would be expected to collapse into five lobes, the liberalization in the 1950 edition would not be exactly 4 to 1. It is to be expected, however, that the proposed method is more liberal and conforms better to theory than the 1949 edition. The lengths of the reference chords by the proposed procedure and the 1950 edition are practically the same.

If this carbon-steel vessel were to operate at 850 F, the required shell thickness would be increased by the rules of Par. UA-33 to 0.470 in. Since the 1950 edition gives no rules for determining allowable out-of-roundness at elevated temperatures, the rules of Par. UG-80(b) might be expected to govern. In this case, the allowable out-of-roundness would be 0.8 t or 0.376 in., or slightly greater than for operation at room temperature. The proposed procedure leads to a value of 0.137 in. or only 71 per cent as much as for operation at room temperature. This relatively great reduction in allowable out-of-roundness results from the reduction in the modulus of failure as reflected in the design stress at the elevated temperature.

Discussion

E. O. BERGMAN.¹ The purpose of the author is to develop a procedure for computing the allowable out-of-roundness of cylindrical vessels that can be applied to all materials and operating

¹ Consulting Engineer, C. F. Braun & Company, Alhambra, Calif. Mem. ASME.

TABLE 1 COMPARISON WITH EXPERIMENTAL RESULTS

Model number	L/D	$100t/D$	A_o/t	Q	$A_o + 1$	P_{ecc}	P_{exp}	P_{AS}
63	2.000	0.193	0.94	0.0420	43.40	8	10	7*
33	1.000	0.197	0.74	0.0450	17.50	18	14	13*
37	1.000	0.192	0.39	0.0450	9.65	38	13	13*
54	0.500	0.190	0.28	0.0500	6.20	50	23*	26
56	0.484	0.200	0.16	0.0490	4.26	77	31	28*
55	0.250	0.200	0.47	0.0570	9.25	36*	48	56
40	2.000	0.312	0.47	0.0429	12.20	42	25	23*
41	1.500	0.330	...	0.0455	39	34*
49	1.500	0.318	0.53	0.0455	13.20	40	36	31*
42	1.000	0.330	0.32	0.0450	8.10	67	58	50*
51	0.937	0.312	0.33	0.0455	8.25	62	54	45*
47	0.750	0.315	0.16	0.0470	4.40	118	65	56*
31	0.547	0.297	0.50	0.0490	11.20	44*	66	69
43	0.500	0.324	0.27	0.0500	8.40	64*	94	92
45	0.500	0.318	0.25	0.0500	6.00	88*	96	97
52	0.500	0.305	0.18	0.0500	4.60	110	84	82*
32	0.375	0.318	0.33	0.0520	7.35	72*	107	119
33	0.250	0.321	0.11	0.0570	2.83	181	139*	190
44	0.250	0.323	0.19	0.0570	4.33	123*	139	192
46	0.250	0.319	0.13	0.0570	3.28	181*	163	206
48	0.187	0.307	0.22	0.0600	4.67	109*	168	235
50	0.125	0.280	0.16	0.0660	3.43	135*	195	300
61	2.000	0.395	0.14	0.0420	4.33	150	48	39*
59	1.000	0.399	0.22	0.0450	5.90	111	89	81*
62	1.000	0.403	0.12	0.0450	3.67	181	89	83*
58	0.500	0.395	0.16	0.0500	4.20	155*	159	163
60	0.250	0.386	0.11	0.0570	2.93	217	199*	347
65	2.000	0.470	0.32	0.0420	8.63	90	67	60*
64	1.000	0.487	0.41	0.0450	10.10	80*	129	142
66	0.500	0.483	0.06	0.0500	2.20	362	235*	278
68	2.000	0.591	0.32	0.0420	8.63	113	112	107*
67	1.000	0.580	0.15	0.0450	4.33	222	209	200*
73	0.500	0.560	...	0.0500	281*	380
70	2.000	0.678	0.13	0.0420	4.57	244	149*	150
69	1.000	0.670	0.16	0.0450	4.55	243*	288	298
71	0.500	0.649	0.14	0.0500	3.80	282*	327	570

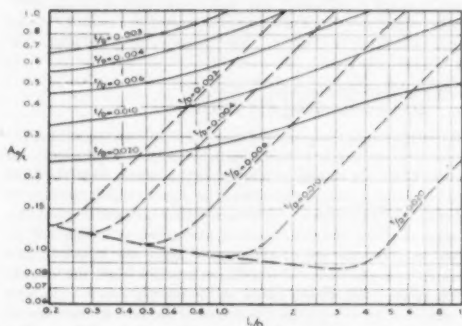


FIG. 4 COMPARISON OF PROPOSED METHOD WITH METHOD USED IN SECTION VIII OF ASME CODE (Solid lines represent Code values; dash lines show proposed values.)

temperatures. This procedure is embodied in his Equation [10] and Fig. 2.

The author compares his method with that of the ASME Boiler Code by applying it to the illustrative example in Par. UA-271 of Section VIII. Fig. 4 of this discussion has been prepared to show how the methods compare over the entire range covered by Fig. UG-80.1 of the Code.

The curves in Fig. 4 represent t/D -values in place of A_o/t -values as in Fig. UG-80.1. This change has been made to facilitate the computation of values for the curves representing the author's method. Values of A_o/t greater than 1.0 are not shown to agree with Fig. UG-80.1. The Code requirement, that the difference between the maximum and minimum diameters shall not exceed 1 per cent of the nominal diameter, limits the out-of-roundness to the following values:

t/D ...	0.003	0.004	0.006	0.010	0.020
A_o/t ...	0.833	0.625	0.417	0.250	0.125

Fig. 4, herewith, shows that for low values of L/D , the permissible out-of-roundness by the author's procedure drops to less than one fourth of that permitted by the Code.

The validity of the proposed procedure can be checked by means of experimental results reported by Windenburg and Trilling.⁵ An expression for the collapsing pressure of an out-of-round vessel is obtained by introducing a factor of 4 in Equation [10] of the paper, and writing it in the form

$$P_{ecc} = \frac{12S}{A_o + 1} \frac{t}{D}$$

Table 1 of this discussion gives data from Windenburg and Trilling's Table 3, including the collapsing pressure at failure, P_{exp} , and the collapsing pressure, P_{AS} , computed by the Windenburg formula now used in the Code. The pressure, P_{ecc} , for collapse of an out-of-round vessel is also given. The lowest of the three pressures for each test model is indicated by an asterisk.

It will be noted that the models for which P_{ecc} is the smallest value, all have small values of L/D , for the most part 0.50 or less. In all except Model 43, the test pressure was less than that figured by the formula for collapse—in many cases, considerably less. The tests show that the reduced values for out-of-roundness given by the proposed procedure are in the right direction.

The present Code rules make no provision for designing vessels with an out-of-roundness, A_o/t , greater than 1.0. It is sometimes necessary to provide for greater values, as in austenitic stainless-steel vessels quenched from high temperatures. The proposed method will make it possible to design vessels for specified values of out-of-roundness.

M. B. HIGGINS.⁶ As author of the rules covering out-of-roundness tolerances in the Code, the writer comments as follows:

The rules in the Construction Code cover a new vessel that has not been subjected to external pressure. The requirement that the difference between the maximum and minimum diameters of a section shall not exceed 1 per cent of the nominal diameter for

⁵ "Collapse by Instability of Thin Cylindrical Shells Under External Pressure," by D. F. Windenburg and C. Trilling, Trans. ASME, vol. 56, 1934, p. 819.

⁶ Supervising Engineer, The Texas Company, New York, N. Y. Mem. ASME.

that section, is for the purpose of eliminating any serious general out-of-roundness.

The second requirement to be met by vessels that are to be subjected to external pressure in service is to detect any bulges or flat spots in the plates that may have occurred during fabrication. At the time this rule was proposed, it was critically reviewed by Drs. Windenburg, Jacobus, and Sturm, and approved by the Special Research Committee on the Strength of Vessels Under External Pressure. The requirement to be met is on the safe side, as the length of the chord specified is twice as long as theoretically necessary.

R. G. STURM.⁷ The author is to be congratulated on developing and presenting such a very clever and useful arrangement of the quantities involved in the collapse of out-of-round vessels. The separation of the terms representing the geometry of the vessel from those governed, primarily, by the properties of the material is of particular value. Such a separation permits consideration of vessels of different materials without duplicating all of the work. His arrangement of the geometric terms so as to obtain a single curve simplifies the problem of presenting rules in the Code.

In determining the out-of-roundness as proposed by the author, it may be desirable to devise a special out-of-roundness meter which can be set up quickly to correspond to a predetermined number of lobes and to a given average diameter of vessel. The writer believes that the intelligent use of such an instrument on vessels that appear to be anomalous at the present time would clarify much of the foggy nature now linked with experience data.

An out-of-roundness pattern that does not agree reasonably well with the natural pattern of collapse for two or more lobes produces a much smaller reduction in strength than if the same out-of-roundness did agree with the pattern of collapse. Disagreement might be in the longitudinal pattern as well as in the circumferential pattern.

The author is correct, however, in basing his design charts on an out-of-roundness pattern that does agree with the collapse pattern, because this is the worst condition. Since out-of-roundness patterns are completely fortuitous, it is possible that at some part of the vessel the conformity might exist.

⁷ Director, Auburn Research Foundation and Engineering Experiment Station, Alabama Polytechnic Institute, Auburn, Ala. Mem. ASME.

AUTHOR'S CLOSURE

The author wishes to thank the discussers for their contributions.

Dr. Bergman's comparison of the proposed requirements and those in Par. UG-80 of Section VIII, 1950 edition, might lead some people to think the proposal is ultraconservative. On the other hand, the data from the paper by Windenburg and Trilling which Dr. Bergman has introduced can be used to show that the proposal is quite reasonable.

Table 2 lists those specimens in Dr. Bergman's Table 1 which failed at average stresses less than 27,500 psi, the probable yield strength of the material used. The computed bursting pressures were obtained by the theory presented in reference 2; first, on the basis that the edges of the tubes were simply supported, and second, that they were fixed. Since many of the test results are greater than the values computed on the basis of simply supported edges and also greater than the value of P_{21} in Table 1, it appears that the condition of fixed edges or, at least, restrained edges prevailed in many cases.

Two values of allowable out-of-roundness also have been determined and compared with the measured out-of-roundness in the last two columns of Table 2. The two values arise from the use of the two values of computed collapsing pressure. The value of S was taken as 55,000 psi.

Fig. 5 shows the relation between the ratios of the computed

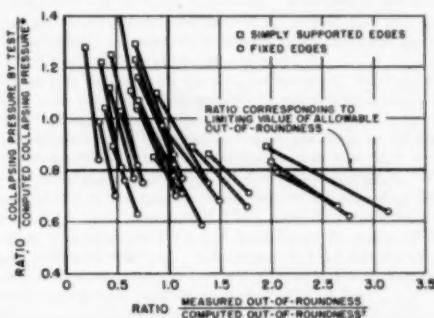


FIG. 5 RATIOS OF MEASURED AND COMPUTED COLLAPSING PRESSURES AND OUT-OF-ROUNDNESSES

TABLE 2 COMPARISON WITH EXPERIMENTAL RESULTS

Spec. no.	L/D	100/L/D	Collapsing pressure, psi			Out-of-Roundness						
			Computed			Computed						
			Simply supported edges	Fixed edges	Test result	Ratio		Simply supported edges	Fixed edges	Measured	Ratio	
			P_1	P_2	P	P/P_1	P/P_2	A_1	A_2	A_3	A_2/A_1	A_3/A_1
63	2.000	0.193	6.3	9.6	10.	1.50	1.04	2.08	1.33	0.94	0.45	0.70
53	1.000	0.197	13.3	19.9	14.	1.05	0.70	1.03	0.69	0.74	0.70	1.07
57	1.000	0.192	12.3	18.5	15.	1.22	0.81	1.11	0.73	0.94	0.35	0.53
54	0.500	0.190	25.8	38.6	22.	0.89	0.63	0.56	0.71	0.29	0.47	0.70
56	0.484	0.200	31.2	44.0	31.	0.99	0.70	0.49	0.33	0.16	0.33	0.48
40	2.000	0.312	29.0	30.4	25.	1.25	0.82	1.04	0.67	0.47	0.45	0.70
49	1.500	0.318	28.0	41.9	30.	1.29	0.86	0.77	0.60	0.53	0.69	1.06
42	1.000	0.330	50.0	75.0	38.	1.16	0.77	0.43	0.28	0.32	0.71	1.14
51	0.937	0.312	44.0	66.0	54.	1.23	0.82	0.49	0.31	0.33	0.67	1.06
47	0.750	0.315	58.0	84.2	65.	1.12	0.77	0.37	0.24	0.16	0.43	0.67
31	0.547	0.297	79.7	109.	66.	0.83	0.62	0.25	0.18	0.20	0.50	2.77
43	0.500	0.324	118.	143.	94.	0.79	0.68	0.18	0.14	0.37	2.06	2.64
45	0.500	0.318	112.	135.	96.	0.86	0.71	0.18	0.14	0.25	1.39	1.78
52	0.500	0.305	99.	119.	84.	0.85	0.71	0.21	0.16	0.18	0.86	1.13
61	2.000	0.395	37.5	57.1	45.	1.28	0.84	0.69	0.44	0.14	0.20	0.32
59	1.000	0.399	83.0	114.	89.	1.07	0.78	0.31	0.21	0.22	0.71	1.05
62	1.000	0.403	85.2	117.	89.	1.04	0.76	0.31	0.21	0.12	0.39	0.57
58	0.500	0.395	179.	241.	159.	0.89	0.66	0.13	0.09	0.16	1.23	1.77
65	2.000	0.470	60.2	114.	67.	1.11	0.69	0.50	0.34	0.32	0.64	1.53
64	1.000	0.487	144.	201.	129.	0.89	0.64	0.21	0.13	0.41	1.95	3.15
68	2.000	0.591	102.	149.	112.	1.10	0.75	0.36	0.23	0.32	0.89	1.39
67	1.000	0.580	213.	306.	209.	0.97	0.68	0.16	0.10	0.13	0.94	1.50
70	2.000	0.678	144.	198.	149.	1.03	0.75	0.28	0.20	0.15	0.54	0.75

and measured pressures and out-of-roundnesses. The points represented by the pairs of ratios determined for the two edge conditions are connected by a straight line, and it is reasonable to believe that the true relation is represented by some point on the line. The data indicate that the collapsing pressure decreases as the out-of-roundness increases. If the data supported the proposal exactly, there would be no data points in the quadrant defined by the ratio of pressures less than 0.8 and the ratio of out-of-roundnesses less than 1.0, nor in the opposite quadrant defined by the ratio of pressures greater than 0.8 and the ratio of out-of-roundnesses greater than 1.0. The fact that 15 of the 23 specimens are correctly graded on the basis of fixed edges indicates that the proposal is quite reasonable. By admitting only slight variations from the condition of fixed edges, one can obtain perfect agreement between the proposal and the test conditions. It is thus shown that the comparisons made by Dr. Bergman in which he omitted the possible effects of restraint at the ends of the specimens may lead to an erroneous conclusion.

Dr. Bergman has showed that the permissible out-of-roundness obtained by the proposed procedure may be as little as one fourth that permitted by the 1950 edition of the Code. This

should not be surprising in view of the fact that between the 1949 and 1950 editions the definition of e was changed but the limits on e were not changed. It is recognized that, in spite of this change, there has been no epidemic of failures; however, the author believes that the factors of safety, in many cases, were lower than anticipated. It is also recognized that, as noted by Mr. Higgins, the present rules were carefully considered by the Special Research Committee on the Strength of Vessels Under External Pressure.

Dr. Sturm's suggestion opens a wide field for the gadgeteer to devise a fixture for making the necessary measurements.

It should be pointed out that the proposed procedure was developed as part of the activity of the Subcommittee on Nonferrous Materials in the preparation of a proposal for the anticipated 1952 edition of the Code which covers many materials for which the rules in the 1950 edition are not satisfactory. It was developed as a branch of a theory which has been satisfactorily verified by tests on vessels of a variety of materials. The adoption of rules such as those proposed would simplify future editions of the expanded Code and would more adequately consider the effects of elevated temperatures.

On the Accuracy of Extrapolated Creep-Test Relations for Plexiglas Subjected to Various Stresses

By JOSEPH MARIN¹ AND YOH-HAN PAO,² STATE COLLEGE, PA.

Most creep-time relations for materials are obtained for short periods of time—usually for 1000 hr or about 40 days. In many applications, however, the life of the member is much greater than 1000 hr. In the design of these members, therefore, it is necessary to provide for creep deformations which cover periods of time much greater than 40 days. To do this, it is common practice to obtain a stress-creep-time empirical relation based on 1000-hr test data, and to extrapolate these relations to periods of time representing the service life of the part. The purpose of this paper is to determine the accuracy of this extrapolation. This is accomplished by comparing the extrapolated tension and compression creep-time relations based on 1000-hr test data with actual 10,000-hr creep-test data. Long-time creep-test data also were obtained for pure bending and pure torsion. These creep-time relations were compared with theoretical values based on empirical relations for 1000-hr tension and compression creep data. For the relations used and for the material tested, it was found that the extrapolated values gave good engineering approximations to the actual values.

INTRODUCTION

It is customary, in design of parts subjected to creep, to determine creep-test data for a period of 1000 hr or about 40 days.

Empirical relations based on this short-time creep data are then extrapolated to determine the creep deformations for longer periods of time equal to the estimated service life of the part. The validity of this extrapolation is questionable. It was the purpose of this study to determine the accuracy of the empirical relations when extrapolated. For this purpose, creep tests covering 10,000 hr and various stresses were conducted, including simple tension, simple compression, pure bending, and pure torsion. In the case of simple tension and compression, empirical creep relations based upon 1000 hr were then extrapolated and compared with the actual creep values at 10,000 hr. Theories developed in references (1)³ and (2) were used to predict bending and torsion creep values up to 10,000 hr. Predicted values were compared with actual 10,000-hr creep values.

The material tested was Plexiglas 1A, manufactured by Rohm and Haas Company. Reported values of the mechanical properties in tension, compression, and flexure are given in Table 1.

TABLE 1 MECHANICAL PROPERTIES OF PLEXIGLAS 1A

Type of stress	Modulus of elasticity E , 10^6 psi	Nominal ultimate strength, 10^4 psi	Nominal fracture strength, 10^4 psi	Ductility, per cent
Tension.....	4.0 to 4.6 ^a	7 to 8 ^b	5.5 to 7.7 ^b	1 to 15 ^c
Compression.....	4.0 to 4.4 ^a	12.5 ^b	12.5 ^b	
Flexure.....	3.85	14.4 ^b		

^a Test data.

^b From technical data supplied by Rohm & Haas Company, as determined by ASTM Standard methods.

^c "Plastics Properties Chart," *Modern Plastics*, 1947.

CREEP-TEST RESULTS

All creep tests were made in a creep laboratory in which the temperature was maintained at 77 ± 2 deg F, and the relative humidity was kept at 50 ± 2 per cent. A humidifier and a dehumidifier with automatic controls were used to maintain constant humidity. A constant temperature was obtained by the use of heating coils with automatic controls.

Creep-time relations for tension, compression, bending, and torsion were obtained using specially designed testing machines as described in references (3) and (1).

The dimensions of the specimens used are given in reference (1). Creep strains in tension were measured to 5×10^{-4} in./in. for a $1\frac{1}{2}$ -in. gage length using SR-4 electric strain gages. The creep strains in compression also were measured using SR-4 gages with a $\frac{1}{2}$ -in. gage length. The creep deflections for pure bending were measured for a 2-in. gage length by means of dial gages reading to 0.0001 in. The angles of twist for the creep-torsion tests were measured over a 4-in. gage length by means of twistmeters equipped with verniers reading to 0.1 deg.

Deformation-time relations are shown in Figs. 1, 2, 3, and 4 for tension, compression, bending, and torsion. Values of the deformations are for periods of time up to 10,000 hr. In keeping with usual practice, the sum of the elastic and creep deformations are shown. Creep-time relations are given in Figs. 1 to 4, for various stress values. In Figs. 3 and 4 for bending and torsion, the stress values given are the values calculated by the elastic theory for the outer fibers and are not the actual stress values.

INTERPRETATIONS OF SHORT-TIME TENSION AND COMPRESSION CREEP TESTS

The creep-time relations in Figs. 1 to 4 show that after the initial creep the rate of change of creep with time or creep rate remains essentially constant and, for engineering design purposes, the creep-time relation may be assumed linear. Using data as represented in Fig. 1, for simple tension, various methods of interpretation have been developed (4, 5) for defining the creep deformation in terms of the stress and time. In selecting an analytical expression for this purpose, complicated expressions of various types can be selected that fit well a given set of test data. The objective in the present investigation is to use an empirical relation which represents a good approximation of the test data and, at the same time, is not so complicated that it

¹ Professor of Engineering Mechanics and Research, The Pennsylvania State College. Mem ASME.

² Research Assistant, Department of Engineering Mechanics, The Pennsylvania State College.

³ Numbers in parentheses refer to the Bibliography at the end of the paper.

Contributed by the Rubber and Plastics Division and presented at the Annual Meeting, Atlantic City, N. J., November 25-30, 1951, of THE AMERICAN SOCIETY OF MECHANICAL ENGINEERS.

NOTE: Statements and opinions advanced in papers are to be understood as individual expressions of their authors and not those of the Society. Manuscript received at ASME Headquarters, November 21, 1951.

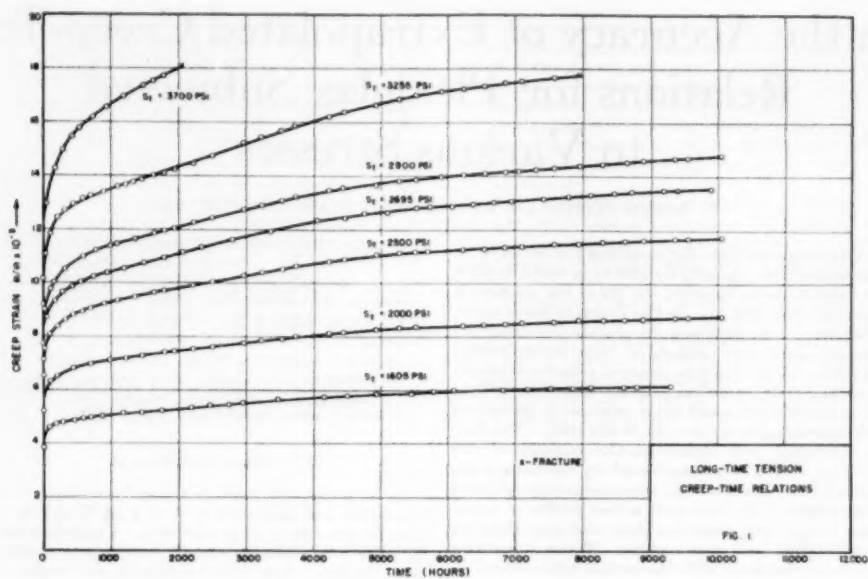


FIG. 1

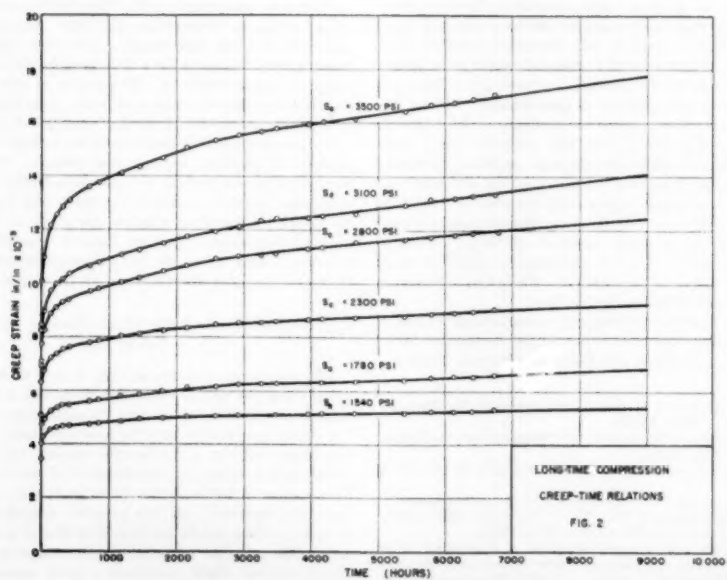


FIG. 2

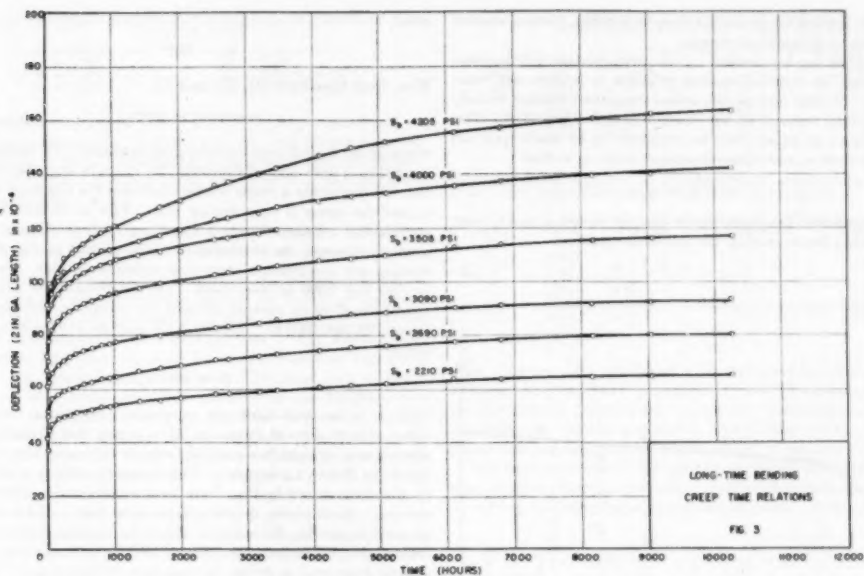


FIG. 3

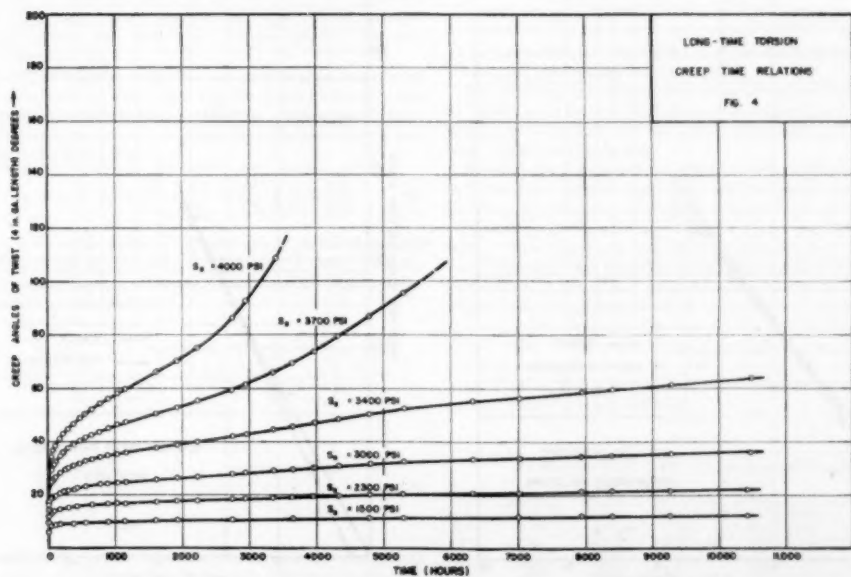


FIG. 4

cannot be applied for predicting creep in bending, torsion, and for various states of combined stresses.

A modified log-log method (1) of interpretation will be used for defining the stress-creep-time relations in tension and compression. By this method the actual creep-time relation *O-A-B*, Fig. 5, will be replaced by the straight lines *O-D* and *D-B*. The creep strain ϵ at a time t can be considered to be made up of an intercept strain ϵ_0 and a time-dependent strain ϵ_p , so that

$$\epsilon = \epsilon_0 + \epsilon_p \quad [1]$$

Considerable test data have shown that the strains ϵ_0 and ϵ_p may be related to the stress S by the following equations

$$\epsilon_0 = D S^m \quad [2]$$

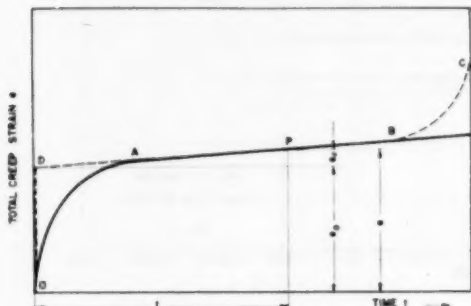


FIG. 5 ASSUMED CREEP-TIME RELATION

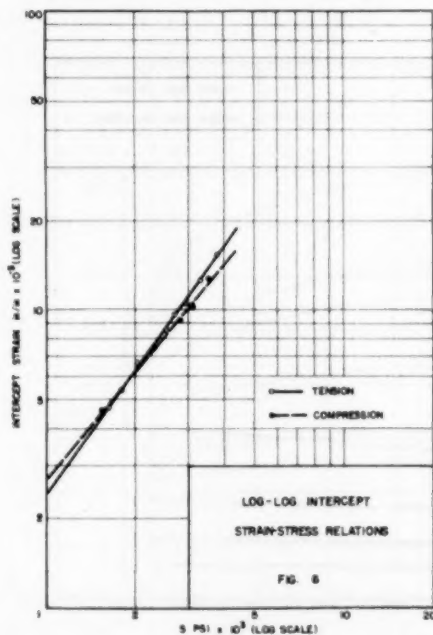


FIG. 6

and

$$\epsilon_p = B S^n \quad [3]$$

Then from Equations (1), (2), and (3)

$$\epsilon = D S^m + B S^n \quad [4]$$

where D , m , B , and n are experimental constants. By taking the logarithm of both sides of Equation (2), it can be seen that Equation (2) represents a linear relation between the intercept strain ϵ_0 and the stress S on a log-log plot. This is verified by the straight-line relations shown in Fig. 6 for both tensile and compressive stresses. In obtaining the data plotted in Fig. 6, the tension and compression creep-time relations in Figs. 1 and 2, for the first 1000 hr were used. The intercepts also were obtained based on an average straight-line creep-time relation between 700 and 1000 hr. Equation (3) may be written as $\epsilon_p/t = BS^n$ or

$$C = BS^n \quad [5]$$

where C = constant minimum creep rate. By taking the logarithm of both sides of Equation (5), it is seen that Equation (5) represents a straight-line relation between the creep rate C and the stress S on a log-log plot. This assumed relation is verified by the plots shown in Fig. 7 for both tensile and compressive stresses. In obtaining the creep rates from Figs. 1 and 2, which are used in plotting the points in Fig. 7, the average slopes of the creep-time relations between 700 and 1000 hr were selected. The straight lines used to define the test data in Figs. 6 and 7 represent the best average of the test points and were obtained by the method of least squares. By the straight lines for tension and

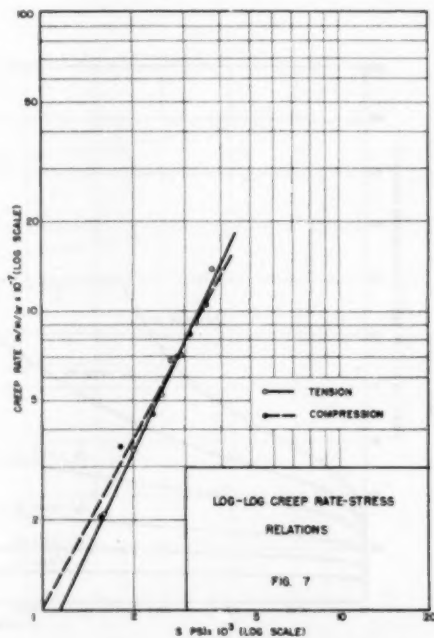


FIG. 7

TABLE 2 VALUES OF CREEP CONSTANTS IN TENSION AND COMPRESSION

$D_t = 2.32 \times 10^{-7}$	$D_c = 6.91 \times 10^{-7}$
$m_t = 1.35$	$m_c = 1.20$
$B_t = 1.83 \times 10^{-11}$	$B_c = 2.49 \times 10^{-11}$
$n_t = 2.19$	$n_c = 1.87$

compression, as given in Figs. 6 and 7, the creep constants D , m , B , and n as expressed in Equations [2], [3], and [5] can be found. The values of these constants for both tension and compression are given in Table 2, based on the first 1000 hr of the creep-time relations of Figs. 1 and 2.

COMPARISON OF THEORETICAL AND ACTUAL LONG-TIME TENSION AND COMPRESSION CREEP-TIME RELATIONS

With the creep constants evaluated in the foregoing, Equation [4] defines the creep-stress-time relation for tension or compression. Then, for any given stress value S , Equation [4] gives the relation between the creep strain ϵ and time t . Fig. 8 shows these theoretical creep-time relations for tension based on Equations [4] for the various stress values used. The solid lines in Fig. 8 represent the actual creep-time relations for the 10,000-hr test period. A comparison between the theoretical relations and actual creep-time relations for tension shows that there is approximate agreement. Table 3 gives a comparison between the theoretical and actual tension creep strains at 10,000 hr. The last column in Table 3 shows that the maximum difference in creep strains is about 20 per cent. Fig. 9 gives a comparison between the theoretical creep-time relations for compression using constants based on 1000-hr tests and the actual creep-time relations. In Table 4 a comparison of the theoretical and actual compression creep strains at 10,000 hr is given for various stress values. The maximum percentage difference is 27.

COMPARISON OF THEORETICAL AND ACTUAL BENDING CREEP-TIME RELATIONS

A theory has been developed by the authors (1) for predicting the creep deflections and creep-deflection rates in bending based upon the tension and compression creep-stress-time relations given in Equation [4].

For a bar of length L subjected to a pure bending moment M at the ends, it can be shown that the center deflection y in terms of the radius of curvature f is $y = (L^2)/(8f)$. In the case of creep, the deflection is made up of two parts, the initial deflection y_0 and the creep deflection y_p , that is

$$y = y_0 + y_p = \frac{L^2}{8f_0} + \frac{L^2}{8f_p} = \left(\frac{L^2}{8}\right)\left(\frac{1}{f_0} + \frac{1}{f_p}\right) \dots [6]$$

where f_0 is the initial radius of curvature and f_p is the creep-time dependent radius of curvature. Reference (1) shows that the value of the curvature f_p is defined by solving the following equations simultaneously to obtain f_p .

$$\left(\frac{1}{f_p D_t}\right)^{\frac{1}{m_t}} \frac{(d - h_t)^{2 + \frac{1}{m_t}}}{\left(2 + \frac{1}{m_t}\right)} + \left(\frac{1}{f_p D_c}\right)^{\frac{1}{m_c}} \frac{(h_t)^{2 + \frac{1}{m_c}}}{\left(2 + \frac{1}{m_c}\right)} = \frac{M}{b} \dots [7]$$

and

$$\frac{(d - h_t)^{\frac{1}{1 + \frac{1}{m_t}}}}{(h_t)^{\frac{1}{1 + \frac{1}{m_t}}}} = \left(\frac{m_c + 1}{m_t + 1}\right) \left(\frac{m_t}{m_c}\right) \frac{(f_p D_t)^{\frac{1}{m_t}}}{(f_p D_c)^{\frac{1}{m_c}}} \dots [8]$$

In Equations [7] and [8], h_t is the distance from the neutral axis to the outer tension fiber; m_t , D_t , m_c , D_c are creep constants in tension and compression corresponding to the constants m and

TABLE 3 COMPARISON OF THEORETICAL AND ACTUAL TENSION-CREEP STRAINS AT 10,000 HR

Spec. no.	Stress, psi	Total creep strains at 10,000 hr		
		Actual, in./in.	Theoretical, in./in.	Difference, per cent
2	2500	11.70×10^{-3}	14.18×10^{-3}	+21
3	2600	14.80	17.42	+15
7	2000	8.78	9.80	+10
8	2695	13.55	16.20	+20
11	1605	6.22	6.82	+10

TABLE 4 COMPARISON OF THEORETICAL AND ACTUAL COMPRESSION-CREEP STRAINS AT 10,000 HR

Spec. no.	Stress, psi	Total creep strains at 10,000 hr		
		Actual, in./in.	Theoretical, in./in.	Difference, per cent
1	1780	7.6×10^{-3}	8.4×10^{-3}	+20
2	1540	5.5	6.9	+20
3	3100	14.4	18.1	+26
4	2800	12.8	16.3	+27
5	2500	9.5	12.1	+27
6	3500	18.3	22.3	+22

D in Equation [2]; and b and d are the width and depth of the specimen cross section. Equations [7] and [8] are based on (a) the stress-creep relations for tension and compression given by Equation [4], (b), the assumption that a plane section remains plane after bending, and (c) the conditions of equilibrium.

In a manner similar to that used for the initial curvature, reference (1) shows that the curvature f_p in Equation [6] is determined by solving the following equations simultaneously to obtain f_p .

$$\left(\frac{1}{f_p D_t}\right)^{\frac{1}{m_t}} \frac{(d - h_t')^{2 + \frac{1}{m_t}}}{\left(2 + \frac{1}{m_t}\right)} + \left(\frac{1}{f_p D_c}\right)^{\frac{1}{m_c}} \frac{(h_t')^{2 + \frac{1}{m_c}}}{\left(2 + \frac{1}{m_c}\right)} = \frac{M}{b} \dots [9]$$

and

$$\frac{(d - h_t')^{\frac{1}{1 + \frac{1}{m_t}}}}{(h_t')^{\frac{1}{1 + \frac{1}{m_c}}}} = \left(\frac{m_c + 1}{m_t + 1}\right) \left(\frac{m_t}{m_c}\right) \frac{(f_p D_t)^{\frac{1}{m_t}}}{(f_p D_c)^{\frac{1}{m_c}}} \dots [10]$$

In Equations [9] and [10], m_t , B_t , m_c , B_c are the creep constants in tension and compression and t is the time.

The predicted deflection y can now be determined by Equation [6] where the values of the radius of curvature f_0 are found by Equations [7] and [8] and the radius of curvature f_p is obtained from Equations [9] and [10].

Based on the tension and compression creep constants, as given in Table 2 for 1000-hr creep data, the theoretical creep deflection-time relations for bending were determined by Equations [6] to [10] for the various values of the moments used in the creep tests. These theoretical relations are compared with the actual creep deflection-time values for a 10,000-hr period in Fig. 10. A comparison of the actual and theoretical creep deflections at 10,000 hr is also given in Table 5. The last column in Table 5 shows that the maximum difference between the theoretical and actual values of the creep deflection at 10,000 hr is 14 per cent. For engineering purposes, this difference indicates good agreement between the predicted theoretical creep-deflection values and the actual values at 10,000 hr.

TABLE 5 COMPARISON OF THEORETICAL AND ACTUAL BENDING-CREEP DEFLECTIONS AT 10,000 HR

Spec. no.	Bending moment M_b , in.-lb	Elastic stress, psi	Creep deflections at 10,000 hr		
			Experimental (in. - 2 in. gage length)	Theoretical	Difference, per cent
2	435	2210	65.8×10^{-3}	67.2×10^{-3}	+2
3	536	2690	81.0	88.8	+10
4	610	3085	93.2	106.7	+14
5	695	3505	117.3	130.0	+11
7	771	4000	142.5	159.8	+12
8	814	4205	153.8	174.5	+8

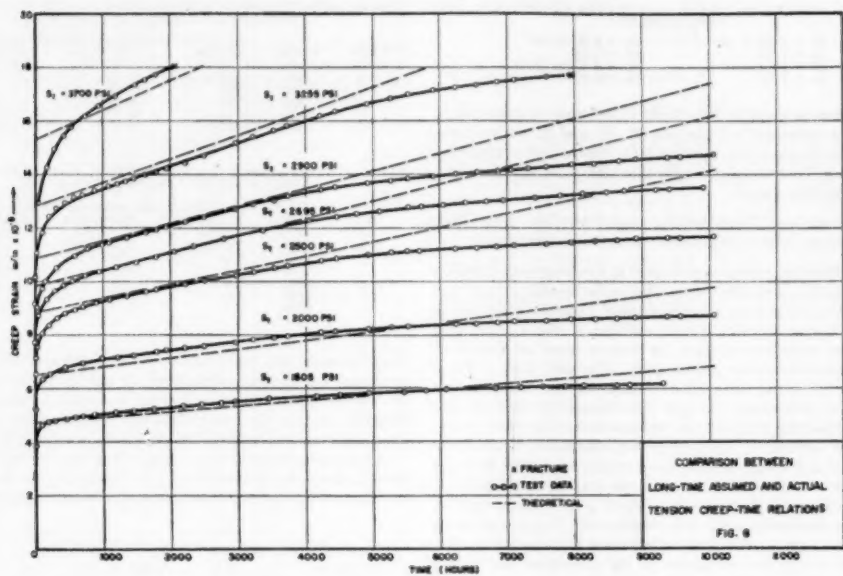


FIG. 8

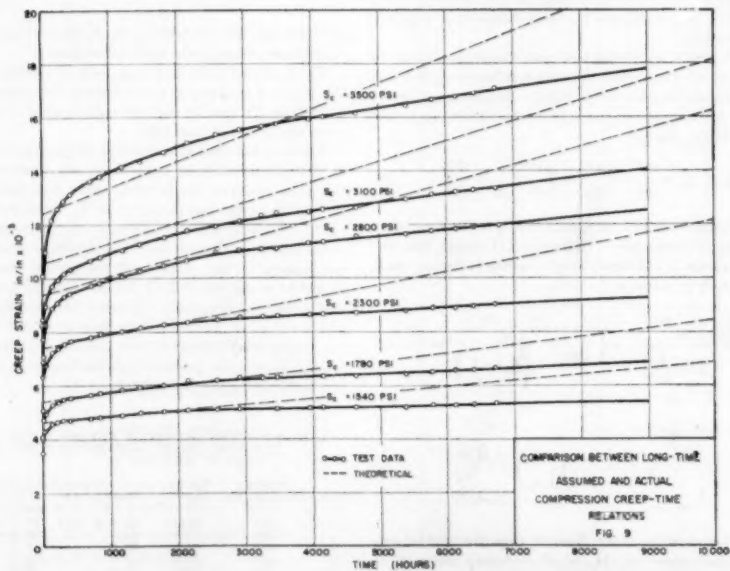


FIG. 9

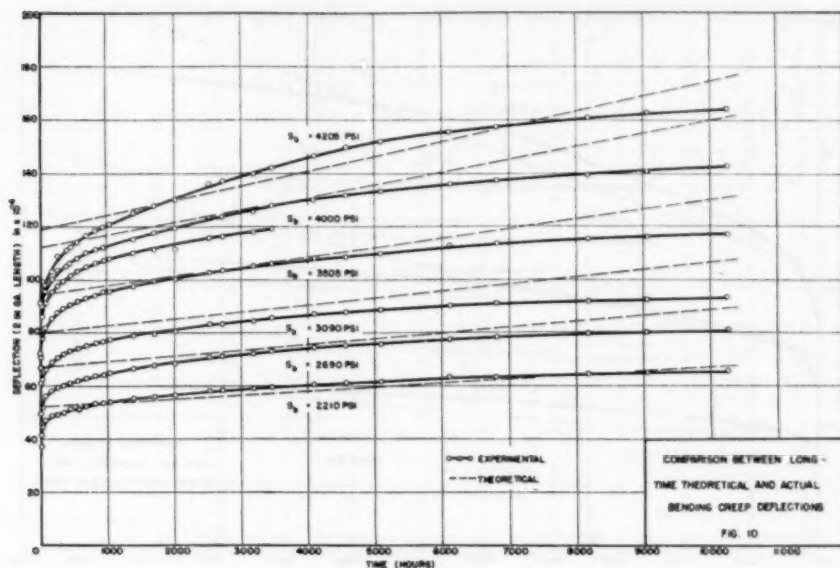


FIG. 10

COMPARISON OF THEORETICAL AND ACTUAL TORSION CREEP-TIME RELATIONS

The creep deformations in torsion of a circular member have been predicted based on theories defining creep strains under combined stresses (6). These theories are based upon the assumption that the tension creep-stress relations are identical with creep relations in compression. As indicated by Table 2, the compression and tension creep strains for a given stress cannot always be assumed equal. A theory for combined creep strain-stress relations for material with different properties in tension and compression was recently developed (2) which can be used for defining torsion creep-stress relations. By this theory, if S_s is the shear stress on the outer fiber of a bar with circular cross section subjected to creep, it can be shown (2) that the shear creep strain is

$$\gamma = \frac{3}{2} \left[D_s S_s^{m_1} (1 + c_d S_s^{c_m} + c_d^2 S_s^{2c_m})^{\frac{m_1-1}{2}} (1 + c_p S_s^{c_n}) + B_d S_s^{n_1} (1 + c_p S_s^{c_n} + c_p^2 S_s^{2c_n})^{\frac{n_1-1}{2}} (1 + c_d S_s^{c_m}) \right] \quad (11)$$

or

$$\gamma = f(S_s) \quad (11)$$

where c_d , c_m , c_p , c_n are material creep constants as follows

$$\left. \begin{aligned} c_d &= \left(\frac{D_s}{D_t} \right)^{\frac{1}{m_1}} \left[\frac{m_1 - m_t}{m_1} \right] \quad (3) \\ c_m &= \frac{m_t - m_1}{m_1} \\ c_p &= \left(\frac{B_s}{B_t} \right)^{\frac{1}{n_1}} \left[\frac{n_1 - n_t}{n_1} \right] \quad (3) \\ c_n &= \frac{n_t - n_1}{n_1} \end{aligned} \right\} \quad (12)$$

and D , B , m , and n in Equations [11] and [12] are the tension and compression creep constants appearing in Equation [4].

Using the conditions of equilibrium and the assumption that a radius remains a straight line during twisting, it is shown in reference (2) that the twisting moment M_t is

$$M_t = \frac{2\pi r^3}{\gamma^2} \int_0^{S_s} [f(S_s')] S_s' \left[\frac{df(S_s')}{dS_s'} \right] dS_s' \quad (13)$$

where $f(S_s')$ = the right-hand side of Equation [11] for S_s' on any fiber instead of S_s for the outer fiber at $r_1 = r$.

If θ is the angle of twist for a length L and β is the angle of twist per unit length, then

$$\theta = \beta L = \frac{\gamma L}{r} \quad (14)$$

where γ is the shear strain defined by Equation [11].

By Equations [11] to [14] the theoretical angle of twist for given twisting moment M_t and time t can be found as follows:

1 For known tension and compression creep constants, as given in Table 2, and as calculated by Equations [12], the values $f(S_s')$ can be obtained by Equation [11] for a series of S_s' values.

2 A graph giving the relation between $f(S_s')$ and S_s' can be plotted and $df(S_s')/dS_s'$ representing the slopes of the $f(S_s')$ versus S_s' can be found.

3 By Equation [13] and the graph $f(S_s')$ versus S_s' obtained in the foregoing, a relation between the twisting moment M_t and the shear strain γ is determined. For a given moment M_t , the shear strain γ can thus be found.

4 With the shear strain γ for a given twisting moment known, by Equation [14] the angle of twist θ for a given moment M_t will be known. The foregoing calculations can be made for various values of time t . Theoretical angle of twist-versus-time relations then can be plotted for selected values of the twisting moment

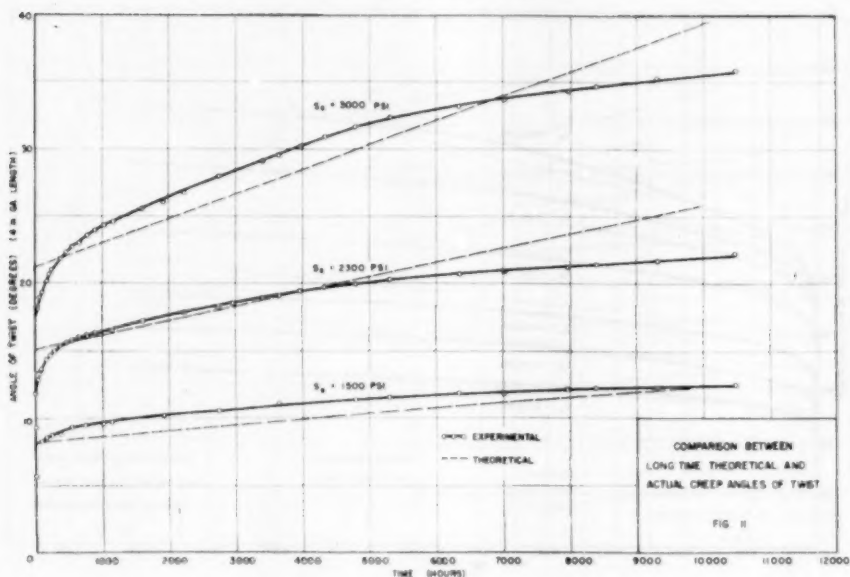


FIG. 11

M_p . These theoretical angles of twist-time relations are shown in Fig. 11 for 10,000 hr and for various values of the twisting moment. Fig. 11 also shows the actual creep angle of twist-time relations. A comparison of the curves shows that there is approximate agreement between the theoretical and actual creep values. The theoretical and actual creep angles of twist at 10,000 hr for various twisting moments are shown in Table 6. The per cent difference between the actual and theoretical creep angles of twist shows that the maximum difference is 18 per cent.

CONCLUSIONS

This investigation shows that for the Plexiglas tested, empirical relations for tension and compression stress creep-time relations based on 1000-hr tests agree well with actual values at 10,000 hr. Furthermore, theoretical bending and torsion creep relations predicted by theories developed in references (1) and (2) and based on 1000-hr tension and compression creep relations are in satisfactory engineering agreement with actual creep deformations at 10,000 hr.

Measurements of recoverable creep deformations for "tension" and "bending" show that the separation of the creep deformation into an instantaneous creep and time-dependent creep as given by Equation [4] is justified.

It appears that the theoretical and empirical relations used in this paper for predicting creep have possibilities for other materials than Plexiglas.

ACKNOWLEDGMENTS

The authors appreciate the sponsorship and financial assistance of the Office of Naval Research and the Research Corporation in making this investigation possible.

BIBLIOGRAPHY

- 1 "Creep Properties of Lucite and Plexiglas for Tension, Com-

TABLE 6 COMPARISON OF THEORETICAL AND ACTUAL CREEP ANGLES OF TWIST AT 10,000 HR

Spec. no.	Twisting moment M_t , in.-lb	Elastic stress, psi	Experimental Creep angles of twist at 10,000 hr, Deg (4 in. gage length)	Theoretical Creep angles of twist at 10,000 hr, Deg (4 in. gage length)	Difference, per cent
4(A)	262.4	3000	35.7	39.6	+11
5(A)	202.2	2300	22.1	26.0	+18
6(A)	131.2	1500	12.4	12.2	-2

pression, Bending, and Torsion," by Joseph Marin, Yoh-Han Pao, and George E. Cuff, Trans. ASME, vol. 73, 1951, pp. 705-719.

2 "A Theory for Combined Creep Strain-Stress Relations for Materials With Different Properties in Tension and Compression," by Joseph Marin and Yoh-Han Pao, presented at the First National Congress on Applied Mechanics, June, 1951.

3 "Static and Dynamic Creep Properties of Laminated Plastics for Various Types of Stress," by Joseph Marin, NACA Technical Note 1105, Washington, D. C., February, 1947.

4 "Metallic Creep," by A. H. Sully, Interscience Publishers, Inc., New York, N. Y., 1949.

5 "The Creep of Metals and Alloys," by E. G. Stanford, Temple Press, Ltd., London, England, 1949.

6 "Mechanical Properties of Materials and Design," by Joseph Marin, McGraw-Hill Book Company, Inc., New York, N. Y., 1942.

7 "Creep of Metals," by L. A. Rotherham, Institute of Physics, London, England, 1951, 80 pp.

Appendix

CREEP-STRAIN RECOVERY ON UNLOADING

It is of practical importance to know what part of the creep deformation produced in a member is recoverable on unloading. In this way the permanent creep deformation produced on removal of stress would be known. To answer this question, the loads were completely removed from the tension and bending creep-test specimens and the deformations were measured at intervals of time as indicated in Figs. 12 and 13. As might be expected, the strain recovery or change to the original dimensions was rapid for the initial periods of time and gradually decreased

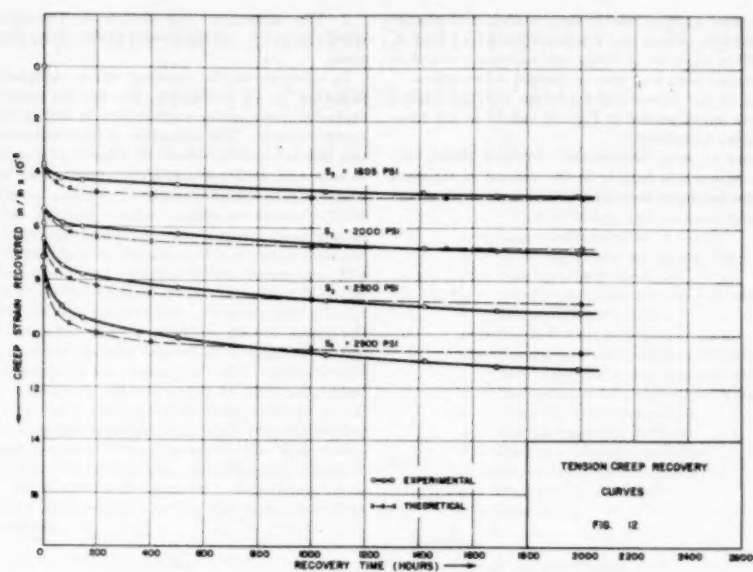


FIG. 12

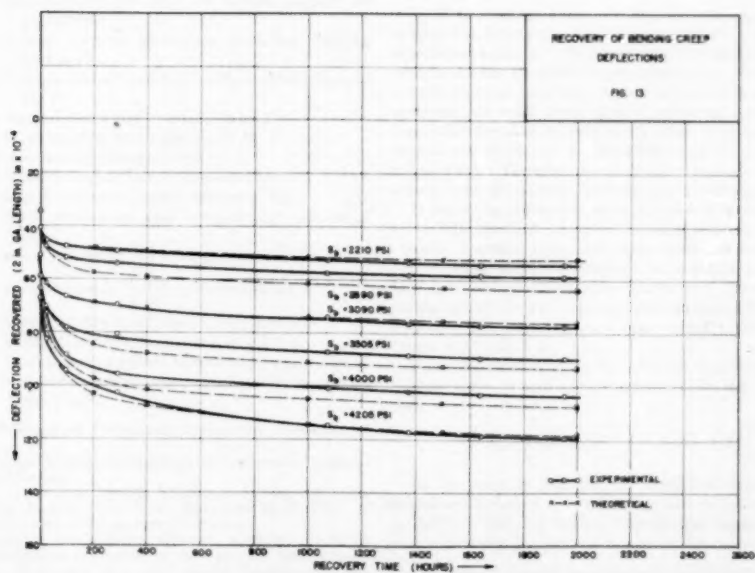


FIG. 13

so that, in most cases, at about 2000 hr there was negligible change of strain for both the tension and bending specimens; that is, after about 2000 hr recovery of strain was essentially complete and the deformations remaining were permanent deformations.

A comparison of the recovery creep curves and the original creep-time curves shown plotted in Figs. 12 and 13 as the theoretical curves shows the following:

1 The amount of creep deformation recovered during any length of time corresponds roughly to the amount of transient creep deformation developed under load for the same time interval.

2 The maximum creep deformation recovered also corresponds roughly to the maximum transient creep strain or intercept strain.

In other words, the intercept strain—designated by DS^* in Equation [4]—is recoverable, whereas the steady rate or time-dependent creep strain—represented by BS^* in Equation [4]—is nonrecoverable. The separation of the resultant creep deformation into two parts as defined by Equation [4] appears, therefore, to have a physical basis and gives support to the method of interpretation adopted in this study.

Heat Transfer From Spheres to a Rarefied Gas in Supersonic Flow

By R. M. DRAKE, JR.,¹ AND G. H. BACKER,² BERKELEY, CALIF.

An approximate analysis is presented for the prediction of the over-all average heat-transfer coefficients from spheres to air in the transition-flow region, that region wherein the mean free molecular path is small but not negligible when compared with the sphere diameter. The analysis is made on the basis of a simplified flow field and the utilization of the continuum formulation of the energy equation with the rarefaction effects being accounted for entirely in the boundary conditions. The results of the analysis are compared with experimental heat-transfer data from spheres to air in the transition-flow region, with heat-transfer data from spheres to air in the continuum-flow region, and with the calculated results of heat transfer from spheres in the free molecule-flow region. Experimental free-stream recovery factors are presented for spheres. Significant flow parameters and flow-region limits for the transition region are discussed.

NOMENCLATURE

The following nomenclature is used in the paper:

- A = surface area of sphere, sq ft
- a = speed of sound, fps
- c_p = specific heat, Btu/lb deg F
- D = sphere diameter, ft
- f = velocity slip coefficient, dimensionless
- F_{1-2} = geometrical shape factor for radiant transfer, dimensionless
- h_c = average over-all convection coefficient, Btu/hr sq ft deg F
- h_r = average over-all radiation coefficient, Btu/hr sq ft deg F
- k = thermal conductivity, Btu/hr ft deg F
- M = Mach number, dimensionless, (U/a)
- N = parameter as defined in text
- Nu = Nusselt number, (hD/k) , dimensionless
- p_i = impact pressure on probe, microns of Hg
- p_s = static pressure on cone probe surface, microns of Hg
- p_∞ = static pressure in free stream, microns of Hg
- Pr = Prandtl number $\left(\frac{\mu c_p}{k}\right)$, dimensionless
- q_r = heat rate by radiant transfer, Btu/hr sq ft
- Re = Reynolds number, dimensionless (UD/ν)
- t = temperature of sphere measured at center, deg F
- t_e = equilibrium temperatures of sphere due to convection, deg F

- t_e' = equilibrium temperature of sphere due to convection, radiation, and conduction, deg F
- t_w = tunnel-wall temperature, deg F
- t_i = initial temperature of sphere, deg F
- U = velocity of free stream, fps
- U_x, U_y, U_z = velocity components in x, y, z -directions
- V = volume of sphere, cu ft
- w = weight density of sphere, lb/cu ft
- α = thermal accommodation coefficient, dimensionless
- γ = ratio of specific heats, dimensionless
- ϵ = thermal emissivity of a surface, dimensionless
- λ = molecular mean free path, ft
- μ = absolute viscosity, lb/ft sec
- ν = kinematic viscosity, sq ft/sec
- σ = Stefan-Boltzmann constant
- ρ = mass density, lb sec²/ft⁴
- τ = time, hr

Subscripts:

- 1 = conditions before shock
- 2 = conditions behind shock
- e = equilibrium temperatures
- T = when written instead of t , means absolute temperature, deg R
- avg = an integrated average

INTRODUCTION

In the usual presentation of analyses on the convective transfer of heat, the transferring media are considered as continua. This is permissible as long as the mean free molecular path is small when compared with significant body dimensions. Even in gases at normal pressures and temperatures where the distances between molecules are much larger than in solids and liquids, the mean free molecular path is very small when compared with those dimensions which are of immediate concern in heat-transfer calculations. Therefore the condition of a small mean free-path length to significant body-dimension ratio is substantially fulfilled.

If the gas is sufficiently rarefied, however, a continuum treatment fails because the mean distance between molecular encounters becomes comparable with significant body dimensions, and the effect of the coarseness of the molecular structure on the flow and heat transfer must be considered. The nature of these rarefaction effects with regard to aerodynamic behavior has been examined by Tsien (1),² and with regard to heat transfer by Drake and Kane (2, 3).

It can be shown that the mean free molecular path λ , may be related to the convenient flow parameters by the following equation

$$\lambda = 1.255 \sqrt{\gamma} \left(\frac{r}{a} \right) = 1.255 \sqrt{\gamma} \frac{DM}{Re} \dots \dots \dots [1]$$

On the basis of Equation [1] three flow regions have been tentatively proposed by Tsien (1); (a) the continuum-flow region, $\sqrt{Re/M} > 100$; (b) the free molecule-flow region, $M/Re > 10$; and in between, (c), the region wherein the mean free molecular

² Numbers in parentheses refer to the Bibliography at the end of the paper.

¹ Assistant Professor of Mechanical Engineering, University of California.

² Associate Research Engineer, Institute of Engineering Research, University of California.

Contributed by the Heat Transfer Division and presented at the Annual Meeting, Atlantic City, N. J., November 25-30, 1951, of THE AMERICAN SOCIETY OF MECHANICAL ENGINEERS.

NOTE: Statements and opinions advanced in papers are to be understood as individual expressions of their authors and not those of the Society. Manuscript received at ASME Headquarters, August 10, 1951. Paper No. 51-A-55.

path is small but not negligible when compared with a significant body dimension—the transition region. These flow regions are shown graphically in Fig. 1.

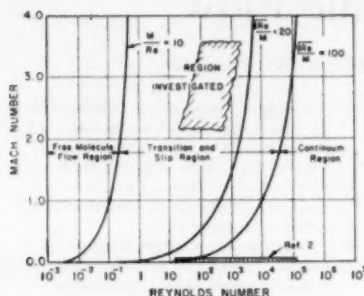


Fig. 1 TENTATIVELY DEFINED FLOW REGIONS OF GAS DYNAMICS

It is the purpose of this investigation to consider the nature of convective heat transfer in this transition-flow region. Silver spheres were chosen as the bodies to be investigated because the geometry and thermal characteristics were well suited to the experimental program.

Heat Transfer From Spheres. The subject of heat transfer from spheres to a moving gas stream (or the converse) has been the objective of several experimental investigations, the range of variables of which are shown in Fig. 2. These available results, while extending over a large range of Reynolds number ($19 \leq Re \leq 8 \times 10^4$) were made under conditions of low Mach number, at or very near atmospheric pressure, thus probably under continuum conditions. There are no experimental data in so far as is known for heat transfer from spheres in supersonic flows or at low ambient densities.

The theory for the heat transfer from spheres is incomplete. While laminar boundary-layer theory probably will yield an expression for the heat transfer from the forward stagnation point

to the point of laminar separation for continuum flow, the general case, including the region after separation, has no solution as yet. Heat transfer from spheres in the free molecule-flow region has been calculated by Sauer (4) on the basis of the kinetic theory of gases. In the transition region, however, the problem is much more difficult and no satisfactory analyses have as yet been made. A brief outline of the outstanding efforts to effect a satisfactory analysis in the transition region has been given in (3).

It is the specific purpose of this paper to present experimental data and approximate analyses for the heat transfer from spheres to a rarefied gas in the transition-flow region for a range of variables $16 \leq Re_t \leq 980$ and $2.24 \leq M_t \leq 3.56$.

ANALYSIS

In the flow region where the mean free molecular path is small but not negligible—the transition-flow region—a direct solution of the momentum and energy equations seems for the moment to present insurmountable difficulties. For this reason another approach to the problem has been utilized (3, 13). This approach consists essentially of using the continuum formulations of the momentum and energy equations for the problem, relegating the slip phenomena to the boundary conditions. In slip flows, two effects have been observed: (a) The flow does not have zero velocity at the wall but “slips” over the surface with a finite velocity. (b) A temperature discontinuity or temperature jump exists between the gas and the wall, i.e., the gas in contact with the wall does not have the temperature of the wall. These effects can be expressed as (14)

$$u_x = 0 - u_w = \left(\frac{2-f}{f} \right) \lambda \left(\frac{du}{dy} \right)_{y=0} \quad [2]$$

and

$$T_x = 0 - T_w = \left(\frac{2\gamma}{\gamma+1} \right) \left(\frac{2-\alpha}{\alpha} \right) \frac{\lambda}{Pr} \left(\frac{dT}{dy} \right)_{y=0} \quad [3]$$

where f is the velocity slip coefficient and α is the thermal accommodation coefficient.

Thus the velocity slip and temperature jump can be expressed

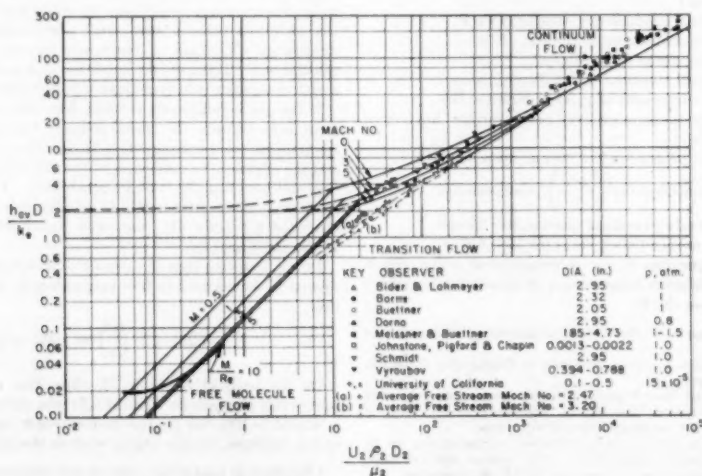


Fig. 2 CONVECTIVE HEAT TRANSFER FROM SPHERES TO AIR

as proportional to the velocity gradient and the heat flux, respectively, at the surface. It is possible to use these characteristic effects as boundary conditions for the differential equations for continuum flows and thus in a manner to account for the rarefaction effects.

Consider a sphere of radius r_1 in a uniform flow field of velocity U , losing heat to the stream, Fig. 3. The energy equation in



Fig. 3 Co-ORDINATE SYSTEM FOR SPHERE

spherical co-ordinates (neglecting the terms concerning compressibility and dissipation of mechanical energy) is

$$\rho c_p \left(U_r \frac{\partial T}{\partial r} + \frac{U_\theta}{r} \frac{\partial T}{\partial \theta} + \frac{U_\phi}{r \sin \theta} \frac{\partial T}{\partial \phi} \right) = k \left[\frac{1}{r^2} \frac{\partial}{\partial r} \left(r^2 \frac{\partial T}{\partial r} \right) + \frac{1}{r^2 \sin \theta} \frac{\partial}{\partial \theta} \left(\sin \theta \frac{\partial T}{\partial \theta} \right) + \frac{1}{r^2 \sin^2 \theta} \frac{\partial^2 T}{\partial \phi^2} \right] \quad [4]$$

As an approximation to the velocity (or velocity-slip) condition let

$$U_r = U_\theta = 0; \quad U_\phi = U$$

and from symmetry

$$\frac{\partial T}{\partial \phi} = \frac{\partial^2 T}{\partial \phi^2} = 0$$

and for small thermal conduction in the θ -direction

$$\frac{\partial T}{\partial \theta} = \frac{\partial^2 T}{\partial \theta^2} = 0$$

the remaining terms of the energy equation are

$$\rho c_p \frac{U}{r} \frac{\partial T}{\partial \theta} = k \left[\frac{1}{r^2} \frac{\partial}{\partial r} \left(r^2 \frac{\partial T}{\partial r} \right) \right] \quad [5]$$

Equation [5] may be solved for the boundary conditions

$$T_{r=r_1} = T_w = \left(\frac{2\gamma}{\gamma+1} \right) \left(\frac{2-\alpha}{\alpha} \right) \frac{\lambda}{Pr} \left(\frac{\partial T}{\partial r} \right); \quad r = r_1$$

$$T = T_\infty = 0; \quad r \rightarrow \infty$$

by means of the Laplace transform to yield for the specification of an average over-all heat-transfer coefficient

$$\frac{h_{avg} D}{k} = 2 + \frac{2}{\pi^2} \int_0^\infty \frac{(1 + e^{-\beta^2 x})(1 + \beta^2)^{-1} d\beta}{\{ [J_1(\alpha\beta) + N\alpha\beta J_0(\alpha\beta)]^2 + [Y_1(\alpha\beta) + N\alpha\beta Y_0(\alpha\beta)]^2 \} \beta} \quad [6]$$

where $\alpha_1 = \sqrt{2(\text{RePr})}$ and

$$N\alpha_1 = \frac{8}{3} \left(\frac{2\gamma}{\gamma+1} \right) \left(\frac{2-\alpha}{\alpha} \right) \frac{M}{\sqrt{2 \text{RePr}}}$$

For small $M/\sqrt{\text{RePr}}$, Equation [6] reduces to an expression

$$\frac{h_{avg} D}{k} = 2 + \frac{2}{\pi^2} \int_0^\infty \frac{(1 + e^{-\beta^2 x})(1 + \beta^2)^{-1} d\beta}{[J_1(\alpha\beta) + Y_1(\alpha\beta)] \beta} \quad [7]$$

which is the solution of Equation [5] when solved for the continuum boundary conditions

$$T_{r=r_1} = T_w; \quad r = r_1$$

$$T = T_\infty = 0; \quad r \rightarrow \infty$$

Comparison of Equation [6] with Equation [7] shows that as the gas is rarefied the Nusselt number becomes dependent upon not only $\sqrt{\text{RePr}}$ but also upon the additional parameter $\sqrt{\text{RePr}}/M$ so that the following functional relationships hold

$$\text{Continuum flow: } Nu_{avg} \sim f(\sqrt{\text{RePr}})$$

$$\text{Slip flow: } Nu_{avg} \sim f\left(\sqrt{\text{RePr}}; \frac{\sqrt{\text{RePr}}}{M}\right)$$

Equation [6] is shown graphically in Fig. 2 with the Mach number as a parameter. The curve shown for $M = 0$ is of course the graphical representation of Equation [7], this being but a specific case of Equation [6]. It can be seen from Fig. 2 that the solution given by Equation [6] for low Reynolds numbers tends to the limit 2 for the Nusselt number. This is clearly the case of zero onflow velocity and the resulting case of heat transfer from the sphere to an infinite body of gas by pure radial conduction. In the physical case, however, the gas may no longer be a continuum if the Reynolds-number variation is obtained by a reduction in density rather than a reduction in velocity. In this case the methods of the kinetic theory of gases may be used for the analysis; therefore predictions for the heat transfer from spheres in free molecule flows have been shown in superposition with the results of Equation [6] in Fig. 2. Strictly speaking, the validity of the calculations made on the basis of the kinetic theory of gases holds only in the free molecule-flow region, the tentative upper limit of which is shown by the line $M/\text{Re} = 10$ in Fig. 2. The curves have been extended, however, to intersect the slip-flow solutions of Equation [6]. Further, the solutions of Equation [6] to the left of these intersections have been shown as dashed lines since it is believed that these results are not to be realized physically under the conditions investigated.

EXPERIMENTAL EQUIPMENT AND PROCEDURE

Wind Tunnel. The required low-density, supersonic air stream was provided by the No. 3 wind tunnel located at the University of California. The constructional features and general operating characteristics of the tunnel are contained in reference (5).

Two axisymmetric nozzles were employed in the investigation—No. 4 and No. 3—giving ranges of Mach numbers 2.24 to 2.75, and 2.78 to 3.56, and a static-pressure range from 36 to 123 microns Hg, and 38 to 115 microns Hg, respectively. The calculated free stream-state temperatures in the working section (151

to 273 deg R) correspond to those obtained by an isentropic expansion of the air from reservoir conditions at approximately room temperature (523 to 546 deg R) to the indicated Mach number at the test section.

The two nozzles used (No. 4 and No. 3) have diameters at the exit plane of 5.5 in. and 5.25 in., respectively. The design of nozzle No. 4 is described in reference (6) and that of No. 3 is described in reference (5).

The flow characteristics at the test section were determined by traversing the section with two probes, Fig. 4, and measuring the pressures associated with each probe. The interpretation of the probe pressure readings to result in a determination of the Mach and Reynolds numbers in the test section has been described in references (7) and (8). The approximate flow-parameter magnitudes characteristic of each nozzle are shown in Table 1.

TABLE 1 PERFORMANCE OF NOZZLES IN NO. 3 WIND TUNNEL

No. 4 Nozzle	p_0 (Microns Hg)	Re ₁ (per in.)
2.75	123	890
2.71	112	780
2.63	98	609
2.50	84	468
2.45	79	410
2.28	62	275
2.23	50	270
2.24	36	155

No. 3 Nozzle	p_0 (Microns Hg)	Re ₁ (per in.)
3.56	115	1860
3.25	95	1140
3.21	72	830
2.88	49	400
2.78	38	280

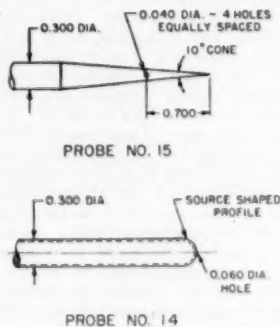


FIG. 4 PROBES FOR DETERMINATION OF FLOW CHARACTERISTICS

A traversing mechanism within the test chamber of the No. 3 wind tunnel provided means for mounting and moving models or probes. Remote operation of this mechanism was accomplished by electric motors connected to each direction of motion, combined with a selsyn system connected to standard 5-place counters for indicating position. Three spheres and the two probes could be mounted at the same time upon the traversing rack, and any one object could be moved into the flow field as required without alteration of the flow. Part of this installation can be seen in Fig. 5.

Experimental Method. The over-all average heat-transfer coefficients were determined by the transient technique described by London, et al. (9), wherein the rate of change of the thermal capacity of a small body of sensibly uniform internal temperature distribution is equated to the heat loss by convection to give the expression

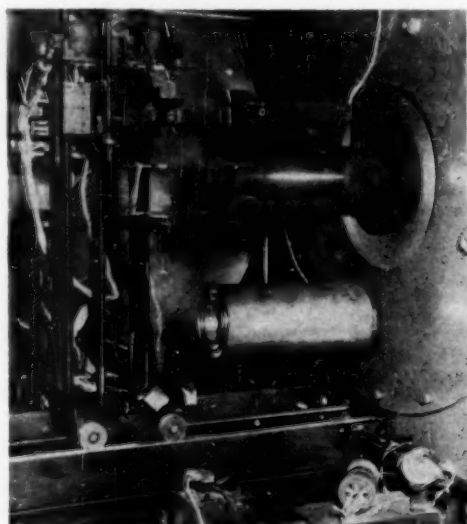


FIG. 5 INSTALLATION OF SPHERES AND PROBES IN NO. 3 WIND TUNNEL, UNIVERSITY OF CALIFORNIA, BERKELEY, CALIF.

$$h_c = -\frac{c_w V}{A} \frac{d \ln \left(\frac{t - t_e}{t_i - t_e} \right)}{dt} \quad [8]$$

In the consideration of continuum-flow conditions, involving small temperature differences, the transfer of heat by radiation is only a very small percentage of the total heat transfer when compared with the transfer of heat by convection, and in this sense the radiation effects are usually neglected. In the present work, however, preliminary calculations (2, 13) indicated that the heat transfer by radiation would be of the same order of magnitude as the heat transfer by convection. Therefore it was necessary to modify the heat balance on the sphere to account for the radiation and to select materials for the construction of the spheres which had low emissivities (as well as high thermal conductivities) to minimize the radiation exchange.

Since the temperature difference for the radiation exchange was not the same as the temperature difference for convection, the following heat balance was written (neglecting for the moment heat conduction along the sphere-mounting sting)

$$-c_w V \frac{dt}{dt} = h_c A (t - t_e) + h_r A (t - t_e) \quad [9]$$

with the boundary conditions

$$t = t_i; \quad \tau = 0 \\ t = t_e; \quad \tau \rightarrow \infty$$

where t_i is the initial sphere temperature and t_e is the equilibrium temperature for the combined effects of radiation and convection. Integrating Equation [9] for h_c and h_r , not functions of the temperature, the following expression is obtained

$$\frac{t - t_e}{t_i - t_e} = e^{-\frac{A(h_c + h_r)}{c_w V} \tau} \quad [10]$$

where

$$t_s' = \frac{h_0 f_0 + h_1 f_0}{h_0 + h_1} \dots \dots \dots [11]$$

The equilibrium temperature due to convection heat transfer alone is given from Equation [11] as

$$t_s = t_s' + \frac{h_s}{h_c} (t_s' - t_a) \dots \dots \dots [12]$$

It was necessary to determine the heat-transfer coefficient for radiation independently. This was accomplished by making transient cooling runs at no flow, with the tunnel pressures reduced to the order of 0.1 microns of mercury so that all convection was eliminated. The heat balance for this case is

$$-c_v V \frac{dt}{dt} = h_r A(t - t_s) \dots \dots \dots [13]$$

and the solution for the boundary condition

$$t = t_0; \quad \tau = 0$$

$$t = t_0: T \rightarrow \mathbb{C}$$

is

$$\frac{t - t_a}{t_i - t_a} = e^{-\frac{A h_{rr}}{c w V}} \dots \dots \dots [14]$$

Making use of the temperature-time histories on a semi-logarithmic plot as suggested by Equation [10], the sum of the heat-transfer coefficients ($h_c + h_r$) is obtained. Utilising the temperature-time history in the radiation run as indicated by Equation [14], the value of h_c can be found. The temperature t'_s and t_e are measured directly, t_e by means of a thermocouple in the tunnel walls, and t'_s the equilibrium temperature attained by the sphere at a very long time. The heat-transfer coefficient for convection h_c , and the equilibrium temperature for convection alone t_e , can be calculated immediately from the results of the two experimental runs just described and Equation [12].

The foregoing discussion presupposes that the heat-transfer coefficients h_1 and h_2 are not functions of the temperature. In so far as h_1 is concerned this is a reasonably sound assumption; but for h_2 there needs to be further consideration, because this coefficient, in general, is a function of the temperature; h_2 is written

$$h_r = \frac{q_r}{t - t_\infty} = \epsilon_1 \sigma F_{1-2} \frac{T^4 - T_\infty^4}{T - T_\infty} = \epsilon_1 \sigma F_{1-2} f(T, T_\infty). \quad [15]$$

However, when the difference $(T - T_*)$ is small, the expression for the coefficient h , becomes, for small error (10 per cent for $T = 2T_*$)

is related to the free-stream static pressure p_∞ and the Mach number M_∞ by the Rayleigh formula (11)

$$p_i = \frac{\left(\frac{\gamma+1}{2} M_\infty^2\right)^{\frac{\gamma}{\gamma-1}}}{\left(\frac{2\gamma}{\gamma+1} M_\infty^2 - \frac{\gamma-1}{\gamma+1}\right)^{\frac{1}{\gamma-1}}} \quad [17]$$

With these assumptions, the two unknowns M_∞ and p_∞ were obtained from the measured values of p_i and p_e .

The temperature-time histories of the cooling spheres were obtained, and from these data the heat-transfer coefficients h_c and the equilibrium temperature t_e were computed as described in this paper.

The heat-transfer coefficients were put into the dimensionless form of the Nusselt number ($h_c D/k$) wherein the thermal conductivity k was evaluated at the equilibrium temperature t_e .

The Reynolds number, corresponding to the conditions of the experiments, was computed. The absolute viscosity μ was determined from Sutherland's Equation [14]

$$\mu_1 = \mu_0 \left(\frac{T_0 + 216}{T_1 + 216} \right) \left(\frac{T_1}{T_0} \right)^{1/2} \quad [18]$$

where

$$\mu_0 = 10 \times 10^{-6} \text{ lb/ft-sec at } 400 \text{ R } [12]$$

The state temperature of the air in the test section was calculated assuming isentropic flow in the core of the tunnel nozzle, and the characteristics of a perfect gas for the air. The relationship is then

$$\frac{T_0}{T_1} = 1 + \frac{\gamma-1}{2} M_1^2 \quad [19]$$

The numerator of the Reynolds number, $U\rho D$, can be expressed in terms of M_1 and p_e by using the perfect-gas law relationship and the definition for M_1 to give

$$Re_1 = \sqrt{\frac{\gamma}{RT_1}} \frac{M_1 p_e D}{\mu_1} \quad [20]$$

Equation [20] when reduced for air becomes

$$Re_1 = 2.14 \times 10^{-4} \frac{M_1 p_e D}{\mu_1 \sqrt{T_1}} \quad [21]$$

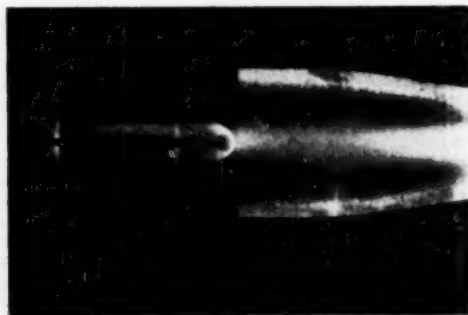


FIG. 7 SHOCK WAVE EXISTING BEFORE SPHERE AS DELINEATED BY NITROGEN AFTERGLOW METHOD

from which expression the free-stream Reynolds numbers were calculated (see Table I).

In addition to the free-stream Mach and Reynolds numbers, it was desirable to consider the effects of the shock wave before the sphere to obtain the Mach and Reynolds numbers behind the shock. In order to calculate this shock effect, the observed curved, detached shock, Fig. 7, was replaced by a detached normal shock. The Mach number M_2 and the Reynolds number Re_2 behind the normal shock were calculated from Equations [22], [23], [24] (11) as well as Equation [18].

$$M_2^2 = \frac{1 + \frac{\gamma-1}{2} M_1^2}{\gamma M_1^2 - \frac{\gamma-1}{2}} \quad [22]$$

$$\frac{T_0}{T_2} = 1 + \frac{\gamma-1}{2} M_2^2 \quad [23]$$

$$\frac{Re_2}{Re_1} = \frac{\mu_1}{\mu_2} \quad [24]$$

SOURCES OF ERROR

Flow System. The probable errors in the determination of the Mach, Reynolds, and static-pressure determinations have been estimated, and the summary of the maximum estimated error in the final results are as follows:

Quantity	Maximum error
M_∞	± 4 per cent
p_∞	± 3 per cent
Re_∞	± 8 per cent

The maximum figures apply to the points of smallest Reynolds number, the per cent error decreasing as Reynolds number increases.

Thermal System. The probable errors in the determination of the heat-transfer coefficients h_c can be broken down into the three modes of heat transfer—conduction, radiation, and convection. Of these, the radiation and conduction effects were measured as one, experimentally, notwithstanding the positive effort made to make these effects negligible. The error that might exist is that which comes about from experimental accuracy and not from outright neglect of the effect. The existing errors are then determined from the least count of the recording potentiometers. The largest least count, 0.5 F, is that of the B-instrument which, when associated with the smallest temperature difference measured and used in the computations, 10 F, gives a possible error of 5 per cent. Since the radiation-conduction correction in the worst case amounts to one third of the total heat-transfer coefficient ($h_c + h_r$) as measured, the maximum error in the calculation for h_c may possibly be 7 to 8 per cent. The error outstanding in the calculation of h_c will be transmitted directly to the Nusselt number with the possibility of further error in the thermal conductivity which is not especially well known for gases.

The actual conduction losses out of the sting are believed to be minute; but, whatever the magnitude, these losses are measured, together with the radiation transfer as mentioned previously, and thus are accounted for.

EXPERIMENTAL RESULTS

The experimental results are shown in Figs. 2, 8, 9, 10, 11, and 12. As is shown in Fig. 2, the representation of the experimental data by the approximate analyses over a wide range of Reynolds numbers is quite satisfactory if consideration is given to the basic assumption of the flow field made in the analysis. The results of other investigators (all in the continuum region) are represented

within 30 per cent by the continuum analysis with the exception of one low group of points.

The presentation of the slip-flow results on the same plot offers some difficulty. The analytical results shown in Fig. 2 contain the Mach number simply as a rarefaction parameter and in no way are the flow-field characteristics of supersonic flow considered, i.e., no acknowledgment of the existence of a shock wave. For the spheres, however, there was observed a detached, curved shock wave since all the experimental data were taken under supersonic as well as low Reynolds number conditions, Fig. 7. For consideration of the shock wave, the observed curved detached shock wave was replaced with a normal detached shock wave, and the heat-transfer coefficient was made a function of the Mach and Reynolds numbers after the normal shock wave for representation in Fig. 2. This approach allows the comparison of the experimental data but somewhat overemphasizes the shock-wave effect on the flow characteristics in the immediate vicinity of the sphere. On this basis the experimental data are lower than predicted by the analysis, but show clearly the expected trend from continuum analysis to free molecule-flow analysis. The

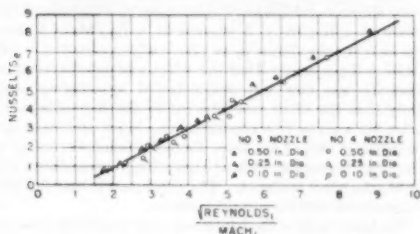


FIG. 8 AVERAGE HEAT-TRANSFER COEFFICIENTS FROM SPHERES TO AIR IN TRANSITION-FLOW REGION—BASED ON FREE-STREAM CHARACTERISTICS

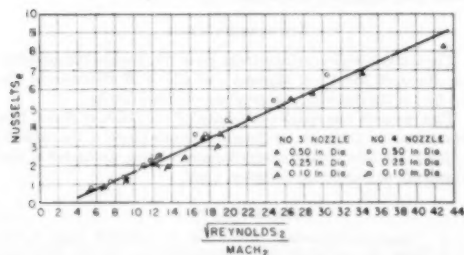


FIG. 9 AVERAGE HEAT-TRANSFER COEFFICIENTS FROM SPHERES TO AIR IN TRANSITION-FLOW REGION—BASED ON FLOW CONDITIONS BEHIND A NORMAL SHOCK WAVE

dashed lines drawn through the experimental data show the average free-stream Mach number for each nozzle. The Mach-number effect is evident.

Equation (6) suggests that the Nusselt number, as obtained by experiment, could be correlated on a single plot if plotted against M/\sqrt{Re} (or the inverse), since the Prandtl number makes only a slight correction in the temperature range considered. Such correlations are shown in Figs. 8 and 9 by plotting the Nusselt number against \sqrt{Re}/M_1 and \sqrt{Re}/M_2 , respectively, the conditions before and after the normal shock. It can be seen that the representation is reasonably good.

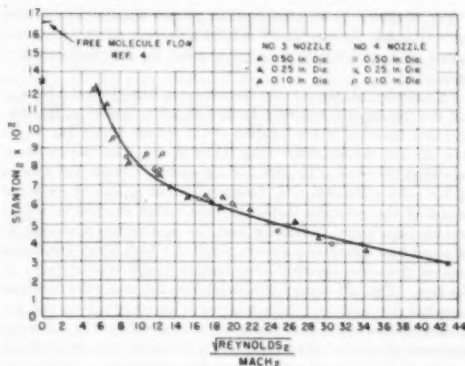


FIG. 10 STANTON NUMBER FOR HEAT TRANSFER FROM SPHERES TO AIR IN TRANSITION-FLOW REGION—BASED ON FLOW CONDITIONS BEHIND A NORMAL SHOCK WAVE

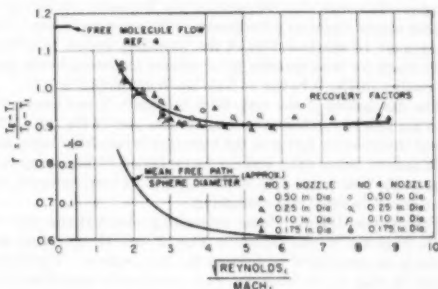


FIG. 11 FREE-STREAM RECOVERY FACTORS FOR SPHERES IN TRANSITION-FLOW REGION

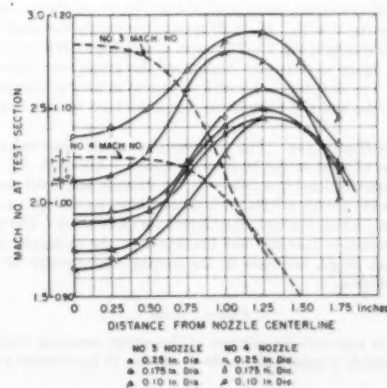


FIG. 12 FREE-STREAM RECOVERY-FACTOR DISTRIBUTIONS IN NOZZLE TEST SECTION

Fig. 10 shows the Stanton number plotted against the parameter $\sqrt{Re_2}/M_2$ for conditions behind a normal shock in relation to the prediction for the Stanton number for free molecule-flow theory (4).

Of considerable interest are the curves in Figs. 11 and 12 showing the free-stream recovery factors as a function of $\sqrt{Re_2}/M_2$, and as a function of the location of the sphere center line in the flow stream, respectively. Fig. 11 indicates that the recovery factors at values of $\sqrt{Re_2}/M_2 > 5$ are sensibly constant at a value of 0.9. At $\sqrt{Re_2}/M_2 < 5$, however, and as $\sqrt{Re_2}/M_2 \rightarrow 0$ the values of the recovery factor increase rather sharply to values greater than unity, indicating that the equilibrium temperature attained by a sphere in a stream of gas at a high Mach number is greater than the reservoir temperature (total temperature) of the flow. This effect would be possible in the event the flow was nonadiabatic and the sphere was receiving energy from the gas stream somehow, but that this is not true is seen in Fig. 12 where the trend of equilibrium temperatures is shown over the working section of the nozzle for a constant-flow setting as a function of the Reynolds number (i.e., sphere diameter). If the effect just described were a result of nonadiabatic flow, there should be no Reynolds-number effect, since the spheres, regardless of size, would come to the same equilibrium temperature in the flow. As can be seen from Fig. 12, however, there is a definite Reynolds-number effect such that the smaller the Reynolds number (i.e., smaller sphere diameter), the greater is the recovery factor. The effect must be characteristic of the transition region. Calculations made for heat transfer from spheres in free-molecule flow (4) predict similar behavior at high Mach numbers, Fig. 11.

The dimensions of the very thick boundary layers associated with the flow of rarefied gases may be seen also in Fig. 12. The rise of the recovery factor in the boundary layer above unity has been noticed before (15), and can be explained by an energy balance on the flow tube. The effect is magnified here, however, for the reasons discussed in the foregoing.

Flow-Region Limits. Some interesting observations can be made from the results shown in Figs. 2 and 11 regarding the limits to be considered in defining the flow regions. The limits shown in Fig. 1, for instance, were tentatively established by Tsien (1) for purposes of analysis. It can be seen from Figs. 2 and 11 that the continuum region may exist for $\sqrt{Re_2}/M_2 > 20$ instead of for $\sqrt{Re_2}/M_2 > 100$ as tentatively suggested by Tsien.⁴ The selection of the limit $\sqrt{Re_2}/M_2 \approx 20$ was based upon the fact that at this value of $\sqrt{Re_2}/M_2$, the recovery factor departs from the continuum value as shown in Fig. 11 and from the fact that the curve $\sqrt{Re_2}/M_2 \approx 20$ approaches closely the continuum analysis shown in Fig. 2. The curve $\sqrt{Re_2}/M_2 \approx 20$ is not shown on the figure since it may complicate the graph with too many lines. The flow-region boundaries denote in no way discontinuous effects, and the boundaries suggested here remain approximate.

Shock-Wave Effect. Fig. 7 shows the curved detached shock wave in relation to the $1/2$ -in.-diam sphere. Although the complete interrelationship is unknown, it is strongly suspected that the shock wave greatly affects the boundary layer by interaction, here especially where the boundary layers are quite thick. The shock wave probably becomes less important as the molecular mean free-path length increases to the lengths characteristic of free-molecule flow.

CONCLUSIONS

1 An approximate solution of the energy equation has been given which is applicable to the prediction of heat transfer from

spheres under conditions of Mach and Reynolds numbers wherein the mean free molecular path is small but not negligible when compared with significant body dimensions. The analysis was performed on the basis of a continuum formulation of the energy equation for the problem relegating the rarefaction effects to the boundary conditions. The results of this solution showed that the Nusselt number becomes dependent upon the dimensionless group \sqrt{RePr}/M as well as \sqrt{RePr} as rarefaction effects become significant. The relationship of these slip-flow solutions to the free molecule-flow solutions was shown graphically.

2 Experimental data were presented for heat transfer from spheres in supersonic flow ($2.28 \leq M_2 \leq 3.56$) and at low corresponding Reynolds numbers ($16 \leq Re \leq 980$). The values represent a range of $1.5 \leq \sqrt{Re_2}/M_2 \leq 9$ which is considered to be in the mid-slip-flow region. The dimensionless heat-transfer coefficient Nu_2 in this region was shown to be a function of the parameter $\sqrt{Re_2}/M_2$ (or $\sqrt{Re_2}/M_2$) over the total range investigated. The experimental data were correlated on this basis. The parameter \sqrt{Re}/M (or the inverse M/\sqrt{Re}) is apparently a significant one in the transition region.

3 The over-all recovery factors, when plotted against $\sqrt{Re_2}/M_2$, were shown to exhibit marked increases to values above unity at values of $\sqrt{Re_2}/M_2 < 5$ whereas at $\sqrt{Re_2}/M_2 > 5$ the recovery factors were shown to be practically constant at a value $r = 0.90 \pm 3$ per cent. That this effect was not the result of a nonadiabatic gas flow was demonstrated by showing experimentally that the effect was inherent in the Reynolds-number variation for a given flow condition (i.e., Mach and static pressure constant); that at the lower Reynolds numbers (low \sqrt{Re}/M) the effect is present, while at higher Reynolds numbers (high \sqrt{Re}/M) the effect is absent. The conclusion is that this effect is one associated with the transition region.

4 The lower limit to the continuum-flow region has been estimated to be somewhat lower than the limit proposed by Tsien. Continuum characteristics seem to exist for $\sqrt{Re_2}/M_2 > 20$ rather than the previously supposed $\sqrt{Re_2}/M_2 > 100$. The flow-region boundaries denote in no way discontinuous effects, and the boundaries suggested here remain approximate.

ACKNOWLEDGMENTS

The authors wish to acknowledge gratefully the not inconsiderable efforts of Mr. G. J. Maslach and Mr. F. S. Sherman in the conduct of the experimental program reported herein.

This research was sponsored jointly by the Office of Naval Research and the Office of Air Research as one phase of the investigation in the field of rarefied-gas dynamics being conducted at the University of California, Berkeley, Calif.

BIBLIOGRAPHY

- 1 "Superaerodynamics, Mechanics of Rarefied Gases," by H. S. Tsien, *Journal of the Aeronautical Sciences*, vol. 13, 1946, pp. 659-664.
- 2 "A Summary of the Present Status of Heat Transfer in Rarefied Gases," by R. M. Drake, Jr., and E. D. Kane, Report No. HE-150-73, Institute of Engineering Research, University of California, Berkeley, Calif., October, 1950.
- 3 "Heat Transfer Problems in High Speed Flows in Rarefied Gases," by R. M. Drake, Jr., and E. D. Kane, General Discussion on Heat Transfer, London, England, September, 1951.
- 4 "Convective Heat Transfer From Spheres in a Free Molecule Flow," by F. M. Sauer, *Journal of the Aeronautical Sciences*, vol. 18, 1951, pp. 353-354.
- 5 "Design and Initial Operation of a Low Density Supersonic Wind Tunnel," by S. A. Schaaf, D. O. Horning, and E. D. Kane, Heat Transfer and Fluid Mechanics Institute, Berkeley, Calif., 1949, pp. 223-242.
- 6 "Boundary Layer Corrections in an Axially Symmetric Low Density Supersonic Nozzle," by D. E. Emerson, Master of Science thesis, University of California, Berkeley, Calif., 1951.

⁴ For comparison of Fig. 2 with Fig. 11 it can be shown that $\sqrt{Re_2}/M_2 \approx 4 \sqrt{Re_2}/M_2$.

7 "Impact Pressure Interpretation in a Rarefied Gas at Supersonic Speeds," by E. D. Kane and G. J. Maslach, Report No. HE-150-67, Institute of Engineering Research, University of California, Berkeley, February, 1950.

8 "Sphere Drag Data at Supersonic Speeds and Low Reynolds Numbers," by E. D. Kane, *Journal of the Aeronautical Sciences*, vol. 18, 1951, pp. 259-270.

9 "Determination of Unit Conductances for Heat and Mass Transfer by the Transient Method," by A. L. London, H. B. Nottage, and L. M. K. Boelter, *Industrial and Engineering Chemistry*, vol. 33, 1941, pp. 467-473.

10 "Tables of Flow of Air Around Cones," by Z. Kopal, Massachusetts Institute of Technology, Cambridge, Mass., 1947.

11 "Aerodynamics of a Compressible Fluid," by H. W. Liepmann and A. E. Puckett, John Wiley & Sons, Inc., New York, N. Y., 1947, pp. 25 and 40.

12 "Thermodynamic Properties of Air," by J. H. Keenan and J. Kaye, John Wiley & Sons, Inc., New York, N. Y., 1945, p. 36.

13 "Forced Convection Heat Transfer From Cylinders and Spheres in a Rarefied Gas," by R. M. Drake, Jr., F. M. Sauer, and S. A. Schaaf, Report No. HE-150-74, Institute of Engineering Research, University of California, Berkeley, Calif., November, 1950.

14 "Kinetic Theory of Gases," by E. H. Kennard, McGraw-Hill Book Company, Inc., New York, N. Y., 1938, pp. 295 and 311.

15 "Introduction to the Transfer of Heat and Mass," by E. R. G. Eckert, McGraw-Hill Book Company, Inc., New York, N. Y., 1950, p. 155.

Discussion

W. DASKIN.⁶ The writer requests that the authors give their estimate of the magnitude of the error introduced by the assumption of complete slip flow at the boundary of the sphere, and also how much this error affects the final results.

AUTHORS' CLOSURE

It is impossible at this time to estimate the error carried into the final results by the assumption of complete slip flow at the sphere boundary, since to make this estimate there is needed either an exact solution considering arbitrary slip conditions or very definitive experimental data. Neither are presently available. However, the complete slip specification should be most serious in the continuum case, $Mach = 0$, and, as is shown in Fig. 2, the variance between the theory and experiment is about 20 per cent. Of course part of this error probably should be attributed to the additional assumption of $U_s = U$ in the flow field about the sphere, which assumption is obviously contrary to fact.

⁶ Instructor in Mechanical Engineering, The Johns Hopkins University, Baltimore, Md. Jun. ASME.



An Experimental Investigation of Convective Heat Transfer to Air From a Flat Plate With a Stepwise Discontinuous Surface Temperature¹

By STEVE SCESA² AND F. M. SAUER,³ BERKELEY, CALIF.

The objective of the investigation described in this paper was to obtain turbulent forced convective heat-transfer data for air flowing parallel to a flat plate with a stepwise discontinuous surface temperature. Heat was supplied by fifteen transverse nichrome ribbons on the upper and lower surfaces of a bakelite plate. The electrical input to each ribbon was controlled separately so that the surface-temperature distribution could be maintained constant or stepwise. Local heat-transfer coefficients were obtained from the measured ribbon temperature and the electrical heat input to each ribbon. The experimental results were correlated with the Colburn equation within ± 6 per cent for a range of local Reynolds modulus from 60,000 to 800,000 by use of the starting-length correction of Rubesin (1).⁴ The starting length is defined as the position where the step occurs in the surface temperature.

NOMENCLATURE

The following nomenclature is used in the paper:

- A = area of ribbon surface, sq ft
- F = local starting-length correction factor
- h = local convective heat-transfer coefficient, Btu/hr sq ft deg F
- h_{avg} = average heat-transfer coefficient, Btu/hr sq ft deg F
- I = electrical current, amperes
- k = thermal conductivity, Btu/hr sq ft deg F/ft
- L = plate length, ft
- Nu_L = local Nusselt modulus
- Nu_L = average Nusselt modulus
- q_{rad} = radiant heat loss, Btu/hr sq ft
- q_{cond} = conducted heat loss, Btu/hr sq ft
- R = nichrome ribbon resistance, ohms
- Re_x = local Reynolds modulus
- Re_L = Reynolds modulus for plate
- s = position of temperature discontinuity from leading edge of plate, ft

- t_b = main-stream temperature, deg F
- t_w = temperature at plate surface, deg F
- Δt = temperature difference between plate surface and main stream, deg F
- U = main stream velocity, fps
- x = distance along plate from leading edge, ft
- ν = kinematic viscosity of fluid, sq ft per sec
- Pr = Prandtl modulus

INTRODUCTION

Investigations of turbulent heat transfer to an air stream in parallel flow over a flat plate have been made previously by Juerges (2), Elias (3), and Segel and Hawkins (4) for an isothermal plate. These investigators neglected the effect on the heat transfer due to the starting length which occurred in their experiments. Drake (5) has made local measurements under the conditions of constant heat rate with a negligible starting length. Jakob and Dow (6) investigated the average turbulent heat transfer over a cylindrical probe in parallel flow with the objective of determining an empirical starting-length correction. Rubesin (1) has developed analytically a starting-length correction for the local heat transfer from a flat plate having a stepwise discontinuous surface temperature for the cases of laminar and turbulent flow.

Considering that data are meager on local turbulent heat-transfer measurements for parallel flow over an isothermal flat plate under conditions of known starting length, this investigation was undertaken to obtain additional local measurements, and further, to provide an experimental check on the analysis of Rubesin.

EQUIPMENT AND INSTRUMENTATION

The flat plate was constructed of laminated canvas-base bakelite, 17-in. wide and 20 1/4 in. long, which included sharp-edged brass nose and tail pieces each 2 in. long, required for structural rigidity. Two pieces of bakelite 1/4 in. thick were bolted together to form the flat plate. Fifteen nichrome ribbons 1 in. wide, 12 in. long, and 0.002 in. thick were bonded by the "cycle" weld process transversely on each of the plate surfaces, Figs. 1 and 2. The ribbons, partially pressed into the bakelite surface, produced spaces between the ribbons of the order of 0.001 in. in depth which were filled with wax to present a smooth surface. Care also was taken to smooth over the joint between the brass nose and tail pieces with wax. Iron-constantan thermocouples spot-welded to the bottom surface of each nichrome ribbon provided for the measurement of the temperature at the center of the ribbon. To minimize the heat conduction out along the thermocouples the 30-gage iron-constantan thermocouples were rolled out at the junction to a thickness of 0.002 in. with subsequent spot-welding to the ribbon. Sixteen surface static pressure taps constructed from Monel tubing, 0.025 in. ID and 0.10 in. OD, were placed between the ribbons on the upper surface.

¹ The experimental results presented in this paper are based on a thesis submitted by S. Scesa to the University of California in partial satisfaction of the requirements for the MS degree.

² Institute of Engineering Research, University of California.

³ Formerly, Assistant Professor of Mechanical Engineering, University of California; at present, California Forest and Range Experiment Station, Forest Fire Research Division. Jun. ASME.

⁴ Numbers in parentheses refer to the Bibliography at the end of the paper.

Contributed by the Heat Transfer Division and presented at the Annual Meeting, Atlantic City, N. J., November 25-30, 1951, of THE AMERICAN SOCIETY OF MECHANICAL ENGINEERS.

NOTE: Statements and opinions advanced in papers are to be understood as individual expressions of their authors and not those of the Society. Manuscript received at ASME Headquarters, February 13, 1952.



FIG. 1 FLAT PLATE USED IN EXPERIMENTAL WORK AS VIEWED FROM LEADING EDGE

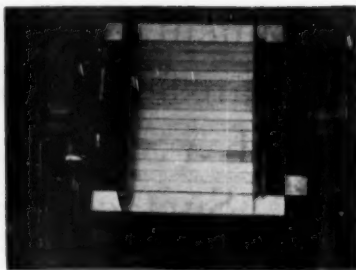


FIG. 2 TOP SURFACE OF FLAT PLATE SHOWING NICHROME RIBBONS

The resistance of the nichrome ribbon at room temperature, as measured in place on the plate, was 0.262 ± 0.001 ohm per ft of ribbon. Previous measurement showed that the ribbon thickness was held to a sufficient tolerance so that this value would be taken as an average for any section of ribbon. No resistivity temperature correction was made due to the low coefficient for nichrome and the relatively small temperature differences used.

The heating current was measured with a General Electric Company magnetic-vane-type a-c ammeter correct to within 0.2 per cent of full-scale value within a frequency range of 0-133 cps. Current readings were taken by the ammeter inserted in a make-before-break jack. The resistance of the ammeter and ammeter leads was adjusted to equal the resistance of the make-before-break jack thus insuring a constant current in the circuit in which the ammeter was placed.

Temperatures were obtained with a Leeds and Northrup Model 8602 precision potentiometer using the Leeds and Northrup calibration for the iron-constantan thermocouple wire.

Alternating-current power at 60 cycles was supplied across the 30 ribbon circuits in parallel. The voltage across this circuit could be controlled in the range from zero to 115 volts by means of a main-line Transtat. The voltage across each individual ribbon was controlled by separate Ohmite rheostats.

EXPERIMENTAL PROCEDURE

The experimental measurements were carried out in the 3-ft Goettingen type wind tunnel of the University of California at Berkeley. To obtain thermal equilibrium the preliminary adjustments required approximately 4 hr. In order to avoid the adverse effects of solar radiation on the tunnel free-stream temperature all experimental work was performed at night.

The required main-stream velocity was set using a Prandtl-type Pitot tube and a Prandtl manometer. The plate was then adjusted transversely to the stream at zero angle of attack by obtaining a zero pressure differential across the first and last pressure taps. Current was supplied to the ribbons by adjusting the main-line Transtat so as to apply a small voltage across the circuit. Continuous adjustments of the individual ribbon rheostats and voltage across the circuit were then made with the objective of obtaining the desired surface-temperature distribution. The ribbon temperatures on the lower surface were maintained equal to the corresponding ribbon on the upper surface. Equilibrium was assumed when the potentiometer readings remained constant within ± 0.005 millivolt while the rheostat settings were no longer adjusted and the Prandtl manometer reading remained as originally recorded. Three sets of readings were taken of the potentiometer, current, and Prandtl manometer at intervals of

$\frac{1}{2}$ hr to further insure no change in the equilibrium of the system.

Ribbon temperatures were measured as a temperature difference from a single radiation-shielded thermocouple placed upstream from the plate. This thermocouple also served as a measure of free-stream temperature.

Fourteen runs were made utilizing five different starting lengths. The ratio of starting length to total plate length varied from 0.104 (the lowest value obtainable due to the brass nosepiece) to 0.528. The Reynolds modulus based on total plate length was varied from 330,000 to 939,000.

Runs 1 through 9 were made with no heating of the starting length. Due to forward heat leak the temperature discontinuity was not stepwise. In order to provide a more stepwise discontinuity the forward ribbons were heated slightly to keep the surface temperature ahead of the step constant during the later runs. This procedure also allowed the calculation of the heat leak and the corresponding corrections to the convective heat loss of ribbons adjacent to the step. Typical surface-temperature distributions for these two cases are shown in Fig. 3.

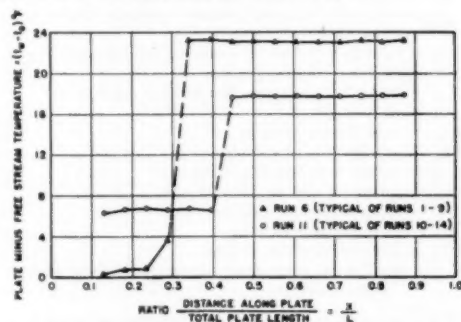


FIG. 3 TYPICAL SURFACE-TEMPERATURE DISTRIBUTIONS (Runs 1 to 9, no heating forward of temperature discontinuity. Runs 10 to 14, slight heating forward of main temperature discontinuity.)

ANALYSIS OF HEAT LOSSES

The local heat-transfer coefficient was calculated from the power loss for each ribbon in the manner of Drake (5)

$$\frac{PR}{A} = q_{\text{cond}} + q_{\text{rad}} + h(t_s - t_\infty) \quad [1]$$

The magnitude of the radiation and the conduction losses were investigated for the conditions of the experiment which introduced

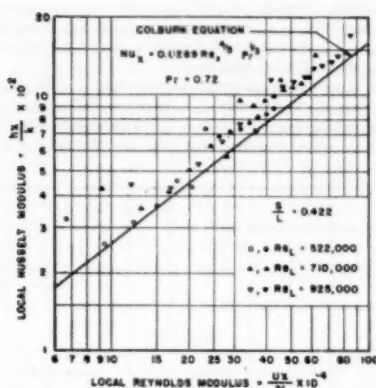


FIG. 4 MEASURED VALUES OF LOCAL NUSSLETT MODULUS UN-CORRECTED FOR STARTING LENGTH FOR A RATIO OF STARTING LENGTH TO TOTAL PLATE LENGTH EQUAL TO 0.422

(Open symbols represent data taken forward of temperature discontinuity; closed symbols represent data taken rearward of discontinuity.)

a maximum error. The value of the long-wave-length emissivity for the nichrome ribbon as measured by the Thermal Radiation Laboratory of the University of California was 0.1. Calculation showed that the radiation heat rates were negligible when compared with the convective heat rates. Conduction through the plate was considered negligible, as the same temperature distribution existed on both sides of the plate.

The effect of transverse conduction was considered negligible in view of the experimental investigation of the temperature distribution along the ribbon as obtained by Ancker (7) which indicated a uniform temperature of the region on both sides of the center portion of the ribbon.

The longitudinal conduction was important only near the brass nose and tail pieces and adjacent to the temperature discontinuity. The heat leakage forward and rearward into the unheated nose and tail pieces resulted in high values of the measured Nusselt modulus for the foremost and rearmost ribbons. The six high points shown in Fig. 5 are typical of this effect. For this reason these data were ignored in later plots.

The forward heat leak at the temperature discontinuity was accounted for in the following manner: The thermal shape factor for conduction from one ribbon to the next was found by the electric-analogy method. Using the measured temperature difference across the discontinuity the forward heat leak was calculated. This value was subtracted from the heat input of the rearward ribbon and added to the heat input of the forward ribbon. This correction amounted to approximately 5 per cent of the convective heat loss of the rearward ribbon and 30 per cent for the forward ribbon.

ANALYSIS OF RESULTS

The experimental results have been corrected for starting length by using the analytical results developed by Rubesin

$$Nu_x = 0.0289 Re_x^{1/2} Pr^{1/3} \frac{1}{[1 - (s/x)^{3/4}]/s^{1/4}} \quad [2]$$

where the last term of the equation represents the correction factor F , due to starting length. The local Nusselt modulus divided by the correction factor was plotted versus the local Reynolds modulus, permitting correlation with the equation

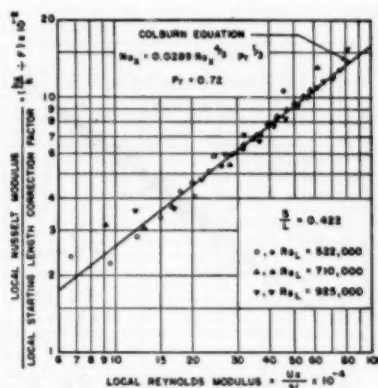


FIG. 5 MEASURED VALUES OF LOCAL NUSSLETT MODULUS CORRECTED FOR STARTING LENGTH FOR A RATIO OF STARTING LENGTH TO TOTAL PLATE LENGTH EQUAL TO 0.422

(Open symbols represent data taken forward of temperature discontinuity; closed symbols represent data taken rearward of discontinuity.)

applying for simultaneous generation of the hydrodynamic and thermal boundary layers (no starting length) which was obtained from the Colburn analogy as

$$Nu_x = 0.0289 Re_x^{1/2} Pr^{1/3} \quad [3]$$

The viscosity and thermal conductivity for air were evaluated at the arithmetic average of the free stream and plate temperatures.

For runs 10 through 14 the method of superposition was applied to obtain the proper correction factor. This procedure is possible because of the linearity of the energy equation. This was necessary because of the two discontinuities in the surface temperature, the first of which was caused by the 2-in. nosepiece. The correction factor for this case becomes

$$F = \frac{1}{\Delta t_1 + \Delta t_2} \left\{ \frac{\Delta t_1}{[1 - (s_1/x)^{3/4}]/s_1^{1/4}} + \frac{\Delta t_2}{[1 - (s_2/x)^{3/4}]/s_2^{1/4}} \right\} \quad [4]$$

Fig. 4 shows the experimental results uncorrected for starting length for runs 10, 11, and 12. The error of measurement in determining the current and temperature ahead of the discontinuity was not very satisfactory because of the small values of these quantities. Below the discontinuity the error of measurement was found to be a maximum of 6 per cent. Thus the points below the discontinuity show the proper trend of asymptotically approaching the curve of simultaneous generation of hydrodynamic and thermal boundary layers.

Fig. 5 shows the same data corrected for starting length. A comparison of Figs. 4 and 5 shows the importance of this correction. If Equation [3] were used to predict the heat rate for a flat plate with an unheated starting length the results would be of the order of 15 per cent too low for the case of Fig. 4.

The data for all runs are shown in Fig. 6 corrected for starting length. The data correlate with the Colburn equation within ± 6 per cent with a maximum spread of ± 8 per cent.

A comparison of the results of the increase in the average heat-transfer coefficient due to starting length as a function of the ratio of the starting length to the total plate length developed by the analysis to the empirical equation determined by the experiments

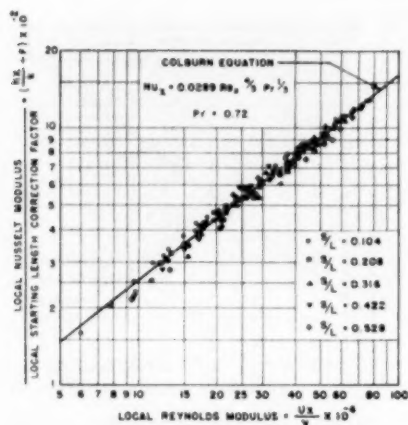


FIG. 6 LOCAL VALUES OF NUSSLETT MODULUS FOR AIR FLOWING PARALLEL TO A FLAT PLATE CORRECTED FOR STARTING LENGTH FOR ALL VALUES OF STARTING LENGTH TO TOTAL PLATE-LENGTH RATIO INVESTIGATED

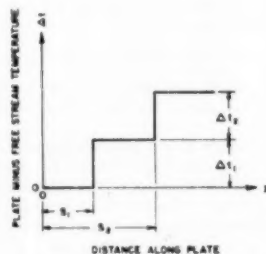


FIG. 7 CO-ORDINATE SYSTEM USED IN EQUATION [4] FOR STARTING-LENGTH CORRECTION DUE TO SUPERPOSED TEMPERATURE DISCONTINUITIES

of Jakob and Dow (6) is presented in Fig. 8. This experiment was performed by use of a cylindrical probe placed parallel to the flow. The experimental results of Jakob and Dow were correlated by the following equation

$$Nu_L = 0.0280 Re_L^{1/2} \left[1 + 0.40 \left(\frac{s}{L} \right)^{2.75} \right] \dots [5]$$

The average Nusselt modulus was obtained from Rubesin's analysis by integration resulting with

$$Nu_L = 0.0361 Re_L^{1/2} Pr^{1/3} \frac{(1 - (s/L)^{9/8})^{17/8}}{1 - s/L} \dots [6]$$

The last terms in Equations [5] and [6] represent the correction factors for the average heat transfer.

As may be seen in Fig. 8, the average correction factor of Jakob and Dow compares favorably with Rubesin's analysis although their results are lower.

By mathematical investigation Jakob and Dow concluded that their experimental results should be 7.5 to 19.6 per cent higher than those of a plane surface because of the curvature of the probe. Inspection of Equations [5] and [6] shows the inverse of

this conclusion. Slack (8) and Little (9) have investigated the heat transfer over cylindrical probes similar to Jakob and Dow in the University of California 3-ft wind tunnel. Their results substantiate those of Jakob and Dow.

Jakob, in his discussion of the results of Siegel and Hawkins (4), reasons that the higher values of Nusselt modulus observed for the plate were due, mainly to secondary flow near the side edges of their plate which increased the heat transfer in that region.

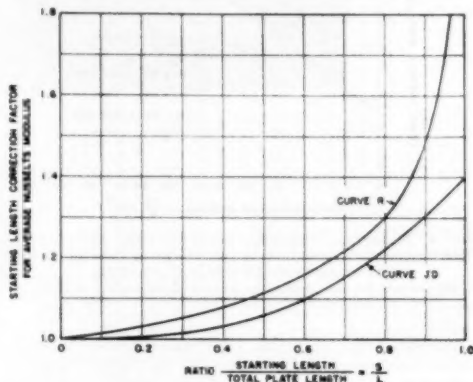


FIG. 8 COMPARISON OF STARTING-LENGTH CORRECTION FACTORS FOR AVERAGE NUSSLETT MODULUS

(Curve R, from analysis of Rubesin, Equation [6]; curve J D, from empirical results of Jakob and Dow, Equation [5].)

During the course of the present investigations string tufts were placed on the side plates used to secure two-dimensional flow over the heated plate. No large-scale secondary flows were detected by this method; however, small-scale secondary flows possibly may have existed at the inside corners. The plate of Siegel and Hawkins was constructed of high-conductivity material allowing the surface temperature to equalize over the width and length of the plate. For constant heat input (electrical heating) this would result in higher measured values of the heat-transfer coefficient. The plate used in the present investigation was constructed of low-conductivity material which would maintain any cross-plate

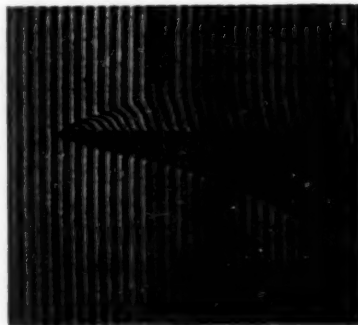


FIG. 9 LEADING EDGE OF PLATE PLACED PARALLEL TO AIR FLOW VIEWED IN UNIVERSITY OF CALIFORNIA INTERFEROMETER (Main-stream velocity equal to 20 fps.)

temperature gradient. Thus the foregoing effect did not influence the measured heat-transfer coefficient.

Fig. 9 shows the leading edge of the plate viewed in the University of California 8-in. interferometer. Even though the plate edge was sharpened ($12\frac{1}{2}$ deg wedge angle) the fringe pattern shows a disturbance of the flow occurring at the leading edge, causing the turbulent boundary layer to form immediately. This disturbance persisted even at very low velocities and could only be removed by tilting the plate downward by several degrees. In experiments where a circular probe is used, the turbulent boundary layer always must be preceded by a laminar boundary layer on the nose section. This difference in boundary-layer growth is believed to represent one of the major sources of discrepancy between heat-transfer data taken on a plate and that taken on a probe.

SUMMARY

Local values of the Nusselt modulus were measured for a flat plate in an air stream for a ratio of starting length to plate length from 0.104 to 0.528. Using the starting-length correction resulting from Rubesin's work, the experimental results were correlated with the Colburn equation within ± 6 per cent for a local Reynolds modulus range from 60,000 to 800,000. The starting-length correction of Jakob and Dow was shown to be slightly low

as compared to the average correction obtained from integration of the Rubesin equation.

BIBLIOGRAPHY

- 1 "An Analytic Investigation of Convective Heat Transfer From a Flat Plate Having a Stepwise Discontinuous Surface Temperature," by M. W. Rubesin, Master of Science thesis, University of California, 1947.
- 2 "Der Wärmeübergang an einer ebenen Wand," by W. Jürges, *Beihfte zum Gesundheits-Ingenieur*, Reihe I, Bieheft 19, 1924.
- 3 "Die Wärmeübertragung einer Geheizten Platte an Strömende Luft," by F. Elias, *Abhandlungen aus dem Aerodynamischen Institut an der Technischen Hochschule Aachen*, No. 9, 1930, pp. 10-39.
- 4 "Heat Transfer From a Vertical Plate to an Air Stream," by L. Siegel and G. A. Hawkins, *Engineering Bulletin*, Purdue University, Research Series No. 97, 1946.
- 5 "Investigation of the Variation of Point Unit Heat-Transfer Coefficients for Laminar Flow Over an Inclined Flat Plate," by B. M. Drake, *Journal of Applied Mechanics*, Trans. ASME, vol. 71, 1949, p. 1.
- 6 "The Heat Transfer From a Cylindrical Surface to Air in Parallel Flow With and Without Starting Sections," by M. Jakob and W. M. Dow, *Trans. ASME*, vol. 68, 1946, pp. 123-134.
- 7 "An Investigation of Local Heat Transfer Coefficients Over an Inclined Flat Plate," by C. J. Ancker, Master of Science thesis, University of California, 1949.
- 8 "Turbulent Heat Transfer With High Surface Temperatures. . . Experimental Investigation With Axial Air Flow," by E. G. Slack, Master of Science thesis, University of California, 1948.
- 9 "Heat Transfer From an Axial Probe From an Air Stream With High Temperature Differences," by E. T. Little, Master of Science thesis, University of California, 1951.



Dynamic Buckling of Thin Elastic Plates¹

By G. A. ZIZICAS,² LOS ANGELES, CALIF.

The behavior of thin elastic plates under loading parallel to their middle plane, constant or arbitrarily varying with time, is considered. The effect of vibrations in the middle plane is examined. In the transverse direction it is shown that by introducing appropriate nondimensional variables and parameters the time dependence reduces to the same type of equation as in the case of columns. Thus the fundamental features of plates and columns are similar. Additional discussion and examples of the solution of the nondimensional equation are presented. Higher modes are related to the fundamental mode of the same plate under appropriate different loading. The need of considering the entire time history of the loading is shown by examples. Shear loading and various boundary conditions are discussed. For loading constant during the time of application initially curved and eccentrically loaded plates are proved equivalent models for the investigation. A slight modification is necessary for a load arbitrarily varying with time.

NOMENCLATURE

The following nomenclature is used in the paper:

- a, b = lengths of sides of a rectangular plate, in.
 A, B = constants
 $D = \frac{Eh^3}{12(1-\mu^2)}$ = flexural rigidity of a plate, lb in.
 e = eccentricity, in.
 E = modulus of elasticity, lb in.⁻²
 f = mid-point (or maximum) displacement of a plate, in.
 f = frequency of vibration, sec⁻¹
 g = gravitational acceleration 32.2 ft per (sec⁻²)
 h = thickness of a plate, in.
 k, m, n = indexes (1, 2, 3, . . .) or separation parameters
 N = force in middle plane, per unit length lb in.⁻¹
 P = external force in middle plane per unit length, lb in.⁻¹
 $\tau(\tau)$ = function of nondimensional time defined by Equation [76]
 $s(t), s_1(t), s_2(t)$ = functions of time introduced by Equations [6] and [8]
 t = time, sec
 T = temperature, deg F
 u, v = displacements in x and y -direction of middle plane averaged over thickness, in.
 U = total potential energy per unit thickness, lb
 V = strain energy per unit thickness, lb in.⁻²

- w = transverse displacement of a point in middle plane of a plate, in.
 x, y, z = rectangular co-ordinates, in.
 X, Y = body forces defined by Equations [10], lb in.⁻³
 \bar{X}, \bar{Y} = functions of nondimensional variables ξ and η
 \bar{X}, \bar{Y} = forces along boundary of middle plane lb in.⁻²
 α = linear coefficient of thermal expansion, deg F⁻¹
 $\beta = \frac{P}{P_{cr}}$ = nondimensional ratio of a loading P to critical or characteristic loading P_{cr}
 γ = specific weight, lb in.⁻³
 γ = angular (shearing) strain
 ϵ = linear strain
 $\xi = \frac{\pi x}{a}$ = nondimensional co-ordinate in x -direction
 $\eta = \frac{f}{f_0}$ = nondimensional displacement in transverse direction
 λ = characteristic values of a differential equation
 μ = Poisson's ratio
 $\zeta = \frac{\pi y}{b}$ = nondimensional co-ordinate in y -direction
 $\pi = 3.1415927 \dots$
 ρ = function of ξ, η and t defined by Equation [70]
 σ = normal stress, lb in.⁻²
 τ = shearing stress, lb in.⁻²
 $\tau = \omega t$ = nondimensional time
 ϕ = stress function in two-dimensional systems
 ω = natural circular frequency, sec⁻¹
 $\nabla^2 = \frac{\partial^2}{\partial x^2} + \frac{\partial^2}{\partial y^2}$
 $\nabla^4 = \frac{\partial^4}{\partial x^4} + 2 \frac{\partial^4}{\partial x^2 \partial y^2} + \frac{\partial^4}{\partial y^4}$

Subscripts and superscripts:

- b = due to bending
 bo = corresponding to bending of a flat plate into form of initial bend of an actual plate
 cr = critical or characteristic
 mn = corresponding to m th natural mode of vibration
 max = maximum
 st = static
 t = total
 x, y, z = in direction x, y, z
 xy = applied to an element normal to z -direction and directed in y -direction
 xy = between x and y -directions (for angular strain)
 0 = initial or constant
 $11, 12, \dots$ = corresponding to the 11, 12, . . . mode of vibration

¹ The investigation presented in this paper was conducted under contract AF 33(038)-14381 sponsored by the Aircraft Laboratory, Engineering Division, Air Research and Development Command.

² Junior Engineer, Department of Engineering, University of California.

Contributed by the Aviation and Heat Transfer Divisions and presented at the Spring Meeting, Seattle, Wash., March 24-26, 1952, of THE AMERICAN SOCIETY OF MECHANICAL ENGINEERS.

NOTE: Statements and opinions advanced in papers are to be understood as individual expressions of their authors and not those of the Society. Manuscript received at ASME Headquarters, November 5, 1951. Paper No. 52-S-8.

INTRODUCTION

The classical theory of buckling is based upon the assumption that the external loads are applied statically (1).² This practically means that their magnitude increases with sufficient slowness that any inertial forces may be neglected. Such an approach cannot be maintained, however, for loads of rapidly changing magnitude.

It has been shown by C. Koning (2) and J. Taub (2, 3) that by applying a constant axial loading on a column for a sufficiently short interval, the Euler critical value may be exceeded by several times without danger of collapse. The column virtually does not have time to experience large deformations. Below the critical load the displacements and stresses may be twice as high as the ones predicted by static theory. Independently, J. H. Meier (4) arrived at essentially the same conclusions. A dynamic investigation of nonlinear or inelastic systems has been obtained by N. J. Hoff (5) and applied to various column models. The same author studied thoroughly the dynamic effects during an actual column-buckling experiment in a testing machine (6). An arbitrary variation of the load with time has been discussed by T. H. H. Pian and J. N. Siddall (7). They considered a column with initial curvature as well as one under eccentric loading, and examined various methods for the solution of the obtained non-dimensional differential equation. Their experiments agreed well with the theory except for the initial stage of buckling. The stability of columns under periodically varying forces has been studied by S. Lubkin and J. J. Stoker (8).

Apparently R. Einaudi (9, 10, 11) has been the only one to investigate the behavior of thin plates under periodically varying forces applied in their middle plane. However, his results do not cover directly the analysis of plates in such important cases as transient loading (landing of airplanes, blast effects on structures) or short duration heat input under boundary constraints. The necessary theory for these cases is developed in the present paper. At several stages comparison is made to the parallel features of columns. For more detailed presentation on certain phases of the paper and additional graphs and numerical tables the reader is referred to a contract report by the author (12).

The effects of shear, rotatory inertia, and structural damping are neglected. They will be reported separately. An extension of the obtained results to anisotropic plates can be readily made.

PLATES WITH INITIAL CURVATURE

Let forces N_x , N_{xy} , N_y varying with time be applied in the middle plane of a plate with initial curvature $w_0(x, y)$. The equation of motion is obtained from the well-known equation of equilibrium (13) by substituting the transverse inertial forces in place of the corresponding external loading. It results in the usual notation

$$\nabla^4(w - w_0) = \frac{1}{D} \left(N_x \frac{\partial^2 w}{\partial x^2} + 2N_{xy} \frac{\partial^2 w}{\partial x \partial y} + N_y \frac{\partial^2 w}{\partial y^2} \right) + \frac{\gamma h}{gD} \frac{\partial^2 w}{\partial t^2} = 0 \quad \dots [1]$$

The equations of motion in the other two directions, in terms of the displacements u and v in the x and y -directions averaged over the thickness h , are (14)

$$\frac{\partial^2 u}{\partial x^2} + \frac{1}{2}(1-\mu) \frac{\partial^2 u}{\partial y^2} + \frac{1}{2}(1+\mu) \frac{\partial^2 v}{\partial x \partial y} = \frac{\gamma(1-\mu^2)}{gE} \frac{\partial^2 u}{\partial t^2} \quad \dots [2]$$

$$\frac{1}{2}(1-\mu) \frac{\partial^2 v}{\partial x^2} + \frac{\partial^2 v}{\partial y^2} + \frac{1}{2}(1+\mu) \frac{\partial^2 u}{\partial x \partial y} = \frac{\gamma(1-\mu^2)}{gE} \frac{\partial^2 v}{\partial t^2} \quad \dots [3]$$

These three equations, however, are not independent. From the stress-strain relations in two dimensions (15) with $N_x = h\sigma_x$, $N_{xy} = h\tau_{xy}$, $N_y = h\sigma_y$, the following relations are obtained

$$\epsilon_x = \frac{\partial u}{\partial x} = \frac{1}{Eh}(N_x - \mu N_y), \quad \epsilon_y = \frac{\partial v}{\partial y} = \frac{1}{Eh}(N_y - \mu N_x) \quad \dots [4]$$

$$\gamma_{xy} = \frac{\partial u}{\partial y} + \frac{\partial v}{\partial x} = \frac{2(1+\mu)}{Eh} N_{xy}$$

They can be solved for N_x , N_{xy} , N_y and written

$$\left. \begin{aligned} N_x &= \frac{Eh}{1-\mu^2} \left(\frac{\partial u}{\partial x} + \mu \frac{\partial v}{\partial y} \right), \\ N_y &= \frac{Eh}{1-\mu^2} \left(\frac{\partial v}{\partial y} + \mu \frac{\partial u}{\partial x} \right), \\ N_{xy} &= \frac{Eh}{2(1+\mu)} \left(\frac{\partial u}{\partial y} + \frac{\partial v}{\partial x} \right) \end{aligned} \right\} \quad \dots [5]$$

A complete formulation of the problem is given by the three partial differential Equations [1], [2], [3] subject to the Relations [5] and appropriate boundary conditions.

DYNAMICAL EFFECTS IN THE MIDDLE PLANE

Equations [2] and [3] show that the vibrations in the middle plane, under the assumptions made, can be treated separately. In order to obtain a solution the following substitutions are used

$$u(x, y, t) = u_0(x, y)u_1(t), \quad v(x, y, t) = v_0(x, y)v_1(t) \quad \dots [6]$$

Dividing through by $u_1''(t)$ in Equation [2] and by $v_1''(t)$ in Equation [3] makes clear that a separation of the time variable requires

$$\frac{u_1''(t)}{u_1(t)} = -m^2, \quad \frac{v_1''(t)}{v_1(t)} = -n^2, \quad \frac{u_1''(t)}{u_1(t)} = -q^2, \quad \frac{v_1''(t)}{v_1(t)} = -k^2 \quad \dots [7]$$

where m, n, q, k are real constants. The negative sign is suggested by the requirement of reversibility which is a direct outcome of the restriction of the investigation in the elastic range—a mathematical justification is beyond the scope of the paper. A comparison of Equations [7] shows that $m^2 = n^2 = q^2 = k^2$ so that $u_1(t) = v_1(t) = \psi(t)$ and

$$\psi''(t) + k^2 \psi(t) = 0 \quad \dots [8]$$

The time dependence can now be eliminated from Equations [2] and [3] and the values k^2 become the characteristic values of the system

$$\left. \begin{aligned} \frac{\partial^2 u_0}{\partial x^2} + \frac{1}{2}(1-\mu) \frac{\partial^2 u_0}{\partial y^2} + \frac{1}{2}(1+\mu) \frac{\partial^2 v_0}{\partial x \partial y} &= -k^2 \frac{\gamma(1-\mu^2)}{gE} u_0 \\ \frac{\partial^2 v_0}{\partial y^2} + \frac{1}{2}(1-\mu) \frac{\partial^2 v_0}{\partial x^2} + \frac{1}{2}(1+\mu) \frac{\partial^2 u_0}{\partial x \partial y} &= -k^2 \frac{\gamma(1-\mu^2)}{gE} v_0 \end{aligned} \right\} \quad \dots [9]$$

Evaluation of k^2 by separation of the variables x and y is in general impossible. Approximate values can be obtained, how-

² Numbers in parentheses refer to the Bibliography at the end of the paper.

ever, by the energy method. It suffices to recognize that Equations (9) are the equations of static equilibrium of a plate which, in addition to forces along the edge, is subject to forces in the middle plane

$$X = k^2 \frac{\gamma}{g} u_0, \quad Y = k^2 \frac{\gamma}{g} v_0 \dots [10]$$

in the x and y -direction correspondingly. In view of this analogy the theorem of minimum of the total potential energy (16) can be applied. The total potential energy U of the system is

$$U = \iint F dxdy - \iint (Xu_0 + Yv_0) dxdy - \int (\bar{X}u_0 + \bar{Y}v_0) ds \dots [11]$$

where

$$F_0 = \frac{1}{2} (\sigma_x \epsilon_x + \sigma_y \epsilon_y + \tau_{xy} \gamma_{xy}) \dots [12]$$

The stresses can be expressed in terms of the strains by the well-known relations (15) and in turn the strains in terms of the displacements. Thus U can be written

$$U = \frac{E}{2(1-\mu^2)} \iint \left(\frac{\partial u_0}{\partial x} + \frac{\partial v_0}{\partial y} \right)^2 dxdy + \frac{E}{4(1+\mu)} \iint \left[\left(\frac{\partial u_0}{\partial y} + \frac{\partial v_0}{\partial x} \right)^2 - 4 \frac{\partial u_0}{\partial x} \frac{\partial v_0}{\partial y} \right] dxdy - \frac{\gamma}{g} k^2 \iint (u_0^2 + v_0^2) dxdy - \int (\bar{X}u_0 + \bar{Y}v_0) ds \dots [13]$$

A judicious choice of expressions for u_0 and v_0 with undetermined parameters can be assumed and U be minimized to give approximate values for k^2 . The procedure will be illustrated for the case of free vibration of a square plate with fixed edges of side length a by taking

$$u_0 = v_0 = A \sin \frac{\pi x}{a} \sin \frac{\pi y}{a} + B \sin \frac{2\pi x}{a} \sin \frac{2\pi y}{a}$$

A and B are unknown constants. The expression for U becomes

$$U = \frac{\pi^2 E (5-\mu)}{2(1-\mu^2)} \left(\frac{A^2}{4} + B^2 \right) - \frac{16 E (3-\mu)}{9 (1-\mu^2)} AB - k^2 \frac{a^2 \gamma}{g} (A^2 + B^2)$$

and in order to be a minimum requires $\partial U / \partial A = \partial U / \partial B = 0$. The obtained system of two linear equations in A and B has a solution different from $A = B = 0$ if and only if the determinant of the coefficients vanishes. An equation is thus obtained which for $\mu = 0.316$ (aluminum) gives

$$k = \frac{3.54}{a} \sqrt{\frac{Eg}{\gamma}} \dots [14]$$

From Equations (14) and (8) the fundamental natural frequency f_0 of extensional vibration is found equal to

$$f_0 = \frac{1}{2\pi} k = \frac{0.56}{a} \sqrt{\frac{Eg}{\gamma}} \dots [15]$$

It is informative to compare this value to the fundamental frequency f_{11} of transverse vibration (17) which for $\mu = 0.316$ is

$$f_{11} = \frac{0.96}{a^2} \sqrt{\frac{Eg}{\gamma}} \dots [16]$$

The ratio of the two frequencies is $f_0/f_{11} = 0.58a/h$. For thin

plates with $a = 50h$ the ratio is roughly equal to 30. Thus, while the plate goes through a complete period in the transverse direction, the fundamental extensional waves travel 30 times back and forth in the middle plane. Accordingly, for times longer than one period in the transverse direction a time average value of the displacements in the middle plane is justified. For higher modes this conclusion can also be used if the comparison is made between the dominant modes in each direction. A modification may be necessary for plates with different ratios a/h . For shorter times the averaging process is not satisfactory. A more accurate analysis (18) may explain discrepancies found by T. H. H. Pian and J. N. Siddall (7) between analytical and experimental results in the initial stages of dynamic buckling of columns. N. J. Hoff (6) has already calculated substantial differences between static and dynamic deflection curves at the initial stages of a buckling experiment.

Further discussion in the present paper is confined to time greater than the period of the dominant modes of transverse vibration. Since from Equation (8) it follows that the time dependence is sinusoidal, the time average of the displacements u and v for a large number of periods of vibration within the middle plane approaches zero. Then the inertial forces in Equations (9) can be neglected and

$$\left. \begin{aligned} \frac{\partial^2 u_0}{\partial x^2} + \frac{1}{2} (1-\mu) \frac{\partial^2 u_0}{\partial y^2} + \frac{1}{2} (1+\mu) \frac{\partial^2 v_0}{\partial x \partial y} &= 0 \\ \frac{\partial^2 v_0}{\partial y^2} + \frac{1}{2} (1-\mu) \frac{\partial^2 v_0}{\partial x^2} + \frac{1}{2} (1+\mu) \frac{\partial^2 u_0}{\partial x \partial y} &= 0 \end{aligned} \right\} \dots [17]$$

These two equations combined give the well-known results

$$\nabla^2 u = 0, \quad \nabla^2 v = 0 \dots [18]$$

As an application, consider a rectangular plate with fixed sides subject to an increase of temperature T in the plate only but not in the supports. The stress-strain relations are (19)

$$\left. \begin{aligned} \epsilon_x &= \frac{1}{Eh} (N_x - \mu N_y) + \alpha T, \quad \gamma_{xy} = \frac{1+\mu}{Eh} N_{xy} \\ \epsilon_y &= \frac{1}{Eh} (N_y - \mu N_x) + \alpha T \end{aligned} \right\} \dots [19]$$

Now $u = v = 0$ satisfy both Equations (18) and the boundary conditions so that, because of the uniqueness of solution (20), they are the actual ones. Thus $\epsilon_x = \epsilon_y = \gamma_{xy} = 0$ and from Equations (19) follows

$$N_x = N_y = -\frac{Eh\alpha T}{1-\mu}, \quad N_{xy} = 0 \dots [20]$$

These values also have been obtained in a different way (21).

Since the calculation of N_x , N_y , N_{xy} has been reduced to a two-dimensional static problem the technique of stress function ϕ (22) satisfying the equation

$$\nabla^4 \phi = 0 \dots [21]$$

can be used. In this way for a rectangular plate under boundary compression forces P_x , P_y and shearing forces P_{xy} per unit length results (22)

$$N_x = -P_x, \quad N_y = -P_y, \quad N_{xy} = -P_{xy} \dots [22]$$

CONSTANT LOADING SUDDENLY APPLIED IN ONE DIRECTION

A simply supported rectangular plate initially curved in the shape

$$w_0 = f_0 \sin \frac{\pi x}{a} \sin \frac{\pi y}{b} \dots [23]$$

is considered. A pressure P in the x -direction is suddenly applied on the plate which is at rest. Then $N_x = -P$, $N_y = N_{xy} = 0$ and Equation (1) specializes to

$$\nabla^4(w - w_0) + \frac{P}{D} \frac{\partial^2 w}{\partial x^2} + \frac{\gamma h}{D} \frac{\partial^2 w}{\partial t^2} = 0 \quad [24]$$

It will be convenient to introduce the nondimensional variables

$$\xi = \frac{\pi x}{a}, \quad \zeta = \frac{\pi y}{b} \quad [25]$$

by means of which the initial curvature becomes

$$w_0 = f_0 \sin \xi \sin \zeta \quad [26]$$

and the Equation (24) of motion is transformed into

$$\pi^4 D \left[\frac{1}{a^4} \frac{\partial^4(w - w_0)}{\partial \xi^4} + \frac{2}{a^2 b^2} \frac{\partial^4(w - w_0)}{\partial \xi^2 \partial \zeta^2} + \frac{1}{b^4} \frac{\partial^4(w - w_0)}{\partial \zeta^4} \right] + \pi^2 P \frac{1}{a^2} \frac{\partial^2 w}{\partial \xi^2} + \frac{\gamma h}{g} \frac{\partial^2 w}{\partial t^2} = 0 \quad [27]$$

The boundary conditions are (23)

$$\left. \begin{aligned} w &= 0 \text{ for } \xi = 0, \xi = \pi, \zeta = 0, \zeta = \pi \\ \frac{\partial^2 w}{\partial \xi^2} &= 0 \text{ for } \xi = 0 \text{ and } \xi = \pi \\ \frac{\partial^2 w}{\partial \zeta^2} &= 0 \text{ for } \zeta = 0 \text{ and } \zeta = \pi \end{aligned} \right\} \quad [28]$$

and the initial conditions can be written

$$w = w_0 \text{ and } \frac{\partial w}{\partial t} = 0 \text{ at } t = 0 \quad [29]$$

A formal solution of the problem is obtained by separation of variables, i.e., by assuming

$$w(\xi, \zeta, t) = X(\xi)Y(\zeta)f(t) \quad [30]$$

Substituting in Equation (27), dividing through by the product XY , and denoting the order of derivatives by superscripts yields

$$\pi^4 D \left(\frac{1}{a^4} \frac{X^{IV}}{X} + \frac{2}{a^2 b^2} \frac{X''}{X} \frac{Y''}{Y} + \frac{1}{b^4} \frac{Y^{IV}}{Y} \right) (f - f_0) + \pi^2 P \frac{1}{a^2} \frac{X''}{X} + \frac{\gamma h}{g} \frac{df}{dt^2} = 0 \quad [31]$$

This equation is satisfied if $X''/X = A$ and $Y''/Y = B$, where A and B are constants. Indeed $X^{IV} = (X'')'' = (AX)'' = A^2 X$ and $Y^{IV} = B^2 Y$ so that Equation (31) becomes a differential equation for $f(t)$ if the values A and B are known. They are evaluated by solving the differential equations $X'' - AX = 0$ and $Y'' - BY = 0$ under the boundary conditions, Equations (28). It follows

$$X = \sin m\xi, \quad Y = \sin n\zeta, \quad (m, n = 1, 2, 3, \dots) \quad [32]$$

Attention is first focused on the values $m = n = 1$, for which

$$\frac{\gamma h}{g} \frac{df}{dt^2} + (f - f_0) \pi^4 D \left(\frac{1}{a^2} + \frac{1}{b^2} \right) - \pi^2 P \frac{f}{a^2} = 0 \quad [33]$$

with initial conditions

$$f = f_0 \text{ and } \frac{df}{dt} = 0 \text{ at } t = 0 \quad [34]$$

The coefficients of Equation (33) have a definite physical significance. They are related to the values of the fundamental char-

acteristic load P_{cr} of a simply supported plate under loading in one direction and the fundamental natural circular frequency ω of transverse vibration (24)

$$P_{cr} = \pi^2 D \left(\frac{1}{a^2} + \frac{1}{b^2} \right), \quad \omega = \pi^2 \sqrt{\frac{gD}{\gamma h}} \left(\frac{1}{a^2} + \frac{1}{b^2} \right) \quad [35]$$

In addition the nondimensional parameter β and the variables τ and η defined by

$$\beta = \frac{P}{P_{cr}}, \quad \tau = \omega t, \quad \eta = \frac{f}{f_0} \quad [36]$$

are introduced and Equations (33) and (34) correspondingly become

$$\frac{d^2 \eta}{d\tau^2} + (1 - \beta) \eta - 1 = 0 \quad [37]$$

$$\eta = 1 \text{ and } \frac{d\eta}{d\tau} = 0 \text{ at } \tau = 0 \quad [38]$$

This nondimensional equation and the boundary conditions are the same as in the case of columns. They have been discussed by various investigators (2, 3, 4, 7). The following three cases are distinguished:

1 $\beta < 1$. The load P is smaller than the critical load P_{cr} .

Then

$$\eta = \frac{1}{1 - \beta} [1 - \beta \cos(\sqrt{1 - \beta} \tau)] \quad [39]$$

The plate undergoes an oscillatory motion around the static displacement η_{st} (obtained by neglecting the inertial term)

$$\eta_{st} = \frac{1}{1 - \beta} \quad [40]$$

The maximum displacement reached during the vibration is

$$\eta_{max} = \frac{2}{1 - \beta} = 2\eta_{st} \quad [41]$$

i.e., twice as large as the one obtained through very slow application of the load.

2 $\beta = 1$. The load P is equal to the critical load P_{cr} . There follows

$$\eta = \frac{1}{2} \tau^2 + 1 \quad [42]$$

The displacement increases according to a parabolic law.

3 $\beta > 1$. The load P is greater than the critical load P_{cr} . The result is

$$\eta = \frac{1}{\beta - 1} [\beta \cosh(\sqrt{\beta - 1} \tau) - 1] \quad [43]$$

The displacement increases following a hyperbolic cosine law.

It was pointed out previously that a time greater than the period of the dominant mode of vibration is essential for the accuracy of the present analysis. This means τ greater than 1. On the other hand, the assumption of small-deflection theory imposes an upper limit on the values of η . The theory holds true for displacements not larger than half or equal to the thickness h of the plate. For initial mid-point eccentricity $f_0 = 0.05h$ the limiting values are correspondingly $\eta_{max} = 10$ and $\eta_{max} = 20$. For higher eccentricities they should be smaller. Beyond such limits large-deflection theory is needed.

The bending stresses σ_x^b , σ_y^b , τ_{xy}^b and corner reaction R can be

expressed easily in terms of the static values σ_x^{bo} , σ_y^{bo} , τ_{xy}^{bo} and R_0 that are developed in an originally flat plate bent in the form given by Equations [23] or [26]. By inserting the values of the displacements in the well-known bending formulas it is obtained

$$\sigma_x^b = (\eta - 1)\sigma_x^{bo}, \quad \sigma_y^b = (\eta - 1)\sigma_y^{bo}, \quad \tau_{xy}^b = (\eta - 1)\tau_{xy}^{bo}, \\ R = (\eta - 1)R_0 \dots [44]$$

These relations hold true in particular for the maximum stresses. The dynamic and static moments and shearing forces are also related by the same factor $\eta - 1$.

HIGHER MODES OF VIBRATION

Formally the most general expression for the displacement is a linear combination of the characteristic functions, Equations [32], i.e.

$$w = \sum_{m=1}^{\infty} \sum_{n=1}^{\infty} f^{mn}(t) \sin m\xi \sin n\zeta \quad (m, n = 1, 2, 3, \dots) \dots [45]$$

Furthermore, a physically possible initial curvature has sufficient continuity to be written in the form

$$w_0 = \sum_{m=1}^{\infty} \sum_{n=1}^{\infty} f_0^{mn} \sin m\xi \sin n\zeta \quad (m, n = 1, 2, 3, \dots) \dots [46]$$

Under the assumption of uniform and absolute convergence of the resulting series, these expressions are substituted in Equation [27] and the coefficients of each product $\sin m\xi \sin n\zeta$ are grouped together. The equation is identically satisfied if the coefficient of each such product vanishes. A simple nondimensional form is given to the obtained equations by introducing the characteristic loads P_{cr}^{mn} and natural circular frequencies ω_{mn} associated with the mn -mode of vibration (24)

$$P_{cr}^{mn} = \pi^2 D \frac{a^3}{m^3} \left(\frac{m^2}{a^2} + \frac{n^2}{b^2} \right), \quad \omega_{mn} = \pi^2 \sqrt{\frac{gD}{\gamma h}} \left(\frac{m^2}{a^2} + \frac{n^2}{b^2} \right) \dots [47]$$

and the nondimensional quantities

$$\beta_{mn} = \frac{P}{P_{cr}^{mn}}, \quad \tau_{mn} = \omega_{mn} t, \quad \eta_{mn} = \frac{f^{mn}}{f_0^{mn}} \dots [48]$$

The result is

$$\frac{d^2 \eta_{mn}}{d\tau_{mn}^2} + (1 - \beta_{mn})\eta_{mn} - 1 = 0 \dots [49]$$

subject to initial conditions

$$\eta_{mn} = 1 \quad \text{and} \quad \frac{d\eta_{mn}}{d\tau_{mn}} = 0 \quad \text{at} \quad \tau_{mn} = 0 \dots [50]$$

The only difference between these two equations and Equations [37] and [38] is the value of β_{mn} . Hence, in nondimensional time τ_{mn} and displacement η_{mn} defined by Equations [48], the time dependence of higher modes is identical to that of the fundamental mode of the same plate under nondimensional loading β_{mn} in place of β . This property apparently is being observed here for the first time. Analytically it shows that only the fundamental mode for various loadings need be considered. It reduces the evaluation of all modes for constant loading to a single graph with various values of the loading, as the one given in Fig. 1. It may lead to an experimental method of evaluating the higher modes by changing the loading and considering the fundamental mode rather than proceeding with a harmonic analysis of the actual pattern under the given loading. It also leads to a better understanding of the features of higher modes. The change from nondimensional parameters to the actual time presents no difficulties. Previous investigators have derived equations for higher modes of columns referred to the same time scale (2, 3, 4, 7).

The characteristic loads P_{cr}^{mn} can be arranged in order of magnitude

$$P_1 = P_{cr}^{11}, P_2 = P_{cr}^{12}, \dots, P_i = P_{cr}^{ij}, \dots \quad (i = 1, 2, 3, \dots)$$

The actual load P may fall between any two of them, say, P_{i-1} and P_i so that $P_{i-1} \leq P < P_i$. Then the modes $1, 2, \dots, i-1$ give $\beta_{mn} \geq 1$ and according to Equation [49] have hyperbolic or linear solutions, i.e., they are unstable. The modes $i, i+1, i+2, \dots$ have sinusoidal solutions; hence they are stable. This result established by J. H. Meier for columns (4) is here found true for plates.

CONSTANT LOADING APPLIED FOR A SHORT TIME INTERVAL

Let the applied constant loading be removed suddenly. The investigation can be carried on a nondimensional basis as for

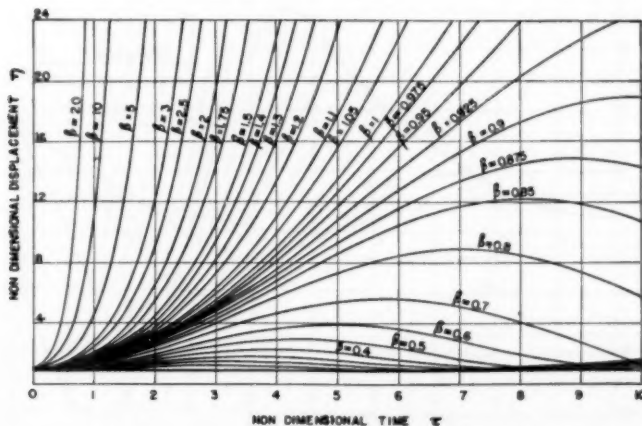


FIG. 1 NONDIMENSIONAL PLATE DISPLACEMENT FOR CONSTANT LOADINGS

columns (4). For the interval τ_0 of the load application the plate behavior was discussed in the previous section. At the end of τ_0 the plate experiences displacements η_0 and velocities v_0 as follows for

$$\beta < 1 \quad \left\{ \begin{aligned} \eta_0 &= \frac{1}{1-\beta} [1 - \beta \cos(\sqrt{1-\beta} \tau_0)] \\ v_0 &= \left(\frac{d\eta}{d\tau} \right)_{\tau=\tau_0} = \frac{\beta}{\sqrt{1-\beta}} \sin(\sqrt{1-\beta} \tau_0) \end{aligned} \right\} \quad [51]$$

for

$$\beta = 1, \quad \eta_0 = \frac{1}{2} \tau_0^2, \quad v_0 = \tau_0 \quad [52]$$

for

$$\beta > 1 \quad \left\{ \begin{aligned} \eta_0 &= \frac{1}{\beta-1} [\beta \cosh(\sqrt{\beta-1} \tau_0) - 1] \\ v_0 &= \left(\frac{d\eta}{d\tau} \right)_{\tau=\tau_0} = \frac{1}{\sqrt{\beta-1}} \sinh(\sqrt{\beta-1} \tau_0) \end{aligned} \right\} \quad [53]$$

The process after the removal of the load is best studied by means of a time origin coinciding with the instant of removal. The governing equation becomes

$$\frac{d^2\eta}{d\tau^2} + \eta - 1 = 0 \quad [54]$$

and the initial conditions

$$\eta = \eta_0, \quad \frac{d\eta}{d\tau} = v_0 \quad \text{at} \quad \tau = \tau_0 \quad [55]$$

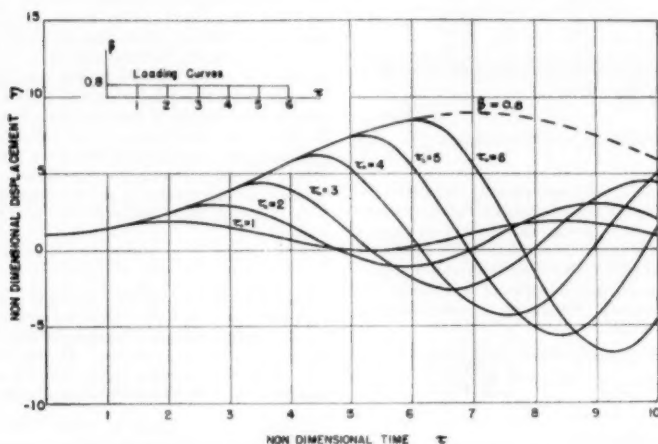


FIG. 2 CONSTANT LOADING $\beta = 0.8$ APPLIED FOR A SHORT TIME

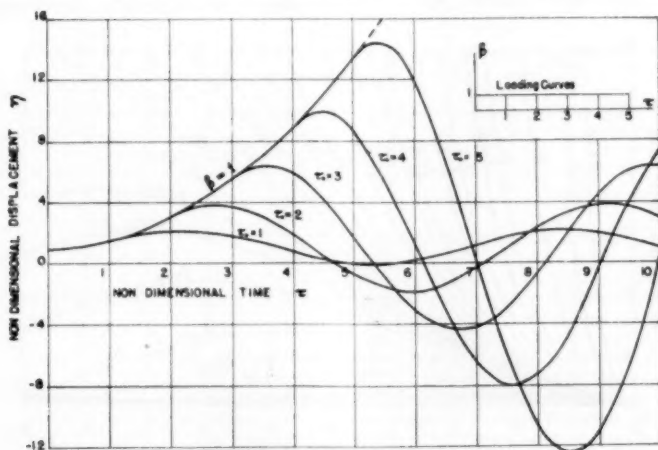
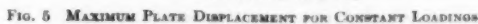


FIG. 3 CONSTANT LOADING $\beta = 1.0$ APPLIED FOR A SHORT TIME



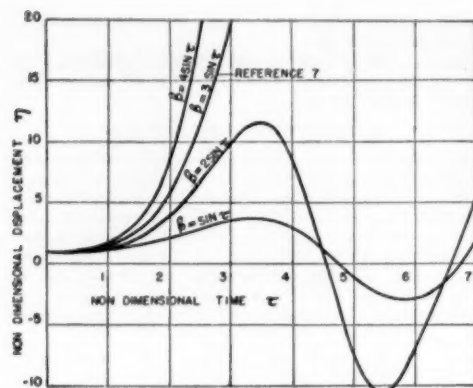


FIG. 6 PLATE DISPLACEMENT FOR SINUSOIDAL LOADINGS

solution using a number of terms of the Taylor series for each step is more practical. If β is given by numerical values at certain intervals, finite difference approximations can be used for its derivatives. The method is discussed by F. B. Hildebrand (25); its application to the particular equation at hand is outlined in a report by the author (12). Figs. 6 and 7 show graphically the results obtained for sinusoidal and linear variation of the loading with time. For a function β given in the form of or approximated by polynomials the standard method of power series also can be applied. Such a procedure was used for the curve of $\beta = 2 - 1/\tau$ in Fig. 9.

EFFECT OF TOTAL LOAD AND MAXIMUM LOADING VALUE

The desirability of obtaining an over-all quantity that would define the dynamical effects without the use of the entire time history of the loading is obvious. Such a possibility will be discussed.

First of all, the previous results show that the displacement may be increasing with time even for $\beta = \text{const}$, so a specific value of β cannot be used as an over-all criterion. Next, the total non-dimensional loading

$$\beta_t = \int_0^{\tau} \beta d\tau \dots \dots \dots [58]$$

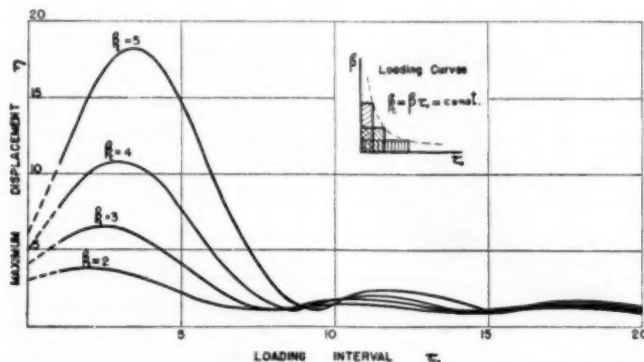


FIG. 8 CONSTANT LOADINGS WITH THE SAME TOTAL LOAD

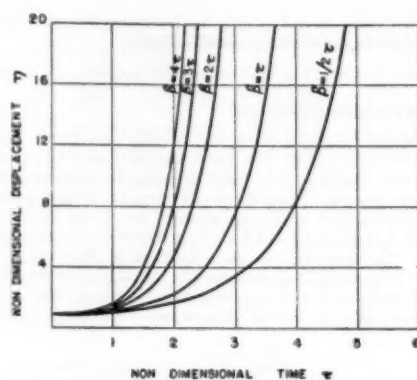


FIG. 7 PLATE DISPLACEMENT FOR LINEAR LOADINGS

is examined. In Fig. 8 curves of η_{\max} for $\beta_t = 2, 3, 4, 5$, and constant loading are drawn. The largest η_{\max} is obtained for approximately $\tau_0 = \pi$, i.e., actual time $t_0 = \pi/\omega$ equal to half a period of transverse vibration. The curves are extended up to $\tau_0 = 20$ and show the effect of intervals higher than the period, which is not included in similar curves by C. Koning and J. Taub (2). It is clear that considerable change of η_{\max} exists under the same β_t ; therefore β_t is not a satisfactory criterion. Finally, loadings of the same β_t and maximum value of β are compared in Fig. 9. A difference up to 25 per cent in η_{\max} is observed.

It can be concluded that the entire time history of the loading is necessary for the description of the dynamic buckling of plates or columns.

LOADING IN TWO PERPENDICULAR DIRECTIONS

If $P_x(t)$ and $P_y(t)$ are compressive forces uniformly distributed along the edges and parallel to the x and y -axes, respectively, Equations [22] show that the equation of motion is

$$\nabla^2(w - w_0) + \frac{P_x}{D} \frac{\partial^2 w}{\partial x^2} + \frac{P_y}{D} \frac{\partial^2 w}{\partial y^2} + \frac{\gamma h}{D} \frac{\partial^4 w}{\partial t^2} = 0 \dots [59]$$

For simply supported rectangular plates the boundary conditions in terms of the nondimensional variables, Equations [25], are

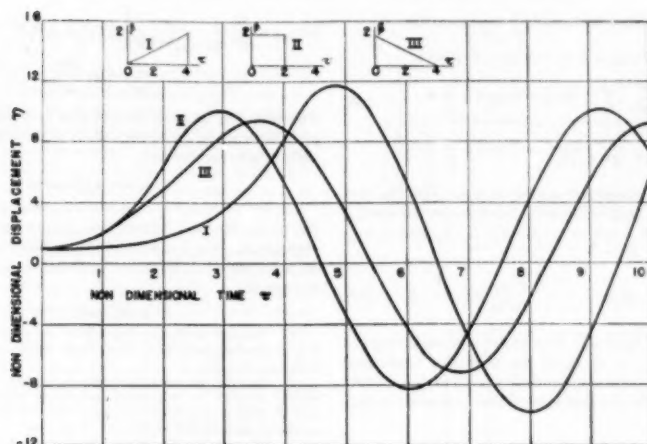


FIG. 9 SAME TOTAL LOAD AND MAXIMUM VALUE OF LOADING

again given by Equations [28]. By introducing the following value for the parameter $\beta_{ms}(t)$

$$\beta_{ms}(t) = \frac{1}{\pi^2 D} \left(\frac{m^2}{a^2} + \frac{n^2}{b^2} \right) \left(\frac{m^2}{a^2} P_x + \frac{n^2}{b^2} P_y \right) \quad [60]$$

and ω_{ms} , τ_{ms} , η_{ms} as defined by Equations [47] and [48], the equation of motion is brought to the form of Equation [49] under initial conditions Equations [50] and can be investigated further on the basis of the results obtained for loading in one direction.

VARIOUS BOUNDARY CONDITIONS AND SHAPES—SHEAR LOADING

For rectangular plates with boundary conditions that allow separation of variables, i.e., solution of the equations $X'' = AX$ and $Y'' = BY$ derived from Equation [31], the previous procedure can be applied directly. The same is true for other boundary shapes where appropriate separable curvilinear coordinates can be used.

For shear loading, and, in general, nonseparable space variables under constant loading, a substitution

$$w_k(x, y, t) = U_k(x, y)f^k(t), \quad (k = 1, 2, 3, \dots) \quad [61]$$

is suggested. For the homogeneous part of Equation [1], i.e., for free vibrations, the separation process gives

$$\nabla^4 U_k - \frac{1}{D} \left(N_x \frac{\partial^2 U_k}{\partial x^2} + 2N_{xy} \frac{\partial^2 U_k}{\partial x \partial y} + N_y \frac{\partial^2 U_k}{\partial y^2} \right) - \lambda_k^2 U_k = 0 \quad [62]$$

$$\frac{\gamma h}{gD} \frac{d^2 f^k}{dt^2} + \lambda_k^2 f^k = 0 \quad [63]$$

The characteristic values λ_k^2 and the associated characteristic functions $U_k(x, y)$ of Equation [62] could be approximated by variational or other methods. Depending on the sign of λ_k^2 the time function $f^k(t)$ may be sinusoidal, linear, or hyperbolic. Thus some modes may be unstable while the remaining higher ones are stable. For plates with initial curvature the corresponding function can be found by expanding w_0 and $\nabla^4 w_0$ in infinite series in terms of the characteristic functions of Equation [62]. Let the obtained coefficients be f_m^k and f_n^k , respectively. The

displacement $w(x, y, t)$ can be expressed as a linear combination of terms of the type of Equation [61] in the form of infinite series with unknown functions $f^k(t)$. After a substitution in Equation [1] use can be made of the Relations [62]. By equating the coefficient of each function $U_k(x, y)$ to zero, the following equations result

$$\frac{\gamma h}{gD} \frac{d^2 f^k(t)}{dt^2} + \lambda_k^2 f^k(t) - f_m^k = 0 \quad [64]$$

In terms of the nondimensional quantities

$$\omega_k = \sqrt{\frac{gD}{\gamma h}} \sqrt{\frac{f_m^k}{f_n^k}}, \quad \beta_k = 1 - \lambda_k^2 \frac{f_m^k}{f_n^k}, \quad \tau_k = \omega_k t, \quad \eta_k = \frac{f^k(t)}{f_m^k} \quad [65]$$

Equation [64] is brought to the form

$$\frac{d^2 \eta_k}{d\tau_k^2} + (1 - \beta_k) \eta_k - 1 = 0 \quad [66]$$

subject to the boundary conditions

$$\eta_k = 1 \quad \text{and} \quad \frac{d\eta_k}{d\tau_k} = 0 \quad \text{at} \quad \tau_k = 0 \quad [67]$$

Any further discussion may be carried out as in the case of Equation [49] with constant β_{ms} .

If N_x , N_{xy} , N_y are functions of time, or functions of both coordinates x , y , and time t , and the boundary conditions do not allow for a separation of the space variables, elaborate numerical techniques or the use of special computing devices are inevitable.

ECCENTRIC LOADING PARALLEL TO MIDDLE PLANE

The motion is governed by the homogeneous part (i.e., with $w_0 = 0$) of Equation [1]. For rectangular plates the use of the nondimensional variables ξ and ζ defined by Equations [25] is again advisable so that

$$\pi^2 D \left(\frac{1}{a^4} \frac{\partial^4 w}{\partial \xi^4} + \frac{2}{a^2 b^2} \frac{\partial^4 w}{\partial \xi^2 \partial \zeta^2} + \frac{1}{b^4} \frac{\partial^4 w}{\partial \zeta^4} \right) + \pi^2 \left(\frac{P_x}{a^2} \frac{\partial^2 w}{\partial \xi^2} + \frac{P_y}{b^2} \frac{\partial^2 w}{\partial \zeta^2} \right) + \frac{\gamma h}{g} \frac{\partial^2 w}{\partial t^2} = 0 \quad [68]$$

For simply supported plates, the boundary conditions are

$$\left. \begin{aligned} w = 0 \quad \text{for } \xi = 0, \xi = \pi, \zeta = 0, \zeta = \pi \\ \frac{\partial^2 w}{\partial \xi^2} = -\frac{a^2}{\pi^2} \frac{P_x}{D} \quad \text{for } \xi = 0 \text{ and } \xi = \pi \\ \frac{\partial^2 w}{\partial \zeta^2} = -\frac{b^2}{\pi^2} \frac{P_y}{D} \quad \text{for } \zeta = 0 \text{ and } \zeta = \pi \end{aligned} \right\} \quad [69]$$

It is well known that the solution can be obtained with the help of any function $\rho(\xi, \zeta)$ with continuous fourth-order derivatives satisfying the boundary conditions. For P_x , P_y , e_x , and e_y constant one such function is

$$\rho(\xi, \zeta) = \frac{P_x e_x}{2\pi^2 D} a^2 \xi(\pi - \xi) + \frac{P_y e_y}{2\pi^2 D} b^2 \zeta(\pi - \zeta) \dots [70]$$

Since the characteristic functions of Equation [68] satisfying the homogeneous part (i.e., $w = 0$), the boundary conditions, Equations [69], are the same as for initially curved plates, already given by Equations [32], the following formal expression is suggested

$$w(\xi, \zeta, t) = \rho(\xi, \zeta) + \sum_{m=1}^{\infty} \sum_{n=1}^{\infty} f^{mn}(t) \sin m\xi \sin n\zeta \dots [71]$$

This expression is substituted in Equation [68] and the contribution of $\rho(\xi, \zeta)$ is expanded in double sine series as follows

$$\frac{e_x P_x}{D} + \frac{e_y P_y}{D} = \frac{16}{\pi^2} \frac{e_x P_x + e_y P_y}{D} \sum_{m=1,3,5,\dots}^{\infty} \sum_{n=1,3,5,\dots}^{\infty} \frac{1}{mn} \sin m\xi \sin n\zeta \dots [72]$$

Equating the coefficients of $\sin m\xi \sin n\zeta$ in Equation [68] to zero yields a set of equations for $f^{mn}(t)$. The variables τ_{mn} and η_{mn} defined by Equations [47] and [48] can be used again, but with

$$\begin{aligned} f_s^{mn} &= \frac{16}{\pi^4} \frac{e_x P_x + e_y P_y}{D^2} \frac{1}{\left(\frac{m^2}{a^2} + \frac{n^2}{b^2}\right)^2 mn} \\ &= \frac{16}{\pi^2} \frac{g}{\gamma h D} \frac{e_x P_x + e_y P_y}{\omega_{mn}^2} \frac{1}{mn} \dots [73] \\ \beta_{mn} &= \frac{1}{\pi^4 D^2} \left(\frac{m^2}{a^2} + \frac{n^2}{b^2}\right)^2 \left(\frac{m^2 P_x}{a^2} + \frac{n^2 P_y}{b^2}\right) \\ &= \left(\frac{m^2 P_x}{a^2} + \frac{n^2 P_y}{b^2}\right) \frac{g}{\gamma h D} \dots [74] \end{aligned}$$

In this way the equations for $f^{mn}(t)$ are again brought to the form of Equation [49] with boundary conditions, Equations [50]. Only the values $m = 1, 3, 5, \dots$, $n = 1, 3, 5, \dots$ give η_{mn} different from zero.

ECCENTRIC LOADING VARYING WITH TIME

The expression ρ of Equation [70] can be used even in the case where P_x , P_y , e_x , e_y are functions of time. Then the coefficients of the expansion in series of the contribution of $\rho(\xi, \zeta, t)$ are also functions of time, and by a similar procedure follows

$$\frac{d^2 f^{mn}}{d\tau_{mn}^2} + (1 - \beta_{mn}) f^{mn} - r(\tau_{mn}) = 0 \dots [75]$$

where

$$r(\tau_{mn}) = \frac{16}{\pi^2} \frac{1}{mn} \frac{g}{\omega_{mn}^2 \gamma h D} \left[e_x P_x + e_y P_y - \frac{\gamma h}{2\pi^2 g} \left(a^2 \frac{d^2 P_x}{d\tau^2} + b^2 \frac{d^2 P_y}{d\tau^2} \right) \right] \dots [76]$$

The numerical methods discussed for load varying with time for a plate with initial curvature can be extended to the present case with a slight modification.

ACKNOWLEDGMENT

The author wishes to express his appreciation to Prof. Walter C. Hurty for his kind interest and encouragement during the investigation. He is also indebted to Messrs. J. D. Revell, J. V. Addison, and D. E. Johnston for their help with the computations and graphs.

BIBLIOGRAPHY

- 1 "Theory of Elastic Stability," by S. Timoshenko, McGraw-Hill Book Company, Inc., New York, N. Y., and London, England, 1936, pp. 325-327.
- 2 "Stoßartige Knickbeanspruchung schlanker Stäbe im elastischen Bereich bei beiderseits gelenkiger Lagerung," by C. Koning and J. Taub, *Luftfahrtforschung*, vol. 10, 1933, pp. 55-64. Also available as NACA TM 748.
- 3 "Stoßartige Knickbeanspruchung schlanker Stäbe im elastischen Bereich," by J. Taub, *Luftfahrtforschung*, vol. 10, 1933, pp. 65-85. Also available as NACA TM 749.
- 4 "On the Dynamics of Elastic Buckling," by J. H. Meier, *Journal of the Aeronautical Sciences*, vol. 12, 1945, pp. 433-440.
- 5 "Dynamic Criteria of Buckling," by N. J. Hoff, Research, Engineering Structures Supplement, Butterworth's Scientific Publications, Ltd., London, England, and Academic Press, Inc., New York, N. Y., 1949, pp. 121-139.
- 6 "The Dynamics of the Buckling of Elastic Columns," by N. J. Hoff, *Journal of Applied Mechanics*, Trans. ASME, vol. 73, 1951, pp. 68-74.
- 7 "Dynamic Buckling of Slender Struts," by T. H. H. Pian and J. N. Siddall, Massachusetts Institute of Technology, Department of Aeronautical Engineering, Aeroelastic and Structures Research, May, 1950, 68 pp.
- 8 "Stability of Columns and Strings Under Periodically Varying Forces," by S. Lubkin and J. J. Stoker, *Quarterly of Applied Mathematics*, vol. 1, 1943, pp. 215-236.
- 9 "Sulle Configurazioni di Equilibrio Instabile di una Piastra Sollecitata da Sforzi Tangenziali Pulsanti," by R. Einaudi, Accademia Gioenia di Scienze Naturali di Catania, Atti, series 6, vol. 1, 1936, Memoria 20, pp. 1-5.
- 10 "Sulle Configurazioni di Equilibrio Instabile di una Piastra Sollecitata da Sforzi Tangenziali Pulsanti, Nota Seconda," by R. Einaudi, Accademia Gioenia di Scienze Naturali di Catania, Atti, series 6, vol. 2, 1937, Memoria 5, pp. 1-20.
- 11 "Sulle Vibrazioni Quasi-armoniche di un Sistema ad Elasticità Quasi-costante," by R. Einaudi, Accademia delle Scienze di Torino, Atti, vol. 72, 1937, pp. 292-298.
- 12 "Dynamic Buckling of Thin Simply Supported Plates in the Elastic Region," by G. A. Zizicas, University of California, Department of Engineering, Los Angeles, Calif., Air Force Contract AF 33(038)-14381 Report, May, 1951, 96 pp.
- 13 See reference 1, p. 319.
- 14 "A Treatise on the Mathematical Theory of Elasticity," by A. E. H. Love, Dover Publications, New York, N. Y., fourth edition, 1944, p. 497.
- 15 "Theory of Elasticity," by S. Timoshenko and J. N. Goodier, McGraw-Hill Book Company, Inc., New York, N. Y.; Toronto, Ont., Can.; and London, England, second edition, 1951, p. 24.
- 16 Ibid., pp. 151-153 and 146-147.
- 17 "Vibration Problems in Engineering," by S. Timoshenko, D. Van Nostrand Company, Inc., New York, N. Y., second edition, eighth printing, 1951, p. 423.
- 18 "The Initial Stages of Dynamic Buckling of Elastic Columns and Plates," by G. A. Zizicas (in preparation).
- 19 See reference 15, p. 421.
- 20 See reference 15, pp. 236-238.
- 21 See reference 15, p. 401.
- 22 See reference 15, pp. 26-27 and 29-32.
- 23 See reference 1, p. 298.
- 24 See reference 17, p. 423.
- 25 "Advanced Calculus for Engineers," by F. B. Hildebrand, Prentice-Hall, Inc., New York, N. Y., 1949, pp. 95-120.

Discussion

GEORGE GERARD.⁴ This interesting paper is an extension to plate elements of the dynamic buckling analyses which have been considered for columns in the recent literature. These analyses are based on a dynamic loading which builds up to the dynamic buckling load by successive reflections of the initial dynamic stress pulse. It has been found for columns and now for plates that dynamic loads in excess of the static buckling loads can be sustained under such loadings.

A point to be raised regarding application of the results of the paper is concerned with the relation between the buckling and failing loads of plate elements. For a column under static loading and presumably under dynamic loading also, the buckling load and failing load are essentially the same. For a plate, however, the failing load may be considerably in excess of the static buckling load when buckling occurs below the proportional limit of the material. Thus, in the case of dynamic buckling of a plate, does the increase in dynamic buckling load over the static value imply any increase in the dynamic failing stress over the corresponding static value or essentially the same failing stress? This important question is probably completely beyond the scope of a mathematical analysis at present but could be investigated experimentally.

Another point is concerned with the application of high impact loadings to plates. Some recently published work⁵ has indicated that under certain conditions of impact, the magnitude of the stress introduced into a column may be sufficient to cause buckling after the initial pulse caused by impact has traversed only a small portion of the column. Although the column can carry loads considerably in excess of the static column load, buckling of the column does occur in which the wave length of the buckle depends directly upon the magnitude of the compressive stress introduced by impact. Under high impact loadings very short wave lengths have been observed experimentally in agreement with the predictions of a simple theory which accounts for the longitudinal propagation of the impact stress.

Although the details of a similar analysis for plates has not been completed, it is interesting to consider the behavior of a plate under conditions of high impact velocity in which the magnitude of the initial impact-stress pulse is greater than the static critical stress of the plate. Such an analysis is beyond the scope of the author's paper since it is tacitly assumed therein that the period of the fundamental extensional wave is much smaller than the fundamental frequency of transverse vibration.

Qualitatively, we can readily construct a conception of the behavior of a plate under impact loading. As the plate is struck at the left end by an impact force, Fig. 10 of this discussion, a stress is immediately set up at that point of a magnitude which depends upon the velocity of the impacting force v , and the velocity of propagation c , in the material. This impact stress is then propagated toward the right, and, when it has traversed a length which depends upon the magnitude of the impact stress, it is possible for buckling to occur in that length.

Essentially, the condition for dynamic buckling is that the impact-stress pulse equals the static buckling stress of the plate for a wave length corresponding to that traversed by the impact stress. Under such conditions it can be shown that the critical length parameter L_{cr}/b , is a function of the parameter $(v/c)(b/t)^2$ as shown in Fig. 10, herewith.

⁴ Guggenheim School of Aeronautics, College of Engineering, New York University, New York, N. Y. Jun. ASME.

⁵ "Column Behavior Under Conditions of Impact," by G. Gerard and H. Becker, *Journal of the Aeronautical Sciences*, vol. 19, January, 1952, pp. 58-61.

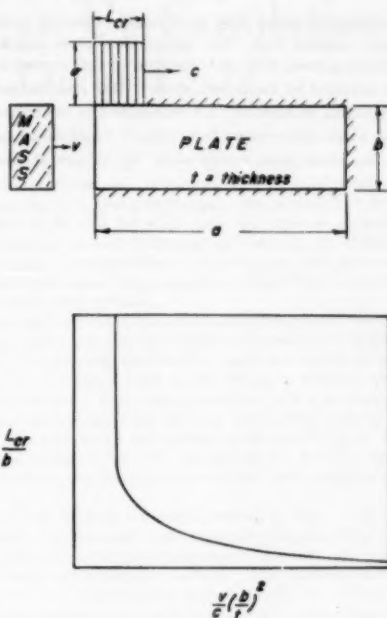


FIG. 10

AUTHOR'S CLOSURE

The author wishes to thank Professor Gerard for his interest in the paper and his stimulating comments. In closing he would like to point out the following:

With respect to the relation between the buckling and failing loads of plate elements, no complete answer can be given without either an analytical or an experimental investigation of the problem of dynamical limit design of the plate under appropriate forces, and such an analysis was beyond the scope of the paper. One thing is certain, however, that the dynamical failing load cannot be lower than the dynamic buckling load that can be sustained by the plate while experiencing only small deflections within the elastic range. Under the latter conditions it is shown in the paper that dynamic loads several times higher than the static-buckling load can be sustained if the interval of application of the load is sufficiently small. Hence a gain in limit design is assured by the results of the paper, at least when the increase of static loading because of dynamical effects is higher than the difference between static failing and static buckling loads. Moreover, there exists a wide range of cases where permanent deformations or large deflections must be avoided and the restrictions assumed in the paper are imposed by the design requirements.

The need for a special investigation for high impact loadings is explicitly stated in the paper.⁴ Professor Gerard's paper⁵ was published after the manuscript of the present paper was already submitted by the author and no reference to his work could be included. The author is considering separately this problem which essentially refers to the initial stages of dynamic buckling⁴ and he feels there exists an oversimplification in Professor Gerard's analytical treatment of the case of columns⁵ and his remark in

⁴ See for instance, reference (18), author's bibliography.

the foregoing discussion that the dynamic buckling condition essentially requires that, "the impact-stress pulse equals the static buckling stress of the plate for a wave length corresponding to that traversed by the impact stress." The essential feature of the buckling phenomenon is a deformation in the transverse direction which occurs with a finite velocity u and during such a motion the stress pulse travels along the column at another

speed c , thus changing the length for which a static buckling may be considered. Accordingly, a simultaneous consideration of these two motions is necessary for an accurate investigation of the phenomenon. For plates the problem is additionally complicated by two-dimensional effects and, from this point of view, the model of Fig. 10 is restricted to a one-dimensional case only which covers problems of plate columns but not the general case of plates.

Friction Surfaces for Spin-Up Simulation in Landing-Gear Drop Tests

By D. W. DRAKE,¹ BURBANK, CALIF.

Current procedures for drop testing of landing gears entail the simulation of wheel spin-up. The use of a fixed reaction surface in conjunction with spinning wheels in the drop tower introduces friction conditions between the tire and reaction surface that do not permit direct use of airport surfaces such as concrete. For this reason the "coefficients of friction" of a number of reaction surfaces have been evaluated and their value for spin-up simulation is discussed.

BACKGROUND

IN the past ten years considerable change has taken place in the laboratory testing of airplane landing gears directed toward a more realistic simulation of the initial impact in landing an airplane. The principal changes have been the simulation of the lift on the wing and simulation of wheel-assembly spin-up with its resultant oscillating drag load. This report discusses the history of the latter change, i.e., the problem of simulating in the laboratory the phenomenon of accelerating the wheel assembly from zero wheel speed just before contact to airplane speed just after contact.

In the past the principal purpose of drop-testing landing gears has been to develop and prove a metering arrangement in the oleo cylinder. Since the performance of an oleo may be affected significantly by friction between the piston and cylinder and since such friction is normally the result of drag force applied at the axle of the gear, tests were conducted by dropping onto an inclined platform which applied an arbitrary proportion (33 per cent) of vertical load normal to the strut axis (1).²

However, when in the early 1940's measurements were made of the forces developed during actual landings, it became apparent that the principal drag forces were associated with spinning-up the wheels, that the applied drag force was often higher than that applied in drop tests, that the applied drag load only lasted until the wheel assembly reached airplane ground speed, and that the dynamic response of gear assembly was important in determining the forces developed (2). Also it was apparent that considerable variation could be expected in the drag loads developed by different gear designs and that spring-back (forward drag load) forces must be considered in gear design. As a result of these studies it was decided that the wheel spin-up phenomenon should be simulated in drop-testing landing gears.

WHEEL ASSEMBLY SPIN-UP SIMULATION

Two methods have been used to simulate wheel spin-up. In one the weighted gear assembly is dropped on a rotating drum of

sufficiently high moment of inertia that drum speed is not changed appreciably in spinning-up the gear-wheel assembly (4, 5). This method works well for small gears but becomes expensive for gears used on modern transports and bombers. In addition, it is not possible to measure directly the drag and vertical forces being applied to the tires during impact and it is difficult to provide for different landing surfaces.

The other method of spin-up simulation consists of dropping the weighted gear assembly on a fixed reaction surface with the wheel assemblies rotating backward at sufficient speed so that, in stopping, the same wheel speed change is obtained as in an actual landing. Using this procedure with a suitable instrumented reaction platform the drag and vertical loads applied to the gear and hence the instantaneous coefficient of friction³ may be measured directly. In addition, by changing the top of the platform, any desired surface may be used to stop the rotating tire.

Lockheed adopted the second method in 1946. Figs. 1 and 2 show the drop-test facility and reaction platforms. Initially, both concrete and black-top surfaces cast to simulate airport surfaces were tried on the reaction platform. The black-top surface was found to be unsatisfactory because with the tire contacting only one spot on the cast surface, as opposed to the airplane landing condition, excessive wear of the surface was encountered. The concrete surface was entirely satisfactory in this regard.

FRICTION CHARACTERISTICS OF CONCRETE

Eight landing gears were tested, using the concrete surface shown in Fig. 2. In Fig. 3 typical variations of the coefficient of friction during the spin-up period are presented for seven of the gears. In Fig. 4 the effect of initial wheel speed on coefficient of friction for two gears is shown. These data indicate the following:

1 There is a wide variation in the coefficient of friction developed by different tires sliding on concrete.

2 All gears developed coefficients which were quite high upon contact but which dropped rapidly after contact and then tended to stabilize at some lower value if the spin-up period was of sufficiently long duration. This characteristic resulted in higher average coefficients of friction for the tests with shorter spin-up periods.

3 Both the average value and instantaneous peak value of coefficient of friction tended to increase with decreasing initial wheel speed.

In Table 1 tire characteristics and average coefficients of friction for the tires tested are tabulated and in Fig. 5 the average coefficient is plotted against tire size and tire pressure. There is some indication that high tire pressures are associated with low coefficients of friction, but the scatter in the data precludes a reasonable evaluation of the relationship. Tire size does not seem to be a significant variable, any effect indicated in Fig. 5 probably being due to the coincidence that the small tires generally used high pressures.

³ Coefficient of friction between the tire and reaction surface is defined as the instantaneous ratio of platform drag load to platform vertical load.

¹ Research Engineer, Lockheed Aircraft Corporation. Jun. ASME.

² Numbers in parentheses refer to the Bibliography at the end of the paper.

Contributed by the Aviation Division and presented at the Spring Meeting, Seattle, Wash., March 24-26, 1952, of THE AMERICAN SOCIETY OF MECHANICAL ENGINEERS.

NOTE: Statements and opinions advanced in papers are to be understood as individual expressions of their authors and not those of the Society. Manuscript received at ASME Headquarters, November 23, 1951. Paper No. 52-8-1.

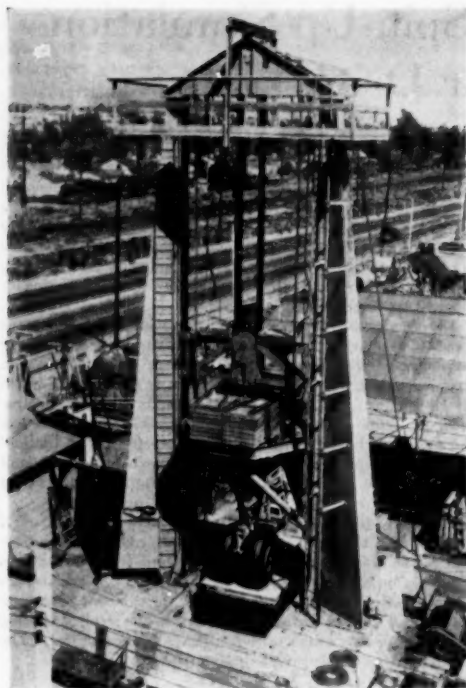


FIG. 1 LOCKHEED DROP-TEST TOWER

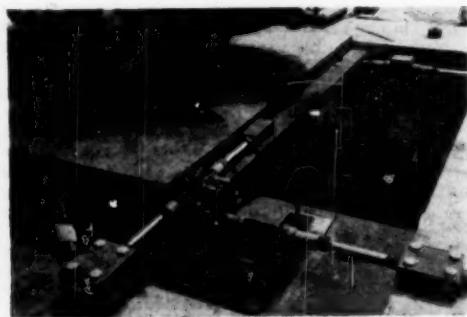


FIG. 2 REACTION PLATFORM WITH CONCRETE SURFACE INSTALLED

The original selection of concrete for a friction surface was based on the assumption that being a typical airport surface material, its friction characteristics in the tower would be typical of friction characteristics in actual landings. In 1949 sufficient data of actual landings were obtained on an instrumented patrol bomber whose gear had already been tested in the drop tower to examine this assumption. Of course, since it is impractical to instrument a runway, drag forces on the gears must be measured in the airplane and hence include dynamic effects. However, by

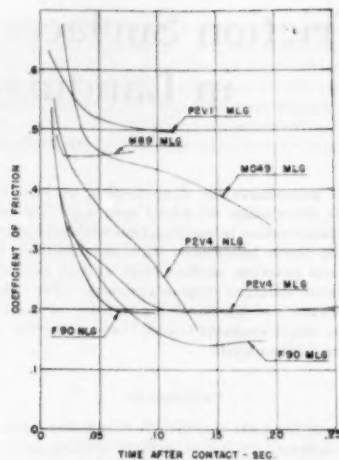
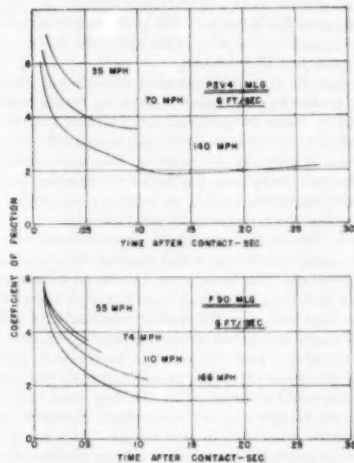
FIG. 3 TYPICAL DROP-TOWER FRICTION CHARACTERISTICS OF CONCRETE SURFACES
(Contact velocity, 6 fps, see Table I.)

FIG. 4 EFFECT OF INITIAL WHEEL SPEED ON DROP-TOWER FRICTION CHARACTERISTICS OF CONCRETE SURFACES

assuming that the coefficient of friction between the tire and runway was constant, it was possible to eliminate the dynamic effects from the measured gear drag loads by a graphical fairing procedure⁴ and hence to estimate the approximate coefficient

⁴ The fairing method used consisted of drawing average load lines through the dynamic drag-load traces during the spin-up period and averaging the instantaneous coefficients of friction obtained from the average drag-load trace. The judgment used in locating the average load line was tempered by the assumption that the coefficient of friction was constant, by comparisons of applied drag load and developed dynamic drag load from drop-tower data, and by previous experience in calculating the response of gears to impulses which varied linearly and sinusoidally with time.

TABLE 1 CHARACTERISTICS AND AVERAGE COEFFICIENT OF FRICTION OF TIRES TESTED

Gear	Tire	Tire press. psi	Free diam. ^a in.	Avg coeff. ^b of friction
M 049 MLG.	17-00-20-16 ply rating	80	48.8	0.5
P2V-1 MLG.	56SC-16 ply rating	60	56.6	0.55
M 89 MLG.	18-00-20-12 ply rating	72	50.3	0.5
P2V-4 NLG.	34 X 9.9-14 ply rating	120	33.4	0.35
P2V-4 MLG.	56SC-20 ply rating	82	56.6	0.38
F-90 NLG.	24 X 5.5-12 ply rating	150	24.6	0.25
F-90 MLG.	34 X 6.9-16 ply rating	160	33.4	0.15

^a Standard maximum free diameter

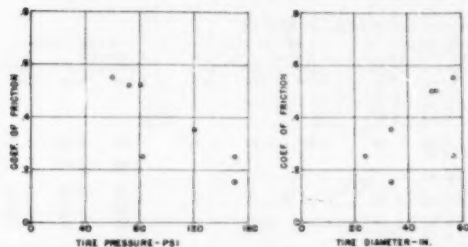
^b Approximate average for normal landing speed on concrete


FIG. 5 EFFECT OF TIRE PRESSURE AND TIRE DIAMETER ON AVERAGE COEFFICIENT OF FRICTION OF CONCRETE SURFACES

of friction that existed during spin-up in the landings. These results are compared with an average coefficient from the drop tests in Figs. 6, 7, and 8.

It may be seen that the average coefficient for the drop tests is below the range of the results for the airplane landings, being about one half the average obtained on the airplane landings.

This somewhat disappointing result forced a complete review of spin-up simulation requirements. This review showed the following factors:

- 1 Friction in the oleo strut during drop tests must be similar in character and magnitude to the actual landing condition in order to develop and select a satisfactory metering arrangement for the oleo strut.

- 2 The difficulty of predicting accurately by analytical methods the dynamic loads developed during spin-up makes experimental verification in the laboratory desirable. Current specifications (3) require a constant coefficient of friction of 0.55 for spin-up design conditions.

- 3 Hydraulic dampers are being used in the drag-load system of some main landing gears. The metering system in such dampers can only be developed satisfactorily by experiment at present, their damping characteristics being determined principally by spin-up conditions.

- 4 All of the available data which could be used to estimate the coefficient of friction developed during spin-up in actual landings indicated that values of 0.5 to 0.6 were typical. Unfortunately, the available data do not include information on the relatively small high-pressure tires used on fighter-type airplanes.

On the basis of the foregoing factors it was decided to try to design friction surfaces for drop testing which would develop a constant coefficient of friction of 0.5 to 0.6 to correspond with landing-gear design conditions.

SPECIAL FRICTION SURFACES

Since initiating a program to develop drop-test reaction surfaces providing coefficients of friction of 0.5 to 0.6, three main landing gears and one nose landing gear have been tested in the Lockheed drop tower. Eight special reaction surfaces have been

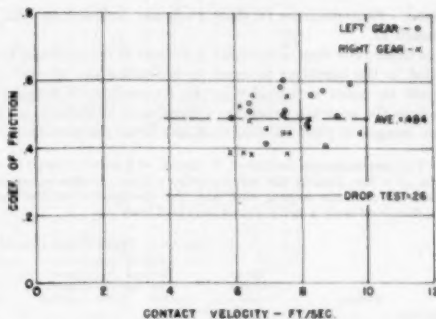


FIG. 6 AVERAGE COEFFICIENT OF FRICTION DURING SPIN-UP, P2V-4 LANDINGS AT PALMDALE ON CONCRETE SURFACE

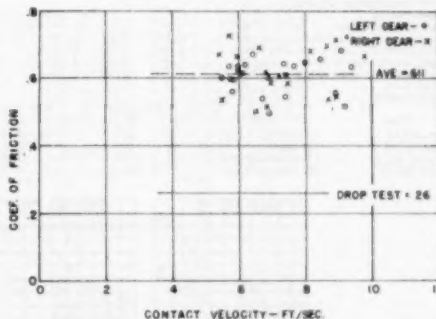


FIG. 7 AVERAGE COEFFICIENT OF FRICTION DURING SPIN-UP, P2V-4 LANDINGS AT LAS VEGAS ON BLACK-TOP SURFACE, APPROXIMATELY TWO YEARS OLD

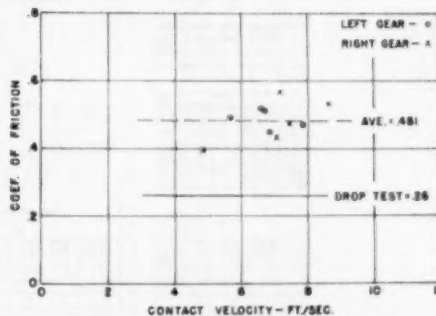


FIG. 8 AVERAGE COEFFICIENT OF FRICTION DURING SPIN-UP, P2V-4 LANDINGS AT LOCKHEED AIR TERMINAL ON BLACK-TOP SURFACE, THREE WEEKS OLD

tested with one or more of the gears (see Figs. 18 and 19). The procedure followed has been to try various surfaces at the start of the program using non-wing-lift spin-up drops, until a satisfactory surface for the particular gear had been found.

Friction data for each drop were obtained by plotting the reaction-platform drag load against the reaction-platform vertical load on an oscilloscope and photographing the trace ob-

tained. Reproductions of these plots are included in Figs. 9 through 17.

In these plots lines of constant coefficient of friction have been added to the negatives to assist in evaluating the curves.⁴ It should be noted in considering the curves that the dynamic loads in the gear are primarily a function of impulse; i.e., the time integral of platform drag load, and hence the portion of the

⁴ The instantaneous coefficient of friction of a point is equal to the slope of a line joining the point to the origin. In the referenced plots, the ordinate is drag load and the abscissa is vertical load. The drag-load scale is twice the vertical-load scale.

curve near spin-up is much more important than the initial slope, since the vertical load is higher and the time spent at load is higher in the final portion of the curves. The sharp drop in the drag load near the end of the curve indicates spin-up. The data have no significance beyond this point.

The data for the various surfaces and landing gears are summarized in Table 2. The longitudinal grating was found to produce satisfactory coefficients of friction for the C124 MLG, the C124 NLG, and the M1049 MLG, although the coefficient at initial contact was somewhat high for the latter two gears.

No satisfactory surface was found for the F-94C MLG. The

TABLE 2 COEFFICIENTS OF FRICTION FOR SPECIAL SURFACES

Surface	Drop height, in.	C124 NLG			C124 MLG			M1049 MLG			F-94C MLG		
		Normal land speed—initial	Normal land speed—avg	Low-speed—avg	Normal land speed—initial	Normal land speed—avg	Low-speed—avg	Normal land speed—initial	Normal land speed—avg	Low-speed—avg	Normal land speed—initial	Normal land speed—avg	Low-speed—avg
Concrete	4				0.35	0.28	0.05						
Concrete	13				0.45	0.22	0.40						
Smooth steel	4	0.30	0.20	0.60	0.25	0.35	0.80						
Smooth steel	13	0.75	0.20	0.40									
Longitudinal grating	4	0.65	0.55	0.55	0.60	0.50	0.45	0.75	0.60	0.55	2.00	0.50	0.65
Longitudinal grating	13	1.50	0.50	0.60	0.60	0.50							
Filled longitudinal grating	4				1.40	0.80					2.00	0.45	0.50
Cross-grating	4										2.00	0.50	0.80
Filled cross-grating	4										1.00	0.28	0.40
Large pattern safety plate	4	0.70	0.37	0.90	0.50	0.40	0.55	0.45	0.35	0.55	1.00	0.25	0.45
Large pattern safety plate	13	1.00	0.37	0.70	0.35	0.30	0.60	0.45	0.30	0.65	1.00	0.20	0.50
Small pattern safety plate	4	0.40	0.30	0.60	0.30	0.27	0.55				1.00	0.50	0.55
Small pattern safety plate	13	1.20	0.33	0.45							2.00	0.65	0.70
Bar surface	4												
Welded plate	4												

Gear	Tire	Tire press. psi	Tire diam. in.
C124 NLG	15:50-20	35	45.4
C124 MLG	25:00-20	64	71.2
M1049 MLG	17:00-20-20 ply	115	48.8
F-94C MLG	26 × 6-12 ply	225	25.8

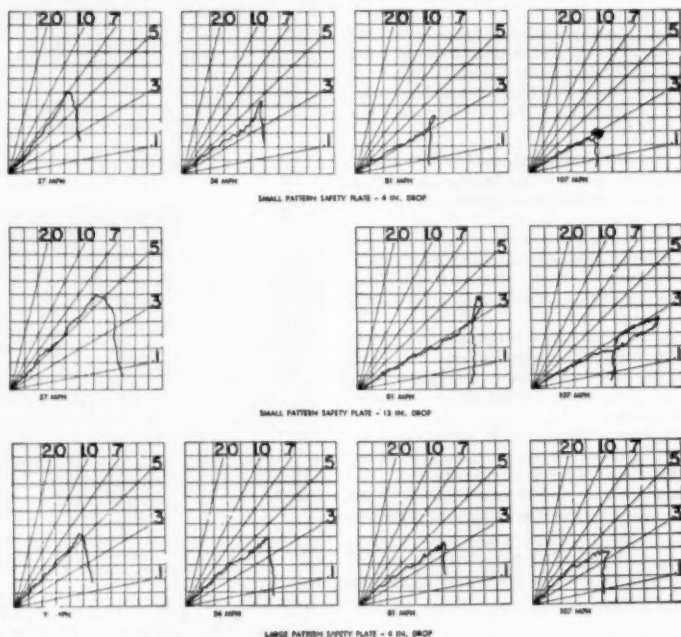


FIG. 9 FRICTION CHARACTERISTICS OF DOUGLAS C124 MLG

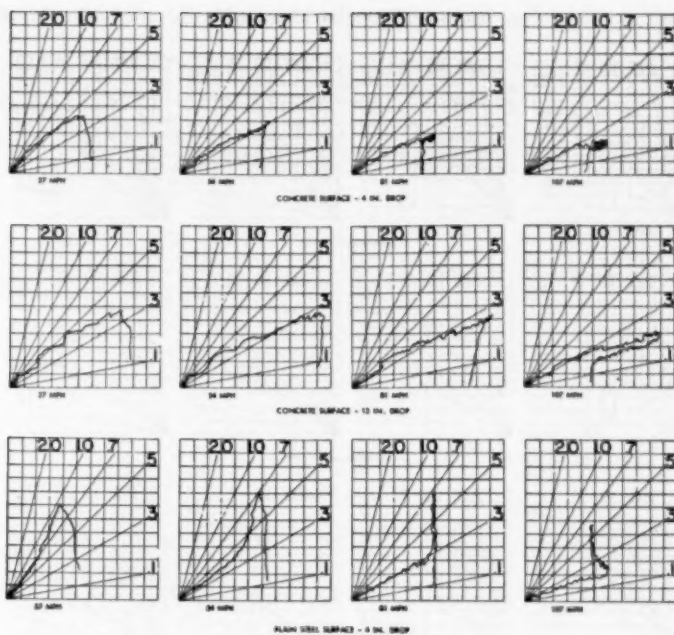


FIG. 10 FRICTION CHARACTERISTICS OF DOUGLAS C124 MLG

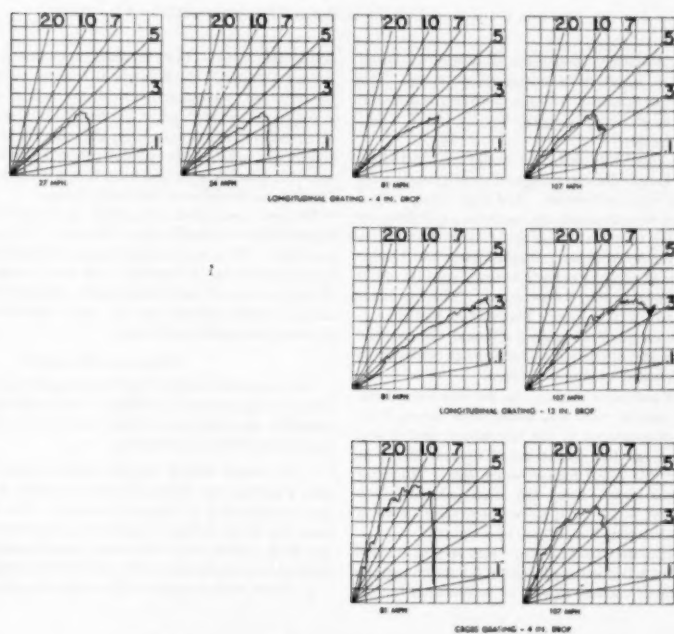


FIG. 11 FRICTION CHARACTERISTICS OF DOUGLAS C124 MLG

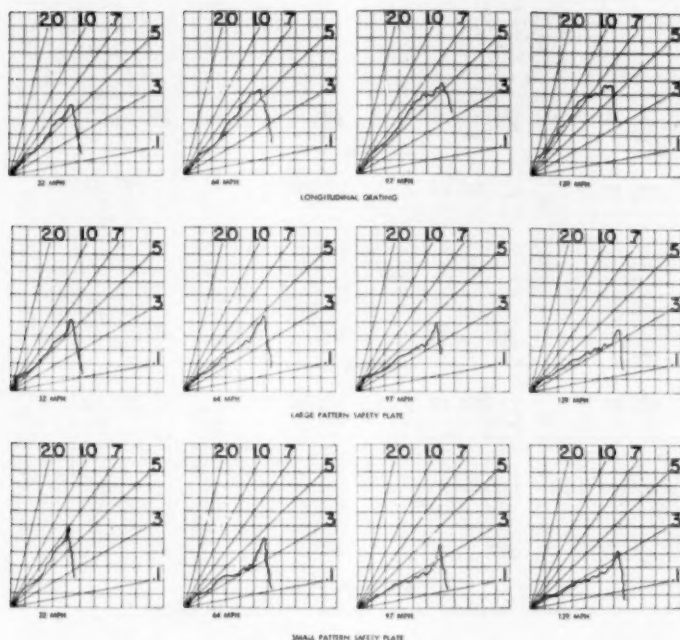


FIG. 12 FRICTION CHARACTERISTICS OF CONSTELLATION M1049 MLG—4 In. Drops

safety plates developed average coefficients of friction of about 0.3 but were somewhat sensitive to initial wheel speed. The longitudinal grating demonstrated average coefficients near 0.5 but had high initial coefficients, was sensitive to initial wheel speed, and badly cut the tire.

In an attempt to control the coefficient better and to reduce tire cutting, both the longitudinal grating and cross-grating were filled to various levels with hydrostone. Although some control of the initial coefficient was obtained, the coefficient still dropped with time, was sensitive to initial wheel speed, and cut the tire regardless of the level of hydrostone. Welded plate had similar characteristics. In an effort to increase the area of contact of the tire, the bar surface shown in Fig. 8 was tested. The top edges of the bars were filed to $1/4$ in. radius. This surface had characteristics similar to the longitudinal grating although the average magnitude of the coefficient of friction was somewhat controllable by varying the thickness and spacing of the bars.

During this series of preliminary tests, the tire was worn down to the fabric. This rate of wear was much more severe than anything previously encountered in the laboratory, and it was concluded that an average test coefficient of friction of 0.5 to 0.6 was too high for this small high-pressure tire. This gear subsequently was proof-tested, using the large pattern safety plate (average coefficient = 0.3), and a few check tests were run with the bar surface developing a coefficient of about 0.5.

On the basis of testing four landing gears with special friction surfaces, it appears that a friction coefficient of 0.5 to 0.6 may be developed readily without causing tearing or severe wear for the

larger tires (over 30 to 35 in. diam) operated with normal pressure (under 150 psi). Coefficients of friction of this magnitude can be obtained conveniently in drop testing using special steel surfaces. For most gears the longitudinal grating used in this laboratory will be satisfactory, although the safety plates may be useful for some of the smaller normal pressure tires. In any event, it appears to be necessary that a friction surface be selected experimentally for each test landing gear.

For gear assemblies using small tires operated at high pressure (over 150 psi) a coefficient of friction of 0.5 to 0.6 appears to be too high. The proper coefficient can be determined only by flight-test measurement in landings with installations using such tires. With the desired coefficient known, experience to date indicates that a friction surface can be found experimentally which will develop the desired coefficient.

GENERAL DISCUSSION

The data collected in this investigation point up the complex nature of the process of adding or removing energy from a wheel assembly by applying a friction force to its surface. Some of the factors involved are as follows:

- 1 In simple sliding friction with a block of material moving over a surface, the friction force is normally proportional to load and independent of area of contact. The force necessary to start the block sliding is higher than the force necessary to keep the block sliding and, with many combinations of materials, the friction force decreases as the velocity of sliding increases.

- 2 With rubber as one of the materials, elastic deformation of

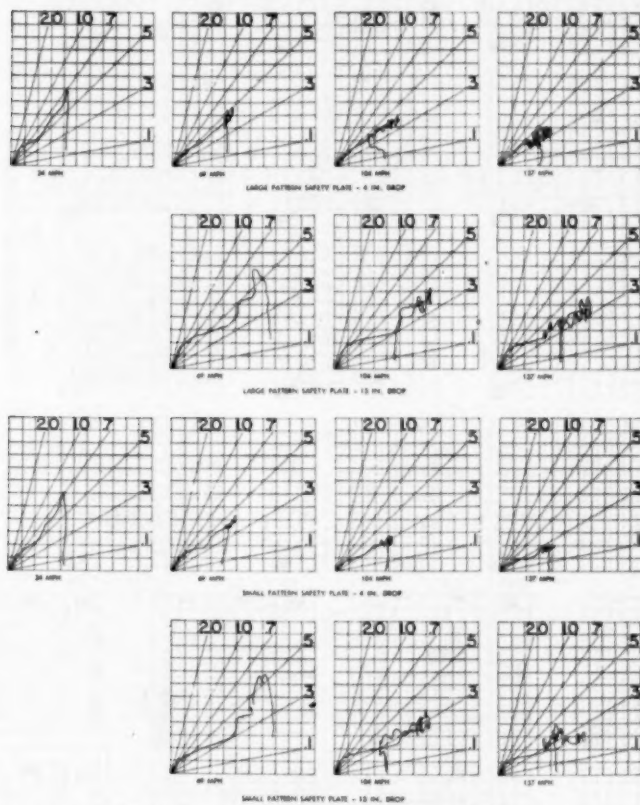


FIG. 13 FRICTION CHARACTERISTICS OF DOUGLAS C124 NLG

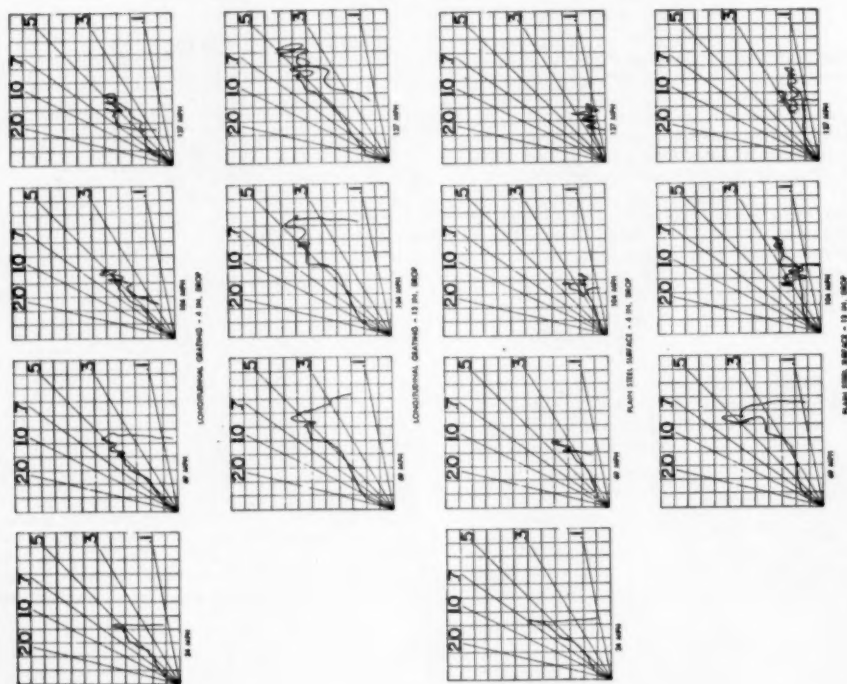


FIG. 14 FRICTION CHARACTERISTICS OF DOCOLAC C124 NLG

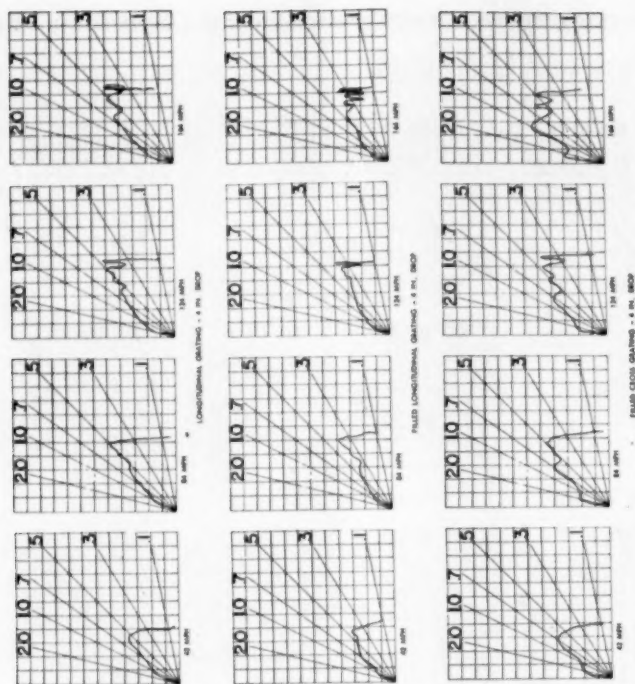


FIG. 15 FRICTION CHARACTERISTICS OF F-94C MLG

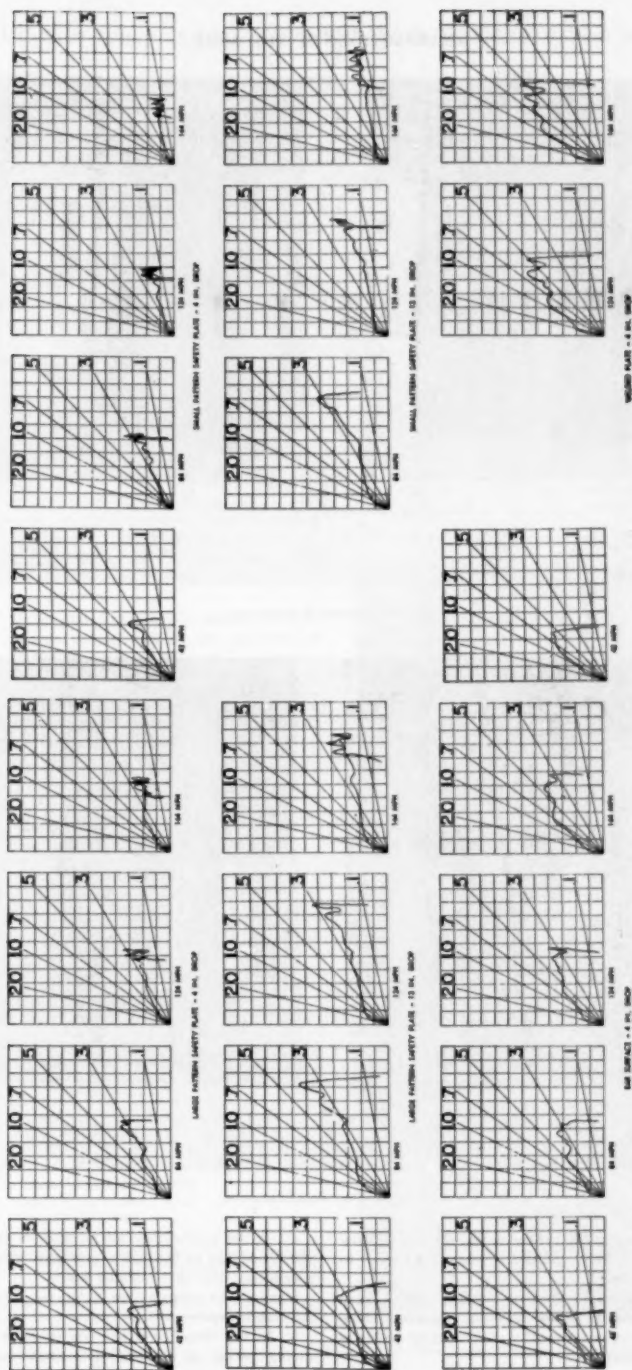


FIG. 16 FRICTION CHARACTERISTICS OF F-94C MLG

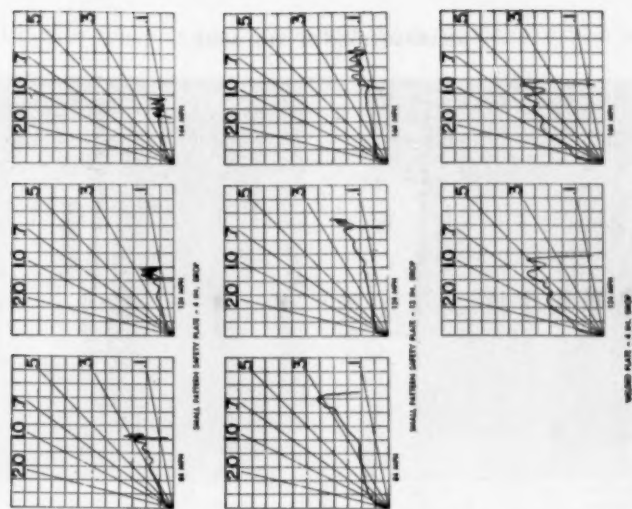


FIG. 17 FRICTION CHARACTERISTICS OF F-94C MLG

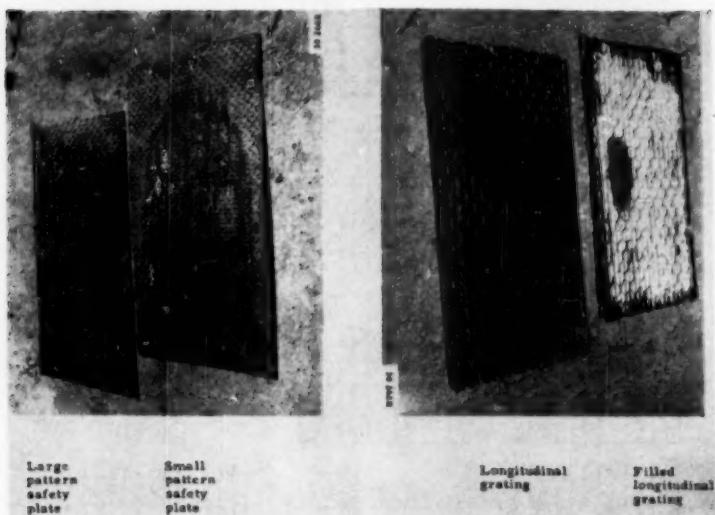


FIG. 18 FRICTION SURFACES

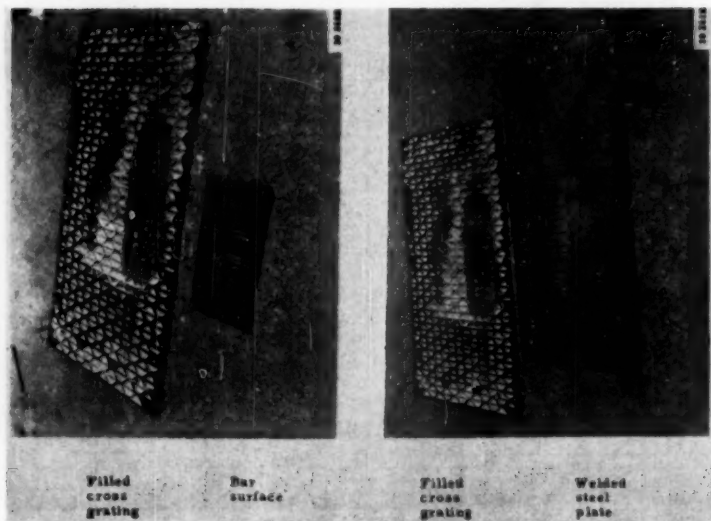


FIG. 19 FRICTION SURFACES

the rubber occurs, permitting the rubber to pass over irregularities in the other surface. This condition is somewhat similar to the action in rolling friction.

3 Rubber can be cut readily or shaved and it softens when subjected to temperatures of a few hundred degrees. These factors lead to the presence of a quantity of soft-rubber particles which may act as a lubricant.

4 A tire is relatively soft in shear in the direction of sliding and hence may go through a process of sticking, breaking loose, translating, and then sticking again.

Some of the irregularities in the curves suggest something of this nature is present.

5 In the drop tower the tire contacts one area during the sliding period as opposed to a continuously new surface in

the landing condition. This can lead to a change in the surface condition during the sliding period.

6 Wheel spin-up is a transient phenomenon with certain of the foregoing factors changing continuously.

The complex interaction of these factors may be shown by considering the variation in coefficient of friction with sliding velocity. Since, in general, friction increases with a decrease in velocity, it would be expected that the coefficient of friction would increase as the tire slows down in the drop tower. Further, with a lower initial wheel speed the average coefficient during the drop should increase. Smooth steel exhibits just such a characteristic (see Figs. 10 and 14). However, the fact that the maximum coefficient is higher for the lower initial speed indicates that the friction surface is being changed and lubricated during the sliding period. The safety plates also exhibit a higher final coefficient of friction to some extent (see Figs. 9, 12, and 13). Concrete, the bar surface, the welded plate, and, in some cases, the gratings, on the other hand, show a drop in coefficient as the wheel slows down.

This drop is not due to a decrease in coefficient of friction with decreasing sliding velocity since the coefficient increases with lower initial wheel speed (see Figs. 9 through 17). Contamination and lubrication by rubber particles will explain most of these cases and probably it is for this reason that the gratings are relatively insensitive to sliding velocity since the rubber particles cut off the tire are deposited between the bars in the grating.

The interaction of the various factors makes the prediction of the characteristics of a friction surface difficult, but consideration of the foregoing will reduce the experimentation necessary to find a satisfactory surface for a given landing gear and also suggest that a wide variety of spin-up characteristics can be obtained if desired.

CONCLUSION

- 1 The need for simulation of wheel spin-up in drop-testing of landing gear is discussed.
- 2 Concrete was found to be unsatisfactory as a friction surface for wheel spin-up simulation in drop testing.
- 3 The information currently available suggests that a coefficient of friction of 0.5 to 0.6 is of the right order for large (over 30 in.) diameter, normal pressure (under 150 psi) tires.
- 4 Small high-pressure tires develop significantly smaller coefficients of friction under similar conditions than the larger normal pressure tires.
- 5 Using special steel surfaces, desired coefficients of friction can be developed in drop tests.
- 6 At present, the proper friction surface for a given landing gear must be selected experimentally.
- 7 Flight-test information relative to the friction developed in the spin-up of small high-pressure tires is needed in order to drop-test such landing-gear installations adequately.

BIBLIOGRAPHY

- 1 "Tests: Landing Gear—Shock Absorber—Drop," Army Air Force Specification No. 40638A, December 7, 1943.
- 2 "Aircraft Wheel Inertia Drag Loads," Army Air Force Report TSELA-2B-4263-46-4, September 30, 1944.
- 3 "Ground Loads," ANC 2a, March, 1949.
- 4 "A New Tyre, Brake, and Undercarriage Testing Machine," by J. R. Green and H. A. Wills, *Aircraft Engineering*, vol. 30, 1949, pp. 22-24.
- 5 "Stress Tests on the Landing Gear of Nose Wheel Airplane Me-262 in Landing," by G. Schmits, *Air Force Translation No. F-TS-966 RE*, October, 1944.

Discussion

D. R. DONALDSON.⁶ This topic has been the subject of much discussion in recent years. As yet, no generally acceptable conclusions have resulted. It is quite possible that different conditions exist for large and for small airplanes. In this regard, this discussion will be limited to conditions existing during landing of large airplanes.

The author's comments direct attention to the complex interaction of many changing factors, but one of the most important is temperature. When a large airplane lands there is a puff of smoke at the instant of tire contact. On investigating the runway one will find a black print of rubber left on the surface followed by several reprints as the tire rolls around, Figs. 20 (a) and (b) of this discussion. This shows that a portion of the tire circumference was heated until the rubber melted. When a large spinning gear is dropped in a drop-test tower, there is a cloud of smoke at the instant of contact. Small rolls of rubber particles are thrown clear and there is a distinct odor of burning rubber. On checking the tire and platform, one will find that they are both quite sticky.

Having noted this phenomenon, a series of laboratory tests were conducted by the writer's company to establish the variation of the coefficient of friction between rubber and concrete at

⁶ Boeing Airplane Company, Seattle Division, Seattle, Wash.



FIG. 20(a) TIRE TRACKS ON RUNWAY AFTER AIRPLANE LANDING

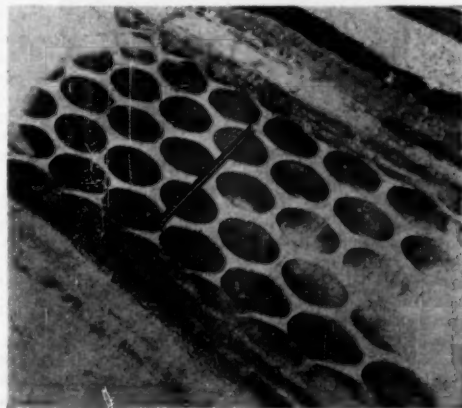


FIG. 20(b) DETAIL OF TIRE PRINTS ON RUNWAY

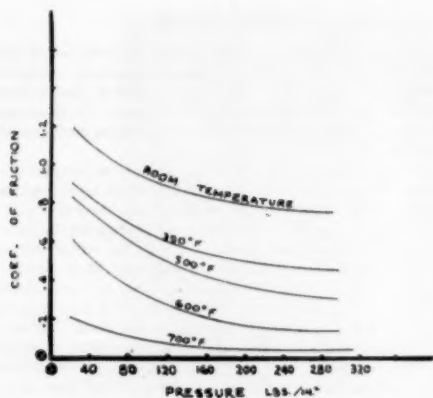


FIG. 21 RESULTS OF TESTS TO DETERMINE VARIATIONS IN COEFFICIENT OF FRICTION BETWEEN RUBBER AND CONCRETE

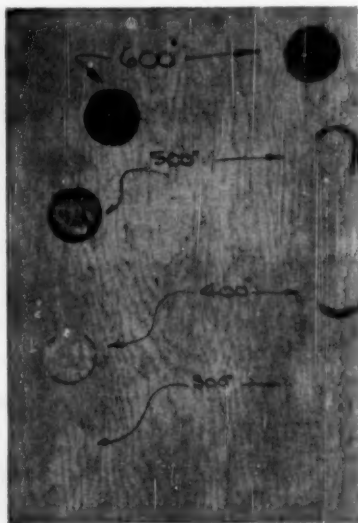


FIG. 22 TEMPERATURE REQUIRED TO MELT RUBBER

various temperatures. The general results of these tests are shown in Fig. 21. Fig. 22 gives an indication of the temperature required to melt the rubber. On this basis it is assumed that the airplane coefficient varies considerably during the very short spin-up time. It presumably starts fairly high, drops almost immediately as the rubber becomes hot, then increases somewhat again as the spin-up is completed.

Another study has been made on recorded gear-load data available on airplanes using 56-in. tires. A statistical record of B-29 landings was made of drag loads against vertical loads on the form of a curve, Fig. 23 herewith. The plot shows that an envelope curve of the points tends to be asymptotic at what might be called a terminal drag value. This can be explained by

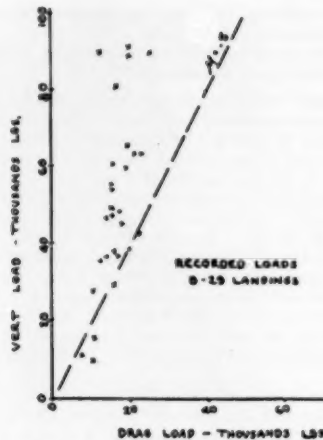


FIG. 23 DRAG LOAD VERSUS VERTICAL LOAD RECORD OF B-29 LANDINGS

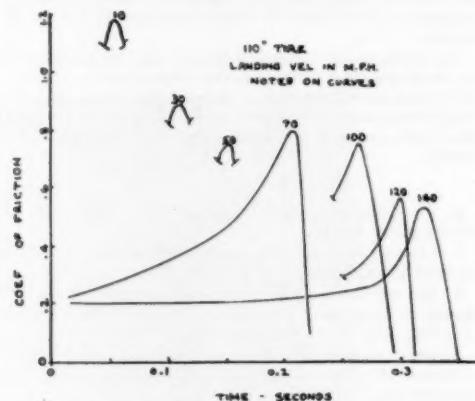


FIG. 24 CONVERSION OF DYNAMOMETER TEST LOADS TO COEFFICIENT OF FRICTIONS

the theory that the greater vertical load results in spinning the wheels to speed in a shorter time, therefore generating more heat and lower coefficients of friction. It is also interesting to note that the scatter of the points is considerable. This scatter would offer considerable difficulty in designing a drag-load system damper to which the author makes reference early in his paper. It appears that a wide variation in the coefficient of friction may be expected both in the case of a landing airplane and in the drop-test tower when all possible variations of surface, airplane attitude, and so on, are considered.

Another interesting investigation was completed by the Air Force at the AMC Laboratory at Wright Field. In these tests, a 110-in.-diam tire was moved against the rotating mass of a large dynamometer and the "vertical" and "drag" loads versus time were recorded for various contact speeds. Converting these loads to a "coefficient of friction," Fig. 24 is obtained. As the contact speed increased, the maximum coefficient decreased (with

one exception). This again would be expected by the theory of heat generation, but unlike most curves, there is not a high coefficient of friction at the instant of contact. However, during the early period of the vertical load build-up, both vertical and drag loads are low and the exact coefficient is difficult to establish.

In conclusion, the author states that steel plates are the most satisfactory drop-test-tower platforms and that other platforms should be determined for a particular gear. The most recent tests by the writer's company have been in tower with platform of heavy boiler plate backed by concrete, and such a platform is believed to be quite satisfactory. However, the necessity for a search for a platform that will produce a uniform coefficient of friction of from 0.5 to 0.6 is very questionable. The foregoing data indicate that one can expect a wide variation in the coefficient.

J. F. McBREARTY.⁷ This paper brings out rather well the decreased coefficients of friction associated with high-pressure tires. The author points out the extreme damage resulting to the tire when a friction surface, designed to produce the design value of 0.55, is used. This latter value has been in use for many years and has been based almost entirely on experience with low-pressure tires. Measurements in actual landings have indicated this same effect, but have been discounted since drag measurements on the structure itself include the dynamic effects present, and precise control and measurement of "boundary conditions" have not been practical. It would now seem that a reduced value of the design coefficient of friction is indeed warranted for the case of high-pressure tires. This value has an important effect on the structural weight not only of the landing gear, but also of other portions of the structure affected by transient accelerations in the wheel spin-up interval—notably nacelles and the rear portion of the fuselage.

G. E. VESCELOU.⁸ It is agreed that a surface moving under the wheel would more closely approach the landing conditions, but the difficulties in achieving this would more than offset any inconsistencies in the backward wheel rotation against a stationary-platform method generally employed.

Our results using a concrete platform have not been too satisfactory as we found the concrete would "load up" with rubber and would then give low friction values due to melting of the rubber during wheel stoppage. This melted rubber acts as a lubricant. It is quite possible, however, that by sandblasting or similar inconvenient means, the concrete surface could be restored between drops.

However, we have achieved fairly satisfactory results by using hot-rolled steel plates with the original rolled surface as a platform. It is our practice to clean the plate between drops with solvent to remove the rubber which has been deposited. Under these conditions we produce apparent coefficients of friction ranging from 0.3 to 0.7 with the greatest portion of the values falling between 0.4 and 0.6. This we believe to be of sufficient accuracy consistent with the other factors now involved in jig drop-testing of landing gears.

From our viewpoint as a strut manufacturer the time and expense involved in conducting tests to determine the particular surface to be used prior to each drop-test program would not be warranted.

⁷ Division Engineer, Structural Engineering, Lockheed Aircraft Corporation, Burbank, Calif.

⁸ Director, Engineering Division, Menasco Manufacturing Company, Burbank, Calif.

AUTHOR'S CLOSURE

Mr. Donaldson's data showing the effect of pressure and local temperature at the contact point is very interesting and, if 600 F is taken as the probable temperature existing in practice, the data certainly substantiate a large drop in the coefficient of friction with increased tire pressure. It seems likely, however, that the reduction in coefficient in an actual landing would be somewhat less than indicated in Fig. 21 since the softened rubber would be continually removed by abrasion.

Referring to the data in Fig. 24, apparently the drum used for the tests had a smooth steel surface. Compare with Fig. 10. Although the drop in peak values of coefficient of friction may be consistent with a theory of heat generation, the low initial values certainly are not. An explanation based on variation in coefficient with velocity as suggested on page 1279 seems more likely.

The data presented in Fig. 23 resemble some Air Force data which the author encountered a number of years ago where the maximum vertical load and the maximum drag load encountered during a landing were cross-plotted. Of course, since coefficient of friction is defined as an instantaneous ratio, it is difficult to draw any conclusions regarding friction conditions from such data. This is made more difficult by the fact that the drag load is a measured gear load and hence includes dynamic effects.

The suggestion of a terminal drag load in Fig. 23 is an interesting possibility. If the wheel is stopped in a small fraction of the fore-and-aft natural period of the gear, the principal reaction for the applied drag force will be the inertia of the gear mass and the friction force impulse will appear initially as velocity of the gear mass. It can be readily shown that under these conditions the maximum drag force developed in the gear will have a constant value. Further, it is quite possible to have gear characteristics which will tend to produce conditions approaching the above so that landing tests will indicate a "terminal drag load."

The foregoing is offered as one of a number of possible explanations for the B-29 data because a terminal drag load is not found in most airplane landing tests. For example, see Figs. 6, 7, and 8. Since this characteristic is not common, it is felt that it is a reflection of the dynamic characteristics of the B-29 gear rather than an indication of the friction between the tire and landing surface.

If the author may be permitted a bit of philosophy, a laboratory test has only limited value unless it adequately simulates service. Certainly the data of this investigation demonstrate that the arbitrary selection of boiler plate or any other friction surface for use in drop tests can produce large errors in simulating landing conditions. Further, the proper friction characteristic cannot be determined in the laboratory but must be derived from actual airplane landings. While the author does not wish to minimize the difficulties of obtaining adequate flight test data nor suggest that much of such data currently available do not show considerable "scatter," his experience in working from such information indicates that as a more detailed understanding of the factors involved develops much of the apparent scatter tends to fade away. In any event, landing-gear evaluation in the laboratory must encompass the range of scatter rather than ignore it if the improvement in shock struts obtained in the past decade is to continue. As Mr. McBrearty notes, the value of such improvement is not insignificant.

The author wishes to thank the contributors of discussion and to acknowledge the valuable guidance in conducting this program provided by Mr. H. W. Foster of Lockheed.

The Mean Flow in Kaplan Turbines

By R. E. MEYER,¹ MANCHESTER, ENGLAND

All theories now in use for the design of the bladings of Kaplan turbines and pumps are based on the assumptions that the fluid moves on concentric cylinders and that no trailing vorticity is shed off the blading. Approximate corrections are here found arising from the fact that the flow does not, in practice, satisfy these assumptions. These corrections are the more important the smaller the ratio of hub diameter to tip diameter. An approximation to them is found from investigation of the axially symmetrical mean flow in the rotor, which is obtained when the velocity components at any point are replaced by their mean values with respect to the angular co-ordinate. This approximation is the more accurate the smaller the pitch-chord ratio. It is found that the three-dimensional effects in the flow are due to the transverse component of the vorticity ("ring vorticity"). Formulas for the velocity components induced by it are given. Two distinct problems arise in connection with the design of a Kaplan blading, viz., (a) to find the shape of the blade and the pressure distribution for a prescribed load distribution, under the optimum working condition, and (b) to find the performance and pressure distribution for a prescribed blade shape, after a change of pitch. The theory applies also to multistage axial-flow turbomachines where the mean velocity is not too high for knowledge of the incompressible flow to be of interest.

1 INTRODUCTION

THE interest of the designers of Kaplan turbine blades has, for a long time, been restricted mainly to the problem of finding blade shapes that will give a prescribed total deflection of the stream. Recently, however, more interest has been taken in the details of the pressure distribution, mainly in connection with the problem of cavitation.

The original theory of turbines, due to Euler, was based on the assumption that the blades are infinitely thin and that all stream surfaces are congruent to them; all the effects due to the finite number of blades, their finite thickness, radial velocities, deviations from the ideal flow upstream of the rotor, viscosity, tip losses, and trailing vortices were neglected. For axial-flow turbomachines, moreover, it has been usual to neglect the effect of deviations of hub and casing from concentric cylinders extending indefinitely upstream and downstream of the blade rings.

There is no prospect of a comprehensive theory of the flow in turbomachines including all of these effects. The great practical success of the simple, original theory has shown, however, that the deviations of the actual flow from that predicted by Euler's theory are relatively small, or confined to narrow regions. This makes it possible to obtain satisfactory results by calculating the corrections arising from these effects separately and independently.

¹ I.C.I. Research Fellow, University of Manchester; Visiting Research Associate, University of Maryland, College Park, Md.

Contributed by the Hydraulic Division and presented at the Annual Meeting, Atlantic City, N. J., November 25-30, 1951, of THE AMERICAN SOCIETY OF MECHANICAL ENGINEERS.

NOTE: Statements and opinions advanced in papers are to be understood as individual expressions of their authors and not those of the Society. Manuscript received at ASME Headquarters, February 8, 1951.

The most important corrections are those resulting from the finite number of blades and their finite thickness. They have been investigated by the help of the theory of aerofoils and aerofoil cascades. These theories are, however, essentially theories of two-dimensional flow (1);² they neglect radial velocities, trailing vortices, boundary layers, and so forth.

In the following, the effects due to radial velocities and trailing vortices are investigated, independently of the cascade effects, by determining the difference between the flow predicted by Euler's theory and that obtained when of its assumptions only the two regarding absence of radial velocities and of trailing vortices are abandoned. These corrections may simply be added to the results obtained by the help of aerofoil-cascade theories, or any other theory neglecting these effects, in order to obtain an improvement of the blade shape and a more accurate estimate of the pressure distribution and of the performance after change of pitch.

The simple procedure of adding the results of two-dimensional cascade theory and three-dimensional mean-flow theory is, of course, not strictly correct. Some information on specifically three-dimensional cascade effects is found in reference (2). But the approximation obtained on the assumption of axially symmetrical flow is the better the smaller the pitch-chord ratio and the thickness ratio of the blade, and hence is well suited to Kaplan turbines with a relatively high number of blades.

The first investigations of the axially symmetrical mean flow in turbines were those of Lorenz (3) and Bauersfeld (4), who recognized the importance of the ring vorticity. The author developed an approximation based on the assumption that the velocity induced by the ring vorticity is small compared with the mean axial velocity, and gave a solution for stationary blade rings without trailing vortices (2). Marble (5) treated the effects of the trailing vorticity of a system of bound, stationary, or rotating vorticity by the help of a more rigorous approximation.

In the following, a simplified, general theory is developed, which includes both those of references (2) and (5). In the presentation, particular emphasis is laid on the application to the design of rotor bladings.

The "Euler" theory is summarized in section 2, and the condition determining the ring vorticity is derived in section 3 for the case of a uniform incident stream, and generalized in section 4 for the case of a nonuniform incident stream. The two design problems are treated in sections 5 and 6; formulas are given, on the one hand, for the ring vorticity, and on the other hand, in terms of the velocities induced by the ring vorticity, for the blade correction, pressure correction, and load correction. Formulas for these velocities are given in section 7, and ways are discussed of constructing simplified, approximate formulas.

The results are relevant to all axial-flow turbomachines where the mean speed is not too high for knowledge of the incompressible flow to be of interest. Some remarks are presented in Appendix 3 to facilitate the application of the results to multistage axial-flow turbomachines.

2 SWIRL AND USEFUL WORK

The purpose of the rotor of a turbine or pump is to transform

² Numbers in parentheses refer to the Bibliography at the end of the paper.

angular momentum³ of the fluid into torque of the shaft. If the process is steady and the fluid gains an amount \mathbf{A} of angular momentum per second on passing the rotor, then the torque experienced by the shaft is $\mathbf{T} = -\mathbf{A}$; and if the angular velocity of the rotor is ω , the work done on it per second is $(\mathbf{T} \omega)$. In a turbine \mathbf{T} and ω have the same sense; in a pump they are of opposite sense.

In a Kaplan turbine or pump the transformation of angular momentum into torque is achieved by the help of a set of aerofoil-shaped blades slightly inclined against the direction of the flow. As a consequence of viscosity, a circulation develops around each blade, and the lift forces thus generated provide a torque about the shaft. The fluid experiences a change in angular momentum and pressure; the mean axial velocity V (equal to the rate of volume flow divided by the area of cross section of the annulus), is the same upstream and downstream of the blade, for reasons of continuity, if the radii of hub and casing are unchanged.

Let us refer for a moment to a system of cylindrical co-ordinates, r, θ, z , fixed in space, with z increasing in the downstream direction on the axis and θ in the sense of rotation, and let c_r, c_θ , and $(V + c_z)$ denote the corresponding components of velocity. Let us ignore for a moment the radial component of velocity as well as the deviation c_r of the axial component from its mean V , and consider the flow between two cylinders of radii r and $r + dr$, respectively. It is desirable that the fluid should have no angular momentum downstream of the rotor blades, in a Kaplan turbine, and if this is to be achieved by N blades, the circulation Γ of the individual blades must at every instant satisfy the relation

$$N\Gamma = \oint (\mathbf{c} \, ds) = -2\pi r \bar{c}_\theta \dots \dots \dots [1]$$

(by Stokes' theorem applied to the closed contour indicated in Fig. 1), if \bar{c}_θ is the mean over the circumference of the tangential component of velocity ahead of the blades. If ρ denotes the



FIG. 1

density, a mass $\rho V 2\pi r \, dr$ will pass through the rotor per second, between the two cylinders considered, and it will acquire an amount of angular momentum

$$dA = 2\pi r \, dr \, \rho V (-\bar{c}_\theta r) = \rho V N \Gamma r \, dr$$

The rate at which work is delivered into the shaft will therefore be

$$(\mathbf{T} \omega) = -\rho V N \Gamma \omega r \, dr = 2\pi \rho V \bar{c}_\theta \omega r^2 \, dr \dots \dots \dots [2]$$

in the case of a turbine. Note that only V and \bar{c}_θ enter into the expression for the total useful work.

From now on, let us refer to a cylindrical system of co-ordinates, r, ϕ, z , with respect to which the rotor blades are fixed and the flow is steady, with z again increasing in the downstream direction on the axis and ϕ in the sense of rotation. Let w_r, w_ϕ , and $(V + w_z)$ denote the components of velocity in this system.

³ Throughout this paper angular momentum is to be understood as taken about the axis of the rotor.

The components of "absolute" velocity \mathbf{c} are given in terms of those of "relative" velocity \mathbf{w} , by

$$\mathbf{c} = \mathbf{w} + \mathbf{c}_\theta = \mathbf{w}_\phi + \omega r, \quad V + c_z = V + w_z \dots \dots \dots [3]$$

If the blades are thin, as in a Kaplan turbine, they may be represented, to a first approximation, by equations of the form

$$\chi(r, \phi, z) = \Pi(r, z) - \phi = \text{const} = \alpha_j \quad (j = 0, 1, \dots, N-1)$$

where, e.g., $\alpha_j = 2j\pi/N$. If they are closely spaced or, more precisely, if the pitch-chord ratio is small, all stream surfaces are nearly congruent to the blade surfaces, and to a first approximation, the blade surfaces and stream surfaces form a family of congruent surfaces given by

$$\chi(r, \phi, z) = \Pi(r, z) - \phi = \text{const} = \beta \quad (0 \leq \beta < 2\pi) \dots \dots \dots [4]$$

In this approximation, the flow shows complete axial symmetry; any one of the surfaces of Equation [4], could be identified with a blade, and the approximation is therefore sometimes referred to as the "theory of an infinite number of blades." In it attention is confined to the mean, with respect to the circumference, of the velocity field.⁴

Let us assume that, in addition to the flow being axially symmetrical, the hub and the casing are concentric cylinders and that the radial velocity vanishes everywhere and the axial velocity is everywhere equal to V . Then the fluid between the cylinders r and $r + dr$ will, on its way from upstream to a height z in the rotor, acquire an amount of angular momentum

$$dA(r, z) = 2\pi r^2 \, dr \, \rho V [c_\theta(r, z) - c_\theta(r)]$$

per second, and the rate at which useful work is delivered by the part of the rotor above the height z will be

$$2\pi \rho V \omega r^2 \, dr [c_\theta(r) - c_\theta(r, z)]$$

where c_θ is again the value of c_θ far upstream. As the total circulation $N\Gamma(r)$ describes the total useful work done by the different cylindrical sections of the rotor, so the "load distribution function"

$$\gamma(r, z) = c_\theta \dots \dots \dots [5]$$

describes its distribution over the blades in detail. It is equal to the local value of the angular momentum per unit mass of the fluid.

The theory just described is the original theory of turbines due to Euler. It goes beyond the theory of "velocity triangles" first outlined in that it considers the mean flow in the rotor, not only far upstream and downstream of it. Its main assumptions are as follows:

- The fluid is inviscid.
- The flow is axially symmetrical.
- The hub and casing are concentric cylinders extending far upstream and downstream.⁵
- The radial velocity vanishes everywhere and the axial velocity is everywhere equal to V .
- The gap between the tip and the casing is negligible.
- No trailing vortices are shed off the blades.

In the following, assumptions (d) and (f) are abandoned and the velocity distribution, pressure distribution, and blade surface

⁴ For simplicity, the mean of the effect on the velocity field of the blade thickness is neglected. It can be treated independently of the mean flow considered here (ref. 2). In practice, the three-dimensional effects due to the blade thickness may be expected to be much smaller than those investigated here.

⁵ For effects due to their deviation from cylinders see, for example, reference (6).

obtained under assumptions (a) to (c), and (e) are compared with those obtained on Euler's theory.

3 BLADE FORCES AND RING VORTICITY

The equations of motion for an inviscid, incompressible fluid, referred to co-ordinates fixed in space, are

$$(\mathbf{c} \cdot \text{grad}) \mathbf{c} = -\text{grad}(p/\rho - gz) + \mathbf{F}$$

where p is the pressure, g the gravitational acceleration, and \mathbf{F} the external field of forces per unit mass that may have to be applied in order to maintain a flow along given stream surfaces. This equation may also be written

$$\mathbf{c} \times \xi = \text{grad} \left(p/\rho - gz + \frac{1}{2} c^2 \right) - \mathbf{F} \quad [6]$$

where $\xi = \text{curl } \mathbf{c}$ is the vorticity, c the velocity magnitude, and \times denotes the vector product. Upon substitution of \mathbf{w} from Equation [3]

$$\mathbf{w} \times \xi = \text{grad} \left(p/\rho - gz + \frac{1}{2} w^2 - \frac{1}{2} \omega^2 r^2 \right) - \mathbf{F} \quad [7]$$

where w is the magnitude of the relative velocity, is obtained as equation of motion referred to the co-ordinate system fixed with respect to the rotor;² it is convenient to retain the "absolute" vorticity, $\xi = \text{curl } \mathbf{c}$.

If the forces are such as can be exerted by solid surfaces fixed with respect to the rotor, then they must be normal to the (relative) stream surfaces, and by Equation [7], $H = (p/\rho - gz + \frac{1}{2} w^2 - \frac{1}{2} \omega^2 r^2)$ must be constant on (relative) streamlines. Moreover, suppose the flow upstream of the rotor is vortex-free; then H must be constant upstream, and hence

$$H = p/\rho - gz + \frac{1}{2} w^2 - \frac{1}{2} \omega^2 r^2 = \text{const.} \quad [8]$$

everywhere. It follows from Equation [7] that

$$\mathbf{F} = -\mathbf{w} \times \xi \quad [9]$$

which is the analog of Joukowski's equation for the force sustained by the circulation around an aerofoil. Since \mathbf{F} must be normal to the blade surface, at every point, it follows that the blade surface is the surface of the relative streamlines and the absolute vortex lines.

Since the flow is axially symmetrical, the velocity components do not depend on θ or ϕ , and the components of absolute vorticity are

$$\left. \begin{aligned} \xi_r &= -\frac{\partial c_\theta}{\partial z} = -\frac{1}{r} \frac{\partial \gamma}{\partial z} \\ \xi_\theta &= \frac{\partial c_r}{\partial z} - \frac{\partial c_z}{\partial r} \\ \xi_z &= \frac{1}{r} \frac{\partial(c_\theta r)}{\partial r} = \frac{1}{r} \frac{\partial \gamma}{\partial r} \end{aligned} \right\} \quad [10]$$

Only the meridional components of vorticity are associated with the load distribution and with the useful work done on the rotor. On the other hand, the "ring vorticity" ξ_θ is associated only with

the variations in the meridional components of velocity, i.e., with the deviations of the flow from that predicted by Euler's theory. It will be shown in section 7 how c_r and c_z may be calculated from any given distribution of ξ_θ .

It can be shown (Appendix 1) that the assumptions (d) and (f) of Euler's theory are equivalent to the assumption that the ring vorticity vanishes everywhere. Bauersfeld (4) has studied turbine bladings for which this assumption is satisfied, and has shown that in that case the mean flow is entirely determined by a single, given streamline. It is found, however, that the lift coefficient of the blade section varies strongly with the radius (2), and this drawback has prevented the technical realization of bladings with a mean flow free of ring vorticity. In practice, the Bauersfeld condition is not satisfied in axial-flow turbomachines.

In general, the relation between the load distribution function γ and the ring-vorticity is a very complicated one (7). However, it has been pointed out (2) that a very good approximation can be obtained in practice by assuming that the velocities induced by the ring vorticity are small compared with the mean axial velocity V . It follows that the blade surface actually required to produce a given load distribution $\gamma(r, z)$ differs only a little from the blade surface obtained by Euler's theory, and that the ring-vorticity may be calculated, to the first order, from the condition that the vorticity surface coincides with the Euler blade surface instead of the corrected blade surface.³

Downstream of the rotor there are no blade forces, so the (absolute) vortex lines coincide with the (relative) streamlines, by Equation [9]. If the blade sections have been matched properly for the optimum working condition, the mean angular momentum will vanish, downstream of the rotor, and there will be no trailing vorticity (except for that due to the tip clearance). But even if the matching is perfect for the optimum working condition, it will cease to be so when the angular momentum upstream and the blade incidence are changed, and the mean angular momentum downstream will then be nonzero and trailing vortices will be shed off the blading. The kinetic energy far downstream resulting from these effects cannot be recovered in the draft tube and contributes to the turbine losses. On the other hand, for the range of working conditions over which the efficiency of the turbine remains high, it may be assumed that the velocities induced by the trailing vorticity are small compared with V , and hence the ring component of trailing vorticity may be calculated, to the first order, from the condition that the (absolute) vortex lines coincide with the (relative) streamlines obtained on Euler's theory.

4 NONUNIFORM INCIDENT FLOW*

In practice, the flow upstream of the rotor cannot be expected to be vortex-free. The guide vanes are cylindrical surfaces and they are placed too near the bend of the duct for their own incident velocity to be uniform over the span, so they shed trailing vorticity into the incident flow of the rotor. To account for this it will be necessary to admit that the axial velocity and the angular momentum, far upstream of the rotor, are both functions of the radius. Let them be denoted, respectively, by $V(r)$ and $\gamma_0(r)$, and assume that $V(r)$ does not vanish anywhere and let V_0 denote the lowest value taken by it.

When the flow upstream of the rotor is not vortex-free, Equations [8] and [9] are not true. On the other hand, the variation with the radius of V and γ_0 does not affect the validity of the Euler theory, which applies primarily to the flow between two concentric cylinders at a small distance apart. Moreover, if

* A more detailed justification for this procedure is given in Appendices 2 and 3.

² The author is indebted to Profs. G. N. Ward and A. F. Hollander for suggesting the inclusion of this section.

³ We are at liberty to imagine that the respective axes of both systems coincide at the instant under consideration. Then the respective components of force are the same in both systems.

the radial and axial-velocity components induced by the blades are small compared with V_0 , the streamlines lie approximately on cylinders, and since Bernoulli's equation [8] holds on streamlines, the total pressure H is approximately a function of r only.

Therefore, if $\xi_0(r)$ denotes the vorticity far upstream of the blades, $\mathbf{w} \times (\xi - \xi_0) + \mathbf{F}$ is small, by Equation [7]; i.e. the surface of the (relative) streamlines and the lines of $(\xi - \xi_0)$ coincides approximately with the blade surface, which, in turn, differs little from the Euler blade surface. Hence the part of the ring vorticity that is due to the blades may still be calculated, to the first order, from the condition that the surface of this part of the vorticity coincides with the Euler blade surface and that, downstream of the rotor, the lines of the corresponding part of the trailing vorticity coincide with the (relative) Euler streamlines. The formulas given in sections 5 to 7 therefore apply also to the case of a nonuniform incident flow, provided ξ is interpreted everywhere to mean $(\xi - \xi_0)$.

It may not always be immediately apparent which functions $V(r)$ and $\gamma_d(r)$ are appropriate to represent the incident flow of a blading. In Kaplan turbines, the rotor is often placed so near the bend of the duct that, even in the absence of the rotor, the axial velocity and the angular momentum would vary appreciably with the height z in the portion of space to be occupied by the rotor. In that case the following method of treatment is suggested: The distribution of axial velocity and angular momentum may be taken as $V(r)$ and $\gamma_d(r)$ that would obtain, in the absence of the rotor, at the station in the duct corresponding, e.g., to mid-chord height of the rotor. At other points in the portion of space to be occupied by the rotor, the velocity field will then deviate from that represented by $V(r)$ and $\gamma_d(r)$, but these deviations will be relatively small and may be treated as corrections ("first" field of velocity corrections). The procedure would then be as follows: (a) The flow in the duct, in the absence of the rotor, is calculated (for instance, by a relaxation method) and from it $V(r)$ and $\gamma_d(r)$ are obtained as well as the first field of velocity corrections. (b) The ring vorticity ξ_0 is calculated from $V(r)$ and $\gamma_d(r)$, as described in sections 5 and 6, and the velocity corrections due to the blades ("second" field of velocity corrections) are calculated from ξ_0 , as described in section 7. Finally, the two fields of velocity corrections are added (vectorially) and the pressure correction, blade correction, and load correction are calculated from the total velocity corrections, as described in sections 5 and 6.

5 BLADE CORRECTION FOR OPTIMUM WORKING CONDITIONS

Assume that the mean axial velocity V , the angular velocity ω , and the load distribution $\gamma(r, z)$ are given. In addition, the intersection, $\phi = \Pi(r, z_0)$ of the blade surface with some plane $z = z_0$ normal to the axis may be chosen; alternatively, the shape of the leading edge, for instance, may be chosen and the following formulas interpreted accordingly.

Since the blade surface is a relative stream surface

$$(\mathbf{w} \cdot \nabla \chi) = w_r \partial \Pi / \partial r - w_\phi / r + (V + w_z) \partial \Pi / \partial z = 0 \quad [11]$$

The Euler blade $\Pi_E(r, z)$ is found by neglecting w_r and w_ϕ altogether, whence

$$\partial \Pi_E / \partial z = w_\phi / (rV) = \gamma / (r^2 V) - \omega / V \dots \dots [12]$$

by Equations [5] and [3], and

$$\Pi_E(r, z) = \Pi(r, z_0) + \frac{1}{r^2 V} \int_{z_0}^z \gamma(r, y) dy - \frac{\omega}{V} (z - z_0) \quad [13]$$

The vorticity is to be determined so that the Euler blade is a vorticity surface, i.e., $(\xi \cdot \nabla \chi) = 0$, whence

$$\xi_z / r = \xi \partial \Pi_E / \partial r + \xi_r \partial \Pi_E / \partial z$$

so

$$\xi_E = \frac{\gamma}{r^2 V} \frac{\partial \gamma}{\partial r} - \frac{\partial \gamma}{\partial z} \frac{\partial}{\partial r} \left[\frac{1}{r^2 V} \int_{z_0}^z \gamma(r, y) dy \right] - \frac{\partial \gamma}{\partial z} \frac{\partial}{\partial r} \Pi(r, z_0) - \frac{\omega}{V} \frac{\partial \gamma}{\partial r} \quad [14]$$

by Equations [10] and [13]. Note that the first three terms depend only on $\gamma(r, z)$; ω enters only into the last term, and $\Pi(r, z_0)$ only into the last term but one. Since the problem has been linearized by our approximation, the contributions to the mean flow of the different terms may be calculated separately, and then added; thus, for instance, the effect of different choices of $\Pi(r, z_0)$ may be studied in a simple way.

The corrected blade surface is found from Equation [11], which, to the first order, becomes

$$\frac{\partial \Pi}{\partial z} = \frac{\partial \Pi_E}{\partial z} - \frac{w_r}{V} \frac{\partial \Pi_E}{\partial r} - \frac{w_\phi}{V} \frac{\partial \Pi_E}{\partial z}$$

whence, by Equation [12]

$$\Pi(r, z) - \Pi_E(r, z) = -\frac{1}{V} \int_{z_0}^z \left[\frac{w_r}{r^2} \left(\frac{\gamma}{r^2} - \omega \right) + w_\phi \frac{\partial \Pi_E}{\partial r} \right] dz \quad [15]$$

It is suggested that this blade correction (in which w_r and w_ϕ are obtained from the ring-vorticity distribution of Equation [14] by the method described in section 7) be applied to the backbone of any blade designed on the basis of a theory neglecting the radial velocity and the deviations of axial velocity from V .

The pressure correction is found from Equation [8], which becomes

$$p_E / \rho - gz + \frac{1}{2} w_\phi^2 + \frac{1}{2} V^2 - \frac{1}{2} \omega^2 r^2 = \text{const}$$

if w_r and w_ϕ are neglected entirely. To the first order of small quantities, therefore

$$(p - p_E) / (\rho V^2) = -w_z / V \dots \dots \dots [16]$$

since all the small terms vanish far upstream. It is suggested that this correction be added to the pressure distribution found from any theory based on the assumptions (d) and (f) of section 2. A numerical example for a fixed blading of hub ratio 0.6 is given in reference (2); the ratio c_p / V is found to reach 0.05 in magnitude, so the pressure correction reaches 10 per cent of the dynamic pressure, $\frac{1}{2} \rho V^2$.

How the mean angular momentum $\gamma = c_\phi r$ is to be chosen or determined in the first place, depends on the theory used for the primary design of the blade, and is therefore outside the scope of this account. Note, however, that it is sufficient to know γ to the first order of approximation in order to evaluate ξ_0 from Equation [14] to the order of accuracy required. Note also that it has been assumed in this section that, in order to minimize induced losses at the optimum working condition, γ is assumed chosen in such a way that the blade does not shed trailing vorticity. This means that $\gamma = \text{const}$ along the trailing edge. If a different choice is made, the ring component of trailing vorticity (see section 6) contributes to the velocity corrections.

6 CHANGE OF PITCH

Assume that the blade shape $\Pi(r, z)$, the mean axial velocity V , the angular velocity ω , and the swirl γ_ϕ upstream of the rotor are given, and that Π and γ_ϕ , at least, differ from their values at the optimum working condition. This situation arises after a change of pitch and load, and it is then required to find the load distribution and the pressure distribution.

On Euler's theory, the load distribution function is

$$\gamma_E(r, z) = r^2(\omega + V \partial \Pi / \partial z) \dots \dots \dots [17]$$

in analogy to Equation [12]. The corrected load distribution γ , for which Π is the corrected blade, differs from γ_E only by small quantities, and ξ_ϕ may therefore be found by substitution of γ_E into Equation [14].

Trailing vorticity, however, must be expected to occur after a change of pitch, and account must also be taken of its ring component. Since, to the first order, the absolute vortex lines coincide with the relative streamlines of Euler's theory

$$\xi_r = 0, \xi_\phi / \xi_z = W_\phi / V \dots \dots \dots [18]$$

downstream of the rotor, where W_ϕ denotes the value of w_ϕ on Euler's theory. Since $\xi_r = 0$, γ is independent of z , by Equations [10], so

$$\gamma(r, z) = \gamma_E^\dagger(r), \text{ and } C_\phi(r, z) = C_\phi^\dagger(r) \dots \dots \dots [19]$$

downstream, where a dagger is used to denote values taken at the trailing edge of the blade, and C_ϕ is the value of c_ϕ on Euler's theory. Therefore, by Equations [10]

$$\xi_z = \frac{1}{r} \frac{d}{dr} \gamma_E^\dagger \dots \dots \dots [20]$$

downstream of the rotor, and by Equations [18], the ring vorticity downstream of the rotor is obtained by substitution of $\gamma_E^\dagger(r)$ for $\gamma(r, z)$ in Equation [14]. To the first order, the vorticity downstream of the rotor depends only on r .

The first-order correction to the load distribution is

$$\gamma(r, z) - \gamma_E(r, z) = r(w_\phi - W_\phi) \\ = r^2(w_r \partial \Pi / \partial r + w_z \partial \Pi / \partial z) \dots \dots \dots [21]$$

by Equations [11] and [12]. The pressure correction is again found from Equation [8]; to the first order

$$(p - p_E) / \rho = -W_\phi(w_\phi - W_\phi) - V w_z$$

and by Equations [21] and [12]

$$\frac{p - p_E}{\rho V^2} = -\frac{w_z}{V} - \frac{r^2}{V} \frac{\partial \Pi}{\partial z} \left(w_r \frac{\partial \Pi}{\partial r} + w_z \frac{\partial \Pi}{\partial z} \right) \dots \dots [22]$$

in the rotor. To find the correction to the tangential velocity downstream of the rotor, note that in the absence of forces the

tangential component of $\mathbf{w} \times \xi$ is

$$\left(w_r \frac{\partial}{\partial r} + (V + w_z) \frac{\partial}{\partial z} \right) (c_\phi r) = 0$$

by Equations [9] and [10]; to the first order, this becomes

$$w_r \frac{\partial}{\partial r} (C_\phi r) + V r \frac{\partial}{\partial z} (c_\phi - C_\phi) = 0$$

by Equation [19], and hence

$$c_\phi(r, z) - c_\phi^\dagger(r) = \frac{1}{rV} \frac{d\gamma_E^\dagger}{dr} \int_{z^\dagger}^z w_r(r, y) dy \dots \dots [23]$$

downstream of the trailing edge, by Equations [19].

7 VELOCITY CORRECTIONS

The problem of finding the meridian velocity components induced by a given distribution of ring vorticity can be solved by classical methods. Equivalent solutions have been given in references (2) and (5). Let

$$U_d(\epsilon_r r) = Y_1(\epsilon_r r_1) J_0(\epsilon_r r) - J_1(\epsilon_r r_1) Y_0(\epsilon_r r)$$

$$U_s(\epsilon_r r) = Y_1(\epsilon_r r_1) J_1(\epsilon_r r) - J_1(\epsilon_r r_1) Y_1(\epsilon_r r)$$

where J_p and Y_p denote the Bessel functions of order p of the first and second kind, respectively, r_1 the hub radius, r_2 the tip radius, and the characteristic values ϵ_n are the positive roots of the equation

$$U_1(\epsilon_n r_2) = 0 \dots \dots \dots [24]$$

Both the Bessel functions and the first 6 roots of Equation [24] are tabulated (8). Then

$$w_r(r, z) = \frac{1}{2} \sum_{n=1}^{\infty} U_d(\epsilon_n r) \int_{-\infty}^{\infty} a_n(\beta) e^{-\epsilon_n(z-\beta)} d\beta \dots [25]$$

$$w_s(r, z) = \frac{1}{2} \sum_{n=1}^{\infty} U_s(\epsilon_n r) \left\{ \int_{-\infty}^z a_n(\beta) e^{-\epsilon_n(z-\beta)} d\beta \right. \\ \left. - \int_z^{\infty} a_n(\beta) e^{-\epsilon_n(\beta-z)} d\beta \right\} \dots [26]$$

with

$$a_n(\beta) = (1/\nu_n^2) \int_{r_1}^{r_2} \xi_\phi(\alpha, \beta) U_1(\epsilon_n \alpha) \alpha d\alpha$$

and

$$\nu_n^2 = \int_{r_1}^{r_2} [U_1(\epsilon_n \alpha)]^2 \alpha d\alpha = \frac{1}{2} \{ [r_2 U_d(\epsilon_n r_2)]^2 - [r_1 U_d(\epsilon_n r_1)]^2 \}$$

These formulas may be interpreted as follows: The axial velocity w_z induced at any point r, z by the total distribution of ring vorticity ξ_ϕ is the sum of the axial velocities induced at r, z by individual disks of ring vorticity of thickness $d\beta$, located at $z = \beta$, and carrying a strength of ring vorticity $\xi_\phi(r, \beta)$ per unit thickness of the disk; and similarly for the radial velocity. The distribution over the radius of the strength of ring vorticity of each disk is analyzed in terms of Fourier-Bessel components, so that

$$\xi_\phi(r, \beta) = \sum_{n=1}^{\infty} a_n(\beta) U_1(\epsilon_n r)$$

in exact analogy to the more common harmonic analysis of a function in terms of Fourier components and its expansion in a Fourier series. Each Fourier-Bessel component induces velocities which are damped exponentially with distance from the disk with a damping factor ϵ_n peculiar to the individual Fourier-Bessel component. The velocity induced by the vorticity disk is the sum of the velocities induced by the individual components.

In view of the approximations introduced for the purpose of determining the ring vorticity in the two preceding sections, it appears unnecessary, at the present stage, to compute the meridian velocities from the exact Equations [25] and [26]. These formulas are, however, useful for the purpose of constructing simpler approximate formulas and of checking the results obtained from those.

How simpler formulas are best constructed depends primarily on the physical setup, and the physical question asked, in any particular case. A useful method would often appear to be first to replace the ring vorticity obtained from Equation [14] by a simpler distribution of ring vorticity, and then to construct simpler, approximate formulas for the purpose of computing the velocities induced by the new distribution of ring vorticity.

As regards the latter point, Marble suggests replacing the damping factors ϵ_n of the individual Fourier-Bessel components by a single, common damping factor, which is to be determined such that the mean square error over the whole field of flow due to the simplification is a minimum; and he describes in detail how this can be done (5).

As regards the first point, Marble suggests replacing the whole blading by a single vortex disk, appropriately located, across which both the angular momentum and the ring vorticity change discontinuously from their distribution over the radius far ahead to that far astern of the blading. This approximation is suitable for the calculation of the velocity field induced by the trailing vorticity, which occupies the portion of space downstream of the trailing edge and is independent of z . However, it is not suitable for the calculation of the velocity field induced by the bound ring vorticity in the blading. For instance, in the absence of trailing vorticity (design for optimum load) this approximation gives $w_r \equiv w_z \equiv 0$, whereas it has been shown in an example (2) that values of w_r and w_z up to 3 and 5 per cent, respectively, of V may arise and lead to an appreciable blade correction.

To construct suitable, simplified distributions of the bound ring vorticity it is useful to consider the constituents which go to make up the ring vorticity in the case of optimum load design. The load distribution at any height z in the rotor may be split in the mean value over the radius γ_1 , and the rest $\gamma_2(r)$, so that $\gamma(r, z) = \gamma_1(z) + \gamma_2(r, z)$, and in practice the first term is the more important one, γ_2 being, at most, locally important (for instance, near the tip). Moreover, the backbone of the blade is usually such that its intersection with some plane ($z = 0$) near the middle of the blade is nearly radial. If it is assumed that $\gamma_2(r, z) = 0$, that the backbone is radial in the middle of the blade, and that the blade extends from $z = -h$ to $z = h$, Equation [14] becomes

$$\xi_\theta = \frac{2}{r^2 V} \left(d\gamma_1/dz \right) \int_0^z \gamma_1(y) dy, \quad (-h < z < h) \quad \dots [27]$$

$$\xi_\theta = 0 \quad (|z| > h)$$

and this may be expected to represent the main part of the bound ring vorticity.

Fig. 2 shows a possible load-distribution function $\gamma_1(z)$ divided

³ For Kaplan turbines, where the choice of a "free-vortex" blading imposes itself.

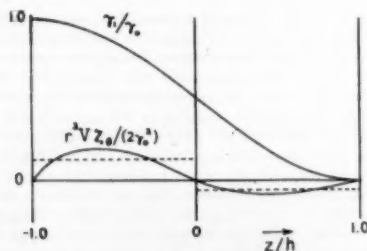


FIG. 2

by the mean angular momentum upstream γ_0 , and the corresponding distribution of $r^2 V \xi_\theta / (2 \gamma_1^2)$ given by Equation [27]. The ring vorticity changes sign at the height in the blade where the backbone is radial. Such a distribution may be approximated, for instance, by a constant distribution with the same total vorticity, for $z < 0$; and similarly for $z > 0$ (dashed in Fig. 2). This approximation is equivalent to three disks (at $z = -h$, $z = 0$, and $z = h$) of discontinuity of the ring vorticity of the same kind as the disk for which formulas for the induced velocity have been given by Marble (5).

Appendix I

The equation of continuity is

$$\partial w_r / \partial r + w_r / r + \partial w_z / \partial z = 0$$

and hence there exists a stream function $\psi(r, z)$ for the meridional components of velocity such that

$$w_r = (1/r) \partial \psi / \partial z, \quad w_z = -(1/r) \partial \psi / \partial r$$

and by Equation [10]

$$\xi_\theta = \partial^2 \psi / \partial r^2 - (1/r) \partial \psi / \partial r + \partial^2 \psi / \partial z^2$$

If ξ_θ vanishes everywhere, the flow in the meridional planes possesses a velocity potential Φ , and $\Phi/z = \text{const}$, if $\partial \Phi / \partial z \rightarrow \text{const}$ for $z \rightarrow \pm \infty$. Hence $w_r \equiv 0$.

If w_r vanishes everywhere, ψ is independent of z . Hence $\xi_\theta \equiv 0$, if it vanishes ahead of the rotor.

Appendix 2

In general, the condition that the blade surface should be the surface of the relative velocity and the absolute vorticity leads to the equation

$$(w \text{ grad}) \left[\frac{\xi_\theta}{r^2 [(V + w_r) \xi_r - w_r \xi_\theta]} \right] = (\xi \text{ grad}) \left[\frac{w_\theta}{r^2 [(V + w_r) \xi_r - w_r \xi_\theta]} \right] \quad [28]$$

connecting the components of velocity and of vorticity (2). If it is assumed that the free vorticity and the bound ring vorticity are small compared with the bound meridional vorticity, so that $\xi_\theta \ll \xi_r$, $w_r \ll V$, $w_\theta \ll V$, the derivatives of these small quantities are also small, and $w_r \partial / \partial r + w_z \partial / \partial z$ may be neglected compared with $V \partial / \partial z$, then Equation [28] becomes, to the first order

$$V \frac{\partial}{\partial z} \left[\xi_\theta / (r^2 V \xi_r) \right] = \left(\xi_r \frac{\partial}{\partial r} + \xi_\theta \frac{\partial}{\partial z} \right) [w_\theta / (r^2 V \xi_r)]$$

Upon integration with respect to z , with partial integration on the right-hand side, this leads to Equation [14], since $\text{div } \xi = 0$.

Appendix 3

REMARKS ON LIMITATIONS OF THE THEORY, AND ITS APPLICATION TO MULTISTAGE AXIAL-FLOW TURBOMACHINES

The assumptions made in the theory presented here are of two kinds. The assumptions discussed in the second section define the role played by the "mean flow theory" within the general theory of Kaplan turbines and pumps. By contrast, the assumption that the velocity corrections w_r and w_z are small compared with the mean velocity is introduced in order to simplify

the mathematical problem of mean flow theory, and it may be worth a brief examination. It is supported by two quite different considerations.

(a) The radial velocity w_r must vanish both on the hub and on the casing, and the axial-velocity correction w_a , as a function of r , for fixed z , must change sign at least once, being defined as a deviation from a mean. Hence both may be expected to be small, if the annulus is narrow.

(b) Since any trailing vorticity downstream of the rotor represents losses, the fact that Kaplan turbines have a high efficiency over a wide range of working conditions suggests that the trailing vorticity is small over a considerable range of working conditions. Moreover, the incident flow does not differ much from one with constant angular momentum, so the rotor blading must be a "free-vortex" blading where γ depends little on the radius, both upstream and downstream of the blade wheel. This suggests a load distribution depending mainly on z , for which the bound ring vorticity changes sign at some station in the rotor (see Equation (27)) and is indeed small, if neither the total load γ_a , nor the local loading $d\gamma_l/dz$, is large. It then follows that the velocity corrections induced by the ring component of both the bound and the trailing vorticity will also be small.

The example given in reference (2) shows that the assumption that w_r and w_a are small compared with V is well founded even for the hub ratios and loads commonly used in Kaplan turbines. However, if the hub ratio is very small; if the total load or the local loading near the leading edge or the trailing edge is large; or if the blade sheds a great deal of vorticity, then the theory may not be expected to predict the mean flow with great accuracy. In any case, it is not designed to treat the extremes of the working range, where the flow separates from the blades.

The theory applies also to multistage axial-flow turbomachines. The mean flow corrections for a stationary-blade wheel are obtained by putting the angular velocity ω equal to zero in the formulas given in the foregoing, and the corrections are then again obtained in the frame of reference with respect to which the blade wheel is at rest. For a multistage machine, the corrections are obtained simply by superposition of those due to the separate stators and rotors; the computation is simplified by the use of Marble's asymptotic expressions (5) for the induced velocities when computing the mutual interference of blade wheels not directly adjacent to one another.

For a multistage machine, however, it is often desirable to employ a blading that is not of the free-vortex type (9, 10). In that case the argument may not apply that has been used to suggest that the bound ring vorticity is small; indeed, the justification (b) may not apply unless the load is light, and the corrections may be predicted less accurately by the theory given here. Moreover, since the flow downstream of the last blade wheel should be free of angular momentum, and since the flow upstream of the first blade wheel is often free of it, it then becomes necessary to provide a first blade wheel designed to convert a free-vortex flow to the type desired in the machine and a last blade wheel designed to reconvert it. That is, these two blade wheels have to be specially designed respectively to shed and absorb a very considerable amount of trailing vorticity (whereas the other blade wheels work in a stream full of free vorticity, but do not contribute much to it), and the corrections due to these

two blade wheels must be anticipated to be predicted less accurately.¹⁰⁾

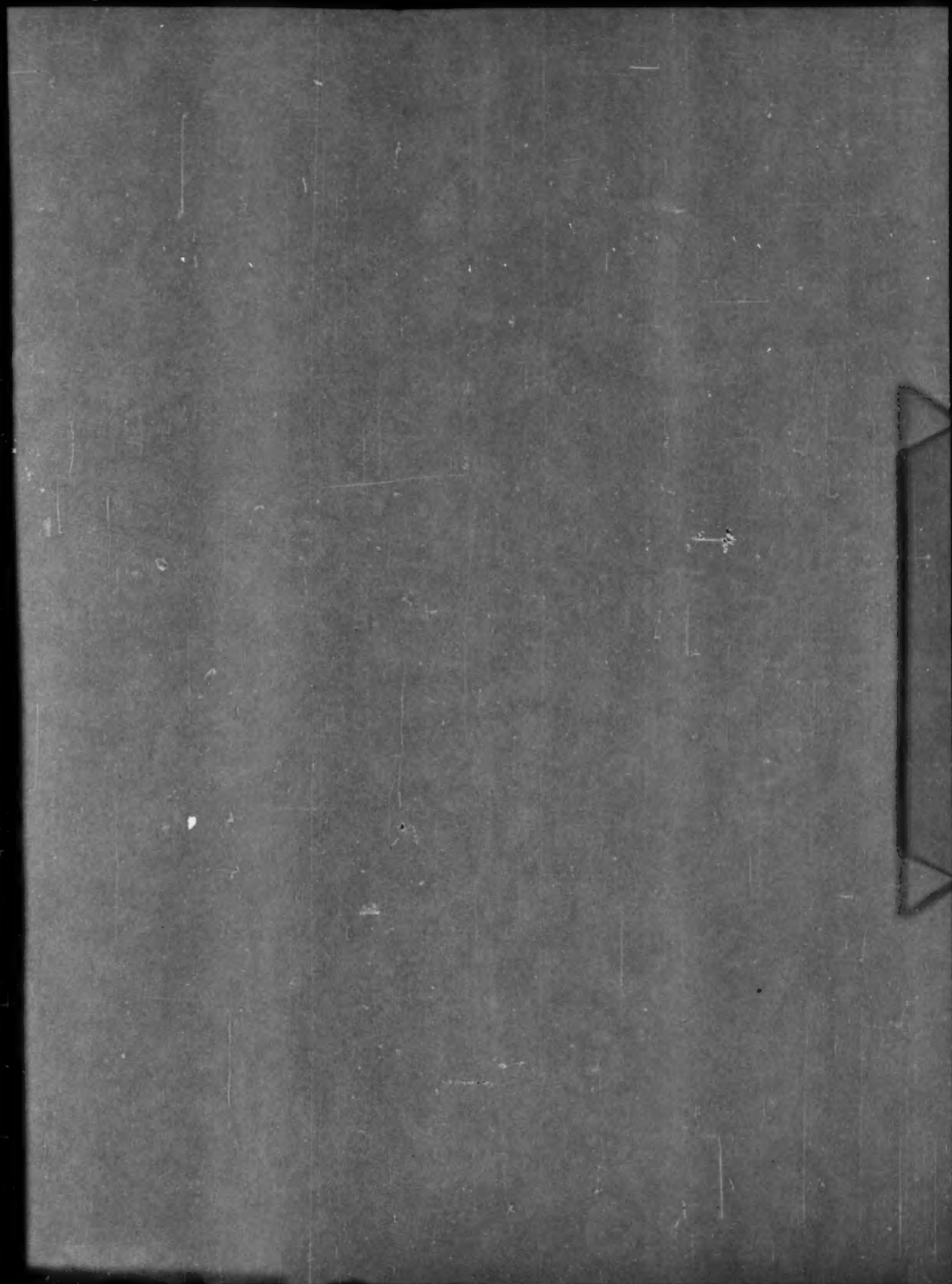
The theory can also be used to investigate a part of the "secondary flow" that is essentially due to viscosity. One of the important effects of viscosity is the existence of large boundary layers on the hub and the casing, already upstream of the blade wheels. In cascade tunnels, for instance, these boundary layers constitute the main effect of viscosity. They can be explored readily, and simulated by a nonuniform distribution of incident velocity represented by suitably chosen functions $V(r)$ and $\gamma_d(r)$. (See section 4; note, however, that the assumption $V(r) \geq V_a > 0$ prohibits excessive realism in simulating such boundary layers. The difficulties that would arise if the boundary conditions for a viscous fluid were applied to the equations of motion for an inviscid fluid are both mathematical and physical). Again, it should be noted that if a blade designed to work in a uniform incident flow is immersed in an incident flow varying strongly in the spanwise direction, then the circulation of the blade sections varies also strongly in the spanwise direction. Therefore a considerable amount of vorticity is shed (which induces a secondary flow), and the justification (b) for the linearizing assumption does not apply.

ACKNOWLEDGMENT

The author would like to thank Prof. S. Goldstein for suggesting this paper, and for his encouragement.

BIBLIOGRAPHY

- 1 "Thin Airfoil Theory and the Application of Analogous Methods to the Design of Kaplan Turbine Blades," by S. P. Hutton, Proceedings of The Institution of Mechanical Engineers, London, England, vol. 163, 1950, pp. 81-97.
- 2 "Beitrag zu Theorie feststehender Schaufelgitter," by Richard Meyer, Eidgenössische Technische Hochschule, Institut für Aerodynamik, Mitteilungen, Nr. 11, Leemann & Company, Zürich, Switzerland, 1946.
- 3 "Theorie und Berechnung der Volutenturbinen und Kreiselpumpen," by H. Lorenz, *Zeitschrift des Vereines deutscher Ingenieure*, vol. 49, 1905, pp. 1670-1675.
- 4 Discussion of reference (3), by W. Bauerfeld, *Zeitschrift des Vereines deutscher Ingenieure*, vol. 49, 1905, pp. 2007-2008.
- 5 "The Flow of a Perfect Fluid Through an Axial Turbo-Machine With Prescribed Blade Loading," by F. E. Marble, *Journal of the Aeronautical Sciences*, vol. 15, 1948, pp. 473-485.
- 6 "A Laminar Theory of the Flow Through a Turbo-Machine," by F. G. Gravalos, Rensselaer Polytechnic Institute, Engineering and Science Series Bulletin No. 62, Troy, N. Y., 1950.
- 7 "Lehrbuch der Hydrodynamik" ("Hydrodynamics"), by Henry von Mises, §§ 5-8 of additions to H. Lamb, second German edition, Teubner, Leipzig, Germany, 1931.
- 8 "Funktionentafeln mit Formeln und Kurven" ("Table of Functions"), by E. Jahnke and F. Emde, second edition, Teubner, Leipzig, Germany, 1933.
- 9 "Application of Radial-Equilibrium Condition to Axial-Flow Compressor and Turbine Design," by C. H. Wu and L. Wolfenstein, NACA Technical Note 1795, 1949.
- 10 "Investigations of Axial-Flow Compressors," by J. T. Bowen, R. H. Sabersky, and W. D. Rannie, Trans. ASME, vol. 73, 1951, pp. 1-15.
- 11 For a blading of hub ratio 0.6 converting a uniform stream free of angular momentum into one of "solid body rotation" the velocity corrections have been worked out numerically by Marble (5), under the assumption that the velocity corrections are small compared with the mean velocity; so for this case quantitative information is available regarding the range over which the assumption may be applied with confidence.



AN ASME PAPER

Its Preparation, Submission and Publication, and Presentation

To a large degree the papers prepared and presented under the ASME sponsorship are evidence by which its professional standing and leadership are judged. It follows, therefore, that to qualify for ASME sponsorship, a paper must not only present suitable subject matter, but it must be well written and conform to recognized standards of good English and literary style.

The pamphlet on "AN ASME PAPER" is designed to aid authors in meeting these requirements and to acquaint them with rules of the Society relating to the preparation and submission of manuscripts and accompanying illustrations. It also includes suggestions for the presentation of papers before Society meetings.

CONTENTS

PREPARATION OF A PAPER—

General Information—Style, Preferred Spelling, Length Limitation, Approvals and Clearances.

Contents of the Paper—Title, Author's Name, Abstract, Body of Paper, Appendixes, Acknowledgments, Bibliographies, Tables, Captions, Photographs, Other Illustrations.

Writing the Paper—Outline Tabulations, Tables, Graphs, Charts for Computation, Drawings, Mathematics, Accuracy, Headings and Numbering, Lantern Slides, Motion Pictures, Typing, Number of Copies.

SUBMISSION AND PUBLICATION OF A PAPER—

Intention to Submit Paper Required in Advance, Meeting Dates, Due Dates for Manuscript, Discussions, Review and Acceptance, Proofs, Advance Copies and Reprints, Discussion and Closure, Publication by Others.

PRESENTATION OF A PAPER—

Time Limit, Addressing Your Audience, Public Address Systems, Use of Slides.

REFERENCES—

References on Writing and Speaking, Engineering Standards.

Price 40¢. No discount allowed. A remittance must accompany all orders for \$5.00 or less. U. S. Postage Stamps are acceptable.

THE AMERICAN SOCIETY OF MECHANICAL ENGINEERS
29 West 39th Street, New York 18, N. Y.